



KIT SCIENTIFIC REPORTS 7650

Proceedings of the 10th IEA International Workshop on Beryllium Technology

September 19 - 21, 2012, Karlsruhe, Germany

P. Vladimirov, J. Reimann (Eds.)

P. Vladimirov, J. Reimann (Eds.)

Proceedings of the 10th IEA International Workshop on Beryllium Technology

September 19-21, 2012, Karlsruhe, Germany

Karlsruhe Institute of Technology
KIT SCIENTIFIC REPORTS 7650

Proceedings of the 10th IEA International Workshop on Beryllium Technology

September 19-21, 2012, Karlsruhe, Germany

by
P. Vladimirov, J. Reimann (Eds.)

Impressum



Karlsruher Institut für Technologie (KIT)
KIT Scientific Publishing
Straße am Forum 2
D-76131 Karlsruhe

KIT Scientific Publishing is a registered trademark of Karlsruhe
Institute of Technology. Reprint using the book cover is not allowed.

www.ksp.kit.edu



*This document – excluding the cover – is licensed under the
Creative Commons Attribution-Share Alike 3.0 DE License
(CC BY-SA 3.0 DE): <http://creativecommons.org/licenses/by-sa/3.0/de/>*



*The cover page is licensed under the Creative Commons
Attribution-No Derivatives 3.0 DE License (CC BY-ND 3.0 DE):
<http://creativecommons.org/licenses/by-nd/3.0/de/>*

Print on Demand 2013

ISSN 1869-9669

Contents

Summary of 10 th IEA International Workshop on Beryllium Technology.....	I
Karlsruhe Institute of Technology (KIT)	
<i>A. Moeslang</i>	1
Beryllide R&D as advanced neutron multiplier for DEMO reactors in Japan <i>M. Nakamichi, K. Yonehara, T. Nishitani</i>	10
Materion: Be supply status <i>K. Smith, K. Smith, L. Ryczek</i>	16
Review of beryllium activities in Russia <i>I. Kupriyanov, G. Nikolaev, R. Giniyatulin, V. Sizinev</i>	55
Development and qualification of beryllium materials for the EU TBM <i>M. Zmitko</i>	66
NRG contribution on the F4E GRT030 Action 3 HIDOBE.01 PIE <i>A.V. Federov, S. van Til, A.J. Magielsen, M. Stijkel, H.L. Cobussen, V.M. Smit-Groen</i>	80
Microstructure characterization of beryllium pebbles irradiated at HFR up to 3000 appm helium production within HIDOBE-01 experiment <i>V. Chakin, R. Rolli, M. Klimenkov, A. Moeslang, P.V. Vladimirov, P. Kurinskiy, H.-C. Schneider, S. van Til, A.J. Magielsen, M. Zmitko</i>	101
Chemical reactivity of irradiated be pebbles under oxidizing atmosphere <i>E. Alves</i>	117
Analysis of tritium retention in beryllium pebbles irradiated in EXOTIC, PBA and HIDOBE-01 experiments <i>A. V. Fedorov, S. van Til, A.J. Magielsen</i>	129
Preliminary results from HIDOBE01 PIE on Russian pellet grades <i>S. van Til, A. V. Fedorov, A.J. Magielsen, M. Stikel</i>	148
Status of material development for lifetime expansion of Be reflectors <i>C. Dorn, K. Tsuchiya, Y. Hatano, P. Charkrov, M. Kodama, H. Kawamura</i>	156
Experimental simulation of beryllium damage under intense transient plasma loads <i>I. Kupriyanov, E. Basaleev, G. Nikolaev, L. Kurbatova, V. Podkovyrov, A. Musichenko, A. Zhitlukhin, L. Khimchenko</i>	172
Tritium behavior in neutron irradiated beryllium pebbles regarding their microstructure <i>E. Pajuste, G. Kizane, A. Vitins, V. Zubkovs, A. Zarins</i>	198
Development of granulation process of beryllide as advanced neutron multiplier for demo reactors in Japan <i>M. Nakamichi</i>	205
Synthesis of beryllides powder for advanced neutron multiplier <i>Y. Natori, J. Suzuki, K. Tatenuma, K. Yonehara, M. Nakamichi</i>	209
Recent progress of irradiation effects study on Be ₁₂ Ti by plasma sintering method <i>T. Shibayama, M. Nakamichi, J.-H. Kim, M. Ando</i>	216

Characteristics of microstructure, swelling and mechanical behavior of titanium beryllide samples after high-dose neutron irradiation at 740 and 873 K <i>P. Kurinskiy, A. Moeslang, V. Chakin, M. Klimenkov, R. Rolli, S. van Til, A. Goraieb</i>	226
Optimization of sintering conditions in plasma sintered beryllide <i>J.-H. Kim, D. Wakai, M. Nakamichi</i>	230
Study on oxidation resistance of titanium beryllide fabricated by spark plasma sintering and surface analysis of the sample exposed to water vapor <i>K. Munakata, K. Wada, Y. Akimoto, H. Takeda, M. Nakamichi, J.-H. Kim, D. Wakai, K. Yonehara</i>	237
Oxidation behavior of beryllium and titanium beryllide fabricated by plasma-sintering method - Direct comparison of oxidation behavior by water vapor <i>K. Munakata, K. Wada, M. Nakamichi, J.-H. Kim, K. Yonehara D. Wakai</i>	245
Oxidation property of plasma sintered beryllide <i>J.-H. Kim, M. Nakamichi</i>	253
First measurements of beryllide vapor pressures <i>J. Reimann, O. Beres, J.-Y. Colle, C. Dorn, H. Harsch, R. Koenigs, P. Kurinskiy</i>	258
Investment casting of Be alloys <i>G. Schuster, C. Pocross</i>	263
Design of a molding process of beryllium and beryllides: from a suspension of metal powder and liquid paraffin to semi-finished parts <i>C. Kräher</i>	275
Beryllium dust explosion experiments <i>P. Humrickhouse, R. Pawelko, L. Moore-McAteer, L. Cadwallader, B. Merrill, M. Jones</i>	285
Anodized coatings for Be and Be-Al alloys <i>G. Schuster, B. Gillenwater</i>	298
Radiation damage in hcp materials: exp. & theory <i>S. Golubov, R. Stoller, A. Barashev</i>	308
Self-interstitial diffusion in beryllium: elementary jumps and overall dynamics <i>V. Borodin, P. Vladimirov</i>	318
Columnar interstitial clusters in Be (and Zr) <i>V. Borodin, M. Gaschenkova, P. Vladimirov</i>	327
Ab initio static and molecular dynamics study of helium behavior in beryllium <i>P. Vladimirov, A. Moeslang</i>	335
Appendix 1: Organisation	344
Appendix 2: BeWS-10 Final Program	346
Appendix 3: List of Attendees	348

Summary of the 10th IEA International Workshop on Beryllium Technology

19-21 September, 2012, Karlsruhe, Germany

The 10th IEA Beryllium Workshop (BeWS-10) was organized by the Karlsruhe Institute of Technology (KIT). The International Organizing Committee (IOC) and all participants expressed their appreciation to the Local Organizing Committee for the truly excellent organization of the workshop at KIT. The participants came mainly from Europe, U.S.A., Russia, Japan, and Kazakhstan. The workshop was supplemented by the BeYOND industrial forum presenting a communication platform for researchers and industry with the aim of bringing the ITER program to life and to prepare a “fast track” for DEMO.

The BeWS-10 was divided into one plenary and five technical sessions. Due to the relatively high number of participants (64), parallel technical sessions had to be organized during the last day. The plenary session delivered a comprehensive overview of the Be-related activities in Europe, U.S.A., RF, and Japan. Of special importance were the reports from the ITER International Organization (IO) and Fusion for Energy (F4E). A separate technical session was devoted to the results of the beryllium irradiation program HIDOBE-01. For the first time, various beryllium grades were irradiated at fusion-relevant temperatures up to approximately one-sixth (1/6) of DEMO expected end-of-life accumulation of helium.

Another highlight was an extensive technical session on beryllide intermetallic compounds where mainly the results of Broader Approach activities were reported. An important breakthrough is a successful fabrication of TiBe₁₂ pebbles at IFERC, Rokkasho, Japan. However, the experimentally obtained two-phase composition should be still optimized in favor of single TiBe₁₂ phase. Important results on oxidation/steam interaction, swelling, and tritium release for beryllides were also delivered. Two sessions were devoted to technology and safety. The modeling session included for the first time presentations related to zirconium as far as Be and Zr are supposed to show certain analogous behavior with respect to their radiation resistance.

The workshop program and the list of participants are attached as appendices.

Following the recommendations of the IOC made at BeWS-9, the BeWS-10 Local Organizing Committee invited key people from the ITER IO and F4E to present their organizations' official views on beryllium activities for fusion applications. Those presentations clearly enhanced the relevance of the technical program.

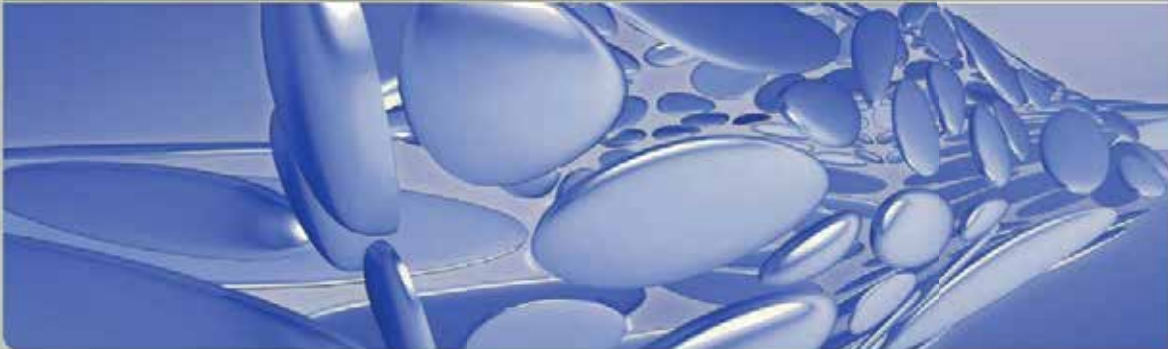
Participation of industry partners was also improved: in addition to Materion Brush Inc. (formerly Brush Wellman Inc.), representatives of IBC Advanced Alloys Corp. (Canada) and Ulba Metallurgical Plant (Kazakhstan) were present. Small business companies were represented by KBHF/GVT (Karlsruhe) and Kompozit JSC (Russia). For the first time, two representatives from CERN, The European Centre for Nuclear Research in Switzerland participated in the BeWS-10.

The following decisions were taken at the IOC meeting on 19.09.2012: Dr. G. Longhurst was awarded an honorary IOC membership for his long-standing activities in the organization of the BeWS series. It was then suggested to pay tribute to the memory of Prof. M. Dalle-Donne (a BeWS founder) by establishing a special review lecture to be given at each future Beryllium Workshop by a distinguished expert.

The current plan is that the next IEA Be Workshop, BeWS-11, will be held in Lisbon, Portugal in September 2013, in conjunction with the ISFNT conference to be held in Barcelona, Spain.

Karlsruhe Institute of Technology (KIT)

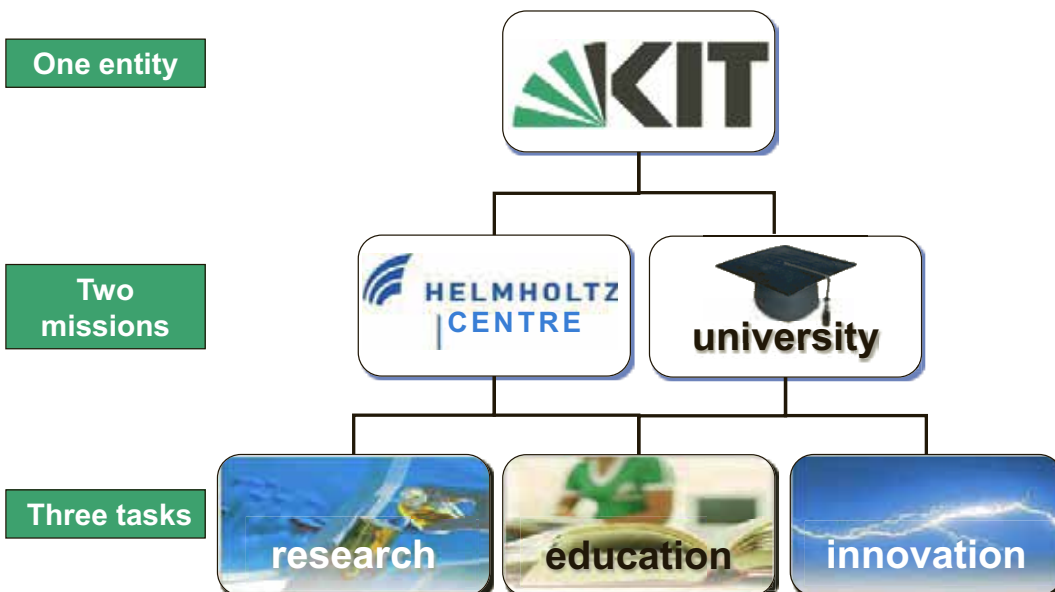
Anton Moeslang – on behalf of the KIT Executive Board and the Institute for Applied Materials



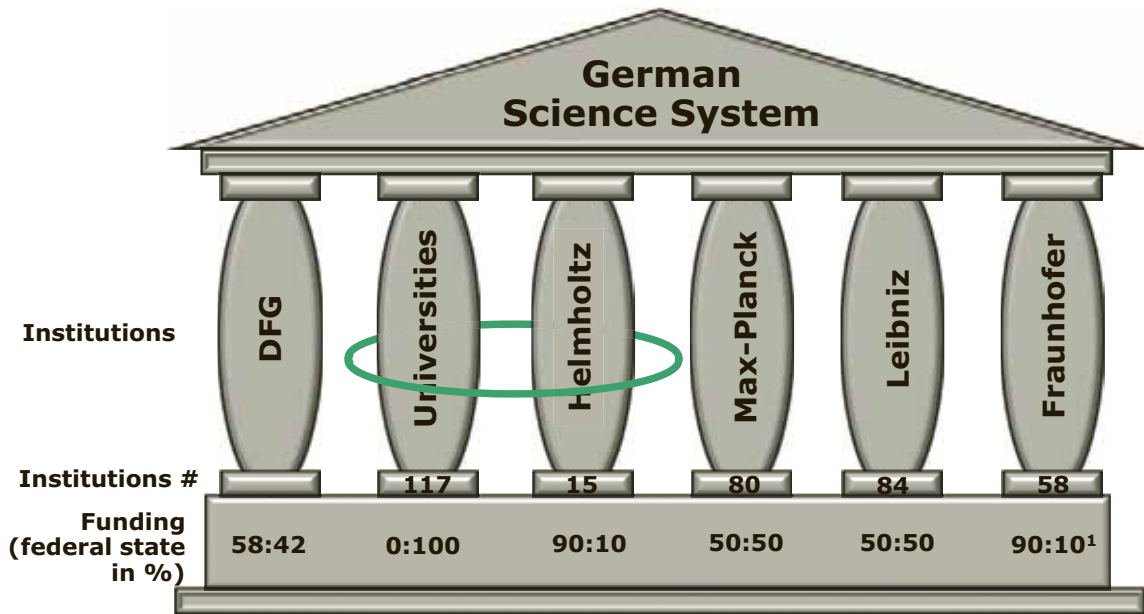
KIT – Universität des Landes Baden-Württemberg und
nationales Forschungszentrum in der Helmholtz-Gemeinschaft

www.kit.edu

KIT – One legal entity, two missions, three tasks



German Science System



(1) Basic public funding only 30 %

KIT - Figures



Campus North



Campus South

<p>Forschungszentrum Karlsruhe GmbH</p> <p>12 programmes</p> <p>3.669 employees</p> <p>351 Mio. € budget</p>	<p>Universität Karlsruhe (TH)</p> <p>11 faculties</p> <p>4.722 employees</p> <p>20.600 students</p> <p>314 Mio. € budget</p>
<p>at large 2200 Ph.D. students</p>	

KIT Large-Scale Research Division



formerly: Research Center Karlsruhe (FZK)

- 1956 Founded as Society for Construction and Operation of Nuclear Reactors
- 1963 Society for Nuclear Research Karlsruhe
- 1978 Nuclear Research Center Karlsruhe GmbH (KfK)
- 1995 Research Center Karlsruhe – Technology and Environment
- 2002 Research Center Karlsruhe – Member of the Helmholtz Association



Programmes:

- Atmosphere und Climate
- Renewable Energies
- Conversion of Energy
- Fusion
- Nuclear Safety
- Technology, Innovation & Society
- Nano- and Microsystems
- BioInterfaces
- Scientific Computing
- Grid Computing
- Synchrotron Source ANKA
- Astroparticle Physics

5

A. Moeslang 10th IEA International Workshop on Beryllium Technology; September 19-21 2012, Karlsruhe, Germany

KIT University Division



formerly: University of Karlsruhe (TH)

- 1825 Founded as Polytechnical School similar to the Ecole Polytechnique in Paris
- 1885 Technical College
- 1902 Additional name „Fridericana“ in honor of the grand duke Friedrich von Baden
- 1967 University of Karlsruhe (TH)
- 2005 Supplemental name: „Forschungsuniversität · founded in 1825“



- Mathematics
- Physics
- Chemistry and Biology
- Humanities and Social Sciences
- Architecture
- Civil Engineering, Geo- & Environmental Sciences
- Mechanical Engineering
- Chemical and Process Engineering
- Electrotechnical Engineering & Information Techn.
- Computer Sciences
- Economics and Business Engineering

6

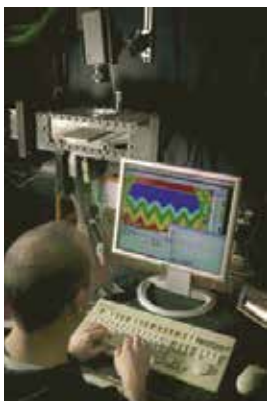
A. Moeslang 10th IEA International Workshop on Beryllium Technology; September 19-21 2012, Karlsruhe, Germany



Strong engagement of Materials Science and Technology

- Simulation and Modeling / HPC Energy
- Measuring Techniques & Diagnostics
- Research infrastructure

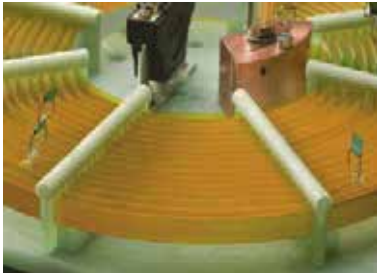
Topic 1: Energy Conversion



- Thermo-Chemical Energy Conversion
- Electro-Chemical Energy Conversion
- Synthetic Fuels
- Heat Transfer and Cooling
- Materials
- Energy Conversion Systems
- CCS

- Modelling and Simulation
- Advanced Instrumentation

Topic 3: Energy Storage and Distribution



- Superconducting Components
- Grid Equipment and Components
- Smart Grids
- Virtual Power Plants
- Battery Storages
- Hydrogen Based Energy Storage

Topic 5: Fusion Technology



- **Fusion Research**
 - Cryogenic test facility TOSKA
 - Tritium laboratory
- **Fusion Technology**
 - Components development
 - superconducting magnet coils
 - gyrotrons
 - blankets
 - divertors
 - materials incl. beryllium
- **Large Fusion Projects**
 - ITER, DEMO, IFMIF, W7X

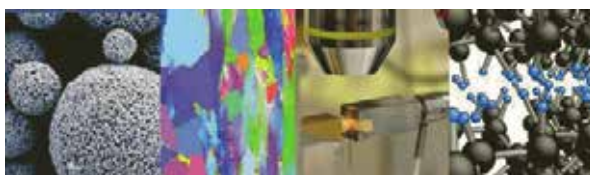
Topic 6: Nuclear Energy and Safety



- Safety of Nuclear Reactors
- Nuclear Waste Disposal
- Radiation Protection
- Nuclear Decommissioning Technologies



Institute for Applied Materials (IAM)

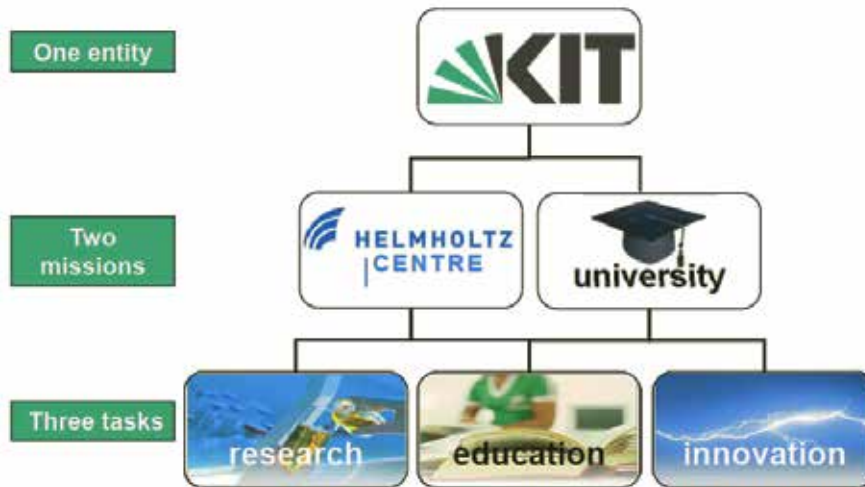


Spokesman:
Prof. Dr. rer. nat. Oliver Kraft

- ❖ IAM – AWP Applied Materials Physics
- ❖ IAM – KM Ceramics for Mechanical Engineering
- ❖ IAM – WBT Materials Process Technology
- ❖ IAM – WK Materials Science and Engineering
- ❖ IAM – WBM Materials and Biomechanics
- ❖ IAM – ZBS Reliability of Components and Systems
- ❖ IAM – ESS Energy Storage Systems

The IAM consists of more than 10 Professors and more an 300 employees, implemented mostly in the Faculty for Mechanical Engineering and/or the governmental Helmholtz Programs

KIT – One legal entity, two missions, three tasks within attractive international partnership



IEA Workshop Series on Beryllium



- 1988: Initiation of the workshop series
- 1993: 1st workshop under IEA sponsorship
- 2012: 10th workshop under IEA sponsorship



International Participation



Beryllide R&D as Advanced Neutron Multiplier for DEMO Reactors in Japan

Masaru Nakamichi, Kazuo Yonehara and Takeo Nishitani

*Fusion Research and Development Directorate, Japan Atomic Energy Agency,
2-166, Omotedate, Obuchi, Rokkasho, Kamikita, Aomori, 039-3212, Japan*

Abstract

Advanced neutron multipliers with lower swelling and higher stability at high temperature are desired in pebble bed blankets, which will give big impact on the DEMO design such as the blanket operating temperature. Beryllium intermetallic compounds (beryllides) such as Be_{12}Ti are the most promising advanced neutron multipliers. However, synthesis and granulation of beryllide is very difficult because it is too brittle. Therefore, the establishment of the fabrication technique for beryllide is a key issue of the advanced neutron multiplier development. Development of advanced neutron multiplier has been started between Japan and the EU in the DEMO R&D of the International Fusion Energy Research Centre (IFERC) project as a part of the Broader Approach (BA) activities. In Japan, beryllide fabrication R&D is being carried out in the Beryllium Handling Room that has been installed in the DEMO R&D Building at IFERC in the Rokkasho BA site. In this facility, synthesis, treatment, machining and characterization of beryllide are performing. Recently, synthesis and granulation of beryllide have succeeded in this facility.

1. Introduction

In parallel to the ITER program, Broader Approach (BA) activities are being implemented by the EU and Japan, aiming at early realization of the fusion energy [1]. The BA activities comprise the International Fusion Energy Research Center (IFERC) [2], the International Fusion Materials Irradiation Facility-Engineering Validation and Engineering Design Activities (IFMIF-EVEDA) [3], and the Satellite Tokamak [4]. IFERC consists of three sub-projects; a fusion demonstration reactor (DEMO) Design and R&D Coordination Center, a Computational Simulation Center, and an ITER Remote Experimentation Center. The IFERC and IFMIF/EVEDA projects are carried out mainly at Rokkasho BA site of the Japan Atomic Energy Agency (JAEA), and the Satellite Tokamak project is at Naka site of JAEA. The construction of the Rokkasho BA site was completed at March 2010 as shown in Fig.1.

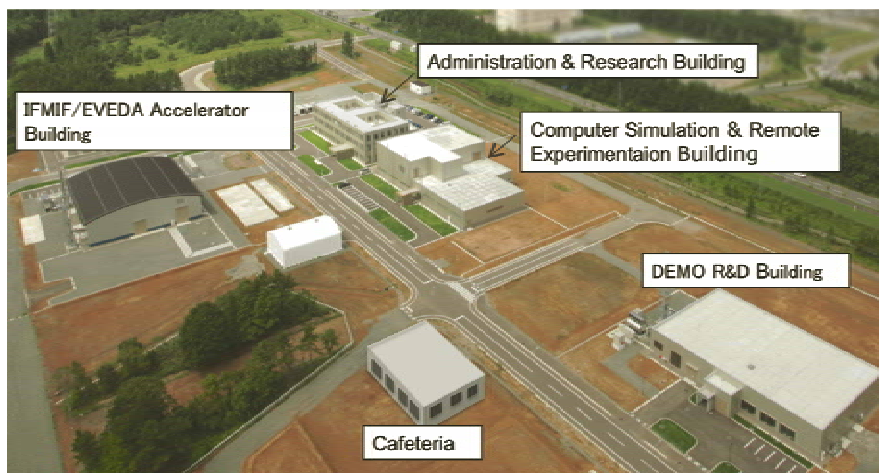


Fig.1 Bird's eye view of the Rokkasho BA site.

Based on the common interests of the EU and Japan in DEMO, R&D on beryllium intermetallic compounds (beryllides) as advanced neutron multiplier [5-6], lithium-containing ceramics as advanced tritium breeder [7], reduced activation ferritic/martensitic (RAFMs) steels as structural material [8], SiCf/SiC composites as a flow channel insert material and/or alternative structural material [9], and tritium technology relevant to the DEMO operational condition are carried out through the BA DEMO R&D program [10].

In the Rokkasho BA site, the DEMO R&D Building with research equipment was completed by March 2011 (see Fig.2). Beryllium handling equipment, a tritium handling glove box, major material analysis apparatuses such as an electron probe micro analyzer (EPMA), a transmission electron microscope (TEM), a scanning electron microscope (SEM), a focused ion beam (FIB), a X-ray diffraction analyzer (XRD) and an inductively coupled plasma mass spectrometer (ICP-MS) have been installed. The Radio-isotope (RI) handling equipment at the Rokkasho BA site is the first and quite unique facility in Japan, where tritium, beta and gamma RI species, and beryllium can simultaneously be used. We obtained the license of the tritium handling with usage amount of 7.4 TBq/day and 29.6 TBq/year, and storage amount of 7.4 TBq. The experiments with tritium and activated specimens started in May 2012.

This paper describes the installation of the Beryllium Handling Room and the recent progresses of R&D on beryllides as advanced neutron multipliers in the IFERC project carried out in the Rokkasho BA site.

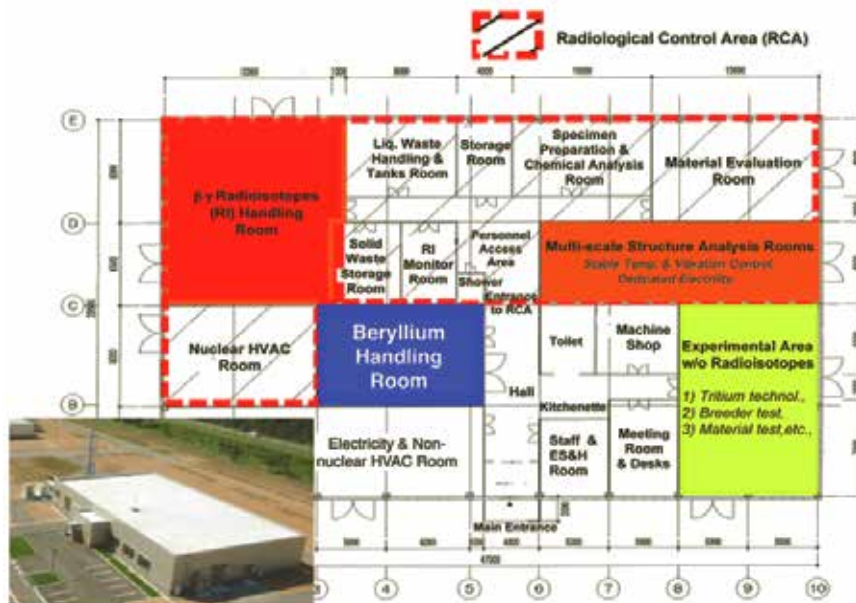


Fig.2 Schematic drawing of the DEMO R&D Building.

2. Beryllium Handling Room

Beryllium and its alloys (> 3 wt.% Be) are defined as specified chemical substances in Japan. Beryllium safety handling is provided in detail in the ordinance on prevention of hazards due to specified chemical substances based on the industrial safety and health act. The administrative government agency is the ministry of health, labour and welfare. Regulating requirement level is different between purpose for manufacturing and that for experimentation and research. The major regulatory requirement compared with purposes is shown in Table 1. Because this purpose of the installation of the Beryllium Handling Room is for experimentation and research, the notification to the regulatory agency is necessary due to a hazardous chemical property of beryllium without manufacturing license.

Table 1 Major regulatory requirement compared with purposes.

Items	Purpose	Manufacturing	Experimentation and research
Manufacturing license		Necessity	Un-necessity ^{*1}
Maximum concentration of Be (<0.002mg/m ³)		Necessity	Necessity
Local exhaust ventilation system		Necessity	Un-necessity ^{*2}
Appointment of operations chief		Necessity	Un-necessity
Establishment of work procedure		Necessity	Un-necessity
Periodical voluntary inspection of machines		Necessity	Un-necessity
Medical examination		Necessity	Necessity

*1: Notification of ventilation system is necessary to regulatory agency without the manufacturing license.

*2: Sealed structure or local exhaust ventilation system is required.

The partitions of the Beryllium Handling Room and the local exhaust ventilations are shown in Figs. 3 and 4, respectively. The room consisted of a beryllium handling area, an exhaust system room and an entrance area. The apparatuses in the beryllium handling area were connected to the exhaust blower of the local ventilation system through the pre-filter and the HEPA filter. The maximum concentration of beryllium was limited to <0.002 mg/m³. The pressure drop and static pressure estimated using the local exhaust ventilation schematics and the controlled air velocity (1 m/s) of the handling port in the hoods were used to decide the specifications of the exhaust blower.



Fig.3 Partitions in the Beryllium Handling Room.

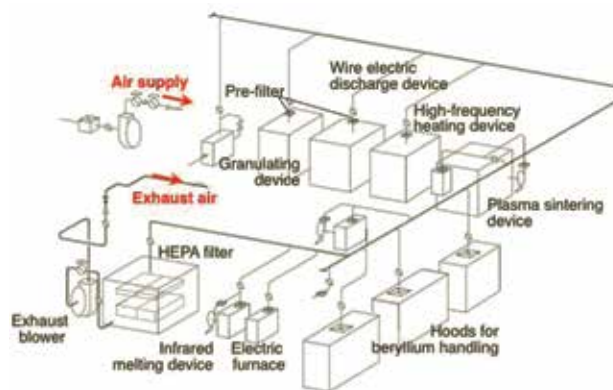


Fig.4 Schematics of the local exhaust ventilation system.



a) Plasma sintering device

b) Beryllium handling worker

Fig.5 Plasma sintering device and workers handling beryllium with personal protective.

Figure 5 shows the plasma sintering device and a worker with personal protective wear handling beryllium. The protective wear included a Tyvek suit, impervious gloves, protective mask and shoes to prevent exposure to beryllium.

3. Beryllide R&D

Metal beryllium (Be) pebbles are the neutron multiplier in test blanket modules for ITER [11]. However, Be pebbles may not be suitable for the DEMO blanket due to swelling and stability issues with water steam [12]. Thus, beryllium intermetallic compounds (beryllides) have become promising materials for advanced neutron multipliers [5-6]. Establishing the fabrication technique for beryllides is a key issue in developing advanced neutron multipliers.

Beryllide synthesis were carried out through plasma sintering, a non-conventional consolidation process. The flow diagram of the plasma sintering method is shown in Fig.6. The plasma sintering process consisted of plasma generation, resistance heating and pressure application [13-15]. The plasma discharge results in particle surface activation that enhances sinterability and reduces high temperature exposure. Pressure application assists the densification process by enhancing sintering and thus further reducing the high temperature exposure of the consolidating powders. Although hot isostatic pressing (HIP) and arc-melting methods have been proposed for beryllide synthesis, the plasma sintering method has the advantages of being a simple process with a lower impurity level in the products, as compared with existing methods.

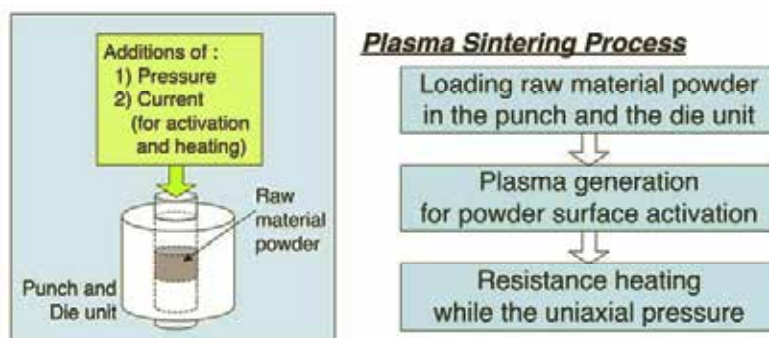


Fig.6 The outline of the plasma sintering method

Synthesis of intermetallic compounds starts with mixed elemental powder particles. In this process, the starting powder is loaded into the punch and die unit, and biaxial pressure is applied for cold

compaction. An electric current is applied to create the plasma environment and thus activate the particle surfaces. The powder compact is resistance heated while uniaxial pressure is still applied to the material in the sintering mold. Synthesis of Be-Ti intermetallic was carried out using mixed Be and Ti powders by the plasma sintering method. The effects of sintering temperature on beryllide consolidation was evaluated. Sintering temperatures used in the experiment were 1073, 1173 and 1273 K. Heating and cooling rates were 100 and 30 K/min, respectively. This preliminary fabrication test of beryllide started with elemental powders. Beryllium powder with 99.9 wt.% purity from RARE METALLIC Co. Ltd. and titanium powder with 99.9 wt.% purity from KOJUNDO CHEMICAL LABORATORY Co. Ltd. were mixed for 30 min using pestle and mortar. The mixed powder composition was 92.3 at.% Be and 7.7 at.% Ti. This ratio is stoichiometric value of Be_{12}Ti composition.

The effects of sintering temperature on beryllide consolidation was evaluated by X-ray diffraction (XRD) and microstructural analysis [6]. The formation of Be_{12}Ti , $\text{Be}_{17}\text{Ti}_2$ and Be_2Ti intermetallics was identified for each temperature from the result of XRD analysis. The area of each element or composition at each sintering temperature was determined in the cross-section micrographs from the results of an Electron Probe Micro Analyzer (EPMA) (see Fig.7). The elemental content of Be and Ti in the plasma sintered material decreased by consolidation enhancement with increasing sintering temperature, with only about 2 % of the elemental phases remaining in 98 % beryllides such as Be_{12}Ti , $\text{Be}_{17}\text{Ti}_2$ and Be_2Ti intermetallics for 1273 K processing. In particular, the area fraction of Be_{12}Ti that is target composition was reached about 90%. This experiments show that the intermetallic compound beryllide can be directly synthesized by the plasma sintering method from mixed elemental powders of Be and Ti at a temperature lower than the melting point.

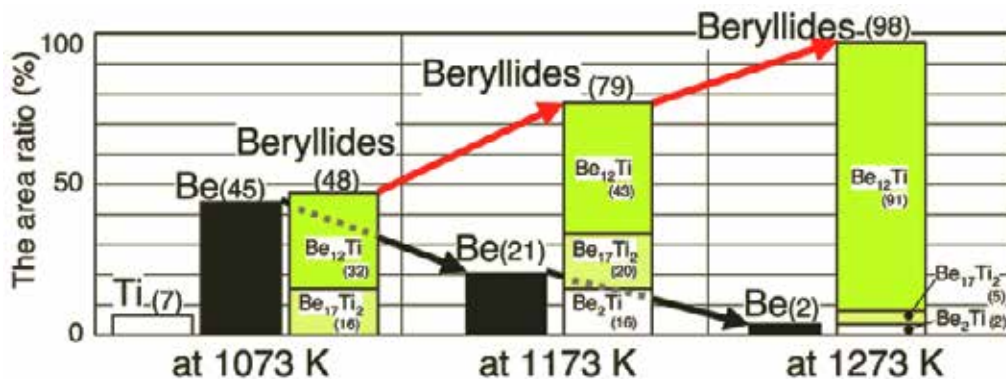


Fig.7 Result of area comparison of each element and composition of Be-Ti intermetallic with sintering temperature by EPMA analysis [6].

In order to fabricate the beryllide pebbles, beryllide with shapes of block and/or rod is necessary when a melting granulation process is applied such as a rotating electrode method. A plasma sintering method has been proposed as new joint technique of beryllide. It was clarified that the beryllide could be simultaneously synthesized and jointed by the plasma sintering method in the insert material region between two beryllide blocks. Beryllide rod of Be_{12}Ti with 10 mm in diameter and 60 mm in length has been successfully fabricated by the plasma sintering method. Using this plasma-sintered beryllide rod, prototype pebble of beryllide was performed by a rotating electrode method as one of the melting methods. The prototype pebbles of Be_{12}Ti with 1 mm in average diameter were successfully fabricated. These recent results concerning joint and granulation of beryllide will be presented and published in this BeWS-10 [16] in detail.

4. Conclusion

Beryllides are the most promising advanced neutron multipliers. The establishment of the fabrication technique for beryllides is a key issue of the advanced neutron multiplier development. In this study, it was reported on the status of beryllide development in Japan.

The Beryllium Handling Room was constructed at the Rokkasho BA site for the R&D of beryllides. Beryllide fabrication trials showed that Be-Ti intermetallic beryllide could be synthesized using the plasma sintering method from mixed elemental powders at a temperature lower than the melting point. The plasma discharge activated the particle surfaces, enhanced sinterability and reduced high temperature exposure. The applied pressure assisted the densification process and further enhanced sintering; this reduced the surface exposure of the consolidated powders at high temperature.

References

- [1] S. Matsuda, *Fusion Engineering and Design* 82 (2007) 435-442.
- [2] M. Araki, Y. Sakamoto, K. Hayashi, R. Ohuchi, T. Nishitani, *Fusion Engineering and Design* 85 (2010) 2196-2202.
- [3] P. Garin, M. Sugimoto, IFMIF/EVEDA Integrated Team, *Fusion Science and Technology* 62 (2012) 219-225.
- [4] T. Fujita, H. Tamai, M. Matsukawa, G. Kurita, J. Bialek, N. Aiba, K. Tsuchiya, S. Sakurai, Y. Suzuki, K. Hamamatsu, N. Hayashi, N. Oyama, T. Suzuki, G.A. Navratil, Y. Kamada, Y. Miura, Y. Takase, D. Campbell, J. Pamela, F. Romanelli, M. Kikuchi, *Nuclear Fusion* 47 (2007) 1512-1523.
- [5] M. Nakamichi, K. Yonehara, *Journal of Nuclear Material*, 417 (2011) 765-768.
- [6] M. Nakamichi, K. Yonehara, D. Wakai, *Fusion Engineering and Design* 86 (2011) 2262-2264.
- [7] T. Hoshino, M. Nakamichi, *Fusion Engineering and Design* (in press).
- [8] H. Tanigawa, T. Hirose, K. Shiba, R. Kasada, E. Wakai, H. Serizawa, Y. Kawahito, S. Jitsukawa, A. Kimura, Y. Kohno, A. Kohyama, S. Katayama, H. Mori, K. Nishimoto, R.L. Klueh, M.A. Sokolov, R.E. Stoller, S.J. Zinkle, *Fusion Engineering and Design* 83 (2008) 1471-1476.A
- [9] T. Nozawa, T. Hinoki, A. Hasegawa, A. Kohyama, Y. Katoh, L.L. Snead, C.H. Henager Jr., *Journal of Nuclear Materials* 386-388 (2009) 622-627.
- [10] T. Nishitani, H. Tanigawa, S. Jitsukawa, T. Nozawa, K. Hayashi, T. Yamanishi, K. Tsuchiya, A., Möslang, N. Baluc, A. Pizzuto, E. R. Hodgson, R. Laesser, M Gasparotto, A. Kohyama, R. Kasada, T. Shikama, H. Takatsu, M. Araki, *Journal of Nuclear Materials* 386-388 (2009) 405-410.
- [11] F. Scaffidi-Argentina, G. R. Longhurst, V. Shestakov and H. Kawamura, *Fusion Engineering and Design* 51-52 (2000) 23.
- [12] R. A. Anderl, et al., *Journal of Nuclear Materials*, 258-263 (1998) 750-756.
- [13] M. Wada and F. Yamashita, New method of making Nb-Fe-Co-B full dense magnet, *Magnetics, IEEE Transactions*, 26 (5), (1990) 2601-2603.
- [14] J. R. Graza, S. H. Risbud and K. Yamazaki, Plasma activated sintering of additive-free AlN powders to near-theoretical density in 5 minutes, *Journal of Materials Research*, 7 (10), (1992) 2643-2645.
- [15] T. Abe and K. Hashimoto, PSZ/Ti functional gradient material by sintering, *FGMnews-015-010*, (1991) 21-25 (in Japanese).
- [16] M. Nakamichi, to be published in BeWS-10.



MATERION



MATERION BERYLLIUM SUPPLY STATUS

Mr. Keith Smith VP Operations & Technology
Mr. Lawrence Ryczek VP Sales & Marketing
MATERION – Brush Beryllium & Composites
Elmore, Ohio USA

BeWS-10 September 2012



- MATERION Overview
- Materion Brush Beryllium & Composites
- Products and Services
- Sustainable Beryllium Supply – New Primary Beryllium Facility

- Appendix:
 - *Upgrading of S-65 Be Specification for ITER First Wall* by Aaron Sayer, Materion, 2011.
 - Materion Markets Overview

You may have known us as:



BRUSHINTERNATIONAL



We are now:



MATERION



- An Advanced Material Company
 - Lighter, stronger, faster, smaller, reliable
- Strong Global Positions in Attractive and Growing Markets
- Solid Record of Long-term Growth
- Strong Value Added* Margins
- Market Cap: \$410 Million
- Annual Sales: \$1.4 Billion (Forecast 2012)
- Strong Balance Sheet: Debt/Debt + Equity <23%
- EBITDA**: \$90-95 Million (Forecast 2012)

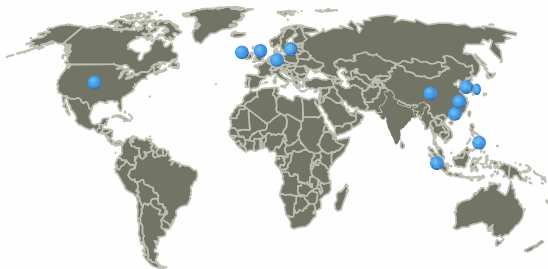
* Excludes metal pass-through

** Earnings before interest, taxes, depreciation and amortization

5

A Global Platform

Operations in US and 11 Countries



- Customers in >50 countries
- Expanded presence in Asia

Significant International Sales* Q2 2012



*Percentage of value added sales

6

Identify High Growth Secular Markets



Market	Q2 2012 % of Value-added Sales	Trends	Key Drivers
Consumer Electronics	26%		<ul style="list-style-type: none"> Smartphone growth Tablet computers & LEDs Miniaturization
Industrial Components & Commercial Aerospace	19%		<ul style="list-style-type: none"> New airplane builds & retrofits Increasing air travel Heavy equipment builds
Defense & Science	11%		<ul style="list-style-type: none"> DoD & foreign military budgets Demand for communications satellites High performance optical devices
Automotive Electronics	10%		<ul style="list-style-type: none"> Increasing global car production HEV/EV lithium ion battery components Engine control & electronic systems
Energy	8%		<ul style="list-style-type: none"> Directional drilling Nuclear Solar, batteries & smart grid devices
Medical	8%		<ul style="list-style-type: none"> Glucose testing Blood analysis test coating for medical diagnosis Diagnostics equipment
Telecommunications Infrastructure	6%		<ul style="list-style-type: none"> Global 3G/4G builds Base stations Undersea fiber-optics expansion

7

Unique Global Positions – Advanced Materials



		Leading Global Position
	<ul style="list-style-type: none"> Only Fully Integrated Producer of Beryllium and Beryllium Alloys in the World <ul style="list-style-type: none"> Over 75 years of reserves at Utah 	<input checked="" type="checkbox"/>
	<ul style="list-style-type: none"> Precision Optical Coatings – Visible to Infrared Bandwidth <ul style="list-style-type: none"> “Go To” Supplier for defense, thermal imaging, space and medical applications 	<input checked="" type="checkbox"/>
	<ul style="list-style-type: none"> High Purity Gold Products for Semiconductor Fabrication (Wireless & LED) <ul style="list-style-type: none"> Offering “full metal management” capabilities 	<input checked="" type="checkbox"/>
	<ul style="list-style-type: none"> Unique Copper-Nickel-Tin Material ToughMet® <ul style="list-style-type: none"> Multiple advanced applications growing at over 30% annually 	<input checked="" type="checkbox"/>
	<ul style="list-style-type: none"> Blood Analysis Test Coatings for Medical Diagnosis 	<input checked="" type="checkbox"/>

8

Successful Repositioning – Snapshot

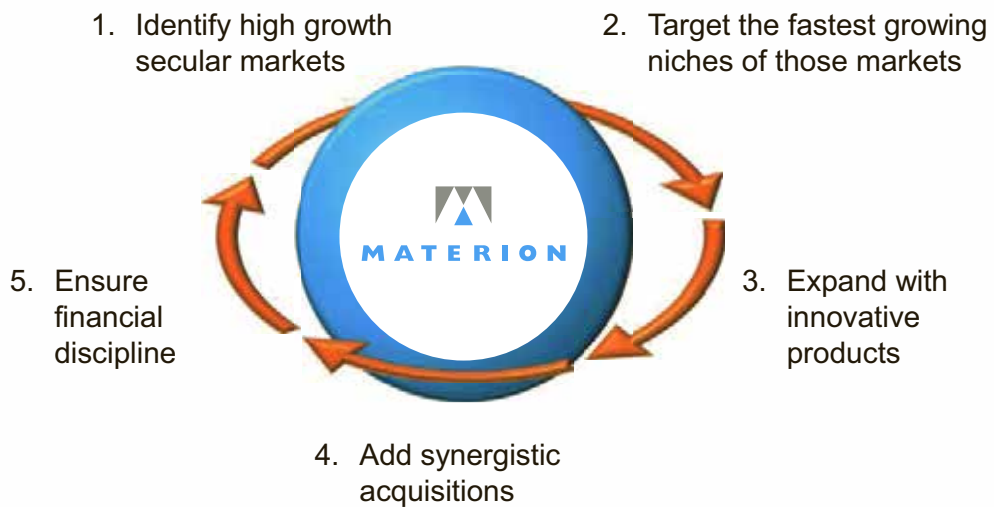


	2002		2011
Revenue	\$373M	→	\$1.5B
Revenue % in Advanced Materials	47%	→	76%
Debt-to-Debt-Plus-Equity	43%	→	17%
Working capital * % of sales	41%	→	23%
Cyclicality	High	→	Lower
Growth	Low	→	Higher

* A/R, Inventory & A/P

9

High Value-Added Business Model



10

A Strong Record of Synergistic Acquisitions



Acquisitions 2005 - 2012	Add complementary products / technology	Impact	
		Expand market position	Accretive in year 1
OMC – shield kit cleaning – 2005	✓	✓	✓
TFT – thin film coatings – 2005	✓	✓	✓
CERAC – inorganic chemicals – 2006	✓	✓	✓
Techni-Met – thin film coatings – 2008	✓	✓	✓
Barr – thin film coatings– 2009	✓	✓	✓
Academy – precious metals – 2010	✓	✓	✓
EIS Optics – thin film coatings – 2011	✓	✓	TBD
AMC – metal matrix composites – 2012	✓	✓	TBD

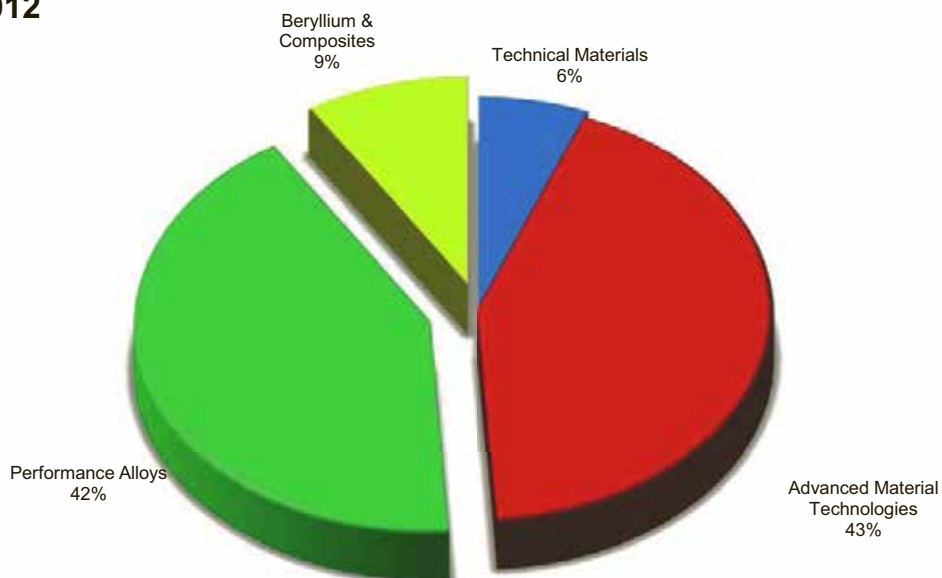
Added over \$440M to sales and approximately 30% of company profit in 2011

11

Value Added Sales: By Segment

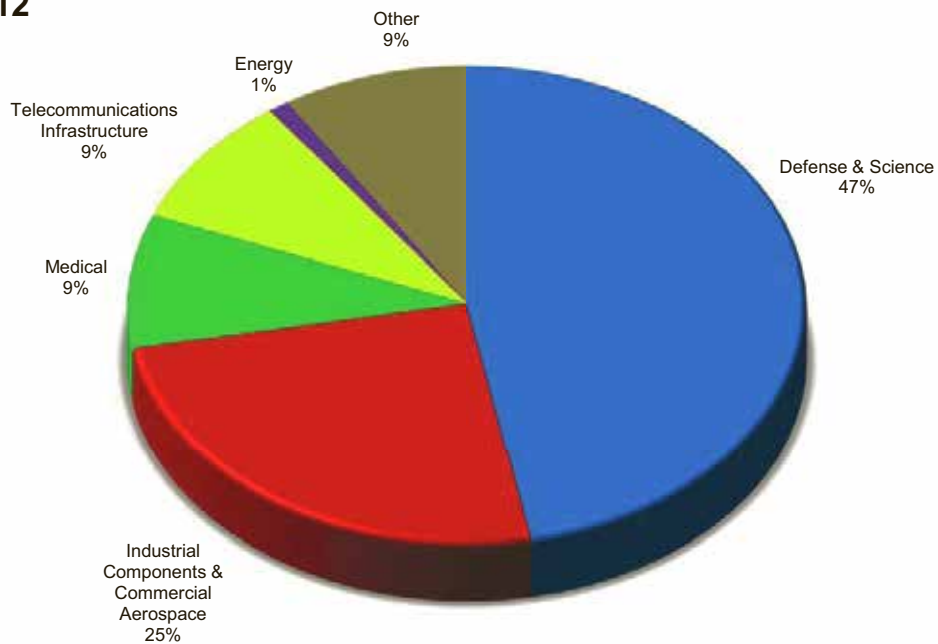


Q2 2012



A-3

Q2 2012



A-6

Continually Develop Innovative Products

- Leveraging customer-centric product development
- Active research programs to take advantage of secular trends
- Key product areas include
 - LEDs
 - Medical
 - Commercial Optics
 - Computer Hard Drives
 - Energy
 - Science
 - Commercial Aerospace
 - Hybrid & Electric Vehicles
 - Wireless



14

1. High Purity Gold and Silver for Industrial Applications
2. Powder Science and Processing (Vacuum, Hot and Cold Isostatic Pressing) ... Metal and Chemical
3. Full Metal Processing Technology (Melting, Casting, Rolling, Extrusion)
4. Selective Electroplating
5. Light Wave Management and Coating Technology
6. Thin Film Large Area Coating
7. Numerous “Specialties” ... Cladding, Electron Beam Welding, Diffusion Bonding
8. Shield Kit Cleaning
9. Chemical Synthesis
10. Amorphous Metals

A-8

Beryllium and Composites

- Nearer net shape fabrication (hot isostatic pressing)
- Truextent™ speaker diaphragms
- Investment Casting
- Amorphous Metals
- SupremEX™ Aluminum Metal Matrix Composites
- Low cost BeO
- Advanced Beryllium processing methods.

Performance Alloys

- ToughMet® Alloy for High Volume Bearing Applications
- BrushForm 158 for Voice Coil Motor (VCM) applications
- Materion R270 Strip
- “Next Generation” Alloy for Oil & Gas

Technical Materials

- Hybrid & Electric Vehicle Battery Components
- Power Electronics
- Smart Grid Meters
- Computer Hard Drives (Dual Stage Activation)
- Medical Applications

A-17

Advanced Material Technologies

Materials

- Optics Coating Materials and Large Format Components
- Thin Film Electrodes (medical diagnostics)
- Expanded refining/chamber services – Complement to Thin Film Materials & Coating businesses
- Nanotechnology Materials
- Materials for High Brightness LEDs
- Specialty Inorganic Compounds (Solar, Security)
- Precious Metal Materials – rod, bar, sheet, slugs, etc.
- Global Refining and Metal Recovery and Management Services
- Ultra high purity Precious Metals for medical and semiconductor applications
- Next generation magnetic data storage thin film head materials

A-15

Advanced Material Technologies

Coatings

- Precision Optical Thin Film Coatings (specialty filters)
- Large format Thin Film Materials for large area coatings (Energy, Solar)
- Solar Panel Thin Film, Concentrator Materials and Barrier Film Coatings

Packaging

- Optical package for New Photonics applications
- RF packages for the latest transistor technology (3G and 4G infrastructure)
- MEMS and Photovoltaic Packaging Materials

A-16

World Leader in Beryllium Containing Materials

- **Fully Integrated Beryllium Materials Supplier**
(mine – manufacture – sales – distribution - technical support)
- Over 1000 Employees at 10 Locations
- Manufacturing:
 - Delta, UT; Elmore, OH; Lorain, OH; Reading, PA , Freemont, CA, Tucson, AZ
- The Elmore plant is the company's largest.
- Sales are 50% outside North America and Growing

19

Delta Facility



Statistics

- 73 employees - 43 hourly
- 1,250 hectares (3,080 acres) -Mill
- 3,000 hectares (7,400 acres) -Mine
- 9,300 m² (100,000 ft²) of building space
- 5th largest private sector employer in Millard Co.
- Facility established in 1968-69 production began in Sept. 1969 (mine land purchases began earlier in the 60's)

Delta Mine Operations



Delta Mill Operations

Wet
Grind



CCD



Leach



Solvent Extraction



Delta Mill Operations

Beryl Ore



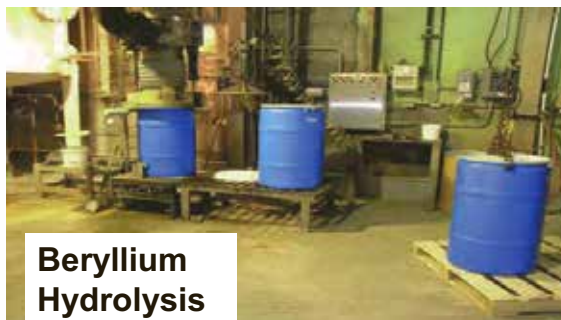
Beryl Plant



Beryl Furnace



Beryllium
Hydrolysis





25

Elmore Facility – Statistics

- 640 employees
- 180 hectares (439 acres)
- 93,000 m² (1,000,000 ft²) of building space
- Second largest private sector employer in Ottawa County

26

Major Product Forms - Alloy



- Strip
- Rod
- Wire
- Plate
- Bar
- Tube
- Billet
- Casting Alloys
- Machined Parts



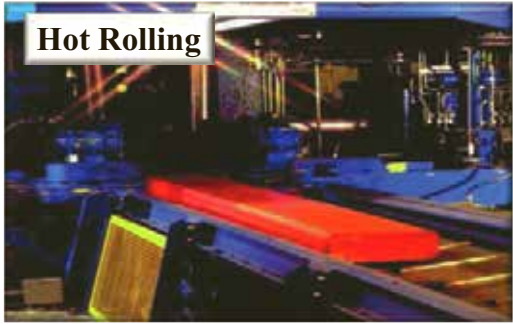
27

Primary Operations

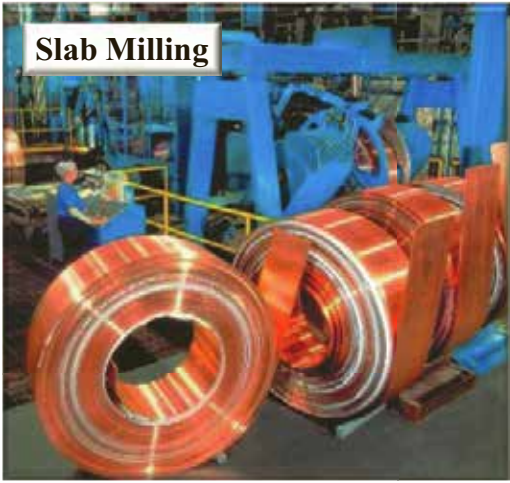


28

Strip Operations



Hot Rolling



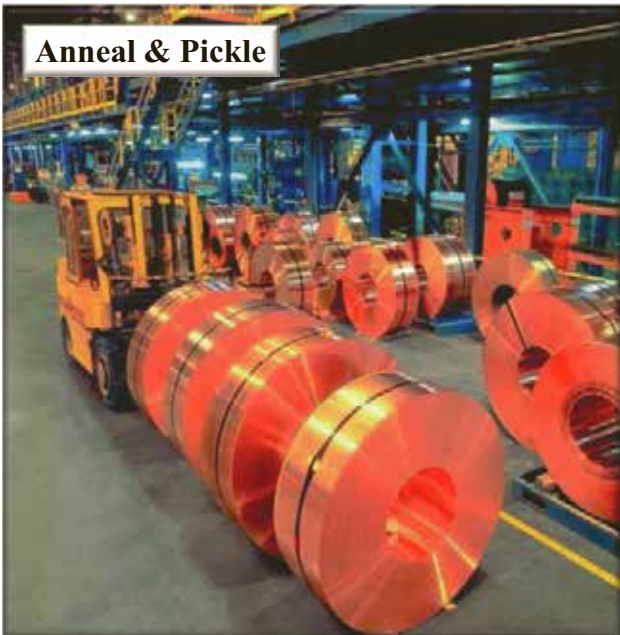
Slab Milling



Cold Rolling

29

Strip Operations



Anneal & Pickle



Age



Finish Pickle

30



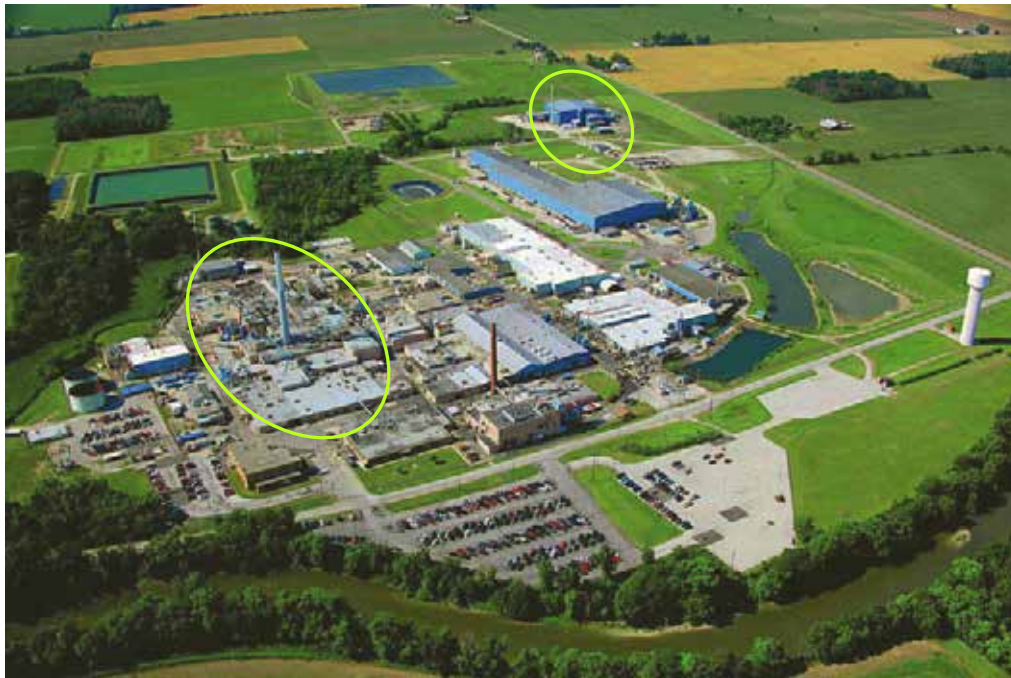
31

Copper Alloys

Material selection is based on combinations of mechanical and physical properties

- Strength*
- Conductivity, resistivity*
- Formability, ductility, crimpability*
- Stability*
- Stiffness*
- Magnetic permeability*
- Corrosion resistance*
- High Temperature Properties*
- Damage tolerance*

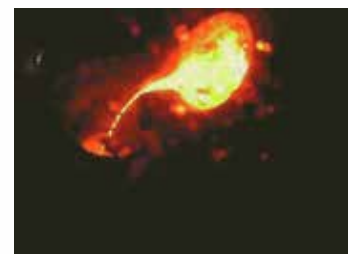
32



33

Beryllium & Composites Manufacturing

- **Business:** Production of Be and Be containing materials.
- **Markets:** Defense, Aerospace.
 - Satellites, optical systems, nuclear, avionics, inertial guidance.
- **Processes:**
 - Extractive metallurgy
 - Powder Metal production and consolidation
 - CNC machining
 - Casting
- **Research and Development:**
 - Advanced materials processing (I/C, amorphous alloys)
- **Applications Engineering and Project Management - SPADE**



34

Why Beryllium?

Our materials **enable** engineers to design and build lighter, faster, accurate, and more reliable systems.

- **Lighter than Aluminum**
 - **Stiff**
- **Transparent to X-rays**
- **Unique nuclear properties**
 - **Dampens vibration**
- **Good thermal properties**

35

Products

Beryllium:

- Seven commercial grades of Beryllium metal:
 - S200F, S200FH, S200FC, I70, **S65**, I220, I220H
 - Block, Parts, Sheet, Extrusions
- Beryllium Foil – multiple grades (Materion Electrofusion)
- Ultra High-purity Beryllium
- Beryllium hydroxide
- Beryllium fluoride



36

Aluminum Beryllium:

- AlBeMet: AM162
- Investment Castings - AlBeCast
 - Grades 910 and 920



Beryllium Oxide: Materion Ceramics, Tucson, AZ

- Powder and consolidated ceramic products.

Composite Materials:

- E-materials: Be – BeO composite (20%, 40%, 60% BeO)
- SupremEX – Metal Matrix Composites (Al based composites)

37

The NEW Pebble Plant



38

Pebble Plant Expansion

Why new plant?

- Old Pebble Plant :
 - 40 years old
 - Obsolete Equipment
 - Poor Condition

**Need for new plant to compete
in 21st Century.**

Government – Industry Cost Share



Pebble Plant cost : \$100 million

- Materion cost share: \$25 M
- US Government share: \$75 M

Defense Production Act Title III Program.







MATERION



Pebble PlantJune 2010

Pebble Plant Opening



Marcy Kaptur – US Congress
Richard Hipple – CEO Materion



Robert Latta – US Congress

Pebble Plant - Today

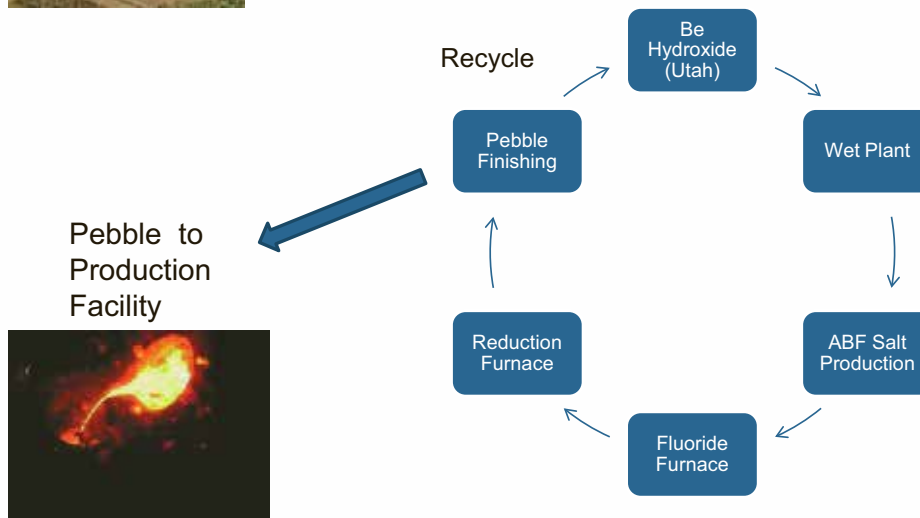


- Use lessons learned from the “old plant”.
- Design with high level of safety.
- Highly automated operation.
- Use best available environmental technology.



47

Pebble Process Overview



Pebble Plant



Pebble Plant



First Pebble April 2011

- Pebble quality meets all specifications.
- Characterization of product completed in mid-2012.




51

We are operating the plant at needed levels to satisfy market demand, with additional available capacity.

52

**Long Term Supply of Beryllium
Assured
at MATERION.**




 M A T E R I O N

MAKING A DIFFERENCE
OUR VISION, MISSION AND VALUES

VISION
We will be a global leader in innovative, advanced material solutions and services that enable our customers to excel in their markets

MISSION
enabling our customers

- We manufacture materials that enable technology to provide a safer and more sustainable future
- We provide advanced systems for our customers globally through innovation, technology and service that continuously exceed their expectations
- We are passionate about creating the necessary next talent
- We commit to building a strong financial future for our shareholders and shareholders, working to consistently grow revenues and earnings
- We always, naturally have had and will continue to produce as a safe, environmentally responsible member

VALUES
an unwavering commitment to integrity and innovation, respect

- Working hard to achieve the best results
- We believe in high quality work, and customer and our support of those higher values for our customers
- We respect all business partners with the highest standards of ethics and integrity
- We leverage the global resources and know-how methods to continuously improve
- We promote innovation and talent to achieve our goals
- We embrace change and rapid development
- We commit to providing and developing services, global talent, and to creating a culture where all employees can do their best work
- We protect the Sustainability of our commitment



MATERION



Appendix



MATERION



October 25, 2011

Upgrading of S-65 Be Specification for ITER First Wall

Aaron B. Sayer, P.E.
Materion

57

Outline



- Grade Comparison
- Reasons for Improvement
- Production Flow Chart
- Micrographs
- Properties
- S-65 Specification Change – What's New?

58

Comparison of Possible Beryllium Grades for ITER First Wall



Chemical element	Published Results					Published Results			
	3MC42Z				Chinese ****	Russian TGP-56FW*****			
	ITER I/O Spec	S-65 E (new)	S-65 C (old)	JET S-65 H	CN-G01	CN-G01m	Sample 1	Sample 2	Spec from BeWs 8, 2007
Beryllium Assay, % minimum *	99.0	99.2	99.0	99.0	>99	>99	99.02	98.84	98.8
Beryllium oxide, % maximum	1.0	0.9	1.0	1.0	0.9-1	0.7	0.95	1.35	1.3
Aluminium, % maximum	0.06	0.05	0.06	0.06	0.006	0.006	0.018	0.012	0.02
Carbon, % maximum	0.10	0.09	0.10	0.10	0.06	0.05	<0.05	0.05	0.1
Iron, % maximum	0.08	0.08	0.08	0.08	0.06	0.06	0.16	0.13	0.15
Magnesium, % maximum	0.06	0.01	0.06	0.06	0.005	0.005			
Silicon, % maximum	0.06	0.045	0.06	0.06	0.01	0.01	0.021	0.013	0.02
Uranium, % maximum **	0.0030	0.015 (will meet 0.0030 for ITER)	0.04	0.04			n/d	0.0005	0.002
Other metallic impurities, % maximum	0.04		0.04	0.04	<0.04	<0.04			
Physical Properties					Per paper*****		Actual Results		
UTS (MPa)	290	290	290	290	340		420		
TYS (MPa)	205	205	205	205	210		303		
Elongation (%)	3	3	3	3	>=3		3		

Items in red do not meet the ITER I/O specification

* Difference (i.e. 100% - other elements)

** Proven method of measurement of Uranium content shall be proposed by Manufacturer of material and agreed with DA and IO.

*** The content of other elements (e.g. Cr, Ni, Cu, Ti, Zr, Zn, Mn, Ag, Co, Pb, Ca, and Mo) shall be reported for information.

*****Recent Progress of Plasma Facing Material Research at SWIP¹, X. Liu, et al, Southwestern Institute of Physics, China

*****Progress in Production and Characterization of RF Beryllium for ITER First Wall, Presentation given at 8th IEA Be WS, Lisbon, Portugal, December 2007.

1. Kupriyanov, et al, Federal Agency of Atomic Energy, Russia

*****Characterization of Chinese Beryllium as the Candidate Armor Material of ITER First Wall, X. Liu et al, Southwestern Institute of Physics, China

Additional Elemental Reductions in S-65 Rev. E

Element	% Maximum
Cr	0.01
Ni	0.025
Cu	0.025
Ti	0.025
Zr	0.025
Zn	0.005
Mn	0.005
Ag	0.005
Co	0.005
Pb	0.005
Ca	0.005
Mo	0.005

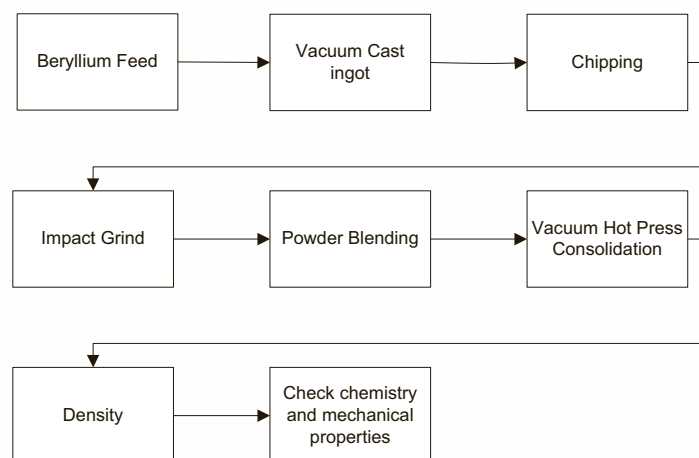
- 3MC42Z ITER I/O Beryllium Specification, “Material Specification for the supply of Beryllium blocks for the ITER First Wall application”
 - Uranium of 30 ppm
- Refinements and adjustments to the process for reduced Uranium led to reduction of other elements and an increase in %Be.
 - BeO, Al, C, Mg, Si, Cr, Ni, Cu, Ti, Zr, Zn, Mn, Ag, Co, Pb, Ca, Mo

- Discovered that steps can be taken to remove uranium from beryllium with the following results:
 - Product A: 3 – 6 ppm Uranium
 - Product B: 20 – 70 ppm Uranium
- In addition, Materion has a process to reduce Product A Uranium further:
 - Less than 5 ppm

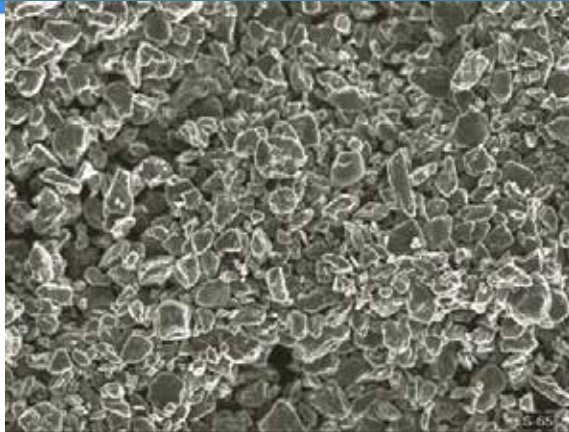
Lot	Fluorometric (ppm U)	Neutron Activation (ppm U)
Lot 1	2	
Lot 2	3	
Lot 3	1	1.0
Lot 4		2.9
Lot 5	1	1.0
Lot 6		1.2
Lot 7		1.9
Lot 8		0.8
Average	1.7	1.5

- First production S-65 lot shipped to ITER IO Specification 3MC42Z in 2011.
 - Not all Uranium reduction methods used
 - Uranium by GDMS: 7 ppm

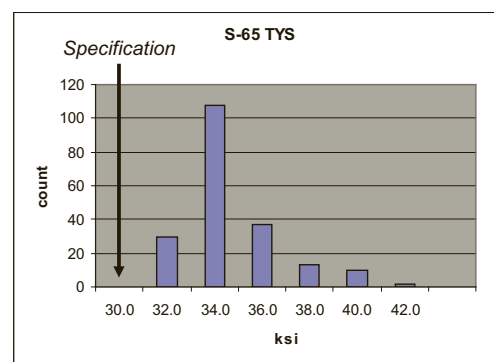
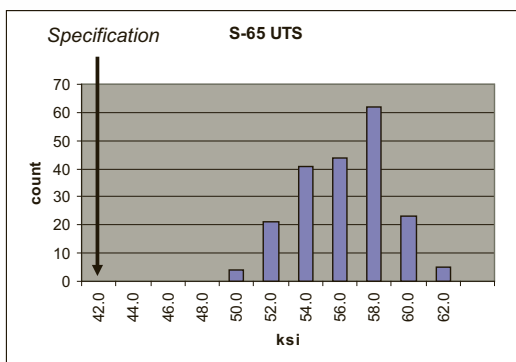
S-65 Flow Chart



Impact Ground S-65 Powder



S-65 Mechanical Properties 2000 – 2011



S-65 Specification Changes



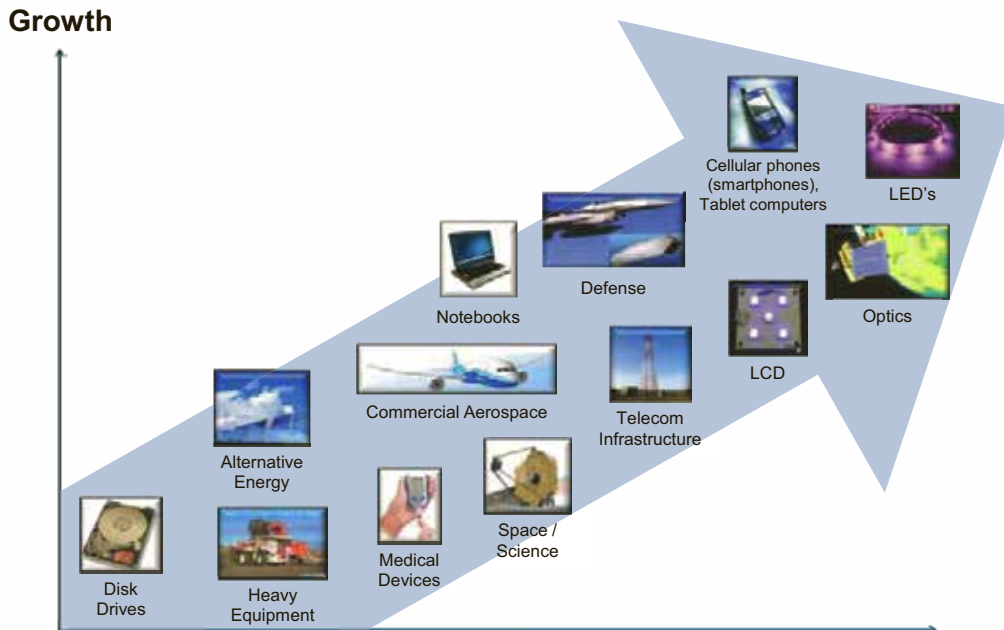
	3MC42Z			
Chemical element	ITER I/O Spec	S-65 E (new)	S-65 C (old)	Typical
Beryllium Assay, % minimum *	99.0	99.2	99.0	99.4
Beryllium oxide, % maximum	1.0	0.9	1.0	0.66
Aluminium, % maximum	0.06	0.05	0.06	0.03
Carbon, % maximum	0.10	0.09	0.10	0.03
Iron, % maximum	0.08	0.08	0.08	0.075
Magnesium, % maximum	0.06	0.01	0.06	0.005
Silicon, % maximum	0.06	0.045	0.06	0.025
Uranium, % maximum **	0.0030	0.015 (will meet 0.0030 for ITER)	0.04	0.001
Other metallic impurities, % maximum	0.04		0.04	
Physical Properties				
UTS (MPa)	290	290	290	386
TYS (MPa)	205	205	205	234
Elongation (%)	3	3	3	4



MATERION



Materion Markets Overview



Entered multiple leading-edge growth markets since 2002

A-18

Applications: Smart Phones

Internal Antenna Contacts

Grounding Clips and Audio Jacks

Micro Mezzanine Connectors for LCD Screen

I/O Connector Contacts

Battery Contacts



Internal Electronics

- Precursor materials for GaAs wafer production

Internal Electronics and LED

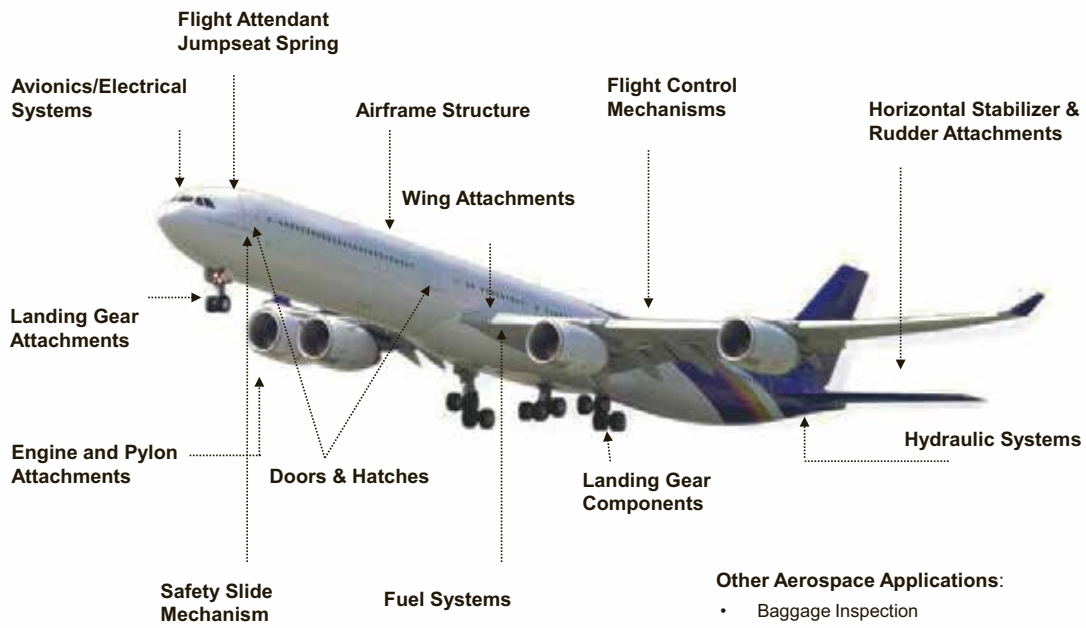
- Thin Film Materials – Power amplifiers, LED, SAW and BAW devices, filters, and ICs
- Hermetic Solutions for SAW
- Refining / Recycling
- Precision Parts Cleaning

Other Smart Phone Applications:

- Circuit Board and IC Inspection
- RoHS Compliance Assurance
- Cellular Infrastructure with High Power RF Packaging
- Voice Coil Motor (auto-focus lens stabilizer)

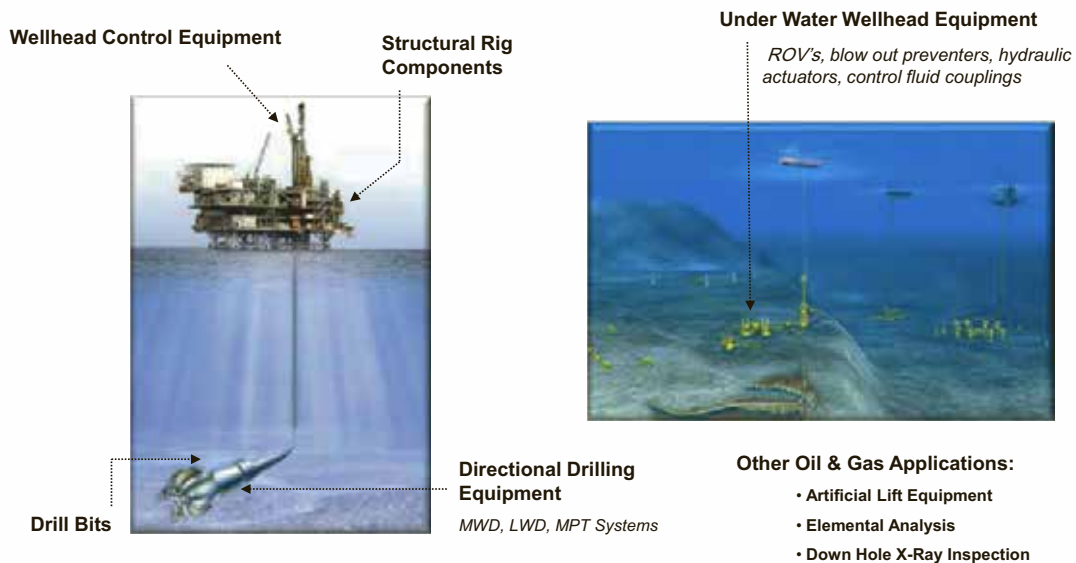
A-19

Applications: Aerospace



A-20

Applications: Oil & Gas



A-21

Applications: Solar Energy



Technology: Crystalline Silicon (Si)

Interconnect Materials

Front and backplane systems for high efficiency designs.

Technology: Flexible Solar Cells / Building Integrated Photovoltaic:

Thin Film Services:

Solar cells built in flexible substrates to accommodate applications such as roofing tiles or defense.

Technology: Cadmium Telluride (CdTe)

Thin Film (PVD) Materials

Cadmium based solar cell architecture. N and P type Cadmium Semiconductor materials
TCO Transparent Conductive Oxide layers
Front and Back-contact layers

Technology: Copper Indium Gallium Selenide (CIGS)

Thin Film (PVD) Materials

as well as Powders for Printing CIGS applications

Copper Indium Gallium Selenide thin film and screen printing applications for flexible and rigid solar cells.



Technology: Concentrator Photovoltaic (CPV)

Thin Film (PVD) Materials

Solar technology based on concentrating Solar rays into a semiconductor device via large lens. Anti-Reflection Coating Materials
Precious metal contact materials

Technology: Amorphous Silicon (a-Si, tandem and multi-junction)

Thin Film (PVD) Materials

Silicon based photovoltaic cells
Front and back contact layers
TCO Transparent Conductive Oxide layers

Micro Electronic Packaging Products:

Bonding Ribbon - Au & Ag
Lead-free Solders
Metalized Ceramic Substrates

A-22

Applications: Medical



Seizure Control

- Thin Film Deposition Implantable Electrode – Parkinson's disease (R&D)

X-Ray Mammography

Subcutaneous Glucose Analysis

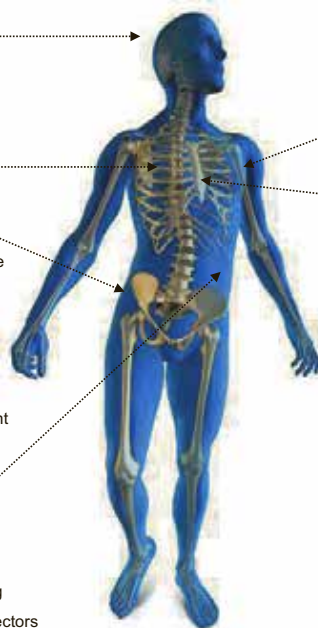
- Thin Film Coatings – Electrode Monitoring device

External Glucose Analysis

- Subcutaneous sensors for glucose measurement

Insulin Pump

- EMI Shielding and Grounding
- Electrical Terminals in Connectors



Radiation Therapy – Neutron Reflectors

Cardiac Rhythm Management

- Electronic Interconnects/Components
- Niobium/Titanium Electron Beam Weld

Other Medical Applications:

- DNA Sequencing Optics
- CT Scan
- Diagnostic X-Rays
- Advanced Drug Delivery Components
- Diagnostic Electronic Components
- Anesthesia Monitoring Components
- Operating Instruments

A-23

Base Stations

- Coaxial Connectors
- High Power Amplifiers

Local Area Networks

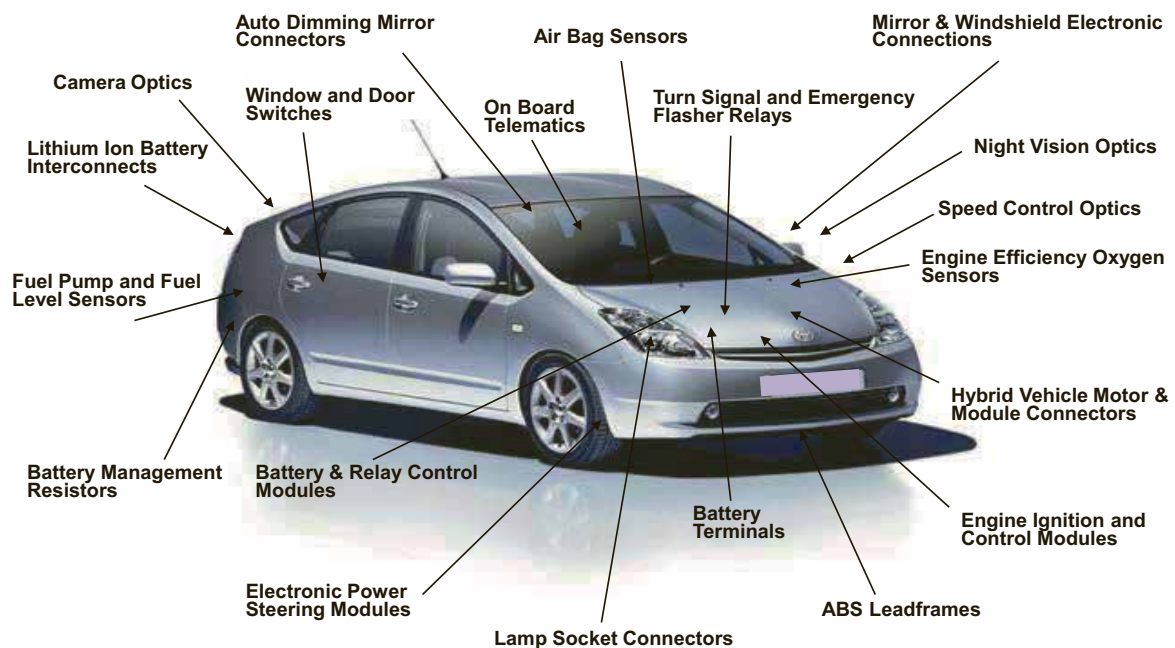
- Shielding
- Modular Jacks
- PCB Sockets
- Processor Sockets

Other Telecommunications Infrastructure Applications

- Undersea Repeater Housings



A-24



A-25

- Infrared Sensors for Fighter Jet and UAV Optical Targeting
- Electronic Packaging for Defense Avionics, Radar and Electronic Countermeasure Systems
- Structural and Electronic Components for Satellites
- X-ray Windows in Security Imaging Systems
- Laser Protection Optical Coatings
- Night Vision System Optics





Overview of Beryllium R&D Activities for Fusion in Russia

I. Kupriyanov¹, G. Nikolaev¹, R. Giniyatulin²,
V. Sizinev³

¹ *A.A. Bochvar Research Institute of Inorganic Materials,
Moscow, Russia*

² *Efremov Research Institute, S.-Peterburg, Russia*

³ *JSC "Compozit", Korolev, Moscow reg.*

September 19-21, 2012

10th IEA Be WS, Karlsruhe,
Germany

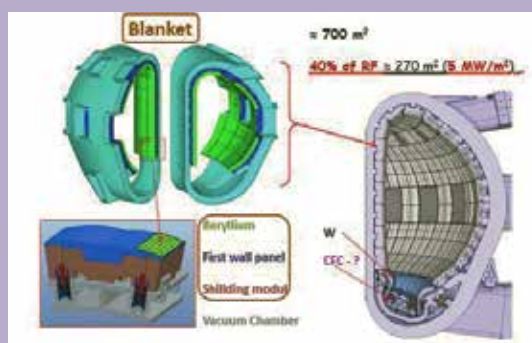
1



Outline

Basis direction of R&D activities:

- 1. R&D for armor of ITER First Wall;**
- 2. R&D for solid breeder blanket**



September 19-21, 2012

10th IEA Be WS, Karlsruhe,
Germany

2



1. R&D for armor of ITER First Wall

R&D has been focused on:

- Complex HHF qualification testing of TGP-56FW grade performed in the frame of ITER IO qualification program;
- Optimization of dimensions of armor plates and further qualification of Be/Cu joints;
- Optimization of process of beryllium plates fabrication for armour of ITER first wall components, focused on the preparation of industrial base for manufacturing beryllium armour plates and the development of more effective method of beryllium plates fabrication;
- Investigation of beryllium for first wall erosion in the ITER-like plasma-wall interaction conditions using QSPA-Be plasma gun facility

September 19-21, 2012

10th IEA Be WS, Karlsruhe,
Germany

3



Performance of complex HHF qualification testing procedure of TGP-56FW grade

Background

Beryllium was chosen as an armour material of the ITER First Wall.

- ITER Final Design Report 2001 identified the reference grades S-65C (Brush Wellman) and DSHG-200 (Russian Federation). The main criterion of this choice was excellent thermal fatigue/thermal shock behavior of these Be grade.
- Later, Russian ITER Parties proposed our advanced grade - TGP-56FW for application as armour of the ITER first wall.
- To assess the performance of this new grade IO and Russian Parties agreed on a program to perform the HHF qualification testing of the TGP-56FW.

September 19-21, 2012

10th IEA Be WS, Karlsruhe,
Germany

4

HHF qualification testing procedure of TGP-56FW grade



The program for HHF qualification included several tests such as:

1. Thermal shock resistance:

Single tests- 1.2-5 MJ/m², Δt = 5 ms, heated area: 5×5mm²

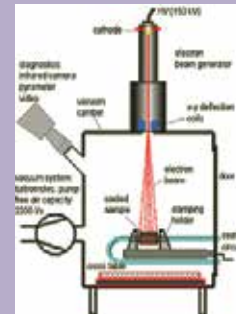
Multiple tests- 1.2 and 1.5 MJ/m², 1000 shots, Δt = 5 ms

2. Vertical displacement event (VDE) simulation testing (at 40 MJ/m², 1 shot, 0.2 s, 10×10mm²) and following thermal shock tests (at 40 MJ/m², 1 shot, 0.2 s, 5×5mm²)

3. Thermal cyclic fatigue tests after VDE simulation testing

(at 80 MW/ m² (2 MJ/m²), 1000 shots, Δt = 25 ms, 10×10mm²)

(All tests were performed in the JUDITH-1 facility at Forschungszentrum Juelich)



September 19-21, 2012

10th IEA Be WS, Karlsruhe, Germany

Design and a view of water-cooled mock-ups (for JUDITH-1 facility)



Before testing

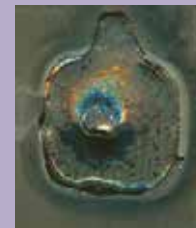


After testing

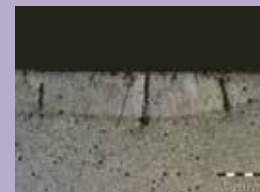
VDE testing (40 MJ/m², 1 shot, 0.2 s, a = 10×10 mm²)



TGP-56FW



S-65C



September 19-21, 2012

10th IEA Be WS, Karlsruhe, Germany

6



Conclusions on HHF qualification tests

- **HHF behavior of TGP-56 grade under different thermal loads expected in ITER FW does not concede the S-65C grade behavior.**
- **TGP-56FW beryllium grade has successfully passed through HHF qualification procedure and approved by the ITER IO for the application as an armor material for the FW.**



Optimization of dimensions of armor plates and further qualification of Be/Cu joints

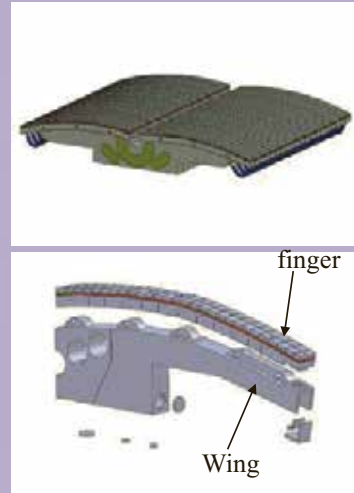
Background

- RF is responsible for production and delivery of $\sim 40\%$ First Wall plates (270 m^2);
- According to recent IO estimations, $\sim 50\%$ ($\sim 350 \text{ m}^2$) of FW surface will be exposed by scaled up stationary heat loads– up to 5 MW/m^2 ;
- All RF share is related to high loaded part of FW
- Because of increase of heat loads, design of FW plates was revised

Optimization of dimensions of armor plates and further qualification of Be/Cu joints

In 2010-2012 some R&D were performed in RF (mainly in Efremov Institute) :

1. Reasoning and development of new design of FW plates adopted to operation at heat loads up to 3-5 MW/m²;
2. Optimization of plates dimensions
3. Further qualification of Be/Cu joints



New design of FW panel (above), consists of individual fingers (below)

September 19-21, 2012

10th IEA Be WS, Karlsruhe,
Germany

9

Optimization of dimensions of armor plates

Original dimensions of Be plates (before revision)
- 80x80x10 mm

Now the following Be plates dimensions are under consideration:

- Thickness of plates - 6-8 mm;
- Plates dimensions - from 50x50 to 12x12 mm.

Reduction of plates dimensions is caused by the necessity:

- To provide required quality of Be/Cu joints by reduction of thermal stress on the interface Be-CuCrZr
- To limit max temperature of Be surface down to 500-600°C at heat loads up to 5 MW/m².

Finalization of Be plates dimensions ~ beginning of 2013

September 19-21, 2012

10th IEA Be WS, Karlsruhe,
Germany

10

Development of process of manufacturing of beryllium plates for armour of ITER FW



General requirements:

1. Totally 180 FW panels ($1.5 \times 1.0 \times 0.2$ m) with beryllium armor to be produced;
2. Total area of beryllium armor 270 m^2 ;
3. Total weight of final products - 4 t (for plates thickness 8 mm)

Preliminary time schedule:

- Signing of PA – end of 2013
- Fabrication of prototype - 2013-2014
- Shipment of products to ITER place - 2014-2019

September 19-21, 2012

10th IEA Be WS, Karlsruhe,
Germany

11

Development of process of manufacturing of beryllium plates for armour of ITER FW



Two general directions of R&D:

1. Manufacturing of Be plates from TGP-56FW (60%):

60% = $160 \text{ m}^2 = 2.4 \text{ t}$ (for thickness 8 mm)

Collaboration of Bochvar Inst., Efremov Inst, Basalt plant and Ulba plant

2. Manufacturing of Be plates from S-65C (40%):

40% = $110 \text{ m}^2 = 1.6 \text{ t}$ (for thickness 8 mm)

Collaboration of Efremov Inst, Materion Brush, Komposit

September 19-21, 2012

10th IEA Be WS, Karlsruhe,
Germany

12

Manufacturing of Be plates from TGP-56FW



General R&D:

1. Development of basis technology of produced of TGP-56FW grade (2007-2010);
2. Development of industrial technology and processes of manufacture of Be plates (2010-2013);
3. Изготовление и ввод в эксплуатацию необходимого оборудования – 2010-2014 (CIP press -2010-2011, VHP press -2011-2012);
4. Изготовление и поставка high quality Be ingots(2012-2015).

September 19-21, 2012

10th IEA Be WS, Karlsruhe,
Germany

13

Manufacturing of Be plates from S-65 C



General R&D:

1. Development and optimization of machining processes of manufacture of Be plates from S-65C blocks (2008-2011);
2. Procurement and implementation of new equipment (2009-2012);
3. Manufacturing and delivery of S-65C blocks (2012-2014).

September 19-21, 2012

10th IEA Be WS, Karlsruhe,
Germany

14



Investigation of Be first wall erosion in the ITER-like plasma-wall conditions

Objectives (important for the ITER lifetime and safety evaluation) :

- Data on Be erosion in the ITER-like plasma-wall interaction for the evaluation of Be armor lifetime;
- Data on erosion products (dust, films) and mix materials under ITER-relevant transient loads (ELMs, disruptions, radiative heat).

- The new plasma gun QSPA-Be facility has been prepared to operating with beryllium at Bochvar Institute.
- Mock ups have been manufactured which design allowed changing beryllium targets.



QSPA-Be: $Q=50 \text{ кДж}$, $t=500 \text{ мкс}$

September 19-21, 2012

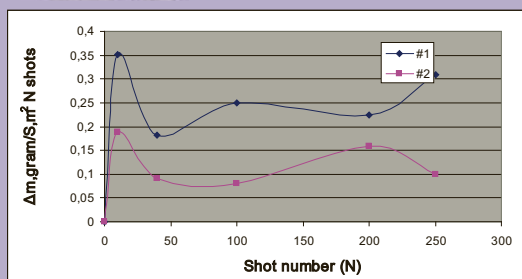
10th IEA Be WS, Karlsruhe, Germany

15

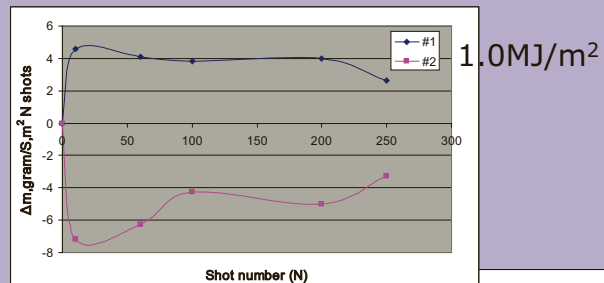
Mass loss/gain and surface structure of Be grade TGP-56FW were studied after plasma heat loads of 0.5-1.5 MJ/ m²



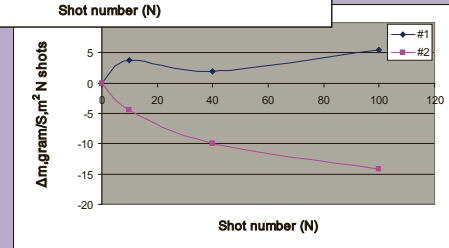
• The dependencies of mass loss/gain on shots number were obtained.



0.5 MJ/m²



1.0 MJ/m²



1.5 MJ/m²

September 19-21, 2012

10th IEA Be WS, Karlsruhe, Germany

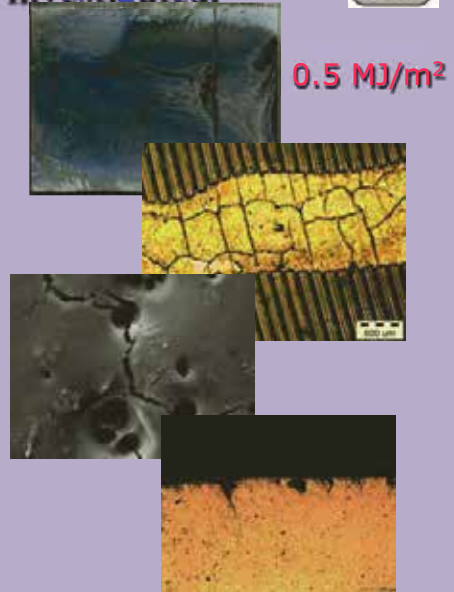
16



Evolution of surface structure was investigated.

Several processes take place simultaneously on the surface areas subjected to plasma stream loading:

- Melting of surface in plasma steam and displacement of melt on the surface of the mock up;
- Re-solidification of displaced melt;
- Porosity formation in re-solidified displaced melt;
- Formation of cracks due to high thermal stresses in surface layer;
- Deposition of sputtered metal in form of films, flakes, macro- and micro- particles.



In spite of the intensive surface melting and a high erosion, the disintegration of all beryllium samples investigated did not happen (see details in I. Kupriyanov present. on BeWS-10)

September 19-21, 2012

10th IEA Be WS, Karlsruhe,
Germany

17

2. R&D for solid breeder blanket



2.1 HIDOBE IEA irradiation experiment

Objective: to gain the necessary information on irradiation properties (swelling, tritium retention, thermal properties, etc.) of various modifications of beryllium (Be-pebbles, dense and porous Be) and Titanium Beryllides ($\text{Be}_{12}\text{Ti}_5$, $\text{Be}_{12}\text{Ti}_7$) under the the irradiation close to the operation conditions of Be in the HCPB DEMO.



Fluence ($E > 0.1 \text{ MeV } 10^{26} \text{ n/m}^2$)	1.5	3
Fluence ($E > 1 \text{ MeV } 10^{26} \text{ n/m}^2$)	0.7	1.4
Helium production in Be (appm)	3000	6000
Tritium production in Be (appm)	250	700
Neutron damage in Be (dpa)	17.9	35.8
Helium production in Be-Ti (appm)	2740	5480
Tritium production in Be-Ti (appm)	235	562
Neutron damage in Be-Ti (dpa)	19.5	38.9
Temperatures ($^{\circ}\text{C}$)	425, 525, 650, 750	425, 525, 650, 750

September 19-21, 2012

10th IEA Be WS, Karlsruhe,
Germany

18



Preparation and performance PIE of Russian beryllium samples irradiated to 3000 appm He in HIDOBE-1 irradiation experiment

Recently, the PIE test matrix of RF Be samples was developed and agreed between NRG and Bochvar Institute. This PIE program are include:

- Standart measurements (weight, dimensions, dose rate, density, helium pycnometry, surface structure observation);
- Tritium release experiments;
- Thermal diffusivity measurements (LFA);
- Microstructure examination (optical, SEM).

Six grade of Be (four densens an two porous grades) will be investigate.

Investigation are on going (complition in Dec. 2012-Jan. 2013)

(see details in S. van Till present. on BeWS-10)

September 19-21, 2012

10th IEA Be WS, Karlsruhe,
Germany

19

2.2 Fabrication and investigation of beryllium pebbles with different grain sizes and fine grain structure

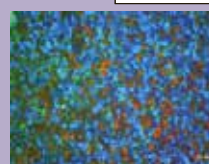
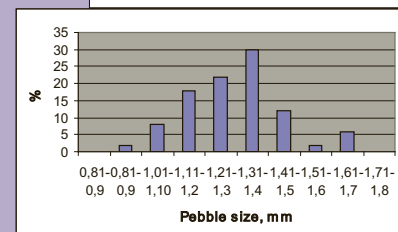
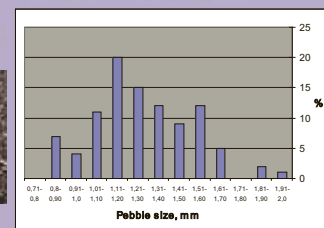


Several experimental batches of Be pebbles with average pebble size of 1.2 – 1.3 mm and different grain sizes have been fabricated by powder metallurgy. Two of them (~0.6-0.8 kg) with average pebble size of 1.2 – 1.3 mm and two average grain sizes (~ 13-14 μm and ~50-55 μm) were characterized.

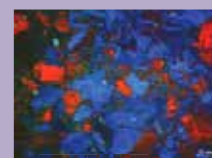
- Packing density at free filling ~59 and 56.8% of theoretical density of beryllium;
- After vibration (50 Hz, 2 hours) packing density increased up to ~66.6 % and ~61.4 %.

(see details in I.Kupriyanov poster on SOFT-27)

(funded by F4E -Contract EFDA 05/994)



~ 13-14 μm



~50-55 μm

September 19-21, 2012

10th IEA Be WS, Karlsruhe,
Germany

20



7. Summary

- **The main R&D activities on Be for fusion in RF are directed on FW application.**
- **R&D activities on Breeder Blanket are performed mainly in collaboration o foreign partners.**



Thank you!



10th IEA Int. Workshop on Beryllium Technology

*Karlsruhe, Germany
September 19-21, 2012*

Development and qualification of beryllium materials for the EU Test Blanket Module: Strategy and R&D achievements

M. Zmitko

TBM & MD Project Team, Fusion for Energy (F4E), Barcelona, Spain



Presentation Outline

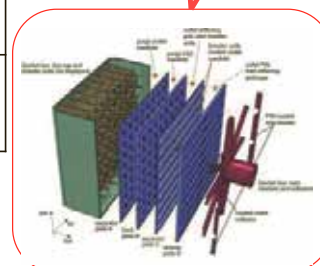
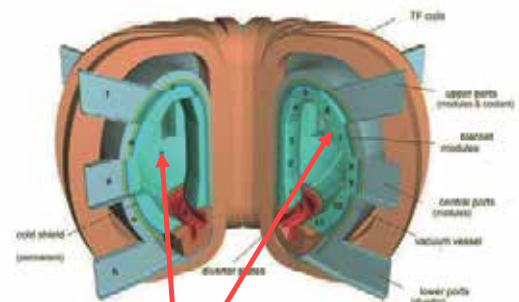
- The European Breeder Blanket concepts
- Test Blanket Modules (TBM)
 - Project organization
 - Technical information
 - Time schedule
 - TBM testing at ITER
- Beryllium as multiplier material for BB
 - Requirements
 - Development and procurement strategy
 - On-going and future activities
 - Some R&D results

The European Breeder Blanket concepts

3

European breeder blanket concepts

	HCPB He-Cooled Pebble Bed	HCLL He-Cooled lithium Lead
Structural material	Ferritic-Martensitic steel (EUROFER)	Ferritic-Martensitic steel (EUROFER)
Coolant	Helium (8 MPa, 300/500°C)	Helium (8 MPa, 300/500°C)
Tritium breeder, multiplier	Solid (pebbles bed) $\text{Li}_2\text{TiO}_3/\text{Li}_4\text{SiO}_4$, Be ⁶ Li enrich. 40-70%	Liquid (liquid metal) Pb-15.7at.%Li ⁶ Li enrich. 90%
Tritium extraction	He purge gas (~1 bar)	Slowly re-circulating PbLi; extraction outside the blanket



**Breeder
Blankets
modules**

4

***ITER, a unique opportunity to test Breeder
Blanket mock-ups:
'Test Blanket Modules' (TBMs)***

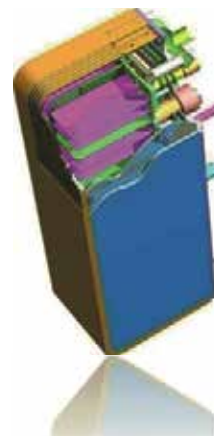
5

TBMs mission in ITER

- To develop and build the European Test Blanket Module (TBM) Systems for ITER
- To develop numerical tools for analysis of TBM tests and design of DEMO breeder blankets

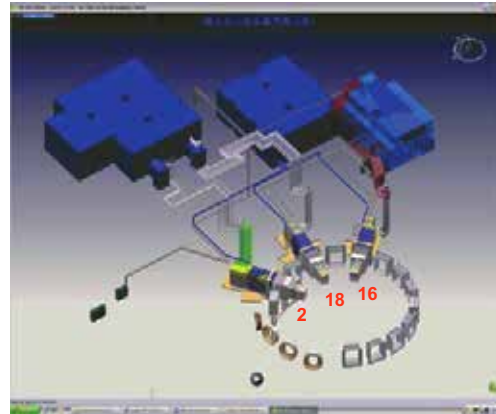
“
ITER should test Tritium Breeding Module concepts that would lead in a future reactor to tritium self-sufficiency and to the extraction of high grade heat and electricity production

”



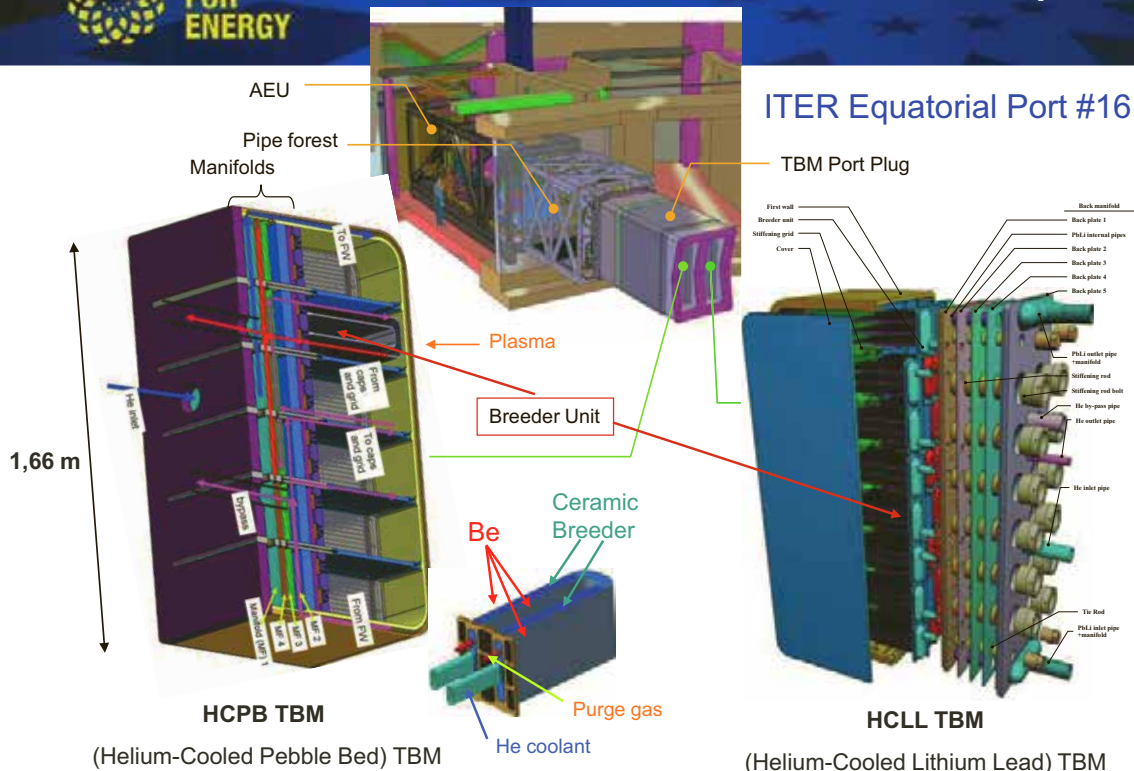
6

- “Council Decision on the Establishment of the Test Blanket Module (TBM) Program”, IC-3, 19-20 Nov.2008
- “Report from the Second Meeting of the Test Blanket Module Program Committee (TBM-PC-2) (29-30 September 2009)”, confirming TBM Port Allocation, endorsed by the IC-5.
- *Recently, proposal from KO to install a Helium-Cooled Ceramic TBS replacing the US DCLL TBS considered up-to-now*



ITER Port # ('Port Master', PM)	TBM Concept 1	TBM Concept 2
#16 (PM: EU)	HCLL (He-Cooled Lithium-Lead) (TBM Leader: EU)	HCPB (He-Cooled Pebble Bed) (TBM Leader: EU)
#18 (PM: JA)	WCCB (Water-Cooled Ceramic Breeder) (TBM Leader: JA)	HCCB (He-Coolant Ceramic Breeder) (TBM Leader: KO)
#2 (PM : CN)	HCCB (He-Cooled Ceramic Breeder) (TBM Leader: CN)	LLCB (Lithium-Lead Ceramic Breeder) (TBM Leader : IN)

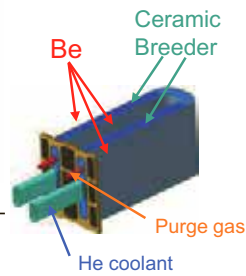
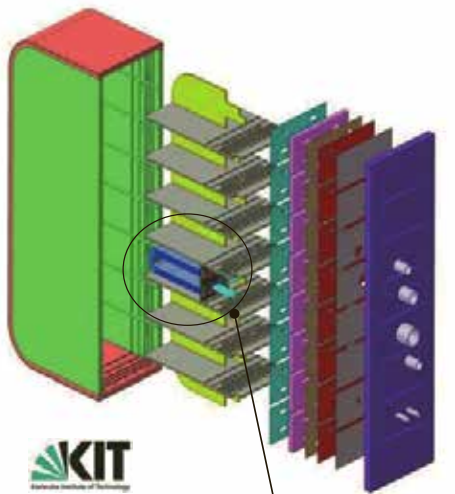
Test Blanket Modules (TBM)



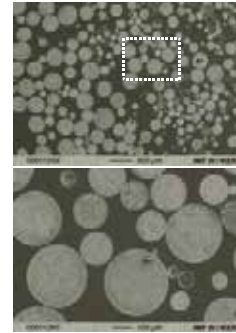


FUSION FOR ENERGY

HCPB TBM (solid tritium breeder)



ceramic pebbles

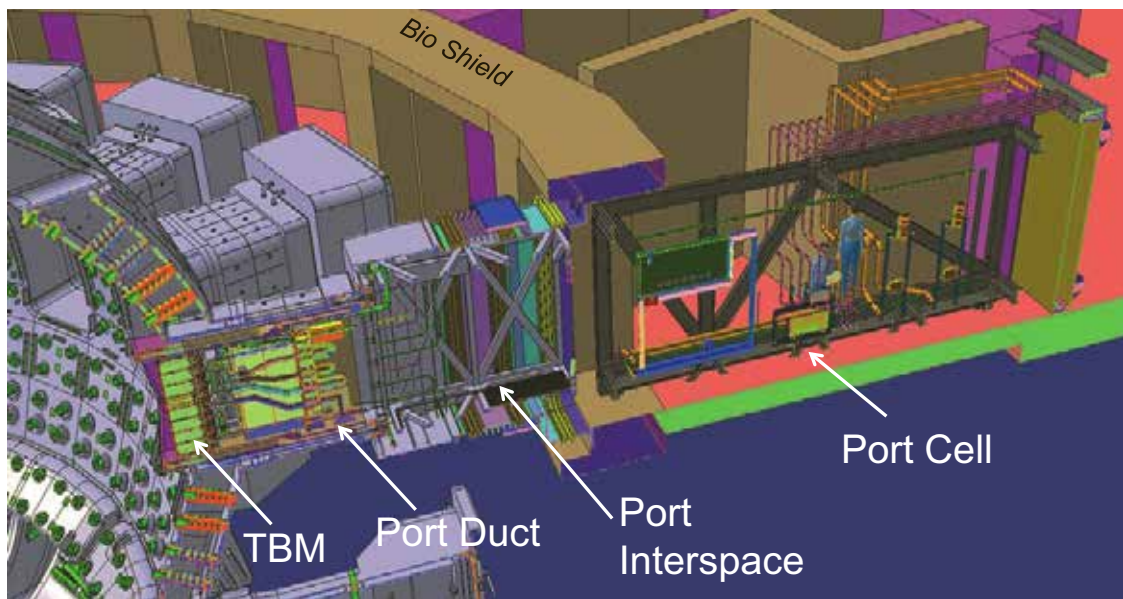


Be pebbles

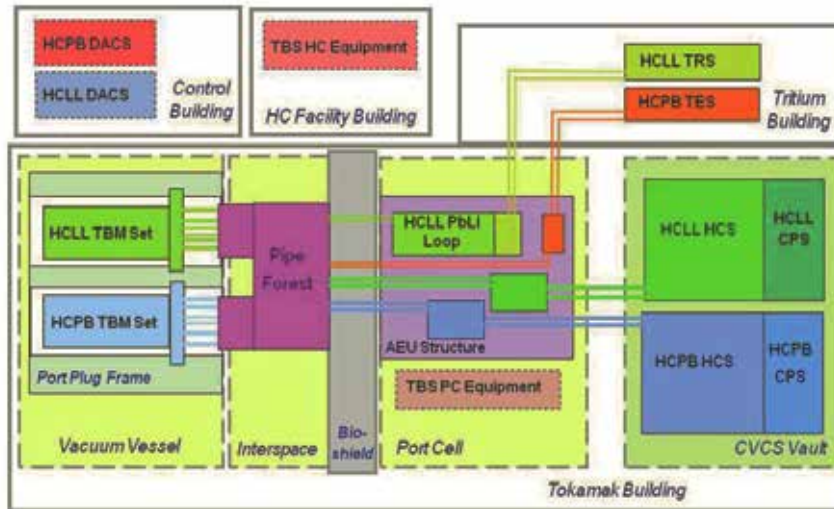


FUSION FOR ENERGY

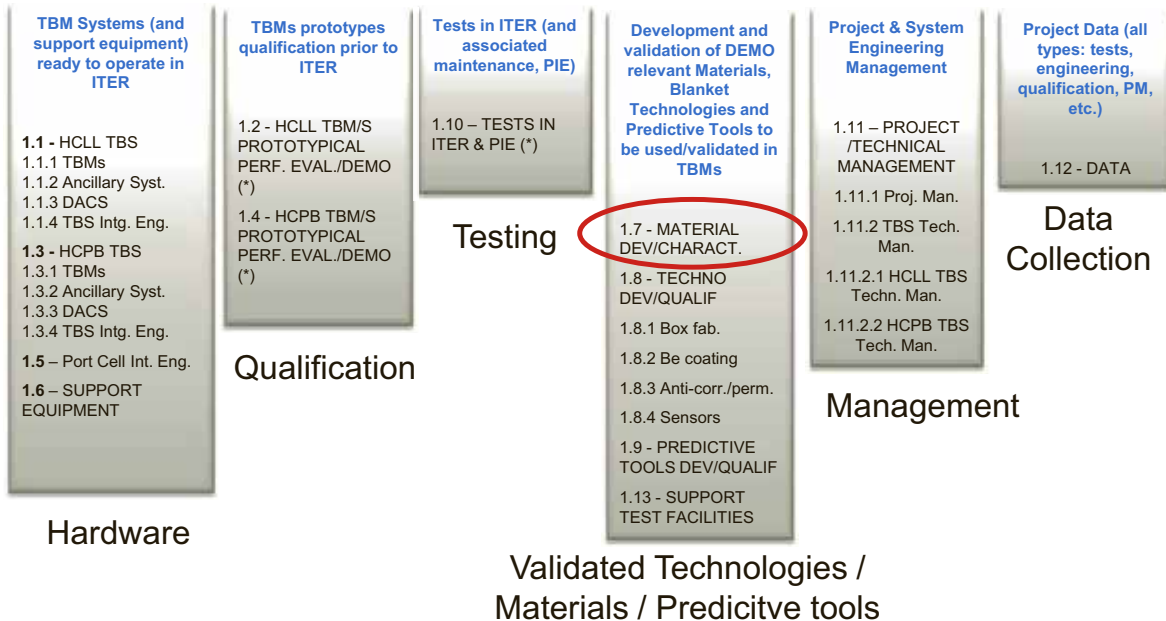
The TBM systems extend from Vacuum Vessel to Port Cell and buildings



– From L.V. Boccaccini, SOFT-2010

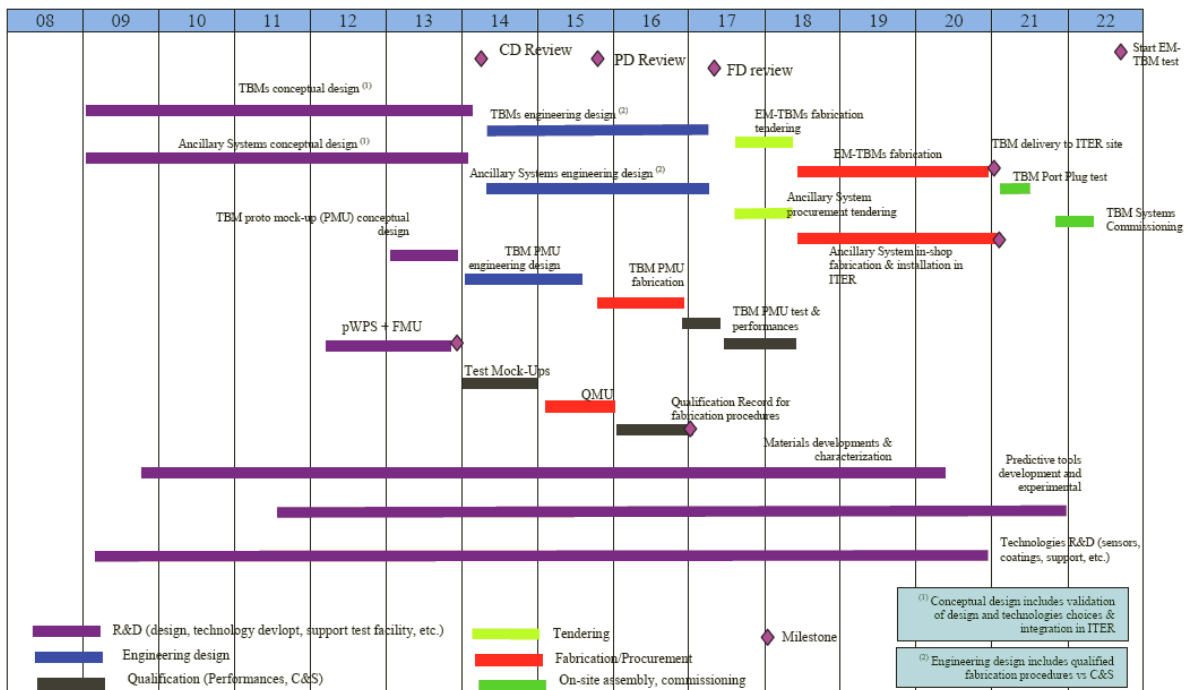


TBMs Project





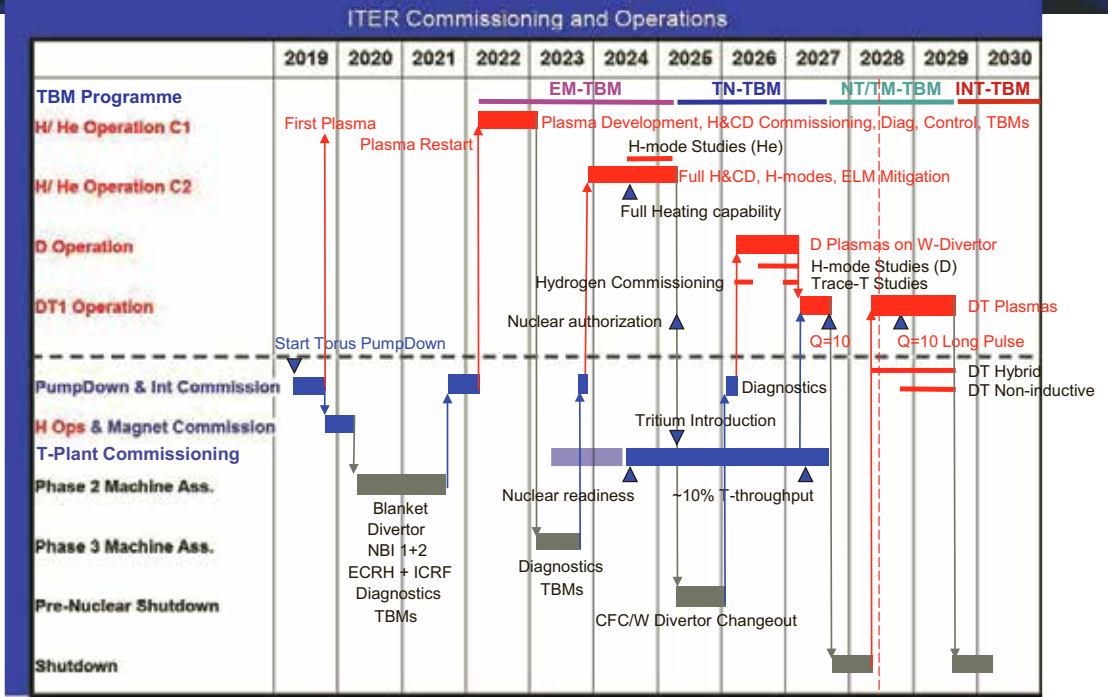
Master schedule (prior to ITER operation)



Adopted Strategy for the TBM Programme Integration (IRP v2.0)

- ◆ 4 versions per each TBM are considered with specific objectives as follow:
 - **Learning/validation phase**
 - ✓ the Electro Magnetic module (EM-TBM): H phase, H-He phase;
 - ✓ the Thermal/Neutronic module (TN-TBM): D-phase;
 - **DEMO-relevant data acquisition phase**
 - ✓ the Neutronic/Tritium & Thermo-Mechanic module (NT/TM-TBM): DT1 phase;
 - **DEMO-relevant data acquisition phase (2nd 10 years)**
 - ✓ the INTEgral TBM (INT-TBM): DT2 (high duty, long pulses)

ITER Experimental Programme



15

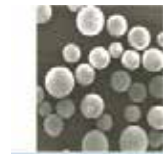


**Breeder Blankets functional materials –
Beryllium multiplier materials development and qualification**

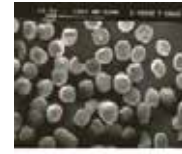
16

General requirements come from DEMO objective with a short-term objective to characterized/qualify Functional Materials (FMs) for a use in the ITER TBM

- Withstand stresses induced under DEMO-relevant operating conditions without excessive fragmentation (CB, Be)
- No degradation of heat transfer parameters of the pebble beds during operation for temperature control (CB: $T_{max} = 920^{\circ}C$; Be: $T_{max} = 650^{\circ}C$)
- Compatibility between the ceramic/Be/Pb-Li and EUROFER (up to max. $T \sim 550^{\circ}C$)
- Neutron irradiation resistance under given operation conditions and for the required life-time (CB, Be); withstand operation conditions without significant changes of thermo-physical and chemical properties (Pb-Li)
- Low tritium residence time/tritium retention in the Li-ceramics and Be pebbles to minimize tritium inventory (safety aspect); possibility to extract efficiently bred tritium => low tritium inventory in Pb-Li
- As low as possible activation under neutron irradiation (impurities level control; e.g. U, Co, Bi)
- Limit hydrogen and passive heat release during accidental conditions below safety limits (Be/steam/water interaction; Pb-Li/water interaction)



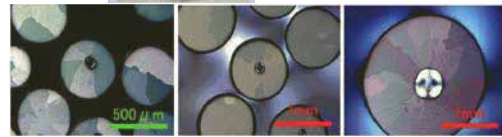
Lithium Orthosilicate (OSi)
 Li_2SiO_3
(FDX-Schott, melt-spray process)
 $\phi = [0.26 - 0.63] \text{ mm}$



Lithium Metatitanate (MTi)
 Li_2TiO_3
(CEA-CTI, extrusion-spherulization-sintering)
 $\phi = [0.8 - 1.2] \text{ mm}$

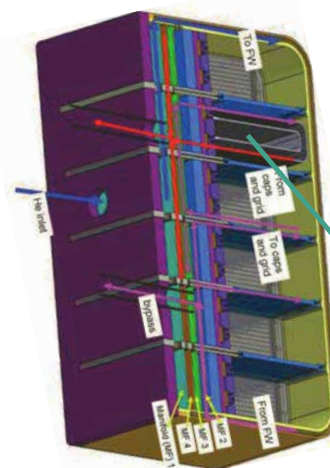


1 mm Be pebbles
NGK (JA)
Rotation Electrode Process (REP)



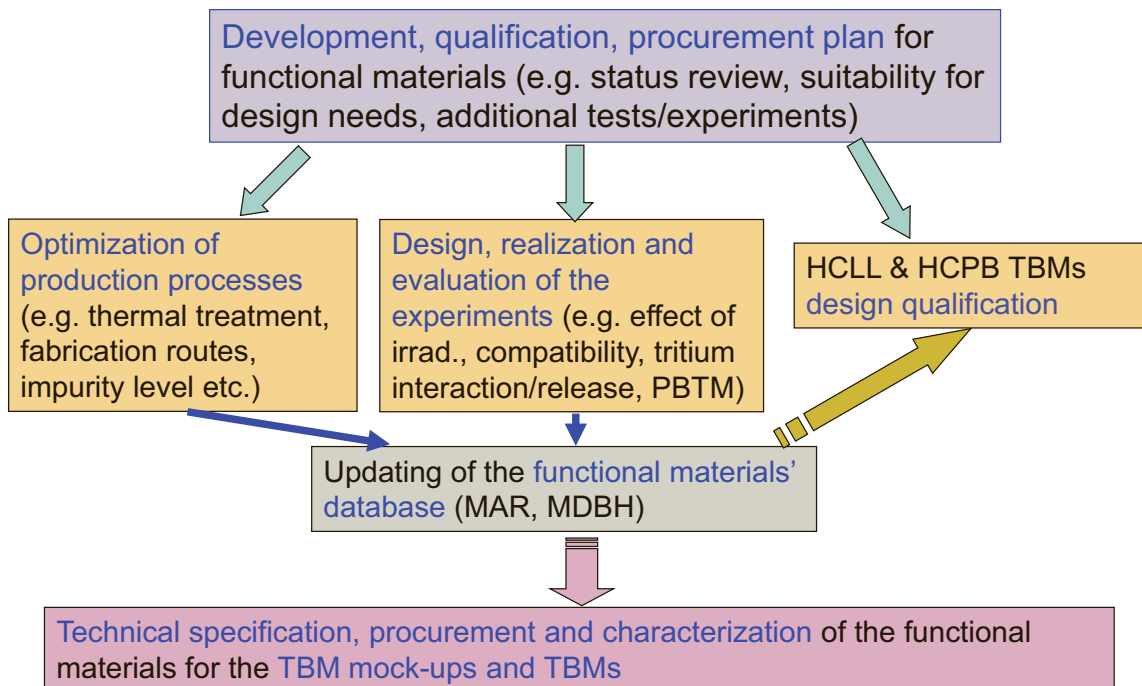
Pb-15.7at%Li alloy ingots
MHD mixing
Hidrovats (Latvia)

- Tritium breeding ratio \rightarrow ceramic breeder/Be volume ratio = 1/4
- Single size pebble bed
- 1 mm Be pebbles produced by Rotation Electrode Process
- Alternative: Advanced Be materials - Beryllium alloys (e.g. $Be_{12}Ti$)
 - Better oxidation resistance
 - Lower swelling
 - Better tritium release characteristics
 - Smaller reactivity with steel



Chemical composition of Be pebbles proposed for TBM application (in wt%)

Be	BeO	Al	Fe	Mg	Si	Co	U
>99	<0.5	<0.09	<0.10	<0.08	<0.06	<0.001	<0.01



19

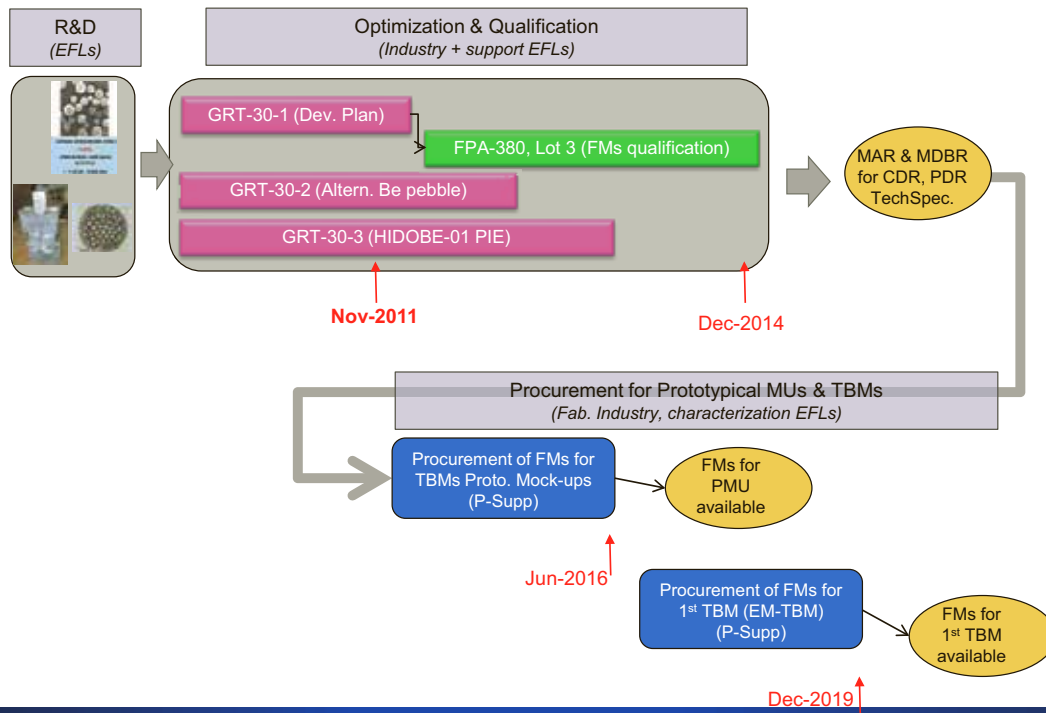
Development and further optimization of fabrication routes

- Optimization of ceramic and Be pebbles fabrication processes with respect to the production yield, pebbles' characteristics and mechanical properties
- Scaling of the laboratory developed production methods
- Production of Be pebbles with small grains (tritium release)
- Development of a suitable fabrication route for Be-alloy material(s) (e.g. Be₁₂Ti)
- Development of an alternative fabrication route for Be pebbles
- Control of undesired impurities level in the functional materials (FM) (e.g. Co, U, Bi)
- In general, availability of Be materials for DEMO and future FPR

Availability of the materials properties needed for a proper TBMs design

- Effect of neutron irradiation on thermo-mechanical properties of Be pebbles and Be pebble bed as function of irradiation temperature and neutron dose taking into account material swelling, thermal expansion and thermal creep
- Tritium retention/release characteristics as a function of irradiation temperature, neutron dose, purge gas chemistry, material properties
- Compatibility with structure material under neutron irradiation
- Interaction of air/steam with Be/Be-alloy pebbles
- Thermal conductivity in pebble beds under compressive loads

20



TBMs functional materials (Be, ceramic breeder, Pb-Li) development/qualification [grant F4E-2009-GRT-030]:

- **Action 1:** Elaboration of the Development /qualification /procurement plan for functional materials
- **Action 2:** Screening of an alternative production route/capacity for Be pebbles
 - **Task 1:** Description/screening of an alternative production route/capacity for Be pebbles and fabrication of a small batch of material for preliminary characterization
 - **Task 2:** Preliminary characterization of the produced the Be material
 - **Task 3:** Characterization of Be pebbles supplied by **Bochvar Institute, RF** [Be pebbles produced by ball milling process using vacuum hot pressed (VHP) Be billets of different grain sizes (10-30 µm, 30-60 µm and >100 µm) as an initial Be material]
- **Action 3:** Post Irradiation Examination of Be materials irradiated in HIDOBE-01 campaign



Framework Partnership Agreement for the Activities in support of the conceptual and preliminary design of the European Test Blanket Systems (F4E-FPA-380)

- **Action 3: Qualification of Functional Materials for TBM Applications** → duration 48 months, Specific grants, max. F4E contribution 2.3M€
 - Optimization/adjustment of the production processes/routes for Be materials in order to improve their properties/characteristics and to allow their scalability to an industrial application level.
 - Characterization of the newly produced Be materials in the terms of geometrical characteristics, chemical and phase composition, porosity, density, microstructure (e.g. revealing a typical grain size), mechanical properties (e.g. mechanical strength, ductility), pebble bed characteristics (e.g. pebble bed density, packing factor), interaction with air/steam and tritium release characteristics.
 - Preliminary qualification of the Be materials under TBM-relevant operative conditions (i.e. temperatures, loadings, purge gas flow and chemistry, neutron irradiation parameters) implying in design and realization of newly identified tests/experiments focused on determination of missing properties and characteristics, and on the materials performance.
 - Evaluation of the performed tests/experiments, including the irradiation campaigns performed under the past EFDA framework (e.g. PIE of HIDOBE, HICU campaign), aiming at determination of the Be materials properties and characteristics (e.g. microstructure, geometrical, chemical and mechanical properties, pebble beds thermo-mechanical behavior, compatibility with structure material, performance under neutron irradiation like swelling, creep, thermal conductivity, tritium retention and release characteristics).
 - Update of the existing materials' properties database in the form of MDBRs (Material Database Report) and MAR (Material Assessment Report) to be used for TBMs design qualification.



HIDOBE irradiation program & PIE

Objectives :

- (i) Beryllium behaviour under DEMO relevant He/dpa ratios and temperatures
- (ii) Tritium inventory as affected by microstructure, swelling, creep
- (iii) Pebble beds thermo-mechanical behaviour under neutron irradiation

HIDOBE-01 irradiation rig:

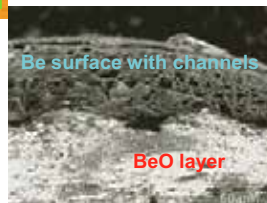
3000 appm He (DEMO: ~18,000 appm)
Irradiation completed - 665 FPD
Start of PIE in 2010, completed 2012 (F4E-GRT-030/A3)

HIDOBE-02 irradiation rig:

6000 appm He
Irradiation completed - 1274 FPD
PIE planned for 2013-14 (F4E-FPA-380/A3)



OM & SEM - Be pebble $T_{irr} = 675^{\circ}C$

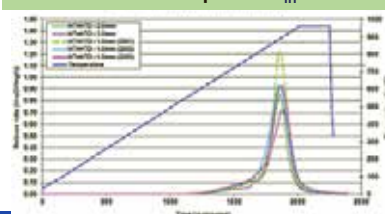


Post Irradiation Examination:

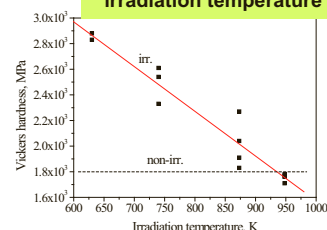
- Dimensional stability, porosity
- Microstructure (OM, SEM, TEM)
- Tritium release (TPD)
- Mechanical / thermal properties
- Interaction with air & steam



Tritium release - Be pebble $T_{irr} = 425^{\circ}C$



Vickers hardness versus irradiation temperature



Unconstrained pebbles					He Pycno	Tritium release			SEM + OM		TEM	CREEP	Oxidation	Chem. Analysis
Grade	Supplier	name	specs	Temperatures	NRG	NRG	KIT	UL	NRG	KIT	KIT	KIT	ITN	ITN
7	EU/FZK	NGK pebbles	0.5 mm	425, 525, 650, 750	4	2	8	3	2	2			2	2
8	EU/FZK	NGK pebbles	1.0 mm (2003)	425, 525, 650, 750	4	4		2	2	2	4	4	2	2
9	EU/FZK	NGK pebbles	1.0 mm (2001)	425, 525, 650, 750	4	2	8	3	2	2	4			
10	EU/FZK	NGK pebbles	2.0 mm	425, 525, 650, 750	4	8		2	2	2	4	4		
Total amount of measurements					16	16	16	10	8	8	12	8	4	4

Constrained pebble beds					Dimensions + Mass	He Pycno	Tritium release			SEM + OM		
Grade	Supplier	name	specs	Temperatures	NRG	NRG	NRG	KIT	UL	NRG	KIT	
7	EU/FZK	NGK pebbles	0.5 mm	425, 525, 650, 750	4	4		4			1	1
8	EU/FZK	NGK pebbles	1.0 mm (2003)	425, 525, 650, 750	7	7	4				2	2
9	EU/FZK	NGK pebbles	1.0 mm (2001)	425, 525, 650, 750	3	3		4			1	1
10	EU/FZK	NGK pebbles	2.0 mm	425, 525, 650, 750	4	4	4				1	1
Total amount of measurements					18	18	8	8	0	5	5	

Beryllides					Dimensions + Mass	He Pycno	Tritium release		Oxidation	Chem. Analysis	XRD
Grade	Supplier	name	specs	Temperatures	NRG	NRG	NRG	KIT	ITN	ITN	NRG
11	JP/JAERI	Be Electrode	ø8x2	425, 525, 650, 750	4	4	2	2	1	1	2
12	JP/JAERI	Be12Ti-5at%Ti	ø8x2	425, 525, 650, 750	8	8	2	2	1	1	4
13	JP/JAERI	Be12Ti-7at%Ti	ø8x2	425, 525, 650, 750	8	8	2	2	1	1	2
Total amount of measurements					20	20	6	6	3	3	8

Characterization of Be pebbles supplied by Bochvar Institute, Russian Federation

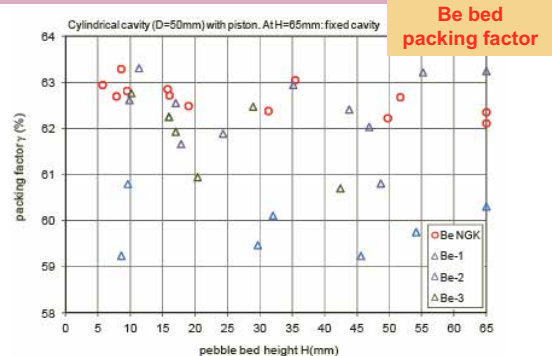
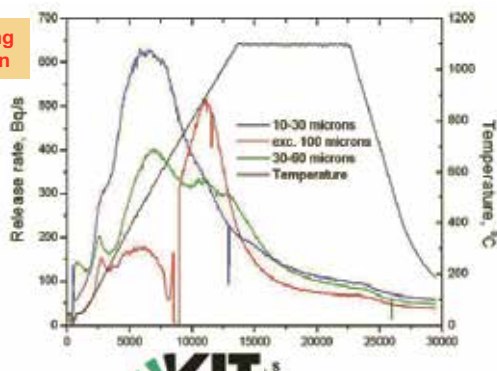
Be pebbles produced by ball milling process using vacuum hot pressed (VHP) Be billets of different grain sizes (10-30 µm, 30-60 µm and >100 µm) as an initial Be material



Be pebbles (10-30 µm grain size)



TPD; heating rate 5 K/min



Preliminary comparison of various properties of Be pebbles from point of view of TBM application

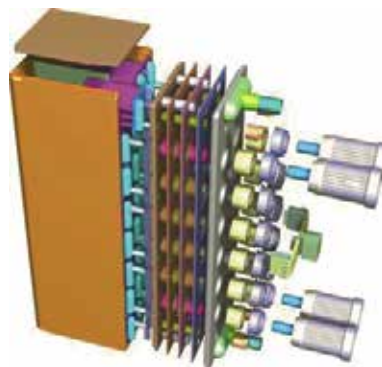
Characteristic of material/Material batch	Be pebbles with the grain sizes of 10-30 µm	Be pebbles with the grain sizes of 30-60 µm	Be pebbles with the grain sizes exceeding 100 µm
Packing density	best	worst	best
Chemical composition	best	medium	worst
Tritium release measurement	best	medium	worst
Material density	medium	best	worst
Pebble size, mm	1.32	1.34	1.37

- **Beryllium multiplier materials**

- The 1 mm Be pebbles at present the reference multiplier material for the EU HCPB concept; will be used in the first HCPB TBMs,
- At later stages of ITER operation beryllides (e.g. Be₁₂Ti) could be tested when the level of maturity achieved,
- HIDOBE-01 and HIDOBE-02 irradiation results → a crucial milestone for the qualification of the reference Be material
- Further development and qualification of Be materials in the view of Conceptual Design Review (CDR) and Preliminary Design Review (PDR) with ITER IO (by 2014/2015)
- Update of MDBR and MAR; finalization of the Technical Specification for Functional Materials procurement
- Procurement and supply of Functional Materials (incl. Be pebbles) for TBM prototypical mock-up by Jun-2016
- Procurement and supply of Functional Materials (incl. Be pebbles) for the 1st EM-TBM by Dec-2019

27

Thank you for your attention



28



NRG CONTRIBUTION TO THE F4E GRT030 ACTION 3 HIDOBE-01 PIE

COORDINATION AND RESULTS

A.V. Fedorov, S. van Til,
A.J. Magielsen, M. Stijkel,
H.L. Cobussen, V.M. Smit-Groen

BEWS-10,
Karlsruhe

Outline



- **Introduction. HIDOBE-01 and HIDOBE-02 experiments**
 - Design
 - Irradiation history
- **HIDOBE-1 PIE (Post Irradiation Examination)**
 - Coordination (NRG, KIT, AEUL, ITN). Sample matrix
 - Results
 - Dimensions and density (emersion & picnometry)
 - Tritium release
 - XRD
 - Microscopy (OM and SEM)
- **Conclusions**

HIDOBE objectives



European programme (EFDA) and IEA collaboration with RF and JP:

- Irradiation behaviour of Beryllium under DEMO blanket relevant dpa/He ratio's and temperatures
- Study tritium inventory and influence of swelling, creep and microstructure on tritium inventory
- Study thermo-mechanical behaviour under irradiation
- **Achieve 30% of DEMO End-Of-Life Helium production**

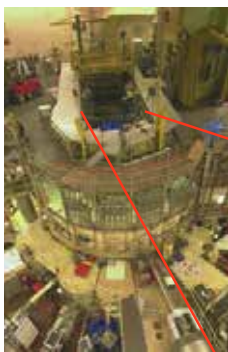
	HIDOBE -01	HIDOBE -02
Fluence ($E > 0.1 \text{ MeV } 10^{26} \text{ n/m}^2$)	1.5	3
Fluence ($E > 1 \text{ MeV } 10^{26} \text{ n/m}^2$)	0.7	1.4
Helium production in Be (appm)	3000	6000
Tritium production in Be (appm)	250	700
Neutron damage in Be (dpa)	17.9	35.8
Helium production in Be-Ti (appm)	2740	5480
Tritium production in Be-Ti (appm)	235	562
Neutron damage in Be-Ti (dpa)	19.5	38.9
Temperatures (°C)	425, 525, 650, 750	425, 525, 650, 750

Irradiation	649 FPD Oct2007	1274 FPD Aug 2011
PIE	2009-2012	

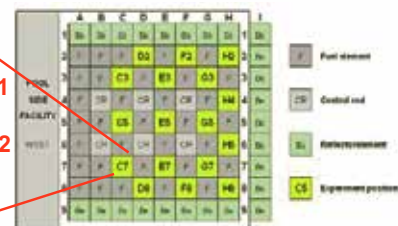
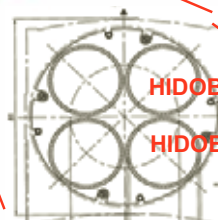
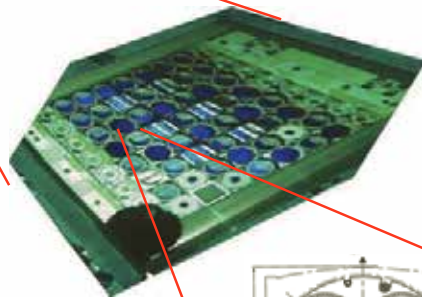
F4E-2009-GRT-030 (Action-1) Task-2 "Development / Qualification / Procurement Plan for Be pebble materials"

Distance, cm	Neutron flux, $\text{cm}^{-2}\text{s}^{-1}$	Temp. °C	Damage, dpa/fpy	He, appm/fpy	T, appm/fpy
2.3 – 3.8	$1.06 \cdot 10^{15}$	615		17	5700
3.8 – 6.8	$1.03 \cdot 10^{15}$		16.5	5539	84
6.8 – 9.8	$0.96 \cdot 10^{15}$		15.4	5162	78
9.8 – 12.8	$0.88 \cdot 10^{15}$		14.1	4732	71
12.8 – 15.8	$0.79 \cdot 10^{15}$		12.7	4248	64
15.8 – 18.8	$0.70 \cdot 10^{15}$		11.2	3764	57
18.8 – 21.8	$0.61 \cdot 10^{15}$		9.8	3280	49
21.8 – 24.8	$0.53 \cdot 10^{15}$		8.5	2850	43
24.8 – 27.8	$0.46 \cdot 10^{15}$		7.4	2474	37
27.8 – 30.8	$0.39 \cdot 10^{15}$		6.3	2097	32
30.8 – 33.8	$0.33 \cdot 10^{15}$		5.3	1775	27
33.8 – 36.8	$0.28 \cdot 10^{15}$		4.5	1506	23
36.8 – 39.8	$0.24 \cdot 10^{15}$		3.8	1291	19
39.8 – 42.8	$0.20 \cdot 10^{15}$		3.2	1075	16
42.8 – 45.8	$0.18 \cdot 10^{15}$	400	2.9	968	15

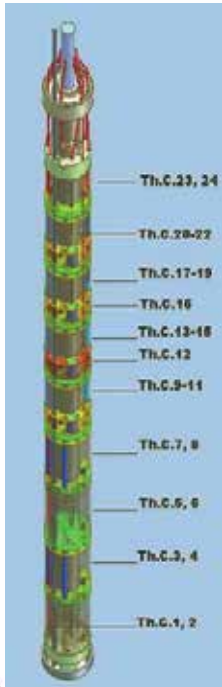
HIDOBE irradiation in HFR, Petten



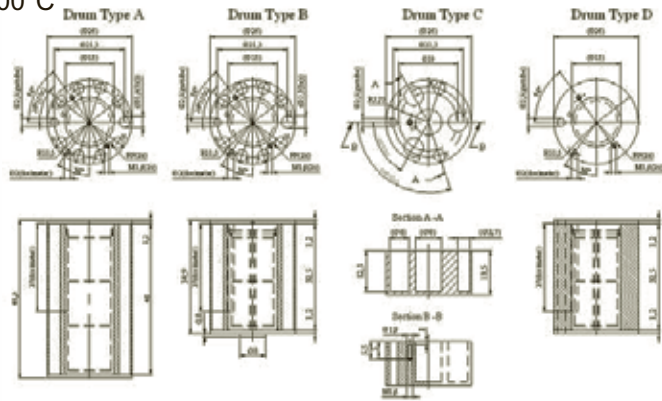
- Irradiation in C7 in two Quattro channels (diameter about 29 mm and about 400 mm total stack height)
- In C7 position $\phi (E_n > 1.0 \text{ MeV})$ is $1.6 \times 10^{18} \text{ n m}^{-2}\text{s}^{-1}$, resulting in $3.3 \times 10^{24} \text{ n m}^{-2}$ per cycle.



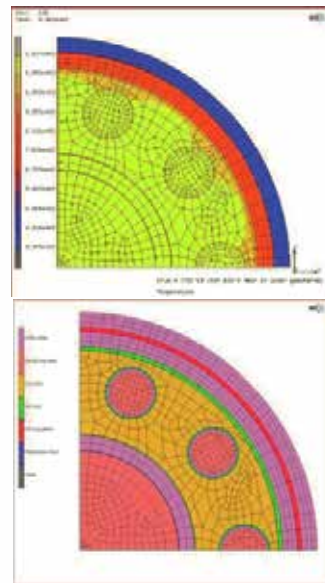
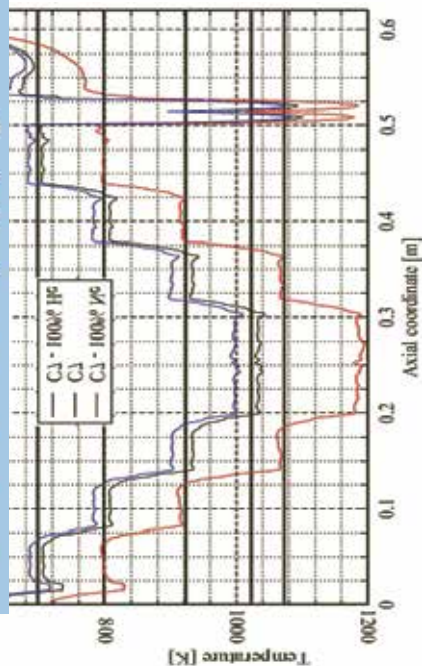
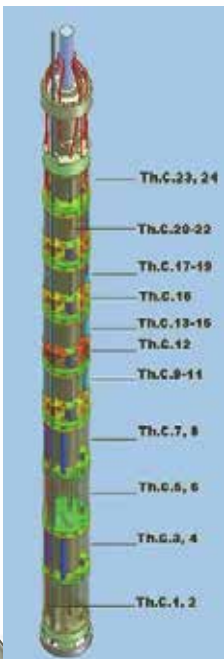
Design of irradiation assembly



- 13 drums in 9 sections separated by heat barriers/radiation shields
- 24 thermocouples distributed in axial and radial direction
- Temperature control by gas mixtures (and gamma heating)
- 4 temperature levels (not independently controlled)
 - 400 to 425°C
 - 525 to 550°C
 - 650 to 700°C
 - 750 to 800°C



Temperature field calculations



Test matrix



	Supplier	Name	BeO (wt%)	Density (g/cm3)	Specimen sizes (mm)	specification
1	RF/VNIINM	DDR grade	3.5-4.0	1.88	Ø6x2, Ø3.5x6, Ø3.5x2.5	grain size 5-8 micron
2	RF/VNIINM	TIP grade	1.2-1.4	1.86	Ø6x2, Ø3.5x6, Ø3.5x2.5	grain size 10-14 micron
3	RF/VNIINM	TIP-56 grade	0.4-0.6	1.85	Ø6x2, Ø3.5x6, Ø3.5x2.5	grain size 20-25 micron
4	RF/VNIINM	TIP-200 grade	0.2-0.3	1.85	Ø6x2, Ø3.5x6, Ø3.5x2.5	grain size 55-60 micron
5	RF/VNIINM	Porous Be	1.5	1.44	Ø6x2, Ø3.5x6, Ø3.5x2.5	~20% porosity
6	RF/VNIINM	Porous Be	1.5	1.25	Ø6x2, Ø3.5x6, Ø3.5x2.5	~30% porosity
7	EU/FZK	NGK pebbles	0.36		0.5	pebbles
8	EU/FZK	NGK pebbles	0.36		1.0	pebbles (2003)
9	EU/FZK	NGK pebbles			1.0	pebbles (2001)
10	EU/FZK	NGK pebbles	0.36		2.0	pebbles
11	JP/JAERI	Be Electrode	0.02	1.84	Ø8x2	discs
12	JP/JAERI	Be12Ti-5at%Ti	0.26	2.12	Ø8x2	discs
13	JP/JAERI	Be12Ti-7at%Ti	0.27	2.25	Ø8x2	discs
14	JP/JAERI	JP pebble 1	0.21		1.0	standard
15	JP/JAERI	JP pebble 2	0.22		1.0	standard
16	JP/JAERI	JP pebble 3	0.23		1.0	low cost
17	JP/JAERI	JP pebble 4	1.10		1.0	low cost
18	JP/JAERI	JP pebble 5	1.35		1.0	low cost

* grade 1 to 4, one specimen D3.5x6 and D3.5x2.5 will be covered with BeO coating, 5 um
 * grade 1 to 4, two TEM specimens will be cold worked

PIE Plan: Test matrix F4E GRT030 ACTION 3

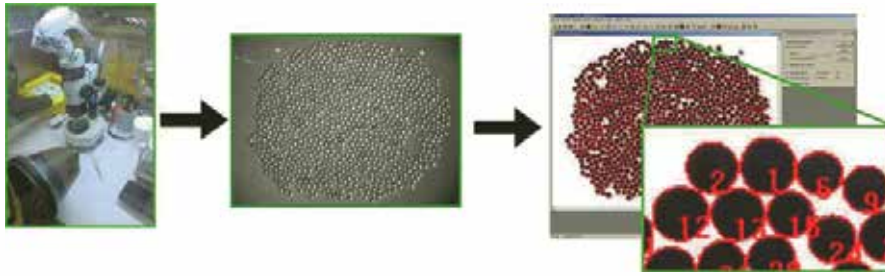


Unconstrained pebbles					Dimensions + Mass	He Pycno	Tritium release			SEM + OM			TEM	CREEP	Oxidation	Chem. Analysis	
Grade	Supplier	name	specs	Temperatures	NRG	NRG	NRG	KIT	UL	NRG	KIT	KIT	NRG	KIT	ITN	ITN	
7	EU/FZK	NGK pebbles	0.5 mm	425, 525, 650, 750	4	4	2	8	3	2	2					2	2
8	EU/FZK	NGK pebbles	1.0 mm (2003)	425, 525, 650, 750	4	4	4		2	2	2	4	4	4	2	2	
9	EU/FZK	NGK pebbles	1.0 mm (2001)	425, 525, 650, 750	4	4	2	8	3	2	2	4					
10	EU/FZK	NGK pebbles	2.0 mm	425, 525, 650, 750	4	4	8		2	2	2	4	4	4			
Total amount of measurements (not in GRT-030)						16	16	16	10	8	8	12	8	4	4		

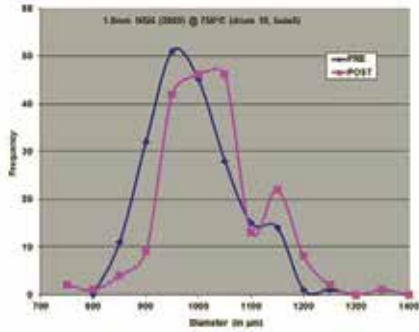
Constrained pebble beds					Dimensions + Mass	He Pycno	Tritium release			SEM + OM		
Grade	Supplier	name	specs	Temperatures	NRG	NRG	NRG	KIT	UL	NRG	KIT	
7	EU/FZK	NGK pebbles	0.5 mm	425, 525, 650, 750	4	4		4			1	1
8	EU/FZK	NGK pebbles	1.0 mm (2003)	425, 525, 650, 750	7	7	4				2	2
9	EU/FZK	NGK pebbles	1.0 mm (2001)	425, 525, 650, 750	3	3		4			1	1
10	EU/FZK	NGK pebbles	2.0 mm	425, 525, 650, 750	4	4	4				1	1
Total amount of measurements					18	18	8	8	0	5	5	

Beryllides					Dimensions + Mass	He Pycno	Tritium release		Oxidation	Chem. Analysis	XRD
Grade	Supplier	name	specs	Temperatures	NRG	NRG	NRG	KIT	ITN	ITN	NRG
11	JP/JAERI	Be Electrode	Ø 8 x 2	425, 525, 650, 750	4	4	2	2	1	1	2
12	JP/JAERI	Be12Ti-5at%Ti	Ø 8 x 2	425, 525, 650, 750	8	8	2	2	1	1	4
13	JP/JAERI	Be12Ti-7at%Ti	Ø 8 x 2	425, 525, 650, 750	8	8	2	2	1	1	2
Total amount of measurements					20	20	6	6	3	3	8

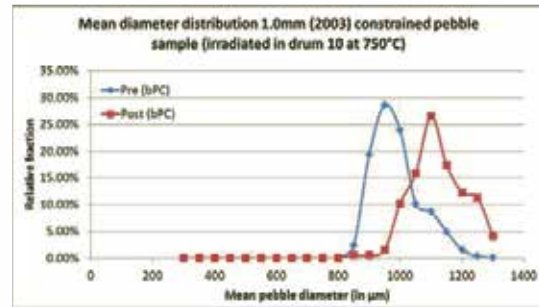
Geometric dimensions



unconstrained



constrained



unconstrained pebbles



1.0mm (2001) NGK



Irradiated at

Non-irradiated 425°C 525°C 650°C 750°C

2.0mm NGK



beryllides

Be-Be5Ti-Be5Ti - 525

Be5Ti - 650

Be5Ti - 750

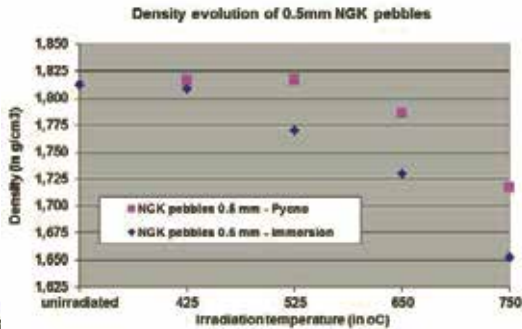


Density measurements. Immersion and Pycnometry.

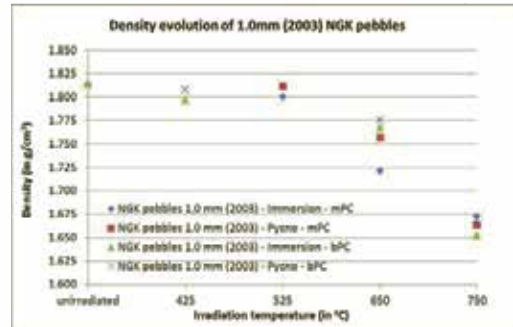


porosity	immersion	pycnometry
open	yes	no
closed	yes	yes

unconstrained



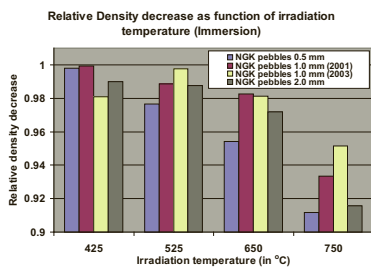
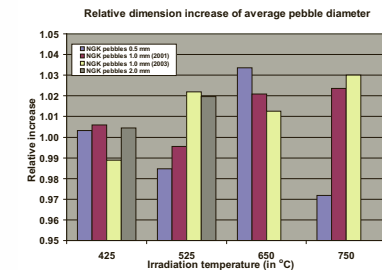
constrained



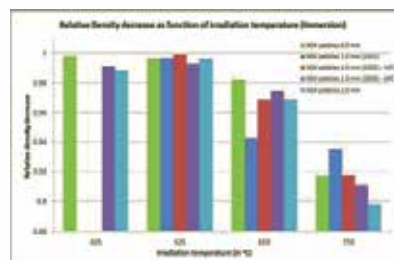
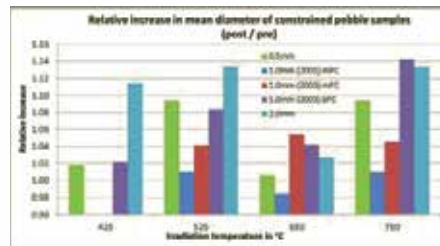
Dimensions and density of pebbles



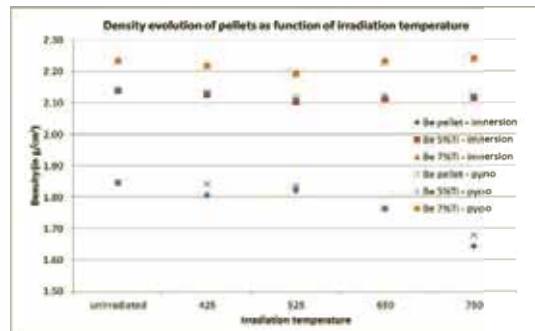
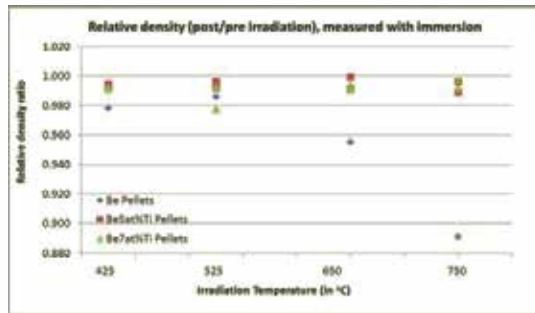
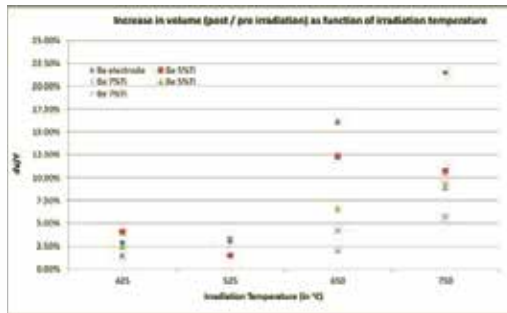
unconstrained



constrained



Dimensions and density of beryllides

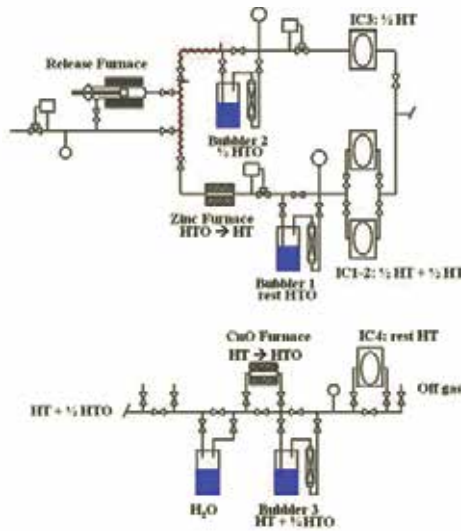


Conclusions on dimensions and density measurements



- Unconstrained pebbles showed moderate swelling which increased with the irradiation temperature (< 3% at 750°C). In accordance, the pebble density measured by immersion and pycnometry decreased with the irradiation temperature.
- Constrained pebbles showed considerably higher swelling, up to 14 %, for all grades, as compared to unconstrained pebbles.
- Beryllides showed significantly less swelling compared to the reference beryllium sample: ~12% versus 22% at 750°C. However, this moderate swelling of beryllides did not result in any measurable decrease in density.

Tritium release measurements



Temperature Programmed Desorption (TPD)

- Heating ramp of 0.5°C/min up to ~950°C
- Purged with reference gas (He+0.1%H₂)
- Distinction between HT and HTO
- Online measurement with ICs
- Cumulative release with bubblers → LSC
- Comparison with 'nuclear' measurements + calculations

Irradiation temperature	'thermal' fluence	'fast' fluence	N _{dpa} ¹⁾ (in Be)	N _{He} ²⁾ [appm]	N _{3H} ³⁾ [appm]
	Φ _{Co} [10 ²⁵ m ⁻²]	Φ _{E>1.0 MeV} [10 ²⁵ m ⁻²]			
750 °C	6.50	8.92	18.1	2950	285
650 °C	6.02	8.07	16.3	2680	252
525 °C	5.21	6.94	13.9	2300	213
425 °C	4.12	5.69	11.3	1890	176

¹⁾ Displacements per atom (N_{dpa}) produced in Be

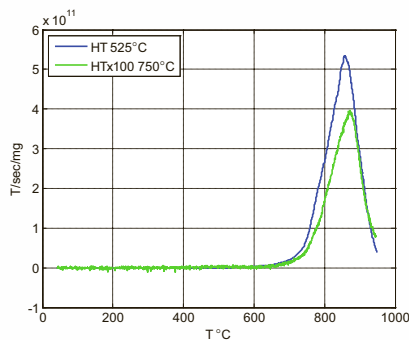
²⁾ amount of Helium produced (N_{He})

³⁾ amount of Tritium produced (N_{3H})

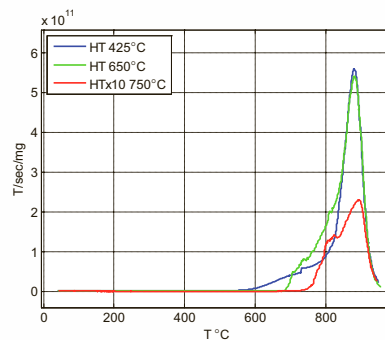
TPD results on unconstrained pebbles



0.5 mm pebbles



2 mm pebbles



Observations:

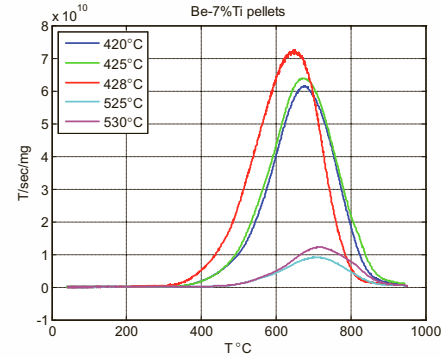
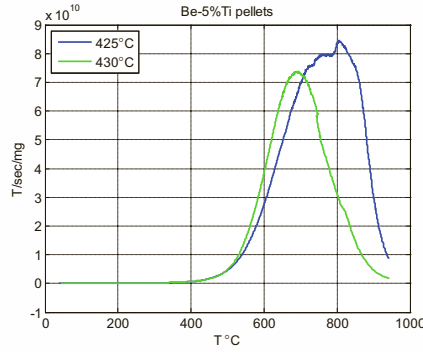
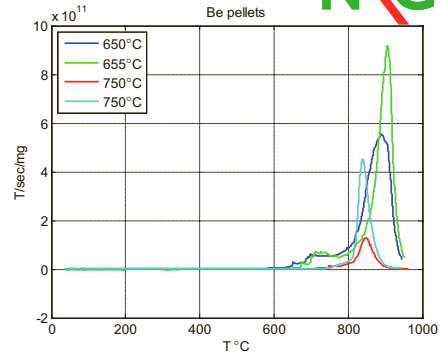
- Two contributions are identified:
 - 1) irregular bursts at 600-820 °C,
 - 2) well defined high temperature release at 880 °C
- Position of the high temperature peak (880 °C) does not depend on the tritium inventory and apparently defined by helium release
- The 0.5 mm pebbles (consisting of 1-2 grains) do not show the burst release at 600-820 °C

TPD results on beryllium and beryllides pellets



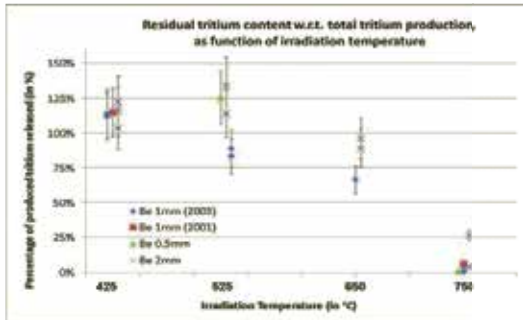
Observations:

- Tritium release in Be pellets proceeds in the way similar to Be pebbles: one well defined peak at ~850-900 °C, preceded by moderate irregular release above 600-700 °C .
- In case of beryllides the release peak becomes broader and shifts to 700-800 °C

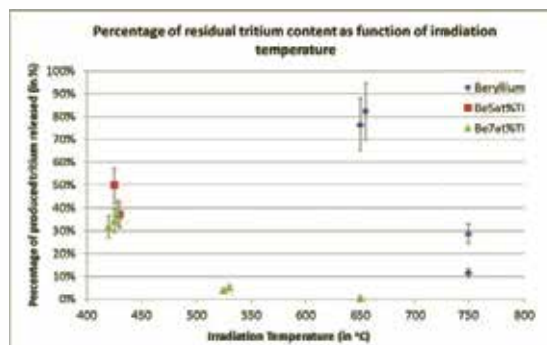
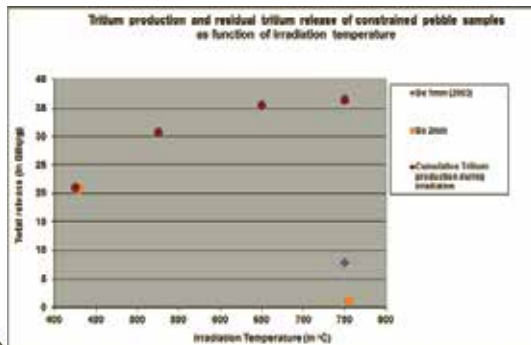


17

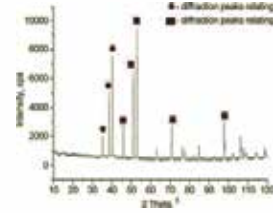
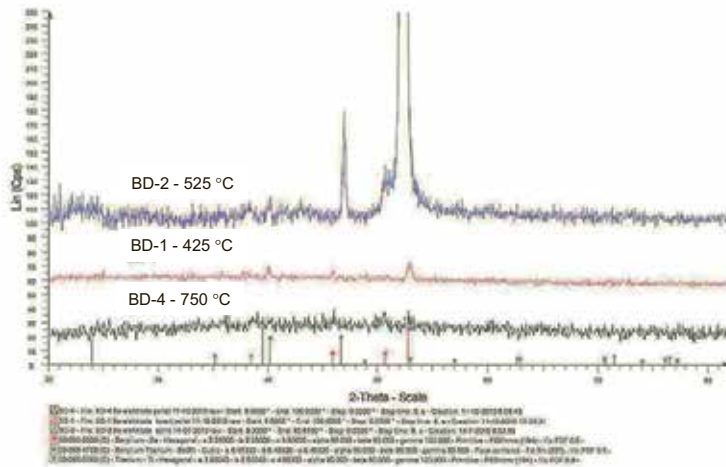
Tritium retention



- Tritium retention in Be pebbles/pellets is about 100% below 525°C and decreases to 75% at 650 °C, and to only few percent at 750 °C
- Both BeTi grades show ≤40% retention at 425°C and virtually no retention at higher temperatures



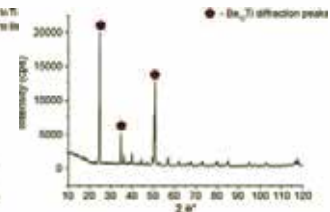
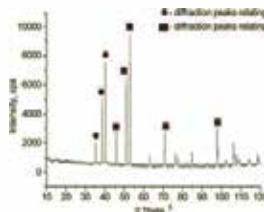
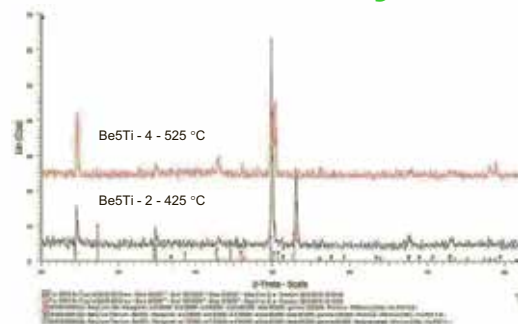
XRD results: Be pellets



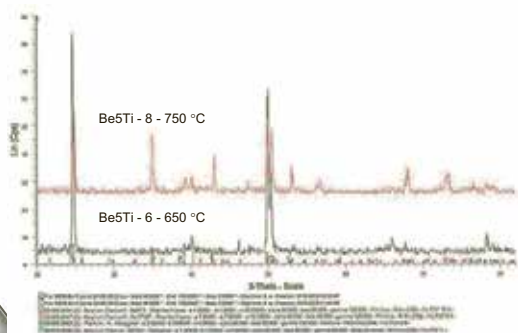
P. Kurinsky et al., JNM 367(2007) 1069

Lattice damage produced during irradiation (15-20 dpa) is expected to be annealed at higher irradiation temperatures

XRD results: Beryllides



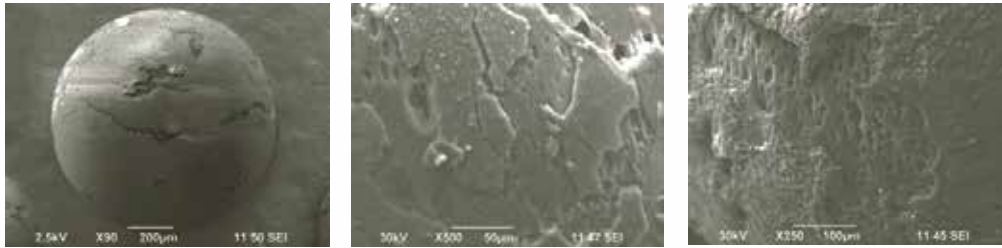
P. Kurinsky et al., JNM 367(2007) 1069



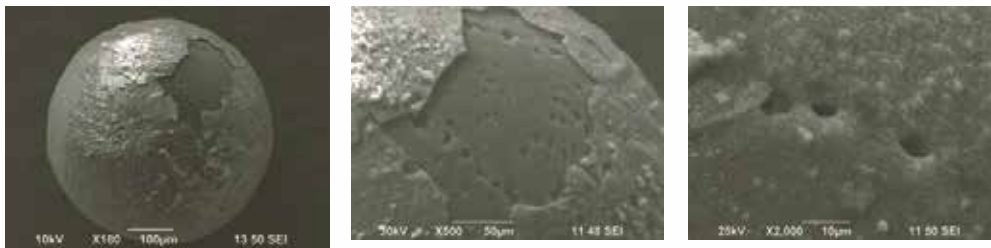
SEM results. State of the surface



1 mm pebbles, $T_{irr} = 525\text{ }^{\circ}\text{C}$



2 mm pebbles, $T_{irr} = 650\text{ }^{\circ}\text{C}$

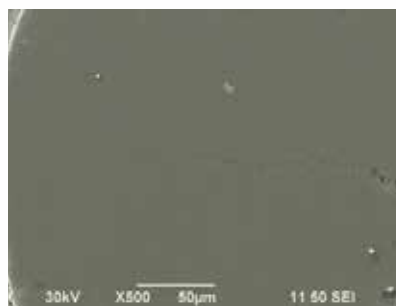


21

OM&SEM results: Interconnected bubbles



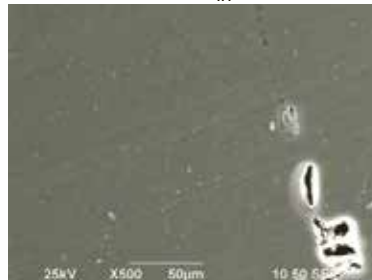
0.5 mm pebbles, $T_{irr} = 650\text{ }^{\circ}\text{C}$



1 mm pebbles, $T_{irr} = 525\text{ }^{\circ}\text{C}$



2 mm pebbles, $T_{irr} = 750\text{ }^{\circ}\text{C}$

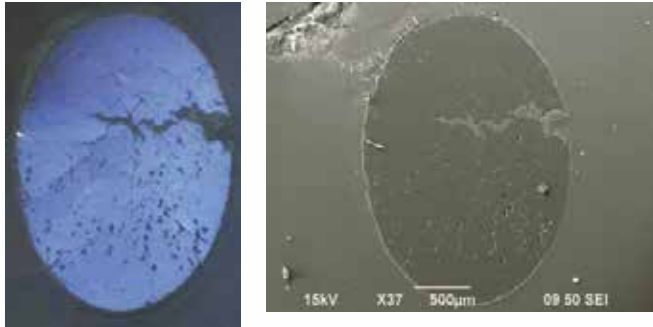


22

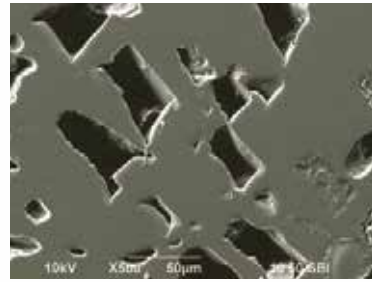
OM&SEM results: Network of channels



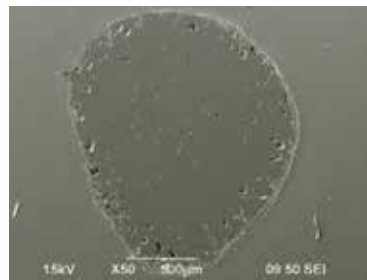
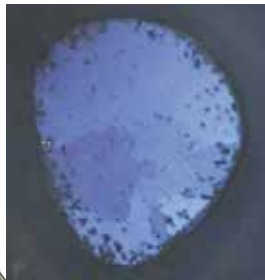
2 mm pebbles, $T_{irr} = 750\text{ }^{\circ}\text{C}$



1 mm pebbles, $T_{irr} = 525\text{ }^{\circ}\text{C}$



2 mm pebbles, $T_{irr} = 750\text{ }^{\circ}\text{C}$



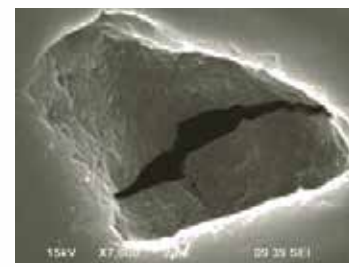
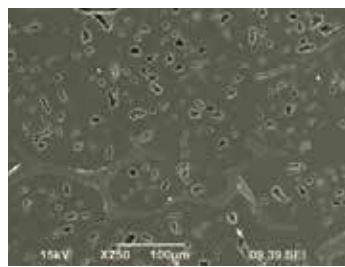
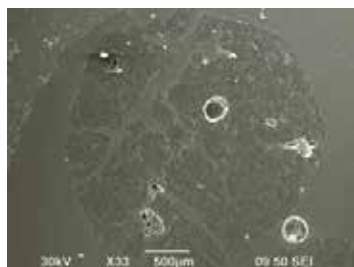
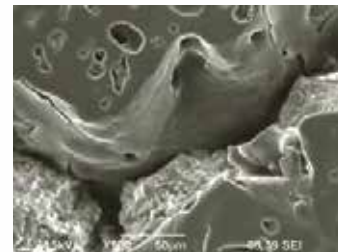
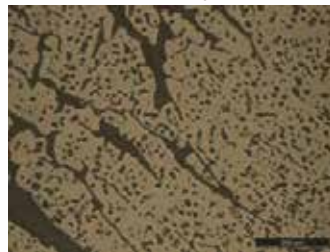
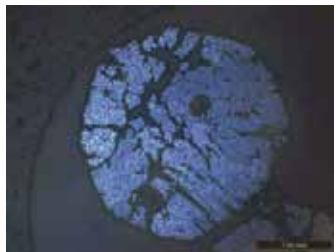
same morphology?



OM&SEM results: irradiation and TPD



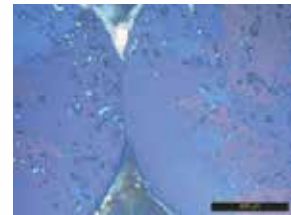
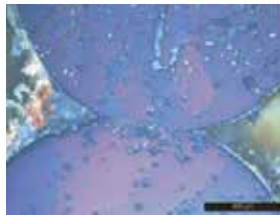
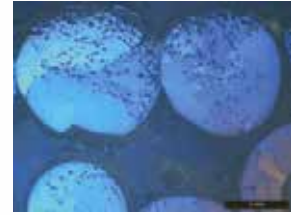
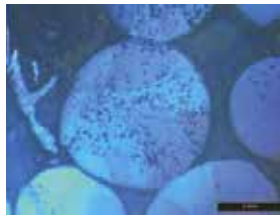
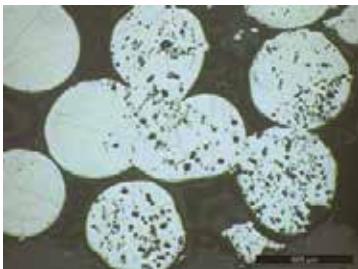
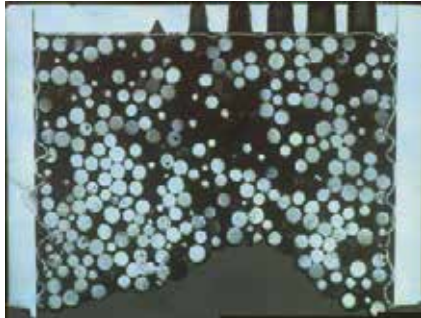
2 mm pebbles, $T_{irr} = 525\text{ }^{\circ}\text{C}$ + TPD at $T_{max} = 900\text{ }^{\circ}\text{C}$



OM&SEM results: constrained pebbles



2 mm pebbles, $T_{irr} = 750\text{ }^{\circ}\text{C}$

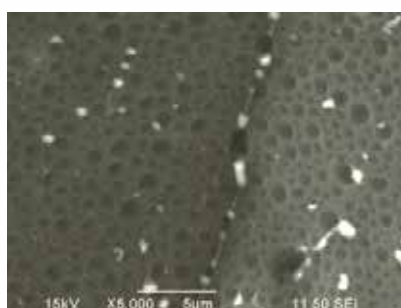


25

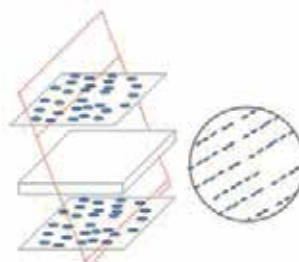
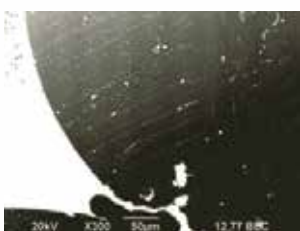
SEM results: constrained pebbles



1 mm pebbles, $T_{irr} = 750\text{ }^{\circ}\text{C}$



PBA, TE#3, $T_{max} = 500\text{-}590\text{ }^{\circ}\text{C}$



SEM observation can be explained if we assume that bubbles are formed in the basal planes separated with $\sim 10\text{-}20\text{ }\mu\text{m}$ bubble-free slabs

26

Conclusions-1/2



1. HIDOBE-01 PIE program gas generated fast amount of experimental data on beryllium behavior under neutron irradiation at the irradiation following irradiation conditions:
 - Helium production ~ 3000 appm (6000 appm per fpy at HCPB DEMO)
 - Tritium production ~ 175-300 appm (50-100 appm per fpy at HCPB DEMO)
 - Temperatures: 425, 525, 650 and 750 °C (300-650 °C in HCPB DEMO)
 - Damage : 11-18 dpa (3-17 dpa per fpy in HCPB DEMO)
2. From all irradiated materials the PIE test matrix (F4E GRT030 Action 3) included NGK (Europe) pebbles (4 grades, constrained and un-constrained), and Be, Be-5%Ti, and B-7%Ti pellets (Japan).
3. Dimensions/density measurements (geometrical, immersion, pycnometry) have demonstrated:
 - moderated swelling of unconstrained pebbles: < 3% (diameter) at 750°C
 - higher swelling of constrained pebbles: < 14% (diameter) at 750°C
 - low swelling for beryllide pellets: < 12% (volume) compared to 22% of reference Be pellet
 - for all materials swelling increased with the irradiation temperature
 - for all materials/grades (except for beryllides) density, measured by immersion and pycnometry, in correspondence with swelling results, decreased with the irradiation temperature.

Conclusions-2/2



4. TPD measurements have shown that:
 - tritium retention in Be pebbles/pellets is about 100% below 525 °C, decreases to 75% at 650 °C, and vanishes to only few per cent at 750 °C.
 - Both BeTi grades show ≤40% of T retention at 425 °C and virtually no retention at higher temperatures
 - all TPD spectra measured on Be pebbles/pellets are dominated by one peak at ~880 °C. The peak position is very little affected the amount of released tritium and irradiation temperature
 - In TPD spectra measured on beryllides the release peak is shifted to lower temperatures: 600-700 °C.
5. In XRD spectra the Be-hcp and Be₁₂Ti were identified. Qualitatively the contribution of the crystalline phases increase with the irradiated at higher temperatures, which suggests that the lattice damage (11-18 dpa) is annealed during irradiation.
6. OM and SEM observations can be summarized as follows:
 - For all irradiation temperatures except for 425 °C the oxide layer is cracked, chipped off, perforated with holes/channels
 - Individual chains of bubbles observed at 425, 550 °C develop into a broad network of channels with walls of hexagonal shape (which suggests recrystallization). These features are most dramatically demonstrated at the pebbles investigated after the TPD studies (maximum annealing temperature 900 °C).
 - Development of this network of channels is apparently governed by helium transport and defines the position of the tritium release peak in the TPD spectra.

THANK YOU FOR ATTENTION

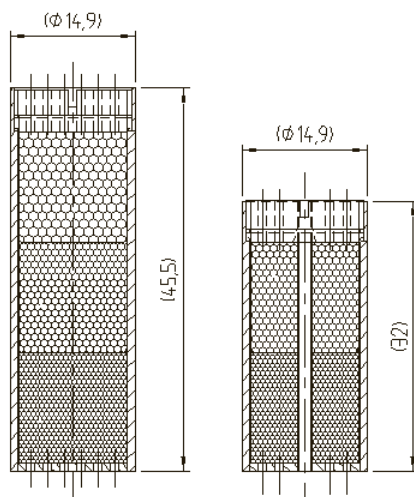


29

Microscopy constrained beds



5 pebble beds from two temperature zones (3x 750 and 2x 525)



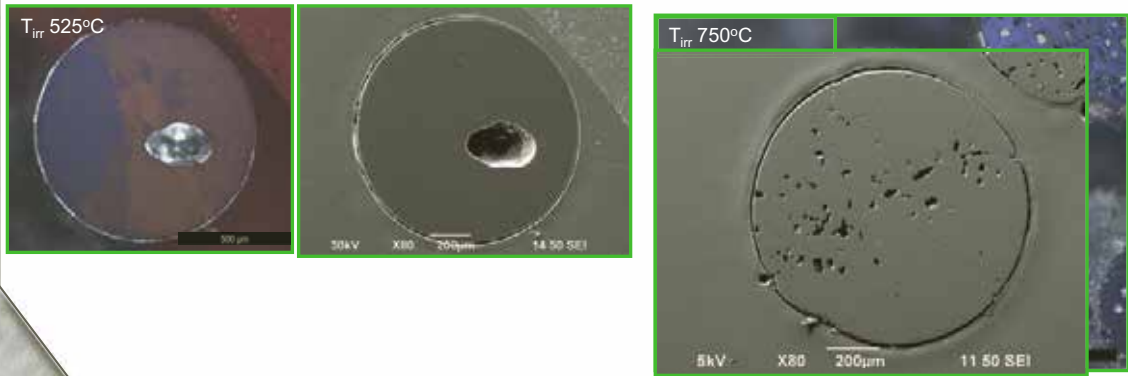
Sample code	SEM code	Grade	T irradiation, °C
Unconstrained			
38sPC	0140-1A	0.5mm	525
2sPC	0140-1B		650
43sPC	0140-2A	1.0mm (2001)	425
42sPC	0140-2B		525
46sPC	0140-3A	1.0mm (2003)	525
9sPC	0140-3B		750
14sPC	0140-4A	2.0mm	650
13sPC	0140-4B		750
Constrained			
2mPC1	0160-6E	1.0mm (2003)	525
2mPC2	0160-6E	1.0mm (2001)	
1bPC3	0160-2A	0.5mm	750
1bPC2	0160-2B	1.0mm (2003)	
1bPC1	0160-2C	2.0mm	

Microscopy cross section



'425°C'- and '525°C'- samples virtually unchanged.
Low amount of small pores in 525°C samples

Show grains with polarized light microscopy,
then use SEM for high resolution images

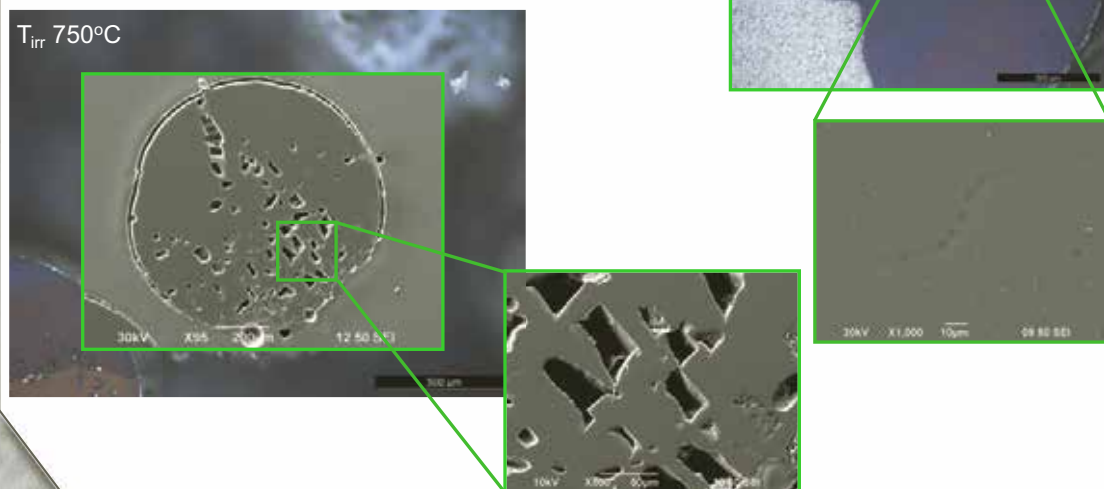


Microscopy cross section (2)



Around $T_{irr} 650^{\circ}C$ varying porosity, at least
coalescence of bubbles at grain boundaries.

$T_{irr} 750^{\circ}C$ show large pores, often rectangular



Microscopy cross section (3)

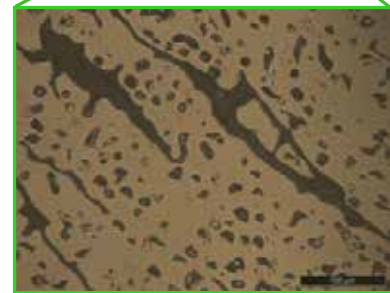
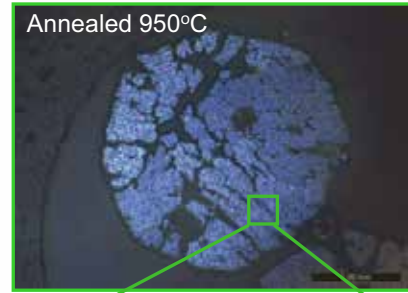


Any sample, annealed to 950°C in out-of-pile tritium release, show high density porosity and intensive cracking

Relation between stresses induced by swelling, He bubbles and vacancy mobility
 → overpressurized bubbles
 → local stresses induce vacancy mobility?

No clear explanation for loss of 'rectangular' pores between 750 and 950°C, but dependency on t and T of anneal seems evident

Possible crystallization of pores at long t (during two year irradiation)



'narrow' pore distribution ~15µm

Dismantling: Extracting issues



Swelling after 2 year irradiation	Swelling [%]	Pill diameter		
		3.5	6	8
T-zone				
425	4	3.70	6.30	8.40
525	5	3.70	6.30	8.40
650	6	3.90	6.50	8.60
750	7	3.90	6.60	8.70

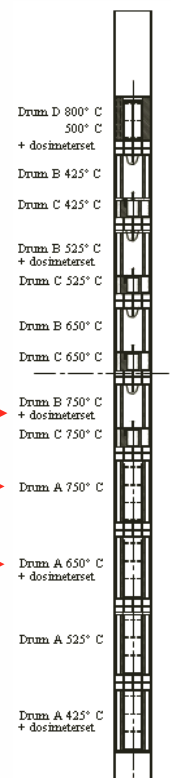
ALL pellets in drums 8 and 9 stuck

~75% (18/24) 2.0 mm pebbles in drum 10 stuck

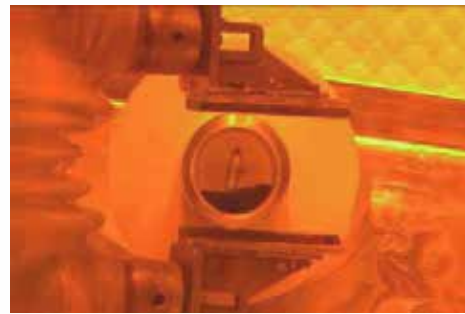
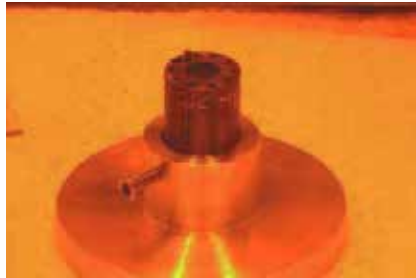
~45% (9/21) 2.0 mm pebbles in drum 11 stuck

(Inner Diameter of small stacks in Drum 10/11: 2.6 mm)

Dismantling experiment succesful;
 Sample recovery >85% succesful



Dismantling: Extracting pebbles



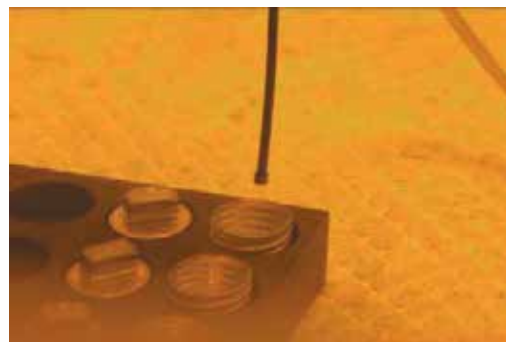
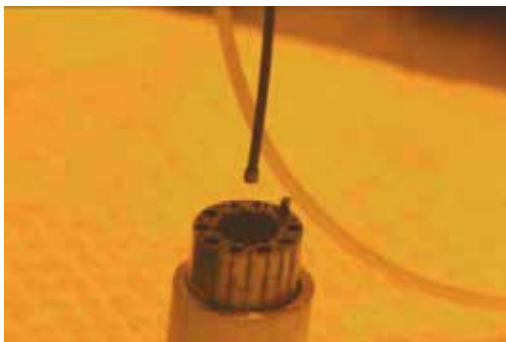
Dismantling: Extracting pellets



First 'pushing device' (left) was developed. This turns out to be 'too imprecise' for pellets.

A 'suction cup device' (bottom) was developed to take out pellets, one by one.

Total of 451 pellets in all B and C drums.



Work detail Task 2 : NRG (3)



Dimension measurements (microscopy):

According to NRG detailed work instructions

- Amount of pebbles
- Maximum, minimum, average size
- Roundness
- Comparison with pre-irradiation data (e.g. swelling)

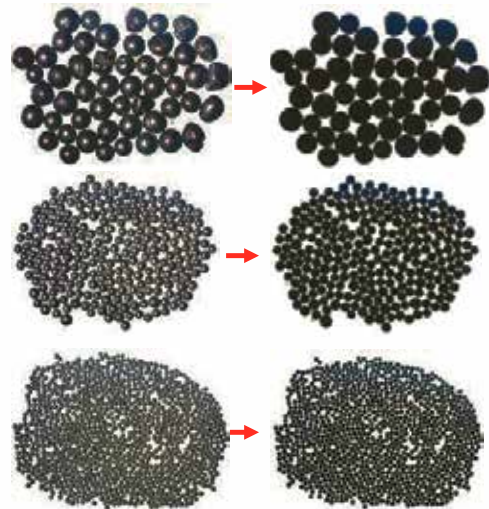
First detailed view of pebbles



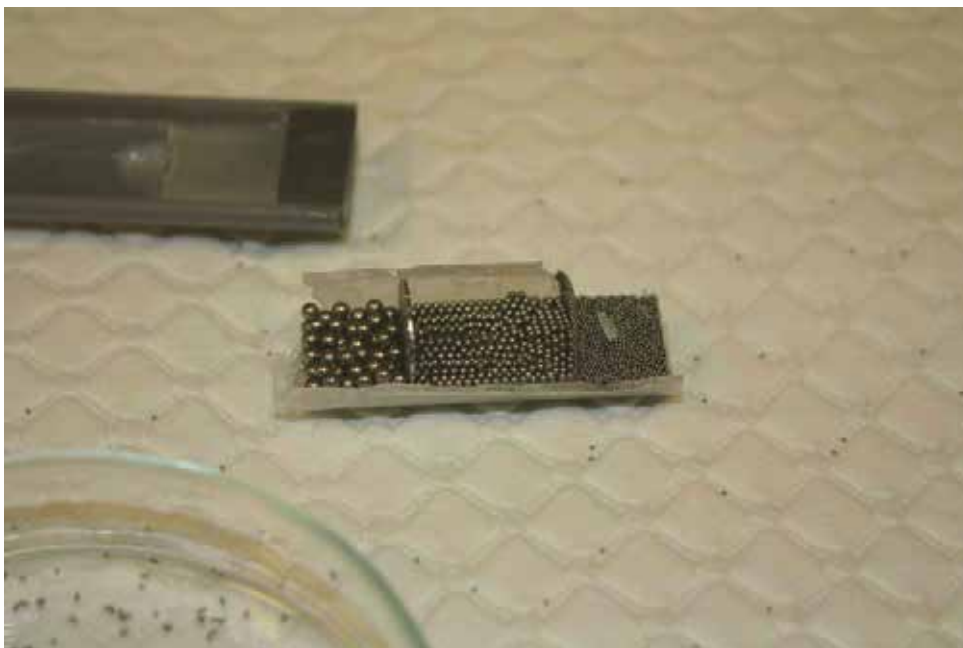
Be 5% Ti

Be 7% Ti

Be electrode



Technical Progress – Dummy study



Technical progress



2010: All measurements completed on:

- unconstrained pebbles (except microscopy)
- pellets samples

2011: - Completed SEM unconstrained pebbles (surface + x-section)
- Performed dummy study on impregnation of pebble beds
- Prepared constrained pebble beds + transport to KIT
- 'Dimensions' and tritium release measurements near completion

Of constrained: 1 drum fully impregnated (microscopy possible)

Due to budget not yet finished:

- Dimension, density (one drum left = 3 samples)
- Half of the agreed upon T-release (= 4 measurements)
- SEM on constrained pebble beds (= 5 beds x 2 views)

Technical progress



2011: - Completed SEM unconstrained pebbles (surface + x-section)
- Performed dummy study on impregnation of pebble beds
- Prepared constrained pebble beds + transport to KIT
- 'Dimensions' and tritium release measurements near completion

Of constrained: 1 drum fully impregnated (microscopy possible)

2012: - Finished remaining dimension / density measurements
- Finished remaining tritium release measurements
- Finished microscopy and SEM on constrained beds

Table 3.2-1 Operation conditions for beryllium pebbles in HCPB DEMO blanket in spherical layers where the distance is measured from the inner surface of the first wall [Fish04] and F4E-2009-GRT-030 (Action-1) "TBMs Functional Materials (Be, ceramic breeder, PB-Li) , Development/Qualification Task-2 Final Report , "Development / Qualification / Procurement Plan for Be pebble materials"



Distance, cm	Neutron flux, $\text{cm}^{-2}\text{s}^{-1}$	Temp. $^{\circ}\text{C}$	Damage, dpa/fpy	He, appm/fpy	T, appm/fpy
2.3 – 3.8	$1.06 \cdot 10^{15}$	615	17	5700	86
3.8 – 6.8	$1.03 \cdot 10^{15}$		16.5	5539	84
6.8 – 9.8	$0.96 \cdot 10^{15}$		15.4	5162	78
9.8 – 12.8	$0.88 \cdot 10^{15}$		14.1	4732	71
12.8 – 15.8	$0.79 \cdot 10^{15}$		12.7	4248	64
15.8 – 18.8	$0.70 \cdot 10^{15}$		11.2	3764	57
18.8 – 21.8	$0.61 \cdot 10^{15}$		9.8	3280	49
21.8 – 24.8	$0.53 \cdot 10^{15}$		8.5	2850	43
24.8 – 27.8	$0.46 \cdot 10^{15}$		7.4	2474	37
27.8 – 30.8	$0.39 \cdot 10^{15}$		6.3	2097	32
30.8 – 33.8	$0.33 \cdot 10^{15}$		5.3	1775	27
33.8 – 36.8	$0.28 \cdot 10^{15}$		4.5	1506	23
36.8 – 39.8	$0.24 \cdot 10^{15}$		3.8	1291	19
39.8 – 42.8	$0.20 \cdot 10^{15}$		3.2	1075	16
42.8 – 45.8	$0.18 \cdot 10^{15}$	400	2.9	968	15



Microstructure characterization of beryllium pebbles irradiated at HFR up to 3000 appm helium production within HIDOBE-01 experiment

V. Chakin¹, R. Rolli², M. Klimenkov¹, A. Moeslang¹, P. Vladimirov¹, P. Kurinskiy¹, H.-C. Schneider², S. van Til³, A.J. Magielsen³, M. Zmitko⁴

¹Institute for Applied Materials - Applied Materials Physics, Karlsruhe Institute of Technology, P.O. Box 3640, 76021 Karlsruhe, Germany

²Institute for Applied Materials - Materials and Biomechanics, Karlsruhe Institute of Technology, P.O. Box 3640, 76021 Karlsruhe, Germany

³Nuclear Research and consultancy Group, Westerduinweg 3, Postbus 25, 1755 ZG Petten, the Netherlands

⁴The European Joint Undertaking for ITER and the Development of Fusion Energy, c/ Josep Pla, n° 2, Torres Diagonal Litoral, Edificio B3, 08019 Barcelona, Spain

ABSTRACT

Beryllium is planned to be used as a neutron multiplier in the Helium Cooled Pebble Bed (HCPB) European concept of a breeding blanket of DEMO. In the neutron multiplier set beryllium will be used in a form of a pebble bed. Small constrained beryllium pebble beds as well as unconstrained beryllium pebbles have been irradiated within HIDOBE-01 experiment at HFR, Petten, the Netherlands. Beryllium pebbles with 1 mm diameter produced by Rotating Electrode Method (REM) were investigated after irradiation at 630, 740, 873, and 948 K up to helium production of 3000 appm. Intensive pore and bubble formation occurs in beryllium after 873 K irradiation. In the contact zones of the pebbles enhanced pore formation takes place. Oxidation of beryllium pebble external surfaces is accompanied by partial destruction of oxide layers owing to their high brittleness. Strong interactions between beryllium pebbles and platinum foil, as well as between beryllium and stainless steel at contact zones occur at 873 and 948 K. The TEM study of beryllium pebbles with a diameter of 1 mm showed the formation of gas bubbles as discs with a hexagonal shape for all four irradiation temperatures. The discs were located in the (0001) basal plane with a height directed along the “c” axis. The average diameters of the bubbles increase from 7.5 to 80 nm with the increase of the irradiation temperature, the bulk densities accordingly decrease from $4.4 \cdot 10^{22}$ to $3.8 \cdot 10^{20} \text{ m}^{-3}$. The calculated swelling of the pebbles increases from 0.5 to 6.5 % with increase of the irradiation temperature from 630 to 948 K.

Keywords: beryllium pebble; neutron irradiation; helium bubble; Wickers hardness.

1. Introduction

In the European Helium-Cooled Pebble Bed (HCPB) blanket of a DEMO fusion power reactor beryllium pebbles with 1 mm diameter are planned to be used as a neutron multiplier [1]. Fusion neutron irradiation causes formation of radiogenic gases in beryllium, in particular, about 20,000 appm of helium can be produced in the beryllium pebbles up to the end-of-life of the HCPB blanket [2]. Fast neutron irradiation in a research nuclear reactor of small beryllium pebble beds at fusion

reactor temperatures allows to reproduce and model thermo-mechanical, swelling and other issues for the beryllium neutron multiplier of the HCPB blanket.

2. Experimental

This work was performed using beryllium pebbles from NGK Insulators, Ltd having diameter of 0.5, 1 (of the 2001 and 2003 heats) and 2 mm produced by Rotating Electrode Method (REM) [3]. These pebbles contain in wt. %: 0.36 BeO, 0.094 Fe, 0.048 Al, 0.029 Si, 0.024 Mg, <0.001 Co, <0.005 Sc, <0.01 U.

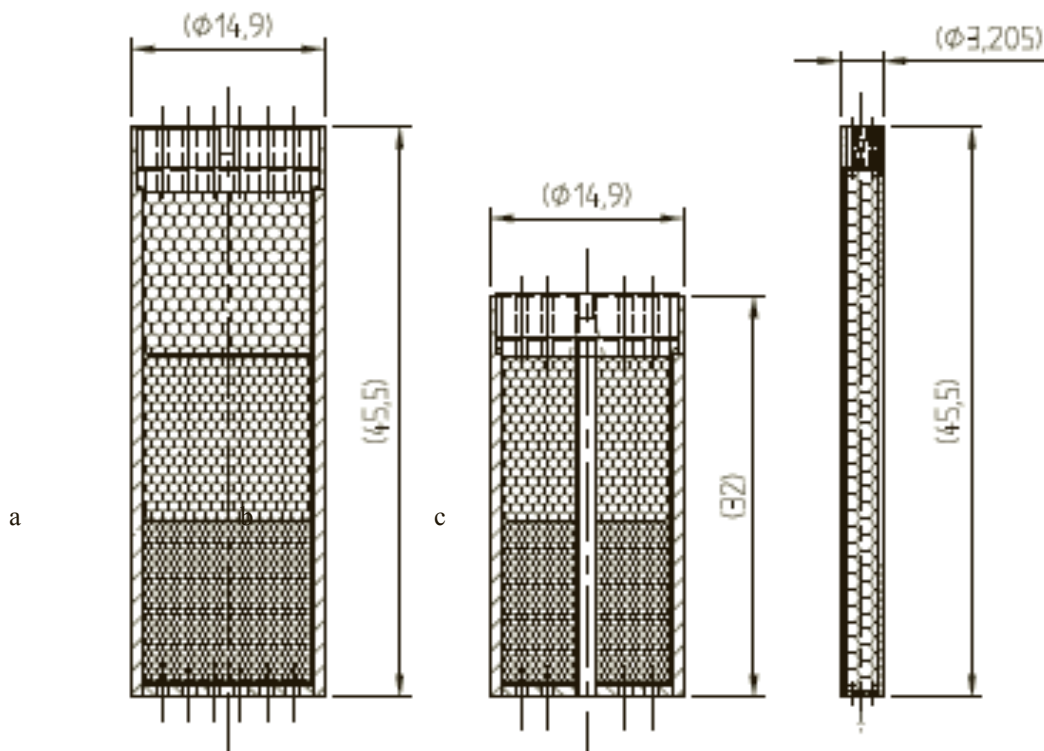


Fig. 1. Containers for irradiation of constrained beryllium pebble beds (a, b) and unconstrained pebbles (c).

Three different container types with beryllium pebbles were used in the HIDOBE-01 irradiation experiment at the HFR, Petten (Fig. 1) [4, 5]. Two of them have been made as small constrained pebble beds which contain 0.5, 1, and 2 mm pebbles located in various sections on height (Fig. 1 a, b). The constrained pebble beds were filled by pebbles and closed with a screw-cap with a torque wrench. To prevent chemical interaction of beryllium pebbles with stainless steel walls a thin platinum foil has been placed between beryllium and steel as a barrier. Third container type was used for irradiation of beryllium pebbles after free filling (unconstrained state) (Fig. 1 c). In the paper the 1 mm pebbles were studied only. Irradiation parameters of the beryllium pebbles and pebble beds are presented in Table 1. Only average irradiation temperatures are presented in the table but the full irradiation history, target and real irradiation temperatures within HIDOBE-01 experiment can be taken from [6].

Table 1. Irradiation parameters of unconstrained beryllium pebbles (P) and pebble beds (PB) from HIDOBE-01.

Type	D _{pebble} , mm	Average T _{irr} , K	F, 10 ²⁶ m ⁻² , E>0.1 MeV	D, dpa	⁴ He, appm	³ H, appm
P	1, 2001/ 1, 2003	630	5.69	11.3	1890	176
		740	6.94	13.9	2300	213
		873	8.07	16.3	2680	252
		948	8.92	18.1	2950	285
PB	0.5	873	8.07	16.3	2680	252
		873	8.07	16.3	2680	252
		873	8.07	16.3	2680	252
		948	9.40	19.2	3090	306
		948	9.40	19.2	3090	306

For transmission electron microscopy (TEM) investigations the irradiated beryllium pebbles were crushed on small pieces (5-10 μm) using a special developed crushing tool. After the crushing procedure the beryllium powder was deposited on a TEM copper greed covered by a thin carbon film (Fig. 1). Only a few places located at edges of the beryllium particle were be transparent for the electron beam and accordingly suitable for the TEM study. The TEM investigations were performed using an FEI Tecnai 20 FEG microscope with an accelerating voltage of 200 kV, the scanning unit for performing scanning TEM (STEM) equipped with a high-angle annular dark field (HAADF) detector, an energy-dispersive X-ray (EDX) detector and also a Gatan image filter for EELS measurements. The microscope was operated at 200 kV accelerating voltage.

3. Results and discussion

3.1 Optical investigations

The microstructures of irradiated unconstrained beryllium pebbles strongly depend on irradiation temperatures (Fig. 2). No pore or bubble formations occur at 630 and 740 K (Fig. 2 a, b). Irradiations at 873 and 948 K cause pore formation resulting swelling up to highest value of about 7 % [5].

Cross sections of high temperature irradiated constrained beryllium pebble beds with remained impregnated pebbles are shown in Fig. 3. The rest of the pebbles from the irradiated pebble beds were used for investigations as separate objects. Overviews of beryllium pebble bed cross sections show intensive pore formation but with peculiar features such as strong non-uniformity of the pore formation process from pebble to pebble and enhanced pore formation near to contact zones of the pebbles. The beryllium pebbles produced by REM have a very non-homogeneous microstructure state because the crystallization of small melted beryllium drops occurs very quickly under production. As a result the pebbles can have different finale microstructure parameters such as technological pore dimensions and their amount, internal stress distribution and so on. These circumstances as well as possible variety of irradiation temperatures on pebble bed cross section can lead to different intensity of radiation-induced pore formation in different pebbles.

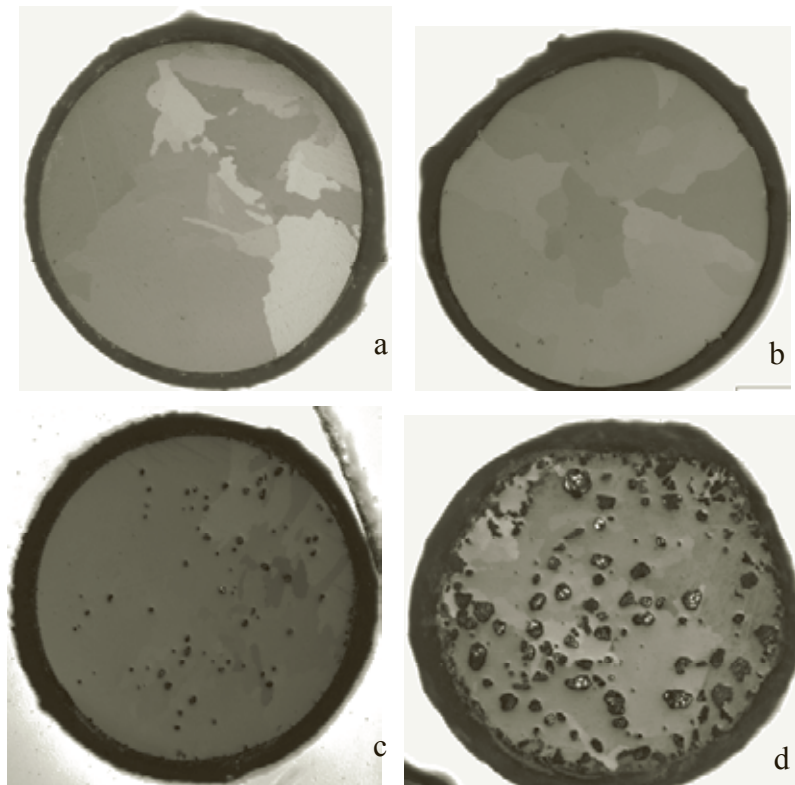


Fig. 2. Overviews of unconstrained beryllium pebbles with diameter of 1 mm, 2003 after irradiation at 630 K (a), 740 K (b), 873 K (c), and 948 K (d).

Partial defragmentation of the pebbles takes place. It can be caused by weakening of grain and sub-grain boundaries after global high temperature condensation of helium atoms on the boundaries with bubble formation. The increase of irradiation temperature from 873 K (Fig. 3 a) to 948 K (Fig. 3 b) results in an acceleration of all radiation-induced processes in the pebbles (growth of pore dimensions, higher swelling and defragmentation, etc.).

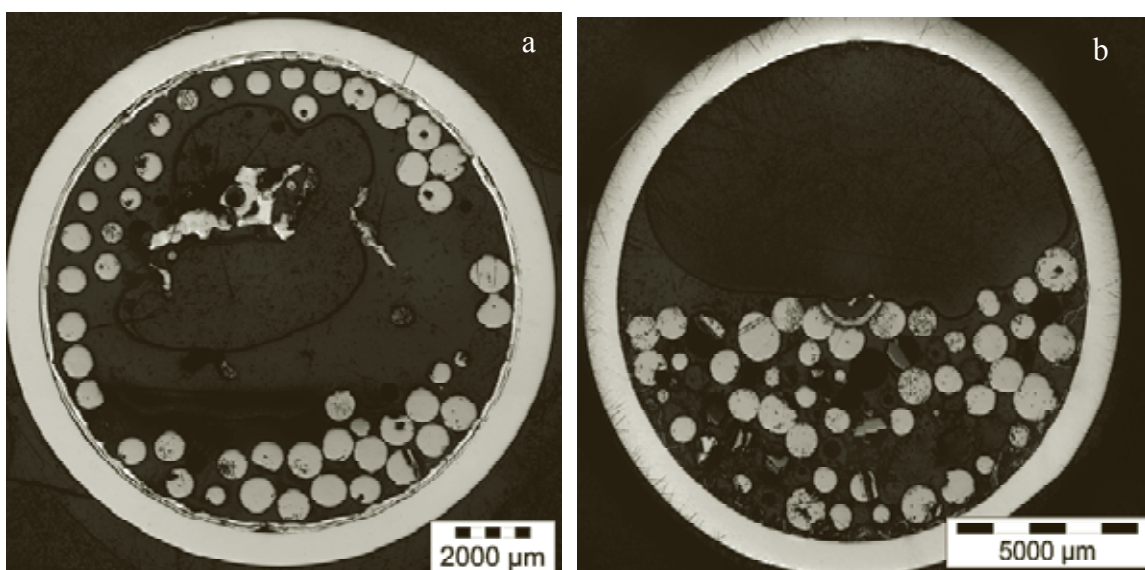


Fig. 3. Overviews of beryllium pebble beds with 1 mm pebbles after irradiation at 873 K (a) and 948 K (b).

Fig. 4 shows changes in beryllium pebbles with a diameter of 1 mm from constrained pebble bed irradiated at 873 K. Strong diffusive penetration of beryllium into platinum occurs at contact zones between pebbles and platinum foil (Fig. 4 a, b) [7, 8]. This is accompanied by intensive pore formation in beryllium (large pores) as well as in platinum (much smaller pores) caused probably by stress-enhanced diffusion of vacancies to the compressed zones [9]. The linear coefficient of thermal expansion for beryllium at 873 K is by a factor of one and a half above platinum [10]. Therefore the temperature variations caused by the reactor cycles have produced cyclic stress loading to the platinum foil. The duration of each loading is equal to the duration of corresponding reactor cycle (in total 649 days at full reactor power for 25 cycles). Strong surface oxidation of the irradiated beryllium pebbles takes place (Fig. 4 c, d). The thickness of beryllium oxide layers may reach 20 μm . But the layers, being friable and brittle, can easily separate from the pebble surface under loading from next pebbles.

The degree of damage at the interface of pebbles and platinum foil can vary significantly (Fig. 4 e). Mostly, a strong embrittlement of platinum under neutron irradiation occurs at 873 K. In the case of intensive pore formation in irradiated pebbles an interconnected pore network with open channels to external surface might be formed. Easy penetration of oxygen from the purge gas along these channels into the pebble causes strong internal oxidation of the pores (Fig. 4 f). An example of pebble bed dense packing after end of irradiation is shown in Fig. 4 g. Ability to local deformation in contact zones of a pebble may be explained by its comparatively lower strength or hardness to next pebbles (non-stability caused by REM production). Other possible reasons for this effect could be local temperature fluctuations under irradiation or different orientations of pebbles to contacting point (micro-hardness varies of 20 % from grain to grain in a pebble). As a result enhanced pore formation in the vicinity of pebble surfaces takes place for more deformed pebbles from the pebble bed. Fig. 4 h shows a formation of solid metallic matrix instead of separate pebble packing. It was established that the white matrix was formed from small platinum foil fragments which could be transported to this place together with interacted beryllium pebble fragments from wall of the pebble bed under the sample preparation for optical examination. As a result the changed orientation of the fragment on 90° creates the impression of permanent metallic matrix. More pronounced damages of the beryllium pebble bed occur under neutron irradiation at higher temperature of 948 K (Fig. 5).

Defragmentation of irradiated pebbles and platinum foil reflects a high brittle state of this materials caused by joint influence of negative factors such as high temperature, damage dose and helium accumulation (Fig. 5 a). Interactions between platinum foil and irradiation container from AISI 321 stainless steel with formation of intermediate phase layer takes place (Fig. 5 b) [11]. It is important to note the strong damage of beryllium pebbles in contact zones with a thermocouple tube from stainless steel (Fig. 5 c) [12]. Some pebbles may poorly contact among themselves in the pebble bed that does not lead to strong damage of beryllium at contact zones however this can lead to sintering of contacting pebbles (Fig. 5 d, e). Fig. 5 e also includes square impressions of the indenter of Vickers micro-hardness measurements. A quite significant difference between their sizes can be noticed that means to be the corresponding large differences in values of the measured micro-hardness for one pebble. Some pebbles have many cracks through the matrix which are sometimes parallel to a contacting damaged zone (Fig. 5 f).

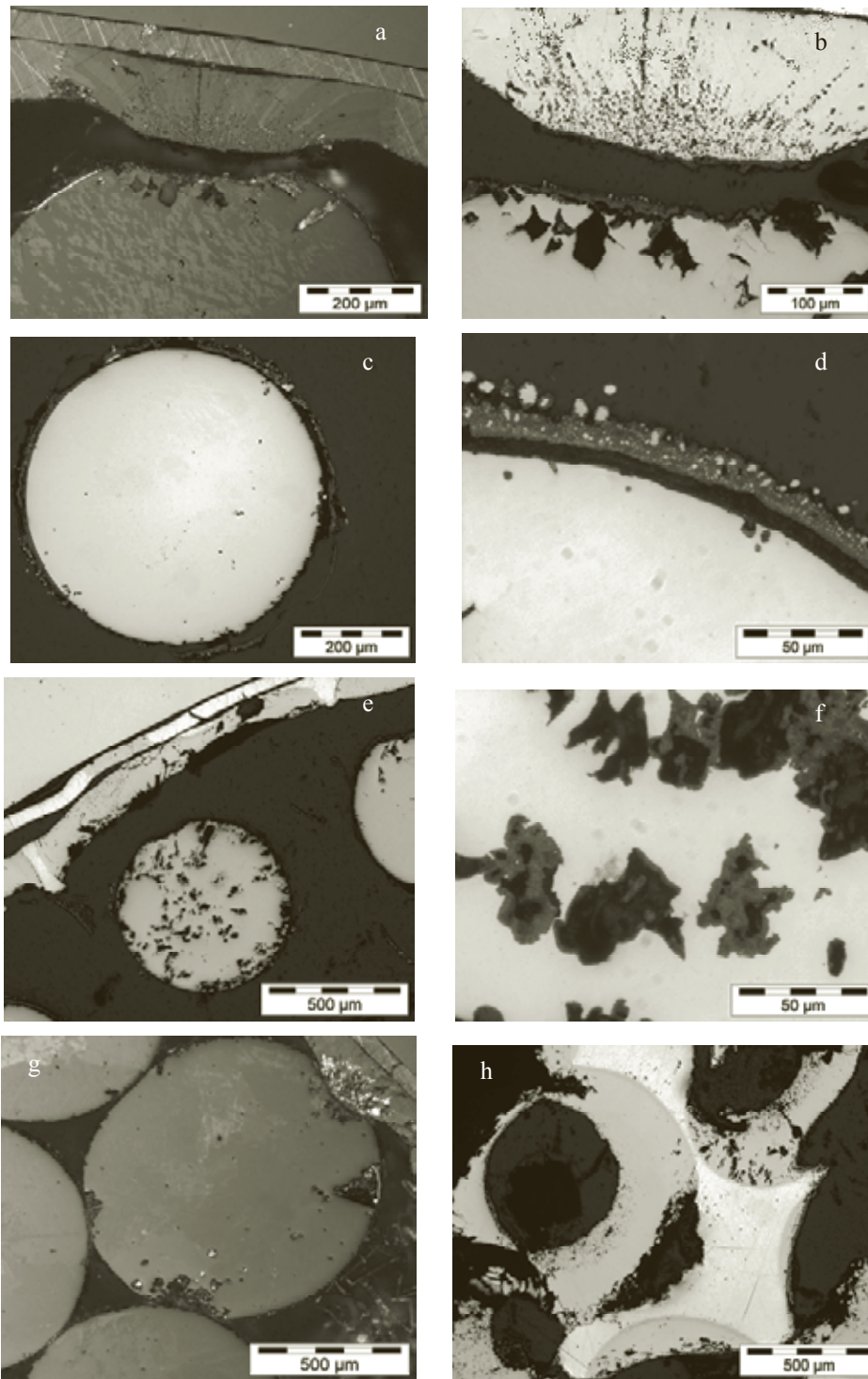


Fig. 4. Irradiation of the beryllium pebble bed with 1 mm pebbles at 873 K results strong interaction of beryllium with platinum foil (a) and pore formation in contact zones both for platinum and beryllium (b), formation of oxide surface layer (c) which often goes from the pebble surface out (d), strong damages of platinum foil and beryllium pebble with cracks formation (e), internal oxidation of large pores in beryllium pebble (f), pore formation in contact zones between pebbles (g), formation of metallic matrix between pebbles (h).

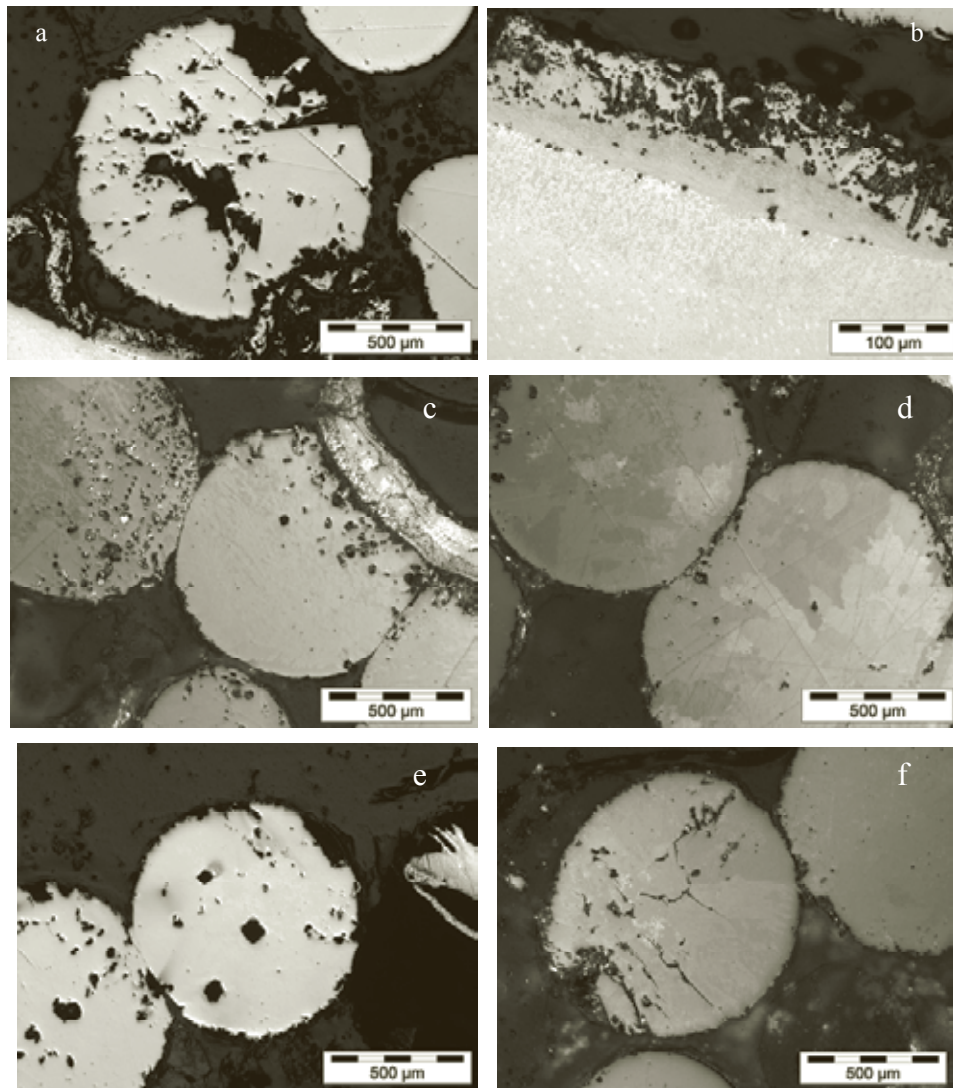


Fig. 5. Irradiation of the beryllium pebble bed with 1 mm pebbles at 948 K results strong interaction of beryllium pebble with platinum foil (a), interaction of platinum foil with stainless steel container (b), interaction of beryllium pebbles with a stainless steel tube of a thermocouple (c), deformation with sintering and pore formation in contact zones between pebbles (d, e), crack formation in a beryllium pebble (f).

Despite of quite large differences in values of Vickers micro-hardness for different investigated pebbles a good reverse linear correlation on irradiation temperature by fitting of the experimental hardness values has been obtained (Fig. 6). The largest radiation hardening occurs at lowest irradiation temperature. The complete recovery of hardness to non-irradiated state values takes place only at the maximum irradiation temperature. The final microstructure of beryllium after high temperature irradiation results in a superposition of several phenomena such as accumulation of radiogenic helium and tritium, subsequent formation and coalescence of pores and bubbles. In addition the high dose neutron irradiation forms point defects, dislocation networks and leads to annealing of internal stresses at higher temperatures. The decrease of micro-hardness with irradiation temperature is a result of above mentioned phenomena. The scatter of the measured values for each irradiation temperature reaches 20 % and can be explained by different orientation of grains of the observed pebbles.

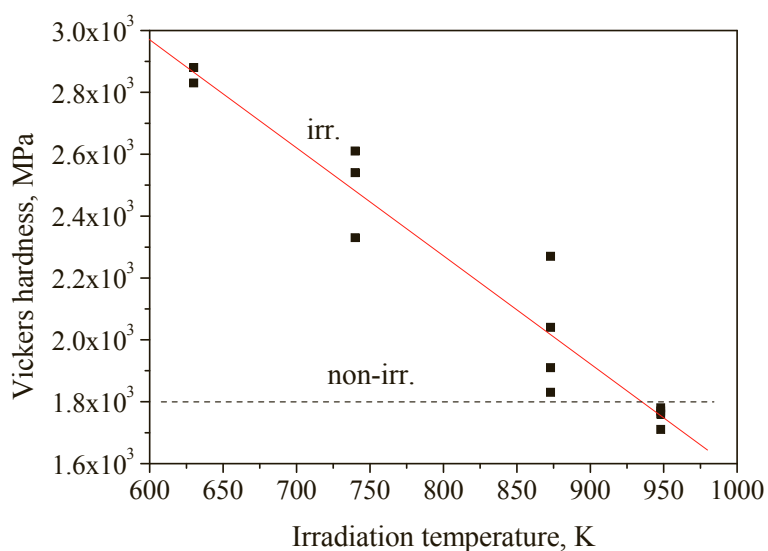


Fig. 6. Vickers hardness of 1 mm beryllium pebbles versus irradiation temperature.

3.2 TEM investigations

The powder pieces of several micrometer size adhere to the carbon film were planned to be characterized in the TEM study. However, the pieces of other compositions (pollution particles) can also be present on the carbon film. Summarizing the investigations results it can be concluded that only from 1/4 to 1/3 of total amount of the adhered particles were detected as beryllium particles from one crushed beryllium pebble. In order to be sure that investigated particles consist of beryllium analytic EELS investigations were performed. The Be-K energy edge is located at 111 eV and herewith it is not detectable with EDX method. In Fig. 7 two beryllium EELS spectra after background subtraction with energy edge at 104 eV are shown. The different energy loss near edge fine structure (ELNES) for both these spectra suggests the different chemical states of beryllium. For example, the spectrum shown in Fig. 7 a was measured on the thinnest edge of the beryllium particle, where the beryllium was possibly oxidized. The spectrum shown in Fig 7 b was obtained from thicker particle area and reflected the fine structure of metallic beryllium. In order to avoid wrong interpretation all investigated particles were verified using EELS method.

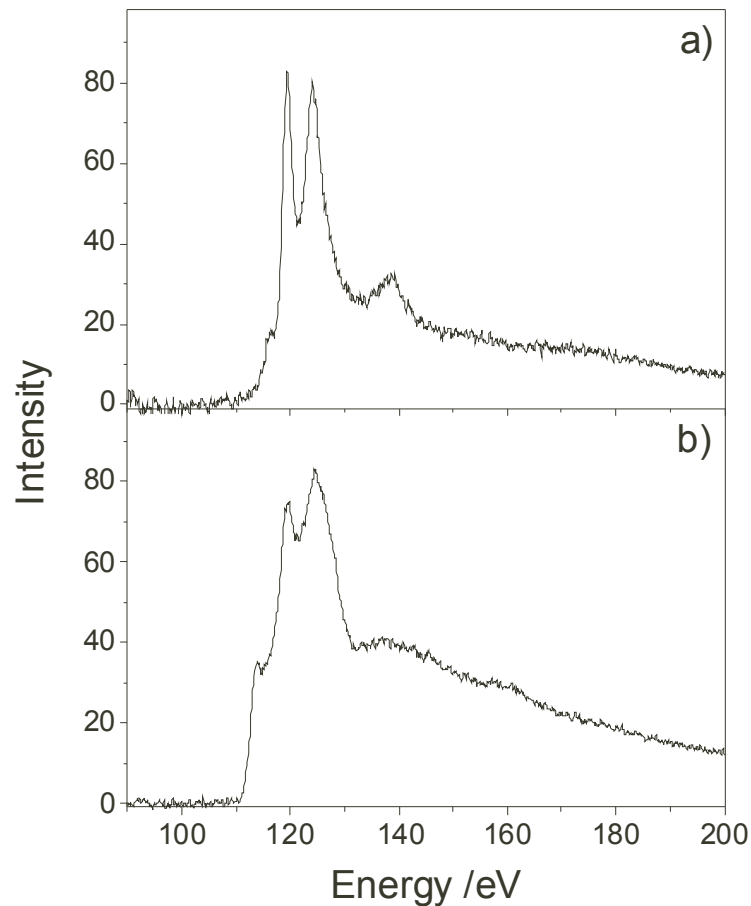


Fig. 2. EELS spectra with energy edge at 104 eV which indicate the presence beryllium but in different chemical states: oxidized (a) and non-oxidized one (b).

The TEM characterization of beryllium powder particles was possible on their thin edges only. The areas on the edges are in the mostly cases wedge-shaped, so the investigated arranges are not homogenously thick. This leads to the strong contrast variation through images. The micrographs obtained by TEM investigations of beryllium pebbles irradiated at 630, 740, 873, and 948 K are shown in Fig. 8-11 respectively. One should be mentioned that beryllium, as the most materials with the hcp lattice, breaks along (0001) basal plane during preparation by crushing method. The beryllium particles with thin edges are oriented in the most cases with “*c*” axis perpendicular to this plane therefore the most bubbles are imaged near “*c*” axis. It could be observed that the bubbles in the most cases are outlined as discs with a hexagonal shape.

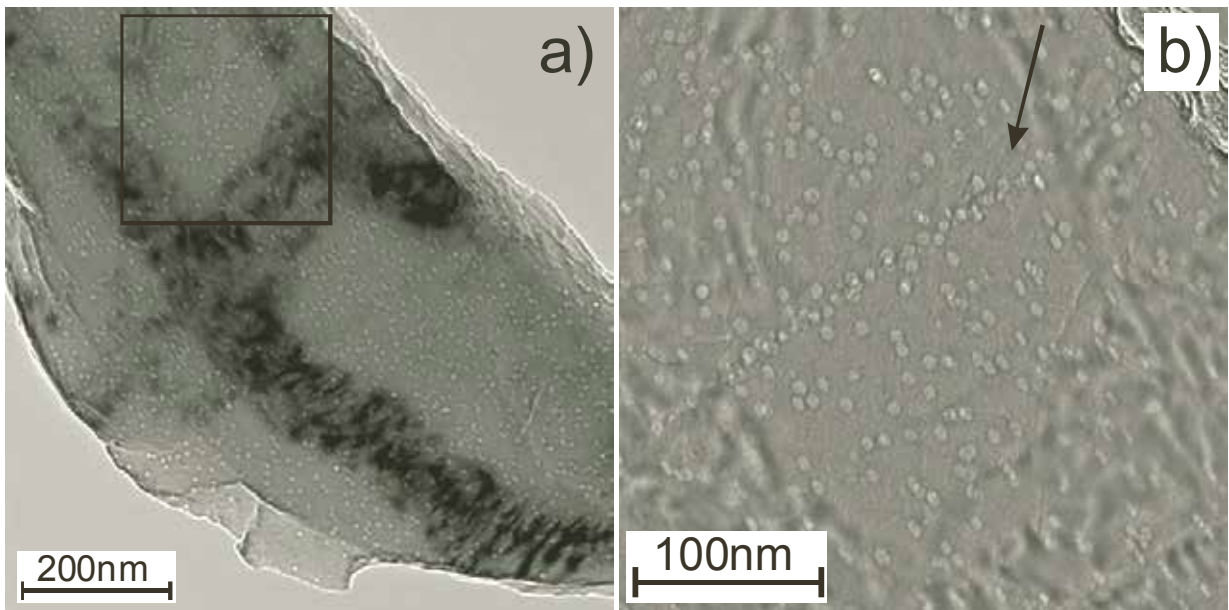


Fig. 8. Bubbles in beryllium pebbles irradiated at 630 K.

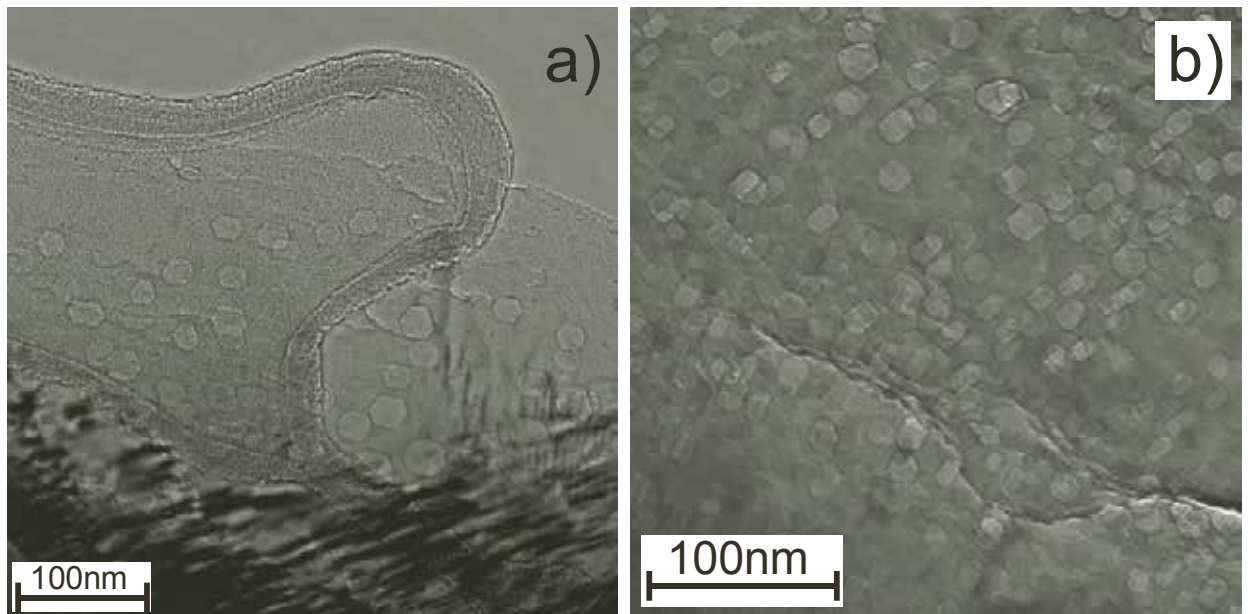


Fig. 9. Bubbles in beryllium pebbles irradiated at 740 K.

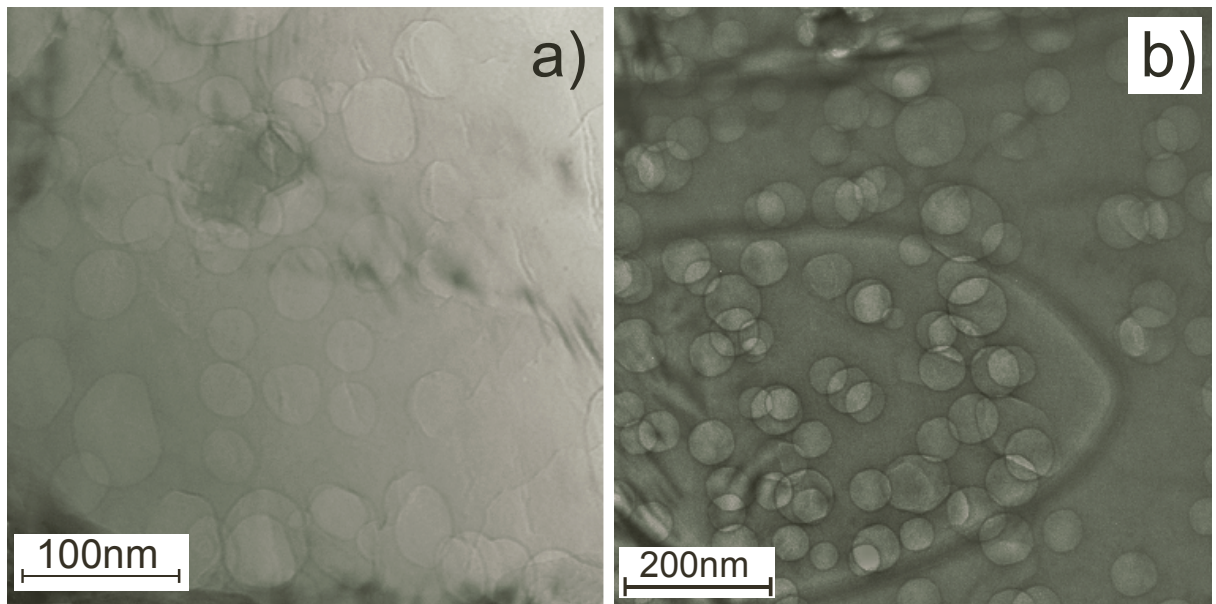


Fig. 10. Bubbles in beryllium pebbles irradiated at 873 K.

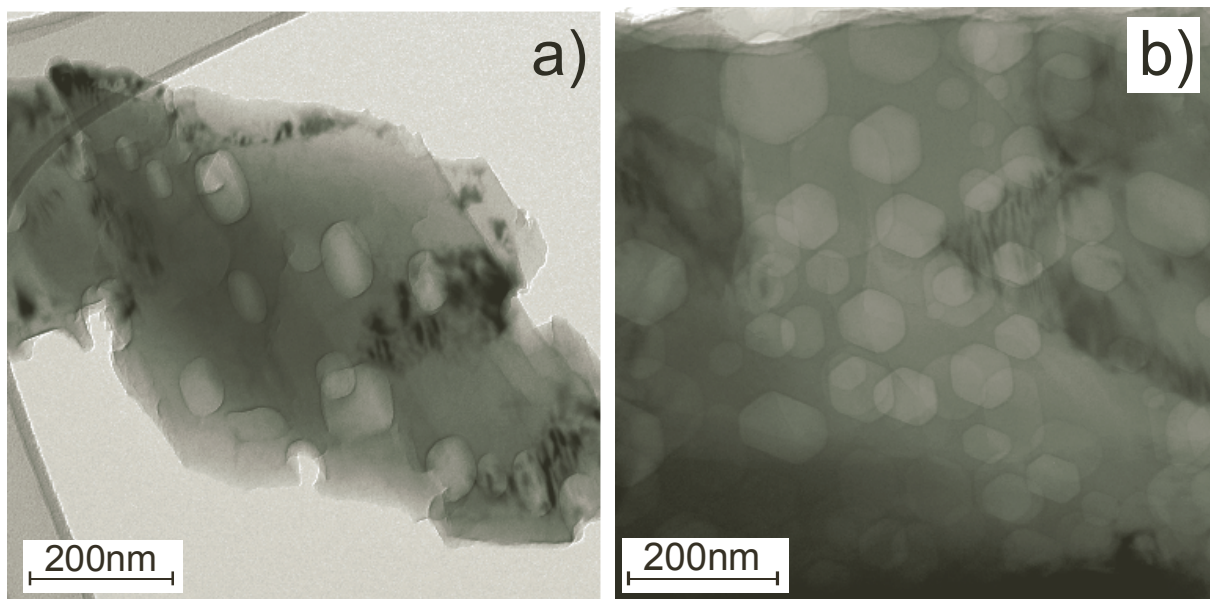


Fig. 11. Bubbles in beryllium pebbles irradiated at 948 K.

The size distributions (Fig. 12) were calculated for all four specimens irradiated at different temperatures. For irradiation temperature of 630 K more than 60 % all bubbles have sizes between 7 and 8 nm. Only small fraction of bubbles shows sizes larger than 10 nm. The bubbles are mainly homogeneously distributed in the specimens. Their sizes or bulk density can be varied on structural inhomogeneity caused by presence of grain and sub-grain boundaries or dislocations. In Fig. 8 an increased concentration of bubbles along a grain boundary is marked by an arrow. For both left and right sites from the grain boundary the closed chains of bubbles are visible. The chains of bubbles

might be formed on former sub-grain boundaries which already were in the pebble before irradiation. The sizes of the bubbles in the 740 K specimen are varied from 12 to 23 nm. 80% of all bubbles have diameters from 14 to 19 nm. For the 873 K specimens the bubble sizes are varied from 40 to 100 nm with a maximum at approximately 75 nm. Bubbles with sizes above 100 nm were not detected in the specimen. The bubbles in the specimen irradiated at 948 K show a width size distribution from 40 to 140 nm. The maximum at approximately 75 nm is only slightly larger than for the 873 K specimen, however the fraction of bubbles which size exceed 100 nm was already estimated to 20%.

Finally, it can be concluded that the observed size distributions of the bubbles are strong depend on irradiation temperature. In particular, for two lowest temperatures (630 and 740 K) the bubbles in irradiated beryllium pebbles have quite small diameters (5-20 nm) which vary in corresponding narrow intervals (sharp peaks in Fig. 4). For two highest irradiation temperatures (873 and 948 K) the bubbles have at several times larger diameters (40-140 nm) with extended distributions on sizes (broad peaks). A threshold temperature can be between 740 and 873 K at which probably the diffusion of helium in beryllium sharply increases.

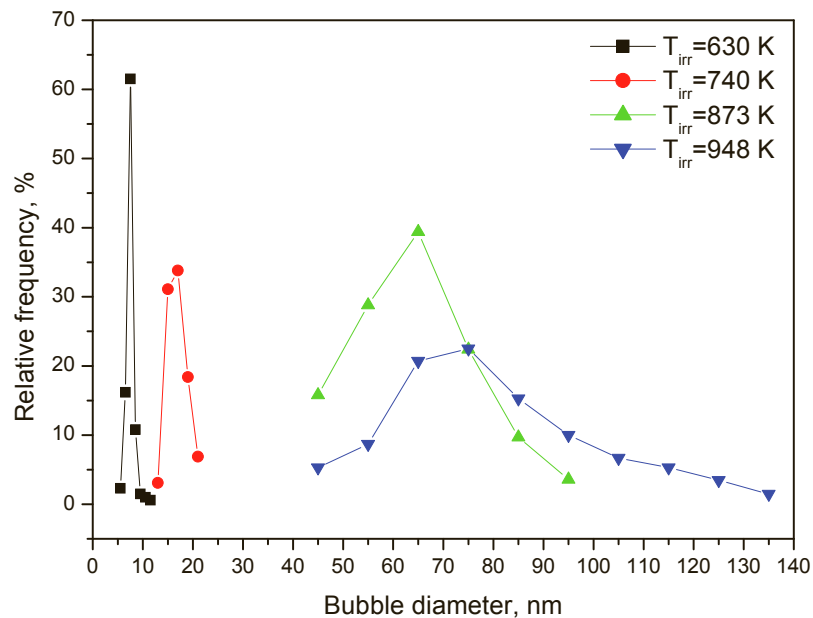


Fig. 12. Distributions on diameters of bubbles in irradiated beryllium pebbles.

The obtained results are in a good agreement with earlier works on TEM investigations of beryllium after irradiation at high temperatures. In particular, D.S. Gelles and H.L. Heinisch in [13] irradiated beryllium in the FFTF/MOTA, USA at 673 K up to 8 dpa (80 appm ^4He) and at 773 K up to 1.25 dpa (10 appm ^4He). Following irradiation at 673 K a high density of small c-type dislocation loops in the bulk and a high density of small helium bubbles (1.5-10 nm) only on grain and sub-grain boundaries were observed. The irradiation at 773 K revealed no small loops and larger bubbles (10-20 nm) which were located on dislocations and grain boundaries. L. Coheur et al. [14] investigated beryllium irradiated in the BR2 reactor, Mol, Belgium at 489, 746 and 880 K up to 2.12-2.55 dpa (560-690 appm ^4He) and observed bubbles on grain boundaries at 746 and 880 K only. But at all three irradiation temperatures there were also found a high density small stacking faults and dislocation loops. I.B. Kupriyanov et al. [15, 16] observed gas bubbles in different

beryllium grades produced by VNIINM, Russia and Brush Wellman, USA after irradiation in the SM reactor, Dimitrovrad, Russia at 923-973 K up to 1.8-3 dpa (640-1140 appm ^4He). It was found that the bubble formation took place on the grain boundaries, inside the grains and on the interface of matrix-second phase. The bubbles had a disk-like hexagonal faceted form and lied in the (0001) basal plane. The average diameters of the bubbles were of 15-20 nm, the thickness was of 2-2.5 nm. In [17] beryllium was irradiated in the BOR-60 fast reactor at 673 K up to neutron fluence of $1.6 \cdot 10^{27} \text{ m}^{-2}$, $E > 0.1 \text{ MeV}$ (9800 appm ^4He). Numerical bubbles with a hexagonal disc shape located in the basal plane were observed by TEM investigations. The bubbles had a diameter around 50 nm, a thickness of 5-10 nm, a bulk density of $8.5 \cdot 10^{21} \text{ m}^{-3}$. So, the published data on TEM investigations of neutron irradiated beryllium reveals that the gas bubbles with small sizes are formed at temperatures since 673 K [13]. The bubbles with identification as disk-like hexagonal faceted form located in the (0001) basal plane were observed in [17] at temperature of 673 K but at high helium accumulation in irradiated beryllium. At higher irradiation temperatures of 923-973 K [15, 16] the hexagonal faceted bubbles like discs were already observed after 640-1140 appm helium production in beryllium.

The parameters of the bubbles as hexagonal faceted discs present in Table 2. The average diameter D_{aver} measured in the (0001) basal plane and the average thickness H_{aver} measured in the “c” axis direction. The average sizes were calculated on the base of statistical date used for calculation of size distribution (see Fig. 7) following the formula:

$$\langle D \rangle = (\text{sum } D_i) / N \quad (1),$$

where D_i is a diameter of a bubble from “i” size interval, N is a total amount of the bubbles in the measurements.

Table 2. Parameters of gas bubbles in beryllium pebbles irradiated at HIDOBE-01.

T_{irr}, K	$D_{\text{aver}},$ nm	$H_{\text{aver}},$ nm	N, m^{-3}	$D_{\text{aver}}/H_{\text{aver}}$	D/H for Be <i>hcp</i> lattice
630	7.5	3	$4.4 \cdot 10^{22}$	2.5	
740	18	9	$2.7 \cdot 10^{21}$	2	1.3
873	70	15	$1.2 \cdot 10^{21}$	4.7	
948	80	28	$3.8 \cdot 10^{20}$	2.9	

Both D_{aver} and H_{aver} increase with the increase of irradiation temperatures but the ratio the diameter to the thickness of the bubbles is not constant value and depends on irradiation temperature. In particular, for 630, 740 and 948 K the ratio values vary from 2 to 3, but for 873 K it is about 5, i.e. much higher. This means that at 873 K the size of a bubble along (0001) basal plane increases much quicker than along “c” axis. Therefore, the accelerated diffusion of helium in beryllium at 800-850 K first starts along basal plane. The increase of the irradiation temperature to

948 K leads to a comparatively increase the helium diffusion along “c” axis that returns the ratio $D_{\text{aver}}/H_{\text{aver}}$ in the typical value between 2 and 3.

The bubbles in the form of hexagonal faceted discs which were observed at this study in highly neutron irradiated beryllium pebbles look like as an elementary hexagonal cell of the beryllium *hcp* lattice but having of course much larger sizes. If to compare the $D_{\text{aver}}/H_{\text{aver}}$ ratio to the D/H for beryllium *hcp* lattice (the last column in Table 2) one could be marked that the bubble ratio is significantly higher than the beryllium cell one. This can mean that the basal plane is a preferable plane for condensation of radiogenic helium atoms during irradiation which probably deform the lattice at this plane more than in the “c” axis direction.

The observed gas bubbles induce a swelling of the irradiated beryllium pebbles. The measured swelling S obtained by calculation using the bubble parameters increases with the increase of the irradiation temperature (Fig. 13). These experimental swelling values can be compared to the theoretical values calculated using the empirical expression from [18, 19]:

$$S_{\text{theor}} = M \cdot T \cdot \exp [-Q/(4kT)] \cdot (F)^{3/2} \quad (2),$$

where T is the irradiation temperature in K, F is the fast neutron fluence with $E_n > 1$ MeV in n/cm^2 , $Q = 2.1$ eV/at is the activation energy, $k = 8.617 \cdot 10^{-5}$ eV/K is Boltzmann's constant, M is a structure-sensitive factor which varies as $(0.31-1.65) \cdot 10^{-34} \text{ K}^{-1} (\text{n/cm}^2)^{3/2}$, at this study $M = 0.8 \cdot 10^{-34} \text{ K}^{-1} (\text{n/cm}^2)^{3/2}$ was chosen. The measured values are in excellent agreement with the calculated ones for lowest irradiation temperatures of 630 and 740 K and in increasing discrepancy at higher temperatures. To explain this effect the existing limitation on bubble sizes observed by TEM should be taken into account. The maximum size of a bubble which is still visible by the electron microscope used at this study cannot exceed 200 nm. Therefore an input of bubbles with larger sizes to the TEM swelling is not included. But observations of cross sections of the same irradiated beryllium pebbles by optical microscope show the presence gas bubbles with sizes up to several tens microns. Hence, the large bubbles give the missing part in the swelling obtained using only TEM observations.

A very limited experimental data on swelling for both high temperature and high dose neutron irradiated beryllium exists in literature. G.A. Sernyaev [20] presents the 18 % swelling for the hot pressed DGP-56 Russian beryllium grade irradiated at 923-973 K up to neutron fluence of $1.02 \cdot 10^{26} \text{ m}^{-2}$, $E > 0.85$ MeV corresponding to 4100 appm helium accumulation. The swelling was measured by hydrostatic method, thereby sure taking into account large bubbles invisible by TEM. In [15, 16] the 2.1 % swelling is revealed for the TshG-56 vacuum hot-pressed Russian beryllium grad after irradiation at the same temperatures but up to lower helium content of 1080-1140 appm.

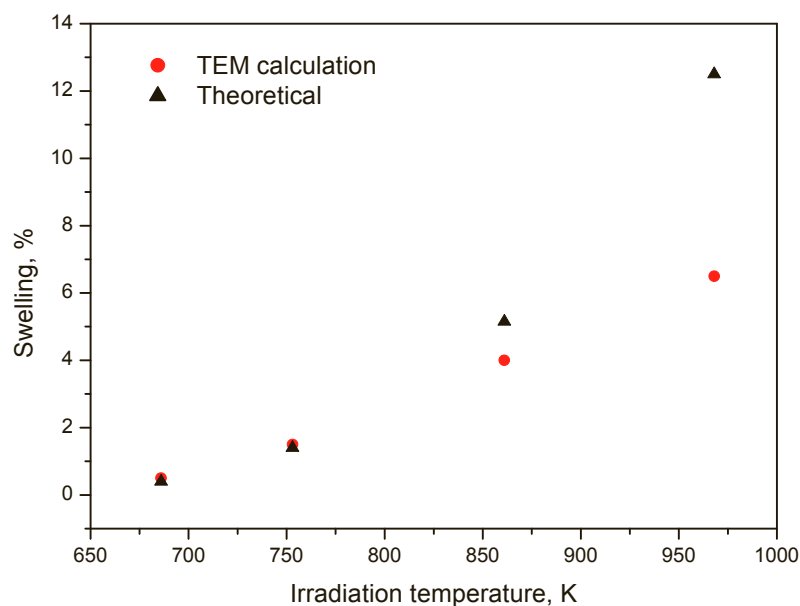


Fig. 13. Swelling of beryllium pebbles from HIDOBE-01 versus irradiation temperature.

4. Conclusions

Internal stresses in beryllium pebbles from the pebble beds caused by swelling are mainly localized in the regions close to contact zones between pebbles. This effect is accompanied by intensive formation of pores in the near surface regions what is probably induced by a stress-enhanced diffusion of vacancies and helium atoms towards stressed zones.

Defragmentation of beryllium pebbles at high irradiation temperatures was observed in some cases. This could be explained by a weakening of grain boundaries and sub-boundaries when condensation of helium atoms in parallel with bubble formation occurs. A transfer of fragments from beryllium pebbles from one part of the pebble bed to another one through free gaps could happen.

Strong oxidation of the external surfaces of beryllium pebbles with formation of thick brittle beryllium oxide layers was observed. Peeling and destruction of the brittle oxide layers can lead to a transfer of small beryllium oxide particles through the gaps between pebbles.

Strong interaction between beryllium pebbles and platinum foil at contact zones takes place. This process is accompanied by a significant damage of the platinum foil caused by beryllium diffusion into platinum with the formation of pores.

Strong interaction between beryllium pebbles and austenitic stainless steel with formation of thick corrosion damage layer occurs.

It was established by TEM investigations that for all four irradiation temperatures gas bubbles were formed as discs with a hexagonal shape. HRTEM investigations showed that the discs were located in the (0001) basal plane with a height directed along the “*c*” axis. The TEM imaging of the bubbles depends on orientation of the image plane varying from a regular hexagon to an elongated

shape as a line segment with an intermediate state as a rectangle. The orientation of the bubbles is the same in a separate grain. The average diameters of the bubbles increase from 7.5 to 80 nm with the increase of the irradiation temperature since 630 until 948 K, the bulk densities accordingly decrease from $4.4 \cdot 10^{22}$ to $3.8 \cdot 10^{20} \text{ m}^{-3}$. The swelling of the pebbles calculated using the bubble parameters increases from 0.5 to 6.5 % with the increase of the irradiation temperature.

Acknowledgements

This work was supported by Fusion for Energy under the grant contract No. F4E-2009-GRT-030-03. The views and opinions expressed herein reflect only the author's views. Fusion for Energy is not liable for any use that may be made of the information contained therein.

References

- [1] Y. Poitevin et al., *Fus. Eng. Des.* 85 (2010) 2340–2347
- [2] M. Zmitko et al., *J. Nucl. Mater.* 417 (2011) 678–683.
- [3] E. Ishitsuka and H. Kawamura, *Fus. Eng. Des.* 27 (1995) 263–268.
- [4] J.B.J. Hegeman et al., *Fus. Eng. Des.* 75–79 (2005) 769–773.
- [5] S. van Til, J.B.J. Hegeman, H.L. Cobussen, and M.P. Stijkel, *Fus. Eng. Des.* 86 (2011) 2258–2261.
- [6] A. Sugonyako and S. van Til, *HIDOBE: final report on irradiation up to 3000 appm He*, NRG-20296/09.96239/P, NRG, Petten, the Netherlands, 2009.
- [7] E.W. Batchelder and R.E. Raeuchle, *Acta Crystallogr.* V. 11, N 2 (1958) 122.
- [8] W. Bronger und W. Klemm, *Z. Anorg. All. Chem. Bd.* 319, N 1/2 (1962) 58–81.
- [9] Ya.E. Geguzin, *Ascending diffusion and the diffusion aftereffect*, *Sov. Phys. Usp.* 29 (1986) 467–473.
- [10] R.M. Treco, *Thermal expansion characteristics of beryllium*, *J. Met.* 188 (1950) 1274.
- [11] T. Tadaki and K. Shimizu, *Scripta Met.*, V. 9, No. 7 (1975) 771.
- [12] H. Kawamura, M. Uchida, and V. Shestakov, *J. Nucl. Mater.* 307–311 (2002) 638–642.
- [13] D.S. Gelles and H.L. Heinisch, *J. Nucl. Mater.* 191–194 (1992) 194–198.
- [14] L. Coheur, J.-M. Cayphas, P. Delavignette, and M. Hou, *Microstructural effects of neutron irradiation in beryllium*, *Proceedings of the 4th IEA International Workshop on Beryllium Technology for Fusion*, September 15–17, 1999, Karlsruhe, Germany, 247–255.
- [15] I.B. Kupriyanov, V.A. Gorokhov, R.R. Melder, Z.E. Ostrovsky, and A.A. Gervash, *J. Nucl. Mater.* 258–263 (1998) 808–813.
- [16] I.B. Kupriyanov, R.R. Melder, and V.A. Gorokhov, *Fus. Eng. Des.* 51–52 (2000) 135–143.
- [17] V.P. Chakin and Z.Ye. Ostrovsky, *J. Nucl. Mater.* 307–311 (2002) 657–663.
- [18] D.S. Gelles, M. Dalle Donne, G.A. Sernyaev, and H. Kawamura, *Radiation effects in beryllium used for plasma protection*, Report PNL-SA-22668, Presented at the ICFRM-6, September 27 – October 1, 1993, Stresa, Italy, 3–6.
- [19] G.A. Sernyaev, *Swelling of beryllium in a mode of high-temperature neutron irradiation*, *Voprosy Atomnoi Nauki I Tekniki*, No. 2 (56), 1991, 16, PNL-TR-488.
- [20] G.A. Sernyaev, *Radiation damageability of beryllium*, Ekateringurg Publishers, Russia, 2001, 274–347.

Chemical Reactivity of Irradiated Be Pebbles under Oxidizing Atmosphere

Eduardo Alves

**Instituto Superior Técnico/Instituto
Tecnológico e Nuclear**

Co-Authors:

N.Catarino, N.P. Barradas, L. C. Alves
Instituto Superior Técnico/ Instituto Tecnológico e Nuclear
Portugal



T.S. van Til
Nuclear Research and consultancy Group,
Netherlands

NRG

P. Barquinha, E. Fortunato
CINEMAT, Universidade Nova de Lisboa

Funding Agency:

EFDA- Fusion For Energy (F4E)

Introduction

Be is very reactive in the presence of oxygen with complete combustion at high temperatures (above 900 °C).

The influence of radiation effects on the oxidation behavior is important for the possible applications in fusion reactors.

We performed oxidation studies of Be pebbles after exposure to neutron irradiation up to 3000 appm of He production (~18 dpa) in the HFR (Petten).

Samples

Be pebbles: (3 pebbles of each batch were measured)

2spc/2: unconstrained 0.5 mm NGK pebble irradiated at 750°C (drum 10)

39spc/2: unconstrained 0.5 mm NGK pebble irradiated at 525°C (drum 12)

46spc/2: unconstrained 1.0 mm (2001) NGK pebble irradiated at 525°C (drum 12)

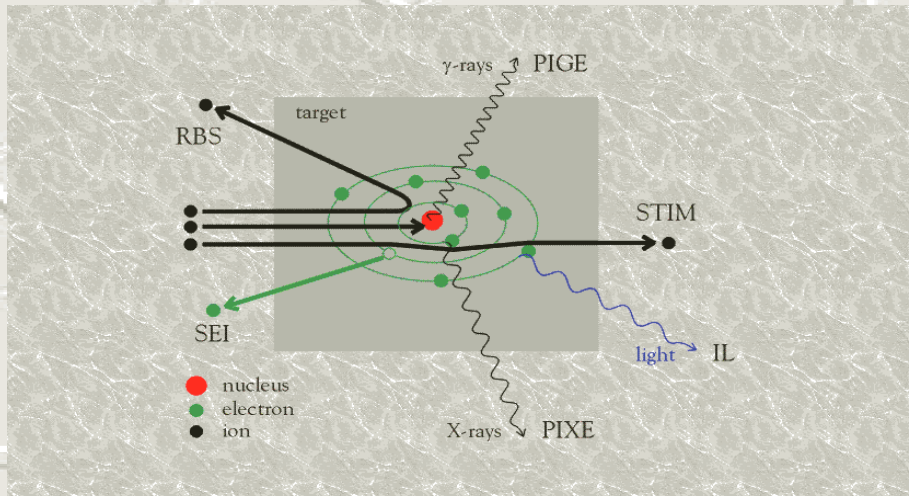
47spc/2: unconstrained 1.0 mm (2001) NGK pebble irradiated at 425°C (drum 13)

Analytical Techniques

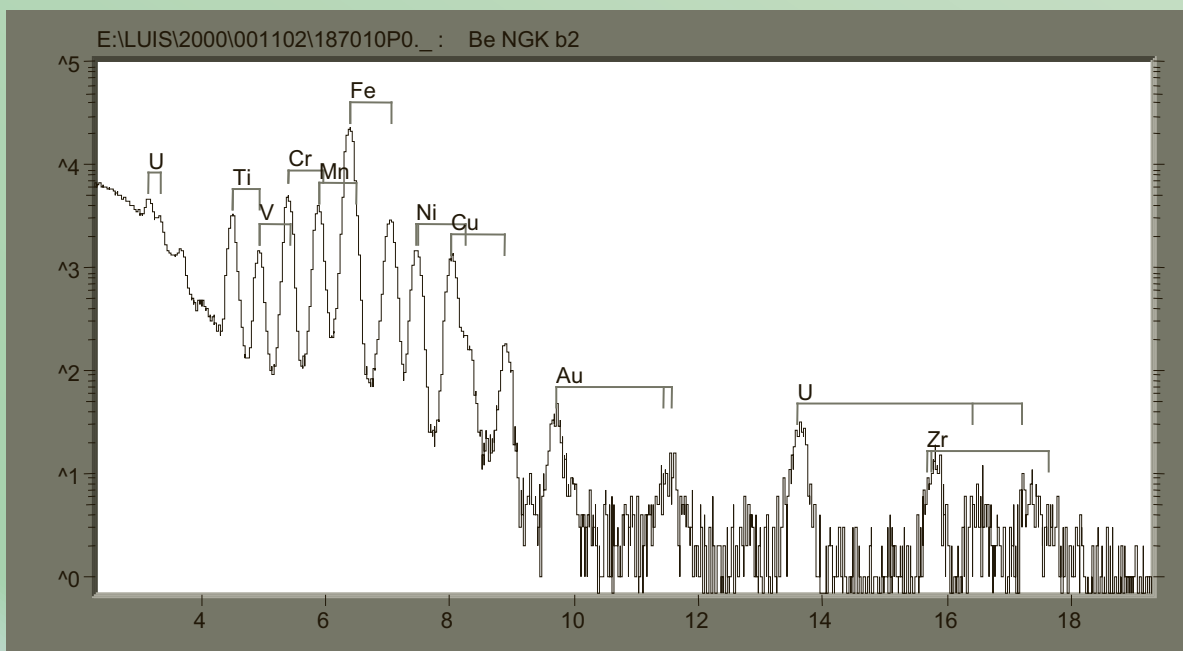
Ion Beam Techniques: Rutherford Backscattering Spectrometry (RBS) and Particle Induce x-Ray Emission (PIXE).

Scanning Electron Microscopy (SEM)

Ion Beam Techniques



Typical PIXE spectrum



Chemical Composition

Concentration ($\mu\text{g/g}$)

	39 s	47 s
Mg	149 \pm 22	49 \pm 7
Al	672 \pm 54	269 \pm 21
Si	635 \pm 51	1387 \pm 111
P	18 \pm 1	
Cl	13 \pm 1	91 \pm 10
K	12 \pm 4	
Ca	129 \pm 19	60 \pm 9
Ti	32 \pm 7	19 \pm 4
V	9 \pm 1	
Cr	131 \pm 10	107 \pm 8
Mn		
Fe	1107 \pm 68	813 \pm 50
Ni	101 \pm 14	81 \pm 10
Cu	62 \pm 7	96 \pm 10

Irradiated samples

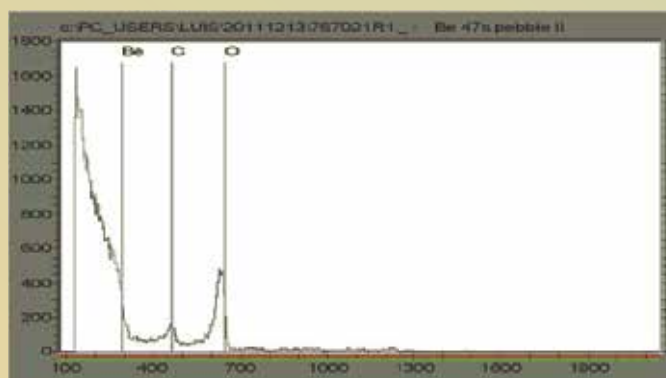
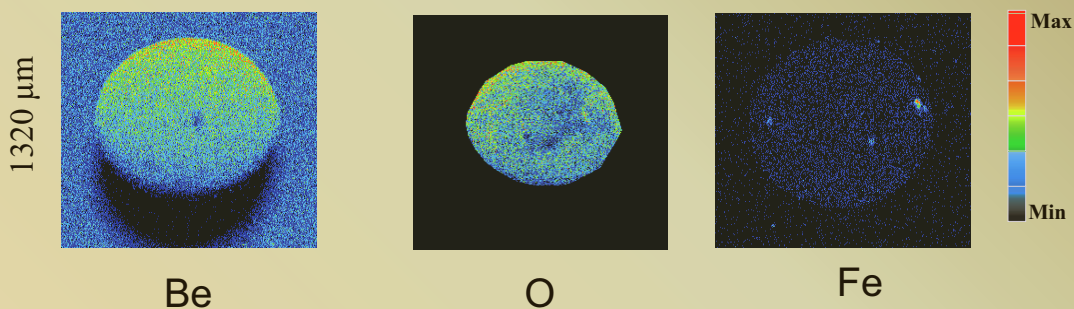
NGK pebbles (1 mm) - 2001

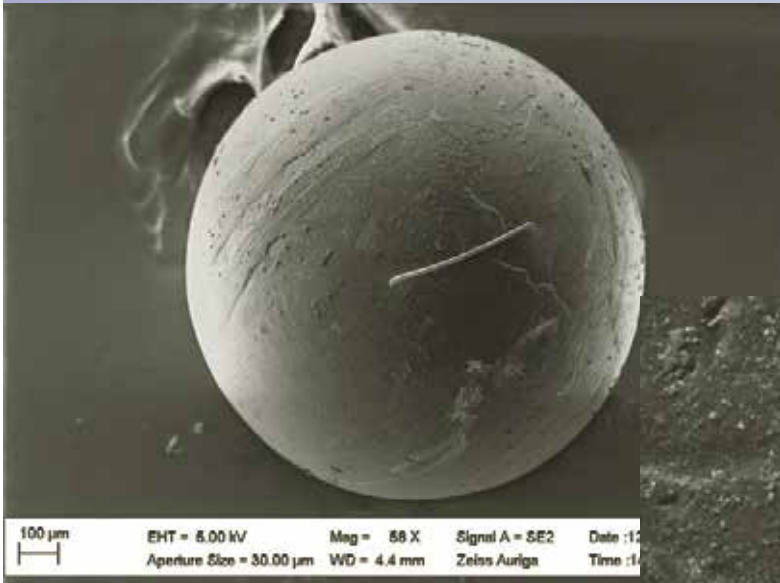
Element	Concentration ($\mu\text{g/g}$)		
Mg	116	\pm	30
Al	376	\pm	35
Si	305	\pm	27
Ti	42	\pm	9
V	19	\pm	3
Cr	102	\pm	12
Mn	104	\pm	13
Fe	1050	\pm	122
Ni	153	\pm	27
Cu	113	\pm	51
Zr	31	\pm	9
Au	20	\pm	2
U	103	\pm	28

47s pc2 - 1 mm, 425°C

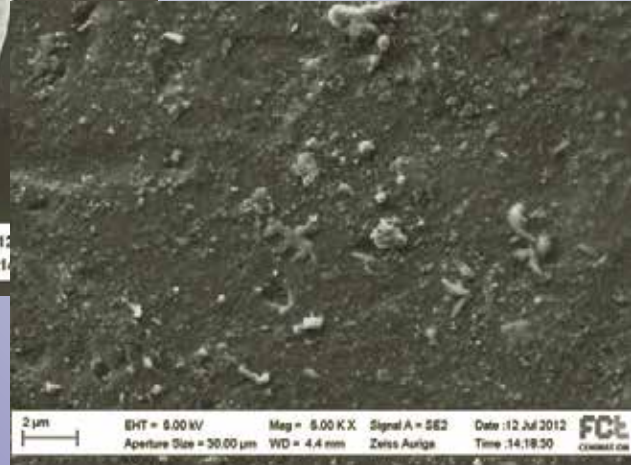
irradiated

Impurity maps





**1 mm Pebble
After irradiation**

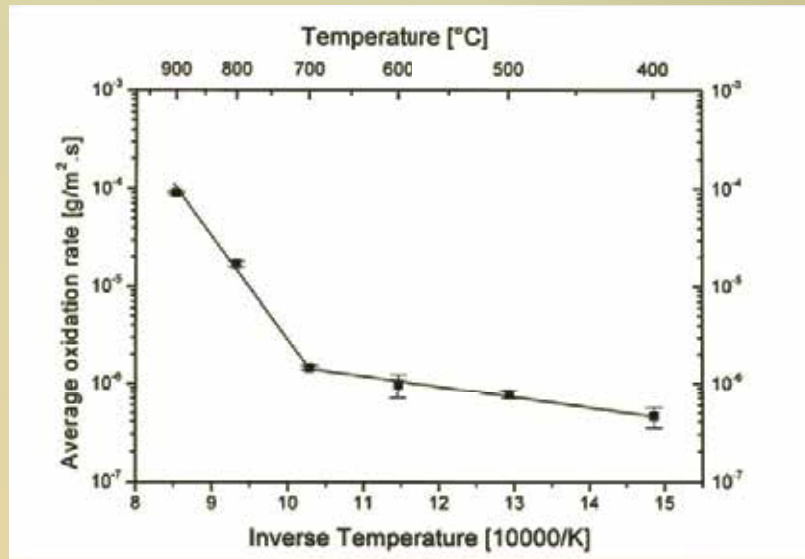


Air/Steam interaction: Chemical reactivity



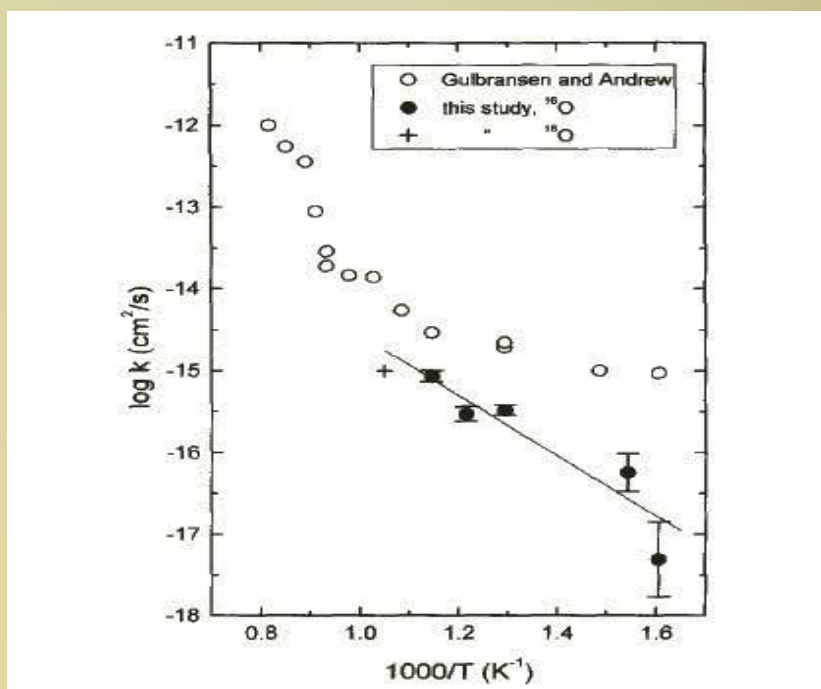
- low temperature (<700 °C)- Parabolic regime ($\Delta m^2 = k_p t$)
- Intermediate range (700-900 °C)- Combination of processes ($\Delta m = k_p t$)
- High temperature >900 °C)- Catastrophic behavior (autocatalytic)

Be Oxidation in air



(F. Druyts et.al. FED 58-58(2001) 695-700)

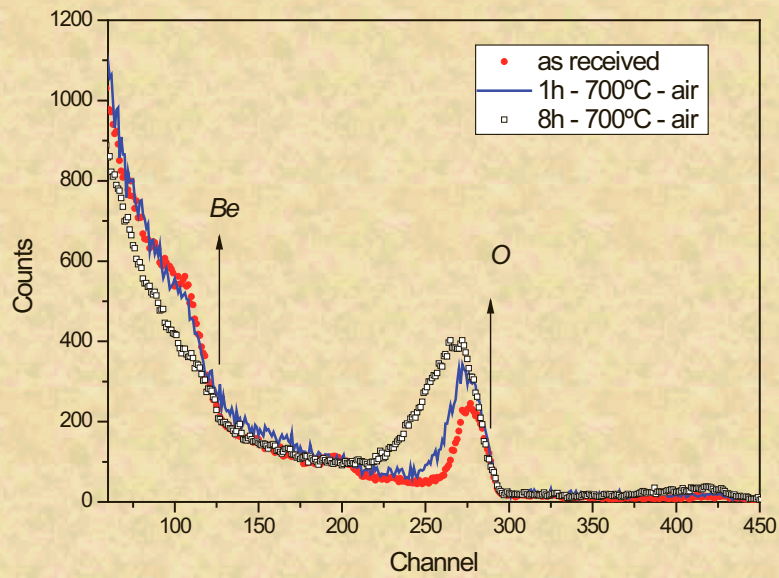
Be Oxidation in O₂



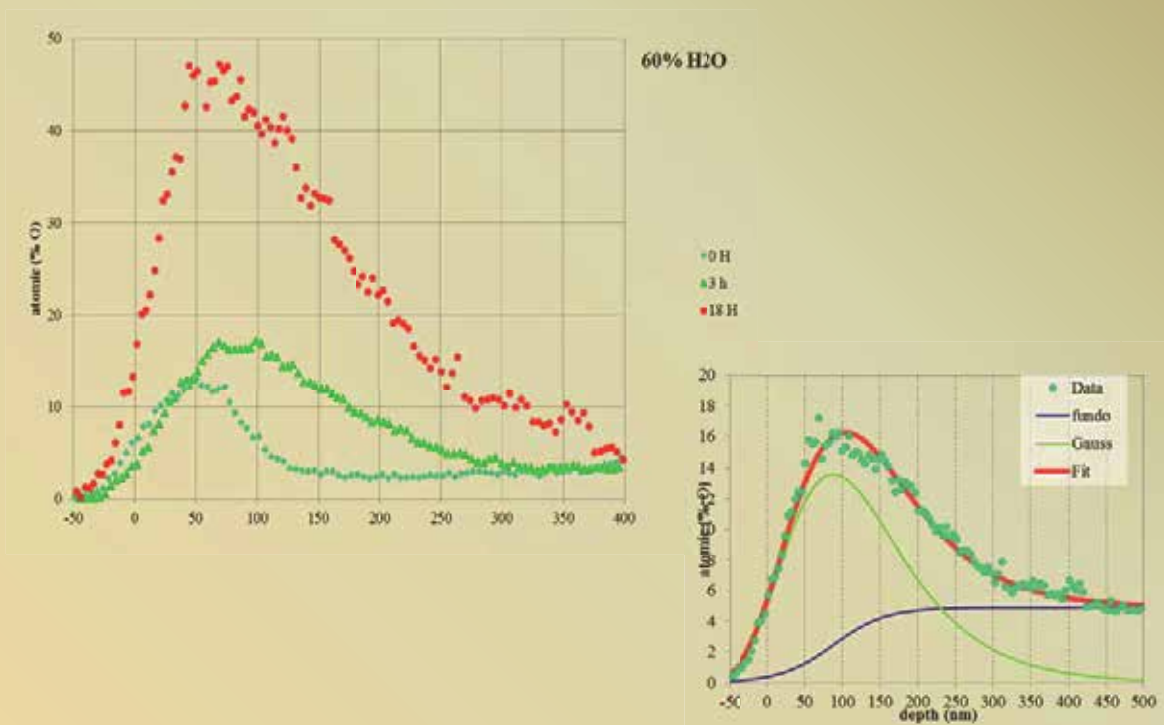
(J. Roth et.al. JNM 250(1997)23-28)

Oxidation in Air (55-60% Humidity)

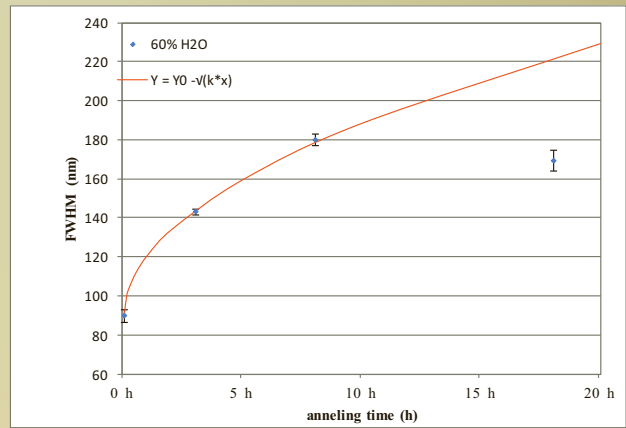
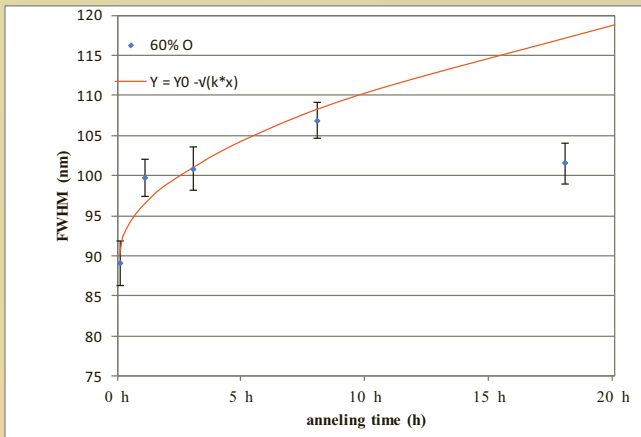
1 mm Irradiated Pebbles



Oxygen profiles

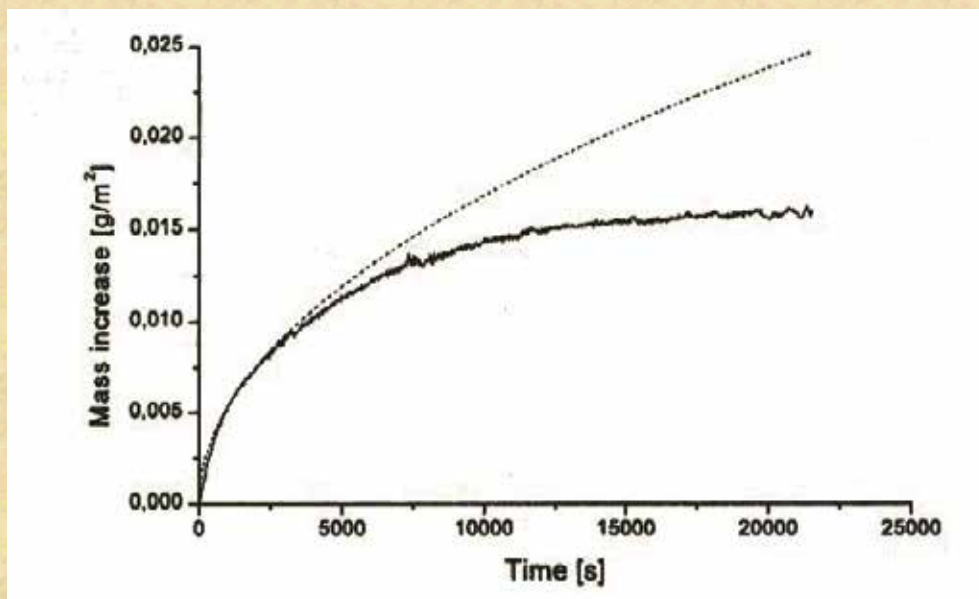


Oxidation Kinetics



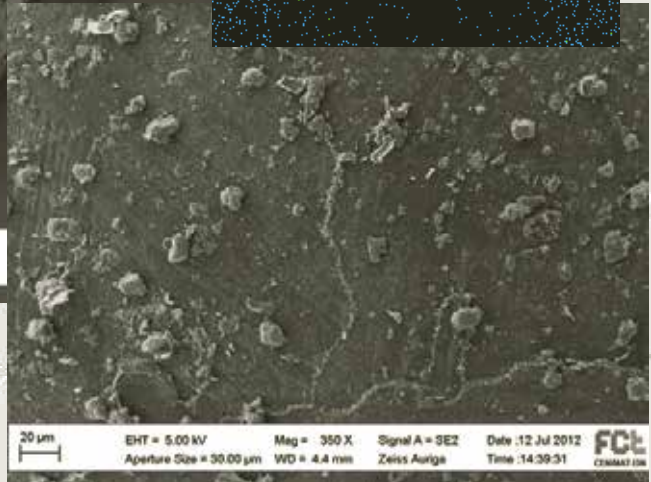
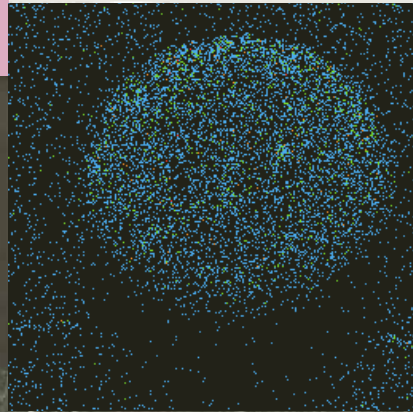
$$\frac{dn}{dt} = D\Delta C/x = Ndx/dt \quad \rightarrow \quad x^2 = x_0^2 + kt$$

Air annealing at 600 °C

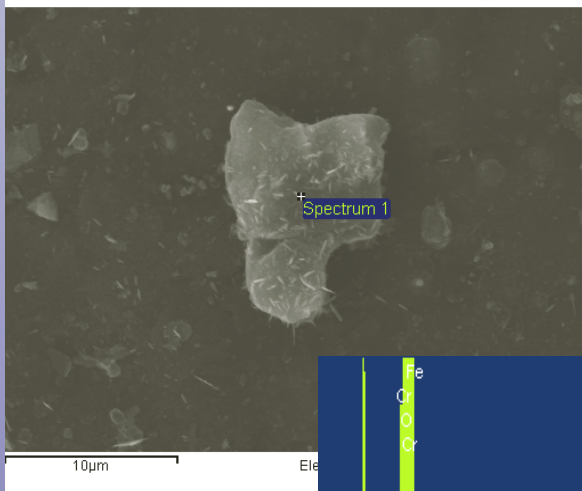


F. Druyts et.al. FED 58-58(2001) 695-700

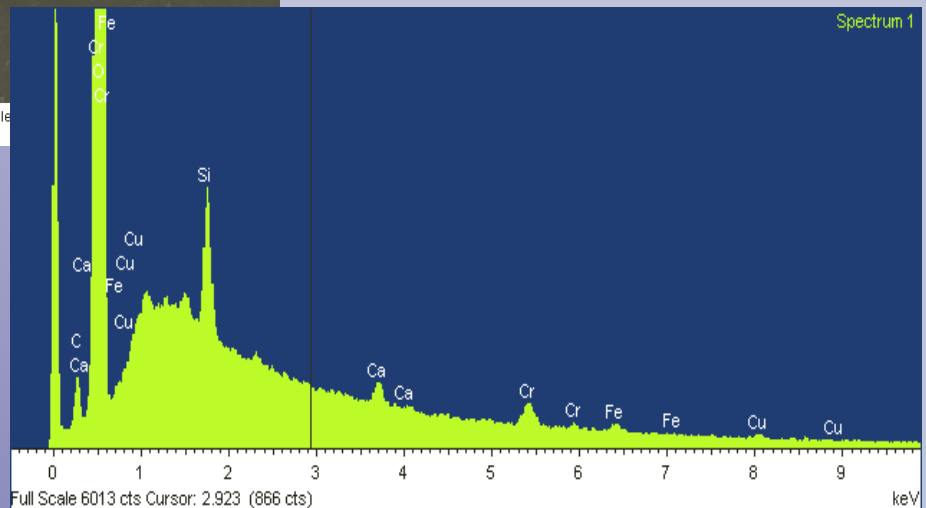
After oxidation 18 h in N₂O₂(60%)



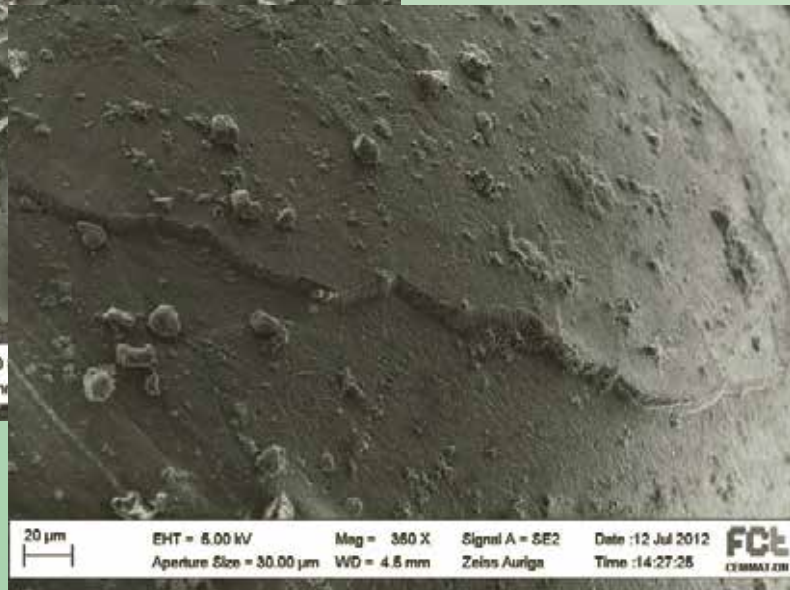
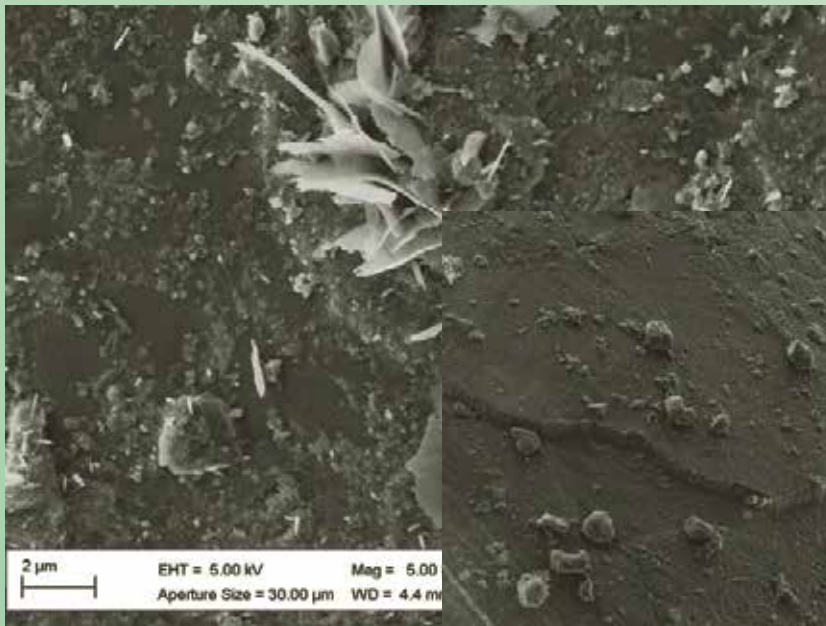
Oxide grains and oxidised grain boundaries



Grain composition:
Mixed oxides



Oxide flaking!

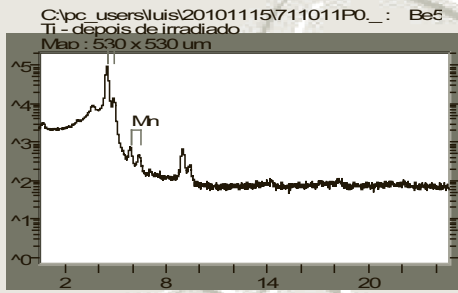


Summary

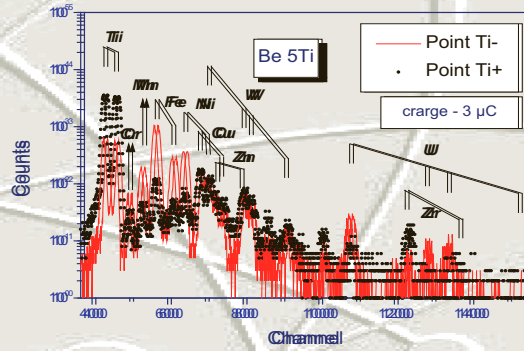
- Irradiated samples up to 525 °C show similar distribution of the chemical species over the near surface region of the samples compared to not irradiated samples.
- At 625 °C an increase on the oxide content is observed.
- Oxidation at 700 °C in air (20% humidity) show little effect on the oxide layer after 1 h.
- Analysis of the oxidation results at 55-60% air humidity and 60%O₂+N₂ at 700 °C shows the formation of a protective oxide layer.
- No evidence for any influence of irradiation on the oxidation behavior at 700 °C.

PIXE spectra

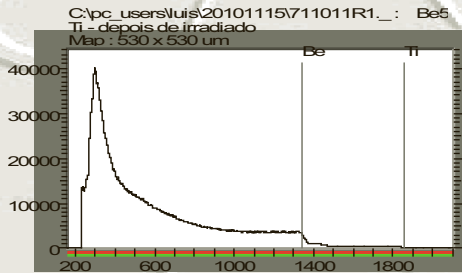
After irradiation



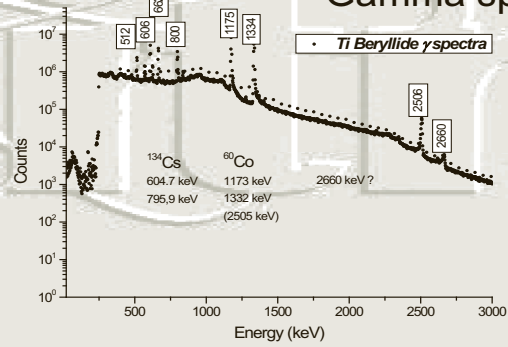
Before irradiation



RBS spectrum



Gamma spectrum



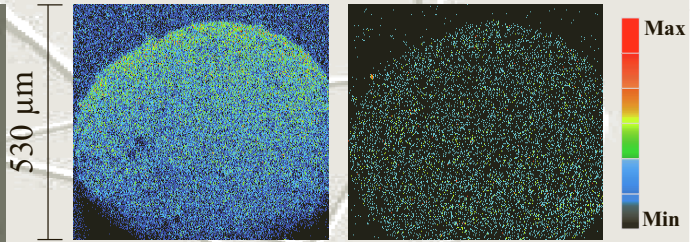
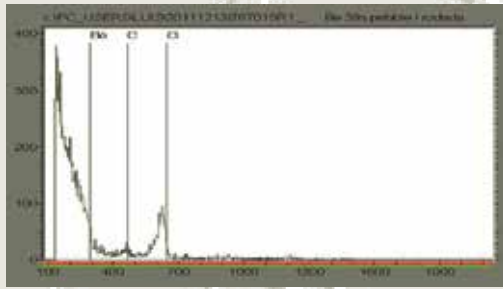
Samples

ITN	Temp	Oxid.	Chem.		total mg
0.5mm	425	30	30	=	60
	525				0
	650	30	30	=	60
	750				0
1.0mm (2001)	425	30	30	-	60
	525	30	30	=	60
	650				0
	750				0
1.0mm (2003)	425				0
	525				0
	650				0
	750				0
2.0mm	425				0
	525				0
	650				0
	750				0
Be elec	425				0
	525	1**	1**	=	100
	650				
	750				
Ti-Be 5%	425				
	525	1**	1**	=	100
	650				
	750				
Ti-Be 7%	425				
	525				
	650	1**	1**	=	100
	750				
Total (in mg)					540

** Number of pellet samples ; ~50 mg each

39s pc2 - 0.5 mm, 525°C

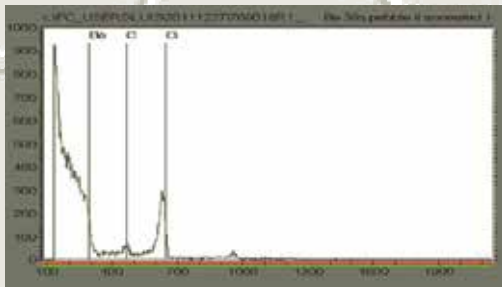
irradiated



Be

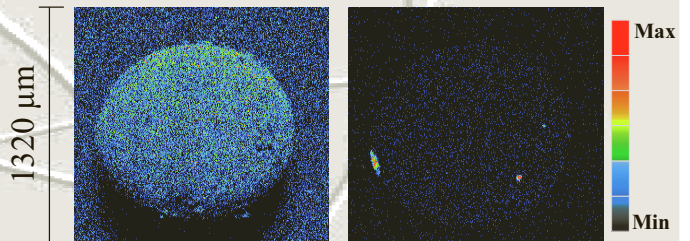
Fe

Annealed 700°C – 1h - air



46s pc2 – 1 mm, 525°C

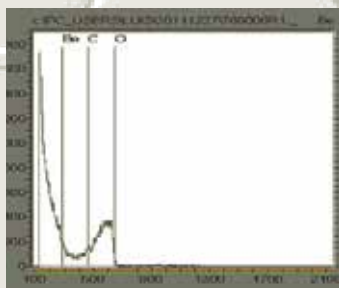
irradiated



Be

Fe

Annealed 700°C – 1h - air



Analysis of Tritium Retention in Beryllium Pebbles in EXOTIC, PBA AND HIDOBE-01 Experiments

Alexander Fedorov,
Sander van Til,
Lida Magielsens,
Marcel Stijkel

NRG, Petten,
The Netherlands

Outline of the talk

- Introduction
- Design of irradiation experiments
- Results of Temperature Programmed Desorption (TPD), Scanning Electron and Optical Microscopy
 - EXOTIC-8
 - PBA
 - HIDOBE-01
- Discussion
- Conclusions

DEMO HCPB. Beryllium operation parameters

parameter	units	
Pebble diameter	mm	1
Packing factor	%	63
Temperature window	°C	300-650
Purge gas		He+0.1%H ₂
Life time	hours	20 000
Amount	tons	300
Neutron flux	$\times 10^{15} \text{ cm}^{-2}\text{s}^{-1}$	0.18-1
Tritium production	appm/fpy	15-86
Helium production	appm/fpy	968-5700
Damage	dpa	3-17

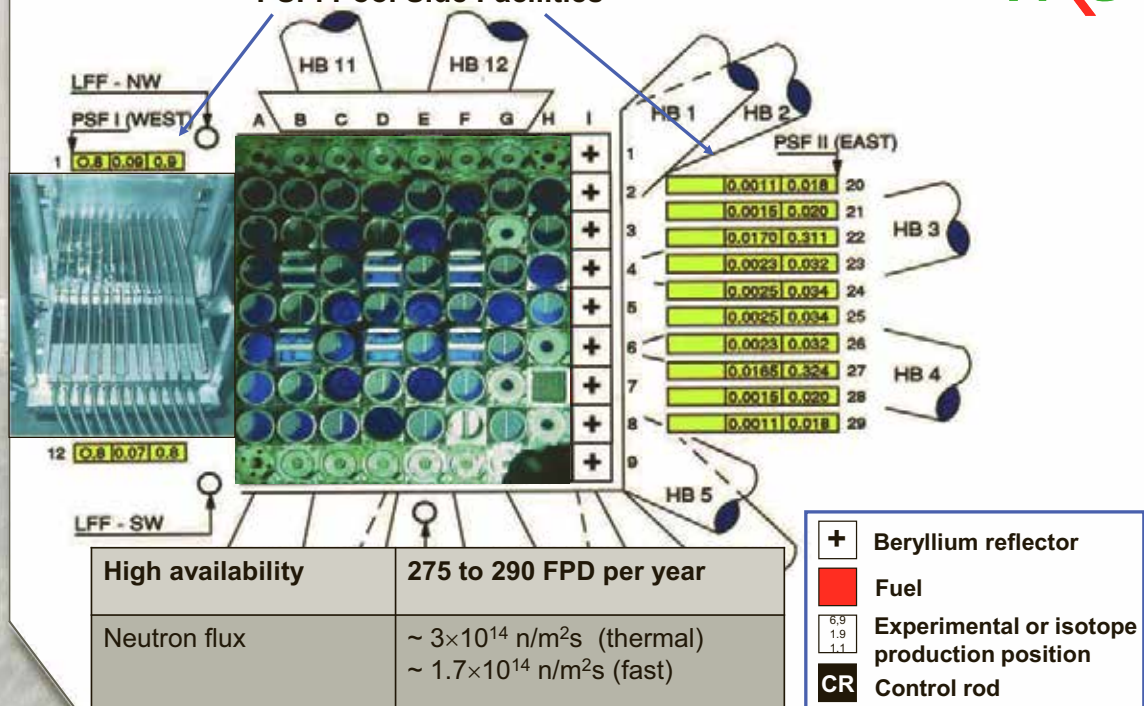
300 tons \times 90 T appm (100% retention) = 9 kg of tritium!

Chakin et al, report F4E-2009-GRT-030 (PNS-TBM) Action 1 – Task 2

3

High Flux Reactor in Petten

PSF: Pool Side Facilities



4

HIDOBE-01



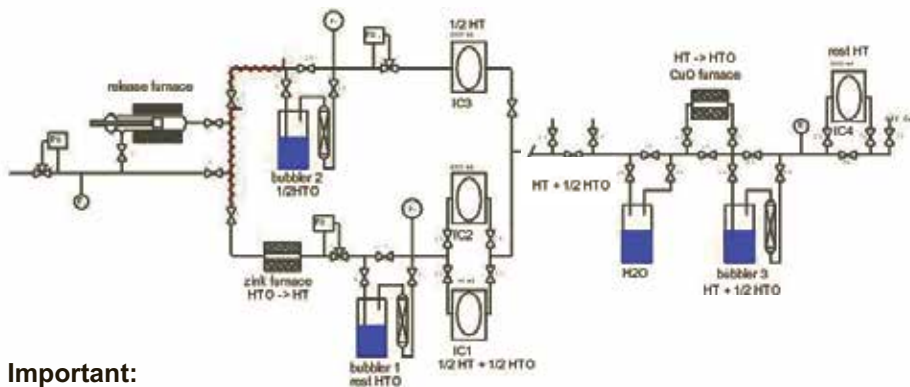
HIDOBE-01 targets of 3000 appm He production, which is about 10 % of the expected end-of-life value for the DEMO reactor

Drum 2-3 B: 425°C
C: 425°C
Drum 4-5 B: 525°C
C: 525°C
Drum 6-7 B: 650°C
C: 650°C
Drum 8-9 B: 750°C
C: 750°C
Drum 10 A: 750°C
Drum 11 A: 650°C
Drum 12 A: 525°C
Drum 13 A: 425°C

HIDOBE-02 with target of 6000 appm He is accomplished

Grade	Supplier	Name	BeO (wt%)	Density (g/cm3)	Specimen sizes (mm)	specification
1	RF/VNIINM	DDR grade	3.5-4.0	1.88	Ø6x2, Ø3.5x6, Ø3.5x2.5	pellet; grain size 5-8 micron
2	RF/VNIINM	TIP grade	1.2-1.4	1.86	Ø6x2, Ø3.5x6, Ø3.5x2.5	pellet; grain size 10-14 micron
3	RF/VNIINM	TIP-56 grade	0.4-0.6	1.85	Ø6x2, Ø3.5x6, Ø3.5x2.5	pellet; grain size 20-25 micron
4	RF/VNIINM	TIP-200 grade	0.2-0.3	1.85	Ø6x2, Ø3.5x6, Ø3.5x2.5	pellet; grain size 55-60 micron
5	RF/VNIINM	Porous Be	1.5	1.44	Ø6x2, Ø3.5x6, Ø3.5x2.5	pellet; ~20% porosity
6	RF/VNIINM	Porous Be	1.5	1.25	Ø6x2, Ø3.5x6, Ø3.5x2.5	pellet; ~30% porosity
7	EU-FZK	NGK pebbles	0.36		0.5	pebbles
8	EU-FZK	NGK pebbles	0.36		1.0	pebbles (2003)
9	EU-FZK	NGK pebbles	0.36		1.0	pebbles (2001)
10	EU-FZK	NGK pebbles	0.36		2.0	pebbles
11	JP/JAERI	Be Electrode	0.02	1.84	Ø8x2	discs
12	JP/JAERI	Be12Ti-5at%Ti	0.26	2.12	Ø8x2	discs
13	JP/JAERI	Be12Ti-7at%Ti	0.27	2.25	Ø8x2	discs
14	JP/JAERI	JP pebble 1	0.21		1.0	pebbles; standard
15	JP/JAERI	JP pebble 2	0.22		1.0	pebbles; standard
16	JP/JAERI	JP pebble 3	0.23		1.0	pebbles; low cost
17	JP/JAERI	JP pebble 4	1.10		1.0	pebbles; low cost
18	JP/JAERI	JP pebble 5	1.35		1.0	pebbles; low cost

Temperature Programmed Desorption set up



Important:

- Ionization chamber IC1 (or IC2) signal is proportional to tritium in both molecular forms: **HTO** and **HT**
- Ionization chamber IC3 signal is proportional to tritium in a molecular form of **HT**
- Absolute amount of released tritium is measured with LSC

Purge gas: 45 ml/min of He+0.1%H₂ Anneal rate = 0.5 °C/min

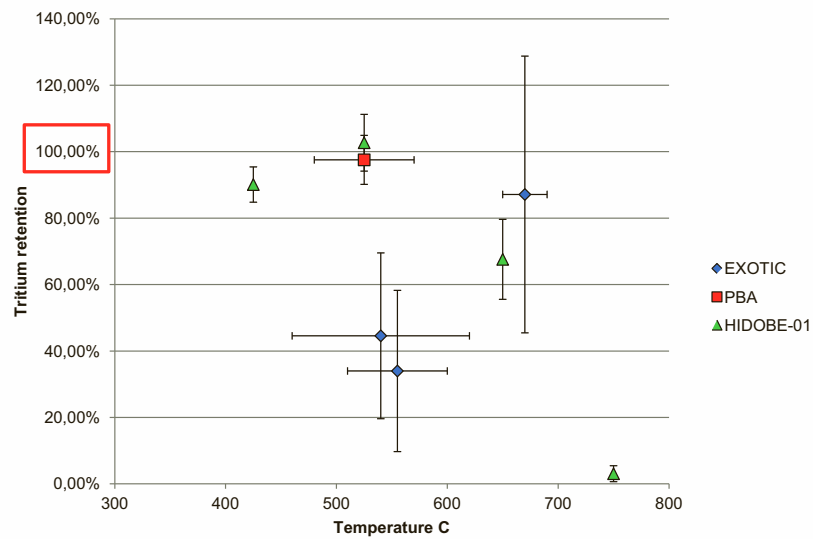
Measured tritium inventory



	units	E-8/3	E-8/7	E-8/8	PBA	HIDOBE-01
T measured	μCi/mg	0.6-1.7	1.1-3.9	0.3-1.8	55-64	480-540 (425°C) 645-762 (525°C) 450-645 (650°C) 6-50 (750°C)
T calculated	μCi/mg	1.32	5.61	3.09	61	566 (425°C) 685 (525°C) 810 (650°C) 917 (750°C)
He calculated	appm	100	283	259	183	1850-2980
T _{irr}	°C	650-690	460-620	510-600	220-480 320-570	425,525,650,750

9

Tritium retention in irradiated beryllium



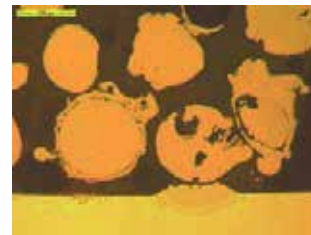
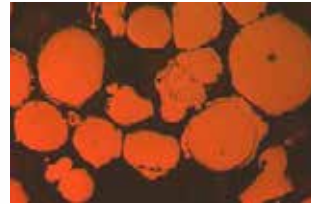
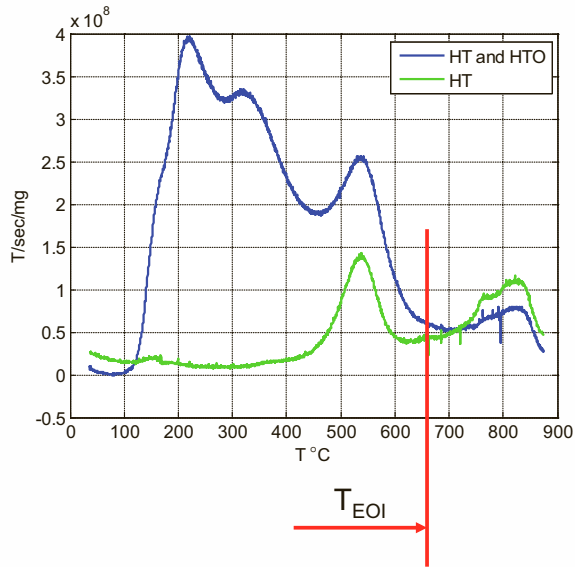
10



EXOTIC-8: Low temperature HTO release



Optical microscopy

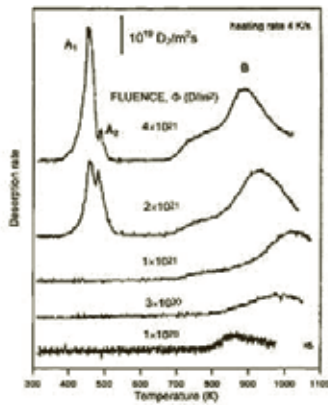


11

Deuterium implantation/exposure experiments in the literature

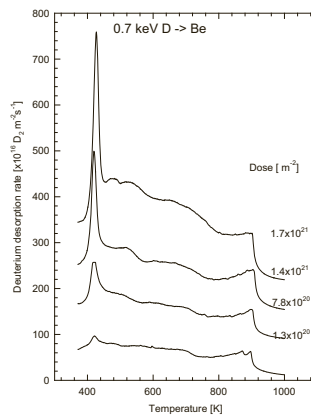


5 keV D implantation



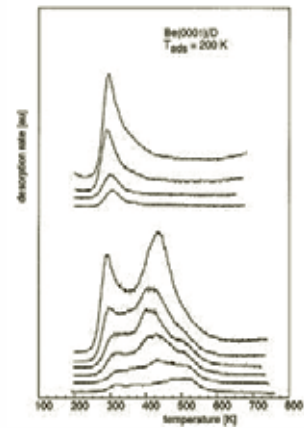
A.V. Markin et al. / Journal of Nuclear Materials 233-237 (1996) 865-869

0.7 keV D implantation



A.V. Fedorov, A. van Veen, G.J. Busker, Proc. 3rd BeWS, 1997, Mito, Japan, p152

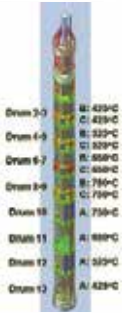
Surface exposure to D



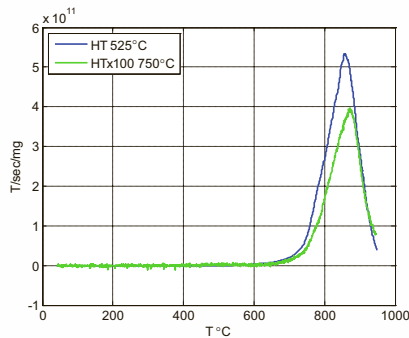
Lossev, J. Kuppens, JNM 196-198 (1992) 953-957

12

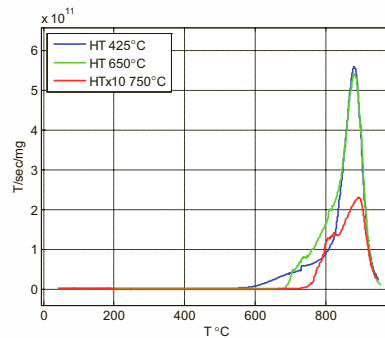
HIDOBE-01 TPD results



0.5 mm pebbles



2 mm pebbles



Observations:

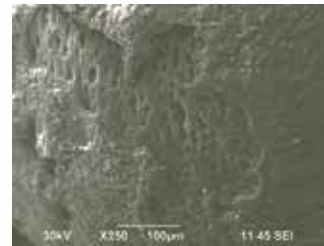
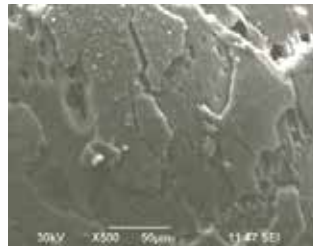
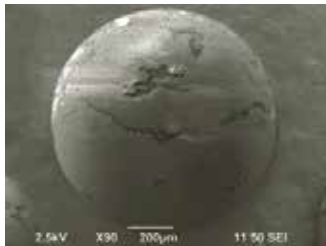
- Two contributions are identified:
 - 1) irregular bursts at 600-820 °C,
 - 2) well defined high temperature release at 880 °C
- Position of the high temperature peak (880 °C) does not depend on the tritium inventory and apparently defined by helium release
- The 0.5 mm pebbles (consisting of 1-2 grains) do not show the burst release at 600-820 °C

13

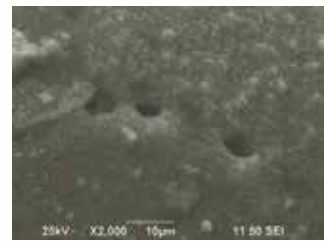
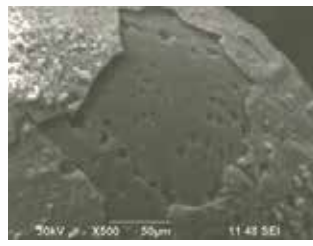
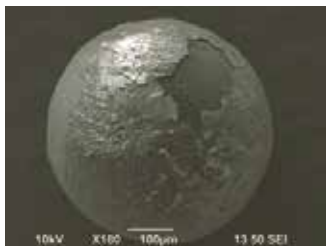
HIDOBE-01: State of the surface



1 mm pebbles, $T_{irr} = 525 \text{ } ^\circ\text{C}$



2 mm pebbles, $T_{irr} = 650 \text{ } ^\circ\text{C}$

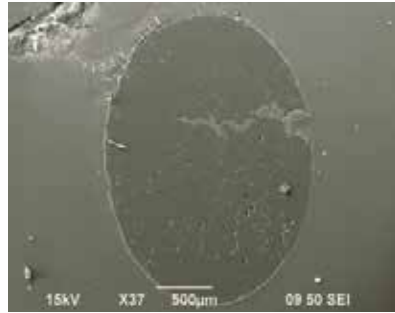
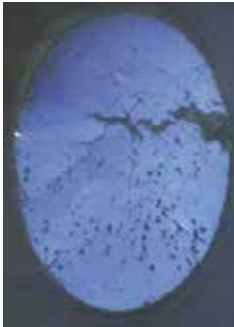


14

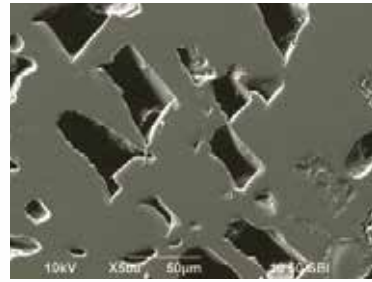
OM&SEM results: Network of channels



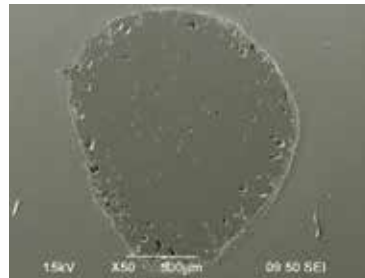
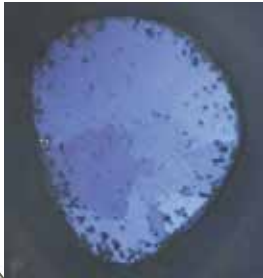
2 mm pebbles, $T_{irr} = 750\text{ }^{\circ}\text{C}$



1 mm pebbles, $T_{irr} = 525\text{ }^{\circ}\text{C}$



2 mm pebbles, $T_{irr} = 750\text{ }^{\circ}\text{C}$



same morphology?

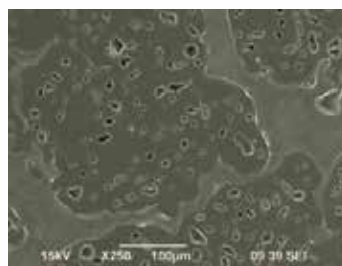
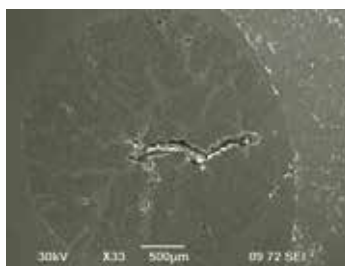


15

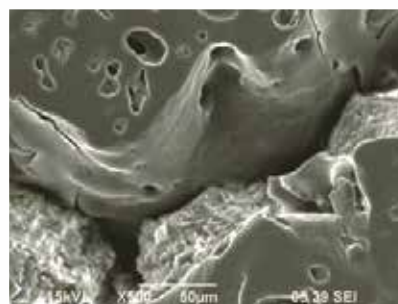
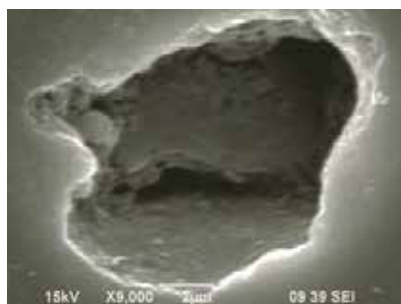
HIDOBE-01: irradiation and TPD



2 mm pebbles, $T_{irr} = 750\text{ }^{\circ}\text{C}$ + TPD at $T_{max} = 900\text{ }^{\circ}\text{C}$



The final structure does not depend on T_{irr} (Tritium content); but is defined by T_{max} and Helium content.

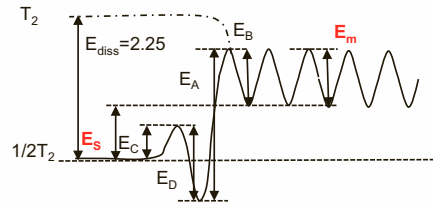


16

Discussion



Why tritium does not permeate from helium filled voids until 800 °C (1023 K) ?



Solubility

$E_S = 1$ eV (Swansiger)

Diffusion

$E_m = 0.3$ eV (Abramov)

$E_m = 0.2$ eV (Jones and R. Gibson)

Dissociation

$E_D = 0.8-1$ eV (Wampler)

$E_D = 0.87$ eV (450 K) (Be, Lossev&Kuippers)

$E_D = 0.61$ eV (320 K) (BeO, Lossev&Kuippers)

Trapping at Helium bubbles

$T_{diss} = 873$ K, $E_S = 2.7$ eV (Wampler)

$T_{diss} = 1000$ K, $E_S = 2.7$ eV (Fedorov)

$T_{diss} = 850-1050$ K, $E_S = 2.2-2.8$ eV (no He, Markin)

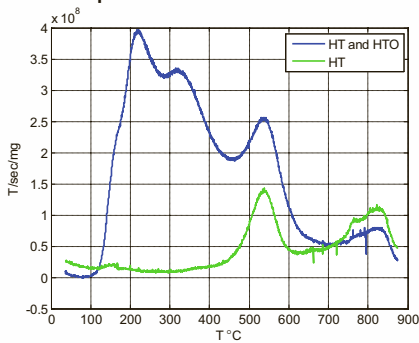
Permeation (gas driven)

$E_S + E_m = 0.28-0.91$ (Al'tovskiy)

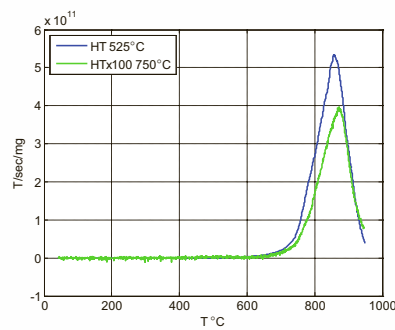
Modeling of TPD results



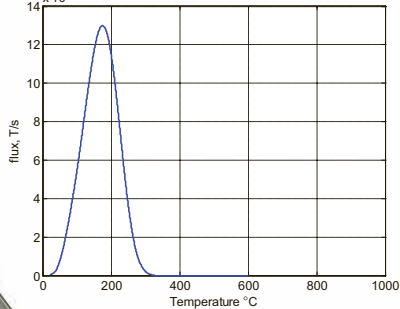
desorption from surface



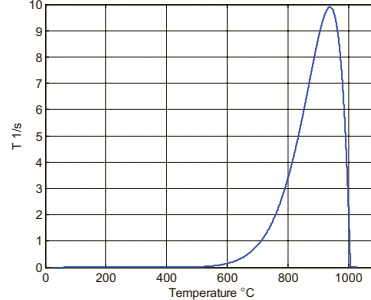
permeation from a cavity



bulk diffusion



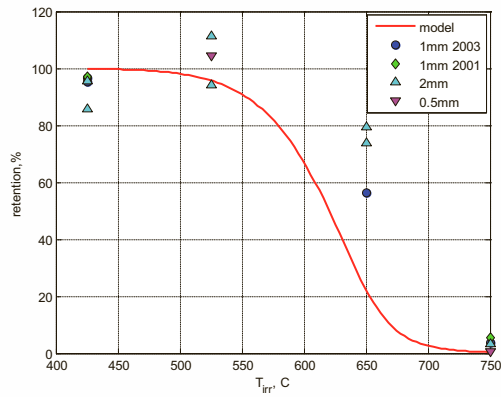
permeation



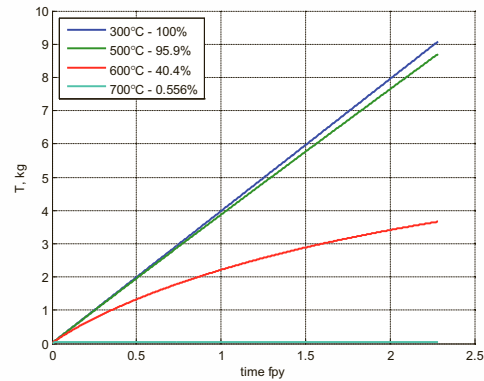
Modeling of HIDOBE and HCPB irradiation conditions



T retention in HIDOBE-01 experiment



T content in 300 ton Be in HCPB



19

Conclusions



1. Tritium retention in beryllium under irradiation below 600°C is ~ 100%. Tritium does not effectively permeate out of the helium-tritium filled bubbles (or cavities) until 650 °C.
2. At irradiation temperatures above 600 °C tritium retention decreases and drops to less than 5% at 750°C
3. At least three release mechanisms are identified:
 1. Surface release at ~ 180-210 °C in HTO molecular form, with associated $E_D = 0.8-1$ eV
 2. Burst type release observed at 600-800 °C (can disappear if pebble size comparable to the grain size)
 3. High temperature release at ~880 °C (does not depend on the tritium content!)
4. At 800-900 °C Helium forms an extended network of channels, which are apparently responsible for the tritium release

20

THANK YOU FOR ATTENTION



21

Discussion



Why tritium does not permeate from helium filled voids until 800 °C (1023 K) ?

Solubility

$E_S = 1$ eV (Swansiger)

Diffusion

$E_m = 0.3$ eV (Abramov)

$E_m = 0.2$ eV (Jones and R. Gibson)

Dissociation

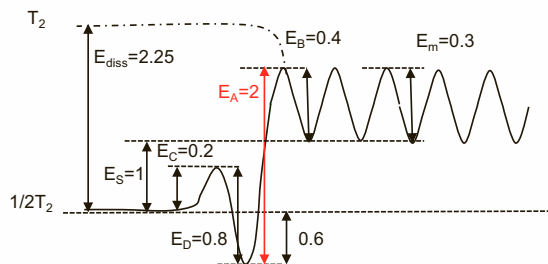
$E_D = 0.8-1$ eV (Wampler)

$E_D = 0.87$ eV (450 K) (Be, Lossev&Kuippers)

$E_D = 0.61$ eV (320 K) (BeO, Lossev&Kuippers)

Permeation (gas driven)

$E_S + E_m = 0.28-0.91$ (Al'tovskiy)



Trapping at Helium bubbles

$T_{diss} = 873$ K, $E_S = 2.7$ eV (Wampler)

$T_{diss} = 1000$ K, $E_S = 2.7$ eV (Fedorov)

$T_{diss} = 850-1050$ K, $E_S = 2.2-2.8$ eV (no He, Markin)

22

Extra slides



Extra slides



Extra slides

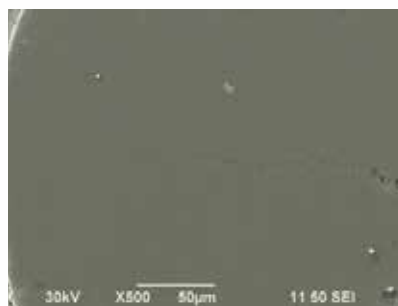


25

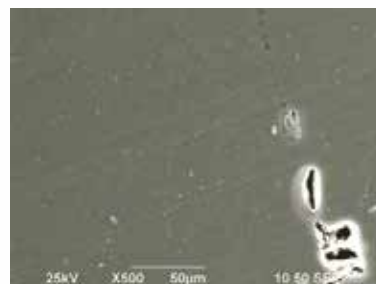
HIDOBE-01: Interconnected bubbles



0.5 mm pebbles, $T_{irr} = 650\text{ }^{\circ}\text{C}$



2 mm pebbles, $T_{irr} = 750\text{ }^{\circ}\text{C}$

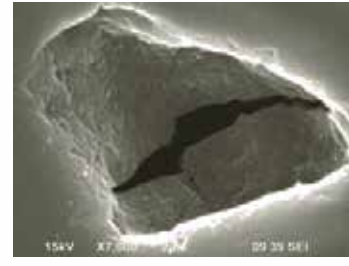
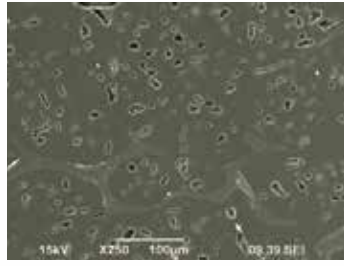
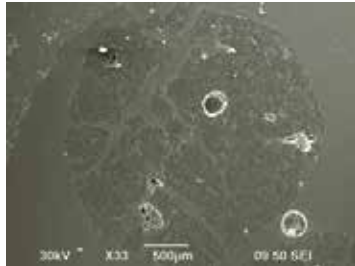
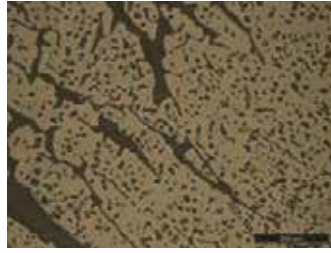
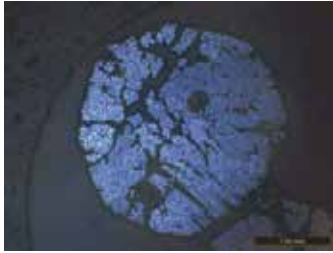


26

HIDOBE-01: irradiation and TPD



2 mm pebbles, $T_{\text{irr}} = 525 \text{ }^\circ\text{C}$ + TPD at $T_{\text{max}} = 900 \text{ }^\circ\text{C}$



27

HIDOBE-01



Experiment	units	HIDOBE-01
Duration	FPD	649
ϕ ($E_n > 1 \text{ MeV}$)	$\times 10^{25} \text{ m}^{-2}$	5.6-8.9
T_{irr}	$^\circ\text{C}$	425, 525, 650, 750
Tritium in Be	appm	176-285
Helium in Be	appm	1890-2950

28

Physical properties of beryllium



	EXOTIC-8/3,-8/7,-8/8	PBA	HIDOBE-01
Producer	Brush Wellman	NGK	NGK
Theoretical density, g/cm ³	1.850	1.850	
Pebble density, % TD	98	n.a.	
Closed pore volume, %	0.86	n.a.	
Pebble size, mm	0.08-0.18	0.7-1.3	0.42-0.6 (0.5 mm) 0.85-1.18 (1mm) 1.70-2.36 (2 mm)
Pebble bed density, g/cm ³	1.17	1.14	

29

Exotic- 8/3, 8/7 and 8/8 irradiations



Experiment	units	E-8/3	E-8/7	E-8/8
Duration	FPD	201	648	450
ϕ ($E_n > 0.1$ MeV)	$\times 10^{25} \text{ m}^{-2}$	1.3	3.7	3.0
T_{irr}	°C	330-680	460-620	510-600
Tritium in Be	appm	0.41	1.73	0.95
Helium in Be	appm	100	283	260
Ceramic material		$\text{Li}_2\text{TiO}_3 + \text{Te}$	Li_2TiO_3	Li_4SiO_4

Be provider: FZK(KIT) plasma spray

30

Pebble Bed Assembly (PBA) Irradiation



Experiment	units	PBA
Duration	FPD	294
ϕ ($E_n > 0.1$ MeV)	$\times 10^{25} \text{ m}^{-2}$	2.4-3.6
T_{irr}	$^{\circ}\text{C}$	220-480 TE#2 (upper bed) 320-570 TE#2 (lower bed)
Tritium in Be	appm	19
Helium in Be	appm	183

Be provider: FZK(KIT) plasma spray

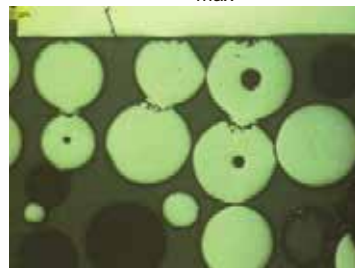
31



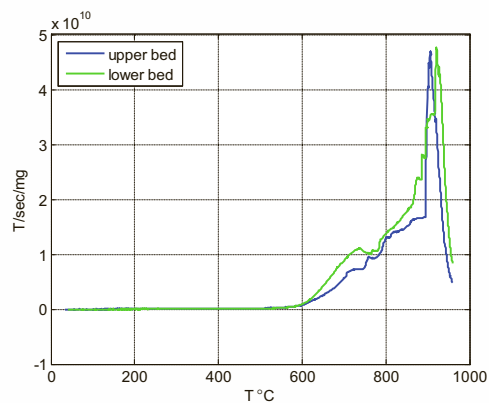
PBA: TPD results



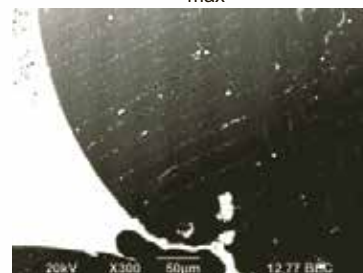
PBA, TE#2, $T_{\text{max}} = 570 \text{ }^{\circ}\text{C}$



PBA, TE#2, HT signal
 $T_{\text{max}} = 480 \text{ }^{\circ}\text{C}$ (upper bed)
 $T_{\text{max}} = 570 \text{ }^{\circ}\text{C}$ (lower bed)



PBA, TE#3, $T_{\text{max}} = 500-590 \text{ }^{\circ}\text{C}$

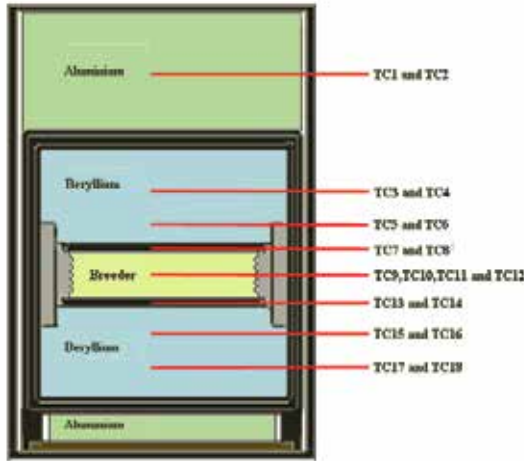


32

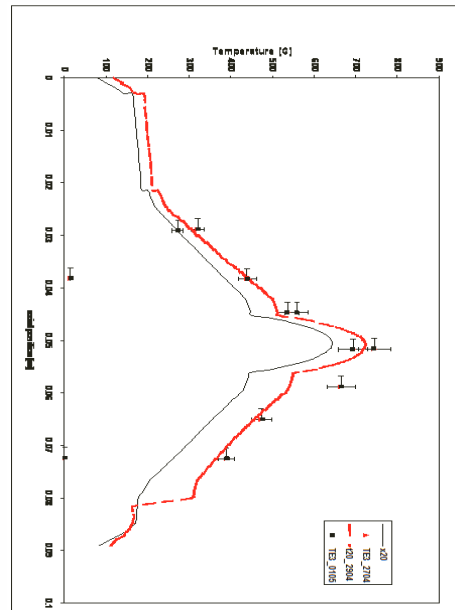
Pebble Bed Assembly (PBA) Irradiation



Positions of thermocouples



Axial temperature profile



33

Chemical composition of beryllium



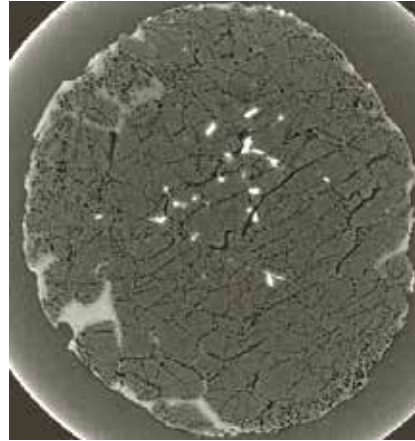
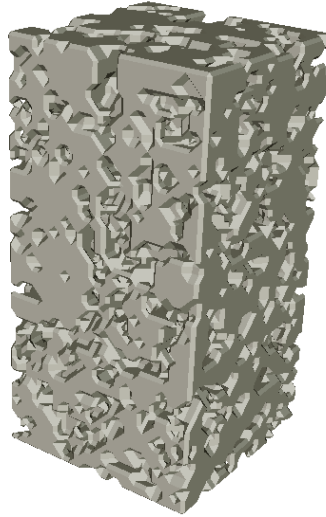
Element	units	EXOTIC-8/3, 8/7, 8/8 Brush Wellman	PBA, NGK pebbles	HIDOBE-01, NGK pebbles
Be	wt %	99.4	n.a.	99.0-99.5
BeO	wt %	0.34	n.a.	0.36
Fe	wt %	0.09	0.09	0.088-0.094
C	wt %	0.07	0.07	
Al	wt %	0.04	0.04	0.047-0.48
B	wt %	-	0.04	
Mg	wt %	<0.01	0.02	0.018-0.024
Si	wt %	0.03	n.a.	0.027-0.029
Cl	wppm	< 100	100	
F	wppm	80	80	
Mn	wppm	80	80	
Ni	wppm	60	60	
Cu	wppm	40	40	
Co	wppm	5	10	< 10
W	wppm	100	100	
U	wppm	30	100	< 100
Cr	wppm	50	50	
Sc	wppm			< 50

34

Computed tomography on neutron irradiated beryllium



Helium 480 appm,
Tritium 12 appm,
 $T_{irr} = 770K$,
 $T_{ann} = 1500 K$

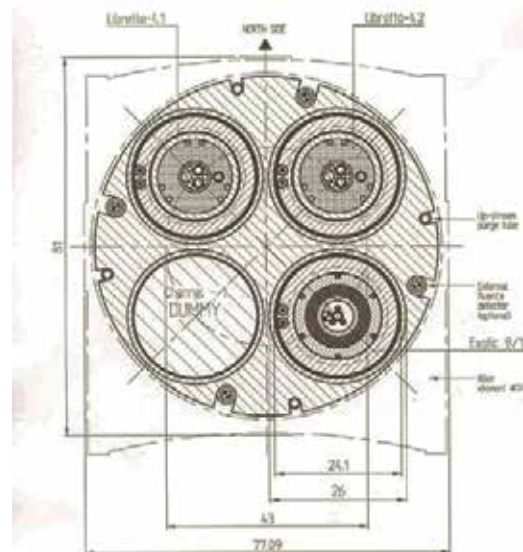


A. Möslang et al, JNM 2008

Irradiation in High Flux Reactor, Petten

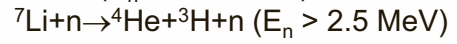
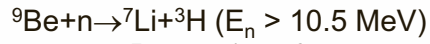
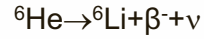
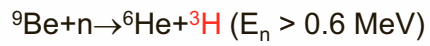
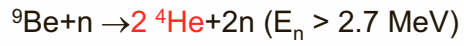
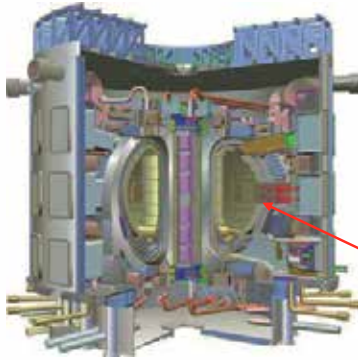


	A	B	C	D	E	F	G	H	I
1									
PSFW 2				1.22E+14 1.13E+14		8.70E+13 8.02E+13		5.42E+13 3.76E+13	
5 3	1.78E+14 3.46E+13		1.32E+14 1.74E+14		1.03E+14 1.35E+14		6.23E+13 8.68E+13		
6 4	1.52E+14 4.37E+13							6.07E+13 6.16E+13	
7 5	1.50E+14 4.42E+13		2.92E+14 1.77E+14		2.37E+14 1.37E+14		7.45E+13 1.02E+14		
8 6	1.42E+14 4.11E+13							5.91E+13 6.20E+13	
9 7	1.59E+14 3.00E+13		1.32E+14 1.73E+14		1.89E+14 1.15E+14		5.75E+13 8.38E+13		
10 8	1.55E+14 1.67E+13			2.01E+14 9.48E+13		8.26E+13 7.55E+13		5.17E+13 3.74E+13	
9									

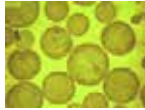


Horizontal cross-section of the TETRA-124 rig

Helium Cooled Pebble Bed EU concept



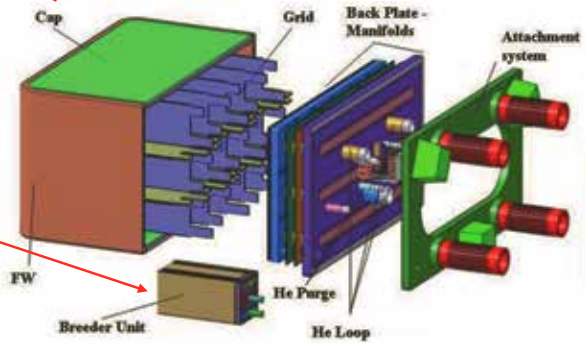
Li₄SiO₄ pebbles



Be pebbles

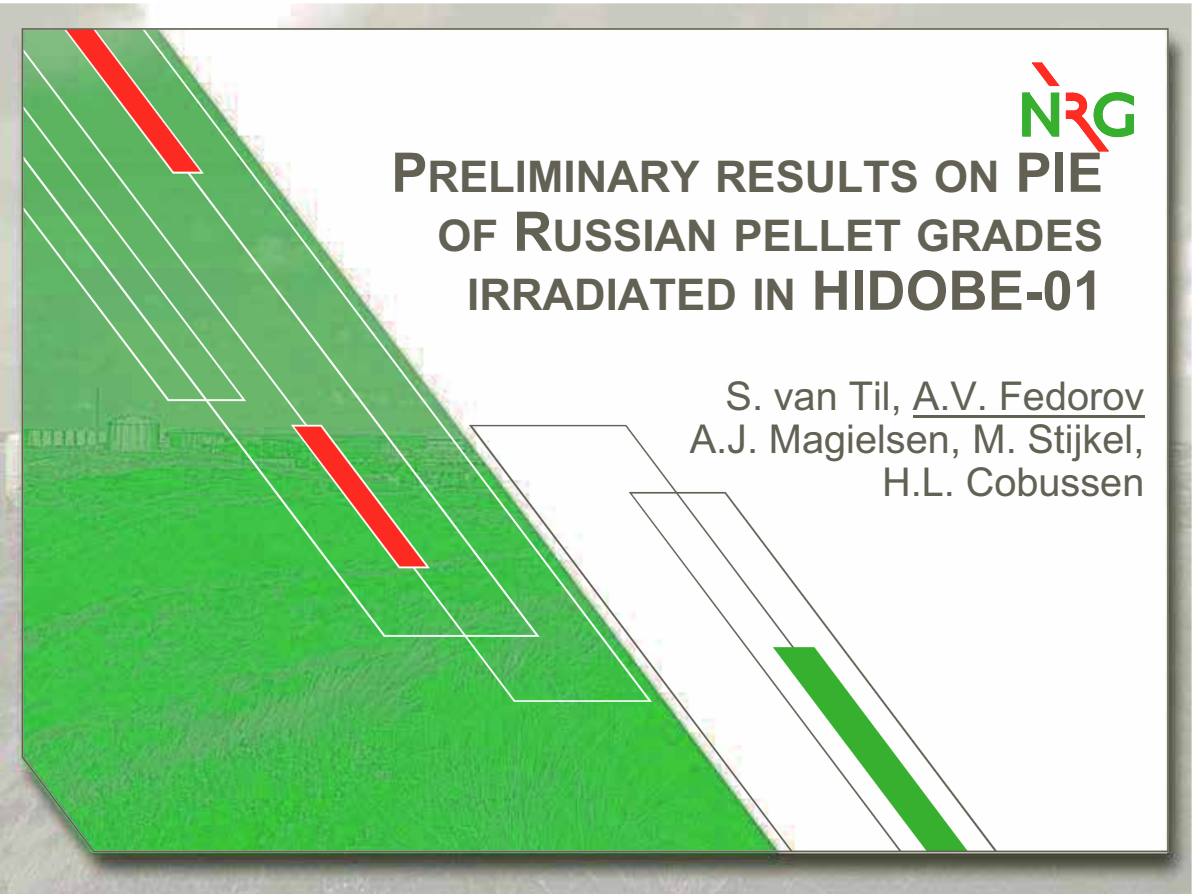


or Li₂TiO₃ pebbles



PRELIMINARY RESULTS ON PIE OF RUSSIAN PELLET GRADES IRRADIATED IN HIDOBE-01

S. van Til, A.V. Fedorov
A.J. Magielsens, M. Stijkel,
H.L. Cobussen



HIDOBE-01

12 drums

3 drum types

19 different grades of beryllium

i.e. - pebbles (4xEU, 5xJP)

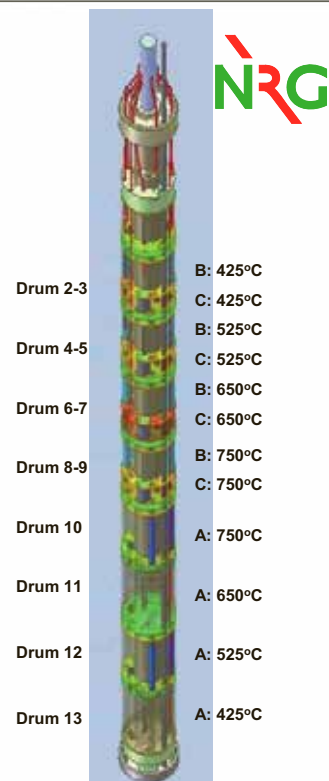
- pellets (6xRF, 3xJP)

4 temperature zones

425°C, 525°C, 650°C, 750°C

	Supplier	Name	BeO (wt%)	Density (g/cm ³)	Specimen sizes (mm)	specification
1	RF/NIINM	DDR grade	3.5-4.0	1.88	Ø6x2, Ø3.5x6, Ø3.5x2.5	grain size 5-8 micron
2	RF/NIINM	TIP grade	1.2-1.4	1.86	Ø6x2, Ø3.5x6, Ø3.5x2.5	grain size 10-14 micron
3	RF/NIINM	TIP-56 grade	0.4-0.6	1.85	Ø6x2, Ø3.5x6, Ø3.5x2.5	grain size 20-25 micron
4	RF/NIINM	TIP-200 grade	0.2-0.3	1.85	Ø6x2, Ø3.5x6, Ø3.5x2.5	grain size 55-60 micron
5	RF/NIINM	Porous Be	1.5	1.44	Ø6x2, Ø3.5x6, Ø3.5x2.5	~20% porosity
6	RF/NIINM	Porous Be	1.5	1.25	Ø6x2, Ø3.5x6, Ø3.5x2.5	~30% porosity
7	EU/FZK	NGK pebbles	0.36		0.5	pebbles
8	EU/FZK	NGK pebbles	0.36		1.0	pebbles (2003)
9	EU/FZK	NGK pebbles			1.0	pebbles (2001)
10	EU/FZK	NGK pebbles	0.36		2.0	pebbles
11	JP/JAERI	Be Electrode	0.02	1.84	Ø8x2	discs
12	JP/JAERI	Be12Ti-5at%Ti	0.26	2.12	Ø8x2	discs
13	JP/JAERI	Be12Ti-7at%Ti	0.27	2.25	Ø8x2	discs
14	JP/JAERI	JP pebble 1	0.21		1.0	standard
15	JP/JAERI	JP pebble 2	0.22		1.0	standard
16	JP/JAERI	JP pebble 3	0.23		1.0	low cost
17	JP/JAERI	JP pebble 4	1.10		1.0	low cost
18	JP/JAERI	JP pebble 5	1.35		1.0	low cost

* grade 1 to 4, one specimen D3.5x6 and D3.5x2.5 will be covered with BeO coating, 5 um
* grade 1 to 4, two TEM specimens will be cold worked



Loading matrix (+ retrieved)



Grd.	Supplier	name	specs	Specimen	size	Temperatures	Num /Temperature			Total samples			
							a	c	O				
1	RF/VNIINM	DDR grade	grain size 5-8 micron, ~3.5-	Swelling	∅3.5x5.5	425, 525, 650, 750	2	1	1	16			
				Tritium	∅3.5x2.5	425, 525, 650, 750	7	2	1	40			
						425, 525	4	4	0	16			
				TEM	∅3x0.4	650, 750	6	2	0	16			
						650, 750	3	0	0	12			
2	T _{irr}	total	RF pellets loaded	RF pellets retrieved		650, 750	2	1	1	16			
					425	drum 2	70	70	650, 750	7	2	1	40
					425	drum 3	22	22		4	4	0	16
					525	drum 4	70	70	650, 750	6	2	0	16
					525	drum 5	22	22	650, 750	3	0	0	12
3	650	drum 6	22	22		650, 750	2	1	1	16			
					650	drum 7	69	53	650, 750	7	2	1	40
					650	drum 8	22	22		4	4	0	16
					750	drum 9	70	0	650, 750	6	2	0	16
4	750	drum 9	22	16		650, 750	3	0	0	12			
						650, 750	2	1	1	16			
						650, 750	7	2	1	40			
		total	367	275		650, 750	4	4	0	16			
			~0.2-0.3wt% BeO	TEM disc 6	∅3x0.4	650, 750	6	2	0	16			
5	RF/VNIINM	Porous Be	~20% porosity	Swelling	∅3.5x6	425, 525, 650, 750	3	0	0	12			
				Tritium	∅3.5x2.5	425, 525, 650, 750	6			24			
					disc 6	∅6x2	425, 525, 650, 750	3			12		
6	RF/VNIINM	Porous Be	~30% porosity	Swelling	∅3.5x6	425, 525, 650, 750	3			12			
				Tritium	∅3.5x2.5	425, 525, 650, 750	6			24			
					disc 6	∅6x2	425, 525, 650, 750	3			12		
a: annealed, c: coldworked, O: BeO coated samples										496			

3

PIE plan



Boundary conditions:

- Budget: ~100k€
- Runtime: ASAP – ~15.12.2012

The following measurements are planned:

- Dimensions and densities
- Tritium release
- Diffusivity / Conductivity : LFA
- Microscopy (SEM/OM + microhardness?)

4

RF HIDOBE-01: global PIE plan



Grd.	Supplier	name	specs	Specimen	size	Total measurements (still decide on a,c or O)					
						DimDens	T-release	LFA	TEM	OM/ microhardness	SEM
1	RFV/NINM	DDR grade	grain size 5-8 micron, ~3.5-4.0w t% BeO	Swelling	∅3.5x5.5	3	3				
				Tritium	∅3.5x2.5	7	2				
				disc 6	∅6x2	2		3	2	2	
2	RFV/NINM	TIP grade	grain size 10-14 micron, ~1.2-1.4w t% BeO	Swelling	∅3.5x5.8	0					
				Tritium	∅3.5x2.5	7	2				
				disc 6	∅6x2	2		3	2	1	
3	RFV/NINM	TIP-56 grade	grain size 20-25 micron, ~0.4-0.6w t% BeO	Swelling	∅3.5x6.1	0					
				Tritium	∅3.5x2.5	7	2				
				disc 6	∅6x2	2		3	2	1	
4	RFV/NINM	TIP-200 grade	grain size 55-60 micron, ~0.2-0.3w t% BeO	Swelling	∅3.5x6.4	0					
				Tritium	∅3.5x2.5	7	3				
				disc 6	∅6x2	2		3	2	1	
5	RFV/NINM	Porous Be	~20% porosity	Swelling	∅3.5x6	3					
				Tritium	∅3.5x2.5	3	3				
				disc 6	∅6x2	4		4	2	2	
6	RFV/NINM	Porous Be	~30% porosity	Swelling	∅3.5x6	3					
				Tritium	∅3.5x2.5	3	3				
				disc 6	∅6x2	4		4	2	1	
						53	18	20	0	12	8

a=annealed ; c = cold-worked ; O = BeO-coated

5

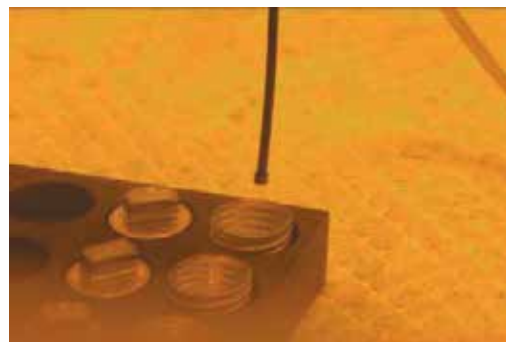
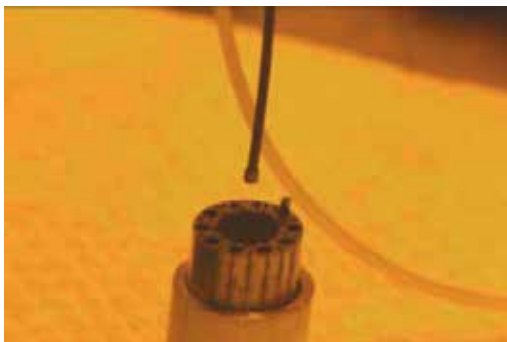
Dismantling: Extracting pellets



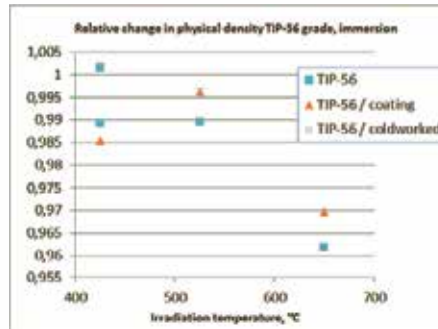
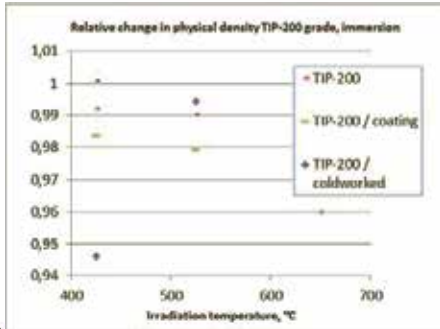
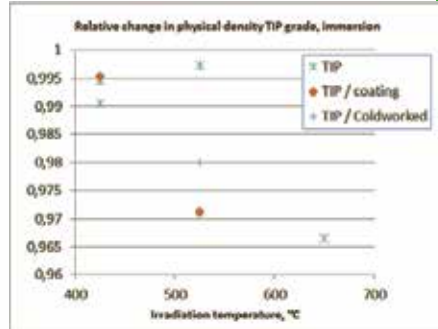
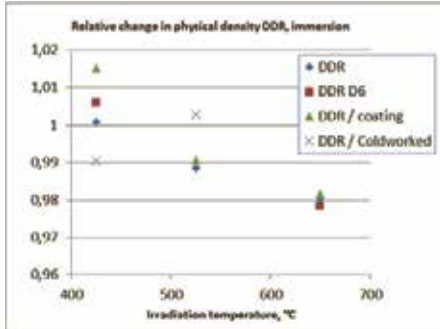
First 'pushing device' (left) was developed. This turns out to be 'too imprecise' for pellets.

A 'suction cup device' (bottom) was developed to take out pellets, one by one.

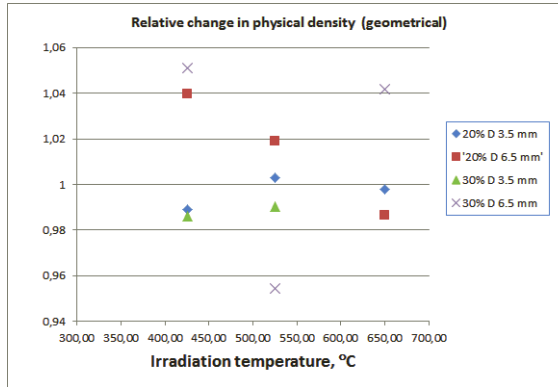
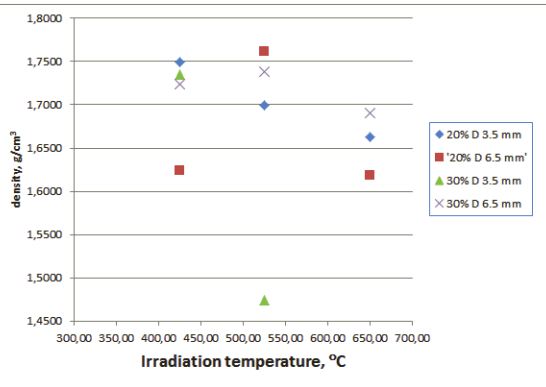
Total of 451 pellets in all B and C drums.



Results on TIP and DDR grades (immersion)



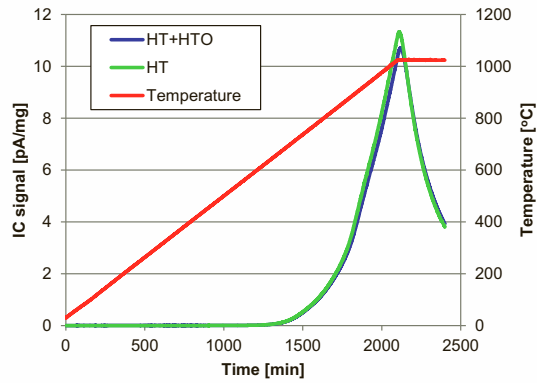
Results on 20% and 30% porous beryllium



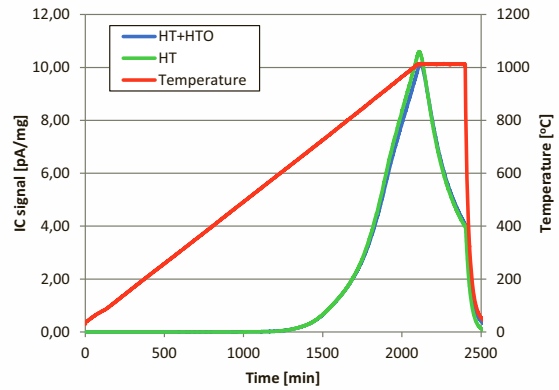
TPD results



1F1: DDR grade 425 °C



3G1: TIP grade 425 °C



9

Conclusions



- The PIE plan and sample matrix are defined
- Most of the specimens are retrieved from the drums and are schedules for measurements
- The measurements and analysis of the data are in progress

10

Dimensions and densities



Dimensions of most pellets:

Ø3.5mm x 2.5mm

→ volume ~ 0.025 cm³

Problem for:

immersion?

(only 40-50 mg)

pycnometry?

(<10% chamber vol.

Incl. calibration volume?)

No hassle of shooting pebbles

Grd.	Supplier	name	size	425	525	650	750
				DimDens			
1	RFV/NINIM	DDR grade	Ø3.5x5.5	a, c, O			
			Ø3.5x2.5	c, O	a, c, O	c, O	
			Ø6x2	a		a	
2	RFV/NINIM	TIP grade	Ø3.5x5.8				
			Ø3.5x2.5	O	a, c, O	a, c, O	
			Ø6x2	a			a
3	RFV/NINIM	TIP-56 grade	Ø3.5x6.1				
			Ø3.5x2.5	O	a, c, O	a, c, O	
			Ø6x2	a			a
4	RFV/NINIM	TIP-200 grade	Ø3.5x6.4				
			Ø3.5x2.5	c, O	a, c, O	c, O	
			Ø6x2	a		a	
5	RFV/NINIM	Porous Be	Ø3.5x6				
			Ø3.5x2.5	1	1	1	
			Ø6x2	1	1	1	1
6	RFV/NINIM	Porous Be	Ø3.5x6				
			Ø3.5x2.5	1	1	1	
			Ø6x2	1	1	1	1
a=annealed ; c = cold-worked ; O = BeO-coated							
total/T				14	16	16	7
total							53

11

Tritium release



volume ~ 0.025 cm³

Either

0.5K/min or

1.0 K/min

Grd.	Supplier	name	size	425	525	650	750
				T-release			
1	RFV/NINIM	DDR grade	Ø3.5x5.5	a, c, O			
			Ø3.5x2.5	a		a	
			Ø6x2				
2	RFV/NINIM	TIP grade	Ø3.5x5.8				
			Ø3.5x2.5	a	a	a	
			Ø6x2				
3	RFV/NINIM	TIP-56 grade	Ø3.5x6.1				
			Ø3.5x2.5	a		a	
			Ø6x2				
4	RFV/NINIM	TIP-200 grade	Ø3.5x6.4				
			Ø3.5x2.5	a, O		a, c, O	
			Ø6x2				
5	RFV/NINIM	Porous Be	Ø3.5x6				
			Ø3.5x2.5	1	1	1	
			Ø6x2				
6	RFV/NINIM	Porous Be	Ø3.5x6				
			Ø3.5x2.5	1		1	
			Ø6x2				
a=annealed ; c = cold-worked ; O = BeO-coated							
total/T				7	2	8	3
total							20

12

LFA



Measurement details?

Ø6.0mm x 2mm

$T_{exp} \leq T_{irr}$?

Other prerequisites?

Grd.	Supplier	name	size	LFA				
				425	525	650	750	
1	RF/VNINIM	DDR grade	Ø3.5x5.5					
			Ø3.5x2.5					
			Ø6x2	a	a	a		
2	RF/VNINIM	TIP grade	Ø3.5x5.8					
			Ø3.5x2.5					
			Ø6x2	a	a	a	a	
3	RF/VNINIM	TIP-56 grade	Ø3.5x6.1					
			Ø3.5x2.5					
			Ø6x2	a		a	a	
4	RF/VNINIM	TIP-200 grade	Ø3.5x6.4					
			Ø3.5x2.5					
			Ø6x2	a	a	a		
5	RF/VNINIM	Porous Be	Ø3.5x6					
			Ø3.5x2.5					
			Ø6x2	1	1	1	1	
6	RF/VNINIM	Porous Be	Ø3.5x6					
			Ø3.5x2.5					
			Ø6x2	1		1	1	
a=annealed ; c = cold-worked ; O = BeO-coated				total/T	6	4	6	4
				total	20			

13

OM/SEM



Grd.	Supplier	name	size	OM				SEM				
				425	525	650	750	425	525	650	750	
<p>Overlap in samples between OM and SEM</p> <ul style="list-style-type: none"> - Microhardness available? - 4 x samples in 1 holder? <ul style="list-style-type: none"> - (same shape / size) - little variation in hardness(?) - Orientation pellets to be decided 							a				a	
					a					a		
					a	a					a	
					a		a				a	
					a	a					a	
							1	1			1	1
5	RF/VNINIM	Porous Be	Ø3.5x6									
			Ø3.5x2.5									
			Ø6x2			1	1		1	1		
6	RF/VNINIM	Porous Be	Ø3.5x6									
			Ø3.5x2.5									
			Ø6x2	1		1	1					
a=annealed ; c = cold-worked ; O = BeO-coated				total/T	3	3	4	2	1	2	3	2
				total	12				8			

Request (actions)



Check estimated hours (once more)

Measurement	Man hours	Man hour Costs (in €)	Required resources	Resource hours	Resource Costs (in €)	Remarks	Cost per test
Dose rate measurements (G1)	0.5	60	G1	0.5	45		105
Set of							
Dimension (optical)	3	375	Glove boxes T-lab	3	60	when done in one 'go' ; incl. dose rate	435
Density (immersion)							
He-Pycnometry							
Mass							
Tritium release (TPD)	5	625	TPD Glove box	(Use >24h)	350	** max. 1 measurements/week; incl LSC (bubbler)	975
Dissolution H-3 (LSC)	3	375	cabinet, LSC	3	60		435
Dissolution Li (MS)	3	375	cabinet, MS	3	350	MS hours + prep in zuurkast	725
LFA (glove box g-cell)	2	240	GB behind G	8	160	Sample limit of 2 mSv/hr	400
OM (x-section)	4	380	F-cells in HCL	4	280	incl. initial sample	760
SEM (x-section)	2	240	F-cells in HCL	4	280		530
TEM	4	480	TEM in JGL	4	280		760

** TPD price alternatively estimated

Planning (work- and runtime)

15

Loading matrix (+ retrieved)



Grd.	Supplier	name	specs	Specimen	size	Temperatures	Num /Temperature			Total samples
							a	c	O	
1	RF/VNIINM	DDR grade	grain size 5-8 micron, ~3.5-4.0wt% BeO	Swelling	Ø3.5x5.5	425, 525, 650, 750	2	1	1	16
				Tritium	Ø3.5x2.5	425, 525, 650, 750	7	2	1	40
				TEM	Ø3x0.4	425, 525, 650, 750	4	4	0	16
				disc 6	Ø6x2	425, 525, 650, 750	6	2	0	16
2	RF/VNIINM	TIP grade	grain size 10-14 micron, ~1.2-1.4wt% BeO	Swelling	Ø3.5x5.8	425, 525, 650, 750	2	1	1	16
				Tritium	Ø3.5x2.5	425, 525, 650, 750	7	2	1	40
				TEM	Ø3x0.4	425, 525, 650, 750	4	4	0	16
				disc 6	Ø6x2	425, 525, 650, 750	6	2	0	16
3	RF/VNIINM	TIP-56 grade	grain size 20-25 micron, ~0.4-0.6wt% BeO	Swelling	Ø3.5x6.1	425, 525, 650, 750	2	1	1	16
				Tritium	Ø3.5x2.5	425, 525, 650, 750	7	2	1	40
				TEM	Ø3x0.4	425, 525, 650, 750	4	4	0	16
				disc 6	Ø6x2	425, 525, 650, 750	6	2	0	16
4	RF/VNIINM	TIP-200 grade	grain size 55-60 micron, ~0.2-0.3wt% BeO	Swelling	Ø3.5x6.4	425, 525, 650, 750	2	1	1	16
				Tritium	Ø3.5x2.5	425, 525, 650, 750	7	2	1	40
				TEM	Ø3x0.4	425, 525, 650, 750	4	4	0	16
				disc 6	Ø6x2	425, 525, 650, 750	6	2	0	16
5	RF/VNIINM	Porous Be	~20% porosity	Swelling	Ø3.5x6	425, 525, 650, 750		3		12
				Tritium	Ø3.5x2.5	425, 525, 650, 750		6		24
				disc 6	Ø6x2	425, 525, 650, 750		3		12
6	RF/VNIINM	Porous Be	~30% porosity	Swelling	Ø3.5x6	425, 525, 650, 750		3		12
				Tritium	Ø3.5x2.5	425, 525, 650, 750		6		24
				disc 6	Ø6x2	425, 525, 650, 750		3		12

a: annealed, c: coldworked, O: BeO coated samples

496

16

Status of Material Development for Lifetime Expansion of Beryllium Reflectors

CHRISTOPHER DORN¹⁾, K. TSUCHIYA²⁾, Y. HATANO³⁾
P. CHAKROV⁴⁾, M. KODAMA⁵⁾, H. KAWAMURA²⁾

1) Materion Brush Inc., Brush Beryllium & Composites, 14710 West Portage River South
Road, Elmore, Ohio, 43416-9500 U.S.A.

2) JAEA, 4002 Narita, Oarai, Higashiibaraki, Ibaraki, 311-1393, Japan

3) University of Toyama, 3190, Gofuku, Toyama-shi, Toyama, 930-8555, Japan

4) INP-KNNC, Ibragimov, 1, 050032, Almaty, Republic of Kazakhstan

5) Nippon Nuclear Fuel Development, Co., Ltd., 2163 Narita, Oarai, Higashiibaraki, Ibaraki,
311-1313, Japan

1. Introduction

Background

Same beryllium has been used as neutron reflector in materials testing reactors for about 50 years.



- Additional considerations rising in importance
- Reduction of irradiated beryllium waste
 - Rationalization of fabrication cost

How many years will be same material used?

JAEA and MBB&C started a cooperative study to find a new grade of beryllium which will offer both **environmental** and **economical** improvements.

Our task is to develop special beryllium which can be used for a longer time under neutron irradiation than the current grade of material

1

Object for Beryllium Reflector of JMTR

Status of Beryllium Frame in JMTR

- Beryllium Grade : S-200F
- Frame Usage Period : about 5 years
(av. 0.3×10^{26} /m² (E>1MeV), 36,000MWD)
- Period for Exchange : about 45 days*
- Used Be Frame : Storage in Canal

* : Actual working in reactor site

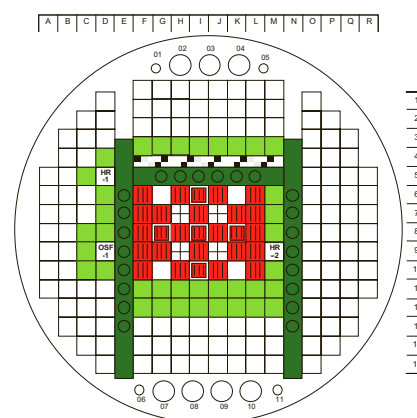
[Conditions]

- Thermal Power : 50MW
- Max. Fast Neutron Flux : 4×10^{18} /m²/s
- Max. Thermal Neutron Flux : 4×10^{18} /m²/s
- Max. Temperature : about 100°C
(Temp. of cooling water : about 50°C)
- Operating Pressure : 1.5MPa
- Flow rate : 11m/s
- Cooling water (Light water) : pH5.5 – pH7.0

Improvement of Beryllium

- Exchange of Be frame : FY2016
- Beryllium Grade : New Grade
- Frame Usage Period : 15-20 years
(av. 1.5×10^{26} /m² (E>1MeV), 180,000MWD)

Core arrangement of JMTR



- : Fuel element
- : Control rod with fuel follower
- : Beryllium reflector element
- : Beryllium frame
- : Aluminum reflector element

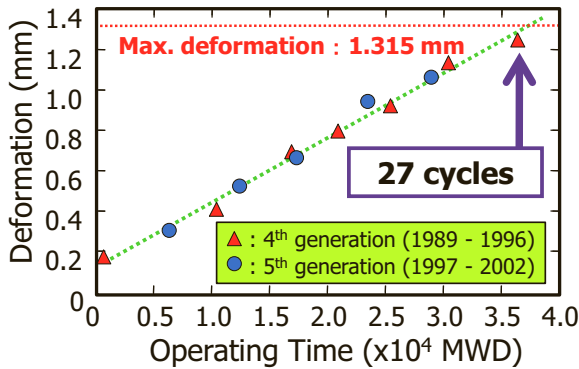
2

Results of Irradiated Beryllium in JMTR

Deformation of Beryllium Frame

JMTR operation : 165 cycles for 38 years
Replacement of Be frames : 6 times

Deformation Measurement

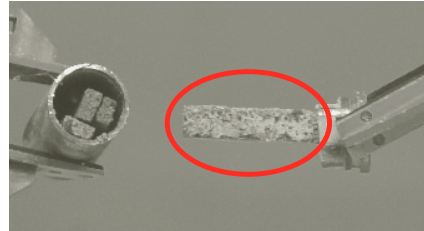


Deformation increased with increasing operation time for accumulation of helium.

Irradiation of Beryllium Samples

[Irradiation Conditions]

Cycle : 100 cycles
Temperature : about 50°C
Atmosphere : Cooling water

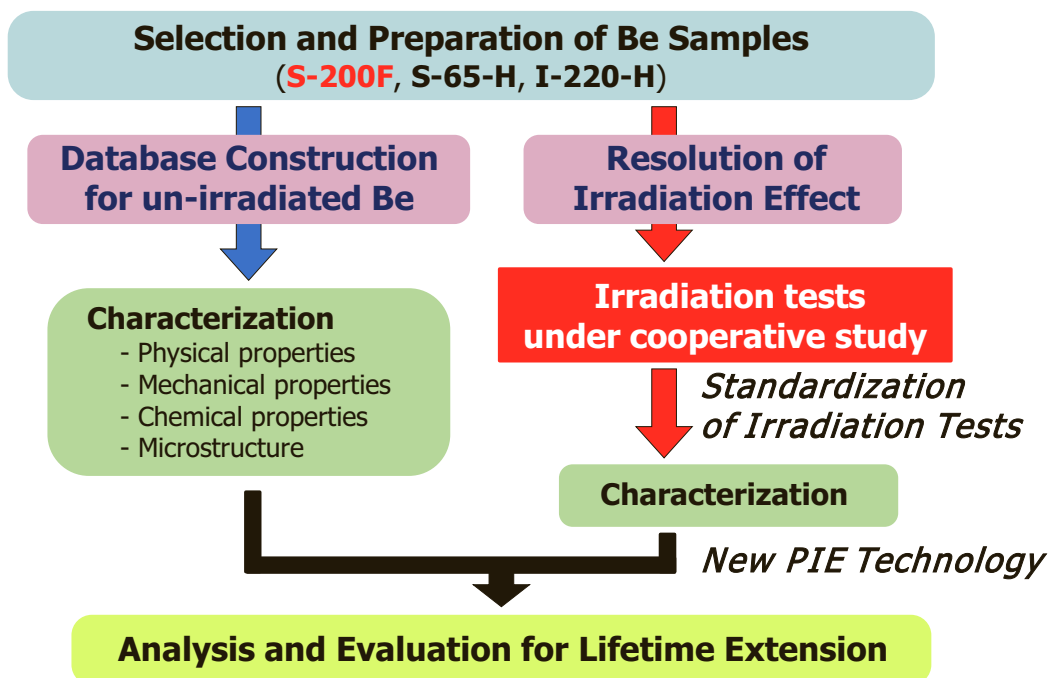


Corrosion of the beryllium surface resulted after a long period of irradiation.

- Evaluation of mechanical properties
- Resolution of corrosion mechanism

3

Test Flow for Lifetime Expansion



4

2. Selection and Preparation

Material Selection for Lifetime Extension

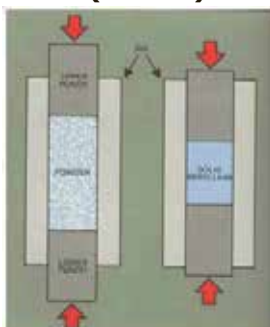
[Target]
Lifetime of beryllium frame : **5 times** (36,000MWd→180,000MWd)

Production of beryllium metal → Powder-Metallurgy

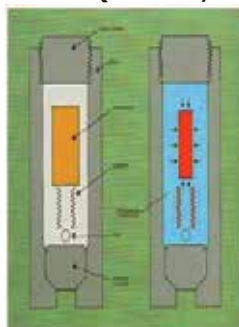
[Effect on properties of beryllium metal due to production method]

- 1) Purity (BeO content, etc.) and particle size distribution of Be powder
- 2) Production methods: VHP (Vacuum Hot Press), HIP (Hot Isostatic Pressing), etc.

VHP
Grade (**S-200F**)



HIP
Grade (**S-65-H, I-220-H**)



Advantages of HIP over VHP

- 1) Superior isotropy and density
- 2) Higher mechanical properties
- 3) Savings of Be powder
- 4) Potential to use near-net shape and reduce machining required

Selection of Beryllium Specimens

S-200F Beryllium (VHP) Reference
Down-Selection Process for Be Grades

- **Purity & Isotropy Combination** **: S-65-H**
- **Strength & Isotropy Combination** **: I-220-H**

	Beryllium metal			
Material Grade	S-200F (1)	S-200F (2)	S-65-H	I-220-H
Dimension (mm)	15x10x1	φ10x1.5	φ10x1.5	φ10x1.5
Density (g/cm ³)	1.856	1.855	1.848	1.861
Grain size (μm)	-	10.3	6.9	5.6
Tensile strength (MPa)	339	365	448	565
Yield strength (MPa)	265	269	271	460
Elongation (%)	3.9	3.4	5.7	3.7
Element (%)				
Be	99.10	99.00	99.40	98.60
BeO	1.10	1.00	0.70	1.90
Al	0.04	0.05	0.04	0.01
Fe	0.10	0.12	0.08	0.06
Si	0.03	0.03	0.02	0.02

Remarks : S-200F (1) is the reserved sample.

6

Preparation of Beryllium Specimens

[Materion Brush Beryllium & Composites, USA]

Name	Shape (Unit : mm)	Photograph	Fabrication Method
Tensile Specimens			Conventional Lathe Machining
Bending Specimens			Conventional Mill Machining
Impact Specimens			Conventional Mill Machining
Disc Specimens			Conventional Lathe Machining followed by Polishing of Surfaces

Fabrication experiences of small size specimens with S-200F, S-65-H, and I-220-H for material testing.

7

3. Database Construction

Mechanical Properties of Beryllium

S-200F Beryllium (VHP) Reference
Down-Selection Process for Be Grades

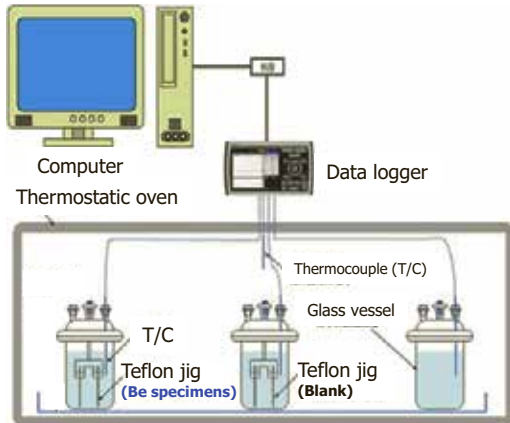
- **Purity & Isotropy Combination** : **S-65-H**
- **Strength & Isotropy Combination** : **I-220-H**

Factor	Grade	Be Assay		YS		UTS		EI		GS
		min	typ	min	typ	min	typ	min	typ	max
		(%)		(MPa)		(MPa)		(%)		(μm)
Ref.	S-200F	98.5	99.1	241	260	324	380	2.0	3.0	20
Purity	S-65	99.2	99.4	206	230	289	386	3.0	5.2	20
Isotropy	S-65-H	99.0	99.4	206	280	345	450	2.0	5.1	15
	I-70-H	99.0	99.4	207	290	345	460	2.0	5.4	12
	O-30-H	99.0	99.5	297	302	400	425	3.0	3.1	15
Strength	S-200F-H	98.5	99.1	296	336	414	450	3.0	4.6	12
	I-220-H	98.0	98.6	345	498	448	577	2.0	3.2	15

Corrosion Test of Beryllium in Pure Water

It is important to perform the characterization of the different grade beryllium for life time expansion evaluation and corrosion test of these beryllium samples were carried out under pure water.

Test Procedure



[Test Conditions]

- Temperature : 50°C
- Corrosion Time : 3300, 5200 and 8300h
- Properties of Water :
 - 1) Electric conductivity : <math><4\mu\text{S}/\text{cm}</math>
 - 2) pH5.5-7

Photograph of Specimens

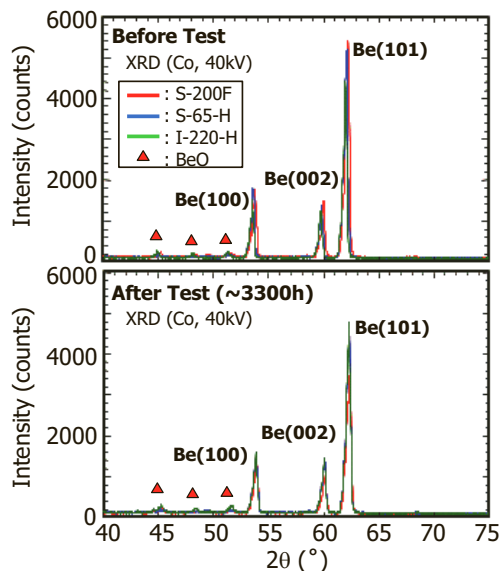
	before	3300h
S-200F		
S-65-H		
I-220-H		

White product was generated on the surface of each Be specimen.

9

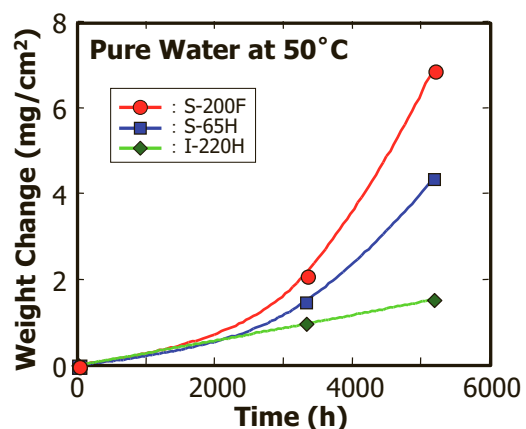
Characterization of Beryllium after Corrosion Tests

XRD Measurement



The Be peaks decreased after the corrosion test, the peaks corresponding to BeO were almost the same intensity before/after the corrosion test.

Weight Change



The weight change of S-200F was larger than that of I-220-H.

White product : $\text{Be}(\text{OH})_2$
Corrosion resistance of beryllium
→ **Content of BeO**

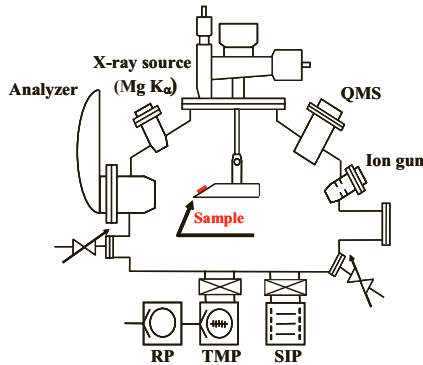
10

Surface Analysis after Corrosion Test

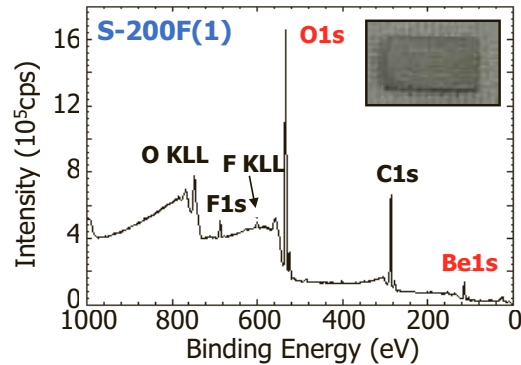
[University of Toyama, Japan]

It is necessary to measure the oxidation property for the elucidation of corrosion mechanism in the cooling water. Thus, the surface analysis of beryllium samples is carried out by X-ray photoelectron spectroscopy (XPS).

X-ray photoelectron spectroscopy



Preliminary Results



[Measuring Conditions]

- (1) Temperature : Room temp. (about 293 K)
- (2) Atmosphere : Vacuum ($<1 \times 10^{-7}$ Pa)

Element (at%)	Be	O	C	F
S-200F	27.6	38.8	31.5	2.1

11

Non-destructive Test of Beryllium Specimens

[NFD, Japan]

It is necessary to detect defects in irradiated beryllium by non-destructive testing for effective reactor management. Therefore, the properties of beryllium samples before irradiation are measured using an Electro-magnetic Acoustic Transducer (EMAT) and electrical resistor.

Preliminary Results for Sound Velocity and Resistivity

Materials	Un-irradiated Beryllium Metal			
	S-200F (1)	S-200F (2)	S-65-H	I-220-H
Grade	S-200F (1)	S-200F (2)	S-65-H	I-220-H
Dimension (mm)	15x10x1	φ10x1.5	φ10x1.5	φ10x1.5
Sound Velocity (km/s)				
Transverse wave (VT)	9.21	9.20	9.17	9.19
Longitudinal wave (VL)	12.86	12.76	12.74	12.68
Resistivity ($\times 10^{-8} \Omega\text{-m}$)	4.41	4.35	3.93	4.34

Consideration and evaluation of measurement data
Calculation of mechanical properties

In future plans, the sound velocity and resistivity of irradiated S-200F, S-65-H and I-220-H will be measured after irradiation testing in JRR-3.

12

4. Irradiation Tests

Candidate Reactors for the Irradiation Tests

<http://www.iaea.or.at/worldatom/rrdb/>

Reactor	JMTR	JRR-3M	OPAL	HFR	BR2	ATR	HFIR	SM-3	WWR-K
Country	Japan	Japan	Australia	Netherlands	Belgium	USA	USA	Russia	Kazakhstan
Reactor power (MW)	50	20	20	45	50-80	250	85	100	6
Coolant	Light water	Light water	Light water	Light water	Light water	Light water	Light water	Light water	Light water
Coolant Temp.	in 49 °C out 56 °C	in 35 °C out 42 °C	-	-	40-50 °C	57-71 °C	-	-	-
Reflector	Be	Be, D ₂ O, H ₂ O	D ₂ O	Be	Be	Be	Be	Be, H ₂ O	H ₂ O
Moderator	Light water	Light water	Light water	Light water	Light water	Light water	Light water	Light water	Light water
Fast Neutron Flux (max.) (m ⁻² s ⁻¹)	4.0×10 ¹⁸	1.4×10 ¹⁸	2.1×10 ¹⁸	4.6×10 ¹⁸	7.0×10 ¹⁸	1.8×10 ¹⁸	1.0×10 ¹⁹	2.0×10 ¹⁹	8.0×10 ¹⁷
Thermal Neutron Flux (max.) (m ⁻² s ⁻¹)	4.0×10 ¹⁸	2.7×10 ¹⁸	3.0×10 ¹⁸	2.7×10 ¹⁸	1.0×10 ¹⁹	8.5×10 ¹⁸	2.1×10 ¹⁹	5.0×10 ¹⁹	2.0×10 ¹⁸
γ Heating (×10 ⁻³ W kg ⁻¹)	0.1-10	0.25-6.6	-	6-12	13-15	0.02-20	-	-	-

Start of irradiation tests : under negotiation for irradiation tests

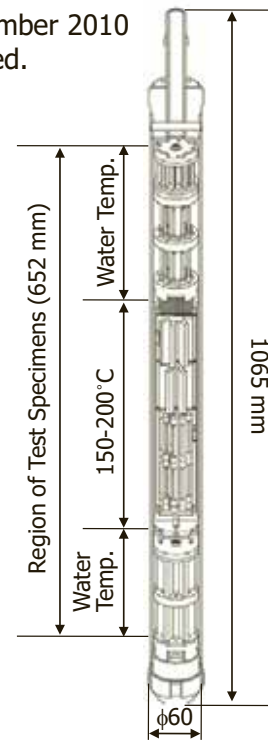
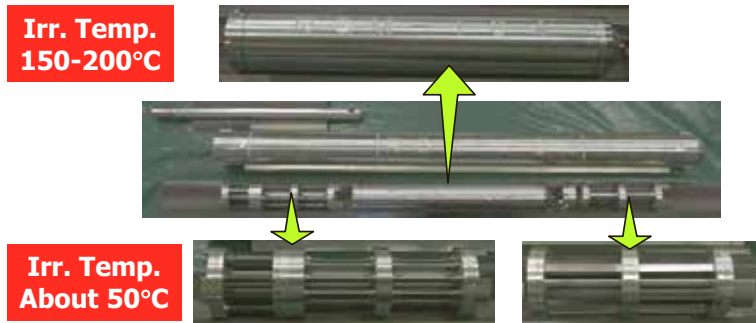
Irradiation Tests in JAEA (1)

The first irradiation test was carried out from March 2010 to November 2010 in JRR-3M. Now, transport from Tokai to Oarai and PIEs are planned.

Irradiation Conditions (1st Test)

- Reactor JRR-3M
- Neutron Fluence ($E > 1\text{MeV}$) 1 point ($3 \times 10^{25} \text{ n/m}^2$)
- Atmosphere 2 points (water, He gas)
- Irradiation Temperature 2 points (water temp., $150\text{-}200^\circ\text{C}$)
- Evaluation of He Generation (Calculated by MCNP, etc.)

Configurations of Irradiation Capsule



14

Irradiation Tests in JAEA (2)

The 2nd Irradiation test is planned in JMTR. The irradiation test began after JMTR re-start and the irradiation capsules were fabricated for the tests.

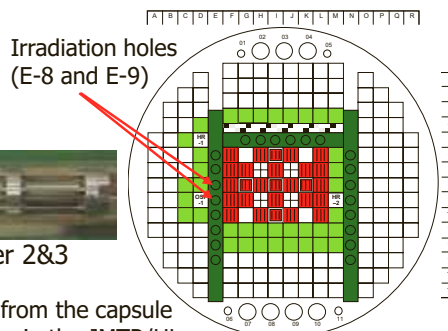
Irradiation Conditions (2nd Test)

- Reactor JMTR
- Neutron Fluence ($E > 1\text{MeV}$) 4 points ($0.3, 1, 1.5$ and $2.0 \times 10^{26} \text{ n/m}^2$)
- Atmosphere 1 points (water)
- Irradiation Temperature 1 points (water temp.)
- Evaluation of He Generation (Calculated by MCNP, etc.)

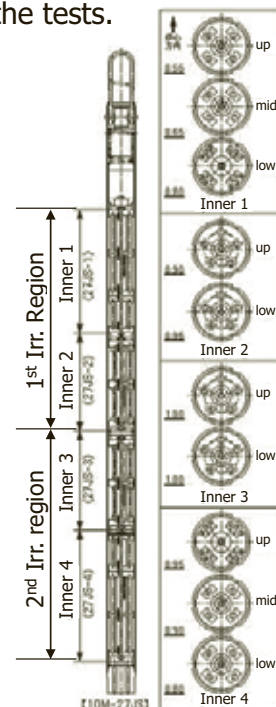
Irradiation Positions and Test Specimens

Test Specimens

- Tensile Specimens
- Bending Specimens
- Impact Specimens



Inner 1 and 2 will be produced from the capsule between the irradiation cycles in the JMTR/HL.



15

Irradiation Test Program under ISTC Project

[INP-NNC, Kazakhstan]

Irradiation testing started at the WWR-K Reactor in Kazakhstan under ISTC partner project from 9 March 2010. Currently, the neutronics of the irradiation test was carried out and the irradiation capsule has been carried out up to December 2011.

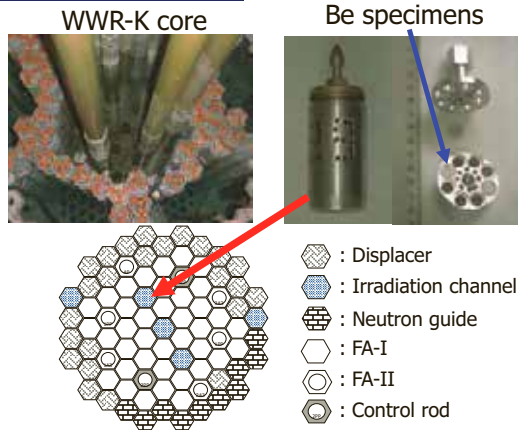
Be Samples

- S-200F $\phi 10 \times 1.5$ mm 3 pieces
- S-65-H $\phi 10 \times 1.5$ mm 3 pieces
- I-220-H $\phi 10 \times 1.5$ mm 3 pieces

Irradiation Conditions

- Neutron Fluence ($E > 1\text{MeV}$) : 1×10^{24} n/m²
- Irradiation Temperature : $\sim 40^\circ\text{C}$ in water

Irradiation Test



Chemical compositions of coolant in WWR-K

Index Name	Index magnitude
pH at 25 °C	5.0 to 6.5
Specific Electric Conduction at 25 °C (mOhm/cm)	4.0
Hardness (mg·equiv./kg)	< 3.0
Ion Chloride Mass Concentration (mg/kg)	< 50
Aluminum Mass Concentration (mg/kg)	< 50
Iron Mass Concentration (mg/kg)	< 50
Copper Mass Concentration (mg/kg)	< 10
Fission Product Total Activity (Bq/kg)	< 2.5×10^7

16

5. Conclusion

Summary

Material Selection of Beryllium Grades as MTR Reflectors was discussed in the Be Specialist Meetings and the following items were decided:

- Selection of beryllium grades
 - Reference (S-200F), Isotropy (S-65-H), Strength (I-220-H)
- High-irradiation tests for lifetime extension
 - Performance of irradiation tests (JRR-3, WWR-K, JMTR)
 - Selection of MTR for irradiation tests (ATR, SM-3, etc.)

Status of Be study

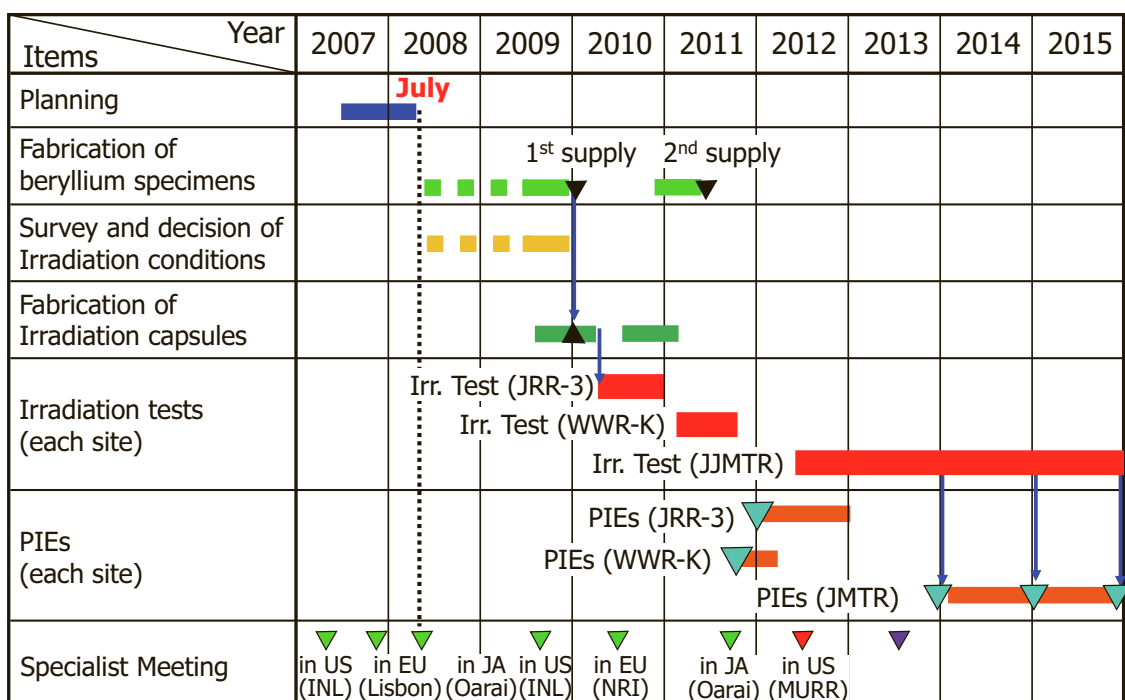
- Preparation of Beryllium Specimens for irradiation tests
- Irradiation tests in JRR-3 and WWR-K
- Preparation of irradiation test in JMTR
- Corrosion evaluation of Be specimens in out-of-pile test
- Development of measurement techniques for new PIEs

Future Plans

- Negotiation for conducting High-irradiation tests in each reactor

17

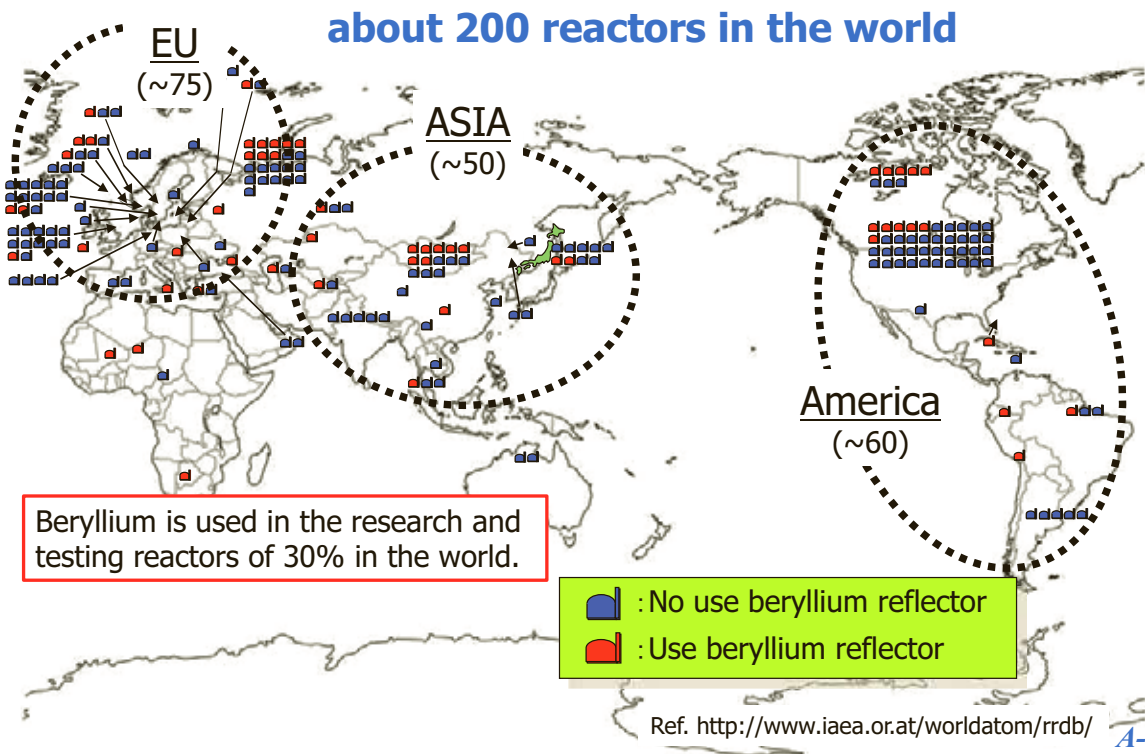
Research Schedule for Lifetime Expansion



18

Appendix

Research and Test Reactors in the World



General Properties of Beryllium

Properties	Values
Density (g/cm ³ , at 25°C)	1.8477±0.0007
Atomic weight	9.013±0.0004
Melting point (°C)	1285±10
Boiling point (°C)	2507-2970
Sublimation point (°C)	482 (BeCl ₂)
Specific heat (J/kg/K, at 25°C)	1923
Thermal conductivity (W/m/K, at 25°C)	188
Thermal expansion (x10 ⁻⁶ °C)	13

Beryllium surface forms a thin oxidation film by interacting with air like aluminum, and beryllium is highly resistant to corrosion in dry gases.

A-2

Status of Used Beryllium in MTR

Understanding of present condition

- How many used beryllium in each testing reactor are all over the world?
- And how does each testing reactor consider concerning the treatment of used beryllium?

Characteristic

- International Regulated Material
- Specific Chemical Material (BeO)
- Tritium included Material
- Activated Material



Waste which handling is difficult and which is produced on and on.

Amount of Storage of used beryllium

Japan	:	3	ton
World	:	30~40	ton

- In USA, the beryllium used at ATR, etc was buried in the desert. However, as the water pollution occurred by ¹⁴C, buried beryllium was digged up and has been kept at surface place briefly.
- In EU, used beryllium has been kept in the pool generally.
- In Russia, there is the situation similar to EU.

A-3

Issues of Used Beryllium

Design Modification

- Lifetime Extension of Beryllium Reflector
- Innovation of Beryllium Reflector Element

We should do our best by the change of material grades or fabrication method for lifetime extension besides.

Recycling Issue

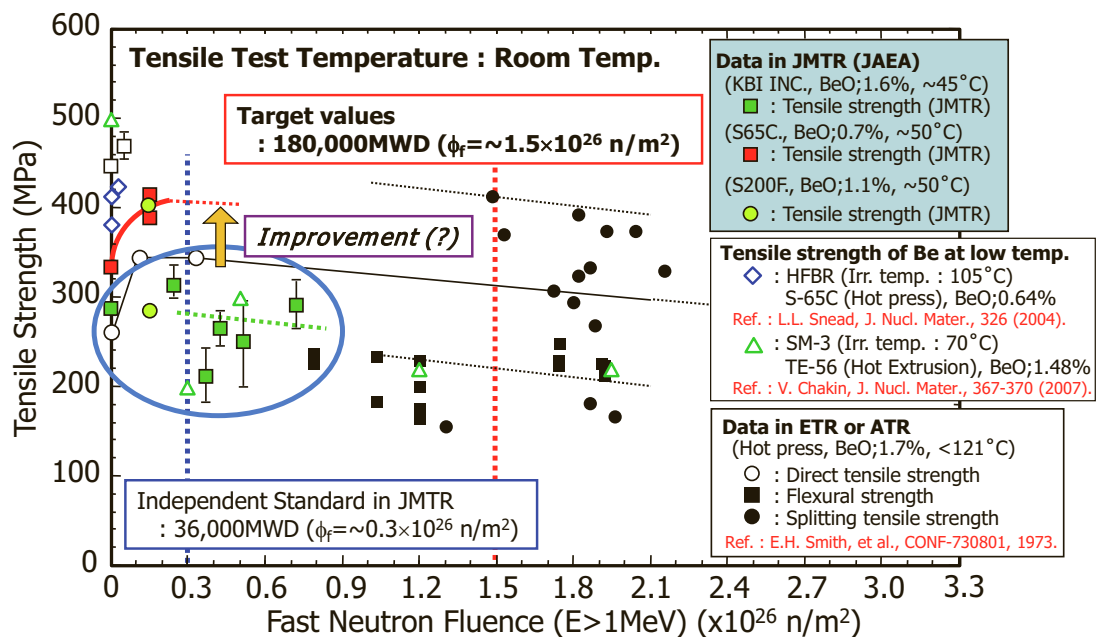
- Recycling of used Irradiated Beryllium

How should "the recycle of used beryllium" which is a common problem, be conducted ?

A-4

Experience in JMTR

Investigation and evaluation of tensile strength of irradiated beryllium

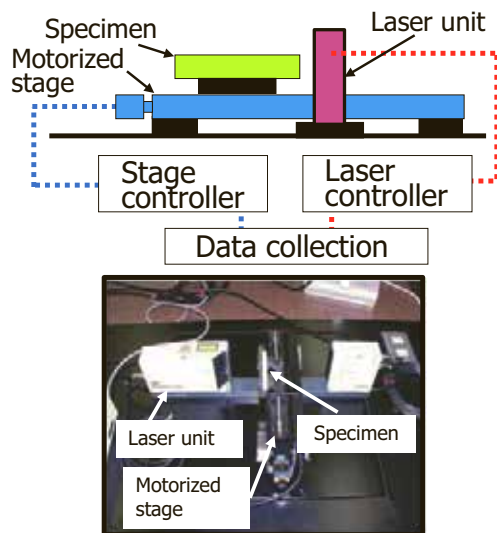


A-5

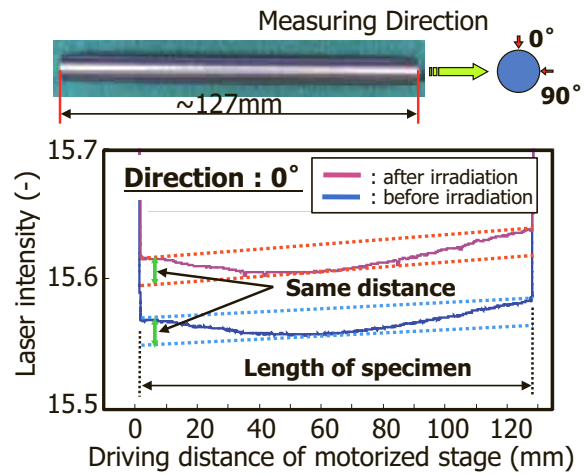
New PIEs (1) - High Accuracy Measurement -

It is necessary to measure the size change and amount of bending of the test specimens after irradiation. Therefore, a highly accurate measurement device was developed.

Outline of Device



Result of Bending Measurement



No bending or swelling of S-65 specimen up to $\sim 1 \times 10^{25} / \text{m}^2$ at $\sim 200^\circ\text{C}$

A-6

Experimental Simulation of Beryllium Damage Under Intense Transient Plasma Loads

I.B. Kupriyanov, E.V. Basaleev, G.N. Nikolaev, L.A. Kurbatova,
A.A. Bochvar Research Institute of Inorganic Materials, 123060, Moscow, Russia

V.L. Podkovyrov, A.D. Muzichenko, A.M.Zhitlukhin
TRINITI, Troitsk, Moscow reg., Russia

L. Khimchenko
Project Centre of ITER, Moscow, Russia

Abstract

Recent results of the experimental simulation of beryllium damage under intense transient plasma loads are presented. The mock-ups of a special design armored with two beryllium targets ($80 \times 80 \times 10 \text{ mm}^3$) made of Russian TGP-56FW beryllium grade were tested by hydrogen plasma streams (5 cm in diameter) with pulse duration of 0.5 ms and heat load of 0.5 - 1.0 MJ/m². Experiments were performed at RT temperature. The evolution of surface microstructure, cracks morphology and mass loss/gain under erosion process on the beryllium surface exposed to up to 250 shots are demonstrated and discussed.

*Corresponding author. Tel.: 7-499-190 8015, fax: 7-499-196-4168. E-Mail address: kupr@bochvar.ru;
igkupr@gmail.com (I.B. Kupriyanov)

Introduction

Beryllium will be used as a plasma facing material in the next generation of tokamaks such as ITER. During plasma operation in ITER, the plasma facing materials and components in fusion reactors will be suffered by different kinds of loading which may affect their surface or their joint to the heat sink. In addition to quasi-stationary loadings which are caused by the normal cycling operation, the plasma facing components and materials may also be exposed to the intense short transient loads like disruptions, edge-localized modes (ELMs). All these events may lead to beryllium surface melting, cracking, evaporation and erosion.

It is expected that the erosion of beryllium under transient plasma loads such as ELMs and disruptions will mainly determine a lifetime of ITER first wall.

To obtain the experimental data for the evaluation of the beryllium armor lifetime and dust production under ITER-relevant transient loads, the advanced plasma gun QSPA-Be (quasi-stationary plasma accelerators) has been constructed in Bochvar Institute.

This paper presents the results of the experiments with Russian TGP-56FW beryllium grade tested at room temperature by hydrogen plasma streams (5 cm in diameter) with pulse duration of 0.5 ms and heat load of 0.5 - 1.5 MJ/m². The evolution of surface microstructure, cracks morphology and mass loss/gain under erosion process on the beryllium surface exposed to up to 250 shots are under consideration.

2. Materials and Experimental Procedur

The QSPA-Be plasma gun facility, a quasi-stationary plasma accelerator [1] provides hydrogen (or deuterium) plasma heat loads corresponding to ITER ELMs and disruptions in the range of 0.2-5 MJ/m² and pulse duration 0.5 ms (Fig. 1).

The samples of TGP-56FW beryllium grade were investigated in form of tiles with 80×80×10 mm in dimensions (Fig. 2).

Initial properties of the TGP-56FW grade are presented in Table 1. Some cuts seen on these samples (Fig. 2) were made to investigate the leading edge melting.

For these experiments the mock-ups have been manufactured which design allowed changing beryllium targets. The mock-up consists of stainless steel body, ceramic plate with heater, two beryllium samples to be changed and protecting beryllium frame. The consequence of assembly of mock-up is shown in Fig. 3 and a planar view of mock-up with beryllium protection frame is shown in Fig.4.

The mock-ups were irradiated by a hydrogen plasma stream (5 cm in diameter) with pulse duration of 0.5 ms and an average heat load of the plasma stream of 0.5, 1.0 and 1.5 MJ/m². The angle between plasma stream direction and mockup surface was 30°. Experiments were carried out at RT. For each tile the area exposed to plasma irradiation was 80 × 60 mm².

The samples were exposed to up to 100-250 shots at different energy density. After 10, 40, 100, 200 and 250 shots, the evolution of surface macro- and microstructure was investigated and beryllium mass loss measurements were performed.

Weight of samples was measured by Shimadzu analytical balance with accuracy of 0.1 mg. Mass loss/gain (Q) were calculated separately for each sample by the equation: $Q = \Delta m / S N$, where $\Delta m = m_i - m_k$ is a mass change of Be tile between shots (i) and (k), S is a

surface area of Be tile ($60 \times 80 \text{ mm}^2$); $N = N_i - N_k$ –number of shots with (i) = 10, 40, 100, 200, 250 and (k) = 0, 10, 40, 100, 200, correspondingly.

Microstructure of the samples was studied both by optical microscopy and SEM.

3. Experimental Results

3.1 Beryllium mass loss/gain

Mass loss/gain dependencies obtained for two samples at 0.5, 1.0 and 1.5 MJ/m² load energy are presented in Fig.5 a,b,c. The sample #1 was situated farther from plasma stream, while the sample #2 was located closer. Distributions of absorbed energy (Fig.6 a,b,c) calculated in [2] using calorimetry data illustrate difference in energy conditions for the samples.

At heat load 0.5 MJ/m² only mass gain was revealed from beginning up to 250 shots for both samples. At loads of 1-1.5 MJ/m² mass loss/gain for samples # 1 and # 2 were directed differently with mass loss for sample # 2 (closer to plasma stream), and mass gain for sample # 1 (farther from plasma stream). Total mass loss after 250 shots at different loads for the sample #2 are presented in Table 2 together with a calculated rate of erosion, which correspond to these mass loss. One can see that the erosion of beryllium in plasma spot nonlinearly increases with transient heat load.

3.2. Evolution of surface structure

Optical microscopy and SEM revealed several surface processes taking place simultaneously on surface areas subjected to plasma stream loading:

- Melting of surface in plasma steam and displacement of melt on the surface of the mock up;
- Re-solidification of displaced melt;
- Porosity formation in re-solidified displaced melt;

- Formation of cracks due to high thermal stresses in surface layer;
- Deposition of sputtered metal in form of films, flakes, macro- and micro- particles.

3.2.1. Surface structure under heat load 0.5 MJ/m^2

Evolution of surface structure of the samples in mock-up subjected to with increase of shots number at heat load 0.5 MJ/mm^2 is presented in Fig.7.

Surface melting of samples was not revealed, except for leading edges. It could be explained by the density of absorbed energy which on the most part of surface is lower than the threshold of beryllium melting ($\sim 0.5 \text{ MJ/m}^2$). According to calculations presented in [2], with the density of absorbed energy 0.5 MJ/m^2 in the center of stream, the distribution of density ranges between 0.5 MJ/m^2 in the stream axis and $\sim 0.1\text{-}0.3 \text{ MJ/m}^2$ on periphery of mock-up (Fig. 6, a).

However, for the leading edges (the angle between plasma stream and edge surface $\beta = 70\text{-}90^\circ$) the impact of plasma was more significant. It was experimentally determined that the threshold of melting for leading edges does not exceed $0.3\text{-}0.35 \text{ MJ/m}^2$. Melted metal spreads and trickles among the surface and then crystallized in intervals between shots (Fig. 8 a, b). Maximal distance of molten beryllium displacement was 60-65 mm.

With increase of shot number, just beyond the melted area the “incrustations” of re-solidified metal with wave-like structure are formed from displaced molten beryllium (Fig. 8 c, d). The same “incrustations” are also found on the periphery of the samples. A height of “incrustations” exceeds 0.5 mm.

After 40 shots the first thin bridges with the thickness of 0.1-0.3 mm formed between the neighbouring elements of mock-up (Fig.8 e, f). Although with increase of shot number a quantity of these bridges increases, their common area does not exceed 15% of total area of gaps between beryllium tiles. It should be noted that the formation of such bridges can play

positive part in ITER FW, since they are able to protect gaps between tiles against plasma touch, and by this means to eliminate a risk of heat sink structure (CuCrZr) damage.

First cracks on beryllium surface were found even after 10 shots. Totally the cracks of 5 types were revealed:

- a net of visible cracks with a cell dimension of 1.5×3 mm (Fig. 9a);
- single visible long (up to 30 mm) macro-cracks (Fig. 9b)
- micro-cracks formed during the re-solidification (Fig. 9c,d);
- single micro-cracks formed at the places of Be melting (Fig. 9e,f);
- micro-cracks at non melted surface (Fig. 9g,h).

The threshold of cracks formation determined experimentally did not exceed 0.2-0.25 MJ/m². With increase of shot number a density of surface cracks increased insignificantly.

The investigations on a crack propagation into the body of samples revealed that a depth of most part of cracks is less than 50 μm (Fig. 10a). In the layer with this type of cracks (closest to surface) a great porosity was found as well. One can also see a limited amount of cracks with a depth of 200-250 μm in Fig. 10a. The only crack with a depth of 400 μm was found (Fig. 10b). Additionally in Fig. 10b one can see that a thickness of melted area is within 5-100 μm .

All cracks propagate perpendicular to samples surface or under a small angles.

3.2.2. Surface structure under heat loads 1.0 and 1.5 MJ/m²

Evolutions of surface structure of samples with increase of shots number at heat loads 1.0MJ/m² and 1.5 MJ/mm² are presented in Fig.11 and 12.

In these cases the most parts of samples surface were melted, and noticeable displacement of molten beryllium over the mock-ups surface took place with a formation of

wave-like surface structure. This behavior corresponds to the distributions of absorbed energy at 1.0 and 1.5 MJ/m² (Fig. 6 b,c), where energy density exceeds the threshold of beryllium melting over the most part of samples surface. Again, the leading edges melted more intensively.

After 10 shots at heat load 1.0 MJ/m² gaps between the samples are partly filled with molten beryllium, and after 60 shots –gaps become fully filled with Be. As for heat load 1.5 MJ/m², gaps between the samples were fully filled with beryllium after 10 shots already.

Under plasma irradiation at heat load 1.0 MJ/m² a cavity was gradually forming on a surface of the sample #2 (Fig. 13) with a depth of ~3-3.3 mm after 250 shots, while the “incrustations” are simultaneously growing on a surface of the sample #1(Fig. 14) with a height of ~3-3.5 mm after 250 shots.

Nevertheless, with all this (the intensive surface melting and a high erosion), the disintegration of all beryllium samples investigated did not happen.

3.3. *Products of erosion (SEM)*

Different products of erosion are found on beryllium surface under plasma irradiation. Several types of erosion products (macro-particles, sub- micron particles, surface films, secondary solidified displaced melts and melt drops) mainly revealed by SEM in this study are shown in Fig. 14.

Summary/Conclusions

A new research instrument - plasma gun QSPA-Be was applied to obtain the data for evaluation of the beryllium armor lifetime under ITER-relevant transient loads. Mass loss/gain and surface structure of Be grade TGP-56FW were studied after plasma heat loads of 0.5-1.5 MJ/m².

As a result of testing:

- The dependencies of mass loss/gain on shots number were obtained. The tendency for a decrease with an increase of shots number was found for mass loss/gain values;
- The products of erosion formed on beryllium surface under plasma irradiation were described, such as: macro-particles, flakes, drops, sub-micron particles and thin films;
- The threshold of cracks formation in beryllium was estimated near 0.2 MJ/m².

References List

- [1] V. Podkovyrov et al. Optimization of QSPA-Be plasma gun facility for ITER ELM, disruption and mitigated disruption simulation experiments, PFMC-13, Rosenheim, Germany, May 9-13, 2011.
- [2] TRINITY Report 10/R&D-6674, Troitsk, Russia, 2011

Figure captions

Fig. 1 The QSPA-Be plasma gun facility: a – a view; b – a scheme

Fig. 2 Be tiles with cuts made to investigate the leading edge melting

Fig. 3 Design and a photo of a mock-up for experiments in the QSPA-Be plasma gun facility:

a – heater, b – assembly of two beryllium plates, c – complete assembly with beryllium protection; d – assembly placement for plasma testing

Fig. 4 Planar view of mock-up with beryllium protection frame

Fig. 5 Mass loss/gain dependencies for two samples at different load energies: a - 0.5 MJ/m^2 ; b - 1.0 MJ/m^2 ; c - 1.5 MJ/m^2

Fig. 6 Distribution of absorbed energy over samples surface area at different heat loads: a - 0.5 MJ/m^2 ; b - 1.0 MJ/m^2 ; c - 1.5 MJ/m^2

Fig. 7 Surface microstructure of beryllium before and after loading with heat energy 0.5 MJ/m^2

Fig. 8 Surface microstructure (optical microscopy) after loading with heat energy 0.5 MJ/m^2 :

a,b,c – 10 shots; d – 100 shots; f - 40 shots

Fig.9 Some types of cracks formed under plasma irradiation with load energy 0.5 MJ/m^2 :

a,b,d,e,f,g – SEM; c,h – optical microscopy

Fig.10 Cross section of samples after 250 shots at heat energy 0.5 MJ/m^2 : a –cracks with the depths of $50 \mu\text{m}$ and $200 \mu\text{m}$; b – the only crack with a depth of $400 \mu\text{m}$

Fig.11 Surface microstructure of beryllium before and after loading with heat energy 1.0 MJ/m^2

Fig.12 Surface microstructure of beryllium after loading with heat energy 1.5 MJ/m^2

Fig.13 A view of beryllium samples after 250 shots with heat energy 1.0 MJ/m^2

Fig.14 Products of erosion found on beryllium surface under plasma irradiation:

a -macro-particles; b - dust particles (aver. size~ 50nm); c, d -secondary solidified displaced melts; e -surface films; f - melt splashing - droplets

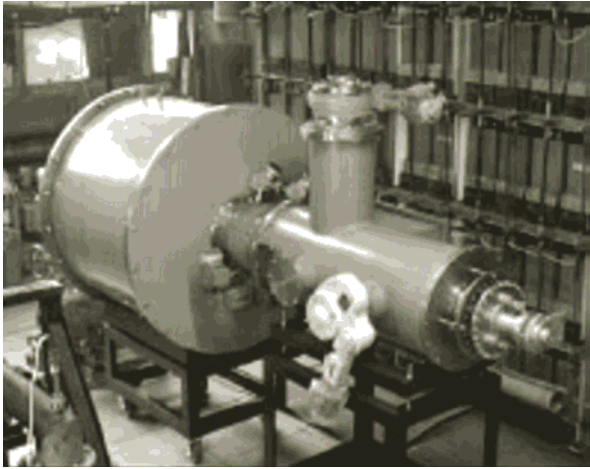
Table 1.

Data on initial characteristics of TGP-56FW grade

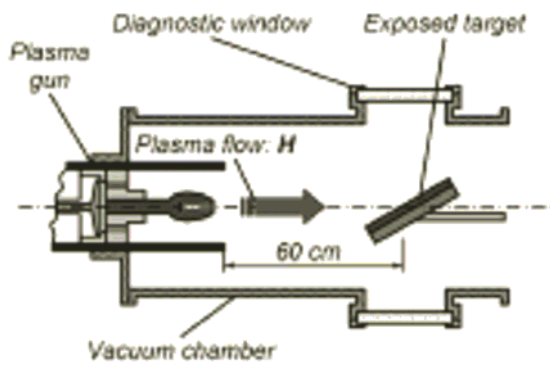
Parameter	TGP-56 FW
<u>Chemical composition, %</u>	
wt.	
Be	99.02
BeO	0.95
C	<0.05
Si	0.021
F	<0.001
Fe	0.16
Al	0.018
Ti	0.016
Cr	0.037
$\Sigma(\text{Mn}+\text{Mg}+\text{Cu}+\text{Ni})$	0.052
Others	
U	n/d
Density, % of theoretical value	99.02
<u>Av. grain size, μm</u>	13-14
<u>Mechanical properties</u>	
Ultimate Tensile Strength (RT), (min), MPa	350
Yield Strength (RT), (min), MPa	250
Total Elongation (RT), (min), %	2.0

I.B. Kupriyanov

Fig. 1



a



b

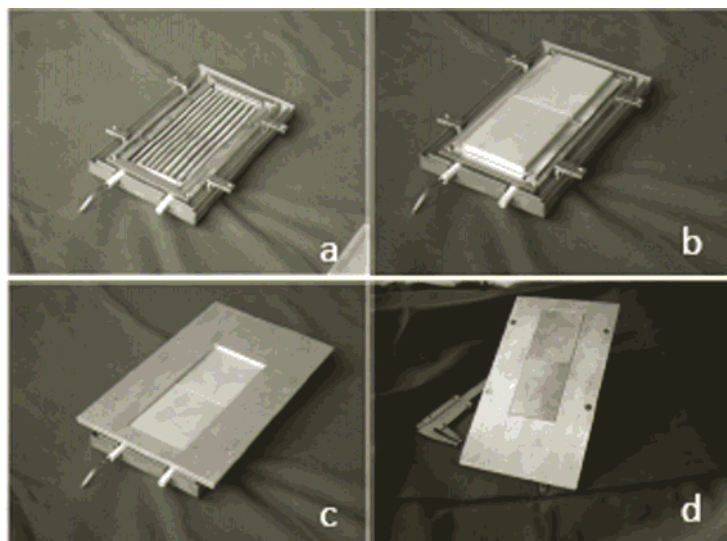
I.B. Kupriyanov

Fig. 2



I.B. Kupriyanov

Fig. 3



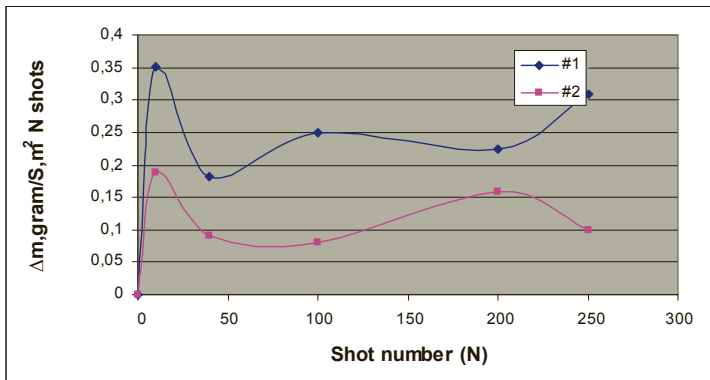
I.B. Kupriyanov

Fig.4

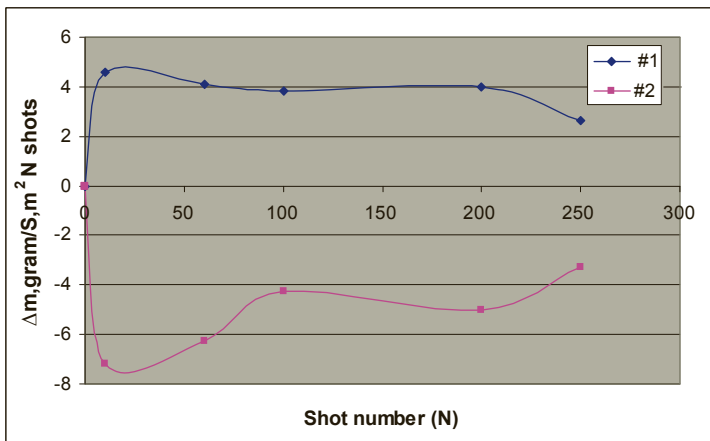


I.B. Kupriyanov

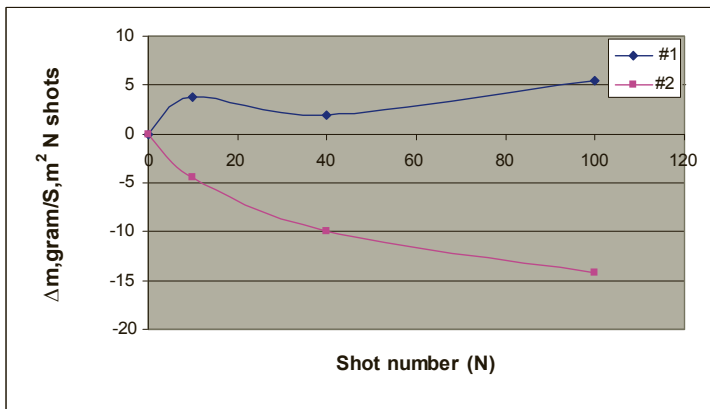
Fig.5



a



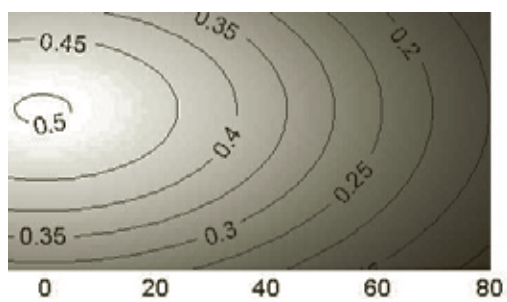
b



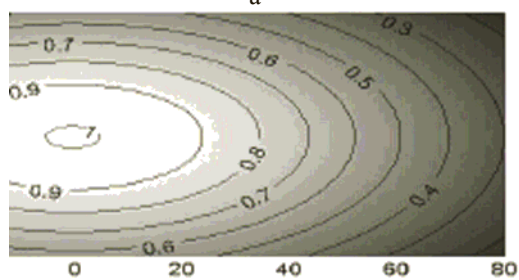
c

I.B. Kupriyanov

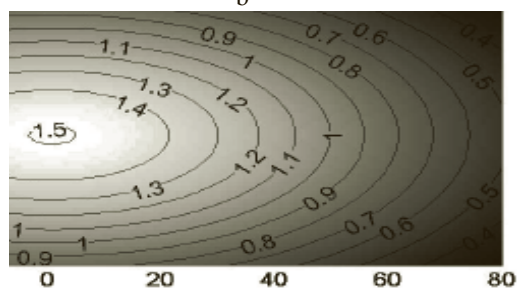
Fig.6



a



b



c

I.B. Kupriyanov

Table 2

Total mass loss of sample #2 after 250 shots at different loads

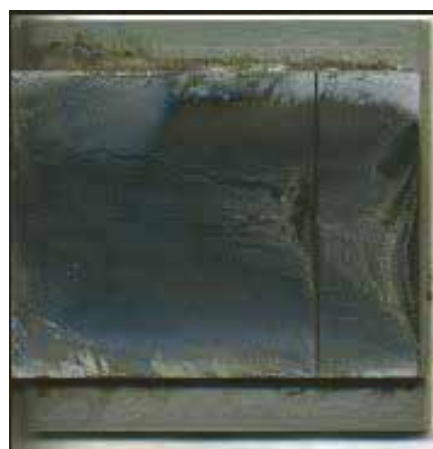
Load energy, MJ/m ²	Mass loss, Δm , g/m ²	Rate of erosion, Δh , $\mu\text{m}/\text{shot}$
0.5	~ 0.44	~ 0.24
1.0	~ 1	~ 0.75
1.5	~ 3.7	~ 2

I.B. Kupriyanov

Fig. 7



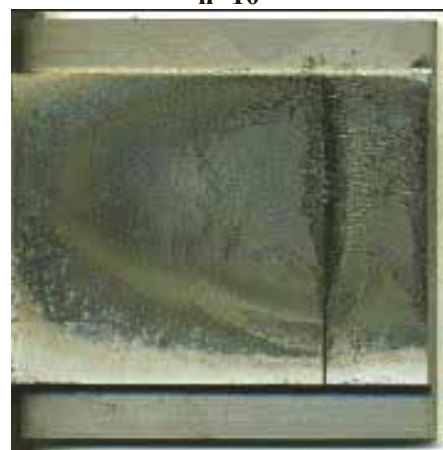
n=0



n=10



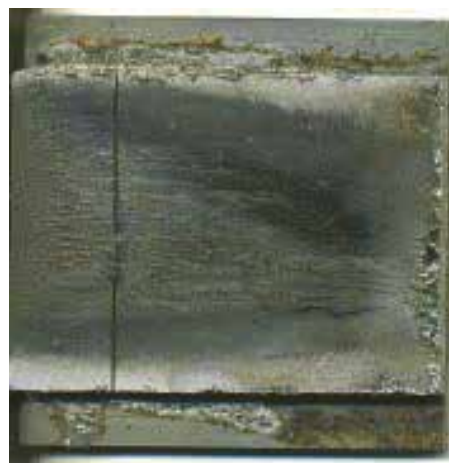
n=40



n=100



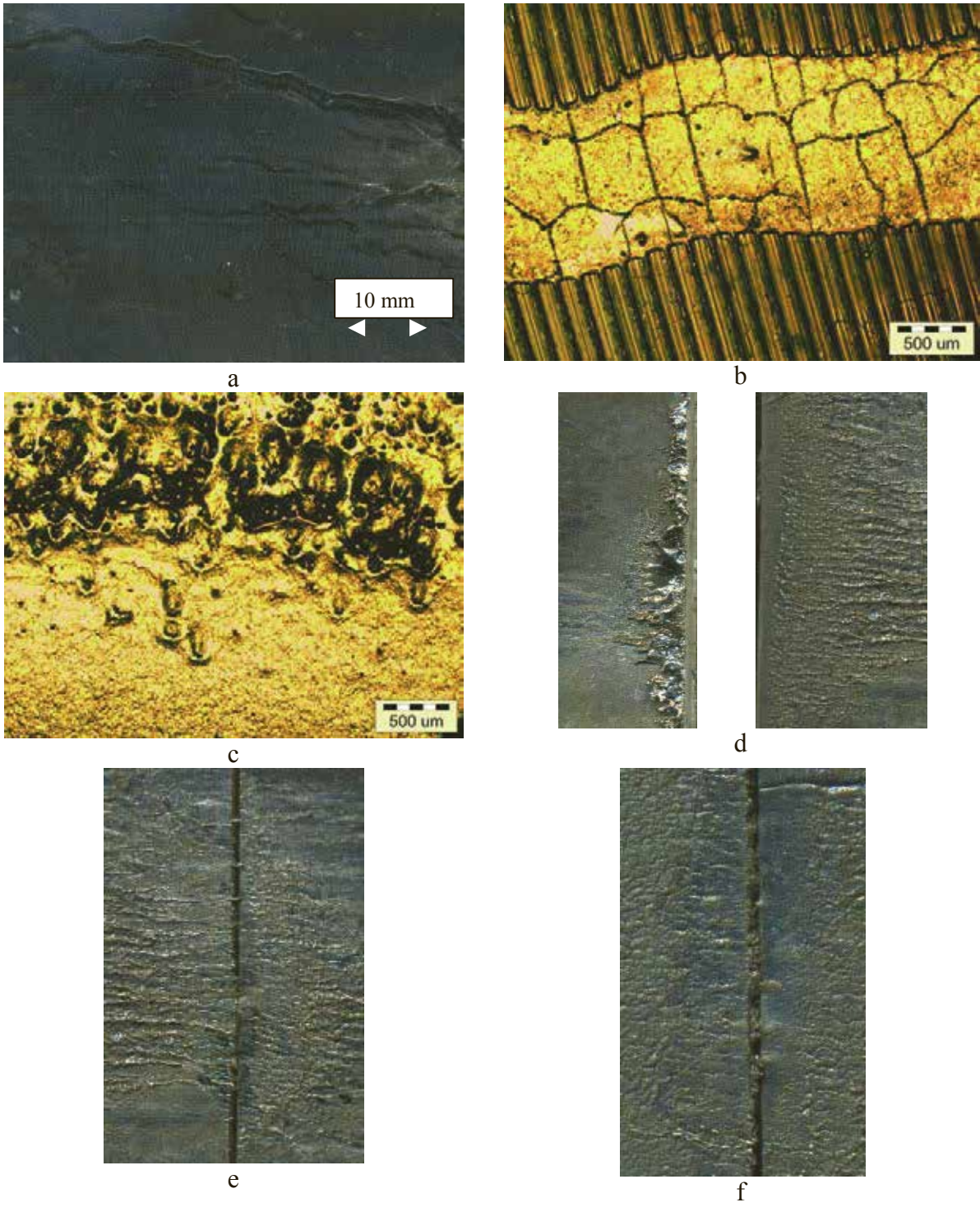
n=200



n=250

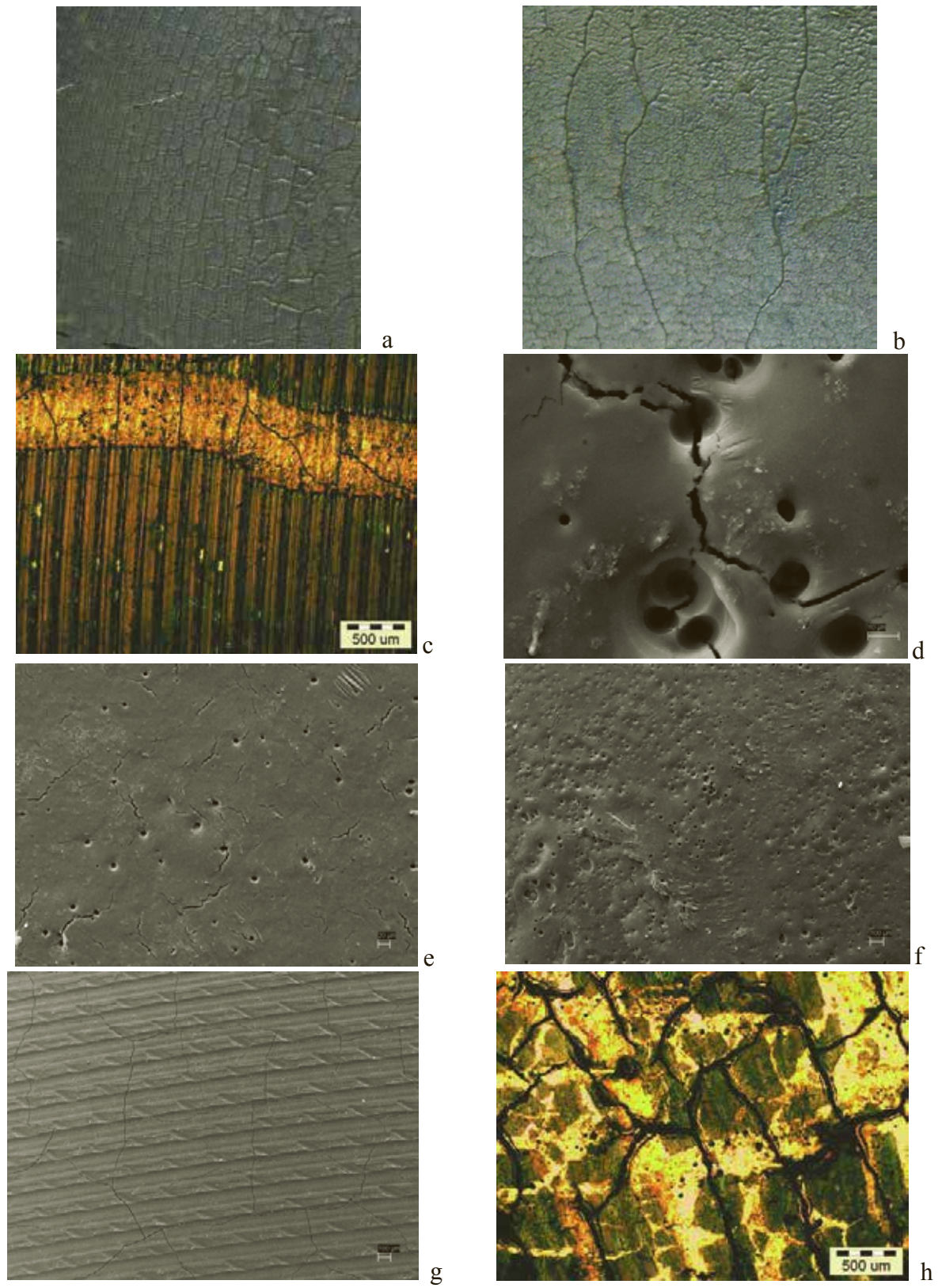
I.B. Kupriyanov

Fig. 8



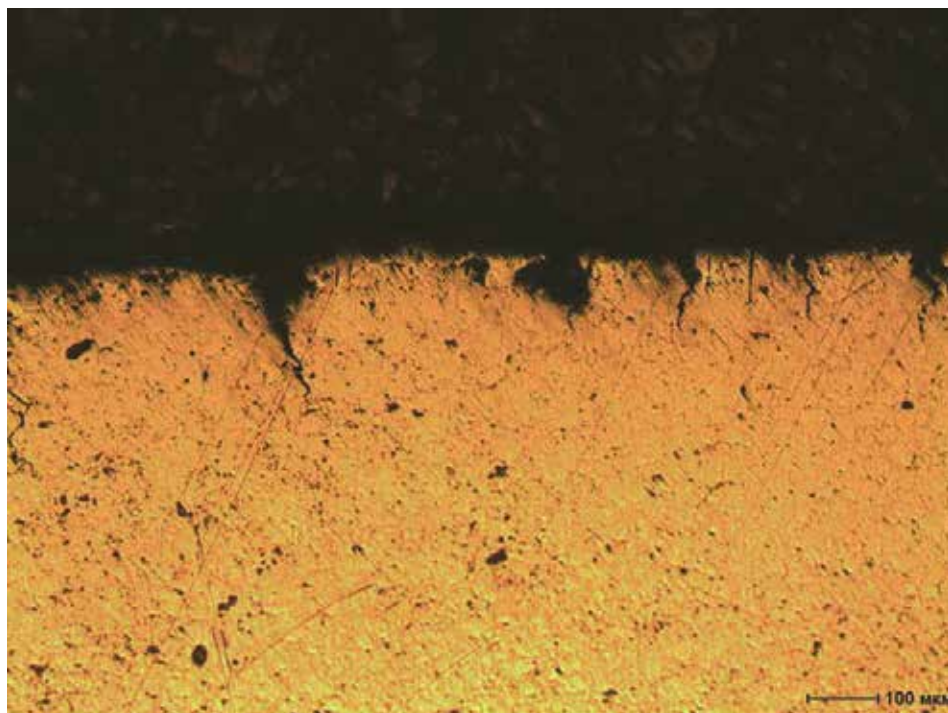
I.B. Kupriyanov

Fig. 9

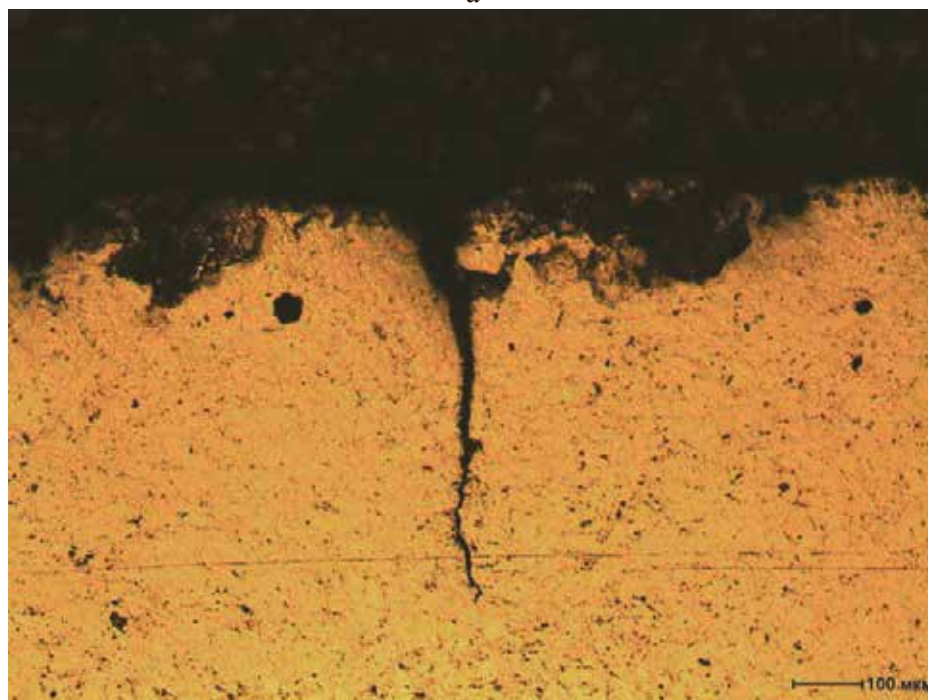


I.B. Kupriyanov

Fig.



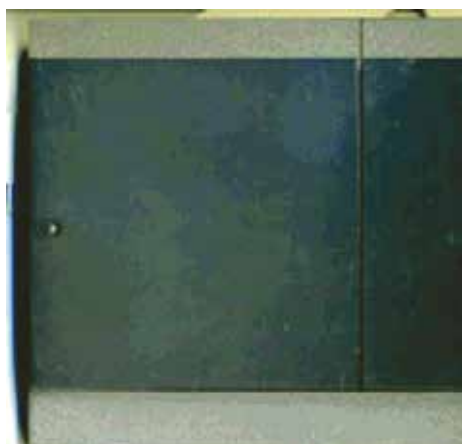
a



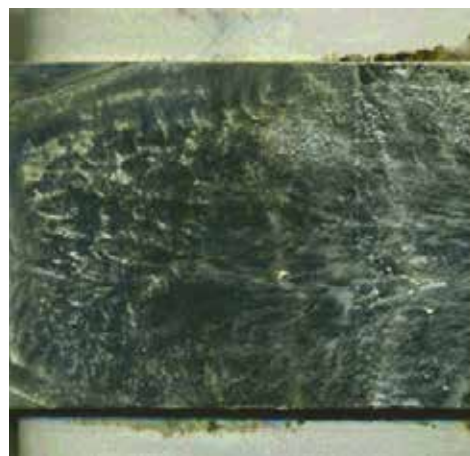
b

I.B. Kupriyanov

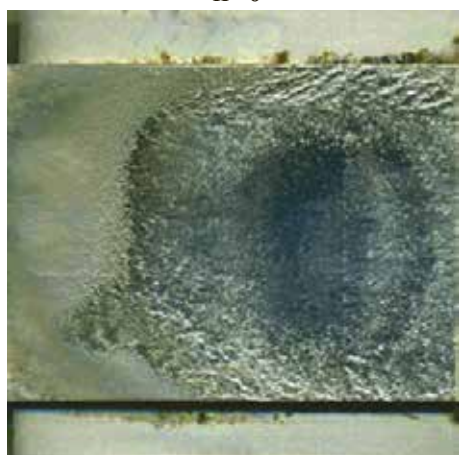
Fig.



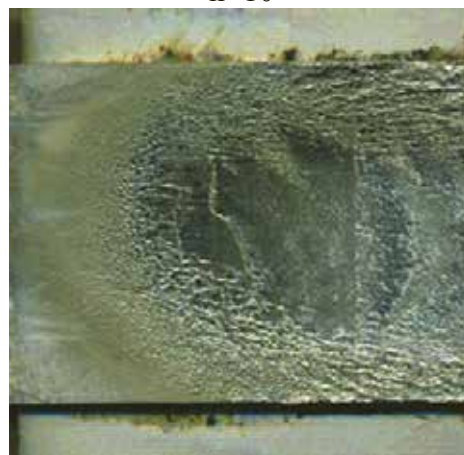
n=0



n=10



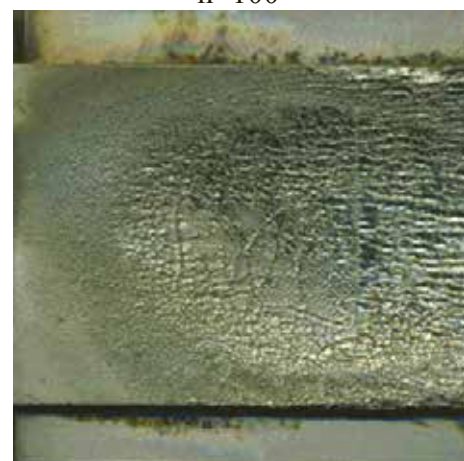
n=60



n=100



n=200



n=250

I.B. Kupriyanov

Fig.



n=10



n=40



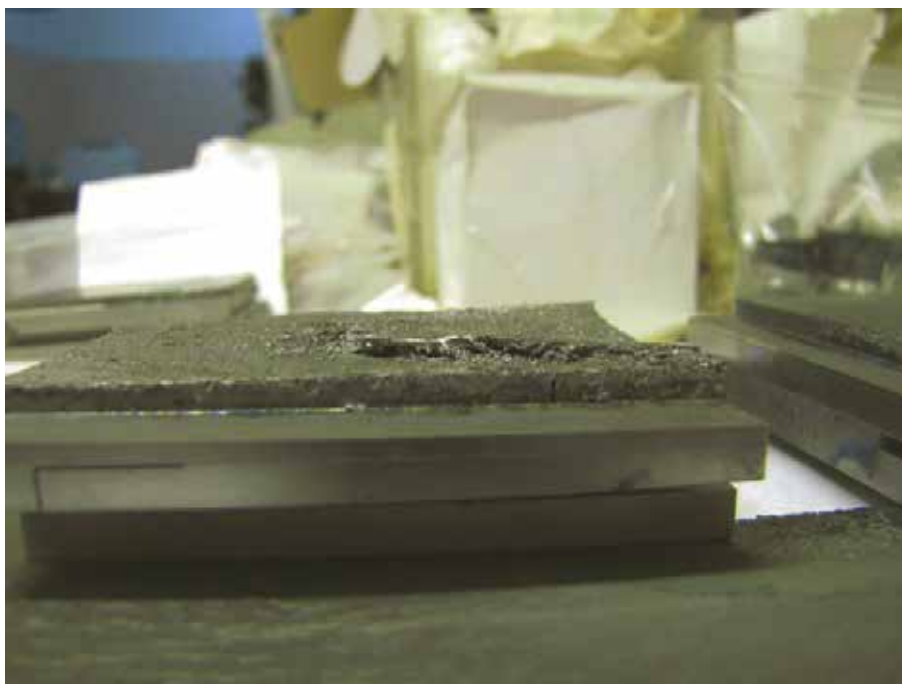
n=100

I.B. Kupriyanov

Fig.



a



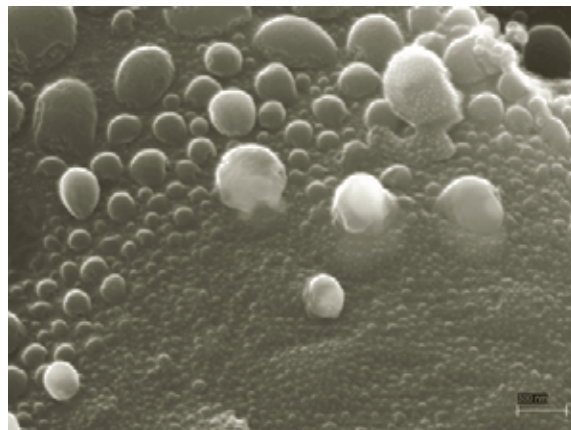
b

I.B. Kupriyanov

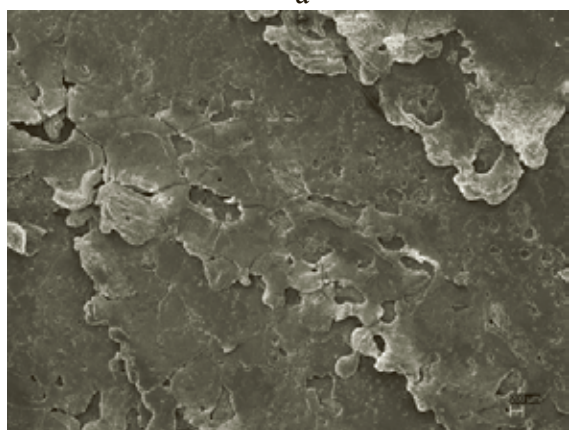
Fig.



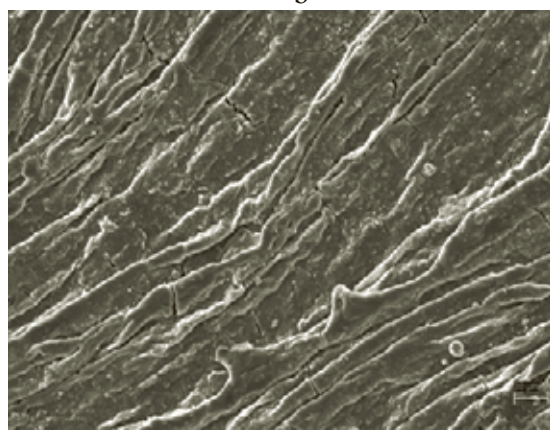
a



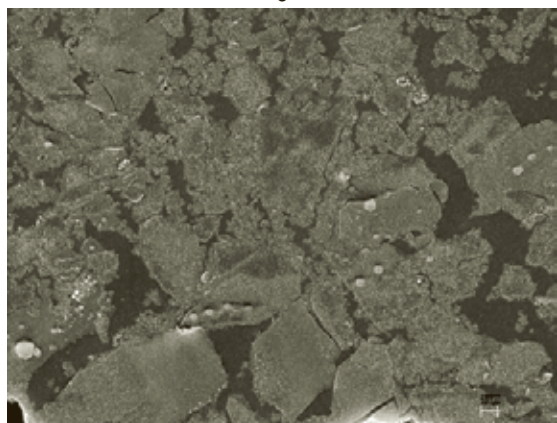
b



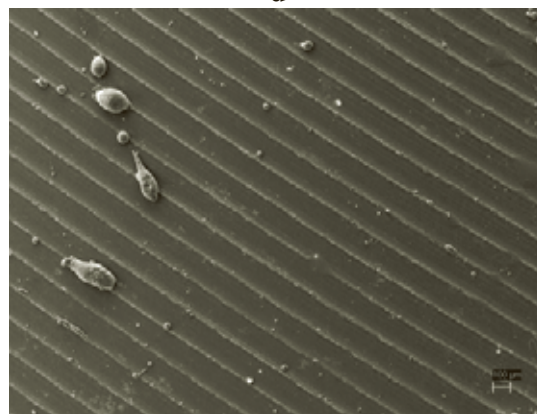
c



d



e



f

I.B. Kupriyanov

Tritium behaviour in neutron irradiated beryllium pebbles regarding their microstructure

Elina Pajuste, Gunta Kizane, Aigars Vitins, Vitalijs Zubkovs, Arturs Zarins

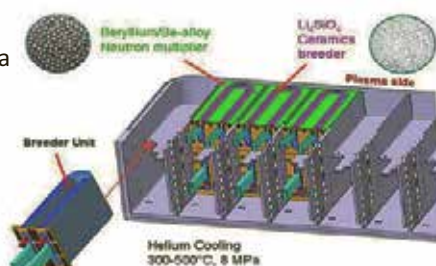
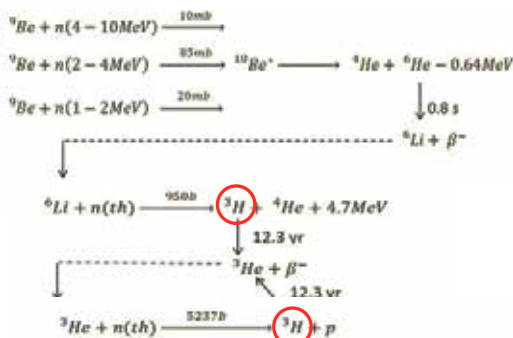
Laboratory of Radiation Chemistry of Solids, Institute of Chemical Physics, University of Latvia

10th IEA International Workshop on Beryllium Technology
 September 19 – 20, 2012, Karlsruhe

INTRODUCTION

In the EU HCPB breeder blanket concept **beryllium pebbles** have been chosen as a reference material for a neutron multiplier.

As a result of neutron induced transmutations of beryllium helium and **tritium** gas is produced in considerable amounts



F. Cismondi et al, 2009

Tritium release into the purge gas during blanket operation depends both on the temperature of pebble bed and on the properties of the pebbles themselves.

Studies on tritium desorption process and its relation to microstructural evolution of beryllium pebbles at a different temperatures could give a better understanding of issues related to tritium inventory in beryllium and possibilities to prevent it.

Aim of this study was to evaluate processes that occur during tritium thermo desorption from neutron irradiated beryllium pebbles.

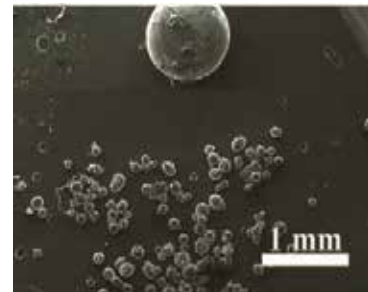
The tasks were:

- Obtain curves of tritium thermo desorption from two types of neutron irradiated beryllium pebbles
- Estimate temperatures where changes in thermo desorption curves are observed and perform treatment of the pebbles at these temperatures
- Study structure of the pebbles after thermal treatment (Scanning Electron microscopy)
- Estimate mass evolution and energies of the processes during thermal treatment (Differential Thermal Analysis and Thermal Gravimetric analysis)

SAMPLES

Two types of **beryllium** samples that have been irradiated in the experiments EXOTIC 8/3 (Extraction Of Tritium In Ceramics) and PBA (Pebble Bed Assembly) have been studied. All these irradiation programs have been performed in the *High Flux Reactor (HFR)* in Petten, the Netherlands

	PBA	EXOTIC 8/3-13
Manufacturer	NGK Insulators Ltd., Handa City, Japan	Brush Wellman Inc., Cleveland, Ohio, USA
Production process	Rotating Electrode Process (REP)	Inert Gas Atomization (IGA)
Pebble diameter, mm	0.9-1.1	0.1-0.2
Main impurities	2300 ppm BeO, 300 ppm Mg	3400 ppm BeO, 100 ppm Mg
Irradiation time	294 days	449.8 days
Neutron fluence (E>0.1 MeV)	$3-4 \times 10^{25} \text{ m}^{-2}$	$2.70 \times 10^{25} \text{ m}^{-2}$
Irradiation temp.	150-550 °C	520 -620°C
⁴He content	300-600 appm	285 appm
Year of end of irradiation	2004	2000



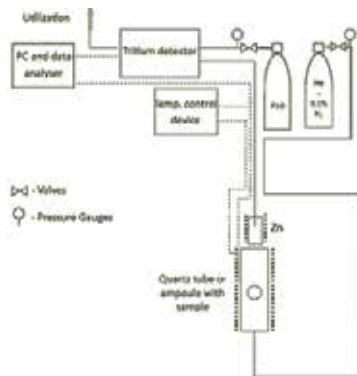
SEM image of PBA and EXOTIC pebbles

METHODS, EQUIPMENT

Samples have been heated in the flow of purge gas He+ 0.1% H_2 at the temperature program 5°C/min and then constant for 2h.

Two experimental setups have been used:

Experimental setup for tritium thermo desorption (Tritium was continuously measured with tritium monitor TEM 2102A



Thermal treatment for structure analysis have been performed in the **DTA/TG*** (*Exstar 6300*) device and therefore also the energy and mass changes were measured.



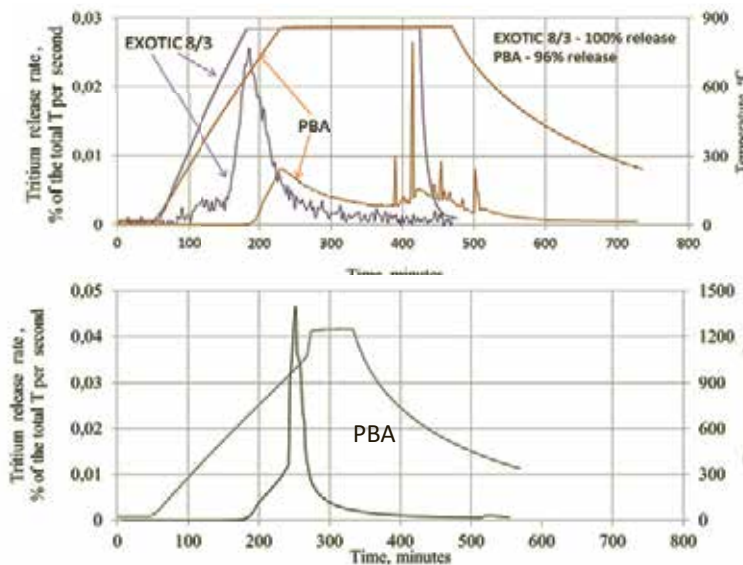
Structure has been studied after treatment in 100, 300, 550, 650, 750, 850, 950, 1050, 1250°C

For structure studies **Scanning Electron Microscope** (*Hitachi S-4800*) has been used (beam energy 3 kV and beam current 15 μ A)

*Differential Thermal Analysis and Thermal Gravimetric analysis

RESULTS

Tritium thermo desorption from neutron irradiated pebbles



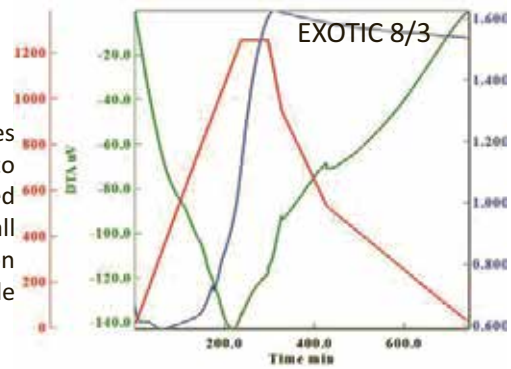
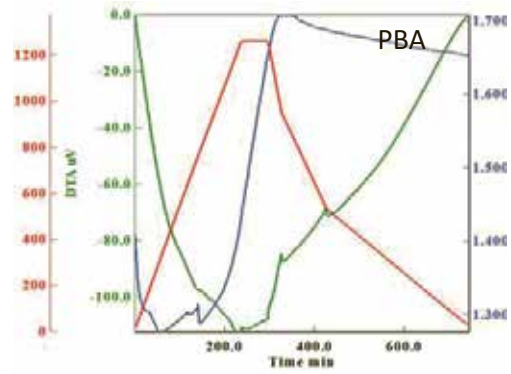
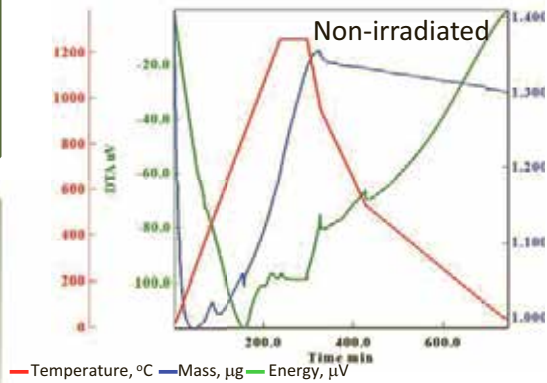
Heating at 850°C is sufficient to release all tritium from the pebbles irradiated in EXOTIC 8/3 experiment, whereas in pebbles from PBA experiment there is still some tritium remaining and higher temperature is needed.

Moreover, tritium desorption from the EXOTIC 8/3 pebbles starts at considerably lower temperature ((90 10)°C than that for PBA pebbles ((682 25) °C.

For PBA pebbles so called burst release starts only at ~950oC.

Thermo desorption of tritium from pebbles irradiated in EXOTIC 8/3 and PBA experiments (published before)

TG/DTA curves during treatment at the 1250oC



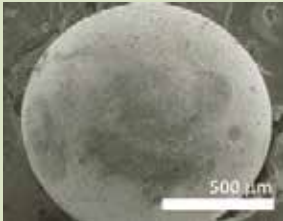


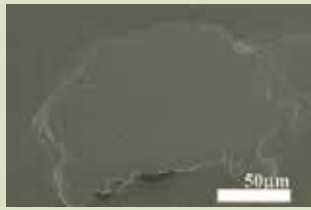
Mass and differential temperature evolution have been measured for non-irradiated (analogous for PBA pebbles) and two neutron irradiated samples. Mass increase indicates beryllium oxidation.

Sample	mass increase, %	Initiation temp., oC
Non-irradiated	~30	~250
PBA	~30	~350
EXOTIC 8/3	>150	~350

Temperature that initiates intense oxidation was found to be higher for the irradiated pebbles, whereas overall oxidation depends mostly on the type of the pebble (fabrication methods, size)

More precise quantities are planned to be obtained by further experiments

Structure of neutron irradiated pebbles before thermal treatment

PBA	EXOTIC
Shape	
<ul style="list-style-type: none"> •Spherical shape, •smooth surface 	<ul style="list-style-type: none"> •Irregular shape, several of them stacked together • surface seems to have layers 
Inner structure	
<ul style="list-style-type: none"> •Void in the bulk of the pebble (∅- 100 250 μm, 0.5 % of the pebble volume) •Few small pores of nm size 	<ul style="list-style-type: none"> •Some small pores (μm) in a fraction of pebbles. • In the areas where two pebbles have stacked together - interlayer 


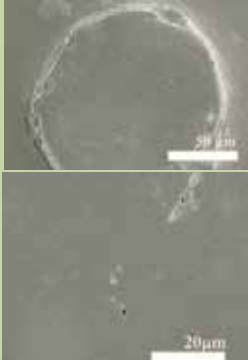
Structure at low temperature (100 -550°C)

No structure changes have been observed in a nanometer scale.

Therefore it might be concluded that tritium desorption at these temperatures (EXOTIC 8/3) is governed by **interstitial diffusion** (in EXOTIC 8/3 approximately 30% of tritium is accumulated as interstitial) and/or **surface processes**.

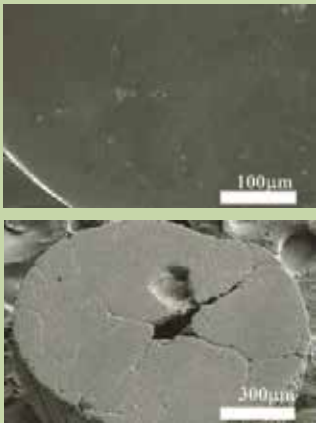
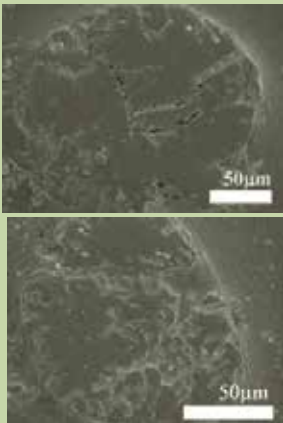
Structure at 550, 650°C (EXOTIC 8/3 and PBA)

First structure changes appears only in temperature range of 550 – 650°C that correspond to the rapid tritium desorption from EXOTIC 8/3 and desorption start form PBA pebbles.

PBA		EXOTIC 8/3
	<p>After treatment in temperature when tritium release starts, porosity has appeared. Pores reaches ~500nm</p> <p>Appearance of pores indicates the start of the gas migration</p> <p>Since in PBA there are almost no interstitial tritium (only gaseous) its desorption starts only at this stage.</p>	

Structure at 950°C (EXOTIC 8/3 and PBA)

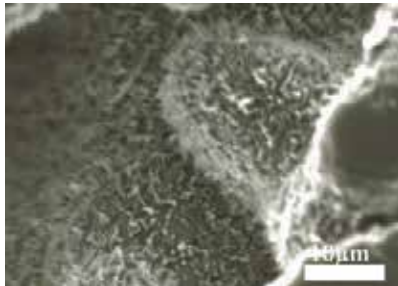
At temperature about 950°C tritium desorption becomes much intense from PBA pebbles, whereas from EXOTIC 8/3 its already released.

PBA		EXOTIC 8/3
	<p>Structure has changed considerably – there are large cracks connecting the technical void with a surface and also the connected pore system has been formed.</p> <p>Moreover, the size of the pores has increased up to several tens of micrometres.</p> <p>No pores and cracks were observed for non-irradiated pebbles.</p>	

Structure at 1050 - 1250°C (PBA)

Structure after treatment in 1250°C has been only studied for PBA pebbles (pebbles after treatment became very brittle).

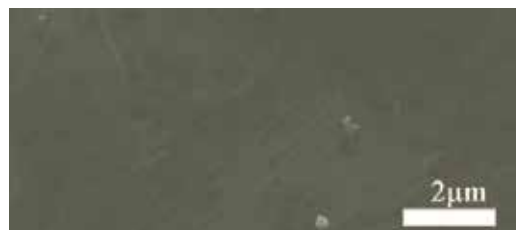
PBA, 1250°C



An interesting phenomena was observed for pebbles treated in high temperature (starting from 1050°C) - the inner structure of cracks and pores were coated with whiskers and «labyrinth type» structures. Moreover these structures were observed only for irradiated pebbles.



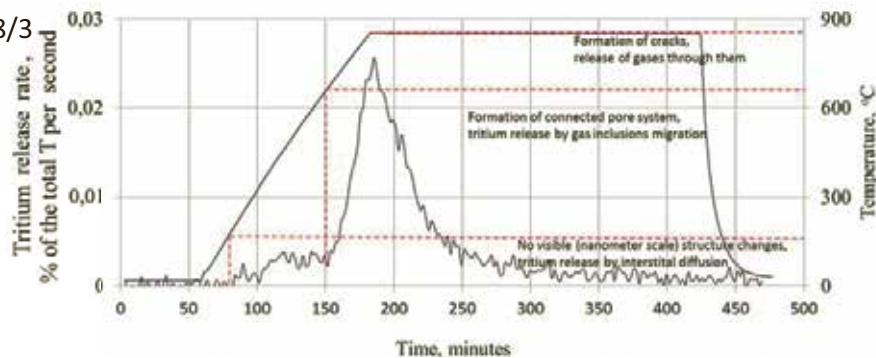
PBA, 1050°C



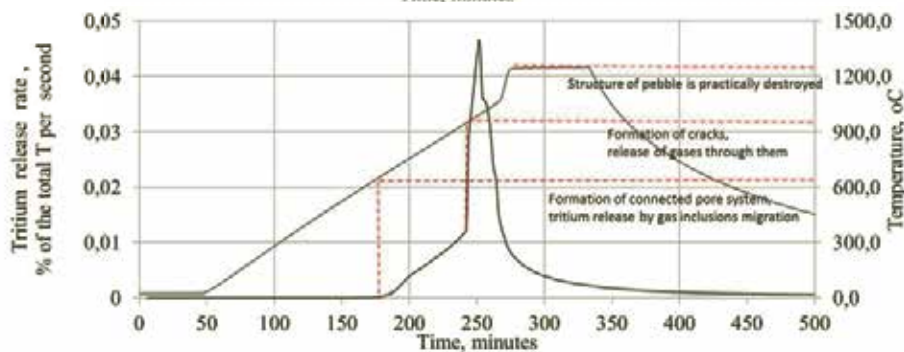
Non-irradiated, 1050°C

Structure evolution in correlation with tritium desorption

EXOTIC 8/3



PBA



CONCLUSIONS

- Tritium desorption from neutron irradiated beryllium pebbles is strongly related to the structure changes of the material. Gaseous products (helium and tritium) deform beryllium lattice that leads to formation of the pores and cracks.
- From EXOTIC 8/3 pebbles tritium release starts before appearance of visible (nanometre scale) structure changes, that might indicate interstitial diffusion that leads to tritium desorption (in previous studies it was found that up to 30% of tritium is accumulated as atomic in EXOTIC 8/3 beryllium pebbles).
- Gas inclusion migration (bubble coalescence and formation of open porosity) starts to appear at the temperatures above 600°C that coincided with the temperature when significant tritium release is started (for PBA pebbles there is no tritium release before this temperature).
- Thermo gravimetry method gives possibility to study oxidation process of beryllium during thermal treatment. It was found that higher temperature is needed to initiate intense oxidation of neutron irradiated beryllium than that for non-irradiated.

Development of granulation process of beryllide as advanced neutron multipliers for DEMO reactors in Japan

M. Nakamichi

Fusion Research and Development Directorate, Japan Atomic Energy Agency,
2-166, Omotedate, Obuchi, Rokkasho, Kamikita, Aomori, 039-3212, Japan

Abstract

Advanced neutron multipliers with low swelling and high stability at high temperatures are desired for pebble bed blankets of demonstration fusion power (DEMO) reactors. Beryllium intermetallic compounds (beryllides) are the most promising advanced neutron multipliers. In order to fabricate the beryllide pebbles, beryllide with shapes of block and/or rod is necessary when a melting granulation process is applied such as a rotating electrode method. A plasma sintering method has been proposed as new technique which uses a non conventional consolidation process. It was clarified that the beryllide could be simultaneously synthesized and jointed by the plasma sintering method in the insert material region between two beryllide blocks. Beryllide rod of Be_{12}Ti with 10 mm in diameter and 60 mm in length has been successfully fabricated by the plasma sintering method. Using this plasma-sintered beryllide rod, fabrication of prototype pebble of beryllide was performed by a rotating electrode method as one of the melting methods. The prototype pebbles of Be_{12}Ti with 1 mm in average diameter were successfully fabricated.

Keywords:

Beryllide, Beryllium, Plasma sintering method, Rotating electrode method, Pebble.

1. Introduction

Advanced neutron multipliers with lower swelling and higher stability at high temperature are desired in pebble bed blankets, which would have a big impact on the demonstration fusion power reactor (DEMO) design, especially the blanket operating temperature. Beryllium intermetallic compounds (beryllides) such as Be_{12}Ti are the most promising advanced neutron multipliers [1-3]. However, beryllide is too brittle to allow production of pebbles. Establishing fabrication techniques for the beryllide is a key issue for development of the advanced neutron multiplier. The development has been started by Japan and the European Union in the DEMO R&D of the International Fusion Energy Research Centre (IFERC) project as a part of the Broader Approach (BA) activities from 2007 to 2016. In specific, the development of fabrication technique for beryllide has been carried out in the Beryllium Handling Room in the DEMO R&D Building at the Rokkasho BA site of the Japan Atomic Energy Agency (JAEA).

It was clear that the intermetallic compound beryllides of Be-Ti could be directly synthesized by the plasma sintering method from mixed elemental powders of Be and Ti at a temperature lower than the melting point [1-2]. Using this plasma-sintered beryllide rod, fabrication examination of prototype beryllide pebble was performed by a rotating electrode method. The present study describes a novel granulation process of beryllide using these methods including synthesis and granulation techniques.

2. Granulation process of beryllide

In order to fabricate the beryllide pebbles, a rod type of beryllide is necessary when a melting granulation process is applied such as a rotating electrode method (see Fig.1). The hot isostatic pressing (HIP) method and the casting method have been proposed for synthesis of beryllides [3]. However, beryllide is too brittle for the fabrication of blocks or rods by these methods. Furthermore, these methods have some disadvantages such as complicated process, difficulty in composition control and contamination by impurities.

In contrast, the plasma sintering process is simple and easy to control. The plasma sintering is a non-conventional consolidation process that consists of plasma generation, resistance heating and pressure application [4-6]. The plasma discharge results in particle surface activation that enhances sinterability and reduces high temperature exposure. Pressure application assists the densification process by enhancing sintering and thus reducing the high temperature exposure of the consolidated powders. The plasma sintering method was decided as a synthesis method for beryllide.

In the previous study, preliminary fabrication of beryllide, namely Be-Ti intermetallic compound, was carried out at sintering temperatures of 1073, 1173 and 1273 K, using mixed Be and Ti powders by the plasma sintering method [1-2]. The formation of Be_{12}Ti , $\text{Be}_{17}\text{Ti}_2$ and Be_2Ti intermetallic compounds was identified by X-ray diffraction analyses. The elemental state fractions of Be and Ti in the plasma sintered material decreased by consolidation enhancement with

increasing sintering temperature, with only about 2 % of the elemental phases remaining in 98 % beryllide for processing at 1273 K. This result showed that the beryllide could be directly synthesized by the plasma sintering method from mixed elemental powders of Be and Ti at a temperature lower than the melting point.

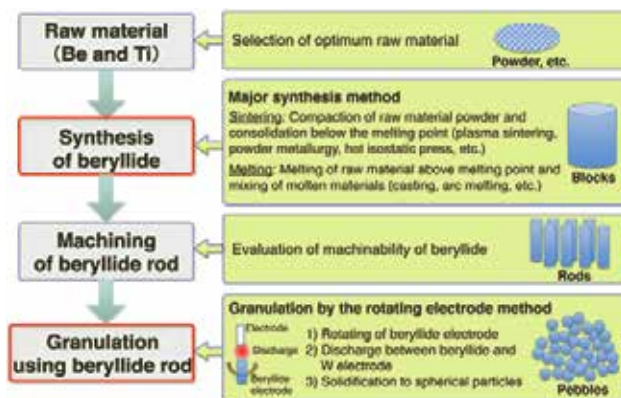


Fig.1 Process flow scheme of beryllide granulation.

3. Synthesis and joining for beryllide by the plasma sintering method

3.1 Synthesis of beryllide by the plasma sintering method

Synthesis of intermetallic compounds starts with mixed elemental powders. In this process, the starting powder is loaded into a die and punch unit applying uniaxial pressure for cold compaction. Electric current is applied to create the plasma environment and to activate the particle surfaces. The powder compact is resistance-heated while the uniaxial pressure is still applied to the material in the sintering mold. In the present study, the plasma sintering apparatus (KE-PasIII) made by KAKEN Co. Ltd. was used.

Schematic drawing of the plasma sintering method and sintering conditions are shown in Fig2. Synthesis of beryllide as a Be-Ti intermetallic was carried out using mixed pure Be and Ti powders. Beryllium powder (Materion Brush Inc., 99.4 wt.%) and titanium powder (Kojundo Chemical Laboratory Co. Ltd., 99.9 wt.%) were mixed with 20 g in weight for 30 min using the automatic mortar (RM200, RETSCH, Co. Ltd.) made of Al_2O_3 . The size of the Be and Ti powders was less than 45 μm . The mixed powder composition was 92.3 at.% Be and 7.7 at.% Ti which is the stoichiometric value of $Be_{12}Ti$ composition. The plasma sintering was carried out at 1273 K for 20 min under a pressure of 50 MPa. Heating and cooling rates were approximately 100 and 300 K/min, respectively. The plasma-sintered beryllide disks were 20 mm in diameter and 28 mm in thickness. Consolidations for Beryllide were evaluated by Electron Probe Micro Analyser (EPMA; JXA-8530F by JEOL Co. Ltd.).

The area fractions of each element or composition were determined in the cross-sectional micrographs of sintered samples by the EPMA. The compositional image in backscattered electron image (BEI) mode of the scanning electron microscope (SEM) in the cross section of the plasma-sintered disk is shown in Fig. 3. Black, dark gray, gray, and white areas of the sample sintered at 1273 K for 20 min were identified as Be, $Be_{12}Ti$, $Be_{17}Ti_2$ and Be_2Ti , respectively. The area fractions of Be, $Be_{12}Ti$, $Be_{17}Ti_2$ and Be_2Ti were about 2, 91, 5 and 2 %, respectively. The plasma-sintered disk has a metallic luster and was a dense material with above 98% of theoretical density.

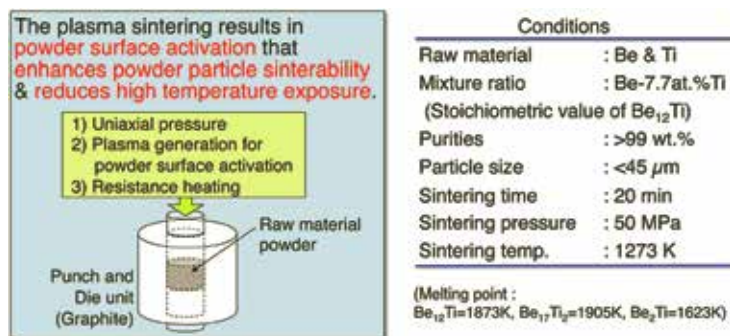


Fig.2 Schematic drawing of the plasma sintering and sintering conditions.

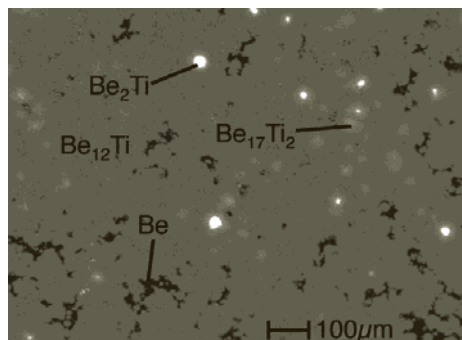


Fig.3 SEM photograph of the cross-section of the plasma-sintered disk.

3.2 Joining of beryllide disks by the plasma sintering method

A joining schematic and appearance and SEM photographs of jointed beryllide are shown in Fig.4. The joining for the beryllide block was carried out using two plasma-sintered beryllide disks. Raw material powder of beryllide with 3 g in weight was inserted between the plasma-sintered disks. This insert material was the same raw material powder as that for the fabrication of disk. The plasma sintering conditions for joining were the same as previous conditions for fabrication of beryllide disk. The size of the jointed beryllide block was 20 mm in diameter and 60 mm in length. Consolidation and joining of beryllide were evaluated by XRD and microstructure analysis using the EPMA.

The result of photograph for the beryllide block joined by the plasma sintering is shown in Fig.4. Neither cracks nor boundary lines were observed on the surface of the plasma-sintered jointed block. There is no defect in appearance. Plasma-sintered jointed block showed metallic luster and was a dense material. There was no change in beryllide compositions before and after plasma-sintered joining. Formations of Be_{12}Ti , $\text{Be}_{17}\text{Ti}_2$ and Be_2Ti intermetallics were identified. The compositional images of the insert material region and the plasma-sintered jointed block with BEI mode of the SEM are shown in Fig.4. These results showed that there was no difference in microstructures between the insert material and the bulk region of the plasma-sintered disk. The Beryllide block with 20 mm in diameter and 60 mm in length has been successfully fabricated by the plasma sintering method.

Because an electrode rod with 10 mm in diameter was necessary in this apparatus, the beryllide rod with 10 mm in diameter and 60 mm in length could be machined by a wire electric discharge (WED) method from the plasma-sintered beryllide block with 20 mm in diameter and 60 mm in length (see Fig.4). It has become clear that difficult-to-machine beryllide could be machined by the WED method accurately and efficiently.

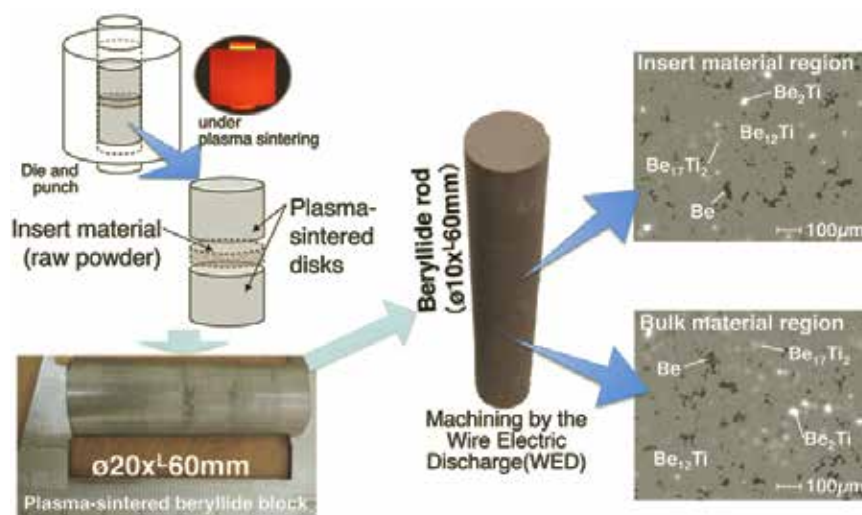


Fig.4 Joining schematic and appearance and SEM photographs of jointed beryllide.

3.3 Granulation of beryllide by the rotating electrode method

A rotating electrode method was applied as a granulation method of beryllide synthesized by the plasma sintering method. This method has a lot of experiences not only for fabrication of beryllium pebble in the fusion field but also for fabrication of metallic pebble in the general industry. In the present study, the granulation apparatus made by MINERVA KIKI Co. Ltd. that has a granulation chamber with 1000 mm in diameter was used. Specifications of this apparatus are 200 A of maximum current and 20000 rpm of maximum rotating speed.

Using the plasma-sintered beryllide rod machined by the WED method, trial fabrication of prototype pebble of beryllide was performed by the rotating electrode method. Figure 5 shows the granulation schematic, real-time photograph of process, and the apparatus. The rotating electrode method is a method for producing metal particle when the end of a metal rod is melted while it is rotated along its longitudinal axis. Molten metal is centrifugally ejected and forms droplets that solidify to spherical particles.

In this study, trial fabrication of beryllide pebble was performed using a commercially available apparatus that has a granulation chamber with 1000 mm in diameter under the conditions with current of 80 A and a rotating speed of 6000 rpm using the plasma-sintered beryllide rod. The pressure of the granulation vacuum chamber with replacement of pure He gas was about 0.1 MPa. Photograph of beryllide pebbles and granulation condition are shown in Fig.6. From the result of trial fabrication, the prototype pebbles of beryllide with 1 mm in diameter were successfully fabricated. However, some molten particles were crushed against the inner surface of the granulation chamber before solidification.

Therefore, the optimization of the granulation condition will be carried out using a custom-built rotating electrode granulation apparatus that has a larger granulation chamber.

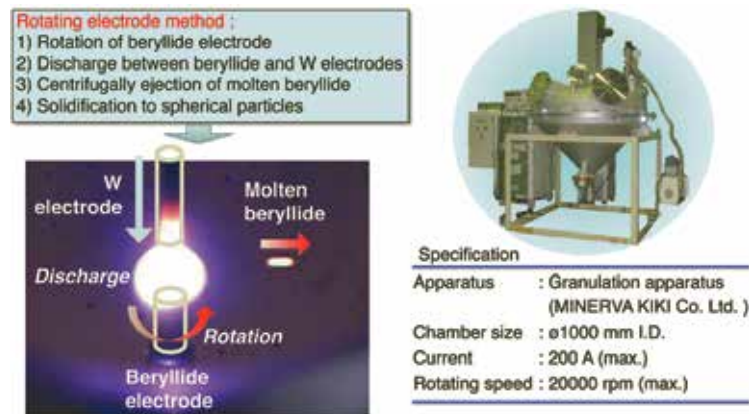


Fig.5 Granulation schematic and the apparatus of the rotating electrode method.

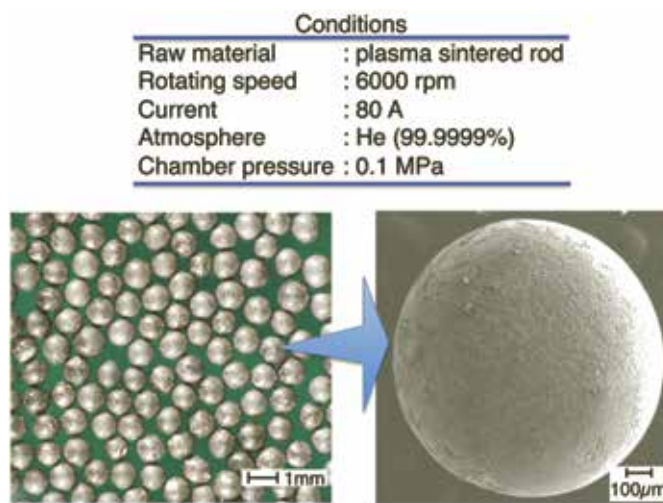


Fig.6 Photographs of the prototype pebbles by the rotating electrode method using the plasma-sintered beryllide rod and granulation conditions.

5. Conclusion

Beryllides are the most promising advanced neutron multipliers. The plasma sintering method has been selected as a new synthesis method for beryllides because this method is very simple and easy to control. It was clarified that the beryllide could be simultaneously synthesized and jointed by the plasma sintering method.

Beryllide rod with 10 mm in diameter and 60 mm in length has been successfully fabricated by the plasma sintering method and machined by the wire electric discharge method. Using this plasma-sintered beryllide rod, trial fabrication of pebbles of beryllide was performed by the rotating electrode method using a commercially available apparatus. Prototype pebbles of beryllide with 1 mm in average diameter were successfully fabricated.

In future, the optimization of synthesis and granulation conditions and characterization of prototype pebble will be performed using the plasma sintering and a custom-built granulation apparatus with larger chamber.

References

- [1] M. Nakamichi et al., J. Nucl. Mater. 417 (2011) 765-768.
- [2] M. Nakamichi et al., Fusion Eng. Des. 86 (2011) 2262-2264.
- [3] Y. Mishima et al., Fusion Eng. Des. 82 (2007) 91-97.
- [4] M. Wada et al., Magnetics, IEEE Transactions 26 (5), (1990) 2601-2603.
- [5] J. R. Groza et al., J. Mater. Res. 7 (10), (1992) 2643-2645.
- [6] T. Abe et al., FGMnews-015-010 (1991) 21-25 (in Japanese).

Synthesis of Beryllides Powder for Advanced Neutron Multiplier

Y. Natori¹, J. Suzuki¹, K. Tatenuma¹, K. Yonehara², M. Nakamichi²

¹ Kaken Inc., 1044 Hori, Mito, Ibaraki 310-0903, Japan

² Fusion Research and Development Directorate, Japan Atomic Energy Agency, 2-166, Omotedate, Obuchi, Rokkasho, Kamikita, Aomori, 039-3212, Japan

Introduction

An advanced neutron multiplier with a higher stability at high temperature is required in DEMO reactors. Beryllium intermetallic compounds (beryllides) are the most promising advanced neutron multipliers. The synthesis method of several kinds of beryllides powder for the raw material of neutron multiplier molding is developed.

Powder Synthesis of Beryllium Intermetallics Compounds¹⁻³⁾

As a method of producing beryllide powders, a simple calcination method was considered. The examined powdery beryllide compounds which were carried out by calcination method are Be_{12}Ti , Be_{13}Zr , Be_{12}V , Be_{12}W , Be_{12}Ta , Be_{12}Cr , Be_{12}Mo , and Be_{12}Nb . The synthesis method is calcination in an inert gas atmosphere: two kinds of metallic powder ($\text{Be} + \text{Metal}$) which serves as materials of beryllide are mixed by stoichiometry value. The properties of beryllide powders synthesized by calcination were then evaluated. The physicality and melting point of the target beryllide compounds are shown in Table 1. The case of Be-Ti is shown for the synthetic method of the examined beryllide powder as an example. As shown in Fig.1, The case of Be_{12}Ti which is one of the candidate material, mixture value of Be and Ti powder were 69.3wt%Be – 30.7wt%Ti. Next, the mixed powders are sintered in an inert gas atmosphere in an alumina crucible. Then, Be_{12}Ti could be synthesized. The most important point of this method is that calcination temperature should be lower than the melting point. The aim of this study is that the synthesis of beryllide powders at lower temperature without melting.

Table-1 Target beryllides

	Target Beryllide	Density [g/cm ³]	Be content [wt%]	Melting point [K]
Be-Ti	Be_{12}Ti	2.26	69.30	1,823
Be-Zr	Be_{13}Zr	2.72	56.22	2,200
Be-V	Be_{12}V	2.37	67.98	1,973
Be-W	Be_{12}W	4.57	37.04	2,020
Be-Ta	Be_{12}Ta	4.18	37.41	2,123
Be-Cr	Be_{12}Cr	2.44	67.53	1,610
Be-Mo	Be_{12}Mo	3.02	45.52	1,973
Be-Nb	Be_{12}Nb	2.88	53.79	1,945

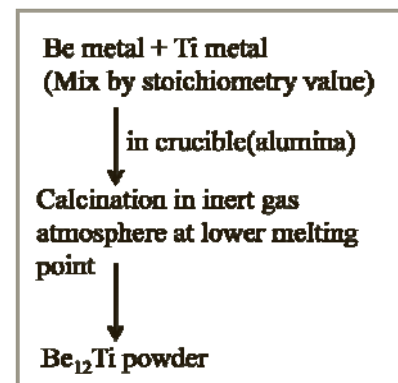


Fig.1 Synthetic method of powdery beryllides

Experimental

Be-Ti Intermetallic Compound^{1~3)}

The synthesis of Be_{12}Ti powder was examined using mixed powders of Be and Ti. The purities of Be and Ti powder used in this study, were 99.6% and 99.9%, respectively and their particles of 45 micrometers or less were used as shown in Fig. 2. The result of thermogravimetry and differential thermal analysis (TG-DTA) of mixed Be and Ti powders is shown in Fig. 3. From the TG-DTA data, it is surmised that the conversion to beryllide compound occurs at the point of exothermic peak at 1373K. Based on this effect, the calcination temperature was decided at 1373 K.

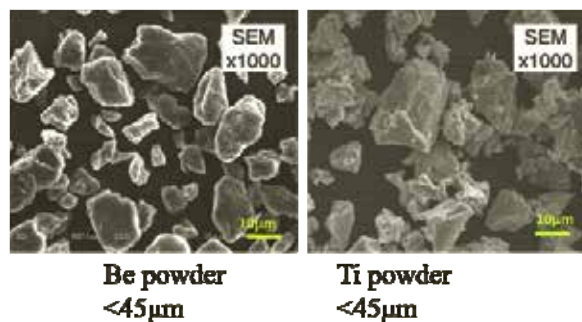


Fig.2 Raw materials of Be and Ti powders

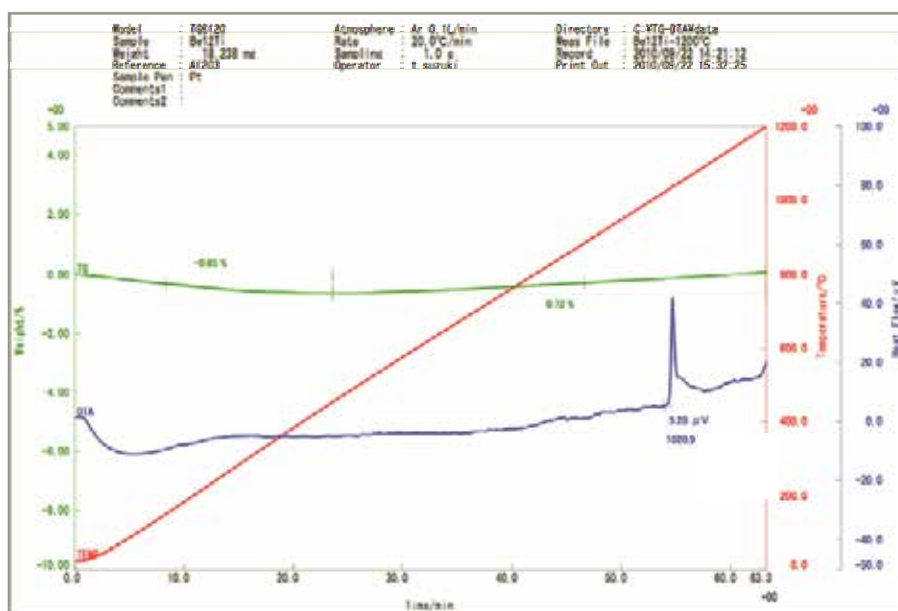


Fig.3 TG-DTA of Be+Ti
rt~1473K(20K/min) in Ar(0.1L/min)

The SEM photographs and X-ray diffraction (XRD) measurement after calcination of the mixed powders at 1373K for 24 h under Ar are shown in Fig. 4 and Fig. 5, respectively. From the result of a crystal structure analysis by using the XRD, the formation of Be_{12}Ti as Be-Ti intermetallics was identified. Therefore it was obvious that Be_{12}Ti powder could be synthesized by calcination at 1373 K..

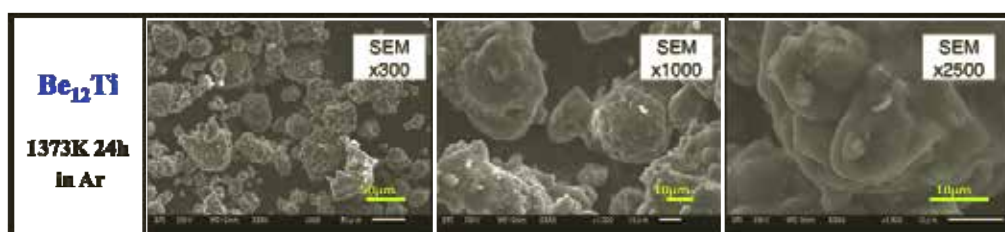


Fig. 4 SEM photograph after calcination of Be+Ti powders at 1373K for 24h in Ar

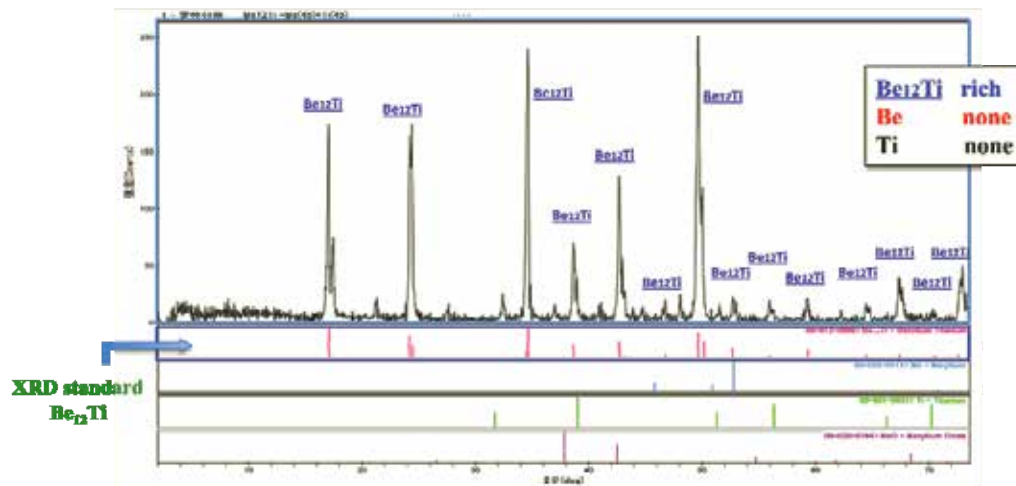


Fig. 5 XRD result of 12Be+Ti powders treated at 1373K for 24h in Ar

To investigate the effect of the calcination holding time, we carried out the calcination at 1373K for 0, 3, 12, 24 and 48 h. The structural analyses using XRD and the electron probe micro analyzer (EPMA) were conducted. From the result of effect of calcination time at 1373K as shown in Fig.6, some parts of Be may be remained and unreacted if the holding time is less than 3 h, but Be_{12}Ti beryllide synthesis could be mostly completed by more than 12 h at 1373K.

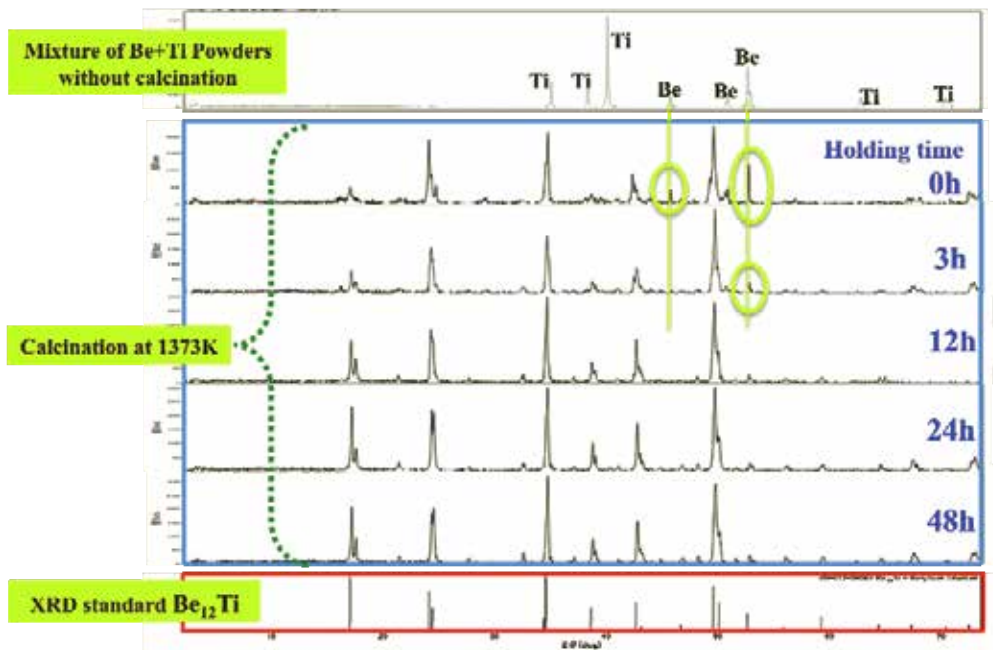


Fig. 6 Effect of calcination holding time of 12Be+Ti at 1373K

The EPMA and SEM photographs of the calcination holding time of 0, 3, 12 24 and 48 h after reached to 1373K are shown in Fig.7. The beryllide powder is composed of two colors, black and white area which corresponds to beryllide and unreacted Be. By the result of increase of Be_{12}Ti area with long holding time, Be_{12}Ti seems to have increased with holding time in proportion. In Fig. 8, the line graph shows the relation between the growth of Be_{12}Ti and the holding time. By judging from the data of EPMA and XRD, it is assumed that the growth of Be_{12}Ti was mostly completed more than 12 h, because this graph shows that the conversion from Be and Ti to Be_{12}Ti is mostly saturated over 12 h.

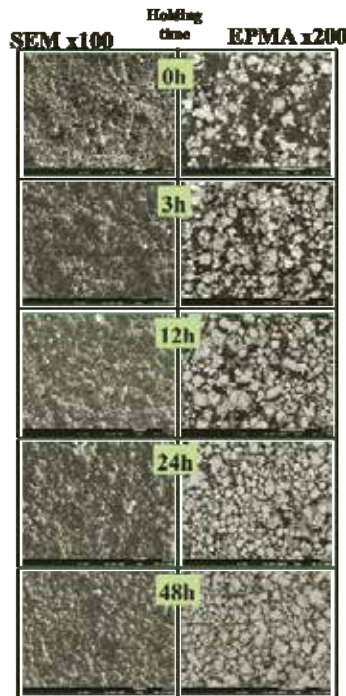


Fig. 7 EPMA and SEM photographs of calcination holding time of 12Be+Ti at 1373K
White area in EPMA is Be_{12}Ti and Black is unreacted Be.

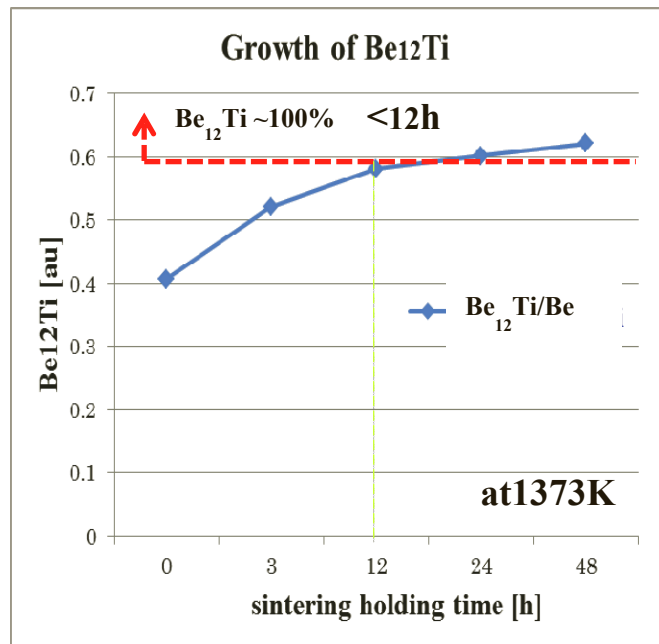


Fig. 8 Relation between the Be_{12}Ti growth and sintering holding time at 1373K

Other beryllium intermetallic compounds¹⁻³⁾

As the other synthesis example of Be intermetallic compounds of Be-Zr, Be-V, Be-Ta and Be-W those examination results are indicated.

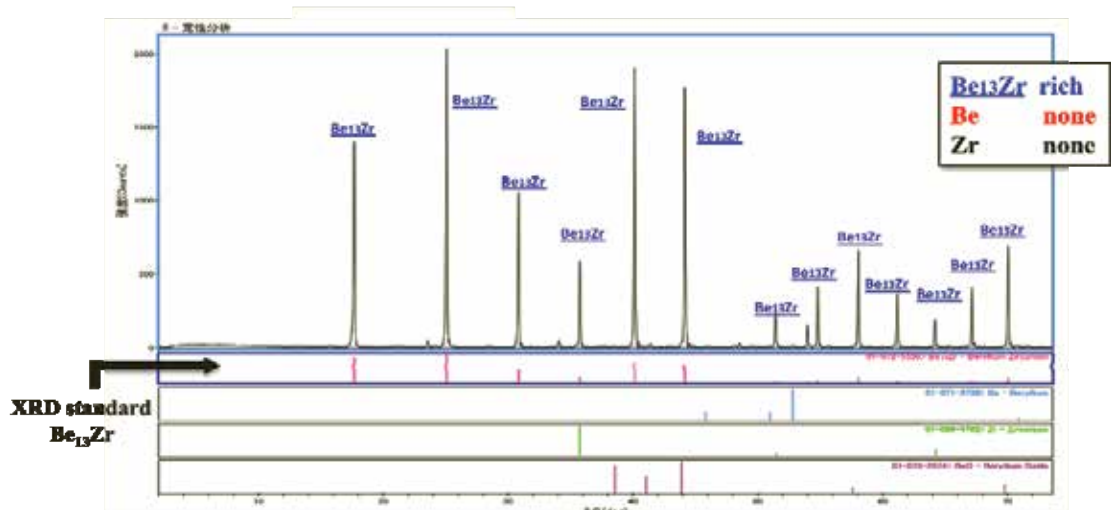


Fig. 9 XRD result after calcination of Be+Zr powders at 1473K for 24h in Ar.

At

first, in the case of the powder of Be and Zr mixed by the ratio of 13 mol and 1 mol, the data of XRD after calcination at 1473K for 24 h under Ar is shown in Fig. 9. From the result, the formation of Be_{13}Zr as Be-Zr intermetallic compound was identified as single phase mostly. Synthesized Be and Zr compound are exactly fitted to Be_{13}Zr peaks with its XRD-standard.

Next, in the case of the powder of Be and V mixed by the ratio of 12 mol and 1 mol, the data of XRD after calcination at 1473K for 24 h under Ar is shown in Fig. 10. From the result of a measurement of XRD, the formation of Be_{12}V as Be-V intermetallics was identified. Some parts of Be seems to remain as it unreacted.

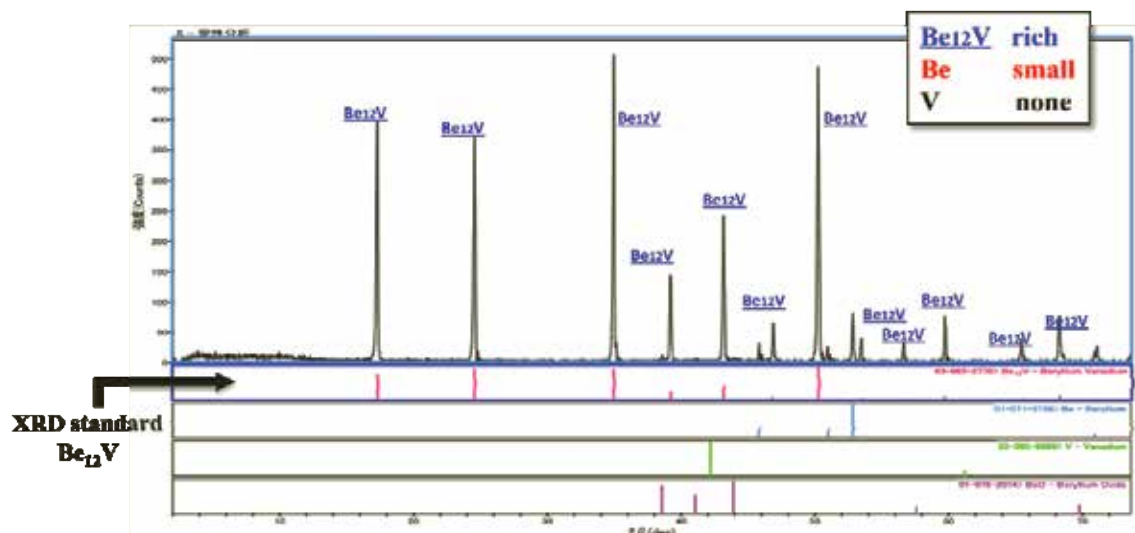


Fig. 10 XRD result after calcination of Be+V powders at 1473K for 24h in Ar.

Next, in the case of the powder of Be and Ta mixed by the ratio of 12 mol and 1 mol, synthesized at 1473K for 24 h under Ar, three kinds of multi-phase mixture of Be_{12}Ta , Be_{17}Ta , Be_3Ta , Be_2Ta were identified as shown in Fig. 11.

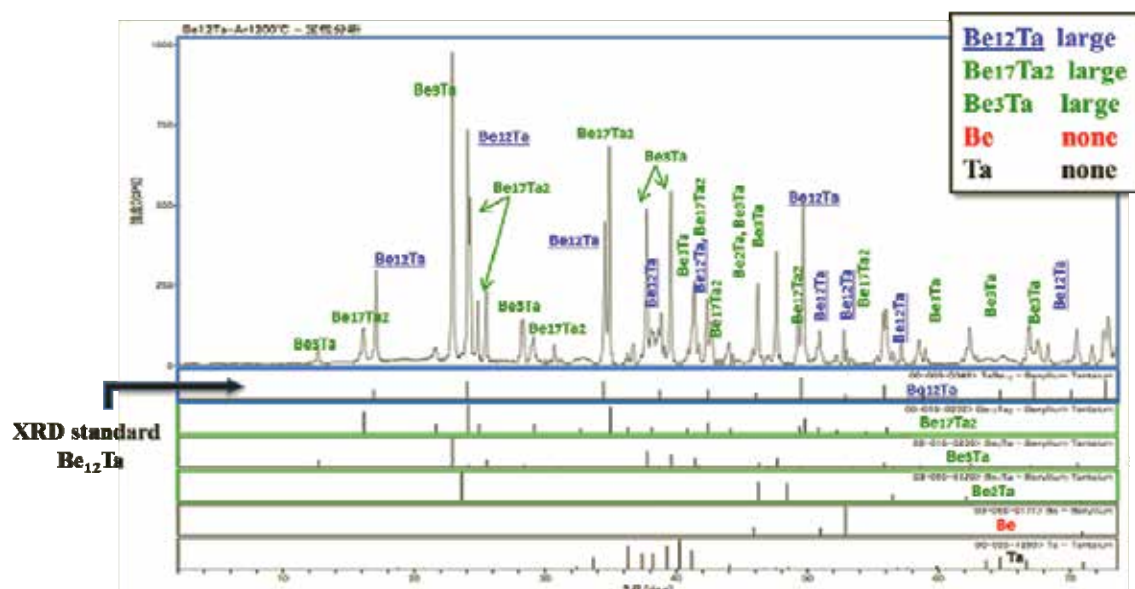


Fig.11 XRD result after calcination of 12Be+Ta Powders at 1473K for 24h in Ar.

Next, in the case of powder of Be and W mixed by the ratio of 12 mol and 1 mol, by synthesized at 1473K for 24 h under Ar. The XRD result indicated that two phases of Be_{12}W and Be_{22}W as Be-W intermetallic were identified (Fig.12). Regarding to Be-W intermetallic compound, it is necessary to find out sintering condition in more detail.

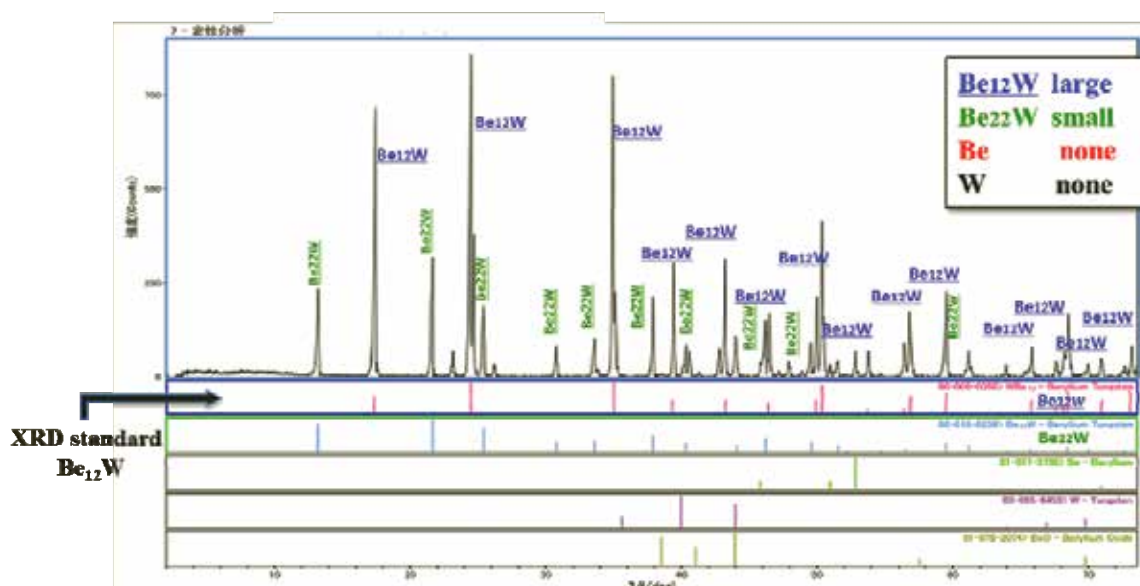


Fig.12 XRD result after calcination of 12Be+W Powders at 1473K for 24h in Ar.

Summary

The target beryllides and their synthesis conditions are shown in Table-2. As the panoptic result of this study, it is possible to fabricate wide variety of beryllide powders by the calcination only using mixed powders of Be and another metal. This method is very simple, by calcination in inert atmosphere only. Because Be-W and Be-Ta are composed of multi-phase compositions, however, it is needed to determine an optimum condition to make a single phase of Be_{12}Ta and Be_{12}W . In a future, the detail examination of calcination temperature and holding time is required.

Table-2 Calcination conditions for synthesizing beryllides powder by mixed elemental powers of Be and metals.

	Target Beryllide	Synthesis condition
Be-Ti	Be_{12}Ti	1373~1473K, 24h in Ar
Be-Zr	Be_{13}Zr	
Be-V	Be_{12}V	
Be-W	Be_{12}W	
Be-Ta	Be_{12}Ta	
Be-Cr	Be_{12}Cr	
Be-Mo	Be_{12}Mo	
Be-Nb	Be_{12}Nb	

Conclusion

The sintering experiments showed that the intermetallic compound beryllide can be directly synthesized by only calcination from mixed elemental powders of Be and Ti (or, others) at a relative lower temperature than the melting point. It is necessary to find out the optimum conditions of the heat-treatment according to the kind of various beryllium intermetallic compounds.

In conclusion, these are the main results of this study, beryllium intermetallic compounds can be directly synthesized by only heating. The synthetic process is very simple and easy to control. And, the beryllide powders can be synthesized with a high reproducibility. On the other hand, as a next step, two additional examinations will be conducted as following: one is to find out the optimum conditions of the heat-treatment. Another is to examine how particle size of the raw materials affects. As a future plan, the fabrication technology of wide variety of beryllide powders with a high quality as single phase will be developed, and the adequate mass-production technology of beryllide powders for advanced neutron multiplier fabrication will be realized.

REFERENCES

- 1) Proceedings of the Sixth IEA International Workshop on Beryllium Technology for Fusion, JAERI-Conf 2004-006, pp.172-183.
- 2) H. Okamoto and L. Tanner, Phase diagrams of Binary Beryllium Alloys, ASM International, Materials Park OH, (1987), pp.211.
- 3) H. Okamoto, Desk Handbook Phase Diagrams for Binary Alloys, ASM International (2000), pp.138-139.

Recent progress of irradiation effects study on $Be_{12}Ti$ by plasma sintering method

Tamaki Shibayama, Masaru Nakamichi*, Jae-Hwan Kim*, Masami Ando* and BA Cooperative Research Team organized by Japanese Universities

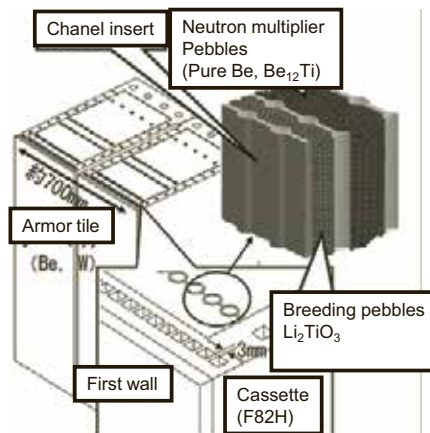
**Center for Advanced Research of Energy and Materials Science, Hokkaido University
 Sapporo, Hokkaido 060-8628, Japan**

***JAEA, Rokkasho, Aomori 039-3212, Japan**

Background (To develop TBM for DEMO)

- Candidate neutron multiplier materials
- Candidate armor tile materials for JET and ITER
- Beryllium intermetallic compounds beyond DEMO due to high temperature melting point, high temperature strength and less

	ITER-TBM	DEMO
Thermal load at surface	0.5MW/m ²	1.0MW/m ²
Wall load by neutron	0.8MW/m ²	3.5MW/m ²
Cooling water temperature	280~325°C	280~510°C
Cooling water pressure	15MPa	25MPa
Structural materials	RAM/F82H	F82H
Breeding pebbles	Li ₂ TiO ₃	Li ₂ TiO ₃
Neutron multiplier	Pure Be	Primary candidate Be ₁₂ Ti



Design concept of Japanese solid breeder/water cooling TBM
 By Suzuki@JAEA

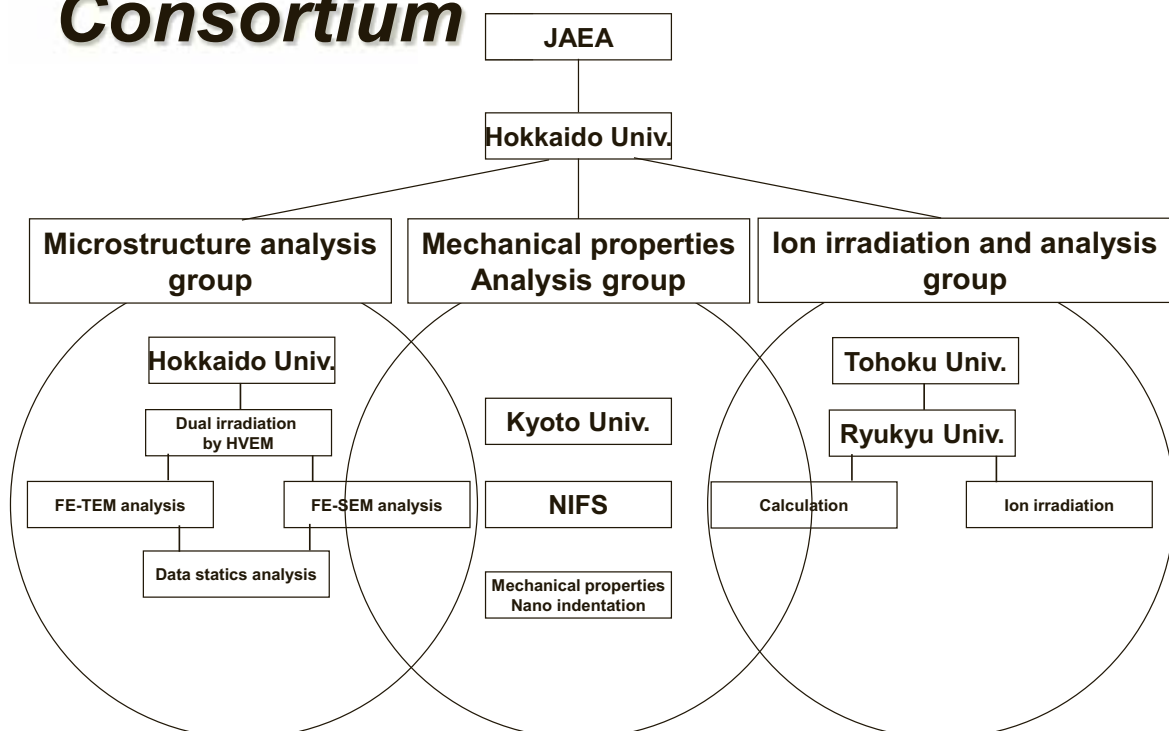
Objective

Basic study on irradiation responses of plasma sintered Be₁₂Ti comparison with HIPed Be₁₂Ti and pure Be.

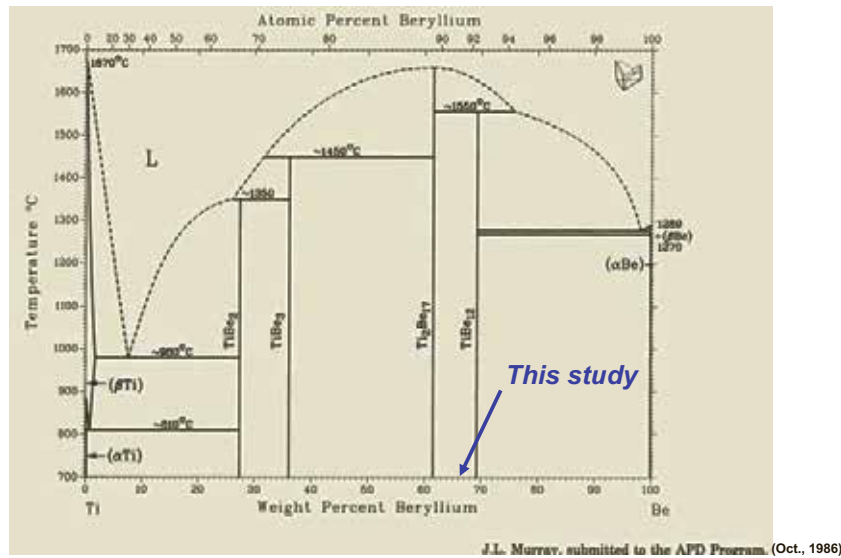
Experimental procedure

- He ion irradiation:
5,000, 10,000, 15,000, 20,000 and 25,000appm at R.T.
under He ion irradiation of 100keV,
- Nanoindentation test
 - pure Be, previous HIPed Be₁₂Ti, plasma-sintered Be₁₂Ti using nanoindentation apparatus of UMIS 2000
 - plasma sintered Be₁₂Ti using apparatus of ELIONIX

Consortium



Assessed Be-Ti phase diagram



Chemical composition of HIPed Be₁₂Ti and pure Be

Table 1
Chemical composition of pure Be and Be₁₂Ti used in this work (mass%)

Heat number	Be	BeO	Mg	Al	Si	Ti	Cr	Fe	Co	Ni	Cu	Sc	W	C
K573 (High Fe)	Bal.	0.15	0.013	0.034	0.009	0.014	0.027	0.18	<0.001	0.007	0.008	<0.005	<0.01	0.043
H1163 (Low Fe)	Bal.	0.35	0.050	0.054	0.031	0.003	0.007	0.069	<0.001	0.002	0.007	<0.005	<0.01	0.043
Be ₁₂ Ti	Bal.	1.32	0.001	0.014	0.025	33.4	0.003	0.044	0.047	<0.001	0.004	-	<0.01	0.026

Fabrication process of HIPed Be_{12}Ti in previous study

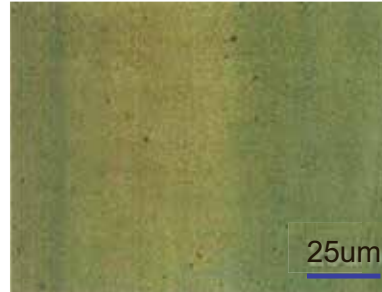
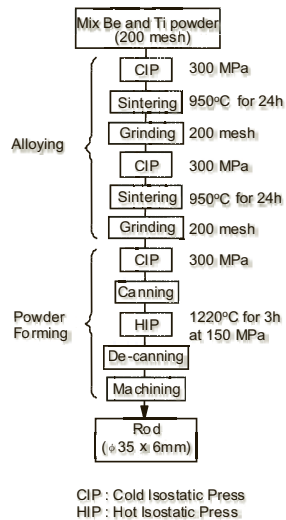
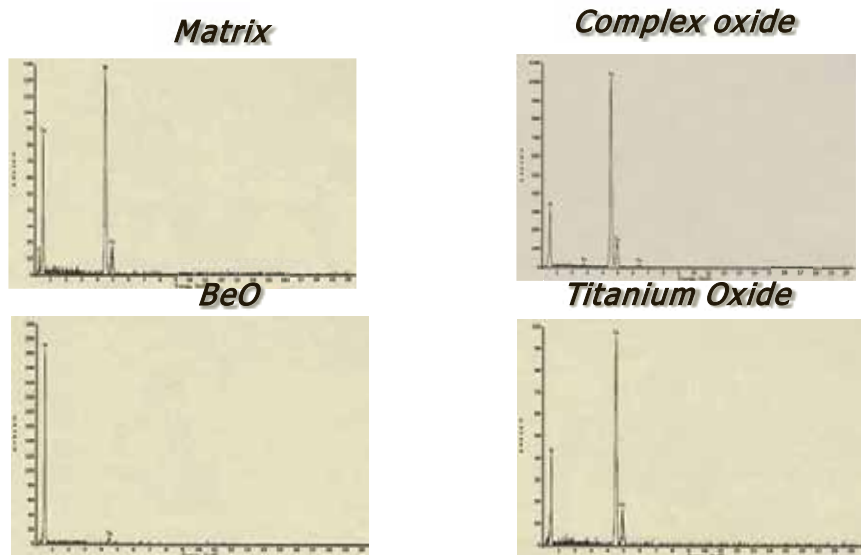


Fig. 1. Optical micrograph of Be_{12}Ti

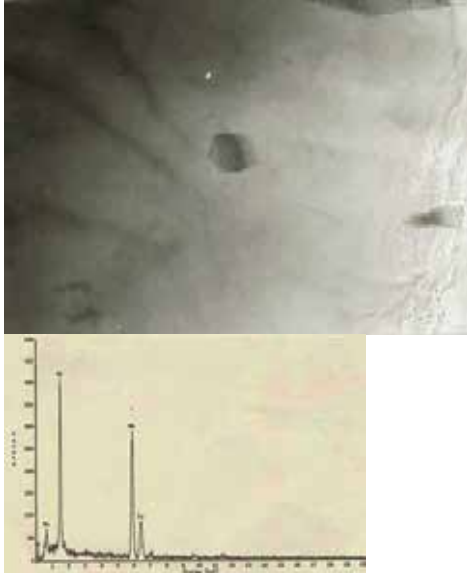
There is no second phase in the matrix.

EDS analysis of matrix and precipitates in HIPed Be_{12}Ti

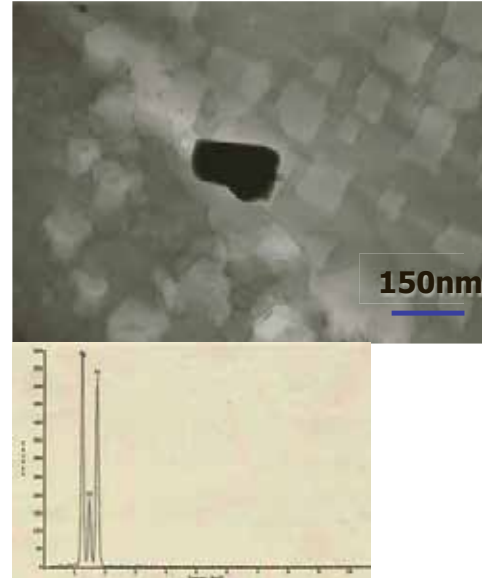


Typical precipitates of pure Be

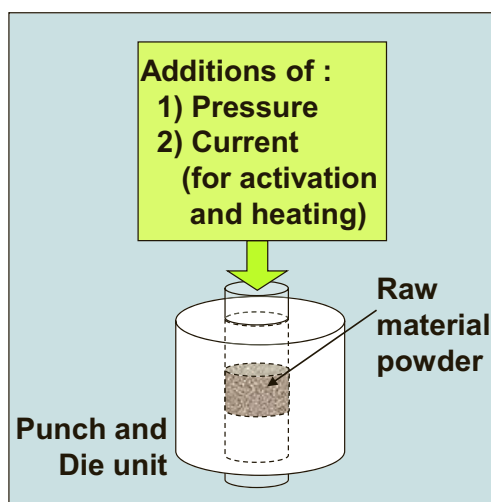
H1163 (Fe 0.069 %, BeO 0.35 %)



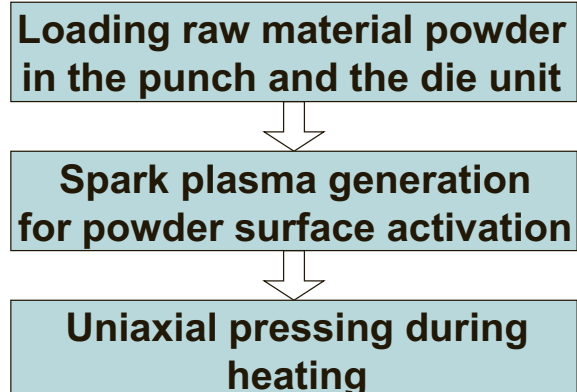
K573 (Fe 0.18 %, BeO 0.15 %)



Plasma sintering process



Plasma Sintering Process



Merit;

- Surface activation (remove surface oxidation layer)
- Relatively lower temperature sintering compare to HIP and HP
- Relatively shorter time sintering compare to the above methods

He ion irradiation at Hokkaido Univ.



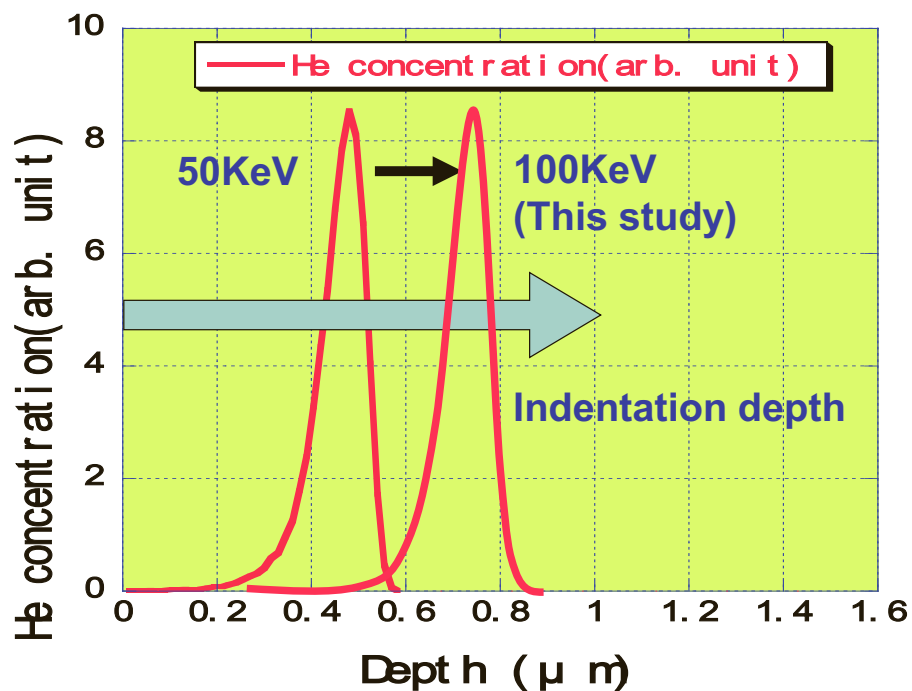
Ion beam irradiation facility in Hokkaido Univ.



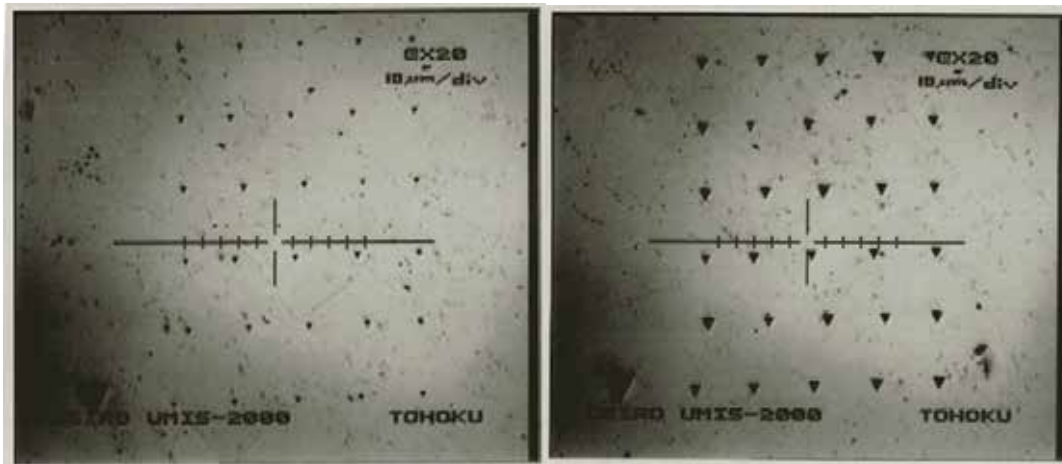
Specimen fixture and specimen

Irradiation conditions;
Irradiation temp.; R.T.
Acc. Voltage; 100keV
Dose; 5,000, 10,000, 15,000, 20,000, 25,000appm

He ion range by SRIM code



Indentation mark by nano indentation testing

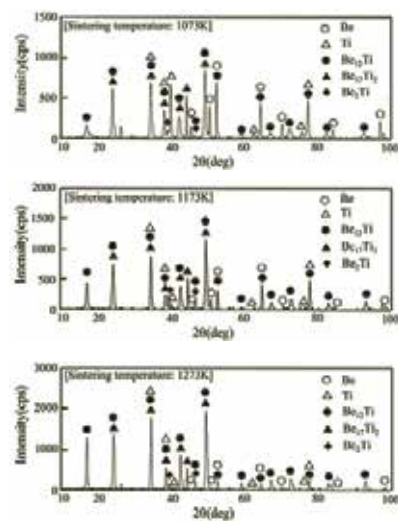
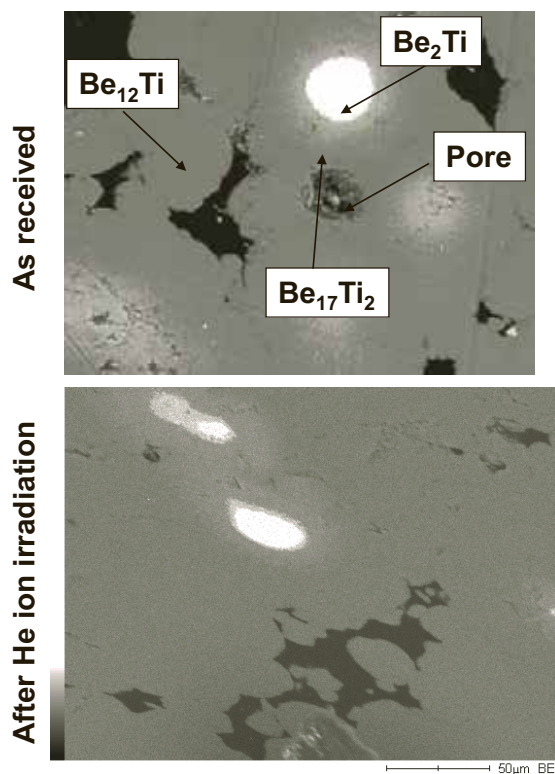


S465C
Before irr., After MCP,
20mN

S465C
Before irr., After MCP,
50mN

Testing by UMIS-2000 in I.M.R. Tohoku Univ

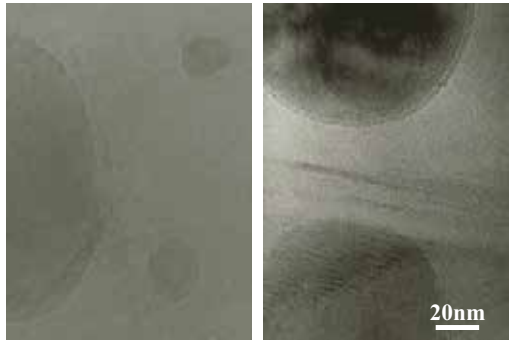
SEM of SPS $Be_{12}Ti$ and



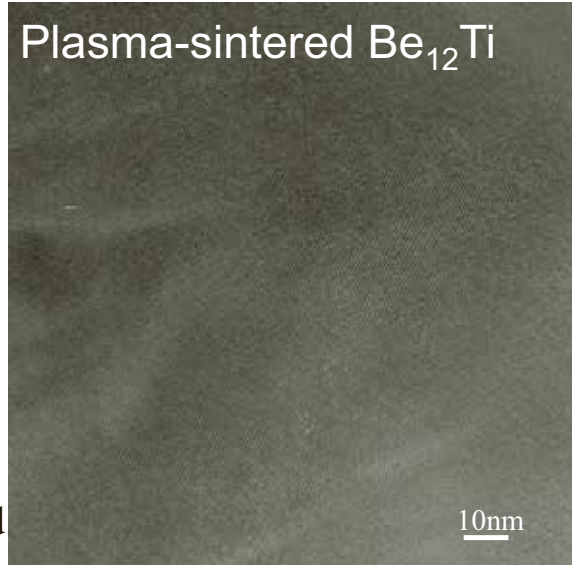
No obvious change of surface morphology after He ion irradiation!

TEM Microstructure of Be₁₂Ti

Previous Be₁₂Ti sample by HIP



Plasma-sintered Be₁₂Ti

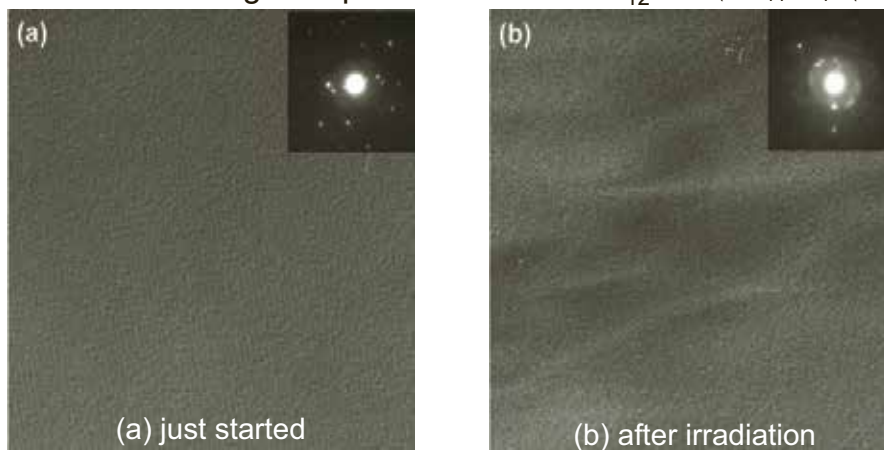


- Plasma-sintered Be₁₂Ti has **low content** of BeO, Ti-oxide and other complex oxides compared with previous Be₁₂Ti by the powder metallurgy method.
- Plasma-sintered Be₁₂Ti is **high crystalline** because lattice images are clearly observed.

1

Electron / He dual irradiation

High resolution TEM images of plasma sintered Be₁₂Ti (~50appm/dpa (~7dpa of Fe) at R.T.)



(1.4×10^{21} electrons/cm² & 9.3×10^{14} He ions/cm²)

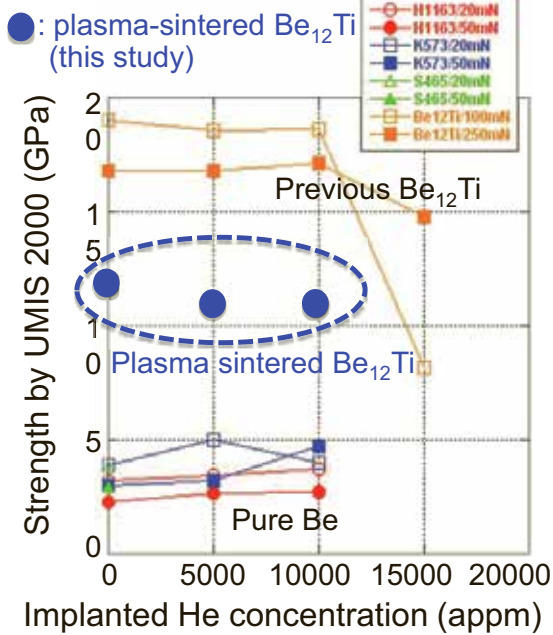
- **Lattice images disappeared** by irradiation.
- Intense undulated **black contrast** was observed after irradiation.
- **Electron diffraction patterns** were also diffused.



The periodic atomic arrangement in the intermetallic phase in Be₁₂Ti was **disordered and became amorphous phase** by irradiation.

Hardening evaluation by He irradiation

Strength change with irradiation

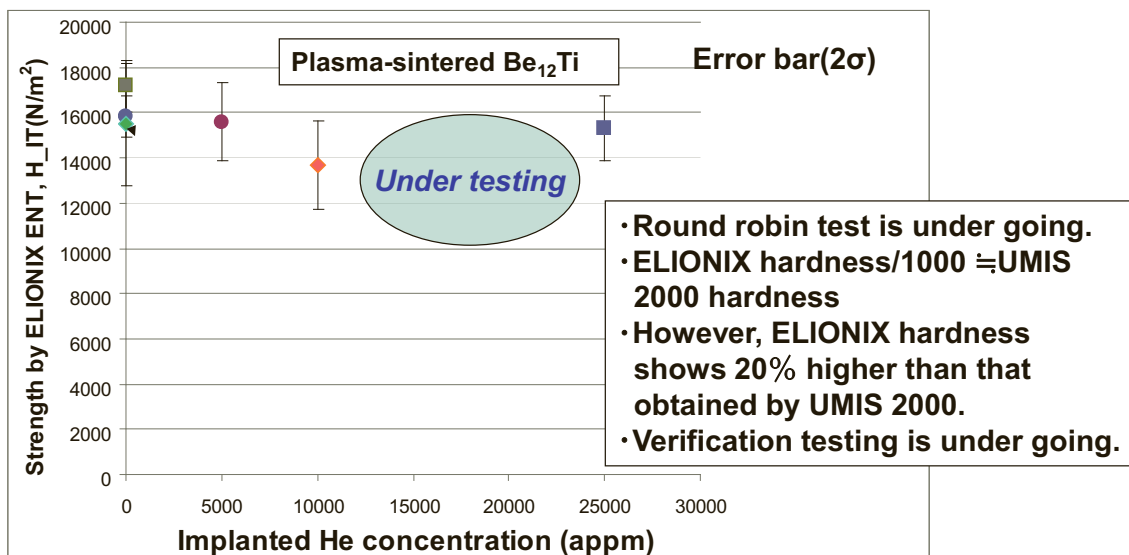


Pure Be : hexagonal closed package crystal structure
 Be₁₂Ti : tetragonal crystal structure

- The strength of plasma sintered Be₁₂Ti is about **two thirds** of that of the previous Be₁₂Ti by the HIP method .
- Irradiation hardening result after 10000 appmHe irradiation shows **no significant degradation** as same as the previous Be₁₂Ti.
- Main reason of these phenomena (difference in strength) would be caused by their **crystal structure** and strongly interacted with **impurities, precipitates** and **inclusions**.
- Plasma-sintered Be₁₂Ti has **lower content** of impurities, precipitates than the previous Be₁₂Ti by the HIP method.

Plasma-sintered Be₁₂Ti showed lower strength than the previous Be₁₂Ti and would also **have higher ductility** compared to the previous Be₁₂Ti.

Effects of He ion irradiation on hardness by ELIONIX ENT



- Round robin test is under going.
- ELIONIX hardness/1000 ≅ UMIS 2000 hardness
- However, ELIONIX hardness shows 20% higher than that obtained by UMIS 2000.
- Verification testing is under going.

Microstructure analysis and irradiation effects

In-situ charged particle irradiation experiments and irradiation hardening testing were conducted.

- 1) Plasma-sintered Be₁₂Ti showed **high crystallinity** before irradiation, and was disordered and became amorphous phase after irradiation.
- 2) The strength of plasma-sintered Be₁₂Ti was about **two thirds** of that of the previous Be₁₂Ti and showed **no significant degradation** after 10000 appmHe irradiation using UMIS 2000 apparatus.
- 3) These results suggested that the plasma sintering method would be **more suitable for a large scale production of neutron multiplier materials** from the view point of **crystallinity and less precipitates and inclusions** in Be₁₂Ti matrices.
- 4) Study of nanoindentation apparatus effects (Round robin test) on hardness is still under going.

1

Characteristics of microstructure, swelling and mechanical behavior of titanium beryllide samples after high-dose neutron irradiation at 740 and 873 K

P. Kurinskiy¹, A. Moeslang¹, V. Chakin¹, M. Klimenkov¹, R. Rolli², S. van Til³, A.A. Goraieb⁴

¹ - Karlsruhe Institute of Technology, Institute for Applied Materials- Applied Materials Physics (IAM-AWP), P.O. Box 3640, 76021 Karlsruhe, Germany

² - Karlsruhe Institute of Technology, Institute for Applied Materials- Materials Biomechanics (IAM-WBM), P.O. Box 3640, 76021 Karlsruhe, Germany

³ - Nuclear Research and Consultancy Group, Westerduinweg 3, Postbus 25, 1755 ZG Petten, the Netherlands

⁴ - Karlsruhe Beryllium Handling Facility (KBHF GmbH), Herrmann-von-Helmholtz-Platz 1, 76344 Eggenstein-Leopoldshafen, Germany

Titanium beryllide Be_{12}Ti is one of the candidate materials for advanced neutron multiplier in the helium-cooled breeding blanket of DEMO reactor.

Cylinder-shaped specimens (diameters of 3 mm) consisting, mainly, of Be_{12}Ti phase were investigated after high-dose neutron irradiation at 740 and 873 K in High Flux Reactor in Petten, Netherlands.

The sizes and shapes of radiation-induced gas bubbles as well as swelling of samples were evaluated by means of transmission electron microscopy (TEM). Mechanical behavior of titanium beryllide specimens in initial and irradiated states was investigated using compression tests under constant loading.

Obtained results are discussed and compared with available data on pure beryllium.

Keywords: titanium beryllide, neutron irradiation, swelling, transmission electron microscopy, compression test.

1. Introduction

Titanium beryllide Be_{12}Ti is considered to be a very promising material in the scope of its use as neutron multiplier in the solid helium-cooled breeding blanket of fusion reactor.

Investigated Be_{12}Ti samples were produced by arc-melting of a cold-pressed Be-Ti disc in argon atmosphere [1] and then irradiated by neutrons at 740 and 873 K in High Flux Reactor (HFR) in Petten, Netherlands, in the frame of HIDOBE-01 irradiation program. The parameters of neutron irradiation corresponded to $6,94 \times 10^{25}$ neutrons/m² ($E > 1$ MeV) with a damage dose of 13,9 dpa for titanium beryllide samples irradiated at 740 K, and to $8,07 \times 10^{25}$ neutrons/m² with a damage dose of 16,3 dpa for irradiation temperature equaled to 873 K [2,3]. Helium production was 2300 and 2680 appm for irradiation temperatures 740 and 873 K, correspondingly.

Cylinder-shaped samples were tested using uniaxial compression loading at 923 K in as-fabricated state and after irradiation at 740 K. Microstructure of neutron-irradiated samples was investigated by means of Transmission Electron Microscope (TEM). Special emphasis was put on evaluation of swelling of irradiated samples using high-resolution TEM images. Obtained results were compared with appropriate experimental data on pure beryllium which is a main candidate material for the use as neutron multiplier in the breeding blanket.

2. Experimental

2.1 Materials

Specimens having diameters of 3 mm and heights of 3-4 mm were used in this work. The phase composition of initial beryllide samples was represented, mainly, by Be_{12}Ti phase. The results of X-Ray diffraction analysis are shown in Fig. 1. It should be emphasized that other beryllides (in particular, Be_2Ti , $\text{Be}_{17}\text{Ti}_2$) which are signed by "X" in Fig. 1 were also formed during the operation of an arc-melting.

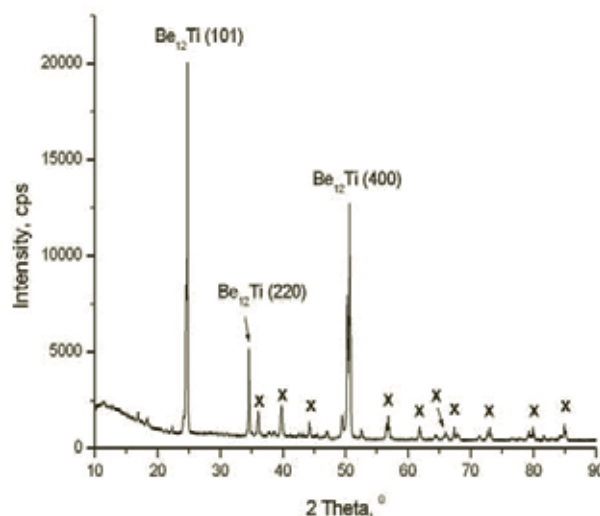


Fig. 1 X-Ray diffraction pattern of arc-melted titanium beryllide sample in initial state

2.2 Specimens and procedure of constant-load compression tests

Constant-load compression tests were performed in the closed glove-box system in Hot Cells (Fusion Materials Laboratory) using two cylindrical specimens: in as-fabricated state and after neutron irradiation at 740 K. The test box was constantly purged with nitrogen in order to avoid the oxidation of specimens during the experiment. Constant load of 1000 N was applied uniaxially by means of ceramic plunger with the duration of 100 hours for all tested specimens. One should note that this value of the compression force was maximal permissible in the glove-box. Having known diameter of the tested cylinders which is 3 mm and the compression load (1000 N), one can estimate the value of the compression stress in this experiment which is about 140 MPa. Titanium beryllide specimens were tested at 923 K. The choice of this temperature corresponds to working conditions of the solid breeding blanket.

2.3 Investigations by TEM

TEM examination was performed using FEI TECNAI-20F (200 keV) microscope. Due to an extremely high brittleness of investigated samples, standard procedure of the preparation of TEM specimens (with diameter of 3 mm and 0.3 mm thickness) was replaced by examination of ultrafine particles produced by crashing of irradiated samples in liquid nitrogen. It was experimentally observed that the particles with the sizes of 100-500 nm were the most suitable for the investigations by TEM. In this case, particles have sufficient volume for representativeness of results and, on the other hand, regions which are transparent for the electron beam can be easily found.

Particles produced by crashing of titanium beryllide samples after neutron irradiation at 740 and 873 K were investigated in this work.

3. Mechanical behavior of Be_{12}Ti samples in as-received state and after irradiation at 740 K

Fig. 2 represents the results of compression tests in the system of axes "absolute deformation – time of testing". In this work, measured "absolute deformation" is the recorded plunger stroke. Both samples, in non-irradiated state and after irradiation at 740 K, have shown nearly equal values of absolute deformation (in the range of 50-70 μm) before the brittle failure occurred. These values correspond to approx. 2% of relative deformation which refers to a formation of cracks in the material volume caused by a uniaxial compression loading. It should be noted that the process of production of initial beryllide samples by an arc-melting led to formation of fabrication-induced pores in the material volume. One can assume that the measured deformation is closely linked to a propagation of cracks and cleavages around these pores. Therefore, the contribution of exact plastic deformation into a change

of the specimens' heights is negligible. Although some difference between the heights of investigated specimens was detected (2.5 and 1.9 mm for initial and irradiated state, accordingly), the mechanical behavior during compression tests at 923 K of both types of samples is very similar.

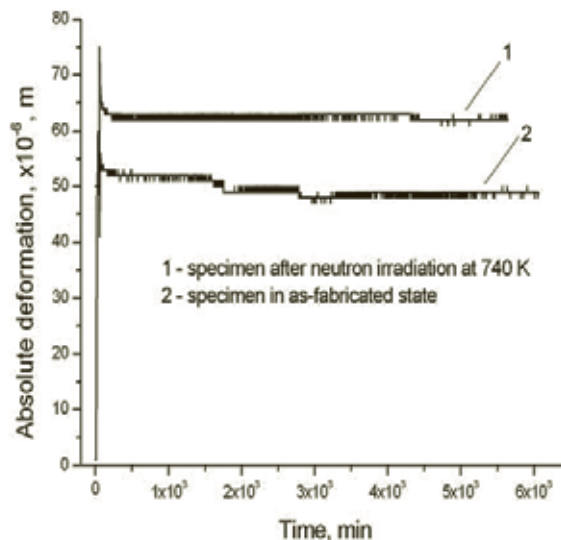


Fig. 2 Results of uniaxial compression tests at 923 K of titanium beryllide samples before and after irradiation at 740 K

Fig. 3 illustrates irradiated at 740 K titanium beryllide specimen after uniaxial compression test. One could observe that the failure occurred at an angle of approximately 45° to a direction of loading with the brittle fracture surface.

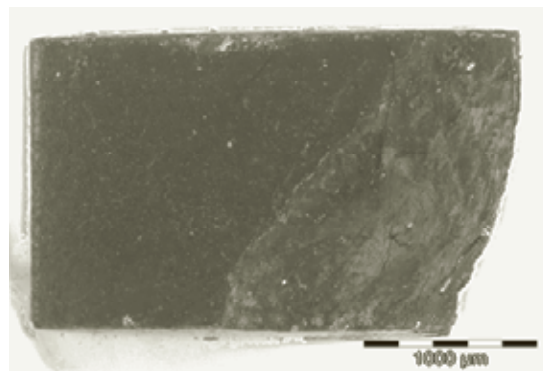


Fig. 3 Titanium beryllide specimen after compression test at 923 K

4. Study of microstructure of titanium beryllide specimens irradiated at 740 and 873 K

4.1. Investigations by high-resolution TEM

In both cases, after irradiation at 740 and 840 K, the formation of radiation-induced bubbles of radiogenic

gases was found. Fig. 4 shows high-resolution TEM image of the particle from irradiated at 740 K titanium beryllide sample. Observed bubbles are homogeneously distributed throughout the investigated material volume and have the average sizes of 1-2 nm.

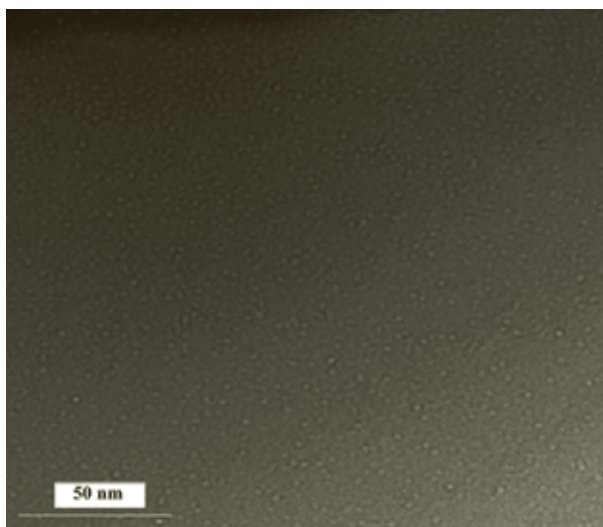


Fig. 4 High-resolution TEM image of the particles from titanium beryllide sample irradiated at 740 K

The sizes of gas bubbles increase along with the temperature grow. It was estimated that the sizes of bubbles were around 15-20 nm after neutron irradiation at 873 K (Fig. 5). Some bubbles have regular geometric shapes (e.g., triangular, hexagonal) what could be an evidence that the preferred bubble growth occurs along certain crystallographic planes.

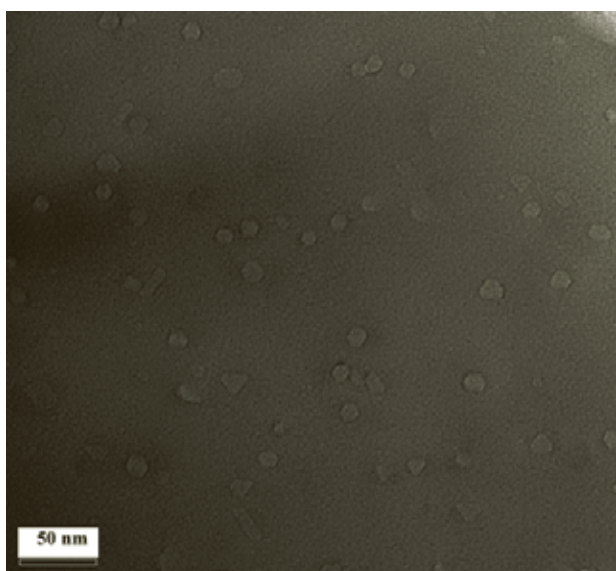


Fig. 5 High-resolution TEM image of titanium beryllide irradiated at 873 K

4.2 Evaluation of swelling using TEM images

High-resolution TEM images were used for the evaluation of neutron-irradiated titanium beryllide samples. One has to emphasize that, in this case, the value of "local" swelling was estimated. This means that the swelling inside the irradiated material has been measured and the volume change which occurred due to an oxidation of near-to-surface layers was not taken into account. On the other hand, the small values of masses of the investigated samples (approx. 30 mg) do not allow the use of the common method for the determination of material density based on the immersion into a liquid media.

Firstly, rectangular cross sections were selected on the TEM images and the number of bubbles N_b located inside these plots was counted. Then, conditionally, was adopted that the bubbles have spherical shapes and their diameters (or the equivalent sizes) were measured knowing the scales on TEM images. Then, the total volume V_b occupied by gas bubbles was evaluated using expression:

$$V_b = \frac{4}{3} \pi \sum_i \left(\frac{d_i}{2}\right)^3 N_i, \quad (1)$$

where d_i – are diameters of bubbles which fit to an interval $d_i \pm \Delta d_i$, N_i – number of bubbles having diameters which correspond to d_i .

High-resolution TEM images were obtained using electrons with energy equaled to 200 keV. The penetration depth of electrons with such energy into titanium beryllide of Be_{12}Ti type is about 220 nm [4]. Therefore, knowing the cross section area on the TEM images and penetration depth of electrons into samples, one can calculate the investigated specimen volume V_s .

Thus, swelling $\frac{\Delta V}{V_0}$ (in %) of neutron-irradiated samples was estimated by expression:

$$\frac{\Delta V}{V_0} = \frac{V_b}{V_s} \times 100. \quad (2)$$

Estimated values of swelling of titanium beryllides irradiated at 740 and 873 K were 0,08 and 0,28%, accordingly.

It was shown in other HIDOBE-dedicated works [2,5] that the values of swelling of neutron-irradiated beryllium pebbles are much higher. In particular, S. van Til et al. reported that the density decrease of beryllium pebbles irradiated at 873 K is around 5%.

5. Discussion and conclusions

Extreme brittleness of titanium beryllide Be_{12}Ti is determined by a factor that the sliding planes in tetragonal lattice of this compound appear only at high strength values. Thus, comparing to hexagonal beryllium

or titanium, the process of plastic deformation of beryllides is sufficiently impeded [6].

Up to now, only one experimental work on neutron irradiation of Be₁₂Ti samples is known from the opened literature sources [7]. Short-term irradiation campaign was performed at Japan Material Testing Reactor (JMTR) in the temperature range of 603-773 K with the neutron fluence of 4×10^{24} n/m². The authors investigated the influence of neutron irradiation on beryllium and Be₁₂Ti specimens. It was indicated that Be₁₂Ti samples have lower swelling (not exceeding 1%) and better release properties of radiogenic gases comparing to pure beryllium. It should be noted that the measured swelling of un-alloyed beryllium samples was around 3%.

The main contribution to the volume change of beryllium-based materials under neutron irradiation makes radiogenic helium ⁴He. One can assume that the formation of gas bubbles in titanium beryllide is impeded compared to un-alloyed beryllium due to a smaller ability of tetragonal lattice of Be₁₂Ti to a deformation under internal stresses which originate during the accumulation of bubbles. The appearance of the point defects (interstitials) leads to a formation of microstresses which are directed towards the volume increase of the elementary cell and, accordingly, of the whole sample volume. The volume change of the irradiated sample is possible due to a deformation of lattice which is, in the case of complex structure of intermetallic compounds, is very difficult. At a certain stage the values of stresses in the crystal lattice of titanium beryllide are too high in order to be compensated by a lattice deformation which is, in turn, accompanied by the bubble growth. The relaxation of stresses runs easier in less brittle beryllium what leads to more intense formation of gas bubbles and, accordingly, higher swelling.

Also, lower swelling of titanium beryllide was measured by Y. Mishima et al. [8] by implantation of helium ions with energy of 50 keV into pure beryllium and Be₁₂Ti specimens at temperatures up to 973 K. In parallel, V. Chakin et al. [9] reported about lower tritium retention properties of Be₁₂Ti specimens saturated with H₂ – 500 appm T₂ gas mixture with the respect to commercially available beryllium grades. Thus, one can suggest that titanium beryllide Be₁₂Ti show lower swelling as well as lower gas retention properties when compared to pure beryllium.

Both, titanium beryllide samples in unirradiated state and after irradiation at 740 K, showed very similar parameters of a brittle failure at uniaxial compression tests using constant loading at 923 K. These experimental results allow to conclude that the high-dose neutron irradiation at 740 K did not lead to a further degradation of mechanical properties of beryllide samples which consist, mainly, of Be₁₂Ti phase.

References

- [1] P. Kurinskiy, A. Moeslang, M. Klimiankou, A.A. Goraieb, J. of Nucl. Mat. **367-370** (2007) 1069-1072.
- [2] V. Chakin, R. Rolli, A. Moeslang, P. Vladimirov, P. Kurinskiy, H.-C. Schneider, M. Kolb, S. van Til, L. Magielsen, M. Zmitko, J. of Nucl. Mat., accepted for publishing, 2012.
- [3] Report NRG-20296/09.96239/P, issued in Sept. 2009.
- [4] T. Malis, S.C. Cheng, R.F. Egerton, Journal of Electron Microscopy Technique, Vol. 8, 1988, 193-200.
- [5] S. van Til, J.B.J. Hegeman, H.L. Cobussen, M.P. Stijkel, Fusion Eng. and Design **86** (2011) 2258-2261.
- [6] G.V. Raynor, Beryllium-rich intermediate phases in beryllium alloys, J. of Less-Common Metals **37(2)** (1974) 247-255.
- [7] M. Uchida, E. Ishitsuka, H. Kawamura, J. of Nucl. Mat., **307-311** (2002) 653-656.
- [8] Y. Mishima et al., Fusion Eng. and Design **82** (2007) 91-97.
- [9] V. Chakin, M. Klimenkov, R. Rolli, P. Kurinskiy, A. Moeslang, C. Dorn, J. of Nucl. Mat., **417** (2011) 769-774.

Proceeding of 10th Beryllium Workshop

Optimization of sintering conditions in Plasma sintered beryllide

Jae-Hwan Kim, Daisuke Wakai and Masaru Nakamichi

*Fusion Research and Development Directorate, Japan Atomic Energy Agency,
2-166, Omotedate, Obuchi, Rokkasho, Kamikita, Aomori, 039-3212, Japan*

Abstract

Beryllides are well-known as advanced neutron multipliers in demonstration power reactor. Many studies on their fabrication have been carried out including conventional methods, arc melting method and hot isostatic pressing method which was not so successful for fabrication of either rod type or pebble type.

In this study, the effect of sintering time on synthesis of beryllides fabricated by plasma sintering was investigated. Most conditions of sintering were fixed such as sintering pressure to 50 MPa, sintering temperature to 1278 K, heating rate to 100 K/min, cooling rate to 200 K /min and surface activation treatment time to 30 seconds and mixture ratio to Be-7.7at%Ti except for sintering time which were 5 min, 10 min, 30 min, 60 min and 90 min.

From the viewpoint of sinterability, it showed the better property because regardless to the sintering times, Be and Ti powders were sintered to more than 98% of their theoretical density value which is higher than that of specimen fabricated by the conventional method. As results of x-ray diffraction and electron probe micro analyzer measurements, the formation of beryllides such as Be₁₂Ti, Be₁₇Ti₂, and Be₂Ti intermetallics was identified at 1278 K for sintering times from 5 min to 90 min. It was obviously confirmed that with increasing time, the area fraction of Be₁₂Ti, which is the compositional target for neutron multipliers, was increased about 96 % whereas the area fraction of beryllium and Be₂Ti decreased.

1. Introduction

Beryllide has been paid attention as a promising candidate of advanced neutron multipliers for DEMO reactor. However, owing to its brittleness, it is considerably difficult to fabricate not only pebble type of beryllide which will be loaded into blanket but rod type of that which is fabricated prior to application of rotating electrode method (REM). Application for some conventional methods such as arc melting method and hot isostatic press method for the rod type of beryllide was not so successful since some problems, complicated process, time-consuming, difficulty on controlling composition as well as eliminating impurities and so on, were anticipated. Therefore, we suggested the plasma sintering method for fabrication of beryllide, expecting that advantages being well-known in general would be applicable to this material. In this study, several sintering conditions, will be introduced in order to investigate the effect of sintering conditions on sinterability of plasma sintered beryllide.

2. Experiments

The specimens used in this study, were prepared by plasma sintering method. For confirmation of the effect of sintering time and temperature, we varied the sintering time and temperature as other conditions were fixed. The synthesis of specimens started with mixed elemental powder particles of beryllium (>99.0%) from Rare Metallic Co. Ltd. and titanium (>99.0%) from Kojundo Chemical Laboratory Co. Ltd. The powders were mixed for 60 min using a RM200 (Retsch, Germany). The mixed powder composition was 92.3 at.% Be and 7.7 at.% Ti. The starting powder was loaded into a graphite punch and die unit and uniaxial pressure was applied for cold compaction. A pulse current is applied to create the plasma environment and thus activate the particle surfaces. The powder compact is resistance-heated while uniaxial pressure is applied to the material in the sintering mold.

The sintering temperatures used in the experiment, was 1273 K, while sintering times were different: 5, 10, 30, 60, and 90 minutes; with heating and cooling rates of 100 and 200 K/min, respectively. For investigation of investigate the sinterability of beryllides, the specimens were cut to $2.7 \times 2.7 \times 4.0 \text{ mm}^3$ and then the density was measured (AccupycII 1340-1CC, Shimadzu, Japan). The measured value was compared with a theoretical one, which was calculated from analytical results of area fractions for each phase. For qualitative analyses of beryllides, back-scattered electron scanning electron microscopic images were obtained using EPMA (JXA-8530F, JEOL, Japan). Additionally, XRD measurements were conducted with scan speeds of 0.01° from 10° to 100° for confirmation of compositional variation of beryllides. To observe the grain size of beryllide, chemical etching was carried out and optical observation was conducted by laser microscopy (VK 9700, KEYENCE)

3. Results and Discussions

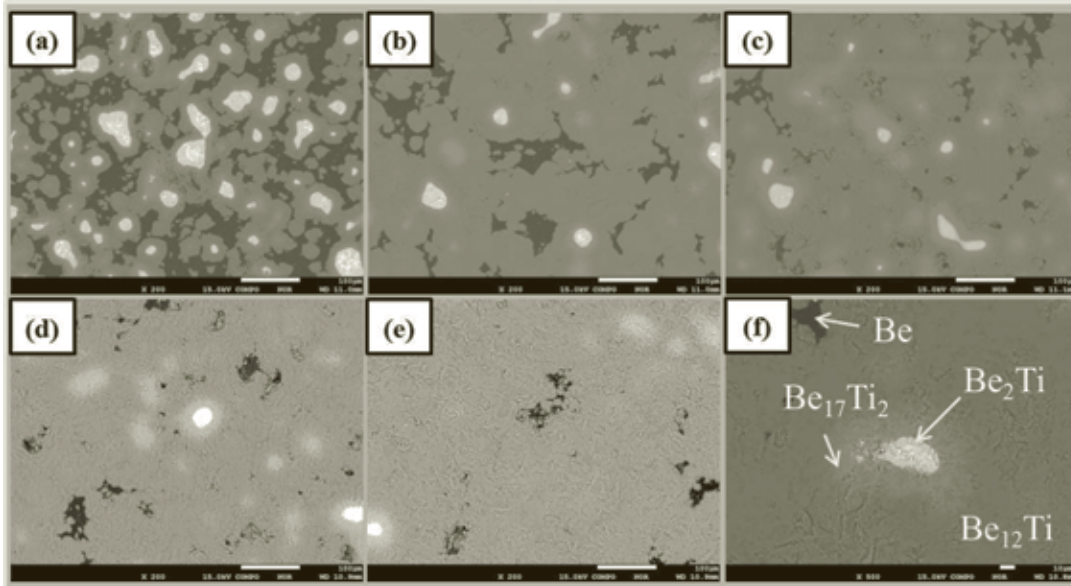


Fig.1 BSE-SEM observation of specimens sintered for (a) 5 min, (b) 10 min, (c) 30 min, (d) 60 min, (e) 90 min and (f) high magnification (x500) of (d), showing qualitative analysis results.

Fig.1 shows the scanning electron microstructure of specimens plasma-sintered for several different times. Since this image is observed using the back scattered electron, different contrast indicates different composition. Therefore, it is obvious that there exist four phases, which are black, gray, light gray and white areas. From the analysis of EPMA, black area was identified to beryllium, gray to Be_{12}Ti phase, light gray to $\text{Be}_{17}\text{Ti}_2$ phase and white to Be_2Ti phase as shown in fig.1 (f). It could be confirmed how each phase transformed to according to sintering time. It was clearly confirmed that beryllium and Be_2Ti phase decreased whereas Be_{12}Ti phase which is stable composition, based on stoichiometry, increased with increase of the time.

In order to investigate the area fraction of each phase in detail, evaluation of area fractions was conducted as shown in fig.2. Area fraction of Be_{12}Ti phase which is targeting composition for specimen sintered for 5 min. was approximately 60 %. However, with increasing the sintering time, the fractions increased to 81%, 84%, 91% and 96%. For beryllium, it was varied to 22%, 7%, 5%, 1% and 0.1%. It means that it can be applicable to fabricate beryllide with different compositions which may lead to improve ductility as adding beryllium into substrate.

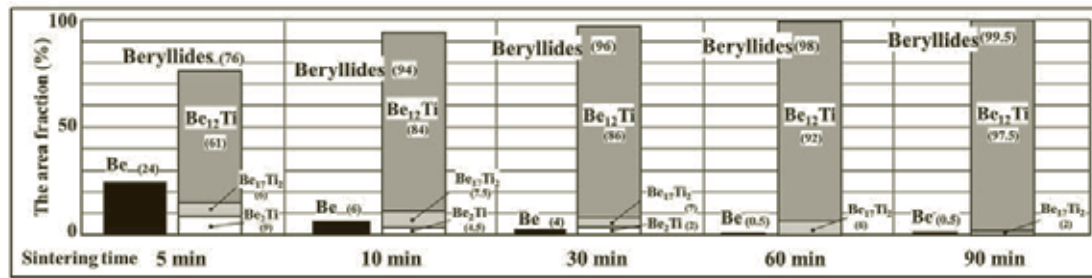


Fig.2 Sintering time dependence at 1273 K on area fraction of each phase

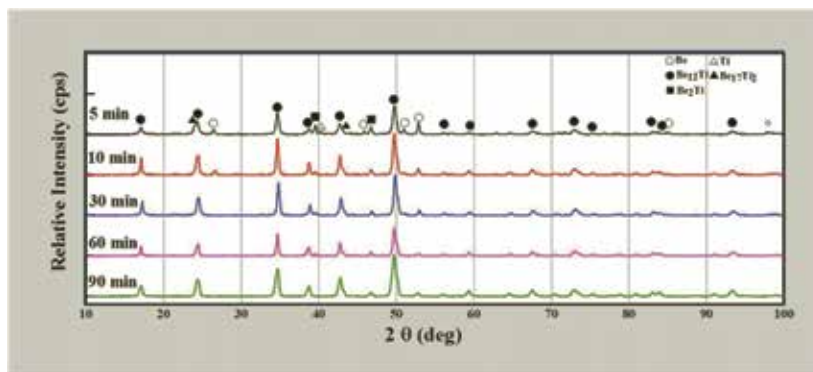


Fig.3 X-ray diffraction analysis of each specimen

XRD profile results are given in Fig. 3. Peaks corresponding to beryllium and beryllides such as Be_{12}Ti , $\text{Be}_{17}\text{Ti}_2$, and Be_2Ti were identified under every sintering time. With increasing sintering time, the beryllium and Be_2Ti peaks decreased while those of Be_{12}Ti increased. This suggests that the sintering of beryllides is enhanced by increasing sintering time. This is in good accord with results on the SEM observation. Nakamichi [1] et al. have reported the effect of sintering temperature on the sinterability, demonstrating that the elemental content of Be and Ti in the plasma sintered material decreased by consolidation enhancement with increasing sintering temperature.

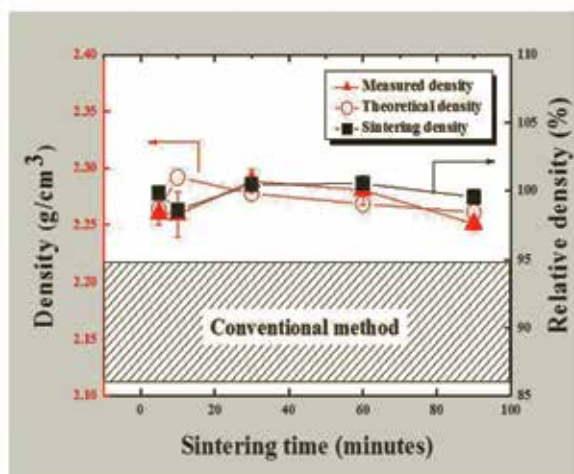


Fig.4 Variation of density according to sintering times

In order to evaluate the sinterability for specimens fabricated by this method, the results for theoretical, measured, and sintering densities with different sintering times for the fabricated beryllides was given in Fig. 4. The mixture of Be and Ti powders (69.3 wt.% Be and 30.7 wt.% Ti) was sintered to more than 98% of the theoretical value. This result clarifies that the value is higher than those for specimens synthesized by arc melting method. In this study, it was clearly confirmed that fabrication by the plasma sintering method resulted in significantly high sinterability. However, sintering time dependency of sintering density could not be observed.

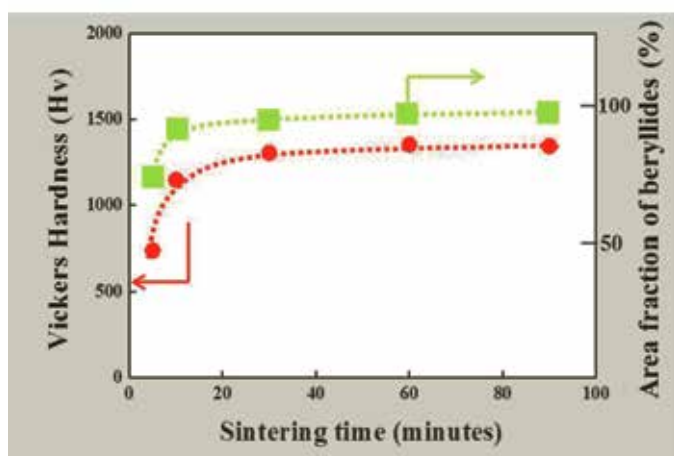


Fig.5 Dependence of sintering time on hardness and area fraction of beryllides.

Fig.5 shows the dependence of sintering time on hardness and area fraction beryllides. With increase of the sintering time, the microvickers hardness increased. Due to increase of beryllides, the

hardness indicated a similar tendency. Accordingly, it is obvious that there is close correlation between the beryllides and hardness.

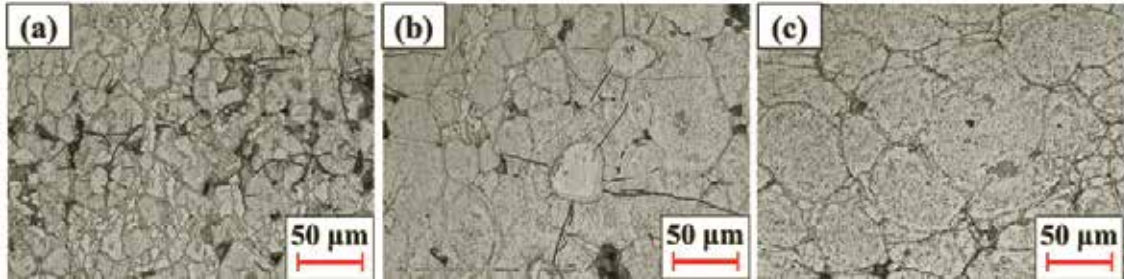


Fig. 6 Grain size of beryllides sintered for (a) 5 min, (b) 30 min, and (c) 90 min

In general, it is well-known that for sintering process, with increase of sintering time, the grain size increases. In the present study, we investigated the grain size of each beryllide with different sintering time. In case of beryllide sintered for 5 min, the grain size was considerably small. However, increase of the sintering time led to increase of the grain size while the grain size grows up to 47 μm as shown in fig. 7. Further studies on the grain size effect are ongoing.

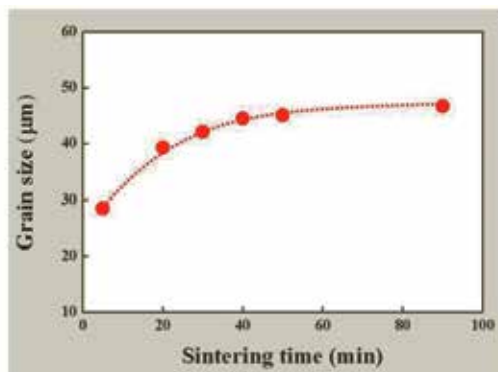


Fig.7 Relationship between the sintering time and grain size.

Conclusions

We investigate the optimization of sintering conditions in plasma sintered beryllide. SEM images and EPMA results clarified that the plasma sintered beryllide was composed of four phases, Be, Be_{12}Ti , $\text{Be}_{17}\text{Ti}_2$, and Be_2Ti . With increase of the sintering time, Be and Be_2Ti phase decreased whereas Be_{12}Ti phase which is stable composition, based on stoichiometry, increased. All beryllides indicated the high sinterability with relative density of over 98 %. For hardness of beryllide, with increasing the sintering time, the hardness increased. This may be attributed by increase of total beryllides which have higher hardness than pure Be. Finally, grain size images of beryllide clearly proved that it was increased with the increase of sintering time. Further studies on the grain size are ongoing.

References

- [1] M. Nakamichi et al. *Journal of Nuclear Materials*, Vol. 417, Iss. 1-3 (2011) 765-768

Study on Oxidation Resistance of Titanium Beryllide Fabricated by Spark Plasma Sintering and Surface Analysis of the Sample Exposed to Water Vapor

Kenzo MUNAKATA¹⁾, Kohei WADA¹⁾, Yusuke AKIMOTO¹⁾, Haruki TAKEDA¹⁾, Masaru NAKAMICHI²⁾, Jae-Hwan KIM²⁾, Daisuke WAKAI²⁾ and Kazuo YONEHARA²⁾

¹⁾*Faculty of engineering and resource science, Akita university, 1-1, Tegatagakuen-cho, Akita, 010-8502, Japan*

²⁾*Fusion Research and Development Directorate, Japan Atomic Energy Agency, 2-166, Omotedate, Obuchi, Rokkasho, Kamikita, Aomori, 039-3212, Japan*

Abstract

The neutron multiplier is indispensable for generation of tritium that is a fuel of fusion reactors. Metallic beryllium is considered as a candidate for the neutron multiplier. Titanium beryllide is an alternative of metallic beryllium as the neutron multiplier of the fusion reactor blanket. The authors examined oxidation resistance of the titanium beryllide sample fabricated by the spark plasma sintering method. Be and Ti powders with grain diameter less than 45 μm were mixed with the mortar for 30 min. The mixed ratio was adjusted to the composition of titanium beryllide (69.3:30.7 wt%). Then, the mixture was sintered with a plasma electrical discharge sintering device.

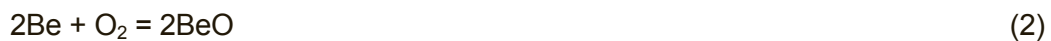
The titanium beryllide samples prepared were placed in a reactor made of quartz. A $\text{H}_2\text{O}/\text{Ar}$ (10,000 ppm) gas was introduced to the reactor with the flow rate of 300 cm^3/min . Experimental temperature of test tube was raised up to 1273 K by the constant rate of 5 K/min using an electric furnace. The reactor temperature was held at 1273 K until it was introduced to the reactor with the flow rate of 300 cm^3/min . The concentrations of hydrogen in the outlet streams of the reactor were measured with a gas chromatograph. The state of oxidized sample surface was characterized by means of the X-ray diffraction analysis (using Ultima IV manufactured by RIGAKU Co. LTD.) and electron probe micro analyzer (using JXA-8230 manufactured by JEOL Co. LTD.). Two samples were used in the experiments to examine reproducibility of oxidation behavior.

The experimental results indicate that hydrogen generation on the surface of the samples is very modest, whereas small difference in the amounts of hydrogen generated from the samples was observed. Comparison of X-ray diffraction patterns taken for the titanium beryllide sample before and after exposure to the Ar gas containing 10,000 ppm of water vapor suggests that diffraction peaks related to BeO arose after on the sample surface after exposure to water vapor. Observations with electron probe micro analyzer (EPMA) before and after

exposure to the Ar gas containing 10,000 ppm of water vapor suggest that the microstructure of the surface consists of four-phase grains before exposure to water vapor while it consists of three-phase grains after exposure to water vapor. After exposure to water vapor, phases attributed to BeO, TiO₂ or complex oxide were observed, whereas diffraction peaks related to Ti or TiO₂ were not observed in the X-ray diffraction analysis

1. Introduction

Metallic beryllium is regarded as a candidate material of neutron multiplier used for increase of the tritium breeding ratio in the tritium breeding blanket of D-T fusion reactors. In the blanket, metallic beryllium could be placed in the high temperature environment, but the material is known to have high reactivity with oxygen and water vapor at high temperature to produce H₂ gas and BeO by following reaction;



H₂ gas is explosive, and BeO is harmful for human body. These are the major drawbacks of metallic beryllium, which poses a threat to the safety of fusion power plants, particularly in the case of water vapor was injected into multiplier layer by breaking of a coolant pipe. Therefore, it is necessary to develop more chemically stable neutron multiplier than metallic beryllium. Titanium beryllides such as Be₁₂Ti is known to have advantages over metallic beryllium in terms of higher melting point, lower swelling, high chemical stability and so forth [1]. Be₁₂Ti had been fabricated by various methods. Japan Atomic Energy Agency (JAEA) has fabricated Be₁₂Ti by a new fabrication method “Spark plasma sintering”. This method is like a combination of direct current pulse generator and hot press [2,3]. In this study, the authors examined oxidation resistance of the Be₁₂Ti sample fabricated by the spark plasma sintering.

2. Experimental

Be and Ti powders with average grain diameter 27 μm and 28μm respectively were mixed with the specify the device such as ball-mill for 30 min. The mixed ratio was adjusted to the stoichiometric composition of Be₁₂Ti (69.3:30.7 wt%). Then, the mixture was sintered with plasma electrical discharge sintering device KE-Pass III(manufactured by KAKEN Co., Ltd). Temperature ramp in heating was 373 K/min, and sintering temperature was 1273 K. The mixture was sintered at the temperature for 40 min, and the pressure was held at 50 MPa during its sintering. The Be₁₂Ti sample was cut into 2 cm diameter and 5 mm thick. Then, the sample disk was cut into dimension of 3×3×5 mm, which was polished up with #800 SiC

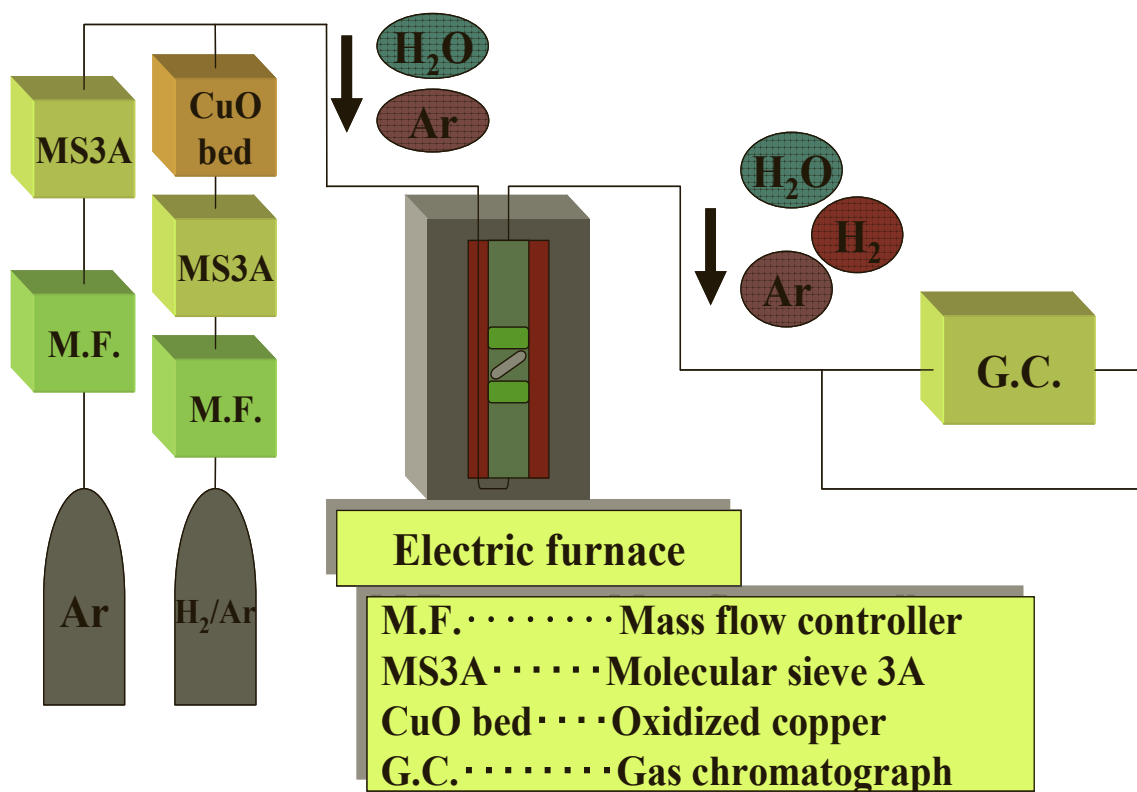


Fig. 1 Experimental apparatus for hydrogen generation.

abrasive paper.

Figure 1 shows the schematic flow diagram of the test apparatus used in the experiment. The Be_{12}Ti sample was wrapped by platinum mesh to avoid direct contact with the test tube, and then it placed between silica wool. Ar gas containing 10,000 ppm of water vapor was generated by passing Ar gas with 10,000 ppm of H_2 gas a copper oxide bed held at 623 K, and then it was introduced to the test tube with the flow rate of $300 \text{ cm}^3/\text{min}$. Experimental temperature of test tube was raised up to 1273 K by the constant rate of 5 K/min using a electric furnace. The test temperature was kept at 1273 K until hydrogen generation terminated.

The concentrations of hydrogen in the outlet streams of the reactor were measured with a gas chromatograph (GC-8A) manufactured by SHIMADZU Co. The state of oxidized sample surface was characterized by means of the X-ray diffraction analysis (using Ultima IV manufactured by RIGAKU Co. LTD.) and electron probe micro analyzer (using JXA-8230 manufactured by JEOL Co. LTD.). In this study, we carried out the same experiment two times in order to examine the reproducibility of the experimental result.

The authors carried out the experiment using a pure beryllium sample [4]. The weight gain and concentrations of hydrogen in the outlet streams of the reactor were measured with thermogravimetry-diferential thermal analysis and mass spectrometry instilment manufactured

by RIGAKU Co. LTD. The pure beryllium sample was placed under the Ar gas containing 10,000 ppm of water vapor. The flow rate of the Ar gas containing 10,000 ppm of water vapor was 300 cm³/min. The temperature of the samples was raised from 313 K up to 1273 K with the constant rate of 5 K/min. After the experimental temperature reached 1273 K, the temperature was held at 1273 K for 24 h. The amount of hydrogen generated from each 1 cm² of the surface of the pure beryllium sample was 2.78×10⁻³ mol.

3. Result and discussion

3.1 Exposure to water vapor at high temperatures

Figures 2 (a) and (b) show change in hydrogen concentration in the outlet stream of the reactor after the 10,000 ppm H₂O/Ar was introduced in the reactor. In the first experiment, the generation of hydrogen was observed when the reactor temperature reached about 673 K. Oxidation reaction continued for about 27 hours. Amount of hydrogen generation from the surface was 1.28 ×10⁻⁴ mol/cm², while that for 24 hours was 1.20 ×10⁻⁴ mol/cm². In the second experiment, the generation of hydrogen was observed above 423 K. Oxidation reaction continued for about 37 hours. The total amount of hydrogen generation was 3.30×10⁻⁴ mol/cm², while that for 24 hours was 3.00 ×10⁻⁴ mol/cm². The amount of hydrogen generation in the first experiment is smaller than that generated in the second experiment. It is thought that this discrepancy is caused by inhomogeneity of Be₁₂Ti sample. The manufacturing process is still under development. As far as the experimental period of 24 hours, there was one order of magnitude difference in the amounts of hydrogen generation between the pure beryllium sample and the Be₁₂Ti sample.

3.2 Surface analysis by XRD

Figures 3 (a) and (b) show the X-ray diffraction patterns of the pure beryllium sample before and after exposure to the Ar gas containing 10,000 ppm of water vapor, respectively. In fig. 3 (b), several diffraction peaks arose, and most of them were attributed to the peak of BeO. Figure 3 (c) shows the X-ray diffraction patterns of the Be₁₂Ti sample before exposure to the Ar gas containing 10,000 ppm of water vapor. For this sample, most of diffraction peaks were attributed to Be₁₂Ti (marked with closed square). Figures 3 (d) and (e) show the X-ray diffraction patterns of the Be₁₂Ti sample after exposure to the Ar gas containing 10,000 ppm of water vapor in the first and the second experiments, respectively. In these cases, diffraction peaks related to BeO were observed on the sample surface. These results also indicate that the diffraction peaks related to BeO possesses different intensity in figs. 3 (d) and (e). However, diffraction peaks related to Ti or TiO₂ were not observed.

3.3 Surface analysis by EPMA

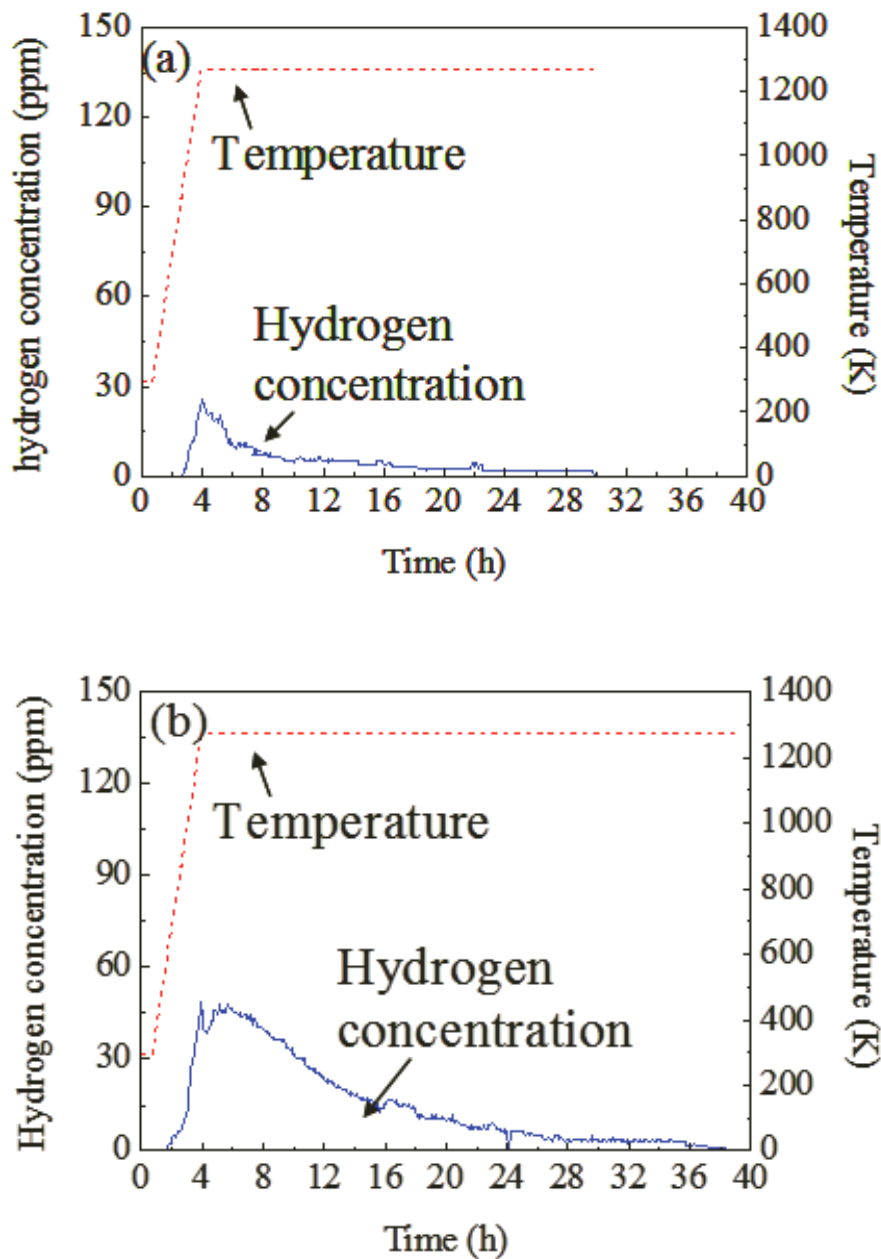


Fig. 2 Change of hydrogen concentration in the outlet stream of the reactor after exposure to gas flow of Ar with 10,000ppm of H₂O for Be₁₂Ti samples (a) and (b)

Figures 4 (a) and (b) show the results of surface analysis of the pure beryllium sample electron microprobe analyzer (EPMA) before and after experiments respectively. On these EPMA images, whiter points correspond to elements with larger atomic weight. As seen in Fig. 4 (b), BeO was generated on the surface of the Be₁₂Ti sample (Be, O : 28.88, 63.60 at%), and many cracks were observed. Figure 4 (c) shows the results of surface analysis of the samples with EPMA before exposure to the Ar gas containing 10,000 ppm of water vapor. Figures 4 (d) and (e) show the results of surface analysis of the samples with EPMA after exposure to the Ar

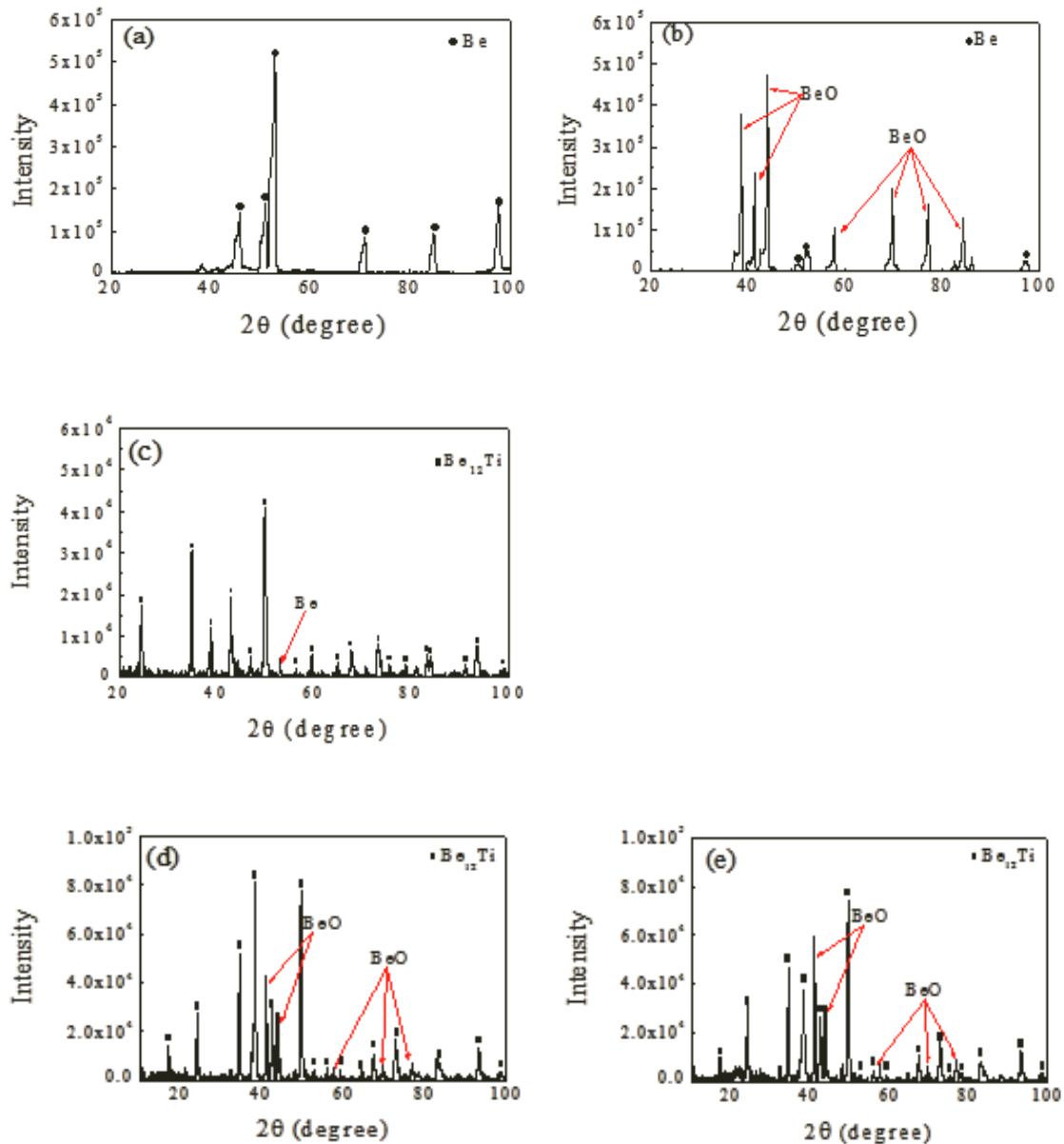


Fig. 3 X-ray diffraction pattern of; pure beryllium (a) before experiment, (b) after experiment, the Be_{12}Ti sample (c) before experiment, (d) after the first experiment and (e) after the second experiment.

gas containing 10,000 ppm of water vapor. Four different contrasts were observed. In fig. 4 (c), black areas were identified as Be, dark gray areas as Be_{12}Ti , gray areas as $\text{Be}_{17}\text{Ti}_2$ and white areas as Ti in the Be_{12}Ti sample. Three different contrast were observed in Fig. 4 (d). As seen in this figure, BeO was generated on the surface of the Be_{12}Ti sample. Furthermore, white (Be, Ti, O : 65.87, 4.44, 29.69 at%) and gray areas (Be, Ti, O : 80.21, 16.24, 3.54 at%) were identified as compounds such as TiO_2 or complex oxide. As seen in Fig. 4 (e), BeO was generated on the surface of the Be_{12}Ti sample, and the white area (Be, Ti, O : 14.28, 21.90, 63.82 at%) was identified compounds such as TiO_2 or complex oxide, as well. Moreover, some cracks were observed on the surface of the Be_{12}Ti samples. However, as mentioned above

diffraction peaks related to Ti or TiO_2 were not observed in X-ray diffraction analysis. Pictures shown in figs. 4 (c), (d) and (e) indicate that areas containing titanium were quite small, and thus X-ray diffraction analysis may not be able to detect diffraction peak of TiO_2 . Further investigation as to how titanium affects oxidation behavior is necessary.

Comparison of the results shown above with the previous result [4] indicates that the

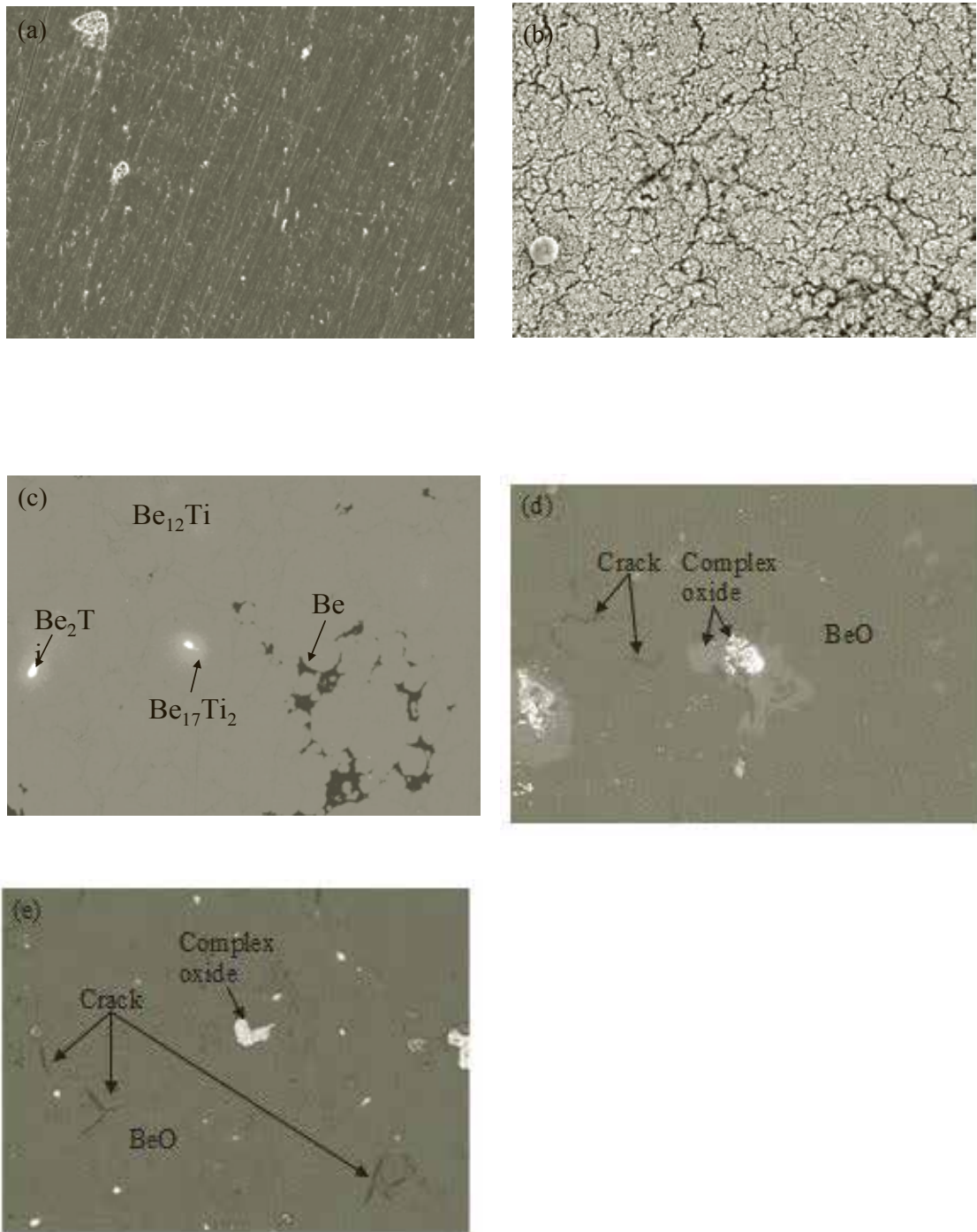


Fig. 4 Electron probe micro analyzer image of (a) pure beryllium before experiment, (b) after experiment, (c) the Be_{12}Ti sample before experiment, (d) after the first experiment and (e) after the second experiment.

Be₁₂Ti sample fabricated by spark plasma sintering possesses demonstrated high oxidation resistance.

4. Conclusion

To examine oxidation resistance of Be₁₂Ti sample fabricated by the spark plasma sintering method at high temperature, the Be₁₂Ti sample were exposed to Ar gas with 10,000 ppm H₂O at 1273 K. After the experiment, the surface of the samples was observed by means of X-ray diffraction analysis and EPMA. As a result, it was found that Be₁₂Ti sample has higher oxidation resistance to water vapor at the high temperature compared with pure beryllium.

5. Acknowledgment

This work was supported by Japan Atomic Energy Agency under the Joint Work contract 23K131, as a part of Border Approach activities.

6. References

- [1] H. Kawamura et al., Fusion Eng. Des. **61-62**, 391-397 (2002).
- [2] M. Nakamichi et al., Fusion Eng. Des. **86**, 2262-2264 (2011).
- [3] M. Nakamichi et al., J. Nucl. Mater. **417**, 765-768 (2011).
- [4] K. Wada et al., J. Nucl. Mater. (presented in ICFRM-15 and under review)

Oxidation Behavior of Beryllium and Titanium Beryllide Fabricated by Plasma-sintering Method – Direct Comparison of Oxidation Behavior by Water Vapor

K. Munakata¹, K. Wada^{1*}, M. Nakamichi², J.H Kim², K. Yonehara², D. Wakai²

¹*Faculty of engineering and resource science, Akita University,*

1-1, TegataGakuen, Akita, 010-8502, Japan

²*Fusion Research and Development Directorate, Japan Atomic Energy Agency,*

2-166, Omotedate, Obuchi, Rokkasho, Kamikita, Aomori, 039-3212, Japan

Abstract

Titanium beryllides such as Be₁₂Ti are alternatives to beryllium as the neutron multiplier of the fusion reactor blanket. Be₁₂Ti is known to have advantages over metallic beryllium in terms of high melting point, lower swelling, higher chemical stability and so forth. This time, the authors examined oxidation behavior of Be₁₂Ti sample fabricated by a plasma-sintering method. The oxidation behavior of a pure beryllium sample was also investigated using the same experimental apparatus for direct comparison of their oxidation behavior by water vapor. In the experiments, the pure beryllium sample and the plasma sintered Be₁₂Ti sample were placed under a flow of an Ar gas containing 10,000 ppm (1%) of water vapor. The temperature of the samples was raised from 313 K up to 1273 K with the ramp rate of 5 K/min.

An experimental result indicates that the weight of the pure beryllium sample drastically increased, which continued for 24 h. On the other hand, the mass gain of the Be₁₂Ti sample observed in the same experiment was very slow. The final mass gain of the pure beryllium sample was 21.75 mg, which corresponds to approximately 50 % of the initial weight of the pure beryllium sample (44.63 mg), while the final mass gain of the plasma sintered Be₁₂Ti sample was 1.10 mg, which corresponds to approximately 1.7 % of the initial weight of the

plasma sintered Be₁₂Ti sample (64.18 mg). Thus, the mass gain of the pure beryllium sample was by far greater than that of the plasma sintered Be₁₂Ti sample. The experimental results suggest that the Be₁₂Ti sample possesses considerably higher oxidation resistance to water vapor compared with the pure beryllium sample.

1. Introduction

Development of the neutron multiplier of the blanket modules is necessary for generating tritium that is the fuel of fusion reactor. Metallic beryllium has been considered as the neutron multiplier of the fusion reactor blanket. However, metallic beryllium is highly reactive with water vapor and oxygen at high temperatures, which produces H₂ gas and BeO via the following reaction:



H₂ is highly explosive, and BeO is harmful to human body. This is one of the major drawbacks of metallic beryllium, which poses a threat to safe operation of the fusion reactor particularly in the case of loss-of-coolant accident (LOCA) in which a coolant line break injects water vapor into the blanket. Therefore, development of new neutron multipliers, which is more chemically stable than metallic beryllium, is necessary. Titanium beryllide is known to possess more attractive chemical properties such as high melting point, lower swelling and more chemically stable compared with metallic beryllium [1]. Be₁₂Ti had been fabricated by various methods. Japan Atomic Energy Agency (JAEA), and JAEA has developed a new fabrication method "Plasma-sintering method". This method is alike of combination of a hot press and a plasma generator. This new method has advantages over the past fabrication process in terms of low fabrication cost and short fabrication period [2,3]. Thus, the authors investigated the reactivity of Be₁₂Ti sample fabricated by the plasma-sintering method (the new process) with water vapor.

2. Experimental

The plasma sintered Be₁₂Ti sample and the pure beryllium sample were cut into 2 cm diameter and 5 mm thick. Then, the sample disk was cut into dimension of 3×3×5 mm, which was polished up with abrasives.

Fig. 1 show the experimental apparatus used in the experiment. The pure beryllium sample or the plasma sintered Be₁₂Ti sample was placed under a flow of an Ar gas containing 10,000 ppm (1%) of water vapor. The temperature of the samples was raised from 313 K up to 1273 K with the ramp rate of 5 K/min. After the experimental temperature reached 1273 K, the temperature was held at 1273 K for 24 h. An Ar gas containing 10,000 ppm of water vapor was introduced to the reactor at the flow rate of 300 cm³/min. The mass gain curve and the concentration of hydrogen generated from the samples in the outlet stream of the reactor were measured with thermogravimetry-differential thermal analysis and mass spectrometry instrument manufactured by RIGAKU Co. LTD., respectively. The state of oxidized sample surface after their exposure to water vapor was characterized by means of the X-ray diffraction analysis using Ultima IV manufactured by RIGAKU Co. LTD.

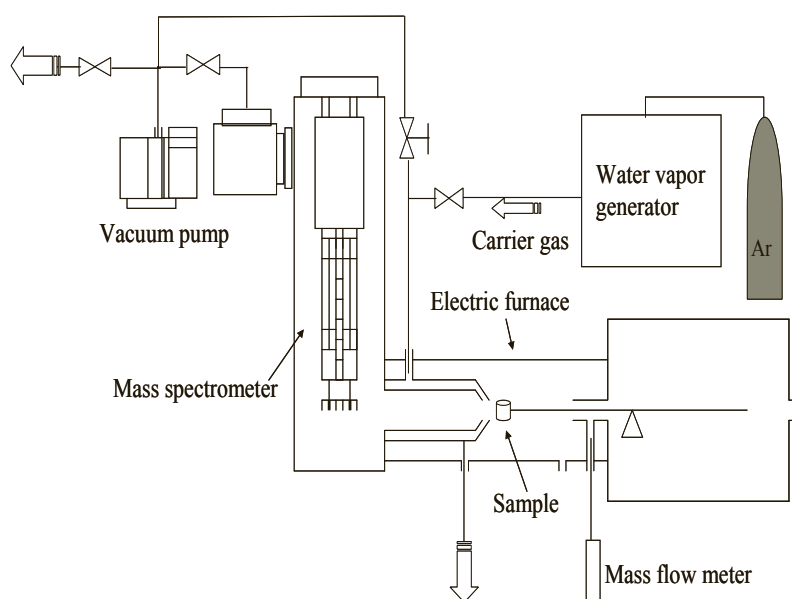


Fig.1 Experimental apparatus

3. Results and discussion

Figs. 2 (a) and (b) show mass gain curves and changes in concentration of hydrogen in the outlet stream of the reactor charged with the beryllium sample and the plasma-sintered Be₁₂Ti samples, respectively. The horizontal and right vertical axes represent duration time and test temperature, respectively. The first left vertical axis and the second left vertical axis represent the concentration of hydrogen generated from the surface of the samples and the mass gain of the samples, respectively. The chained line shows the mass gain of the samples, and the broken line shows the test temperature, respectively. In the case of pure beryllium, it is known that a catastrophic oxidation reaction takes place under the conditions of high temperature and high water vapor pressure [4]. As previous works suggests, the weight of the *pure beryllium sample drastically increased in the experiment, which continued for 24 h.* The result of the previous studies by Aylmore et al. [5] indicates that the catastrophic oxidation reaction takes place at temperatures higher than 973 K. On the other hand, the mass gain of the Be₁₂Ti sample was very slow. The final mass gain of the pure beryllium sample was 21.75 mg, which corresponds to approximately 50 % of the initial weight of the pure beryllium sample (44.63 mg), while the final mass gain of the plasma sintered Be₁₂Ti sample was 1.10 mg, which corresponds to approximately 1.7 % of the initial weight of the plasma sintered Be₁₂Ti sample (64.18 mg). The average mass gain rate of the pure beryllium sample and the plasma sintered Be₁₂Ti sample were 2.8×10^{-4} and 6.6×10^{-6} mg/sec, respectively. The mass gain of the pure beryllium sample was by far greater than that of the plasma sintered Be₁₂Ti sample. The experimental results shown above suggest that the Be₁₂Ti sample possesses higher oxidation resistance to water vapor compared with the pure beryllium sample.

The solid-line curves in the figures show changes in the concentration of hydrogen in the outlet stream of the reactor. In the case of the pure beryllium sample, a considerable amount of hydrogen was produced throughout the experiment. The amount of hydrogen generated from each 1 cm² of the surface of the pure beryllium sample was 2.78×10^{-3} mol. On the other

hand, in the case of the Be₁₂Ti sample, the amount of hydrogen generated from each 1 cm² of the surface of the plasma sintered Be₁₂Ti sample was only 1.14×10⁻⁴ mol. The amount of the hydrogen concentration of the pure beryllium sample was 24 times of that of the Be₁₂Ti sample.

Figs. 3 (a) and (b) shows the X-ray diffraction patterns of the pure beryllium sample before and after exposure to the Ar gas containing 10,000 ppm of water vapor, respectively. Photographs of the samples are shown in the figures, as well. Several diffraction peaks arose

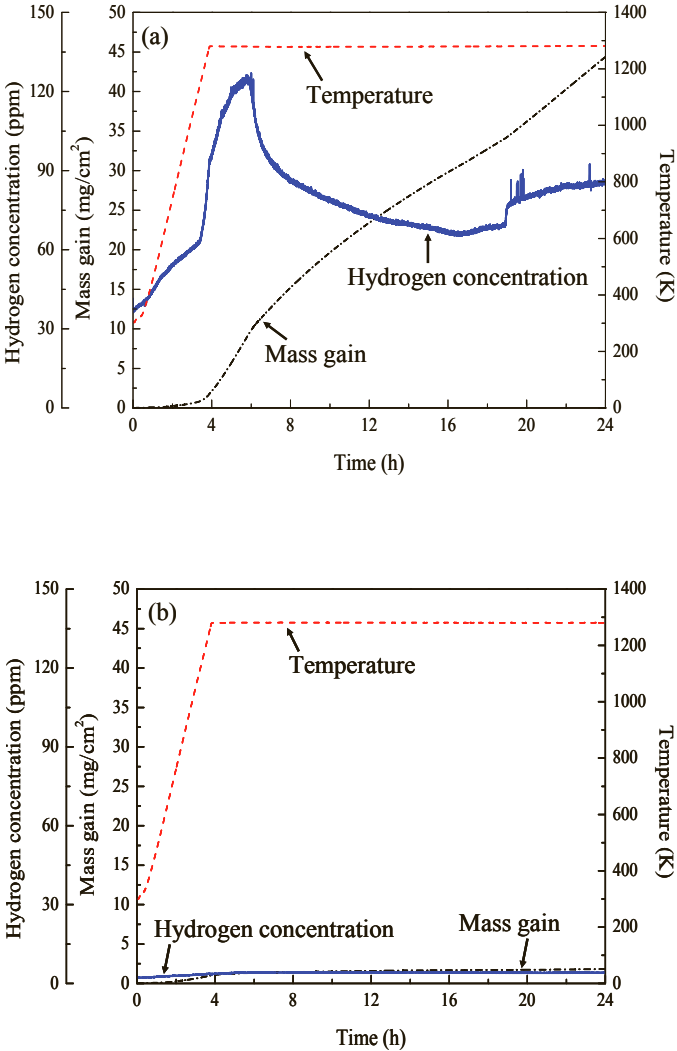


Fig.2 Mass gain curve and hydrogen concentration of (a) the pure beryllium sample and (b) the Be₁₂Ti sample fabricated by the plasma-sintering method.

(see Fig.3 (b)), and most of them were attributed to the peak of BeO (marked with closed triangle). After the experiment, a large amount of white products were observed on the surface of the pure beryllium sample. Furthermore, in the case of the pure beryllium sample, volume expansion and peel off of these white products took place. Fig. 3 (c) shows the diffraction pattern of the Be₁₂Ti sample before exposure to the Ar gas containing 10,000 ppm of water vapor. For this sample, most of diffraction peaks were attributed to Be₁₂Ti (marked with closed square), and diffraction peaks related to metal oxides were not observed. Fig. 3 (d) shows the diffraction pattern of the Be₁₂Ti sample after exposure to the Ar gas containing 10,000 ppm of water vapor. In the case of the Be₁₂Ti sample, white products had appeared

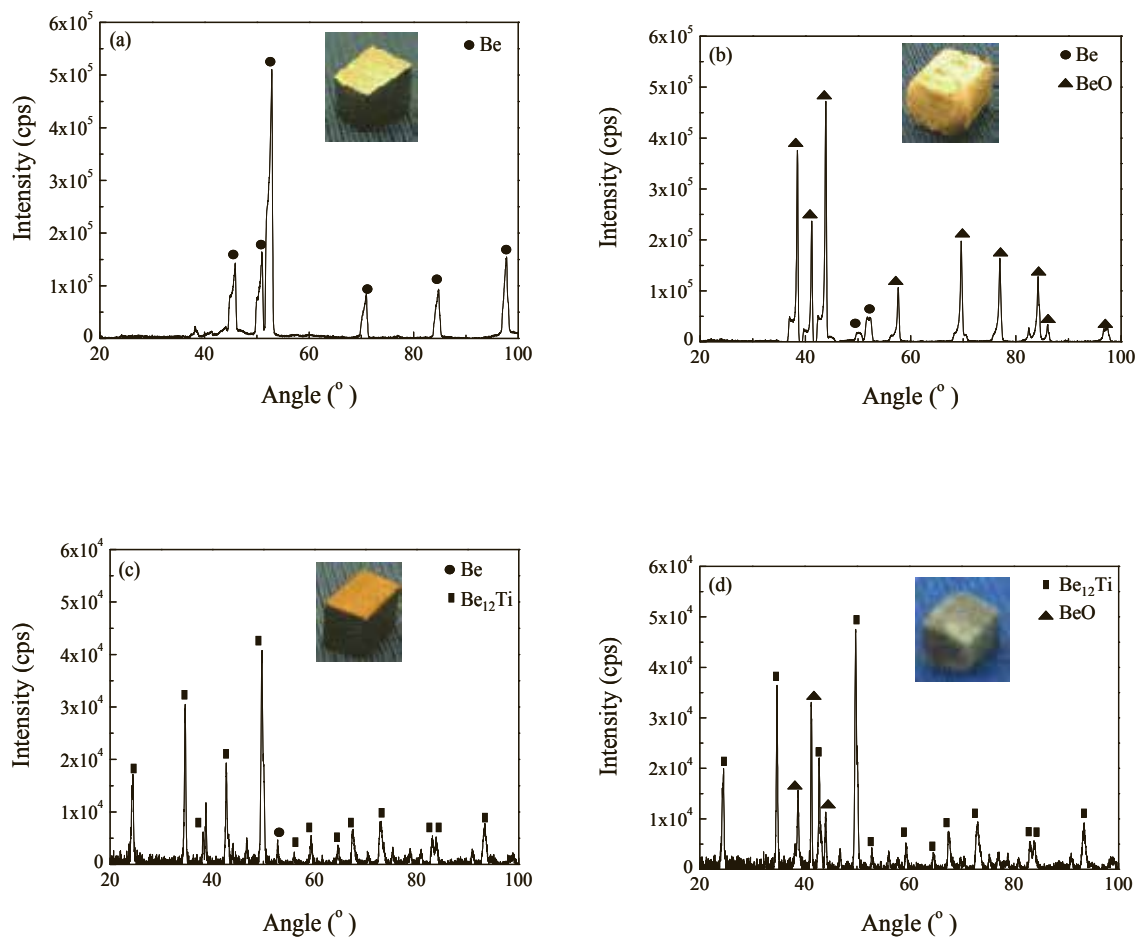


Fig.3 X-ray diffraction pattern of (a) the pure beryllium sample before the experiment, (b) the pure beryllium sample after the experiment, (c) the Be₁₂Ti sample before the experiment and (d) the Be₁₂Ti sample after the experimentt

only as limited number of spots on the surface, and neither swelling nor peel off of the surface products was observed. Diffraction peaks related to BeO were observed on the sample surface, whereas the intensity of the diffraction peak attributed to BeO was quite small compared with the pure beryllium sample. The results of this analysis and the experiments shown above indicate that the Be₁₂Ti sample possesses high oxidation resistance.

4. Conclusion

The oxidation resistance of the Be₁₂Ti sample, fabricated by a plasma-sintering method, under water vapor was investigated. In the experiments, the pure beryllium sample and the Be₁₂Ti sample were placed under an Ar gas containing 10,000 ppm of water vapor at the temperature of 1273 K for 24 h. The catastrophic oxidation reaction was not observed for the Be₁₂Ti sample. The mass gain and the amount of hydrogen generated were by far smaller than the pure beryllium sample. Furthermore, in the case of the pure beryllium sample, volume expansion and peel off of the surface of white products were observed.

After the experiment, the surface of the samples was observed by means of X-ray diffraction analysis, which suggests the presence of beryllium oxide on the samples surface. However, in the case of the Be₁₂Ti sample, the intensity of the diffraction peak attributed to BeO was quite smaller compared with the pure beryllium sample.

5. Acknowledgment

This work was supported by the Japan Atomic Energy Agency under the Joint Work contract 23K131, as a part of Border Approach activities.

6. Reference

[1] H. Kawamura et al., Fusion Eng. Des. 61-62 (2002) 391-397.

- [2] M. Nakamichi et al., Fusion Eng. Des. 86 (2011) 2262-2264.
- [3] M. Nakamichi et al., J. Nucl. Mater. 417 (2011) 765-768.
- [4] D. A Petti et al., J. Nucl. Mater. 283-287 (2000)
- [5] D.W Aylmore et al., J. Nucl. Mater. 3, No. 2 (1961) 190-200.

Oxidation property of plasma sintered beryllide

Jae-Hwan Kim, Masaru Nakamichi

Japan Atomic Energy Agency

*Fusion Research and Development Directorate, Japan Atomic Energy Agency,
2-166, Omotedate, Obuchi, Rokkasho, Kamikita, Aomori, 039-3212, Japan*

Abstract

Beryllides which have been paid attention as an advance neutron multiplier in demonstration power reactor, are too brittle to fabricate either pebble type or rod type by use of conventional methods, which are arc melting and hot isostatic pressing method. As plasma sintering method has been suggested as a new method for beryllide, studies on the plasma sintered beryllide are ongoing.

In this study, oxidation property of plasma sintered beryllide was investigated under dry air as an evaluation of high temperature property. It was obvious from the result of thermal gravimetry that specimen with larger amount of Be_{12}Ti phase which corresponds to longer-sintered specimen had superior oxidation resistance. As results of electron probe micro analyzer and x-ray diffraction analyses, oxidation behavior of Be_2Ti phase had different mechanism showing formation of TiO_2 scale while those of Be and Be_{12}Ti phase were not so different as compared to studies conducted so far. The TiO_2 scales were crystallized upon Be_2Ti phase, being formed outside of the island-like oxide scales while BeO scales were formed inside of the scales. In addition, the result that some cracks were formed either near to or cross to the island-like scale, may result in degradation of mechanical property at high temperature. Further studies on high temperature property are ongoing.

Introduction

Beryllide is well known to a material with brittleness which can be problematic for the fabrication of pebbles by conventional methods. The establishment of fabrication techniques for solid beryllide rods is a key issue in advanced neutron multiplier development. So a new method for synthesis of this beryllide was suggested by Nakamichi [1] and studies on the effect of the sintering time were reported [2]. Compared to beryllium, high temperature properties for beryllide are considered as the most important aspect because beryllium is known to exhibit poor high temperature properties above 873 K [3].

In this study, the oxidation resistance of the plasma sintered beryllides is reported using the weight gain measurement.

Experiments

Starting powders of Be (>99.0 %) and Ti(>99.9%) were blended with stoichiometric composition of Be_{12}Ti , that is, 92.3 at% Be and 7.7 at% Ti, and mixed for 60 min by using a RM200 (Retsch, Germany). The powder is loaded in a punch and die, made by graphite and pressed by uniaxial pressure for cold compaction. To generate the plasma environment and activate the particle surfaces, on-off pulsed direct current with 500 A was applied. The compact was resistance-heated during applying the uniaxial pressure to the material. For comparison, sintering temperature was fixed to 1273 K and sintering times were varied to 5, 10, 30, 50 min with heating and cooling rates of 100 and 200 K/min, respectively.

The plasma sintered beryllides were cut to $2.7 \times 2.7 \times 4.0 \text{ mm}^3$ and polished up to $15 \mu\text{m}$. To evaluate the variation of each phase according to oxidation, back-scattered electron scanning electron microscopic images were observed with exact same position before and after thermal-gravimetry (TG) measurements using electron probe micro analyzer (JXA-8530F, JEOL, Japan). The TG tests were conducted at 1273 K for 24 hr under dry air with flow rate of 300 ml/min. In addition, x-ray diffraction measurements were conducted with scan speeds of 0.01° from 10° to 100° for confirmation of compositional variation of beryllides.

Results and Discussions

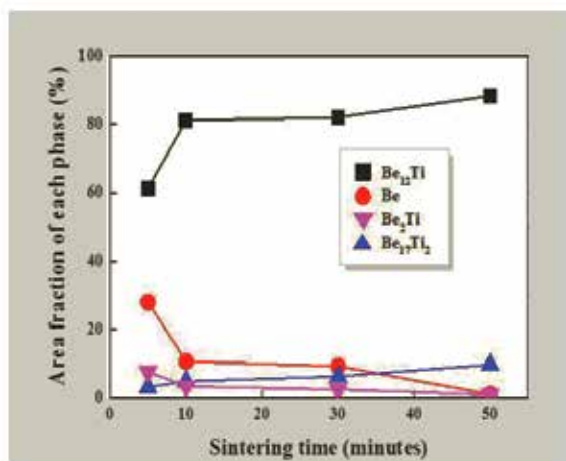


Fig.1 Difference of area fraction for plasma sintered beryllides tested in thermal gravimetry.

Fig.1 shows the area fractions for the beryllides sintered for different times, 5 min, 10 min, 30 min, and 50 min. For the beryllide sintered for 5 min, area fractions of Be_{12}Ti phase and Be were approximately 61 % and 29 %, respectively, including small fractions of $\text{Be}_{17}\text{Ti}_2$ and Be_2Ti phase. The sintering time of 5 min was not enough to consolidate the Be_{12}Ti phase as its stoichiometric

composition. However, as the sintering time increased to 10 min, area fraction of Be_{12}Ti phase increased to 81 % while that of Be decreased to 10 %. From the total variation of each phase, with increasing the sintering time, Be_{12}Ti phase increased to 87 % while Be phase decreased to almost 0 %. Although small fractions for $\text{Be}_{17}\text{Ti}_2$ and Be_2Ti phase were confirmed, $\text{Be}_{17}\text{Ti}_2$ phase increased while Be_2Ti phase decreased with the sintering time.

In order to investigate the oxidation resistance of the plasma sintered beryllides fabricated by different sintering times, weigh gains for each beryllide were measured at 1273 K for 24 h under dry air with gas flow of 300 ml/min.

Fig.2 exhibited the results of weight gains for the beryllides with a reference by Sato [4]. For the beryllide sintered for 5 min, with increase of the exposure time at 1273 K, weight gain increased with parabolic rate. On the other hands, it was clear that the longer sintering time the beryllides have, the better oxidation resistance they have. This result suggested that the beryllide with larger fraction of Be_{12}Ti phase as well as smaller fraction of Be phase, exhibited to the better oxidation resistance. To investigate the oxide scale in detail, the SEM surface images

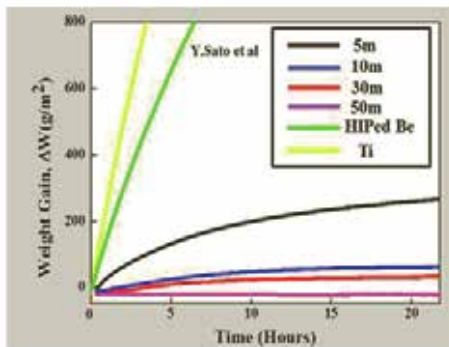


Fig.2 Weight gains of plasma sintered beryllides under isothermal condition with 1273 K.

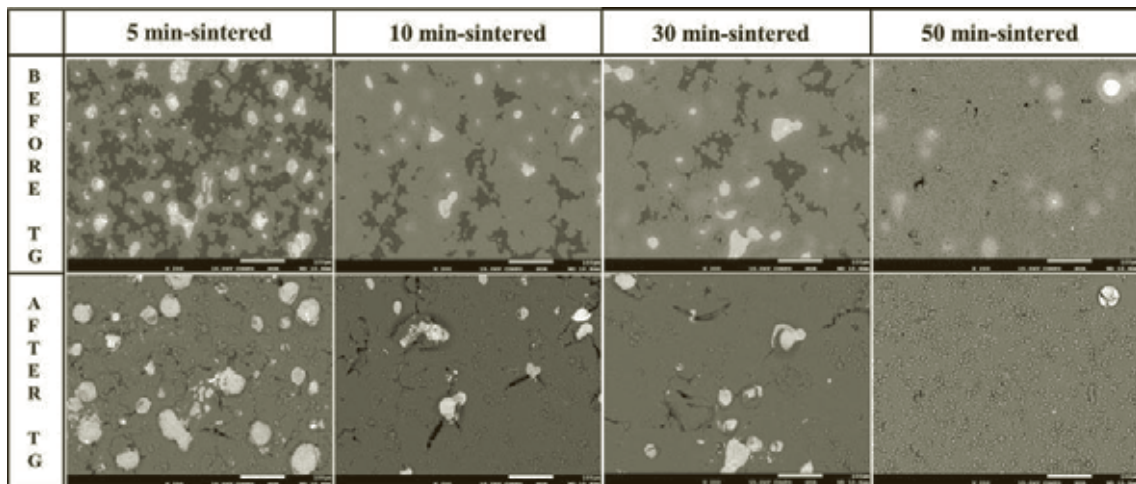


Fig.3 SEM images for plasma sintered beryllides before and after TG test.

Fig. 3 shows the SEM images for the beryllides before and after TG test, observing the exact same position for comparison. It was obvious that for 5 min-sintered beryllide after TG test, white area detected on the exact same position of Be_2Ti phase. EPMA results clearly clarified that the white substance corresponded to TiO_2 phase which was oxidized and formed with rugged type on the surface. In addition, many cracks near to TiO_2 phase were observed. This may be caused by stress between BeO and TiO_2 . Further studies on this are ongoing. Moreover, the gray areas for the beryllide after TG test, were identified to BeO . However, its morphology tends to have different type of BeO , depending on the position. As results of TG test, BeO on the Be was formed to be porous scale while that on the Be_{12}Ti and $\text{Be}_{17}\text{Ti}_2$ phase seemed to be dense.

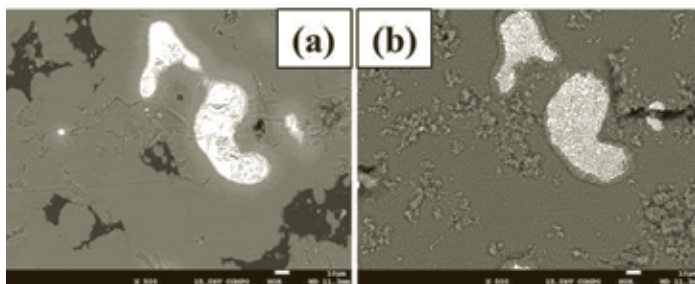


Fig.4 SEM images of the plasma sintered beryllide (a) before TG test and (b) after TG test.

Fig. 4 shows the SEM images of the beryllides, explaining that Be_{12}Ti and $\text{Be}_{17}\text{Ti}_2$ phases have higher oxidation resistance while Be and Be_2Ti phases were severely oxidized. Be phase in the beryllide tends to be oxidized as the single Be phase is oxidized. It is clear that BeO formed on the Be phase is porous and non-protective scale. On the other hand, BeO formed on the Be_{12}Ti phase is considerably dense and protective. Sato [4] demonstrated that the difference of oxidation behavior between Be and Be_{12}Ti is caused by compressive stress to keep the coherency of Be lattice between scale and substrate.

The oxidation behavior of $\text{Be}_{17}\text{Ti}_2$ was similar with the Be_{12}Ti , forming the dense and protective scale. However, Be_2Ti was severely oxidized with rugged type of scale. The cross sectional image demonstrated that the scales are composed of TiO_2 and BeO , which were formed outside and inside of the rugged scale, respectively. Accordingly, existence of Be_2Ti phase may lead to degradation of not only oxidation resistance but mechanical property due to cracks.

Conclusions

As a new method for fabrication of beryllide, we have suggested the plasma sintering method. In this study, the oxidation resistance for each phase in the beryllide plasma-sintered for 5 min, 10 min, 30 min, and 50 min will be investigated. The SEM images indicated that with increase of sintering time, area fraction of Be_{12}Ti and $\text{Be}_{17}\text{Ti}_2$ phases increased while Be and Be_2Ti phases decreased. The weight gain result for the beryllides clarified that the longer sintering time the beryllide has, the higher oxidation resistance it has. From the surface observations, it was obvious that Be was severely oxidized with porous and non-protective scale while Be_{12}Ti and $\text{Be}_{17}\text{Ti}_2$. In addition, Be_2Ti was oxidized with rugged scale which was composed of TiO_2 and BeO scales, formed outside and inside of the scale, respectively. And some cracks were identified near to TiO_2 formed on the Be_2Ti phase. For the plasma sintered beryllide, accordingly, Be_2Ti phase may result in degradation of oxidation resistance and mechanical property.

References

- [1] M. Nakamichi et al., J. Nucl. Mater., Vol. 417, Iss. 1-3 (2011) 765-768
- [2] J.H. Kim et al., ICFRM 15, J. Nucl. Mater., in review, (2011)
- [3] Anderl, R. A., et al, J. Nucl. Mater., 258-263(1998) 750-756
- [4] Y. Sato, M. Uchida and H. Kawamura, Proc. 6th IEA Int. Workshop on Beryllium Technology for Fusion (2003) JAERI-Conf 2004-006, 203

First Measurements of Beryllide Vapor Pressure

J. Reimann¹, O. Beneš², J.-Y. Colle², C. Dorn³, H. Harsch⁴, R. J. M. Konings², P. Kurinskiy¹

¹KIT, Karlsruhe, Germany, joerg.reimann@partner.kit.edu,

²JRC-ITU, Karlsruhe, Germany,

³Materion Inc., Elmore, Ohio, USA,

⁴GVT, Karlsruhe, Germany

For the beryllium tiles protecting the ITER First Wall, the low vapor pressure of beryllium is a fundamental issue because considerable amounts of beryllium are evaporated from thermally high loaded areas and are deposited in cooler zones.

The beryllides, namely $Be_{12}Ti$, $Be_{12}V$ and $Be_{12}Cr$, have become of interest for ceramic breeder blankets because of better performance in several areas. This would be also the case for the use as First Wall material if beryllium evaporation is considerably smaller. In the paper, first results from measurements of the beryllium vapor pressure above $Be_{12}Ti$ in the temperature range from 1250 K to 1600 K are described. It showed that the beryllium vapor pressure above the $Be_{12}Ti$ alloy is of the same order of magnitude as the vapor pressure of pure beryllium metal.

I. INTRODUCTION

In the ITER fusion reactor, beryllium will be an important material mainly in two areas: first, in ceramic breeder blankets where it is required as a neutron multiplier and second, as a material for plasma facing components (PFCs) in the shape of tiles at the First Wall¹.

For First Wall applications, the low vapor pressure of beryllium is a fundamental issue because considerable amounts of beryllium are evaporated from thermally high loaded areas and are deposited in other zones. Especially, the deposition of beryllium on the tungsten divertor surface is of special concern²⁻⁴ because it might result in the formation of Be-W compounds with considerably lower melting temperatures compared to pure tungsten.

Figure 1 shows vapor pressures of different metals from Ref. (5). The data were fitted to an expression of the form

$$\log p = A - B/T, \quad (1)$$

where the vapor pressure p is in Pa and the temperature T is in Kelvin. The constants A and B are listed in the figure.

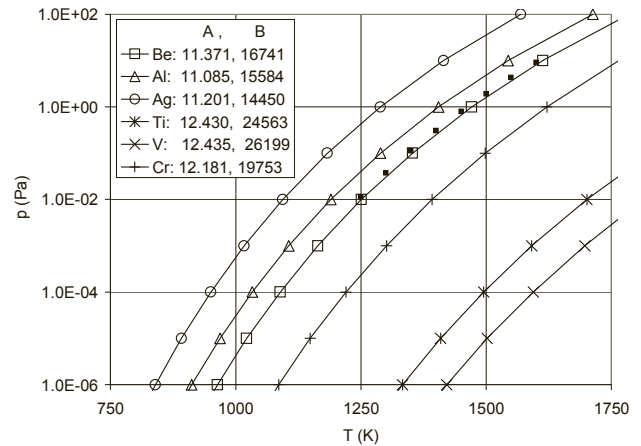


Fig. 1. Metal vapor pressures from Ref. (5).

The vapor pressure of beryllium is in between of that of silver and aluminum and larger compared to metals of interest as structural materials. The beryllium data are in good agreement with data from Refs. (6-7) which were used in the data evaluation described in Section II.

For the use of multiplier material in blankets, beryllium intermetallic compounds, beryllides, have proven to perform better compared to pure beryllium in respect to upper temperature limit, compatibility with structural materials, chemical reactivity with air and steam, and tritium release⁸⁻¹⁵. Drawbacks are the difficulty of fabrication and the brittleness of these materials at lower temperatures.

From the neutronic point of view, the compounds $Be_{12}M$ with titanium, vanadium, and chromium as metal constituent are of interest. Up-to now work concentrated on $Be_{12}Ti$. The present material data basis for these beryllides is very limited compared to that for pure beryllium; vapor pressures of beryllides were not

experimentally determined yet. If it would prove that beryllide vapor pressures are significantly smaller compared to pure beryllium, the attractiveness of these compounds would increase considerably.

The vapor pressures of ideal alloys can be assessed with Raoult's law, expressed by

$$p_{\text{alloy}} = N_{M1}p_{M1} + N_{M2}p_{M2} \quad (2),$$

where N_{M1} and N_{M2} are the mole fractions of the metal constituents M1 and M2, respectively, and p_{M1} and p_{M2} are the corresponding vapor pressures above the pure metals. With the data from Fig. 1, according to Raoult's law, no essential vapor pressure differences are expected between the Be_{12}M compounds of interest and pure beryllium.

However, because of the complicated phase diagram of beryllides¹⁶ which in general contain many intermediate phases with various ranges of stability, see e.g. Fig. 2, the accuracy of Raoult's law is questionable and experiments are required.

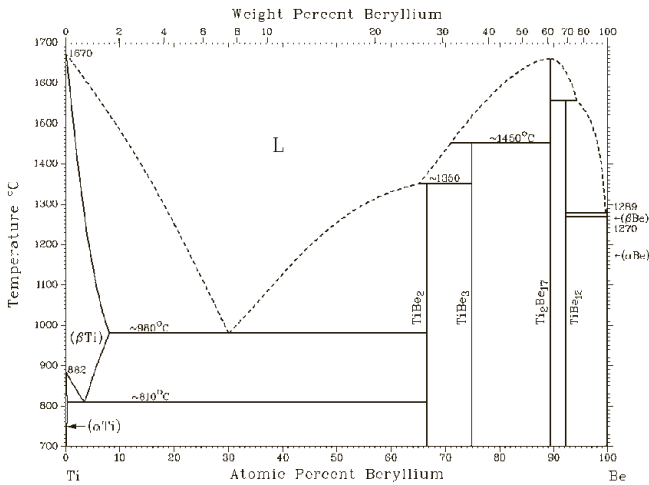


Fig. 2. Ti-Be phase diagram, Ref. 14.

In the following, results from screening experiments with Be_{12}Ti are described, performed in the Institute for Transuranium Elements (ITU) of the Joint Research Center (JRC) of the European Commission.

II. EXPERIMENT

To determine the vapor pressure of Be above pure beryllium metal and Be_{12}Ti alloy a Knudsen Cell technique coupled with a quadrupole mass spectrometer (KCMS) has been used¹⁷. Both materials have been measured from room temperature up to 1600 K, just above the melting temperature of pure beryllium ($T_m(\text{Be}) = 1560 \text{ K}$).

The samples used in this study were solid pieces of the total weight of 3.03 mg and 4.56 mg for Be metal and Be_{12}Ti alloy respectively, which were loaded in the tungsten Knudsen Cell, see Fig. 3. The cell was centered in a high temperature furnace made of tungsten coil-heating element surrounded by seven cylindrical thermal shields. To avoid any contact of evaporated Be species with other gas molecules the whole system is placed in a high vacuum chamber ($p \sim 10^{-7}$ mbar). The scheme of the whole equipment as well as the Knudsen in detail cell is shown in Fig. 3.

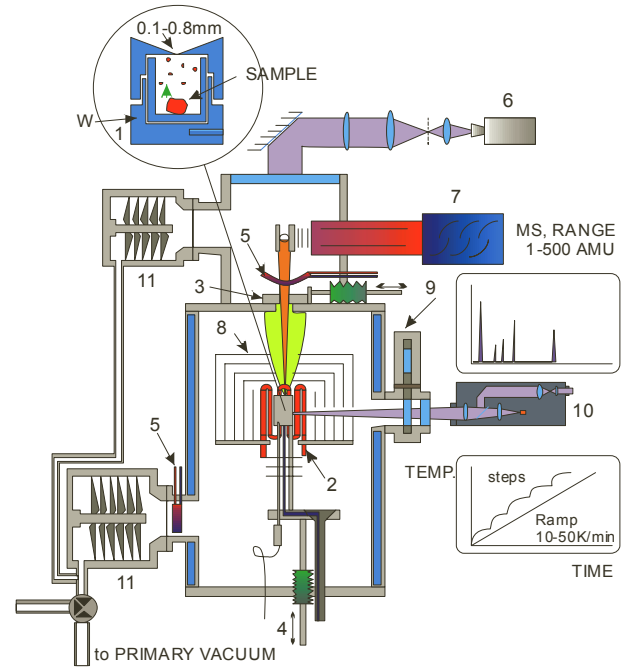


Fig. 3. Scheme of set-up: (1) Knudsen Cell with black-body hole; (2) W resistance heating coil; (3) molecular beam chopper; (4) cell lift apparatus; (5) LN cold trap; (6) CCD camera for cell and chopper hole alignment; (7) quadrupole mass spectrometer; (8) thermal shields; (9) revolving protection windows; (10) linear pyrometer; (11) turbo molecular pump.

KCMS technique is an equilibrium study which measures the intensity of gaseous species escaping from the Knudsen cell through a small aperture (of 0.5 mm diameter), which are further ionized in an ionizing chamber forming cations to be detected in a mass spectrometer. Based on the intensity of a signal, I_i^+ , the vapor pressure, p_i , is determined according to Equation 3, where T is the absolute temperature and K_i is the calibration factor. This factor generally contains an instrumental term, which is independent of measured gaseous species, and a term which is dependent on the species measured and includes the ionization cross

section, the efficiency of the secondary electron multiplier and the isotopic abundance of given species.

$$p_i = (I_i^+ T)/K_i \quad (3)$$

The calibration factor is determined from the vapor pressure measurement of a standard material which is measured at the same time as the analyzed sample. Usually as a standard material pure silver metal is used, however in this study this was not possible as it was observed in several initial experiments that loading silver together with Be-containing samples in one cell resulted in an abnormal curve shape of the silver signal indicating some reaction of silver with beryllium, most likely on the solid surfaces of two metals, in the molten state and possibly in the gaseous phase. Therefore, silver was not feasible to be used as calibrating metal.

However, as the aim of this study was to measure the difference between the vapor pressure of Be atomic species above pure beryllium metal and Be₁₂Ti alloy, the vapor pressure was determined directly from the measured intensity signal assuming that the conditions of the two consecutive measurements (1. Be(g) above pure Be metal, and 2. Be(g) above the Be₁₂Ti alloy) are identical. This assumption is also supported by the fact that no other vapor species than Be(g) have been detected during the performed measurements, thus the total vapor pressure above Be metal and Be₁₂Ti alloy is attributed to Be(g) only.

During the first experiment the intensity of the Be signal above pure beryllium metal was measured and the obtained curve was correlated with the vapor pressure of beryllium using the database⁶⁻⁷. The relation between the theoretical vapor pressure and the signal intensity is shown in Fig. 4. The data were fitted by:

$$\log p_{Be}(\text{Pa}) = -0.3215 - 1.0081 \log I - 0.0928 (\log I)^2 \quad (4)$$

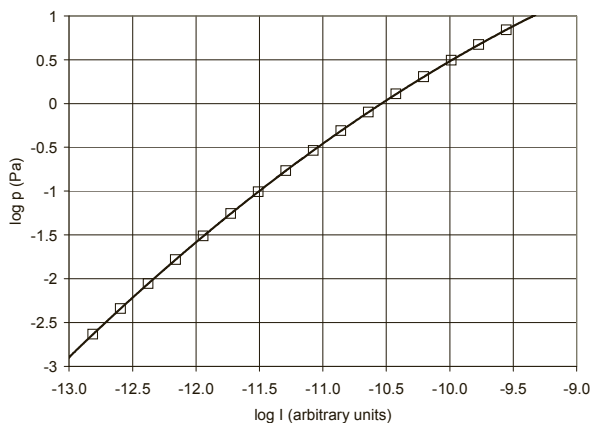


Fig. 4. Relation between vapor pressure of pure beryllium and measured intensity.

In the second step the vapor pressure of Be gaseous species above Be₁₂Ti alloy was measured and from the intensity of the signal the vapor pressure was determined using the Equation (4).

III. RESULTS

The vapor pressure of Be(g) above Be₁₂Ti alloy obtained from the mass spectrometric measurements as described in the previous section is shown in Fig. 5. The solid line is the calculated vapor pressure of Be above Be metal according to Refs (6-7), taken as a reference in this study.

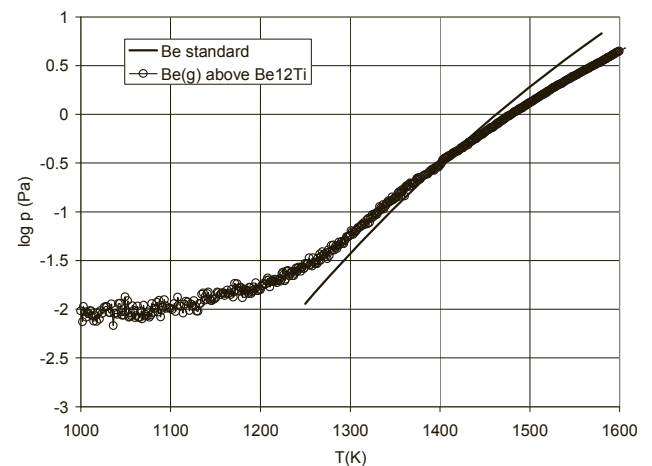


Fig. 5. Vapor pressure of Be above Be₁₂Ti alloy.

Fitting the experimental results for the temperature range from 1250 K to 1650 K, the following relation is obtained:

$$\log p_{Be12Ti}(\text{Pa}) = -18.87 + 0.0194T - 4.53 \cdot 10^{-6} T^2 \quad (5)$$

The data below 1250 K were not taken into account as the vapor pressure of Be is very low below that point and falls within the background signal of the detector. This is shown in Fig. 5 resulting in an inflection on the vapor pressure signal between 1200 K and 1300 K.

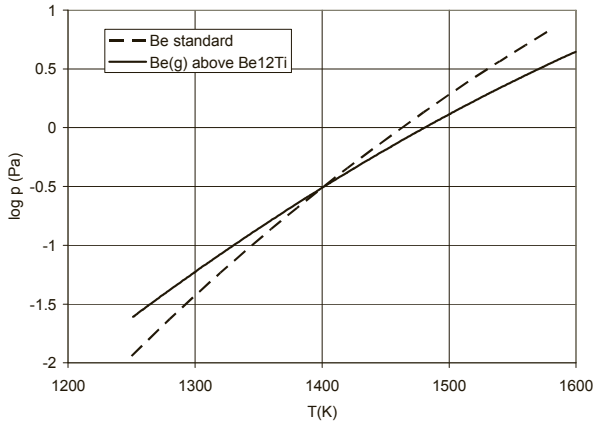


Fig. 6. Vapor pressure of Be metal and of Be above the Be_{12}Ti alloy as a function of temperature.

Figure 6 shows the comparison between the vapor pressure of Be above pure beryllium metal and the vapor pressure of Be above Be_{12}Ti alloy obtained in this study and described by Eq. 5.

At low temperatures the vapor pressure of $\text{Be}(\text{g})$ species is slightly higher above the Be_{12}Ti alloy compared to pure beryllium whereas at around 1400 K this trend changes and the vapor pressure above pure metal becomes higher. This is due to the different slopes of the temperature functions of the vapor pressure which are explained by different equilibria above pure metal and the alloy as shown in the following relations 6 and 7.

1. Equilibrium with pure Be metal:



2. Equilibrium with Be_{12}Ti alloy:



It is evident that the second equilibrium assumes a composition modification of the initial sample and can be expressed by the general formula:



however, as the Ti-Be phase diagram¹² does not indicate hypostoichiometry of the Be_{12}Ti phase, as shown in Fig. 2, equilibrium from Equation 7 is suggested.

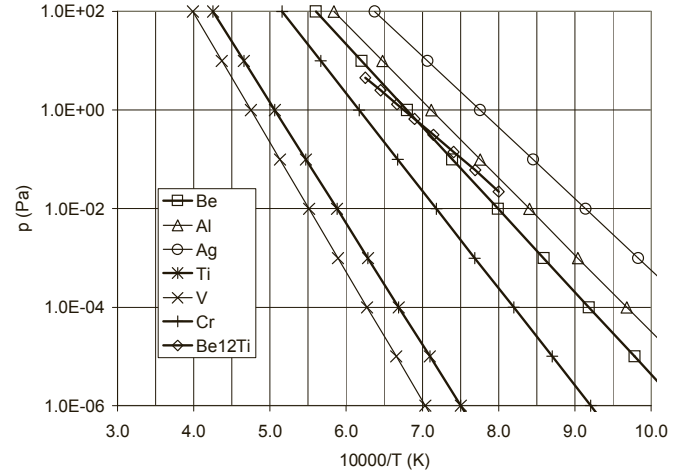


Fig. 7. Vapor pressure of different metals and of Be above the Be_{12}Ti alloy as function of reciprocal temperature.

The differences of the curve slopes are also obvious from Fig. 7 where plots of $\log p$ versus reciprocal temperature are presented. Fitting the data for Be above the Be_{12}Ti alloy according to Equation (1), the following constants are obtained: $A=11.371$, $B=16741$.

IV. CONCLUSIONS

From the mass spectrometric data, taking into account the experimental error of the used method, we conclude that the vapor pressure of the Be_{12}Ti alloy is of the same order of magnitude as the vapor pressure of pure beryllium metal in the temperature range from 1250 K to 1600 K. Similar results are expected for the other beryllides of interest, Be_{12}V , and Be_{12}Cr .

REMARK

The content of this paper was first presented at the 19th TOFE Conference, Las Vegas, USA, Nov. 7-11, 2010. Because of technical reasons the paper was not published in the conference proceedings.

REFERENCES

1. G. JANESCHITZ, Overview of the status of the ITER Project, ISFNT-9, Dalian, China, Oct. 12-16 (2009).
2. C. LINSMEIER, K. ERTL, J. ROTH, A. WILTNER, K. SCHMID, F. KOST, S. R. BHATTACHARYYA, M. L. BALDWIN, R. P. DOERNER, Binary

- beryllium-tungsten mixed materials, *J. Nucl. Mater.* 363-365 (2007) 1120-1137.
3. M. J. BALDWIN; R. P. DOERNER, D. NISHIJIMA, D. BUCHENAUERER, W. M. CLIFT, R. A. CAUSEY, K. SCHMID, Be-W alloy formation in static and divertor-plasma simulator experiments, *J. Nucl. Mater.* 363-365 (2007) 1179-1183.
 4. A. WILTNER, CH. LINSMEIER, Formation of a surface alloy in the beryllium–tungsten system, *J. Nucl. Mater.* 337–339 (2005) 951–955.
 5. I. S. GRIGRIEV, E. Z. MEILIKHOV(Ed), *Handbook of Physical Quantities*, CRC Press, (1997).
 6. C. W. BALE et al., *FactSage Software v. 5.5*.
 7. C. W. BALE, et al., *FactSage Element Database* (Revised Jan. 2006).
 8. C. DORN, W. HAWS, E. VIDAL, A review of physical & mechanical properties of Titanium beryllides with specific modern application of TiBe₁₂, *Fusion Eng. Des.* (2009) in press.
 9. H. KAWAMURA, T. TAKAHASHI, N. YOSHIDA, V. SHESTAKOV, Y. ITO, M. UCHIDA, H. YAMADA, M. NAKAMICHI, E. ISHITSUKA, Application of beryllium intermetallic compounds to neutron multiplier of fusion blanket, *Fusion Eng. Des.* 61-62 (2002) 391-397.
 10. H. KAWAMURA, M. UCHIDA, V. SHESTAKOV, Compatibility between Be₁₂Ti and SS316LN, *J. Nucl. Mater.* 307-311 (2002) 638-642.
 11. K. MUNAKA, H. KAWAMURA, M. UCHIDA, Surface reaction of titanium beryllide with water vapor, *Fusion Eng. Des.* 81 (2006) 993-998
 12. M. UCHIDA, E. ISHITSUKA, H. KAWAMURA, Tritium release properties of neutron-irradiated Be₁₂Ti, *J. Nucl. Mater.* 307-311 (2002) 635-656.
 13. M. UCHIDA, E. ISHITSUKA, H. KAWAMURA, Thermal conductivity of neutron irradiated Be₁₂Ti, *Fusion Eng. Des.* 69 (2003) 499-503.
 14. J. REIMANN, C. DORN, A. GORAIEB, H. HARSCH, W. HAWS, P. KURINSKIY, R. LINDAU, CH. LINSMEIER, A. MOESLANG and M. ROHDE, “Beryllides for Fusion Reactors,” *Proc. 23rd Meeting on Fusion Engineering*, San Diego, USA, May 31-June 5 (2009).
 15. K. A. WALSH, *Beryllium Chemistry and Processing*, ASM International, (2009).
 16. H. OKAMOTO, *Phase diagrams for binary beryllium alloys*, ASM International, Materials Park, OH 44073-0002 (1987).
 17. J.-P. HIERNAUT, J.-Y. COLLE, R. PFLIEGER-CUVELLIER, J. JONNET, J. SOMERS, C. RONCHI, A Knudsen cell-mass spectrometer facility to investigate oxidation and vaporisation processes in nuclear fuel, *J. Nucl. Mat.* 344 (2005) 246–253.

Investment Casting of Be Alloys

Gary Schuster¹ and Chuck Pokross²

Abstract:

Investment casting is a near net shape manufacturing process that typically reduces both the amount of alloy and machining time needed to produce a part. The reductions in these two areas frequently lead to significant decreases in the total cost of the part. Materion has developed procedures for the investment casting of three Be-Al alloys (AlBeCast® 910, 920 and 930). These alloys are composed primarily of Be and Al, and also contain smaller concentrations of other elements (Si, Ge, Ni, Ag, Co and Sr). The Be and Al have very little solubility for one another. Also, they have quite different solidification temperatures (1285 and 660 C respectively). As a result Be-Al alloys solidify with a large mushy zone and form two phases, one being Be and the other Al. In general the alloying elements are selected to improve the mechanical and casting properties of the Al phase, although they also have an impact of the Be phase. X-ray dot maps of alloy cross sections show that the Si, Ge, Ag and Sr tend to stay in the Al phase whereas the Ni and Co forms solid solutions with both the Be and Al. The addition of Ag has the largest impact on the strengths of the alloys due to its tendency to form a Widmanstatten plate, δ' , phase with the Al. Additions of Co and Ni increase strength but also produce a large decrease in thermal conductivity. The high concentrations of Be in these alloys result in high specific modulus values.

1 Introduction

1.1 Investment Casting Process

Casting is a “near-net-shape” fabrication process. Cast components typically need relatively little subsequent machining. For some components there are design features that cannot be readily produced by machining, but can be incorporated during casting. Furthermore, for many components, the amount of metal needed for fabrication is significantly reduced by casting as compared to machining from a block. Because of these advantages, casting can frequently produce a component at significantly less cost as compared to alternative fabrication processes.

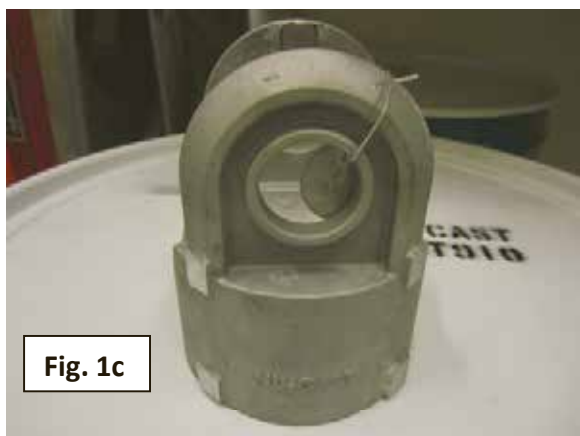
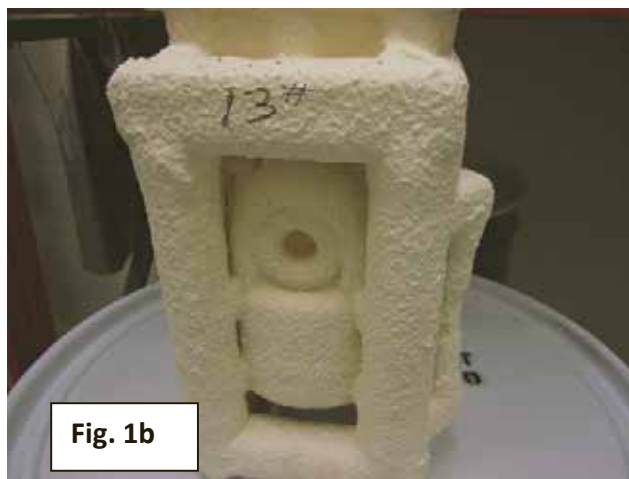
Investment casting is a casting process that uses a ceramic shell as the mold. By using a ceramic shell one can cast alloys that are more reactive and have higher melting temperatures

¹ Director of R&D, Materion Brush Beryllium & Composites, Elmore, OH, USA

² Senior R&D Engineer, Materion Brush Beryllium & Composites, Elmore, OH, USA

as compared to alloys typically cast using other methods such as die and sand casting. Beryllium (Be) has a fairly high melting temperature (1285 C) and is quite reactive. Because of this, investment casting is the only practical casting method for alloys containing high concentrations of Be. The highly reactive nature of Be also means that Be alloys cannot be practically melted and cast in air. The best method is to melt and pour in vacuum. This complicates the investment casting process, but it can still be accomplished.

In order to produce the ceramic investment shell, a piece, having the shape of the desired component, must first be made. Typically this piece is made from wax. Frequently a mold/die is machined to have the desired shape of the component. Wax is injected into this mold to make a wax part. The wax part is then dipped, multiple times, into ceramic slurries to form a ceramic shell around the wax. When the shell is sufficiently thick the wax is removed by heating. The shell is then fired and is ready to be used as a mold for investment casting. Molten metal is poured into the shell and allowed to solidify. Once solidified the shell is removed—a shell is only used once. Figures 1a-c show a wax part, shell and an investment casting.



Figures 1a-c—Photos showing: (a) The wax part; (b) The ceramic shell and; (c) An AlBeCast® 910 casting produced by filling the shell.

2 Discussion

2.1 Be-Al Casting Alloys

Materion offers three Be-Al alloys for investment casting. The alloys (AlBeCast® 910, 920 and 930) are characterized in Tables Ia&b. They vary in composition and properties. Each will be briefly reviewed.

2.1.1 AlBeCast® 910

The 910 alloy is a relatively simple, three-component, alloy with a nominal composition of 61 wt % Be, 3 wt. % Ni and the balance Al (Table Ia). Be and Al have little solubility for one another and melting temperatures of 660 C and 1285 C respectively. As a result, during solidification, a Be phase forms first and freezes throughout the casting before the Al phase starts to freeze. This produces a two-phase microstructure having a dendritic appearance. Figure 2a shows a SEM image of the 910 microstructure. Ni is soluble in Be¹ and also forms an aluminide. X-ray dot maps (Figures 2b-d) show the distributions of the three metals in the 910 microstructure. These dot maps indicate that the Ni largely stays within the Be phase forming a solid solution. At low concentrations, Ni increases the strength of Be². The Ni also causes the Be phase to significantly increase its absorption of x-rays. This is useful because pure Be is naturally transparent to x-rays. The presence of this Ni in the Be makes its absorption of x-rays roughly equal to that of Al. As a result, it is much easier to identify porosity, and other casting defects by x-ray examination. The Ni also acts to increase both the strength and hardness of the Al phase and causes the Al's thermal expansion coefficient to decrease.

AlBeCast® 910 has a high specific modulus and intermediate strength as compared to the 920 and 930 alloys (Table Ib). For applications where a high specific modulus is required, and strength is not so important, the 910 is a good option.

Table Ia—Nominal Compositions of the three AlBeCast® Alloys

Element	units	910*	920**	930***
Be	wt.%	61	64	47
Al	wt.%	bal	bal	bal
Si	wt.%			4.5
Ag	wt.%		3	2
Ni/Co/Cu	wt.%	3 (Ni)	1 (Co)	
other	wt.%		0.75 Ge	0.04 Sr

*Covered by Materion U.S. patent 5667600.

**Equivalent to AMS 7918 alloy.

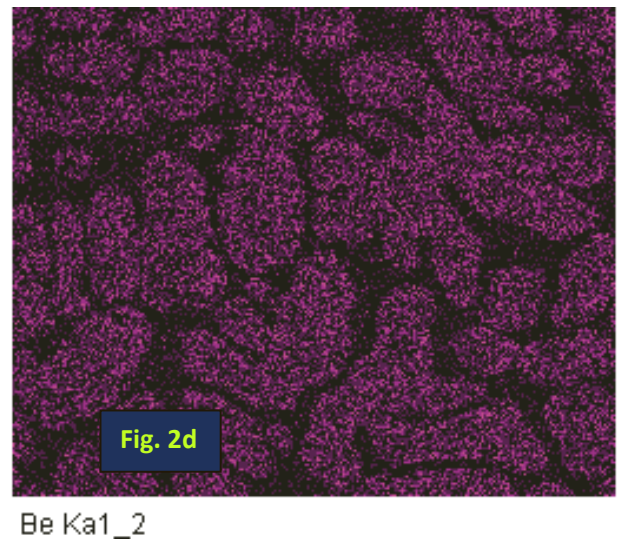
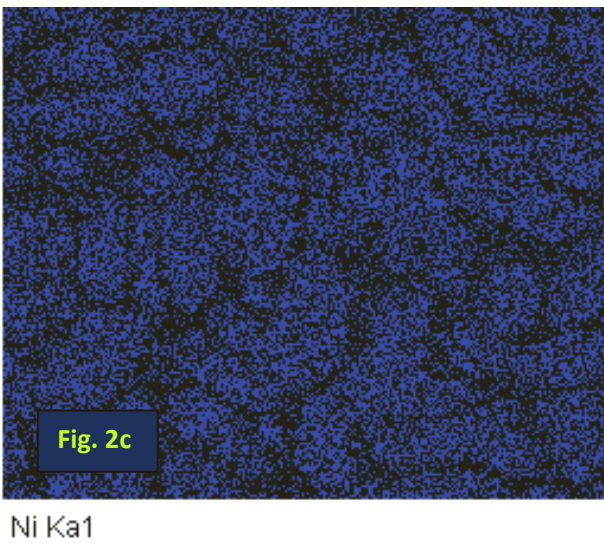
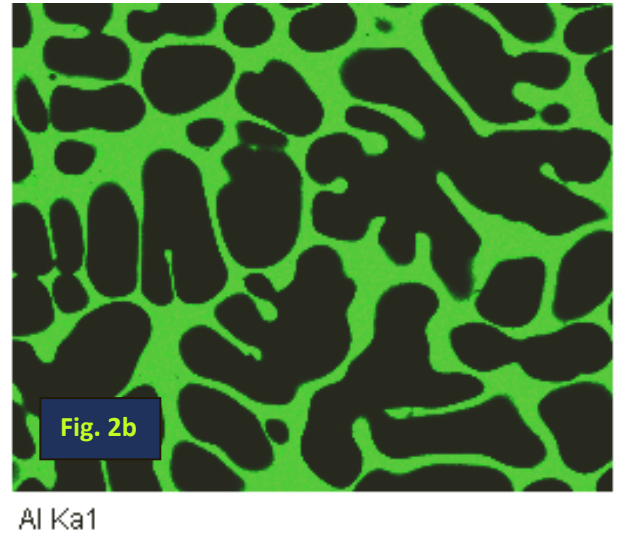
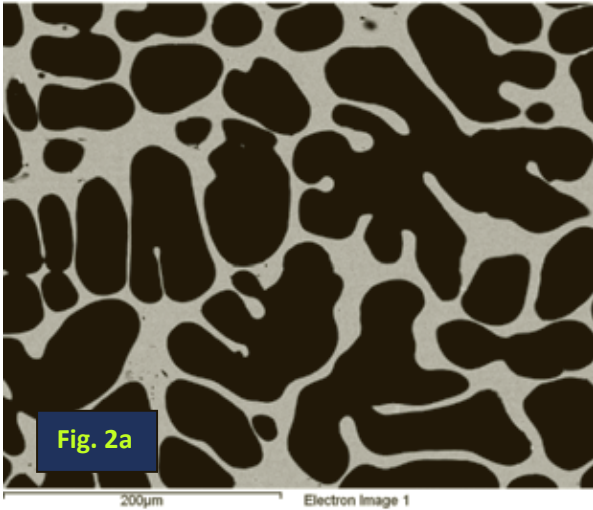
***Patent application filed in 2012.

Table Ib—Properties of the three AlBeCast® Alloys

Properties	units	910*	920**	930*
Density	g/cm ³	2.16	2.16	2.21
Melt (Liquidus)	°C	1287	1287	1287
CTE	µm/m	14.6	14.2	13.6
Thermal Conductivity	W/M-°K @ 30°C	110	105.5	186
Modulus of Elasticity in Tension	GPa @ 25°C	202	202	167
Specific Stiffness	GPa-cm ³ /g @ 25°C	93.5	93.5	75.5
0.2% YS	MPa	152	200	145
UTS	MPa	200	255	200
% Elongation	% @ 25°C	5.4	3.4	3.0

*Average values generated from testing at Materion.

**AMS 7918 minimum mechanical properties and values from testing at Materion.



Figures 2a-d—Fig. 2a is a SEM photo showing the typical microstructure of an AlBeCast® 910 cross section. The microstructure has two phases, a Be phase (dark) and an Al phase (gray). Fig 2b shows an Al dot map of the region. Fig. 2c shows a Ni dot map and Fig 2d shows a Be dot map. The Ni is seen to reside primarily in the Be phase.

2.1.2 AlBeCast® 920

Materion's AlBeCast® 920 is equivalent to the AMS 7918 alloy. It has a nominal composition of 65% Be, 3% Ag, 1% Co and 0.75% Ge (all wt.%)--balance of Al. Figure 3a shows a SEM image of a 920 alloy cross section and Figures 3b-e show corresponding x-ray dot maps (Al, Be, Ag, Ge and Co respectively) of the image. The SEM image, similar to the 910 alloy, shows a two-phase dendritic microstructure. Binary phase diagrams show that Co is soluble in Al up to concentrations of about 32 wt % and in Be to about 7wt %¹. Ge forms a eutectic phase with Al at 420 C (48 wt % Al) and two eutectic phases with Be at 1210 C (53 wt.% Be) and 875 C (2 wt. % Be). Be forms a eutectic phase with Ag at 880 C (99 wt.% Ag) and an intermetallic having a stoichiometry AgBe₂¹. Ag is soluble in Al to about 1 wt.% and, for Al rich Al-Ag alloys, forms a δ' phase¹ during thermal aging. This δ' phase has a Widmanstatten plate structure.

The dot maps show that the Ag and Ge metals are concentrated in the Al phase and that the Co is distributed roughly uniformly in both phases. Some of the Ge seems to form a eutectic phase within the Al, but some of the Ge also occurs in the Al as a solid solution (Figures 3c&4b). Figure 4a shows a higher magnification image of the Al phase. It shows that Widmanstatten plates, associated with the δ' phase, have formed. The slow cooling, that normally occurs during solidification for investment casting, seems to serve as the thermal aging process that forms this phase.

Figures 4b-c respectively show Ge, Al and Ag dot maps of the area in Fig. 4a. The presence of the Ge, Co and particularly Ag within the Al phase causes it to have greater hardness and strength. This increase in strength for the Al phase is the primary reason for the high yield and tensile strengths of the 920 alloy. The 920's high Be concentration gives it a high specific modulus. These properties make 920 a good choice for applications where both high strength and high specific modulus are needed.

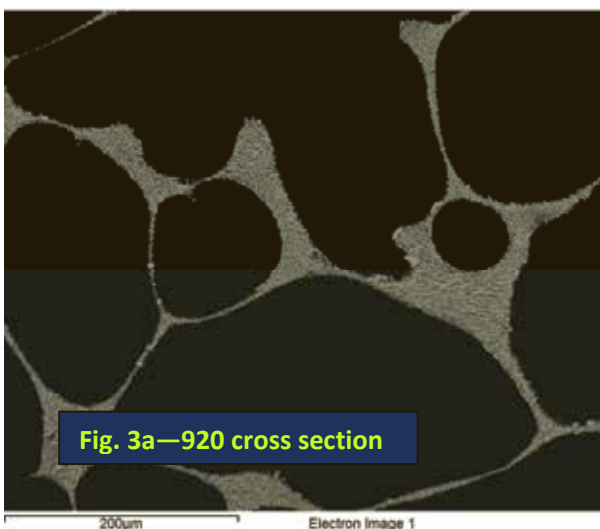


Fig. 3a—920 cross section

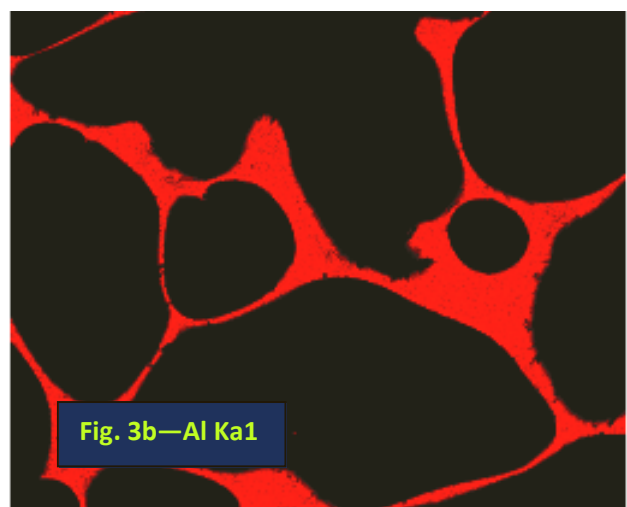
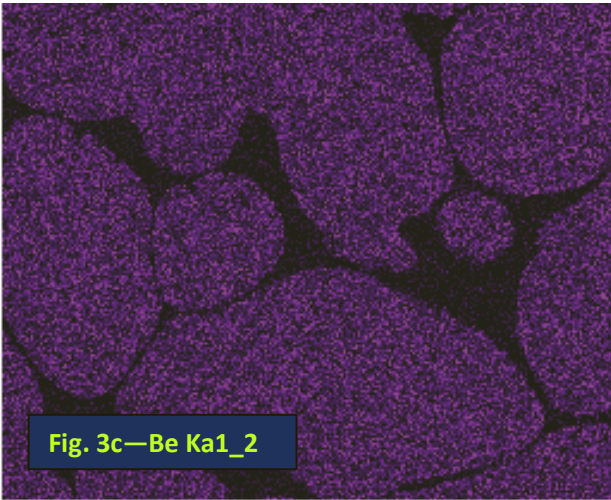
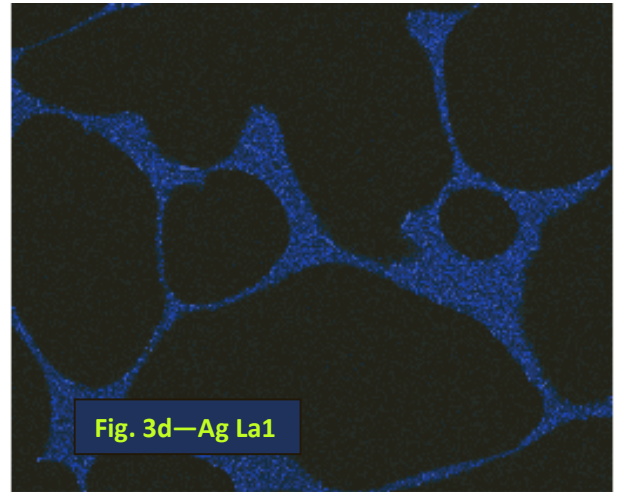


Fig. 3b—Al Ka1

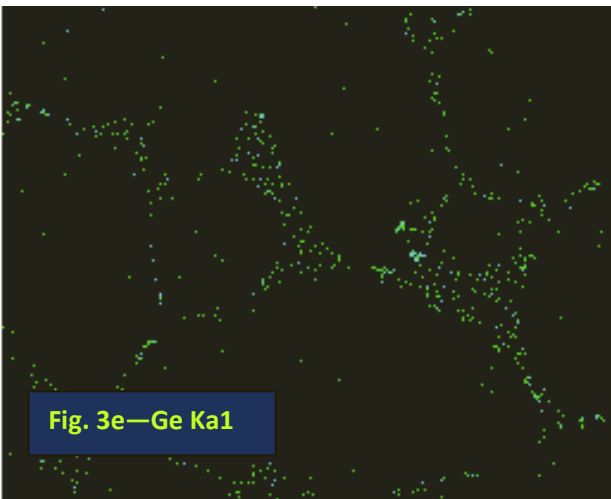
Al Ka1



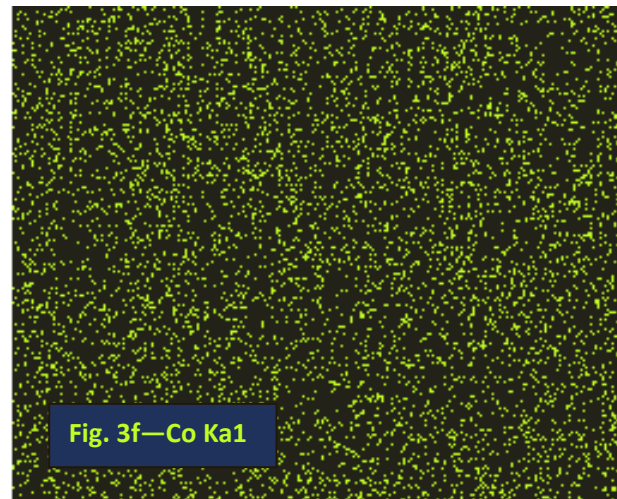
Be Ka1_2



Ag La1

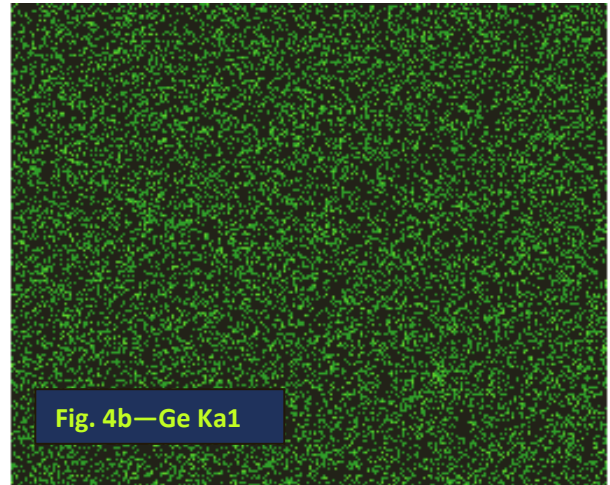
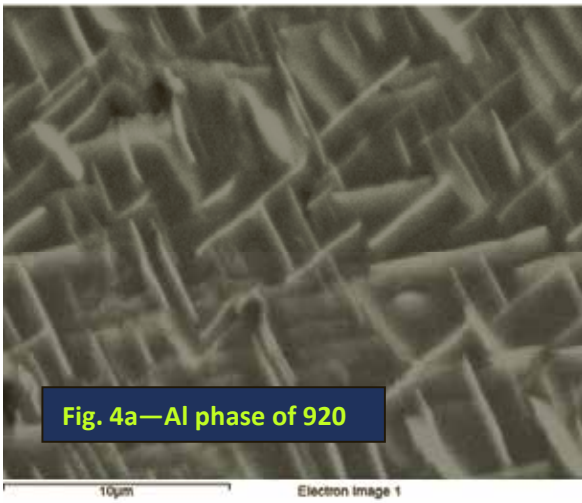


Ge Ka1

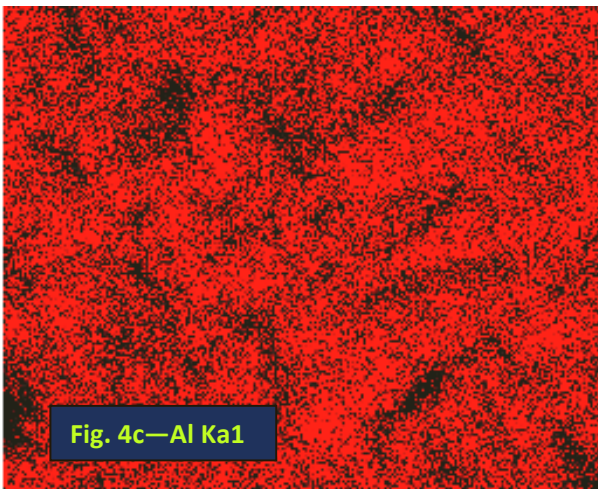


Co Ka1

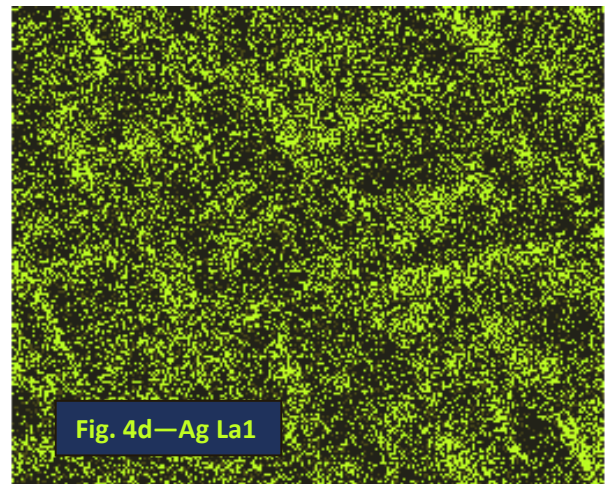
Figures 3a-f—Cross section of 920 alloy showing distributions of Al (3b), Be (3c), Ag (3d), Ge (3e) and Co (3f).



Ge Ka1



Al Ka1



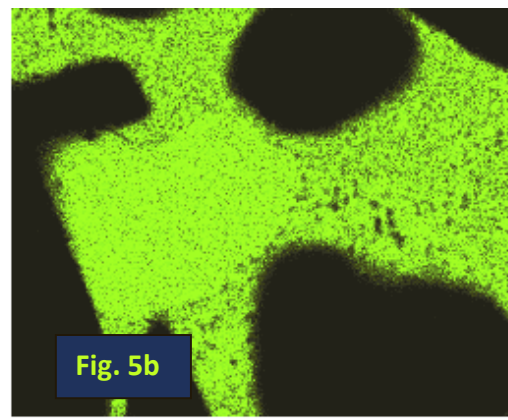
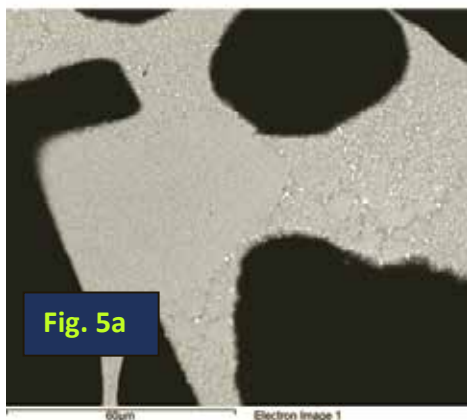
Ag La1

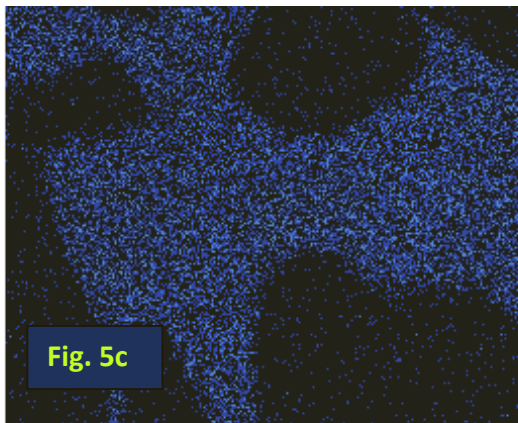
Figures 4a-d—Cross section from a AlBeCast®920 casting. Fig 4a is a high magnification SEM photo of the Al phase. It has a Widmanstatten plate structure. The dot maps indicate that the plates contain a higher concentration of Ag. This phase is believed to be the δ' phase for Al-Ag alloys.

2.1.3 AlBeCast® 930

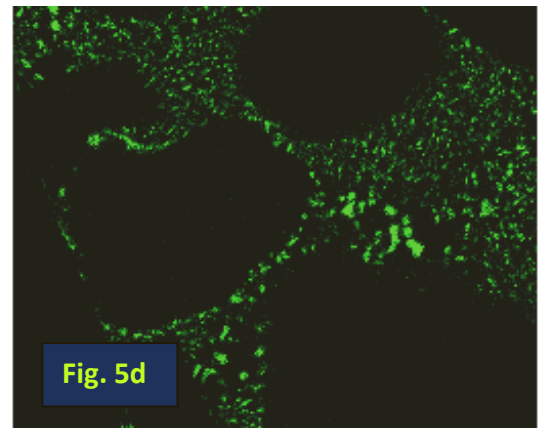
Materion's AlBeCast 930 alloy has a nominal composition of 47% Be, 4.5% Si, 2.0% Ag, 0.04% Sr (all wt %) with the balance Al. Figure 5a shows a SEM micrograph of a 930 cross section. As with the 910 and 920 alloys, the 930 has a dual-phase (Be and Al) dendritic microstructure. Figures 5b-e are x-ray dot maps showing how the alloying elements distribute themselves within the phases. Essentially the Si, Ag and Sr all go to the Al phase. The Si and Sr form a eutectic with the Al. The Ag, as before, stays with the Al phase and forms a Widmanstatten structure—this increases the alloy's strength and hardness. Unlike the 910 and 920 alloys, 930 contains no elements that form solid solutions with both Al and Be—i.e. no Ni or Co. These elements increase the strengths of the Al and Be phases, but they also affect physical properties such as thermal conductivity. By excluding these elements the 930 has a significantly higher thermal conductivity than either the 910 or 920 (Table Ib).

The 930 has a couple of advantages over the 910 and 920 alloys. First, as just explained, its thermal conductivity is much higher—186 W/m-K Vs roughly 110 W/m-K. Second, due to having a Be concentration below 50 wt. %, this alloy does not need a U.S. Department of Commerce license for export. The requirement for such a license can add time and uncertainty to the procurement of a component. Of course the reduced Be concentration also results in a decreased value for specific modulus as compared to the 910 and 920. However, it is still much higher than for most alloys. The reduction in the Be concentration also reduces the alloy's cost. Materion's 930 alloy is intended for applications requiring high specific modulus, moderate strength and high thermal conductivity.

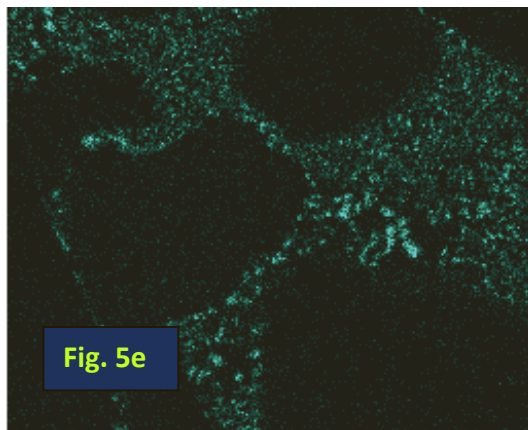




Ag La1



Si Ka1



Sr La1

Figures 5a-e—5a is a SEM photo of a AlBeCast® 930 cross section. As before, the alloy essentially has two phases Be (dark) and Al (mottled gray). 5b-Al dot map; 5c-Ag dot map; 5d-Si dot map and 5e-Sr dot map. The Ag, Si and Sr all stay within the Al phase, although the Si and Sr tend to concentrate in eutectic phases.

2.2 Casting Process Challenges

There are two major challenges with cast Be-Al alloys. First is the highly reactive nature of Be. This essentially forces one to cast under vacuum. Also the Be will reduce most oxides. This makes it more difficult to identify suitable refractory materials for making the investment shells. Second, the two major components (Be and Al), have a large difference in their solidification temperatures and low solubility for one another. As a result, Be-Al alloys solidify with two distinct phases--one nearly pure Be and the other nearly pure Al phases. This behavior produces a large “mushy” zone—i.e. the temperature range over which solidification starts and ends. Alloys with large mushy zones typically are prone to casting defects such as shrinkage porosity and hot tearing.

Materion is working with its partner, (Nu-Cast Inc of Londonderry, NH, USA), to overcome the challenges inherent with casting these alloys. Vacuum melting and pouring procedures have been developed. A refractory composition has been identified and successfully used for the fabrication of investment shells. Also Materion and Nu-Cast have developed shell designs, (gating, runners and reservoirs) that minimize the occurrence of defects. Materion is now able to produce a range of castings. Efforts continue to increase our capabilities to cast objects which are more intricate or have larger thin-walled sections.

3 Summary

Materion has internally developed two Be-Al alloys, AlBeCast® 910 and AlBeCast® 930, and offers its own version of AMS 7918 alloy which is designated as AlBeCast® 920. Together these three alloys offers customers a range of values for specific modulus, strength, thermal conductivity and cost. Materion has also developed investment casting procedures to fabricate components from these alloys. Figure 6 shows some components that have been cast using our 910 alloy. Materion is ready to begin working with customers to determine if their performance requirements can be met with our Be-Al alloys and, if so, whether investment casting is the most economical manufacturing process.



Figure 6—A variety of components that have been investment cast at Materion using AlBeCast® 910.

4 References

- (1) Binary Alloy Phase Diagrams-Vol. 1, T. B. Massalski, ASM, Metals Park, OH (1987)
- (2) Metallurgy of the Rarer Metals-7 (Beryllium), G.E. Darwin and J.H. Buddery, Pg. 313, Academic Press Inc., London (1960)
- (3) Beryllium Chemistry and Processing, ed. K. A. Walsh, ASM International, Materials Park, OH (2009)

Design of a powder metallurgical molding process for Be-Alloys

Christian Kräher

GVT

Abstract

In the process of building a fusion reactor in the future there will be an increasing demand of bigger amounts of components made of beryllium alloys. For this purpose a pilot production facility is under construction in the Karlsruher Beryllium Handling Facility (KBHF) on campus north of the Karlsruhe Institute of Technology (KIT).

The facility is made up of three basic process steps: Milling of the powder (wet), molding and sintering. The special characteristic of this process is the machining of a powder-paraffin-suspension instead of a dry, free flowing powder.

After some experimental experience there are technical solutions for the milling and the sintering process. But there are still efforts in researching the molding process.

Favored products are: Spheres with 1 – 2 mm diameter, cylinders with 1 -2 mm height and diameter and bars with 10 mm diameter and 100 mm length.

In the context of a bachelor thesis single action pressing in a die was tested on suitability to boundary conditions. With the results die pressing turned out to be not suitable to the wet conditions of the process. The main issue of this process is the handling of a wet powder, which causes the following problems:

- A very difficult filling of the mold
- Extreme oscillations in the density allocation of compacts
- A lack of reproducibility of density and size of the compacts because of the use of a multi cavity mold

In Fact, without an automated filling of the mold the productivity of the process is too low. However, the effort of developing the filling process obviously is too extensive because of the exotic application and therefore the general lack of know how. Furthermore as a result of the small dimensions of the favored products combined with the necessary high pressing force, the endurance of the filigree tools decreases steeply.

As an alternative, extrusion is about to be tested on suitability for the molding process.

Extrusion is expected to have following advantages compared to pressing in a die:

- An easier filling of the mold due to a bigger diameter of the cavity

- A higher reproducibility (no multi cavity tools)
- A more constant density allocation
- A higher productivity
- Massive tools → higher endurance
- An easier maintenance

The objective is, to be able to make a decision in context of machinery acquisition in September 2012 with the results of the testing.

1. Introduction

In the process of building a fusion reactor (ITER) in the future there will be an increasing demand of bigger amounts of components made of beryllium and beryllium alloys (beryllides). Beryllium and beryllide is particularly suitable for the use in the nuclear field because it

- reflects/multiplies neutrons,
- is extremely temperature resistant,
- is heavy radioactive activated.

For the Test Blanket Modules (TBM) which will be used in ITER, there will be a large demand of beryllium pebbles. Because of isotropic material properties, powder-metallurgical (pm) beryllium is the preferred material. For this purpose a facility is under construction in the Karlsruher Beryllium Handling Facility (KBHF), for pm production of beryllium and beryllide parts.

1.1 *Beryllium vs. Beryllide*

An extensive overview on beryllium chemistry and processing was published recently by Walsh [1], including also beryllides. Beryllides are expected to release better tritium. Higher melting points could make beryllides attractive for the use as plasma facing components (PFC). Beryllides are expected to have a better oxidation resistance at higher temperatures. However, beryllides are more brittle than beryllium.

TABLE I. PHYSICAL AND THERMO-MECHANICAL PROPERTIES

Material Property	TiBe ₁₂	VBe ₁₂	Be [23]
Crystal structure	tetragonal	tetragonal	hexagonal
Melting point, (°C)	1600	1700	1283
Density, (g/cm ³)	2.26 [1]	2.37 [24]	1.85
Vapour pressure			700°C: 10 ⁻⁸ 900°C: 10 ⁻³
Young's elastic modulus, (GPa)	20°C: 280 1260°C: 21.69 [1, 25]	20°C: 300 [24]	20°C: 300 650°C: 260
Ultimate tensile strength, (MPa)	1260°C: 30-90 1371°C: 24 1510°C: 16-21 [1]	20°C: 140 [24]	20°C: 580 500°C: 280
Compressive strength, (MPa)			20°C: 1530
Thermal expansion coefficient, (10 ⁻⁶ /K)	100°C: 13.2 500°C: 16.8 [FZK]	100°C: 14.5 500°C: 17.1 [FZK]	100°C: 11.5 500°C: 15.6
Thermal conductivity, (W/m/K)	100°C: 41 500°C: 38-41 [7, FZK]	100°C: 38 500°C: 35 [FZK]	100°C: 155 500°C: 100
Thermal creep		1150°C exps [24]	
Microhardness, (GPa)	20°C: 10 600°C: 8 [26]	20°C: 11 600°C: 8 [26]	20°C: 2.25
DBTT (°C)	880, [26]	790, [26]	
Fract toughness, (MPa√m)		20°C: 0.8 [24]	20°C: 9.8

Fig. 1-1: Physical and thermo-mechanical properties [2]

Fig. 1-2 (from [2]) shows that the thermal conductivities of beryllide materials are significantly smaller than that of beryllium. However, this effect is much less expressed considering pebble beds in helium atmosphere, compare Fig. 1-3 (from [2]).

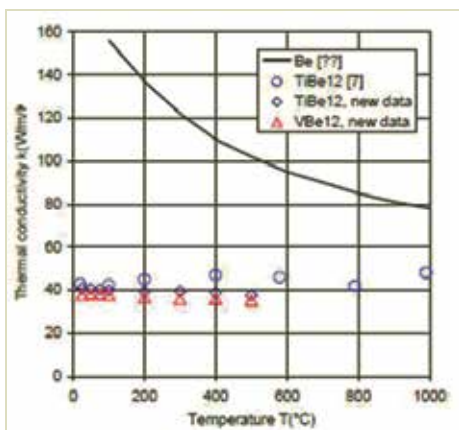


Fig. 1-2 [2]

TABLE II. CALCULATED PEBBLE BED THERMAL CONDUCTIVITY

A_c/A	$k_{pb\ Be}$	$k_{pb\ Beryl}$	$k_{pb\ Beryl}/k_{pb\ Be}$
0	2.33	2.2	0.94
0,001	3.76	2.82	0.75
0,002	4.9	3.32	0.67

Fig. 1-3 [2]

1.2 Process

The production process at the KBHF consists of three essential process steps

1. Mixing and milling of beryllium powder with tetradecane (liquid)
2. Molding, which has not defined in detail yet
 - Two possibilities:
 - Production of semi finished products (rods) for the rotating electrode method (state of the art in pebble production)
 - Direct pebble production
3. Sintering in a tube furnace

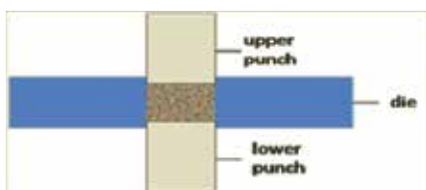
1.3 Challenges

On our way to a suitable solution for the molding process there are some important challenges that have to be managed. The most challenging aspect is the fact that the basic material is a suspension and not a dry powder. For this issue there is a general lack of knowledge and experience, so we have to develop a lot on our own. Another aspect is the space limitation in a glove box. Furthermore the high affinity of Be and Ti to oxygen causes additional efforts in handling the material.

To be able to satisfy the beryllium pebble demand for the ITER fusion test reactor, the process should be able to produce large amounts of pebbles at low cost.

2. Tested Molding Processes

1. Die pressing



2. Extrusion

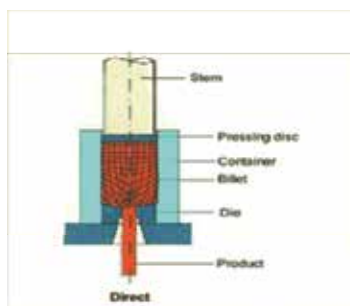


Fig. 2-1 [figure on the right from 3]

Two molding processes were tested in order to assess the suitability in respect to our specific requirements:

1. Cold die pressing for production of pebbles and cylinders (\varnothing 1 – 2mm, height 1 – 2mm)

- Extrusion of capsules filled with powder for production of rods (\varnothing 10mm, 100mm length)

For the screening tests, instead of beryllium, non-toxic titanium powder was used.

2.1 Cold Die Pressing

Fig. 2-2 shows the design of the multi cavity tool, which was used for the cold die pressing tests. A multi cavity tool was used because of the desired minimum output of one pebble/sec. It is a simple tool with four upper punches, four lower punches and a plate with four holes which functions as a die (all made of hardened steel). The punches have a diameter of 3 mm. The products are cylinders with diameters and heights of 3 mm (in the tests we did not intend to produce pebbles yet). A 50 kN hydraulic press was used.

Experimental procedure:

- Filling the holes with suspension
- Pressing
- Baking out compacts (400°C, under vacuum) or baking out + sintering (1000 - 1300 °C, under vacuum)
- Determination of density → weighing compacts in air, coating compacts with wax, again weighing in air, weighing in tetradecane → density determination with the principle of archimedes (from [4])

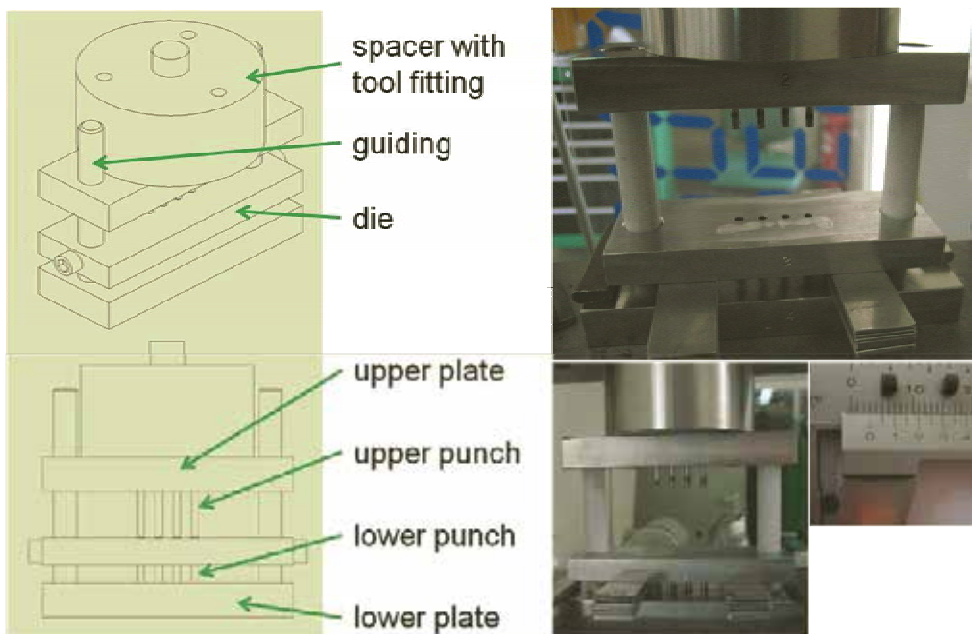


Fig. 2-2

2.1.1 Cold Die Pressing: Results

Fig. 2-3 shows the measured relative density of the compacts as a function of the used pressing forces 10 kN, 20 kN, 30 kN, and 40 kN. The average relative density increases, as

expected, with increasing pressing force. However, there is a strong variation of up to 30 % in the compact density.

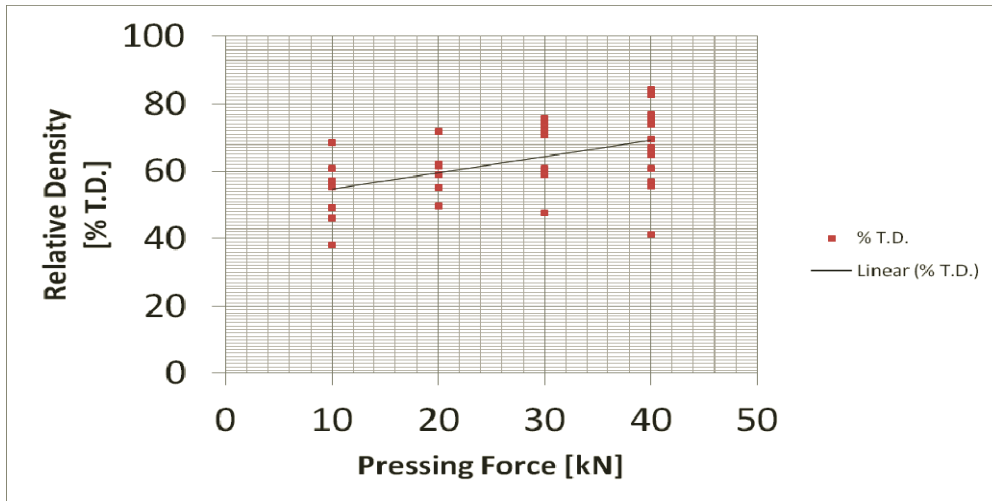


Fig. 2-3

Fig. 2-4 shows the density variations with the heat treatment temperature as a parameter. Green: Mean value of relative density of compacts which were baked out at 400-500°C for 2-3.5 h. Blue: Mean value of relative density of compacts which were baked out at 500°C for 2 h and sintered at 1000°C for 2 h. Red: Mean value of relative density of compacts which were baked out at 400°C for 0.5 h and sintered at 1200-1300°C for 2 h. The figure shows that the density variations are not dependent on heat treatment temperature.

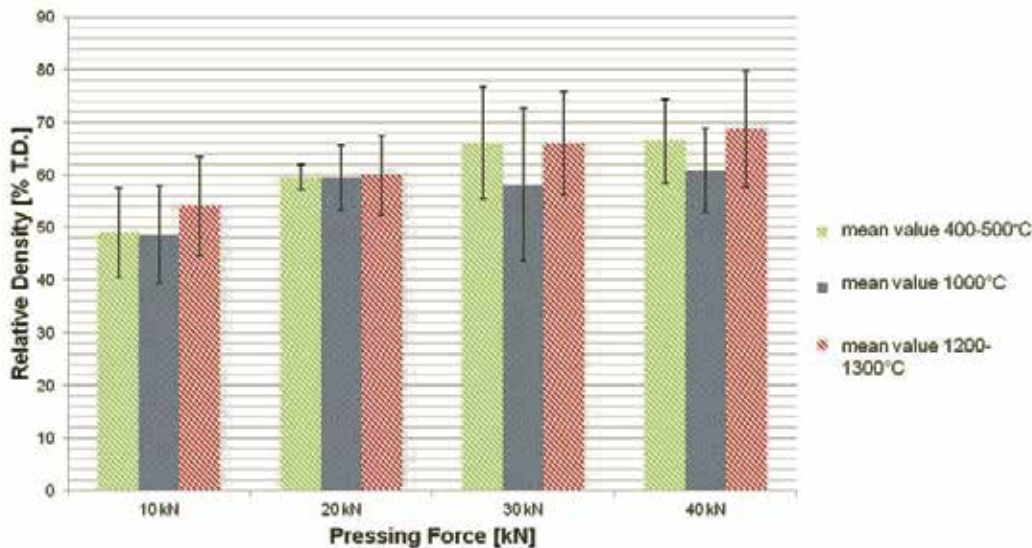


Fig. 2-4

2.1.2 Cold Die Pressing: Conclusions

In our opinion, the density variation is mainly caused by three effects:

- Manual filling of the multi-cavities with the suspension:
Differences in mass occur and therefore also in the composition of the material between each filling process. These differences cause different densities and size of compacts. Moreover, a disproportionate filling of the 4 cavities causes a variation of load and consolidation of the powder and therefore an inhomogeneous density distribution. This is the expected reason for differences in density even between the compacts of one pressing batch. Small dimensions of the cavities increase this variation effect.
- Removal of the liquid part of the suspension during pressing:
In connection with the removal of fluid there is also an unavoidable loss of powder-particles which is not calculable. In case of small dimensions this powder leakage has a significant effect on size and density of compacts.
- Fabrication tolerances of the multi-cavity tool worsen the whole situation additionally.

The gained experiences affect the applicability of the process:

- In terms of reproducibility and productivity (1 pebble/sec), an automated filling of the mold instead of a manual one is necessary. But because of a lack of knowledge the development of an automated filling device would be too extensive and costly for GVT.
- Even if the filling process could be controlled there is a quite high probability that the leakage of powder during pressing will not allow to produce compacts with a density variation between desired tolerances with a multi cavity tool.

In summary, the die pressing does not fulfill the anticipated requirements. Therefore, we decided to change our focus from the direct pebble production to the processing of semi finished products for the rotating electrode method.

2.2 Extrusion

With the results of the experiments of cold die pressing we could deduce requirements for an alternative molding process. The following points motivated the decision to choose extrusion as an alternative:

- We can produce electrodes for the rotating electrode method.
- Extrusion allows an easier filling of the mold due to a bigger diameter of the cavity.
- We expect a higher reproducibility of size and density of compacts because we have a single instead of a multi cavity tool with significantly bigger dimensions.
- Another point is that extrusion is performed with massive tools. Therefore we expect a higher endurance.

For the testing of extrusion molding we started a cooperation with the Extrusion Research and Development Center (ERDC) at the TU Berlin [3].

2.2.1 Cold Extrusion

At the ERDC Berlin we tried to combine the two steps, i) extraction of the suspension, and ii) extrusion at room temperature. We put the wet titanium material into a small extrusion press cavity with 30 mm diameter, moved the punch into it and tried to push the material through a 2 mm hole. Indeed it was not possible to push it through, but the material consolidated by extracting the liquid from the solid part of the suspension. It was not possible to extrude the material at room temperature even with the maximum pressing force of 500 kN, however after this consolidation the produced compact had a relative density of nearly 80 % T.D. With this result we plan to extrude in the future at higher temperatures to enhance formability.



Fig. 2-5: Cold Extrusion Tests

2.2.2 Hot Extrusion: Process Steps

The production process of rods by extrusion differs from the first presented production process of cylinders/pebbles by die pressing.

The considered process includes following steps:

1. Mixing and milling of powder with tetradecane (liquid).
2. Filling a steel capsule with the suspension.
3. Extraction of the liquid part in a hydraulic press.
4. Closing of the capsule by tungsten-inert gas welding.
5. Removal of the residual content of the liquid by baking out the capsule (in step 4, the capsule is not closed air-tight, there is a pipe with 8 mm in diameter which is connected to the capsule's lower cover plate by welding).
6. Insertion of the capsule into a 2nd containment (also a steel capsule), closing by electron beam welding (EBW).
7. Heating up the specimen to 1000°C and extrusion.

2.2.3 Hot Extrusion: Step 3

Fig. 2-6 shows a prototype tool which was designed for the extraction tests. In the center of the tool there is a capsule made of a steel pipe with 70 mm outside-diameter. There is a

welded lower cover plate with a 8 mm hole in which a small pipe is welded. Additionally there is a deepening in the cover plate where we put in a disk of sintered metal with a thickness of 2-3 mm. To fill the whole capsule with extracted material we have to fill the tool with suspension of a volume which is more than the double of the capsule volume. After filling the cavity with suspension we move the punch with the Teflon (PTFE) pressure disk at the front down into the cavity. By pressing the fluid out of the cavity through the porosities of the sintered metal the material will be extracted, consolidated and simultaneously jacketed inside the capsule.

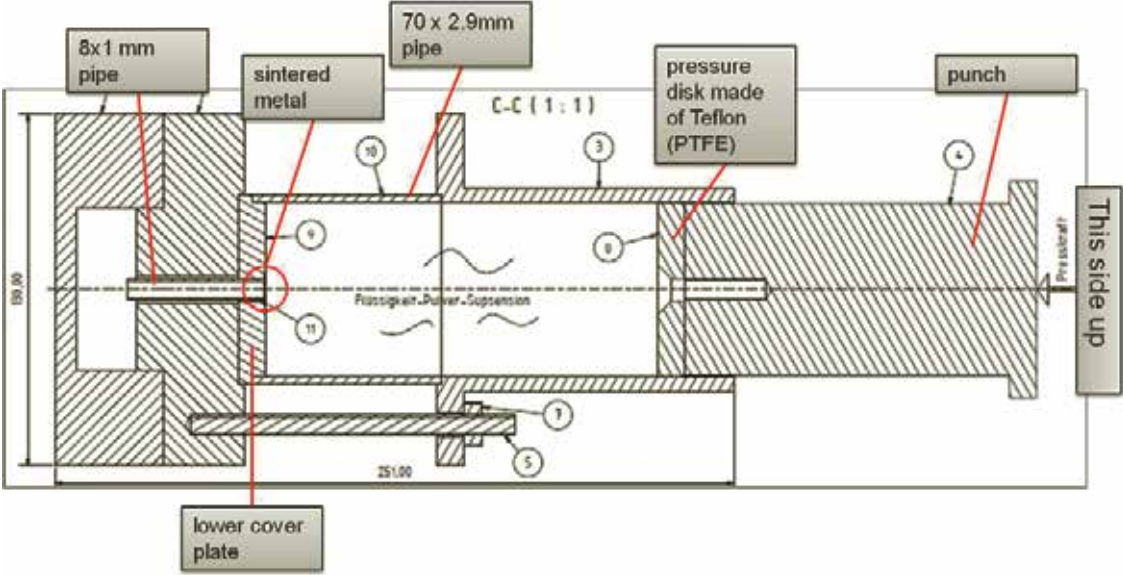


Fig. 2-6

Fig. 2-7 shows the prototype tool and its components. All components are made of stainless steel, except the pressure disk which is made of Teflon (PTFE). After extraction the upper cover plate will be welded on the capsule.



Fig. 2-7

2.2.4 Hot Extrusion: Step 5, Baking Out

After extraction, the next step is baking out the capsule. For 6 hours, at a temperature of 400°C the residual content of tetradecane is evaporating. Fig. 2-8 shows the assembly for this process step. The capsule is put in a small furnace. The 8 mm pipe of the capsule is connected to a vacuum pump. Interconnected is a heat exchanger to condense and accumulate the evaporated tetradecane so that it can be recycled. After baking out, the pipe has to be squeezed to tighten the capsule (which is under vacuum) from the environment.

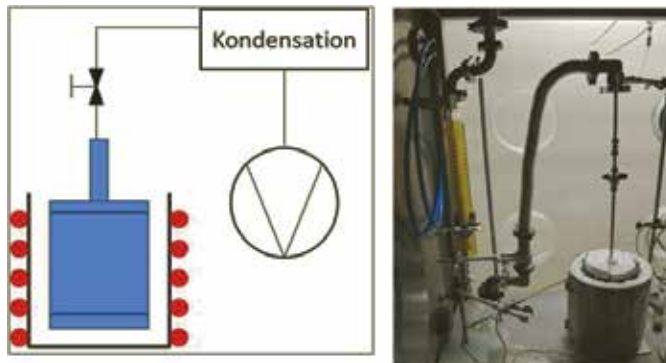


Fig. 2-8

2.2.5 Hot Extrusion: Step 6 and 7

To ensure the safety for the environment and the material we decided to put the capsule into another, bigger capsule (4 mm thickness) which functions as second containment. The second containment is welded with the electron beam welding method. This happens in a vacuum atmosphere, so that there is only few oxygen left that could affect the material or the surface of the capsule (scaling). The produced specimen – consisting of two capsules - will be transported to the ERDC Berlin. Here it will be heated up to 1000°C and extruded in a press with 8 MN press capacity. The diameter reduction will be from 80 mm diameter down to about 15 mm. The produced rods will be cut to defined length and machined to remove the steel jacket. The end product will be rods of 10 mm diameter and 100 mm lengths.



Fig. 2-9: Second Containment, capsule, extraction tool

2.2.6 Hot Extrusion: Present Results

Extraction and jacketing has successfully been tested with titanium powder as non toxic testing material. We produced an extracted block, see Fig. 2-10, that is stable and has an approximated relative density of about 60 % T.D. A higher press capacity will increase green density after extraction. The components for upgrading the press will be installed after we will have the results of the first extrusion (results are expected end of 2012).



Fig. 2-10

2.2.7 Hot Extrusion: Perspectives

The devices for extraction and the baking out process have been successfully tested. Baking out and hot extrusion of the first capsule with titanium powder will be tested October 2012. Testing with beryllium will start in January 2013. The next capsule prepared for extrusion in February 2013 will contain beryllium-titanium powder with a titanium jacket in order to separate the powder from the steel wall.

With this process we hope to be able to produce electrodes for pebble production.

3. References

- [1] Walsh, Beryllium chemistry and processing, ASM International, 2009
- [2] Reimann et al., Beryllides for fusion reactors, Sofe-Conf, San Diego, June 09
- [3] <http://www.fzs.tu-berlin.de/>, homepage Extrusion Research and Development Center of the TU Berlin
- [4] Schatt, Pulvermetallurgie, Springer, Dresden 2007

Commissioning and Calibration of the ExCEED Facility for Beryllium Dust Explosions

P. W. Humrickhouse, R. J. Pawelko, L. D. Moore-McAteer, L. C. Cadwallader, B. J. Merrill, and M. G. Jones

Idaho National Laboratory

Abstract

In order to assess the risk of dust explosions in future fusion devices that may use beryllium as a plasma facing material, the Experimental Chamber for Evaluation of Exploding Dust (ExCEED) has been commissioned at the Safety and Tritium Applied Research (STAR) facility at the Idaho National Laboratory. The experiments are performed in a 20 liter spherical pressure vessel manufactured by Kühner AG designed specifically to contain dust explosions. While a number of facilities operate such devices, the toxicity of beryllium dust necessitates complete secondary containment; in ExCEED, the vessel is located inside a glovebox to achieve this. We describe here the commissioning of the facility and an initial round of calibration experiments with a standard niacin powder. The explosion indices (maximum pressure and volume-independent maximum rate of pressure rise) of niacin measured in ExCEED are $P_{max} = 8.6$ bar and $K_{max} = 236$ bar·m/s ($dP/dt_{max} = 869$ bar/s). These are well within plus or minus 10% of the mean values from all other facilities that have reported their data, which is the established calibration criterion. Having completed the calibration of ExCEED, the facility is now ready for beryllium operation.

1. Introduction

Dust explosions, long known to be a safety issue in agriculture and industry [1], are also a potential safety concern for next-step magnetic fusion devices in which large quantities of dust are expected to be generated by plasma-surface interactions (see [2] for a recent review of dust related issues in fusion). In order to better assess this risk of dust explosion, various plasma facing materials (such as carbon and tungsten) have been the subject of dust explosion experiments [3]-[4]. Since beryllium is also a candidate first wall material, a complete understanding of the explosion risk necessarily requires some data on beryllium; however, the necessarily large quantities (~100's of grams) of dust required for explosion testing make such experiments extremely challenging due to the well known toxicity of inhaled beryllium dust. The difficulties associated with handling large quantities of beryllium

make it impractical or impossible for many facilities to do so, but Idaho National Laboratory (INL) and the Fusion Safety Program (FSP) in particular are experienced in handling beryllium at the Safety and Tritium Applied Research (STAR) facility (see, e.g., [5]). In order to assess the beryllium dust explosion risk, the Experimental Chamber for Evaluation of Exploding Dust (ExCEED) has been commissioned in the STAR facility at INL.

2. Facility Description

2.1 Kühner 20 Liter Sphere

The characteristics of a dust explosion (such as the maximum pressure) are in general dependent not only on the properties of the dust, but also on the test method (volume, ignition method, degree of mixing, etc.). This has led to a standardization [6] of vessels and methods for dust explosion testing, and the 20 liter sphere (such as that manufactured by Kühner AG [7]) is one such standard; it is operated by at least 70 facilities around the world [8], including DUSTEX at KIT and ExCEED at INL.

A schematic and a photo of the INL Kühner sphere are shown in Fig. 2-1; it consists of two volumes connected by a pneumatic outlet valve. The standard procedure for a single explosion is to load the desired quantity of dust into the 0.6 liter dust container and pressurize it to 21 bar (absolute). The sphere itself, which is 20 liters in volume, is evacuated to 0.4 bar (absolute). Mixing the two results in a total of 20.6 liters of the dust/air mixture at 1 bar initial pressure. The dust is dispersed with a “rebound nozzle” shown in the schematic, the outlet valve closes, and ignition in the 20 liter volume is initiated with chemical igniters of a specified energy after a fixed delay (typically 60 ms), chosen to allow sufficient time for the pressures in the two volumes to equilibrate, but no further time for settling or other transport to result in an inhomogeneous dust cloud. Pressure measurements are made with two Kistler pressure sensors (which, along with the control units and KSEP software, were provided by Kühner), immediately adjacent to each other at the right side of the sphere, near the vacuum ball valve. This valve is connected to a vacuum pump which is used to pull partial vacuum on the sphere before each test; the outlet ball valve at the opposite side opens the sphere to exhaust gas and particulate after each test and is connected directly to a high efficiency particulate air (HEPA) filtered vacuum cleaner in ExCEED. The double-walled vessel is water-cooled to rapidly reduce its temperature following each test and ensure a uniform temperature prior to each explosion.

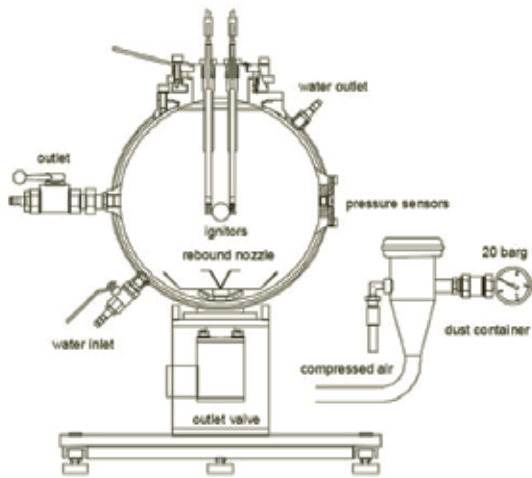


Fig. 2-1. Schematic [7] and photo of the Kühner 20 liter sphere in ExCEED. The vacuum ball valve and vacuum gauge, not shown in the schematic, are visible at the right in the photo.

Though a number of standard tests can be performed in the Kühner sphere, at present we are primarily concerned with measuring the explosion indices that characterize beryllium dust. In order to determine the explosion indices, a series of explosions are carried out with different concentrations of the same powder. We perform the tests in the intervals prescribed by Kühner [7], beginning with 60 g/m^3 ($1.2 \text{ g} / 20 \text{ l}$), continuing with 125 g/m^3 ($2.5 \text{ g} / 20 \text{ l}$), 250 g/m^3 ($5 \text{ g} / 20 \text{ l}$), and in 250 g/m^3 ($5 \text{ g} / 20 \text{ l}$) increments from there. An example pressure trace from a 750 g/m^3 niacin test is shown in Fig. 2-2. Both the maximum pressure (P_m) and maximum rate of pressure rise (dP/dt_m) are identified by the software. Note that P_m is always given in bar gauge (relative to 1 bar absolute), according to convention.

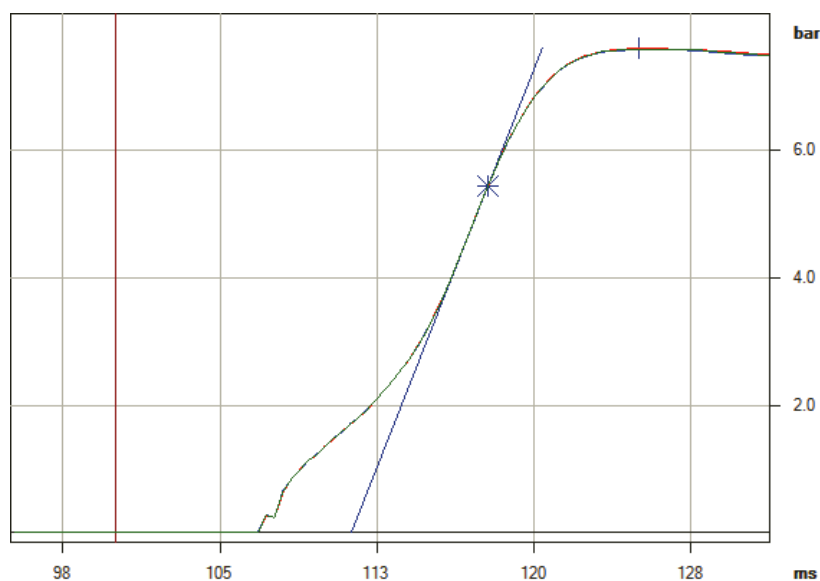


Fig. 2-2. A representative pressure transient during a 750 g/m^3 niacin explosion.

The values of P_m and dP/dt_m extracted from each explosion initially increase with the dust concentration, but eventually peak and begin to decrease with the addition of more dust, which acts as a heat sink when the reactions are oxygen starved. The highest of these values obtained over the entire range of concentrations are the explosion indices P_{max} and dP/dt_{max} , the identification of which is the primary objective of this work. Because dP/dt_{max} is dependent on the volume of the explosion chamber, for comparison between different devices (e.g. the 1 m³ sphere and 20 l sphere) the following, volume-independent parameter K_{max} , a measure of the explosion violence, is typically used instead:

$$K_{max} = V^{1/3} \left(\frac{dP}{dt} \right)_{max} \left[\frac{\text{bar} \cdot \text{m}}{\text{s}} \right] \tag{2.1}$$

In keeping with the practices recommended by Kühner, we repeat three times the explosion at the concentration where P_{max} and K_{max} are found to occur, as well as the next lowest and next highest concentrations. The reported value for the dust in question is the average of the three. K_{max} is taken as an indication of the explosion violence, and the following qualitative categories have been established [9]:

Table 2-1. Classification of explosive dusts (St = Staub, “dust” in German).

Explosion class	K_{max} (bar·m/s)	Characteristic
St 0	0	No explosion
St 1	0 to 200	Weak explosion
St 2	200 to 300	Strong explosion
St 3	> 300	Very strong explosion

2.1.1 Igniters

As noted previously, standardization requires uniformity in all aspects of the explosion test, and the ignition is no exception. In the Kühner sphere, two igniters of identical energy are wired facing opposite each other on the leads extending from the lid of the sphere. For measurements of the explosion indices P_{max} and K_{max} , these are to be 5 kJ each, for a total of 10 kJ ignition energy. Until relatively recently, there was only one manufacturer of suitable igniters, Sobbe GmbH in Germany. Because the Sobbe igniters contained some toxic materials in the form of lead, barium, and barium compounds, and were also fairly susceptible to accidental ignition by electrostatic spark or friction, Simex Control of the Czech Republic have developed a replacement. The Simex igniters contain environmentally benign materials, and are much more resistant to accidental ignition, see Table 2-2. A series of

tests with different dusts and at different facilities has verified that the Simex igniters give results no different than Sobbe [10]-[11], a fact further confirmed by a number of participants in the recent calibration round-robin test with Niacin powder in the Kühner sphere [8]. In light of these facts and the heightened consequences of an accidental ignition when beryllium containment is imperative, we used Simex igniters in all tests.

Table 2-2. Comparison of Sobbe and Simex 5 kJ chemical igniters [10].

Parameter	Sobbe	Simex
ESD sensitivity (μJ)	10-20	10,000-20,000
Friction sensitivity (g)	200	4,000
Safety current (A)	0.18	0.4
Toxic materials:	Yes	No

Because the risk of accidental ignition still must be mitigated, numerous safety precautions were taken to minimize static electricity. All components involved in the testing were grounded (including the operators, by a wrist strap as shown in Fig. 2-3), igniters were handled only two at a time and transferred in ESD-safe Mylar bags, and a pulsed DC anti-static bar (Cole Industries) is mounted in the handling area and operated continuously with alternating polarity.



Fig. 2-3. Wiring igniters in ExCEED.

2.2 Glovebox

In order to contain all beryllium dust used in future explosion tests, The Kühner sphere and all dust handling operations are located in a Vacuum Atmospheres DRI-LAB He series glovebox. Because removal of the lid from the sphere requires considerable clearance, an addition to the glovebox had to be made to accommodate the required height. A custom fabricated extension (the “attic”) was added in place of one of the external light fixtures for this purpose. The attic section includes swiveling metal hooks so the lid can hang at the top during wiring of the igniters and cleaning. Since the containment provided by the glovebox was not necessary during the niacin calibration testing, this was carried out without gloves and with only one window in place (as a shield while wiring igniters, Fig. 2-3). The glovebox as configured for niacin testing is shown in Fig. 2-4.



Fig. 2-4. The ExCEED facility during niacin calibration testing.

3. Niacin Calibration

As a means of calibration, and in order for facilities operating a Kühner sphere to identify any issues that may exist with their instrumentation or test procedures, Kühner provides

for a calibration-round-robin (CaRo) test to be conducted by all owners of the device every two years. Since our sphere was received in November 2011, it was accompanied by the powder and instructions for participation in CaRo11. Since adequate work controls (including preparations for beryllium operation) had to be devised and implemented, our facility was not ready for operation until 2012, at which time CaRo11 had already been completed and the results published [8], so ours were not able to be included. On the other hand, the results of tests in 69 other facilities are readily available for comparison with ours. We have performed the test series as instructed [7], the results of which are summarized in this section.

The standard powder provided by Kühner for this calibration testing is niacin, otherwise known as vitamin B₃ (C₆H₅NO₂) or nicotinic acid, a white (Fig. 3-1), odorless powder. Some basic information about the size distribution of the particles is provided: the median diameter is 19 μm, with 10% of particles < 4 μm and 90% < 83 μm.

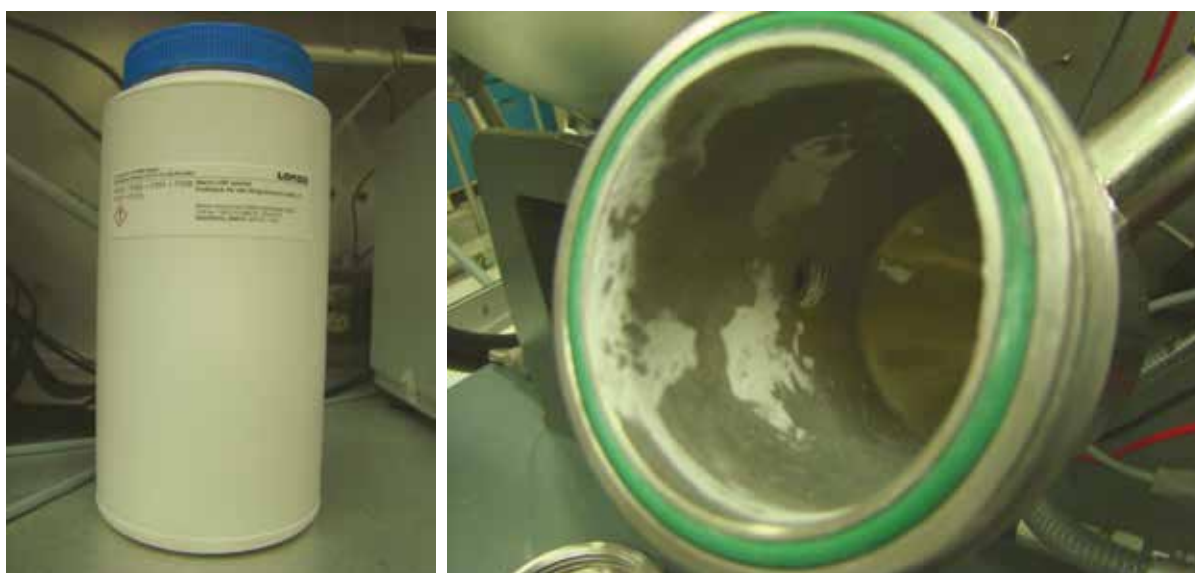


Fig. 3-1. Niacin powder as packaged (left), and deposited on the inside of the dust container (right). The (unoxidized) powder is white.

Qualitative observations after each test indicated the increasing explosion violence as the mass was increased in the approach to the peak. This was evident in the damage to the remains of the igniters themselves (Fig. 3-2), and also to the insulators to igniter leads, which were initially white but became permanently fouled over the course of the testing (Fig. 3-3). A black film coated all interior surfaces after each niacin explosion (Fig. 3-4), which had to be removed by wet-wiping; it did not consist of loose material that could be easily removed by vacuuming as recommended by Kühner.

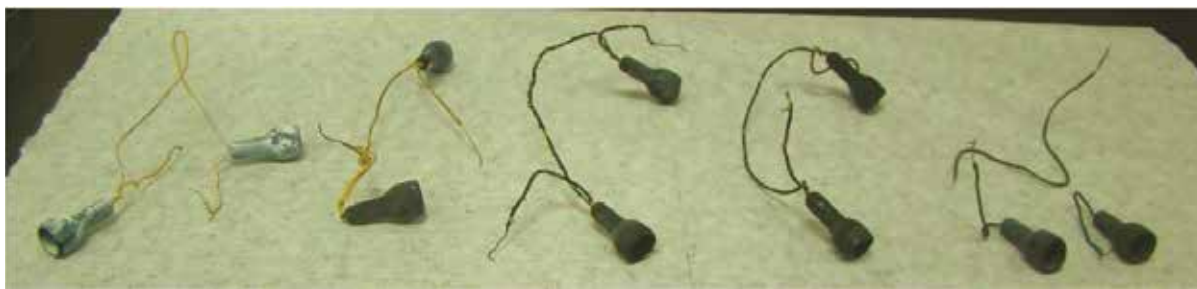


Fig. 3-2. Damage to igniters during niacin testing. From left: 0, 60, 125, 250, and 500 g/m³ niacin. Note that without dust, the igniters are only covered with a white film and are not charred. The yellow coating on the wires remains intact until 125 g/m³, at which point it melts. At 500 g/m³, they have separated into several pieces.

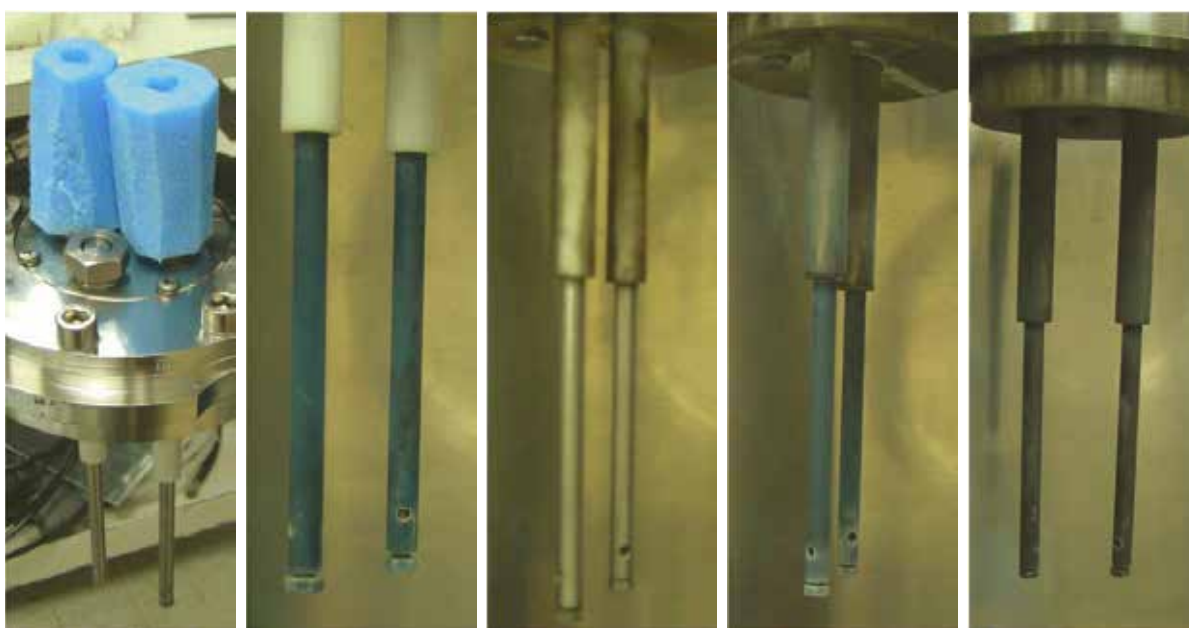


Fig. 3-3. Progression of fouling on the igniter lead insulators, the top portions that are initially white, beginning prior to first use at the time of receipt (left). Note the blue color of the lower metal portion of the leads in the second and fourth pictures (center left and center right), which was characteristic of, and unique to, a dust loading of 250 g/m³ (5 g / 20 l) niacin. In the center photo, the metal portion of the leads has been wiped down, and they were similarly cleaned after the other photos were taken (and after all other tests), but the discoloration of the insulators was permanent.

During the course of operation, it became apparent that even though any remaining loose particles were being effectively filtered during HEPA vacuum cleaning after each explosion, some gaseous combustion products were entering the room. Subsequent analysis of filtered exhaust gases remaining in the sphere after a 500 g/m³ (10 g / 20 l) explosion revealed the mixture to contain approximately 19% CO, 8% CO₂, 5% H₂, and the balance presumably N₂. Only traces of other gases (including oxygen) were present. A ventilated enclosure for the vacuum cleaner was added at this time, as well as a 0.01 μm Matheson filter in the vacuum

pump line, and in subsequent tests exhaust was removed with the vacuum pump prior to vacuum cleaning (as was intended, for other reasons, during beryllium operation).

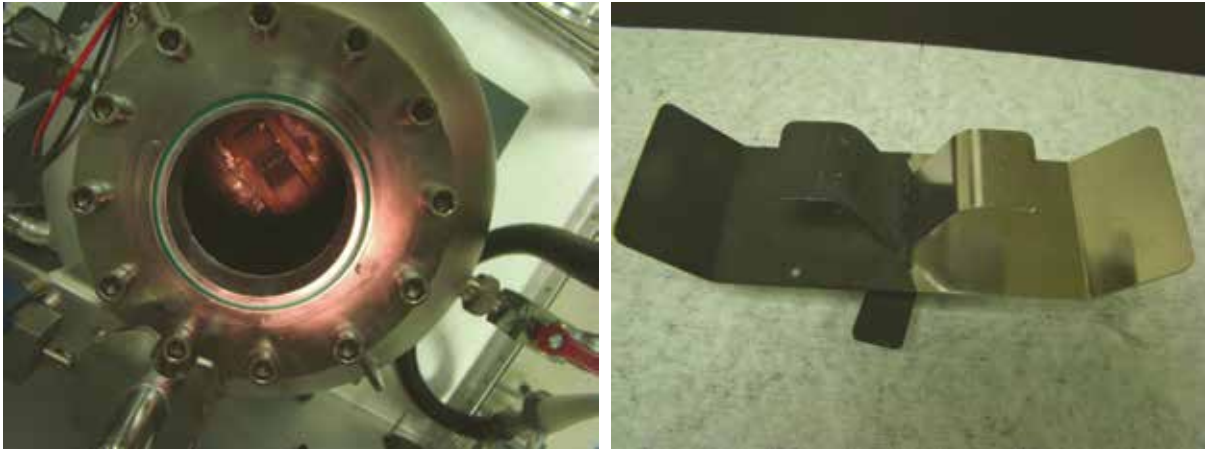


Fig. 3-4. The black film coating interior surfaces of the sphere following a niacin explosion. Half of the rebound nozzle, visible in place at the bottom of the sphere at left, has been cleaned (with water) at right.

4. Results and Future Work

14 tests were required to identify the explosion indices of the niacin powder; the measured values of P_m and dP/dt_m for niacin are plotted in Fig. 4-1 and Fig. 4-2. Many of the dP/dt_m values were not correctly identified by the KSEP software due to pressure oscillations during the firing of the igniters, prior to the actual dust explosion. This problem has been noted for both Simex and Sobbe igniters by other users [8]. In these cases, the correct dP/dt_m was identified “manually” by a linear fit to no less than seven data points (a span of 2.4 ms). One test was so plagued by such oscillations throughout the pressure transient that meaningful identification of dP/dt_m was not possible, and so this point had to be repeated.

On each pass, P_{max} was found to occur at 500 g/m^3 . In two of the three passes, dP/dt_{max} was found at 500 g/m^3 , and at 750 g/m^3 in the other. Averaging the three values for each, we find $P_{max} = 8.6 \text{ bar}$ at 500 g/m^3 and $K_{max} = 236 \text{ bar}\cdot\text{m/s}$ ($dP/dt_{max} = 869 \text{ bar/s}$) at 583 g/m^3 . Both values are within the 10% (required for calibration) of the mean of all facilities, reported as $P_{max} = 8.1 \text{ bar}$ by 505 g/m^3 and $K_{max} = 243 \text{ bar}\cdot\text{m/s}$ by 623 g/m^3 in [8]. A relative comparison between our results and those of the other facilities is shown in Fig. 4-3 and Fig. 4-4.

With the calibration of ExCEED established, the facility is now ready to commence beryllium operations following installation and testing of the glovebox windows and gloves. The beryllium powder to be tested has been obtained from Materion Brush Beryllium and

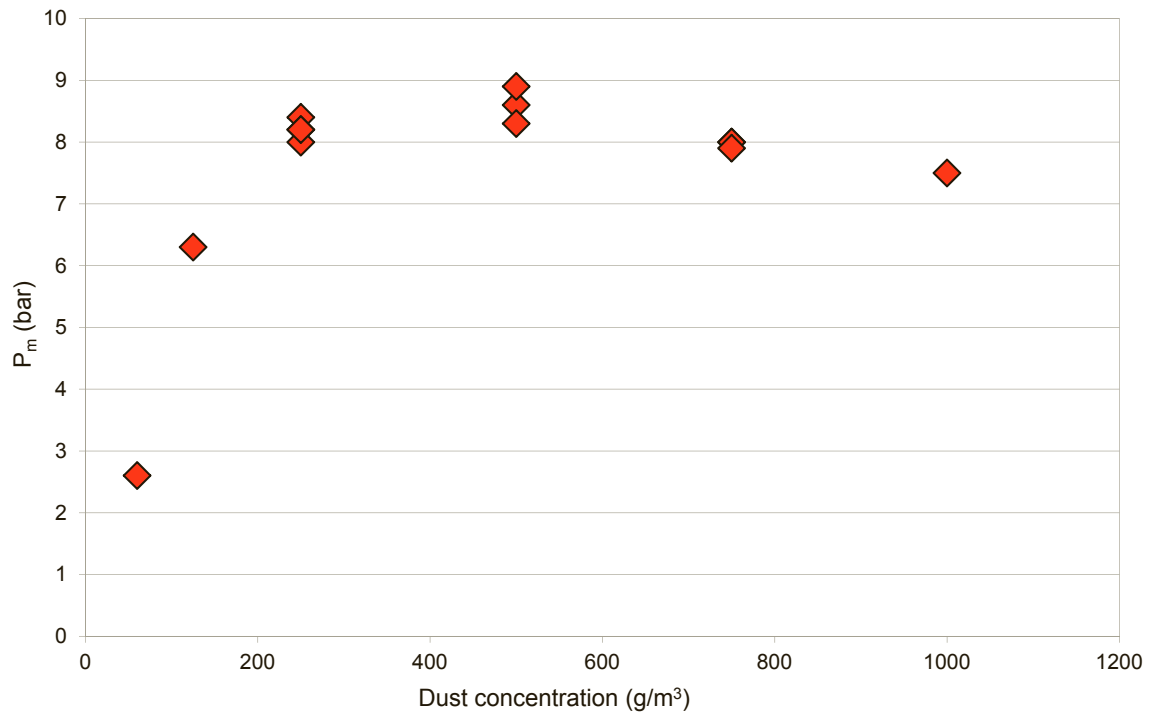


Fig. 4-1. P_{\max} for niacin dust as a function of concentration. Note that two identical points occur at $(750 \text{ g/m}^3, 8.0 \text{ bar})$.

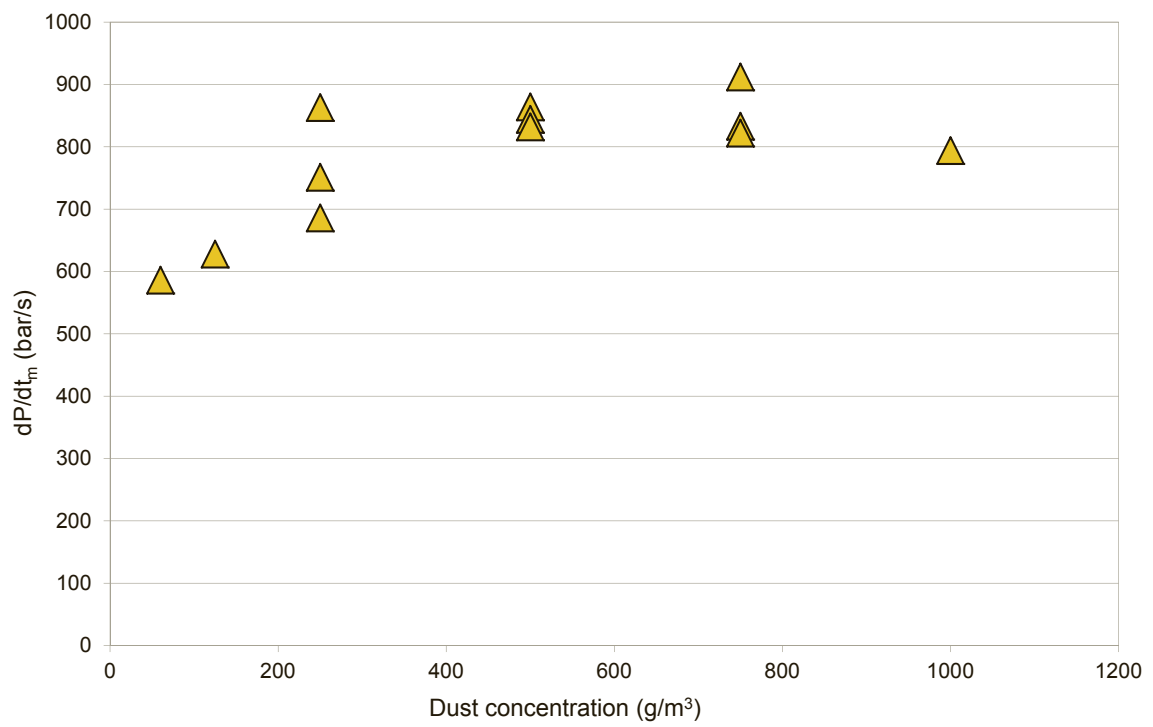


Fig. 4-2. dP/dt_{\max} for niacin dust as a function of concentration.

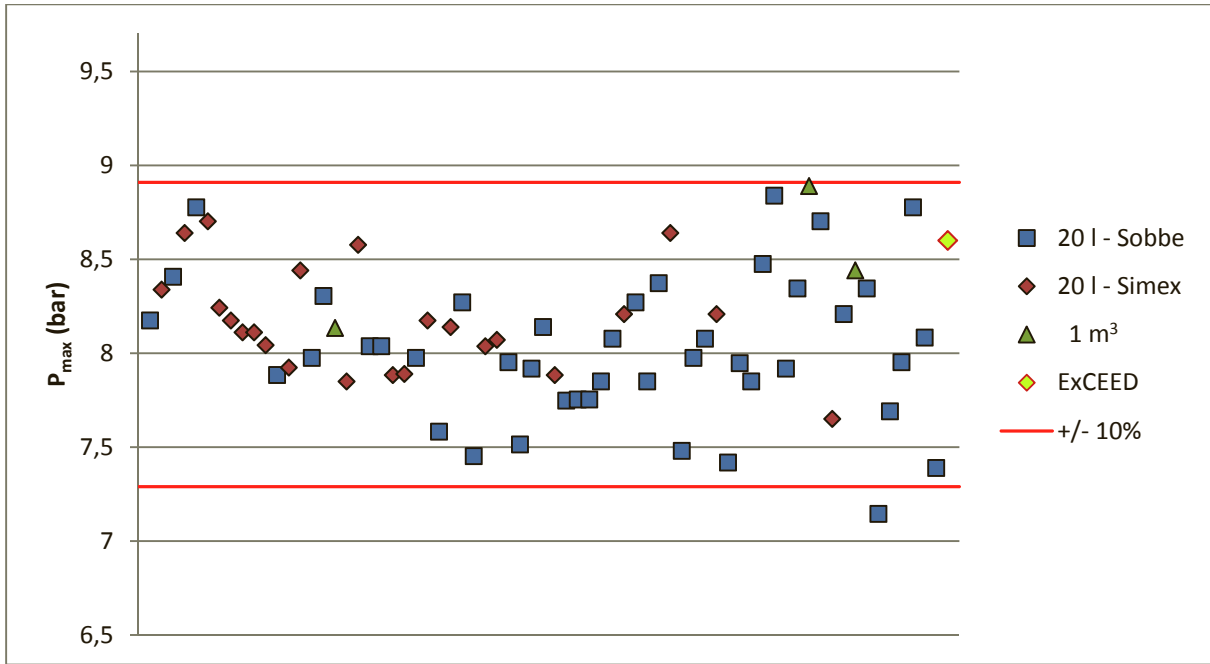


Fig. 4-3. P_{max} for niacin dust measured in ExCEED and compared to CaRo11 participants [8].

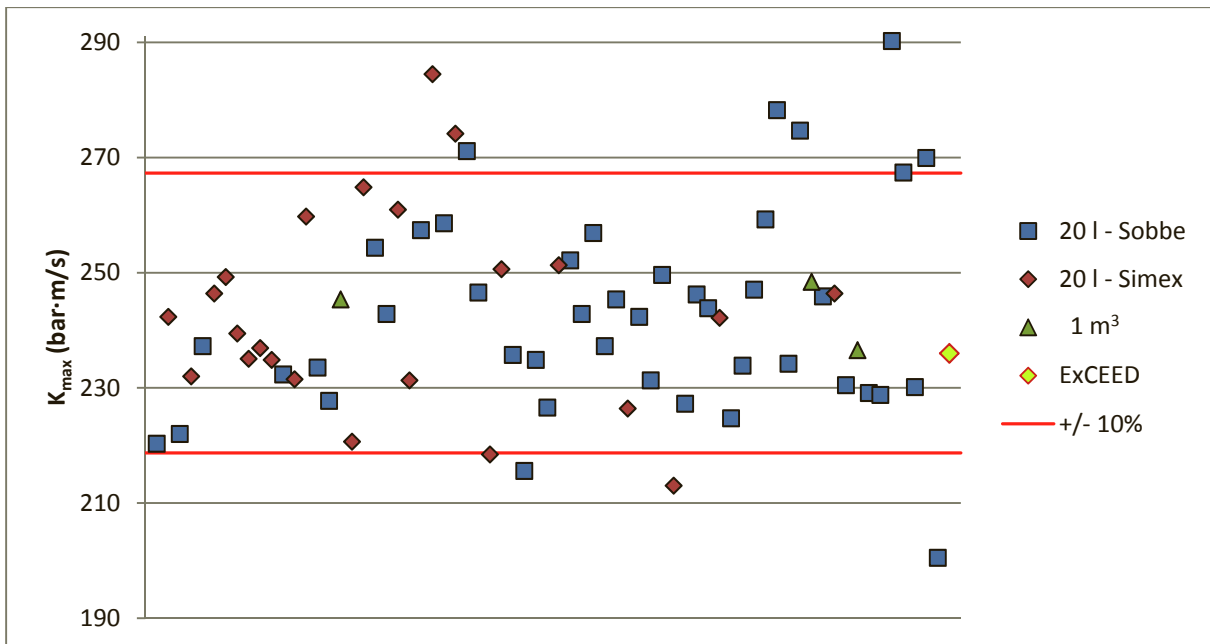


Fig. 4-4. K_{max} for niacin dust measured in ExCEED compared to CaRo11 participants [8].

Composites and has a range of particle sizes from 0.1 to 20 μm with a median of about 6 μm , reasonably representative of tokamak dust. A series of measurements identifying the explosion indices of this beryllium dust will be completed by the end of December 2012.

5. References

- [1] Bartknecht, W., *Dust Explosions: Course, Prevention, Protection*, Springer-Verlag, Berlin, 1989.
- [2] Krasheninnikov, S. I., Smirnov, R. D., and Rudakov, D. L., *Dust in magnetic fusion devices*, *Plasma Physics and Controlled Fusion* **53** (2011) 083001.
- [3] Denkevits, A. and Dorofeev, S., *Dust explosion hazard in ITER: Explosion indices of fine graphite and tungsten dusts and their mixtures*, *Fusion Engineering and Design* **75-79** (2005) 1135-1139.
- [4] Denkevits, A. and Dorofeev, S., *Explosibility of fine graphite and tungsten dusts and their mixtures*, *Journal of Loss Prevention in the Process Industries* **19** (2006) 174-180.
- [5] Longhurst, G. R., Anderl, R. A., Adler-Flitton, M. K., Matthern, G. E., Tranter, T. J., and Hollis, K. J., *Beryllium Technology Research in the United States*, 7th IEA International Workshop on Beryllium Technology, Santa Barbara, CA, Report INL/CON-05-00920, 2005.
- [6] ASTM Standard E1226-10: Standard Test Method for Explosibility of Dust Clouds, ASTM International, 2010.
- [7] Kühner 20 liter sphere manuals, (<http://safety.kuhner.com/en/product/apparatuses/safety-testing-devices/id-20-l-apparatus.html>).
- [8] Kühner 20 liter sphere: Final Report CaRo11, (http://kuhnersafety.com/tl_files/kuhner/product/safety/PDF/B052_256CaRo11.pdf).
- [9] Occupational Safety and Health Administration, *Hazard Communication Guidance for Combustible Dusts*, OSHA 3371-08, 2009.
- [10] Krietsch, A., Scheid, M., Lasry, M., Suter, G., Teske, H.-J., Stahmer, K. W., Arnold, A., Nemcak, O., Cesana, C., and Siwek, R., *Validation of alternative igniters for the determination of explosion characteristics of dust clouds in 20-l-sphere and 1-m³-vessel*, 13th International Symposium on Loss Prevention, Bruges, Belgium, June 6-9 2010.
- [11] Krietsch, A., and Scheid, M., *Tests on suitability of a new pyrotechnical igniter for the determination of explosion characteristics of dust clouds in 20-L-sphere and 1-m³-vessel*, *Science and Technology of Energetic Materials* **72(5-6)** (2011) 174-178.

Anodized Coatings for Be and Be-Al Alloys

Gary Schuster¹ and Bryan Gillenwater²

Abstract:

Be and Be-Al alloys can be readily anodized. Results from salt fog testing indicate that anodized coatings, formed on AlBeMet®162 (62 Be-38Al (wt %)), are more effective in preventing corrosion than anodized coatings formed on Be. Metallographic examinations of test coupons show that cracks tend to form much more commonly in anodized coatings formed on Be as compared to AlBeMet®. This higher occurrence of cracking is suspected to be reason why Be's anodized coatings are less protective against corrosion. The cause for the coating cracking is believed to be the relatively large volume expansion associated with the oxidation of Be (71%) versus Al (28%). This large volume expansion generates stresses which produce the cracks. Also the Al, in the anodized AlBeMet® coatings, does not fully oxidize. This further reduces the volume expansion associated with the formation of the anodized coatings on AlBeMet® and also provides some relatively ductile material, Al, to accommodate the stresses. In order to improve the corrosion performance of the anodized coatings on Be, work is being pursued to determine the coating thickness at which cracking begins to occur.

1 Introduction:

1.1 Anodizing Basics

Anodization is a process in which an oxide coating is formed on the surface of a part through an electrochemical reaction. The part to be coated is made to be the anode of a cell. The cell is set up to produce oxygen at the surface of the part. This oxygen reacts with the metal to form an oxide coating.

Anodizing typically produces coatings that are 5 to 25 microns in thickness. In order for the oxidizing reaction to proceed, oxygen must reach the metal. To do this it needs to diffuse through previously oxidized metal. Diffusion is a slow process. If the diffusion distance increased with coating thickness then the rate at which the coating grows would rapidly decrease as its thickness increases. This is not the case. Typically the coating thickness increases roughly proportional to anodizing time. The reason for this is that the distance over which the oxygen diffuses remains approximately constant with increasing coating thickness. This is because a cell structure develops in the coating. The cells have pores that run perpendicular to the coating. The "barrier layer" is the portion of the coating starting at the bottom of the pore (Figure 1a). The thickness of this barrier layer is the distance that the oxygen must diffuse through in order to reach the metal. The thickness of this barrier layer is roughly constant

¹ Director of R&D, Materion Brush Beryllium & Composites, Elmore, OH, USA

² R&D Senior Research Technician, Materion Brush Beryllium & Composites, Elmore, OH, USA

during anodizing because the depth of the pore increases along with the thickness of the coating. Figure 1b show SEM photos of the cell structure of three samples of anodized Al.

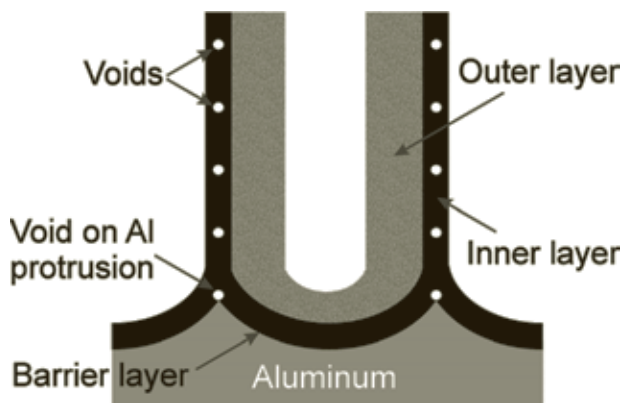


Figure 1a—Schematic showing the cross section of a cell that is part of an anodized coating. The cells have pores in their centers. The depths of these pores increase with coating thickness so that the thickness of the barrier layer remains approximately constant. Figure taken from reference (1).

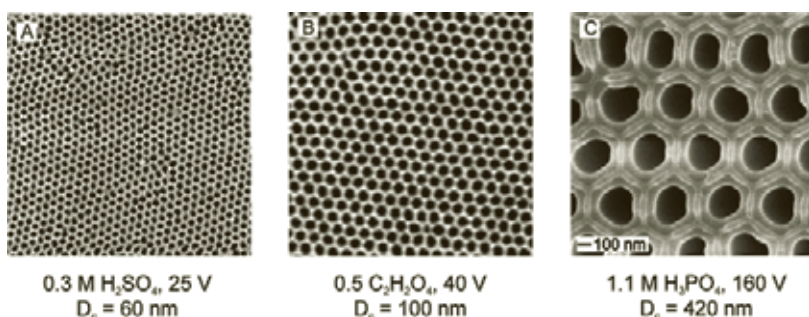


Figure 1b—SEM photos showing the cell structures on the surfaces of three anodized Al coupons. Figure taken from reference (1)

The pores in the coating offer little protection. Typically anodized coatings are sealed to plug these pores. To accomplish this, the anodized part is immersed into a solution that reacts with the oxide coating causing it to swell. The swelling closes the pores. In addition sometimes the pores are partially filled with organic material—e.g. Teflon or dye. The dye can improve the appearance of the coating as well as provide some additional protection.

2 Discussion:

2.1 Anodizing Beryllium and Beryllium-Aluminum Alloys

Both Be and Al can be anodized. Be-Al alloys are characterized by two-phase dendritic microstructures. Be and Al have little solubility for one another. When a Be-Al alloy solidifies the two metals separate to form a dendritic microstructure with a Be and an Al phase. Figure 2 shows the microstructure of AlBeMet® 162—an alloy with nominally 62 wt. % Be and the balance Al. The two-phase dendritic microstructure is readily apparent. Given that both Be and Al can be anodized, it is reasonable to expect that Be-Al alloys can also be anodized. This turns out to be true.

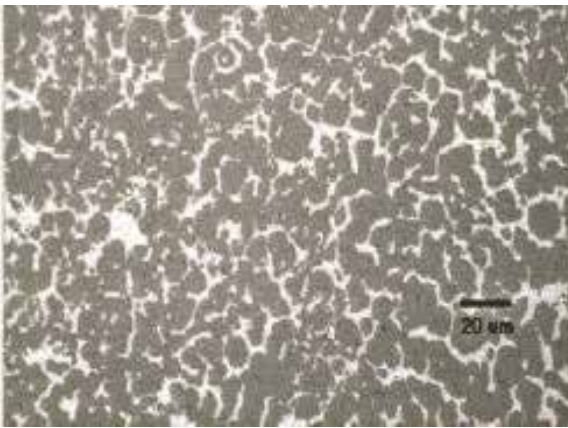
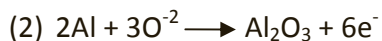
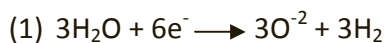


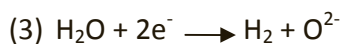
Figure 2—Cross Section of an AlBeMet® 162 sample. The dark phase is Be and the light phase Al.

The basic reactions for anodizing these two metals are as follows:

Al Anodizing



Be Anodizing



For each anodizing process, oxygen ions are formed from the electrolysis of water. These ions react with the metal after diffusing through a layer of previously formed oxide—the barrier layer. Anodizing typically occurs in an acid solution. The acid both increases the conductivity of the solution and aids in the dissolution of the oxide to form the pores.

2.2 Volume Expansion due to Oxide Formation

There is a volume expansion of the coating material associated with the oxidation reaction. This volume expansion is characterized by the ratio “R” where:

$$R = (\text{volume of the metal oxide})/(\text{volume of the metal})$$

R can be computed from the equation:

$$R = M_{\text{oxide}}(d_{\text{metal}})/M_{\text{metal}}(d_{\text{oxide}})$$

Where:

M = molecular wt.

d = density

Tables Ia&b show the molecular weights and densities for Al, Be and their oxides as well as the calculated R values for the two oxidation reactions. For Al R is 1.28 and for Be it is 1.71. Note, these computed values of R are not equal to the volume expansion that will actually occur. The oxidation reactions typically does not go to completion. Also, the densities of the oxides that form will likely be less than the values given in Table Ia. Nevertheless these computed R values indicate that the volume expansion associated with the anodization of Be is likely to be much greater than that for Al.

Table Ia—Molecular Weights and Densities

	Molecular Wt	Density (g/cm ³)
Al	27	2.70
Al ₂ O ₃	102	3.97
Be	9	1.85
BeO	25	3.01

Table Ib—Volume Expansion (R Values) Associated with Be and Al Oxidation

Oxidation Reaction	Al → Al ₂ O ₃	Be → BeO
R value	1.28	1.71

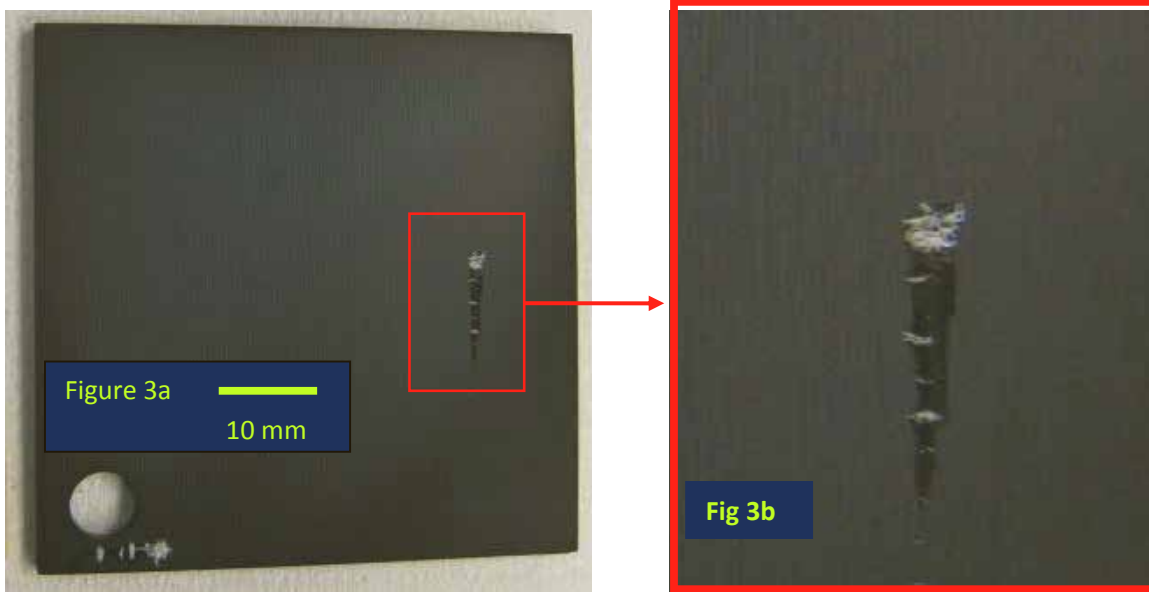
2.3 Performance Requirements for Anodized Coatings

Coatings are applied for a variety of reasons. The performance of the coating depends upon what it is intended to do! For Be and Be-Al alloys one major concern is the prevention of oxidation and corrosion. Anodized coatings are frequently applied when a metal is going to be exposed to a corrosive environment. Be readily forms chlorides. Unprotected Be will experience significant corrosion when exposed to a salt (NaCl) solution. Consequently, for Materion, one of the important performance characteristics of an anodized coating is its ability to protect Be from the corrosion that results from exposure to salt water.

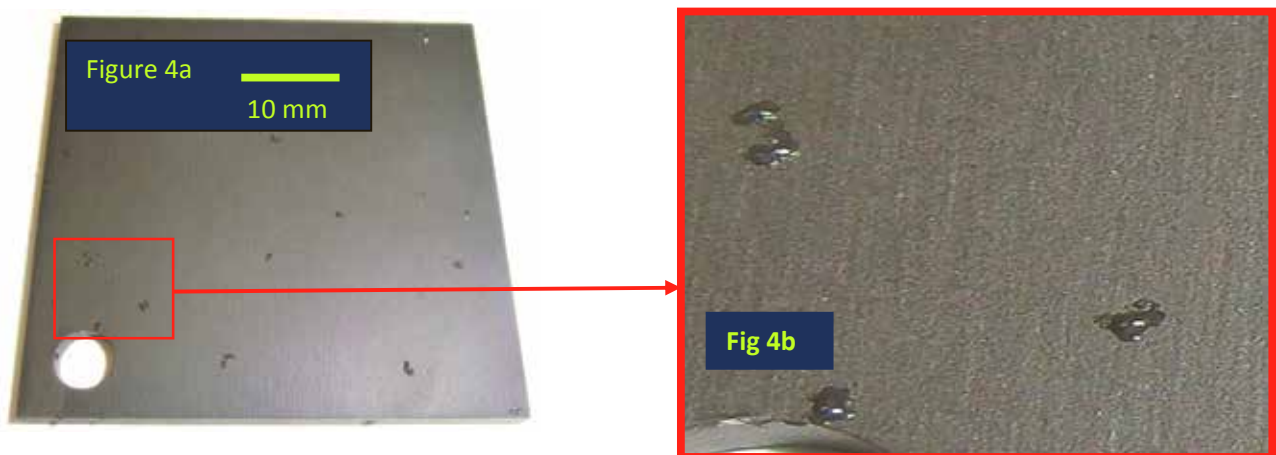
To measure the performance of coatings Materion uses a salt fog tester. For this, test coupons are placed in a chamber. This chamber exposes the coupons to a fine mist of saline solution. The water temperature, salt concentration and misting rate are all carefully controlled and maintained within specified ranges. The performance requirements that are perhaps the most commonly specified are the ones cited in the U.S. Military Specs. There are no anodizing MIL Specs for Be alloys. However, there are anodized coating specifications for Al alloys (MIL-A-8625F). This is the performance specification that Materion strives to achieve for its anodized coatings for both its AlBeMet® and Be grades.

2.4 Coating Performance Metrics

The corrosion performance of a coating, per MIL-A-8625F, is essentially determined by the amount of corrosion that has occurred at the end of the test period. The MIL Spec defines what constitutes an indication of corrosion. Pits and “stains” are considered indications of coating failure. The MIL Spec defines a coating’s performance based on the number and sizes of these corrosion indications. Figures 3a&b show a pit, along with some corrosion product, that formed on an anodized AlBeMet® 162 coupon during a salt fog test. Figures 4a&b show blisters. These blisters appear to be small droplets of amorphous material. An analysis of these blisters indicate that they are composed primarily of Be, O and Cl. They typically begin to appear on the surfaces of test coupons a day or more after the coupons are removed from the salt fog chamber. These blisters are precursors to pits. They form because defects in the coating allow Cl ions to penetrate and react with the Be in the substrate. The reaction produces a Be-Cl-OH compound. There is a volume increase associated with the formation of this compound. Consequently the compound seeps up through the coating. During the time the coupon is in the salt fog chamber it is continuously washed with a fine salt fog mist. When the test is completed, and the washing no longer occurs, the compound accumulates on the surface and thereby marks the spot where a coating defect exists. Observing the formation of these blisters is a very sensitive method for measuring the performance of an anodize coating, on Be alloys, for salt fog testing.



Figures 3a&b—Anodized AlBeMet[®] coupon after two weeks in a salt fog test chamber. Pits and corrosion product have developed on the surface due to corrosion from the salt water.



Figures 4a&b—Anodized AlBeMet[®] coupons after two weeks in a salt fog chamber. This coupon shows blisters. The blisters are a Be-Cl-OH compound. They form because the coating has locally failed thereby allowing Cl ions to penetrate and react with Be. The compound slowly bubbles up and accumulates above the coating defect.

2.5 General Performance of Anodized Coatings on AlBeMet® and Be

Materion is seeking to develop anodizing procedures for both AlBeMet® and Be that will meet the performance requirements of MIL-A-8625F. Findings to date indicate that the anodized coatings on the AlBeMet® alloy perform significantly better than those on Be grades. The superior performance of anodized AlBeMet® over Be has been a surprise. The AlBeMet® has two phases, Al and Be, making it a more complicated metal to anodize. A fair amount of work has been conducted to understand why this performance difference exists?

Figure 5a shows a micrograph of a cross section of an anodized AlBeMet® coated coupon. The coating is approximately 30 microns thick. Figures 5b-d respectively show Al, Be and O dot maps of this same region of the coating. The dot maps indicate that the Be in the coating has oxidized, but a fair amount of the Al in the coating has not. Be has a more negative free energy of formation for its oxide. As a result the Be phase oxidizes preferentially over the Al. Depending upon the anodizing parameters, 10-80% of the Al in an anodized AlBeMet coating may be un-oxidized.

In contrast the Be anodized coating appears to be uniformly oxidized. Figures 6a&b, 7a&b and 8a&b show Be coupons having anodized coatings with thicknesses of roughly 3, 10 and 30 microns respectively. The thickness of the Be anodized coating in Figures 8a&b is approximately equal to the thickness of the anodized AlBeMet® coating in Figure 5a. The Be anodized coating is seen to be full of cracks. In contrast the AlBeMet® anodized coating has no significant cracks.

Cracks in the coatings are defects. Cracks can allow Cl ions to reach the underlying Be metal. Once there corrosion will occur. The large number of cracks forming in the coatings of anodized Be is believed to be the cause for the relatively poor performance of these coatings in a salt fog environment.

The reason for the cracking is believed to be the stresses that are generated from the volume expansion of the coating due to oxidation. As previously explained, the volume expansion associated with the oxidation of Al is 28%. For Be it is 71%. Actual volume expansions are probably well below these values, but the Be is likely to produce much larger volume expansion than the Al. When the coating first forms the oxidation is occurring on a free surface. At this time growth is only constrained by the substrate. As the coating's thickness increases, the newly formed coating is constrained both by the substrate and the coating that has already formed. The thicker the coating becomes the more it constrains the new oxidation from its volume expansion. This generates large stresses within the coating. In general the coating will develop compressive stresses near the metal/oxide interface and tensile stresses near the free surface. There will also be shear stresses throughout the coating. These stresses can be partially relieved by cracking.

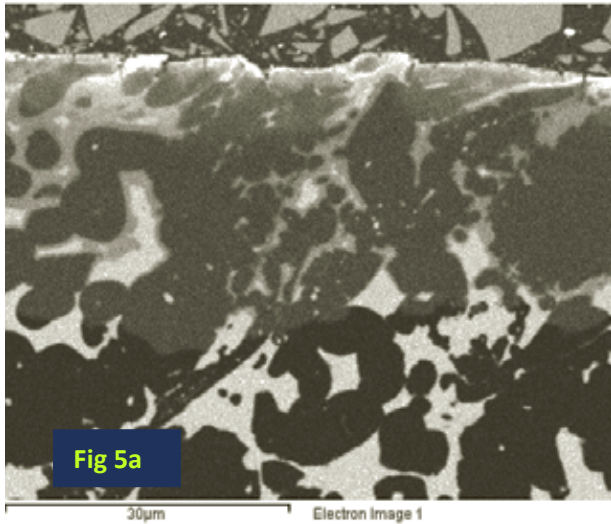


Fig 5a

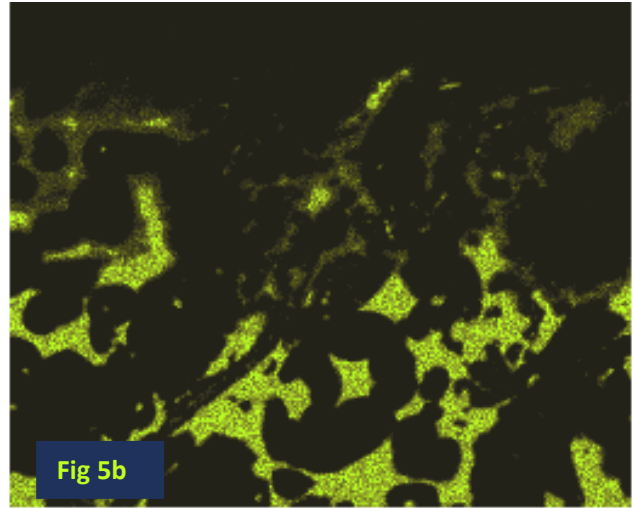


Fig 5b

Al Ka1

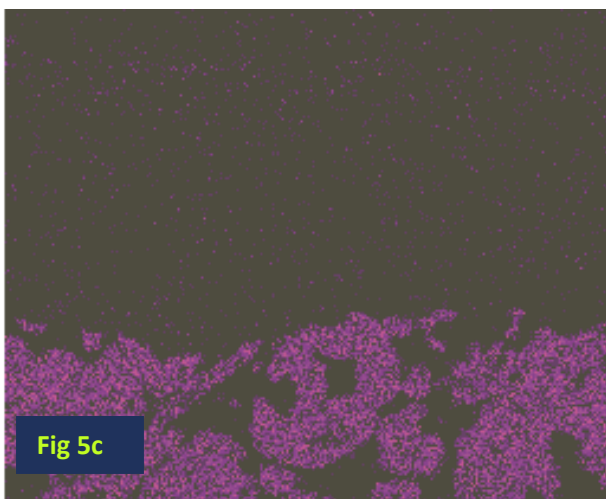


Fig 5c

Be Ka1_2

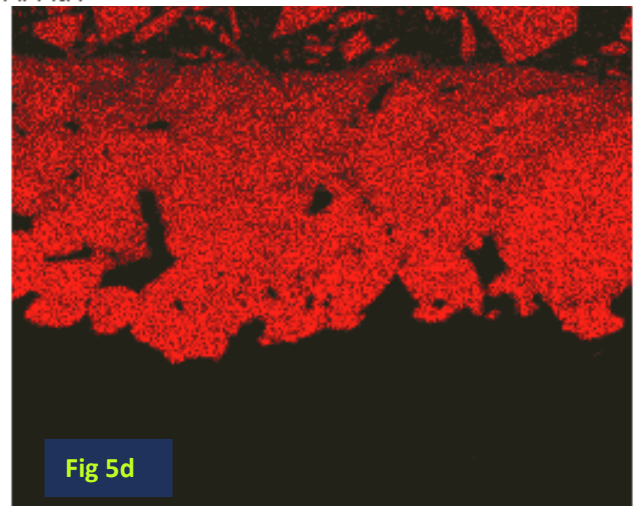


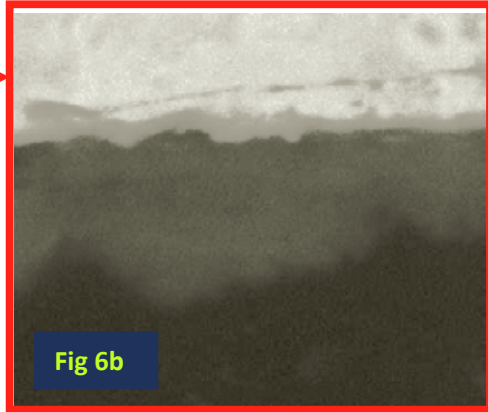
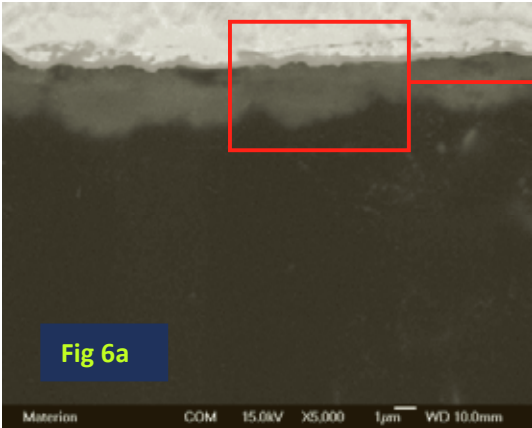
Fig 5d

O Ka1

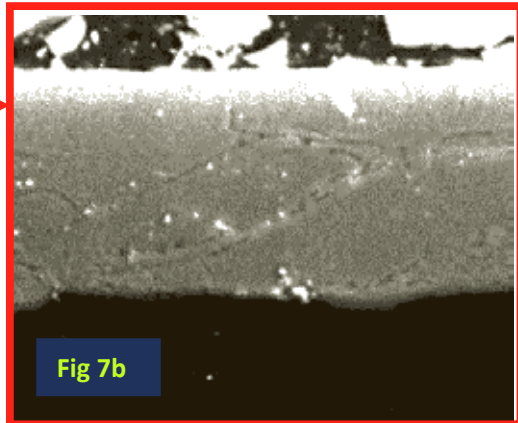
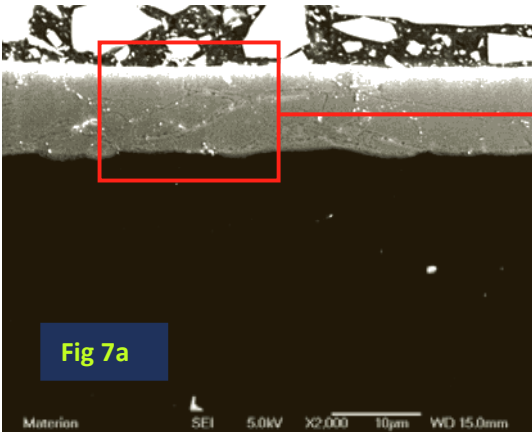
Figures 5a-d—5a-SEM micrograph of an anodized AlBeMet® coupon. The coating thickness is roughly 30 microns. Figures 5b, 5c and 5d respectively show Al, Be and O dot maps of the region in 5a. The O dot map indicates that the Be in the coating is oxidized but that roughly half of the Al in the coating is not.

The AlBeMet® coatings will develop less stress. Part of the reason for this is because 38 wt. % of the AlBeMet® is composed of Al and it has a much lower R value, so the volume expansion will be less. Furthermore a significant fraction of the Al in the coating tends not to oxidize. The dot maps on Figures 5b&d show that roughly 50% of the Al in that coating is not oxidized. This is typical. When the Al does not oxidize it both adds nothing to the volume expansion and also serves as a relatively ductile material

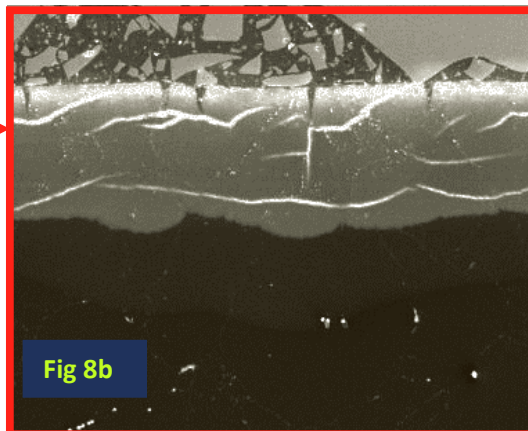
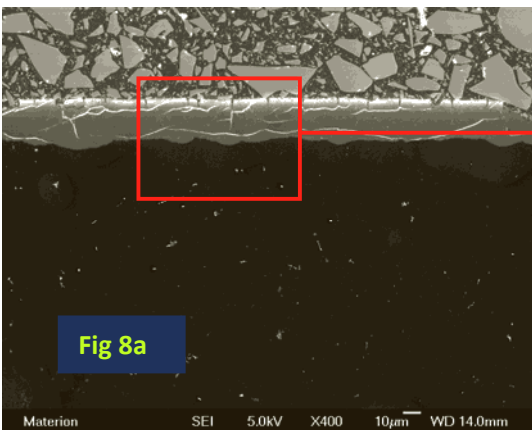
that can more readily accommodate the volume increase caused by the oxidation of Be. The metallic Al also acts to hold the relatively brittle oxide phase together thereby again reducing the incidence of cracking.



Figures 6a&b—Three micron thick Anodized Be coating. Cracking is not apparent.



Figures 7a&b—Ten micron thick Anodized Be coating. Many cracks.



Figures 8a&b—30 micron thick Anodized Be coating. Many major cracks.

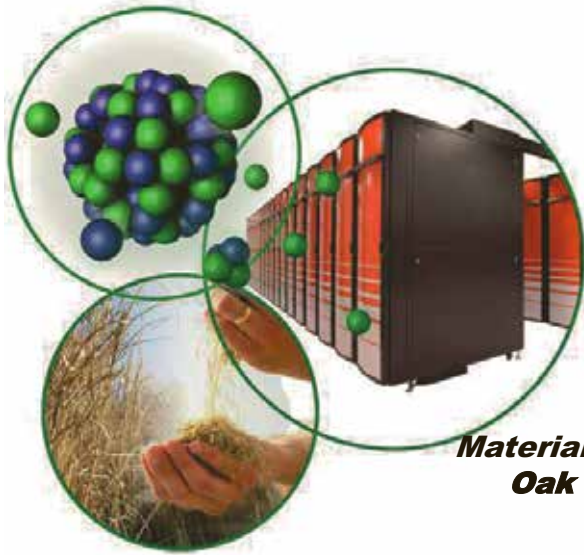
3 Conclusions

Assuming that the cracks in the Be oxide are the cause for poor corrosion performance then there should be an optimal coating thickness for corrosion protection. If the coating is too thin then its coverage may be incomplete or it may be too susceptible to damage. If the coating is too thick then it is likely to form cracks that will allow corrosive materials to reach the substrate. Based on preliminary testing, cracks are not common for coatings less than 5 microns in thickness. Trials need to be conducted on Be to determine if anodized coatings, that are 5 microns or less in thickness, can actually provide corrosion protection in a salt fog environment.

4 References:

- (1) Nanostructured Materials in Electrochemistry, Ed Ali Eftekhari, WILEY-VCH Verlag GmbH & Co, KGaA, Weinheim, ISBN: 978-3-527-31876-6 (2008)

Radiation Damage in HCP Metals. Experiment and Theory



**Stas Golubov
Roger Stoller
Alexander Barashev**

*Materials Science and Technology Division
Oak Ridge National Laboratory, USA*

Managed by UT-Battelle
for the Department of Energy

10th IEA International Workshop on Beryllium Technology
19-21 September, 2012



OUTLINE

- ❖ **Damage accumulation in irradiated structural materials**
- ❖ **Theory of damage accumulation**
- ❖ **Theory of radiation growth in HCP crystals**
- ❖ **Modeling of gas bubble evolution**



Radiation- induced phenomena

- ❑ **Swelling:** dislocations climb, voids nucleation and growth
- ❑ **Growth:** inelastic deformation without stress at constant volume
- ❑ **Creep:** inelastic deformation under stress at constant volume
- ❑ **Hardening & Embrittlement:** radiation defects - obstacles for moving dislocations
- ❑ **Phase transformation, radiation-induced segregation, etc.**

Radiation changes drastically mechanical properties

3 Managed by UT-Battelle
for the Department of Energy



The Essence of RD Theory

- ❑ **To reveal mechanisms responsible for damage accumulations**
- ❑ **To describe**

Nucleation and growth of point defect clusters:

- ❖ **Voids/bubbles, vacancy loops and stacking-fault tetrahedra**
- ❖ **Interstitial loops**
- ❖ **Secondary phase precipitates**

Change in dislocations and grain boundary properties

4 Managed by UT-Battelle
for the Department of Energy



Radiation Damage Theory Brief History

~1959 - 1990 Earlier Models (all solids)

- Point defects production only
 - 3-dimensional diffusion of PDs
 - No spatial correlations in microstructure
- Failed to explain basic observations**

1990 – 2005 Production Bias Model (PBM) (cubic crystals)

- Defect clustering in cascades
 - 3-dimensional diffusion of PDs and 1-D diffusion of self interstitial clusters (SIA) clusters
 - No spatial correlations in microstructure
- Many basic observations explained**
Problems still remain

2005 - now: Self-consistent PBM

- dislocation decoration by SIA clusters
- inclusion of spatial correlations (e.g.void lattice)
- radiation growth model for HCP crystals (2011)

PBM is equally applicable for all metallic crystals at least

Recent review:

S.I. Golubov, A.V. Barashev, and R.E. Stoller, *Radiation Damage Theory*. In: Konings R.J.M., (ed.) *Comprehensive Nuclear Materials*, volume 1, pp. 357-391, Amsterdam, 2012: Elsevier.

5 Managed by UT-Battelle
for the Department of Energy



Primary damage from cascades

20keV cascade in iron

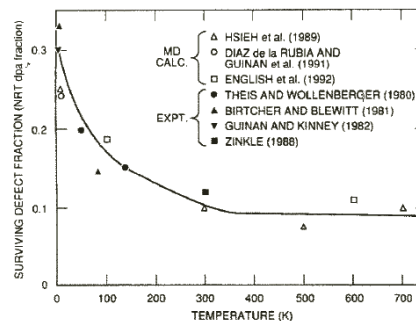
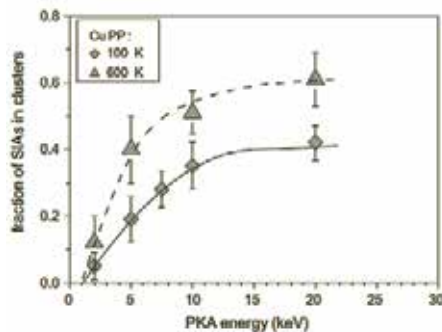


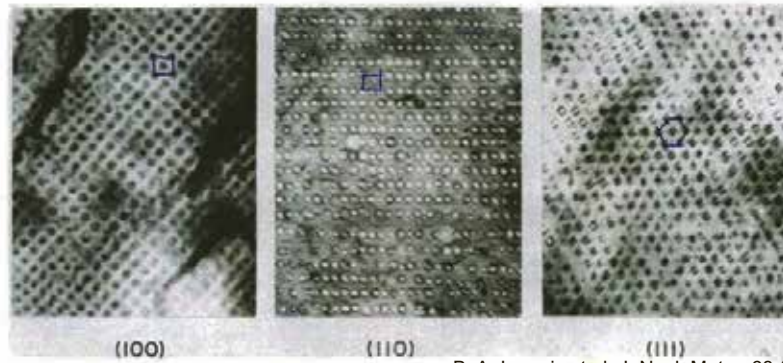
Fig. 4. Temperature-dependent fraction of defects surviving the cascade quench and correlated recombination (SDF) in copper irradiated under cascade conditions. The open symbols [20,43,74] refer to MD calculations performed with PKA energies of 3 to 5 keV and the filled symbols [52,53,72,73] refer to lower-bound estimates obtained from electrical resistivity measurements on neutron-irradiated copper (see text).

- ❑ Formation of thermally stable one-dimensionally migrating SIA clusters
- ❑ The process is not depend on type of lattice and material composition since $E_{PKA} \gg E_{coh}$

6 Managed by UT-Battelle
for the Department of Energy



Void lattice (VL) in neutron-irradiated Niobium



B. A. Loomis et al, J. Nucl. Mater. 68 (1977) 19

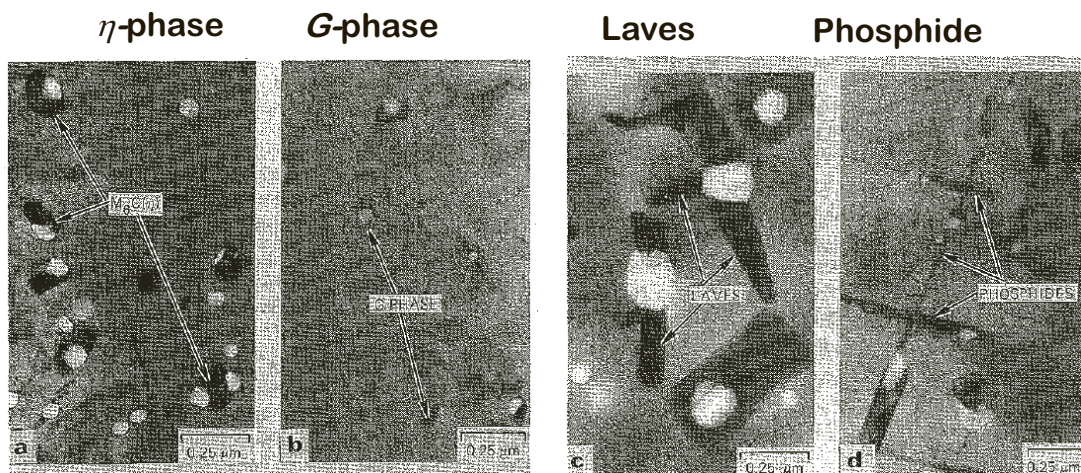
- ❖ VL has the same symmetry and orientation as the host lattice (BCC in BCC metals and so on)
- ❖ It forms under neutron and heavy ion but never under 1 MeV electron irradiation

Explanation of VL formation is out of capability of FPPM

7 Managed by UT-Battelle
for the Department of Energy



Spatial correlations between voids and second-phase particles

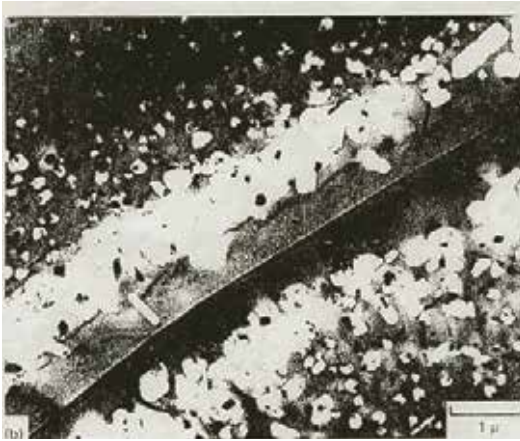


**Pedraza & Maziasz (1987):
Solution-annealed type 316 stainless steel.**

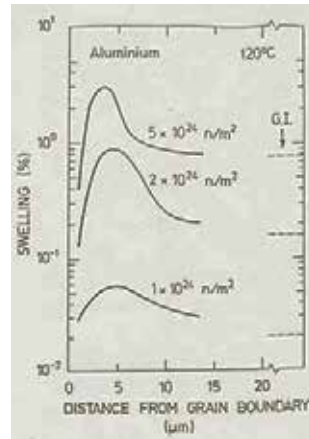
8 Managed by UT-Battelle
for the Department of Energy



Grain boundary effect in Al under neutron irradiation



K. Farrell et al., Albany 1971, p.376 (Al)



Foreman, Singh, Horsewell
Mater. Sci. Forum 15-18 (1987) 895

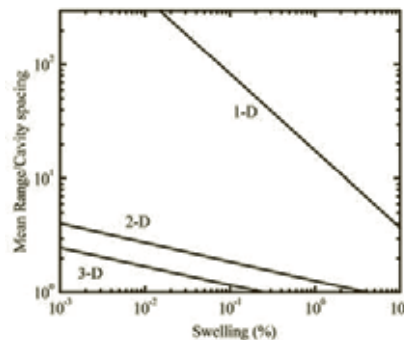
Length scale orders of magnitude larger than that is provided by 3-dimensional diffusion of PDs

9 Managed by UT-Battelle for the Department of Energy



3-D and 1-D Reaction Kinetics

Mean free paths of 3-D and 1-D migrating defects



$$\lambda_{(3)}^{-1} = (4\pi RN)^{-1/2}$$

$$\lambda_{(1)} = (\pi R^2 N)^{-1}$$

Observations explained by PBM:

- High swelling rate at low dislocation density
- Void lattice
- Grain boundary/size effects
- PKA energy effect
- Raft formation
- Segregation of voids and dislocations

10 Managed by UT-Battelle for the Department of Energy



PKA Energy Effect

Irradiations:

- 2.5 MeV electrons
- 3 MeV protons
- fission neutrons

Material & conditions

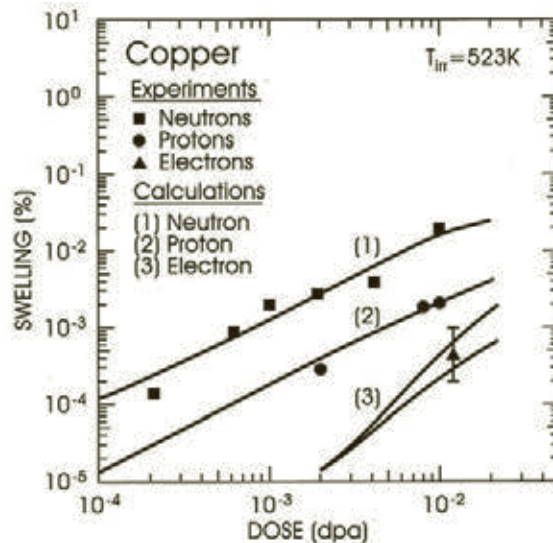
Copper

$G_{NRT} = 10^{-8}$ dpa/sec

T=520 K

Cascade parameters for neutrons

$$(1 - \varepsilon_r) = 0.1, \quad \varepsilon_i = 0.2.$$



Singh et al. *Phil. Mag. A* 80 (2000) 2626

Golubov et al. *Phil. Mag. A* 81 (2001) 2533

**50 times higher swelling level
 at 10 times smaller defect production**

11 Managed by UT-Battelle
 for the Department of Energy



Radiation Growth in Zr alloys

The first radiation growth model:

S.N. Buckley, in: *Proc. Int. Conf. on Properties of Reactor Materials and the Effects of Radiation Damage*, Ed. D.J. Littler (Butterworths, London, (1962) p. 413.

Recent reviews:

Holt, *Journal of Nuclear Materials* 372 (2008) 182.

'Although the means to predict polycrystalline behavior from the behavior of individual crystals now exist as described above, the basic physical parameters that would be needed to construct reliable mechanistic models to predict the deformation of even a pure Zr single crystal are not known ... We therefore still rely a phenomenological approach.'

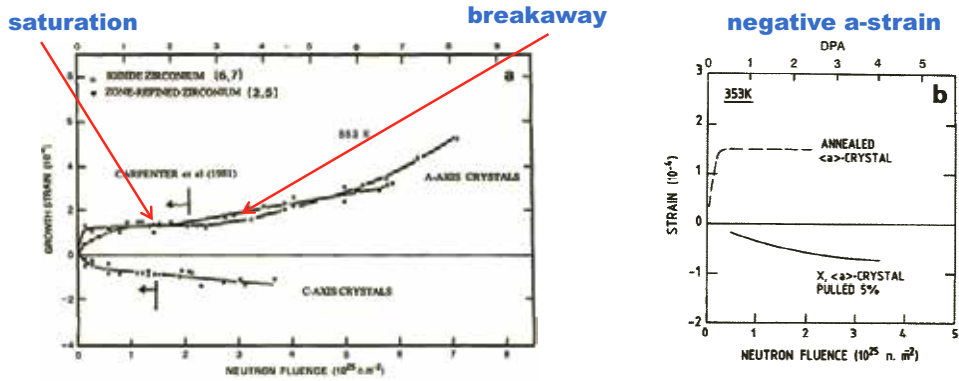
Adamson *et al.*, A.N.T. INTERNATIONAL (2009).

'... equations and models are needed to enable useful predictions and analyses for current or future reactor components. In addition, as reviewed earlier, understanding of the basic creep mechanisms in anisotropic materials like zirconium alloys is still not strong enough to be truly predictive.' *'... Today, most models are empirical in nature, ...'*

12 Managed by UT-Battelle
 for the Department of Energy



Radiation growth of Zr



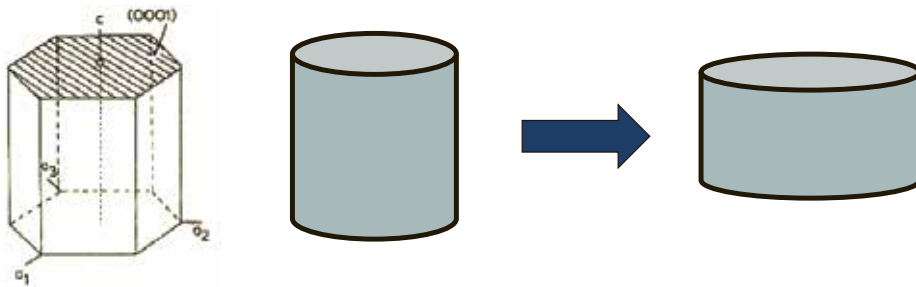
Observations, which have never been explained in framework of a single model for over 50 years :

- Strain saturation**
- Breakaway growth**
- Coexistence of about the same sizes vacancy and SIA type prismatic loops**
- Occasionally negative a-strain**

13 Managed by UT-Battelle for the Department of Energy



Radiation growth in Zr metals



- Expansion in prismatic directions (*a-directions*)**
- Contraction in along perpendicular to basal ones (*c-direction*)**
- Volume conservation**



Radiation growth in Zr-7%Pt binary alloy (strain ~100%)

14 Managed by UT-Battelle for the Department of Energy



Void Alignment in HCP Metals

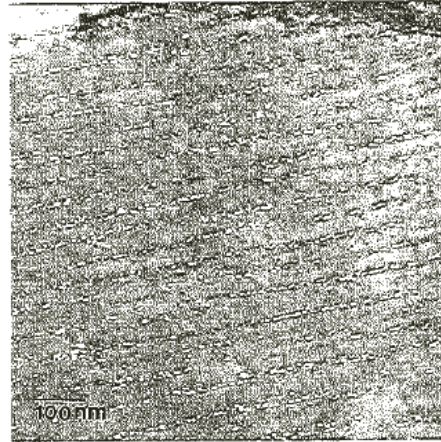
Magnesium



Fig. 1. Magnésium irradié à 3×10^{22} n/cm² ($E > 0,1$ MeV)
 $T = 55^\circ\text{C}$. Plan de lame: 1110. $\times 24\,000$.

Risbet & Levy, J. NUCL. MATER 50 (1974) 116-118.

Zirconium



MD: SIA clusters migrate 1-D along close packed directions on basal planes

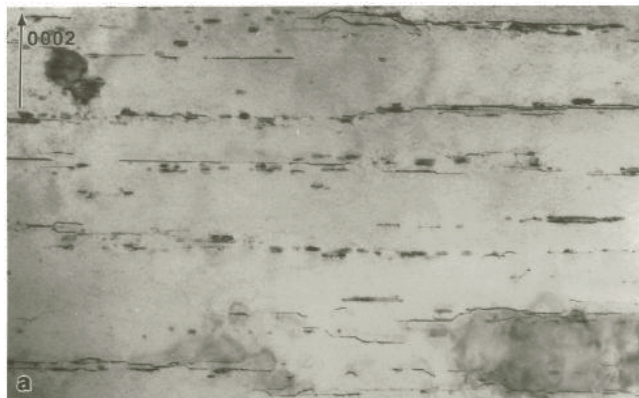
15 Managed by UT-Battelle
for the Department of Energy



Vacancy basal loop alignment in Zr

252

M. Griffiths et al. / Journal of Nuclear Materials 225 (1995) 245-258



16 Managed by UT-Battelle
for the Department of Energy



Radiation growth in framework of PBM

Basic equations for mobile defects

$$\frac{dC_v}{dt} = G_{\text{NRT}}(1 - \varepsilon_r) - D_v C_v k_v^2, \quad 3 - D,$$

$$\frac{dC_i}{dt} = G_{\text{NRT}}(1 - \varepsilon_r)(1 - \varepsilon_i^g) - Z_i D_i C_i k_i^2, \quad 3 - D,$$

$$\frac{dC_{\text{gm}}}{dt} = \frac{G_{\text{NRT}}}{3}(1 - \varepsilon_r)\varepsilon_i^g - D_g C_{\text{gm}} k_{\text{gm}}^2, \quad 1 - D.$$

Strain rates

$$\frac{d\varepsilon_x}{d\phi} = \chi \left(\frac{1}{2} - \frac{\rho_x}{\rho} \right), \quad \chi = (1 - \varepsilon_r)\varepsilon_i^g$$

$$\frac{d\varepsilon_y}{d\phi} = \chi \left(\frac{1}{2} - \frac{\rho_y}{\rho} \right),$$

$$\frac{d\varepsilon_z}{d\phi} = -\chi \frac{\rho_z}{\rho},$$

ρ_x, ρ_y are density of prismatic dislocation

ρ_z is density of basal ones
 ρ is total dislocation density

Z-axis is perpendicular to basal planes

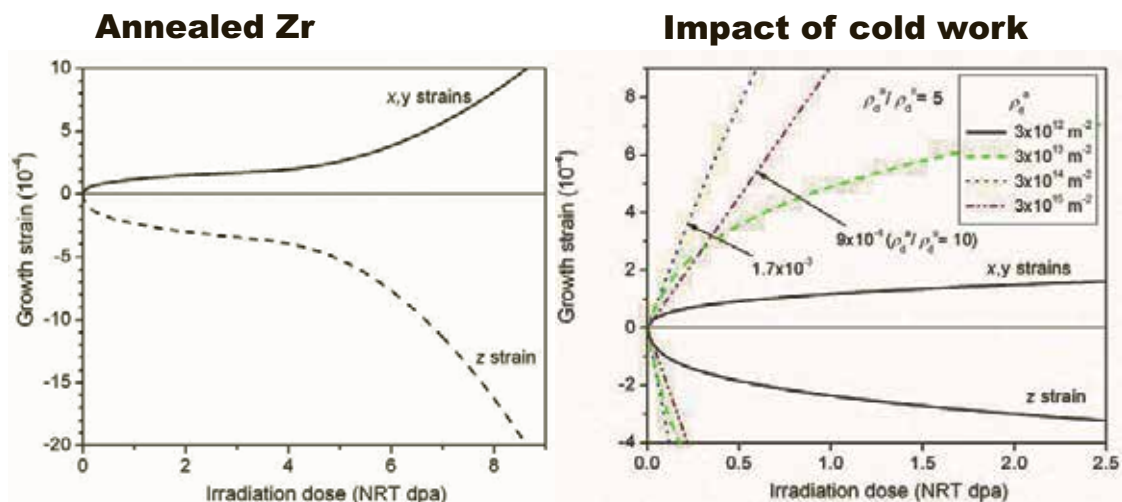
Strain rates are determined by cascade parameters

$$\chi = (1 - \varepsilon_r)\varepsilon_i^g$$

17 Managed by UT-Battelle for the Department of Energy



Dose dependence of RG strains predicted by the model



The calculations reproduce all strike features found experimentally

18 Managed by UT-Battelle for the Department of Energy



**End of presentation
Thanks for your
attention**

19 Managed by UT-Battelle
for the Department of Energy



Self-interstitial diffusion in beryllium: elementary jumps and overall dynamics

V.A. Borodin^{1,2} and P.V. Vladimirov¹

Institute for Applied Materials - Applied Materials Physics

¹ *Karlsruhe Institute of Technology, Karlsruhe, Germany*

² *NRC Kurchatov Institute, Moscow, Russia*

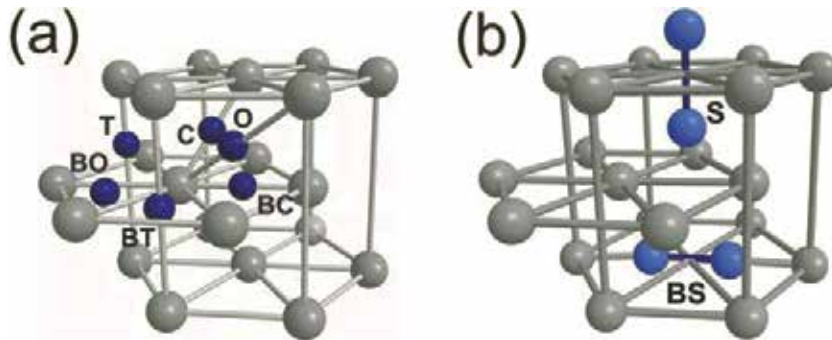
BeWS10 – Karlsruhe, 20-22.09.2012

Outline

- Background
- Simulation techniques
- Interstitial jumps – types and energy barriers
- From individual jumps to diffusion coefficients
- Summary

Interstitial configurations in Be

Symmetry Based Possibilities



- ❑ “True” interstitial positions: either between basal planes or inside basal planes
- ❑ Dumbbell configurations

Which configurations are stable and how interstitials move?

2

Simulation techniques:

First-principles DFT:

- ❑ VASP / GGA / PAW and US potentials
- ❑ supercells:
 - 96 - 512 atoms for static relaxation
 - 96 atoms for jumps
- ❑ Monkhorst-Pack k -points : from $9 \times 9 \times 9$ down to $2 \times 2 \times 2$ (depending on the supercell size)
- ❑ Transitions : NEB

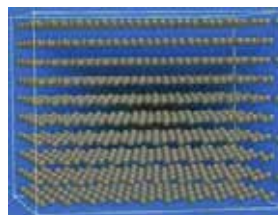
Molecular dynamics:

Potential: ABOP (C.Björkas et al. J. Phys.: Condens. Matter 21 (2009) 445002)

Simulation cells : $(1\div 6) \times 10^3$ atoms

Simulation runs: up to 2 ns

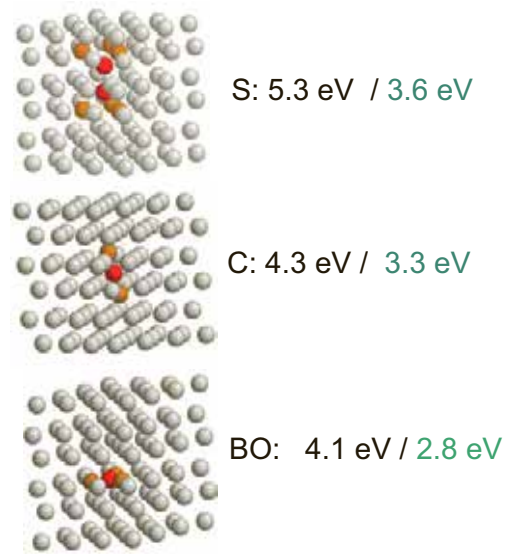
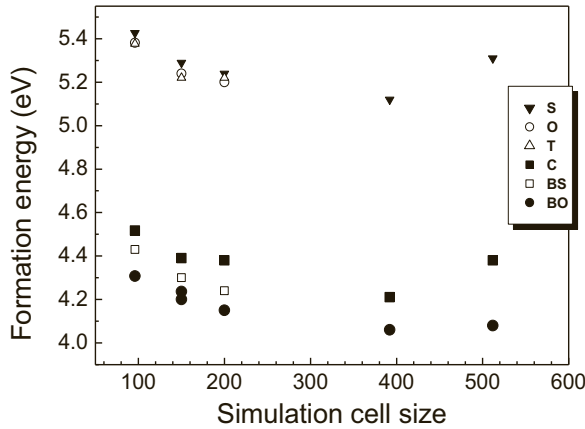
700 - 1000 K



3

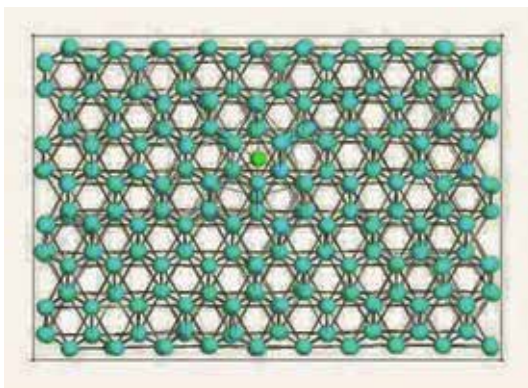
Stable interstitial configurations

Convergence with the simulation cell size

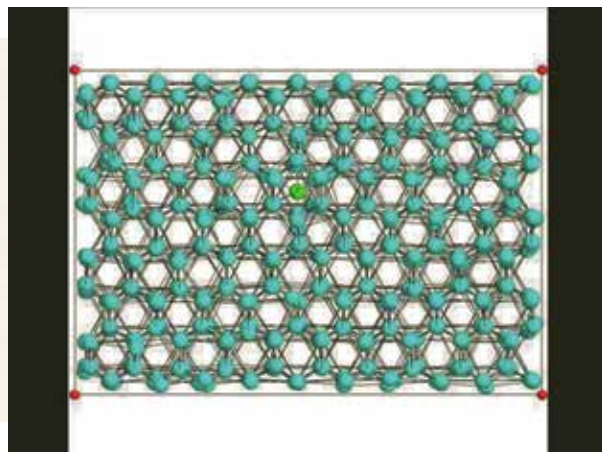


- Only three configurations remain stable in the largest supercells
- The lowest energy configuration is BO

Interstitial diffusion in Molecular Dynamics



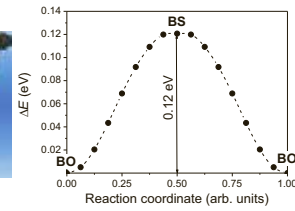
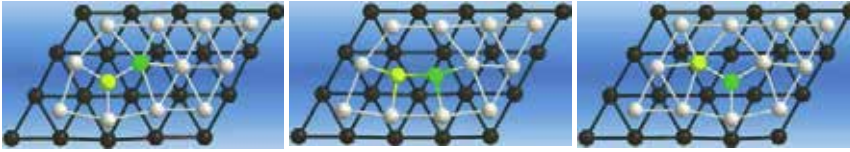
500 K



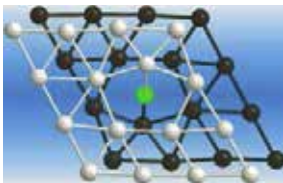
900 K

Possible diffusion jumps

I: In-plane jumps



- Though BO is a true interstitial, its in-plane diffusion occurs via dumbbell configuration (replacement jump)
- Migration barrier for in-plane diffusion is only 0.12 eV

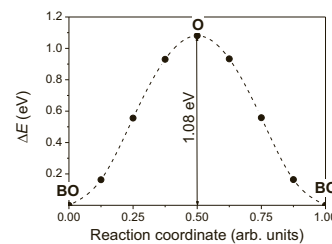
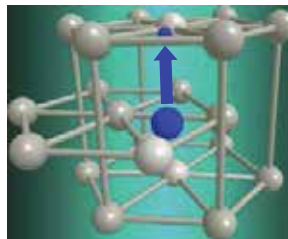


- No valid NEB trajectory: intermediate images relax to BO
- But dynamically observed as a part of „long“ jumps at high T

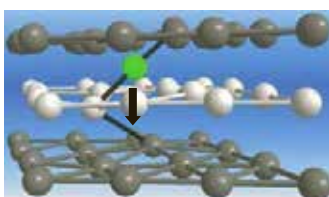
6

Possible diffusion jumps

II: Jumps normal to basal plane



- The same atom remains interstitial after the jump
- Migration barrier (1.1 eV) is notably higher than for in-plane diffusion

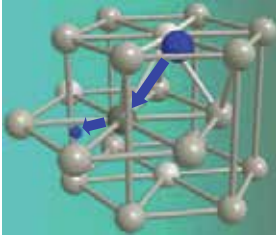


- No valid trajectory: intermediate position is a BO configuration, where the jumping atom is one of BO neighbours
- Not observed in MD

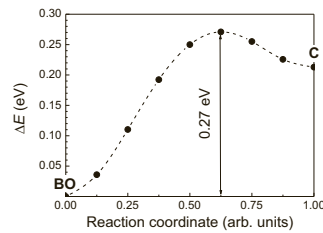
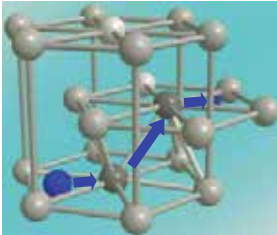
7

Possible diffusion jumps III: Mixed (a+c) jumps

Direct replacement



Indirect replacement (BO → C → BO)



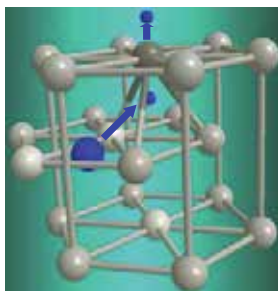
- The jump is symmetric with respect to the intermediate C position
- Migration barrier (0.27 eV) is higher than for in-plane diffusion, but still quite low

8

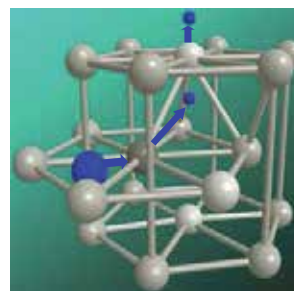
Possible diffusion jumps IV: Jumps through S-configuration

Jumps consist of 2 “half-jumps” of type BO ↔ S

Version 1



Version 2



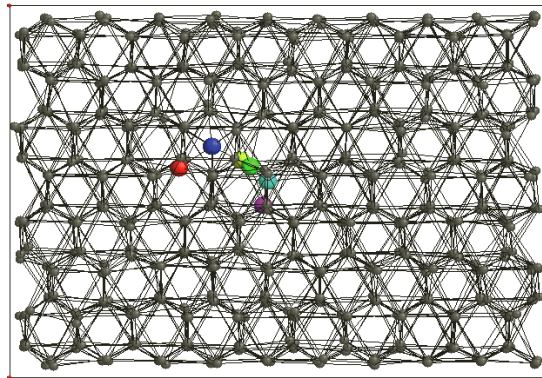
- The configuration energy of S is 1.2 eV higher than BO, thus the jumps are relatively rare
- Stay in S is usually short (1-2 ps), but sufficient to decorrelate the ‘forward’ and ‘backward’ half-jumps
- As a result, the jump length can reach 2a in plane and 2c along c-axis

9

Possible diffusion jumps

V: "Long" jumps

- ❑ Sometimes an interstitial jump involves a long trajectory (several interatomic distances), even though the distance between the initial and final atom position can be only 1-2 interatomic distances
- ❑ Sometimes these long trajectories can be separated into chains of several consecutive correlated jumps, but equally well the interstitial trajectory can be quite chaotic
- ❑ No long jump is like another

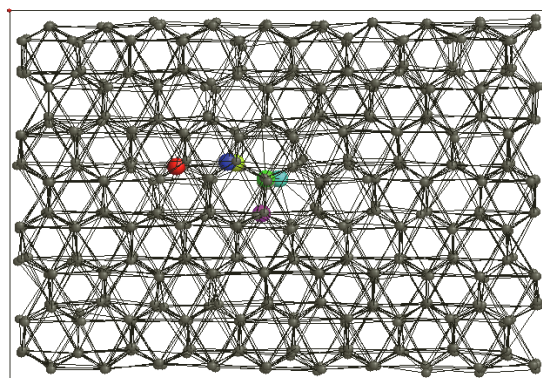


10

Possible diffusion jumps

V: "Long" jumps

- ❑ Sometimes an interstitial jump involves a long trajectory (several interatomic distances), even though the distance between the initial and final atom position can be only 1-2 interatomic distances
- ❑ Sometimes these long trajectories can be separated into chains of several consecutive correlated jumps, but equally well the interstitial trajectory can be quite chaotic
- ❑ No long jump is like another

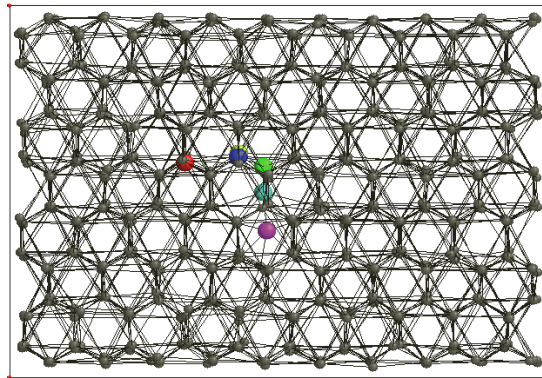


11

Possible diffusion jumps

V: "Long" jumps

- ❑ Sometimes an interstitial jump involves a long trajectory (several interatomic distances), even though the distance between the initial and final atom position can be only 1-2 interatomic distances
- ❑ Sometimes these long trajectories can be separated into chains of several consecutive correlated jumps, but equally well the interstitial trajectory can be quite chaotic
- ❑ No long jump is like another

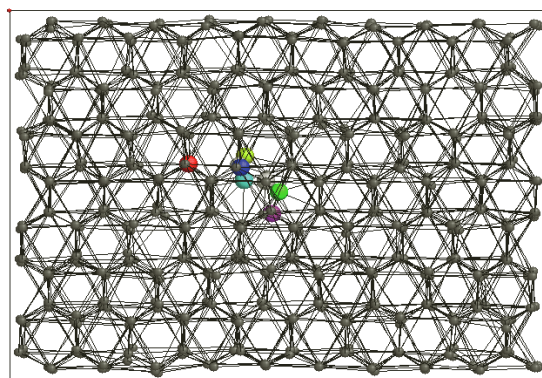


12

Possible diffusion jumps

V: "Long" jumps

- ❑ Sometimes an interstitial jump involves a long trajectory (several interatomic distances), even though the distance between the initial and final atom position can be only 1-2 interatomic distances
- ❑ Sometimes these long trajectories can be separated into chains of several consecutive correlated jumps, but equally well the interstitial trajectory can be quite chaotic
- ❑ No long jump is like another

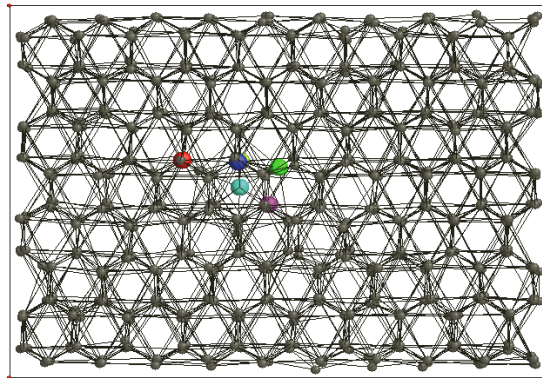


13

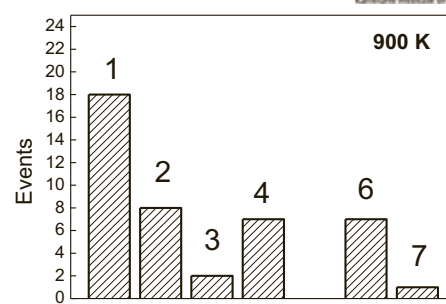
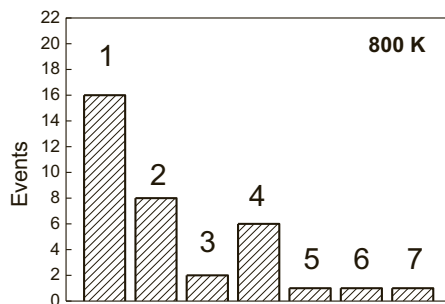
Possible diffusion jumps

V: "Long" jumps

- ❑ Sometimes an interstitial jump involves a long trajectory (several interatomic distances), even though the distance between the initial and final atom position can be only 1-2 interatomic distances
- ❑ Sometimes these long trajectories can be separated into chains of several consecutive correlated jumps, but equally well the interstitial trajectory can be quite chaotic
- ❑ No long jump is like another



Jump statistics



- 1 - BO-BS-BO (in-plane) : ~ half of the jumps
- 2 - BO-C-BO (a+c)
- 3 - BO-BO dr (a+c)
- 4 - BO-S-BO (a+c)
- 5 - BO-O-BO (c)
- 6 - other
- 7 - long/chains

Interstitial diffusion is 3D, but notably anisotropic

$$D_a = D_{a0} \exp(-0.1eV/kT), D_c = D_{c0} \exp(-0.3eV/kT)$$

Summary



- Interstitials easily move in beryllium
- Multiple jump transitions are possible
- Most transitions are replacive, even though the interstitial itself is a “true” one
- Interstitial diffusion is generally 3D, but there is notable diffusion anisotropy (preferential diffusion in basal planes)

Columnar interstitial clusters in Be (and Zr)

Institute for Applied Materials - Applied Materials Physics

V.A. Borodin^{1,2} M.G. Ganchenkova³, and P.V. Vladimirov¹

¹ *Karlsruhe Institute of Technology, Karlsruhe, Germany*

² *NRC Kurchatov Institute, Moscow, Russia*

³ *Aalto University, Helsinki, Finland and NRNU MEPhI, Moscow, Russia*

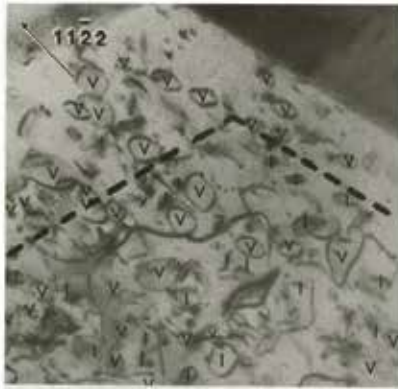
BeWS10 - Karlsruhe, 20-22 September 2012

Experimental background

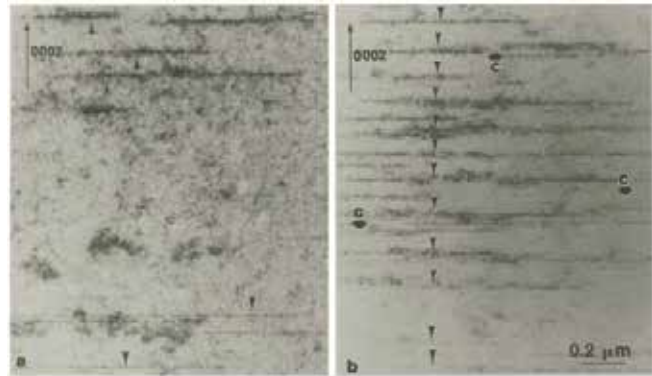
- Be and Zr have much in common:
both are hcp with $c/a < 1.633$
- Both are used as reactor materials.
- Both have very similar energy ranging of basic mono-interstitial configurations
- Are they similar in interstitial clustering behavior?

Dislocation loops in Zr

Griffith et al: JNM 159 (1988) 405



Griffith et al: JNM 205 (1993) 225



- Prismatic loops lie mostly on $\{11-20\}$ planes and can be both **interstitial-** and vacancy-type
- Basal loops are exclusively vacancy-type

2

Dislocation loops in Be

Gelles and Heinisch: JNM191-194 (1992) 194

- The microstructure of specimens irradiated at 400 and 500°C included a low density of dislocation tangles of $\sim(a/3)(1120)$ a-type Burgers vectors, which were possibly present before irradiation.
- At 400°C a high density of small loops with $c(0002)$ c-type Burgers vectors, while at 500°C **no small loops were found.**
- Small bubbles on **grain boundary** dislocations.

Gelles et al: JNM212-215 (1994) 29

- At irradiation temperatures of 400°C and below, damage consists of black spot or loop damage
- At higher temperatures, the microstructural product of irradiation is mainly bubbles, preferably at grain boundaries.
- Dislocation loops are annihilated following annealing in the temperature range 500-600°C

3

Dislocation loops in Be

G. P. Walters et al., JNM, 11 (1964) 335



Fig. 1a. Electron micrograph showing loops on {1120} planes in irradiated beryllium.

Plane of foil (0001)
Reflecting Plane (0110)



Fig. 2. Electron micrograph showing loops on {1120} planes in quenched and annealed hot pressed beryllium.

Plane of foil (0001)
Reflecting Plane (0110)

- After irradiation ($2 \times 10^{20} \text{ cm}^{-2}$, 350°C) {11-20} loops are formed,
- but :
- The same {11-20} loops (only smaller) are formed by quench from 1000°C

4

Dislocation loops in Be

Chakin & Ostrovsky, JNM, 307–311 (2002) 657

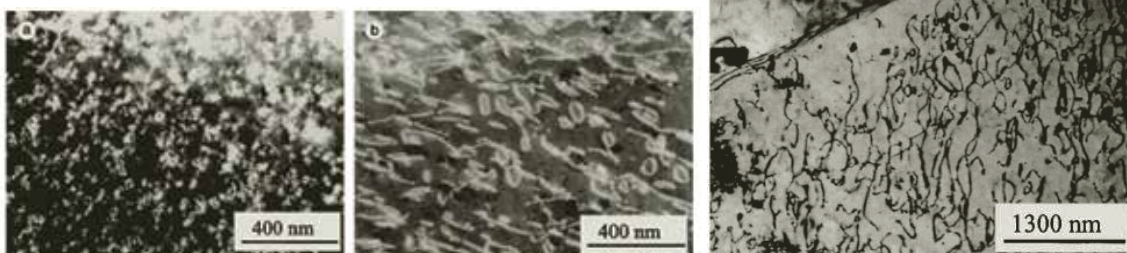


Fig. 2. Dislocation structure of the TE-56 beryllium grade irradiated in the SM reactor up to $2.5 \times 10^{22} \text{ cm}^{-2}$ ($E > 0.1 \text{ MeV}$) at $70\text{--}120^\circ\text{C}$: (a) after irradiation; (b) irradiation+annealing at 300°C , 1 h; (c) irradiation+annealing at 500°C , 1 h.

- Loops are of interstitial type.
- At least two planes of location, one of which is the basal plane.
- Loop distribution is extremely non-uniform; there are regions free from loops.
- After annealing loop size increases and bulk density decreases significantly.

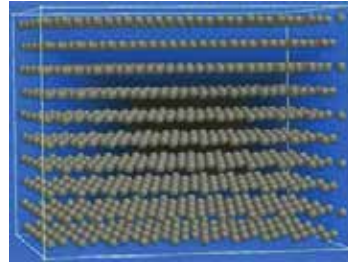
5

Simulation techniques:

Molecular dynamics:

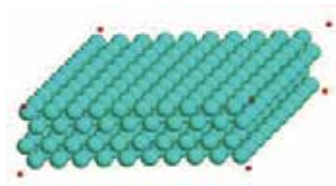
Potential: ABOP (C.Björkas et al. J. Phys.: Condens. Matter 21 (2009) 445002)

Simulation cells : from 10^3 to 6×10^3 atoms
T = 800 K



First-principles DFT:

- VASP / GGA / US (Be) and PAW (Zr) pseudopotentials
- supercell: 400 atoms
- Monkhorst-Pack k -points : up to $4 \times 4 \times 4$

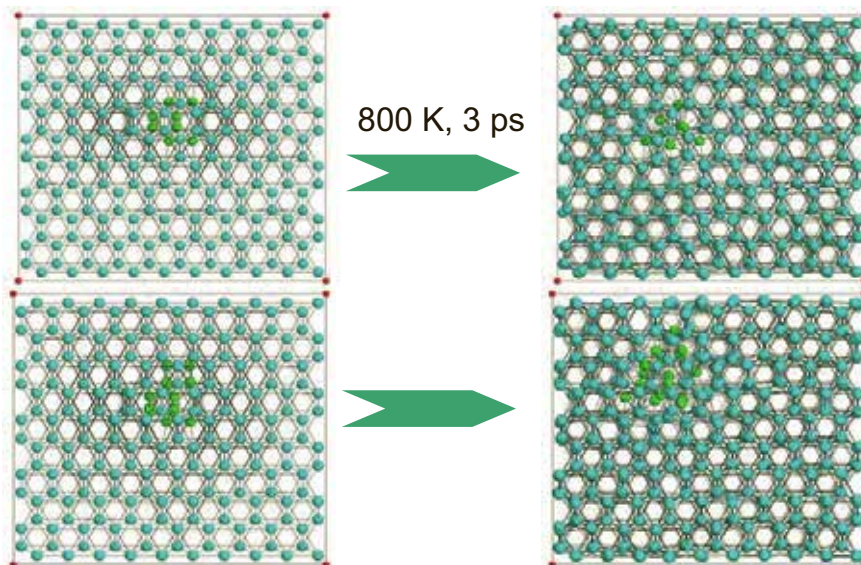


6

Instability of prismatic dislocation loops in Be

What is the structure of prismatic loops ?

Clusters of BS interstitials (De Diego et al. Met. Trans. A , 33 (2002) 783) ?

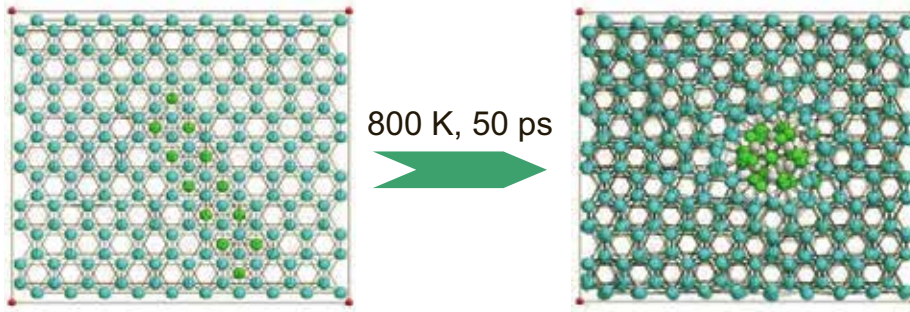


□ BS-type loops are unstable in Be

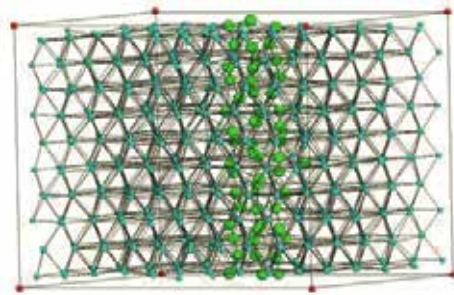
7

Instability of prismatic dislocation loop in Be

Alternative structure of prismatic loop (only BO interstitial configurations)



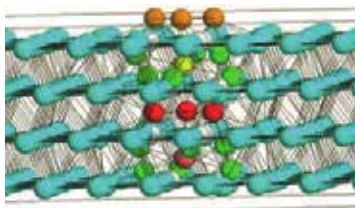
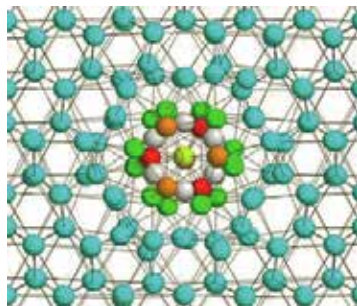
Resulting structure =
c-axis aligned interstitial column



8

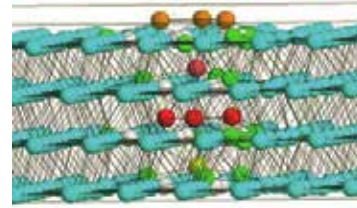
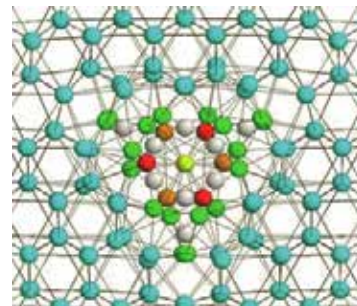
Refined column structure (DFT)

Be



$E_f/int = 1.74 \text{ eV}$ (ABOP: 1.45 eV)
Cf. $E_f(I_1) = 4.2 \text{ eV}$ (ABOP: 2.5 eV)

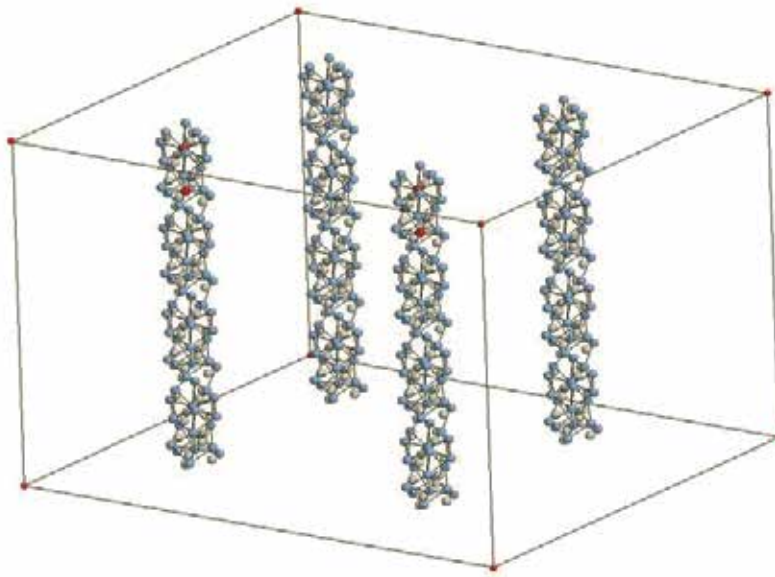
Zr



$E_f/int = 1.32 \text{ eV}$
Cf. $E_f(I_1) = 2.4 \text{ eV}$

9

Thermal stability of infinite columns



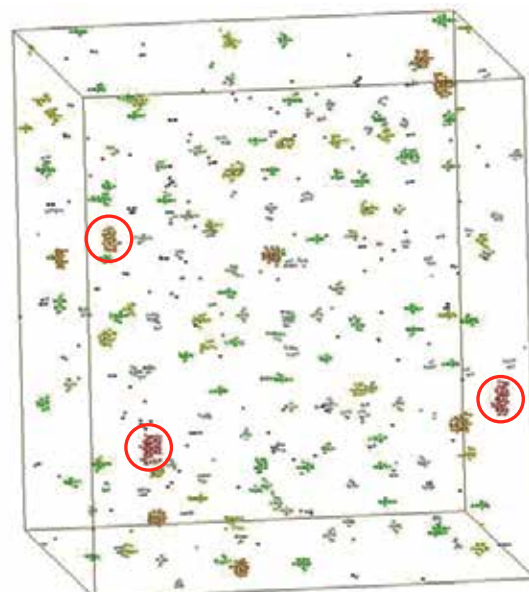
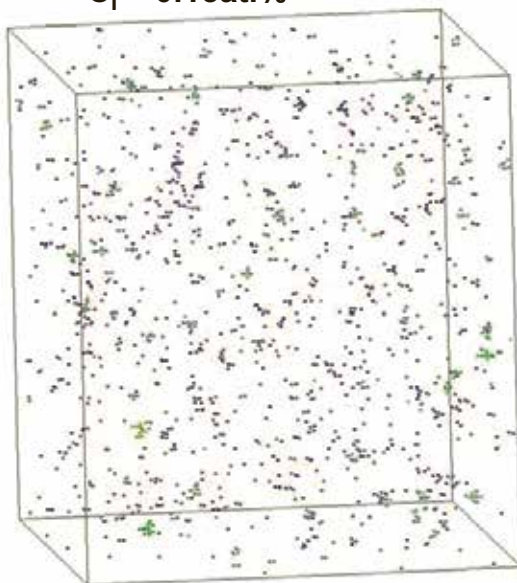
- Infinite columns show no signs of decay even when kept for 1 ns at 1000 K

10

Column nucleation from interstitial ensemble

$C_i = 0.15\text{at.}\%$

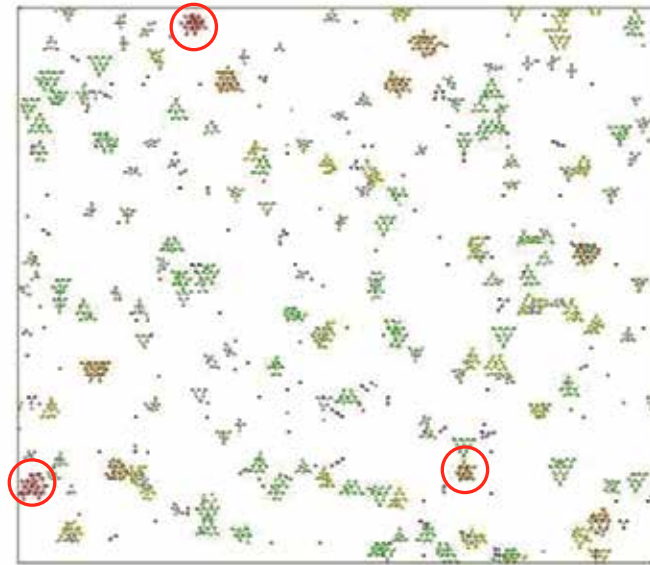
after 1 ns at 800 K



- Larger clusters (> 15 interstitials) tend to extend along c-axis

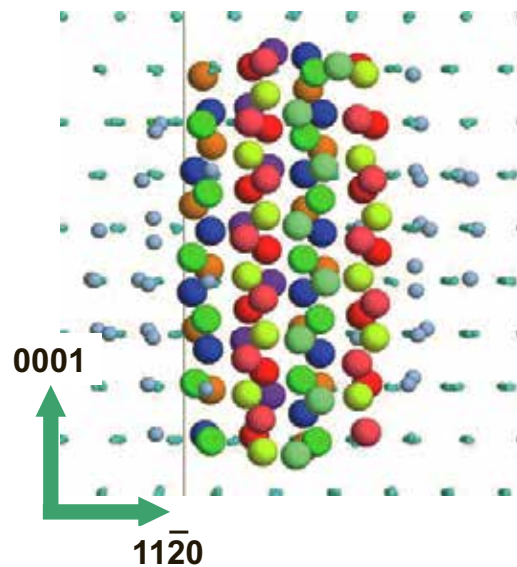
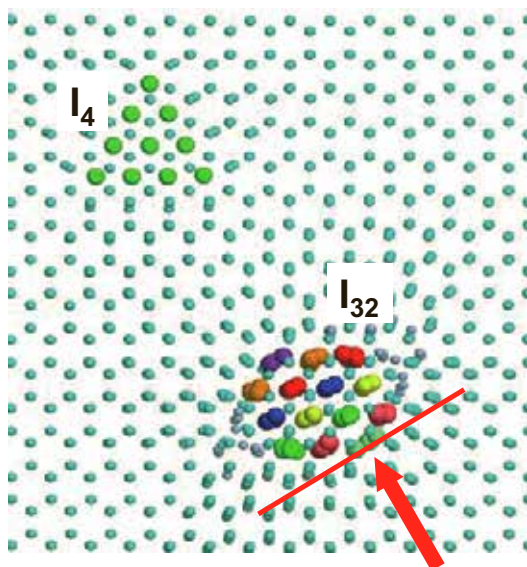
11

Column nucleation from interstitial ensemble



□ Larger clusters are compact in projection to basal plane

Atomic structure of finite-length column



Columns = sets of (zigzag) atom chains in open interstitial channels along c-axis

Summary



- ❑ Interstitial clusters in Be tend to grow as columnar structures elongated in *c*-direction, rather than prismatic loops
- ❑ Finite-length interstitial columns are sets of atom chains in open interstitial channels aligned along *c*-axis
- ❑ Columnar interstitial clusters in Zr are energetically favorable, so possibly they coexist with dislocation loops

AB INITIO STATIC AND MOLECULAR DYNAMICS STUDIES OF HELIUM BEHAVIOR IN BERYLLIUM

P.V. Vladimirov, A. Moeslang
Karlsruhe Institute of Technology, Karlsruhe, Germany;*

Beryllium is an effective neutron multiplier material widely exploited in nuclear applications. It will be used in the helium-cooled beryllium pebble bed of fusion reactor blankets for increasing the efficiency of tritium production. Macroscopic effects of irradiation (e.g., swelling) on beryllium are greatly influenced by accumulated transmutation helium. Atomic scale simulations of beryllium behavior under irradiation are necessary for understanding the basic mechanisms and reliable prediction of microstructural changes.

In this study, we investigate the behavior of interstitial and substitutional helium, its diffusion pathways and interaction with point defects present in irradiated beryllium by means of static and molecular dynamics *ab initio* simulations. It was shown that a mixed dumbbell consisting of self-interstitial and helium atoms represents the ground-state configuration for interstitial helium. At low temperatures, the mixed dumbbell migrates in the basal plane through a series of in-basal-plane rotations, while at higher temperatures it jumps also between adjacent basal planes.

It was revealed that, as in many other metals, interstitial helium atoms are bound to each other ($E_b \sim 1$ eV). In beryllium, two mixed dumbbells meet each other so that helium atoms are the nearest neighbors, whereas the helium pair can be oriented either in- or out-of-basal plane. Diffusion modes of the pair are discussed.

In addition, it was found that helium is very strongly bound to vacancies: the binding energy of more than 3 eV found by static *ab initio* calculations suggests that helium is unlikely to be released from a mono-vacancy at temperatures below the melting point. As has been shown previously, vacancy clusters are unstable in beryllium. This study shows that the addition of helium stabilizes di-vacancies. Thus, it is confirmed that the presence of transmutation gas is necessary for the development of a porous microstructure in beryllium.

Keywords: helium, beryllium, ab initio, first principles molecular dynamics

* Corresponding author:

Karlsruhe Institute of Technology, IAM, Campus Nord

Hermann-von-Helmholtz Platz 1

76344 Eggenstein-Leopoldshafen

Germany

Phone: +49 0721 6082 4243

Fax: +49 0721 6082 4567

e-mail: pavel.vladimirov@kit.edu

1. Introduction

Beryllium is widely used as neutron reflector and multiplier in fission reactors. Numerous experiments performed on beryllium irradiated below about 673 K suggest that its swelling is directly proportional to accumulated helium concentration. Large amounts of helium generated by nuclear reactions and accumulated under such conditions considerably affect material properties.

Helium accumulation will play an even more important role for fusion reactors, which possess a much harder neutron spectrum with a pronounced 14 MeV peak. In the helium-cooled fusion reactor blanket, beryllium will be used as the neutron multiplier material in the form of single-sized pebble beds. One of the important tasks for fusion reactor design is the assessment of tritium accumulation in beryllium pebbles.

In addition, tritium is produced by nuclear reactions and partly accumulated inside helium bubbles. In most cases approximately ten times more helium is generated than tritium. Therefore, gas bubble growth is mainly driven by helium accumulation, while tritium is captured by small helium-vacancy clusters and helium bubbles. Hence tritium retention and release is intimately connected with helium-bubble nucleation and growth. To reliably simulate this process, one should know the atomic scale mechanisms of helium diffusion and interaction of helium with traps. The properties of vacancy and interstitial type defects as well as preliminary results on helium behavior in beryllium were previously studied using *ab initio* methods [1, 2, 3, 4].

In this paper, we discuss atomic configurations and diffusion mechanisms of interstitial and substitutional helium as well as the binding between interstitial helium atoms and the binding of helium to vacancy clusters.

2. Computational details

In this work, static and dynamic first principles density functional theory (DFT) based calculations are used to identify possible defect configurations and their diffusion pathways.

Ab initio calculations were performed with plane-wave VASP computer code [4]. Full geometry optimization was carried out using generalized gradient approximation (GGA) with Perdew-Wang non-local exchange-correlation functional [5] and the scalar relativistic projector augmented wave (PAW) method [6]. The calculations typically involve 13x13x13 Monkhorst-Pack k-point mesh [7] and 450 eV for cutoff energy. Calculations with various k-point meshes has shown that starting from a 12x12x12 mesh the energy of the ground-state interstitial helium configuration deviates from the converged value (reached for the 19x19x19 mesh) by less than 0.01 eV. These results justify our selection of a 13x13x13 k-point mesh. Rhombohedral supercells with sizes of 64 and 96 lattice sites were used.

Migration barriers were estimated by means of independent relaxations of intermediate configurations. The jumping atom was fixed along the jump direction (and was moving freely in two other directions) at a position obtained by interpolation between its positions in the initial and final configurations. In addition, one or two lattice atoms were fixed in all three directions to avoid shifting of the lattice as a whole.

First principle molecular dynamics (FPMD) calculations are usually assumed to be rather time consuming and therefore only performed on very small systems and

for short simulation times. In general, this is still true; however, with increasing computer power computations not achievable five years ago are now possible. The case of beryllium is easier than for heavier elements as it has only four electrons and requires lower computational resources. Using a time step of 3 fs, it is possible to perform 3,000-4,000 step simulations (9-12 ps), which last about three days on a powerful computer cluster (HP XC3000 at Steinbuch Centre for Computing, in our case).

The number of k-points and the cut off energy values for static calculations were obtained by performing set of tests until configuration energy convergence was reached. These parameters are already quite demanding with respect to computer resources. To speed up the calculations we downsized the requirements as follows: 7x7x7 Monkhorst-Pack k-point mesh and 250 eV energy cut off were used for the FPMD calculations. This choice was justified by the fact that FPMD runs were used to elucidate helium diffusion pathways and defect cluster configurations qualitatively.

To obtain quantitative information, we have relaxed helium and defect cluster configurations observed in FPMD simulations using static first principles calculations with higher requirements and found that all configurations were stable. This confirms that reducing the requirements does not produce artificial configurations that would not be found with a more demanding set of parameters.

FPMD simulations are performed by VASP code on the so-called exact adiabatic Born-Oppenheimer surface [8]. In metals, fast moving electrons can adapt their motion to the much slower motion of nuclei. This means that total electronic energy minimization (ground-state search) is performed at each step of the FPMD. Simulations are performed in the NVT¹ ensemble where the system temperature is controlled using a Nose-Hoover thermostat. Temperature equilibration requires simulation runs longer than those used in this study. Therefore, notable temperature variations occur during our FPMD runs stimulating diffusion jumps of investigated defects. These variations, however, do not have an effect on the observed migration pathways.

3. Results and Discussion

3.1 Single helium interstitials

Eight possible high symmetry configurations for interstitial helium atoms have been tested: octahedral (O), basal octahedral (BO), tetrahedral (T), basal tetrahedral (BT), non-basal crowdion (C_N), basal crowdion (BC), split along c-axis (S), and basal split mixed dumbbell (BS_m). We found most of these configurations stable for self-interstitial atoms; therefore, we checked their suitability for interstitial helium. After relaxation four of the configurations appear to be stable: C_N, BO, BT, and BS_m (only two have been previously reported [3]). Formation energies of various interstitial helium configurations are collected in Table 1.

Formation energy of interstitial He was calculated as follows:

$$E_f = E(\text{He}_{\text{Int}}) - E_{\text{cryst}} - E(\text{He}), \quad (1)$$

¹ NVT ensemble means that the number of particles (N) and system volume (V) are constant and the ensemble has a well-defined temperature (T).

where $E(\text{He}_{\text{int}})$ is an energy of interstitial helium configuration, E_{cryst} is an energy of ideal hcp crystal lattice of Be, and $E(\text{He})$ is the reference energy of helium atom in vacuum.

Table 1: Formation energies (eV) of interstitial helium at various positions calculated for supercells containing 64, 96, and 128 atoms

Configuration:	O	BO	T	BT	C _N	BC	S	BS _m
64 atoms	unstable	5.74	unstable	5.70	6.05	unstable	unstable	5.39
96 atoms	6.17	5.81	6.01	5.78	6.11	unstable	5.77	5.46
128 atoms		5.73		5.67	6.11		5.93	5.39
Comment	→ BO		→ BT			→ BT → BO	→ BT	ground state

Calculations were performed using supercells containing 64, 96, and 128 atoms to assess the effect of the supercell size. As can be seen from the Table 1, the difference for stable configurations does not exceed 0.06 eV. Thus, we can conclude that a supercell with 64 atoms can reliably predict interstitial helium atom behavior in beryllium.

Note that the ground-state configuration for interstitial helium in beryllium is a basal split mixed dumbbell located in basal plane (BS_m). In most cases, this configuration was observed in the FPMD snapshots supporting the results of static simulations. The same ground-state configuration was recently reported [10, 11] using Quantum-ESPRESSO and Wien2k, while this configuration was unnoticed in [12].

Nudged elastic band calculations show that the BO configuration is a metastable shallow minimum: only 0.1 eV is required for decay to a mixed dumbbell configuration, while about 0.37 eV is necessary for the reverse jump. Accordingly, FPMD runs have revealed that at temperatures from 800 to 1000 K helium atom avoids the neighborhood of BO being effectively caged around the BT position. Helium can form mixed dumbbell with any of the three atoms at the triangle corners; however, jumps between triangles occur by rotation: the mixed dumbbell goes out of basal plane, while helium atom jumps into the other triangle. All diffusion jumps observed during the simulation runs in this interval of temperatures occurred within the basal plane (i.e. at low temperatures, interstitial helium diffuses two-dimensionally).

Temperature limits obtained by FPMD calculations should not be used for direct comparison with the real world. Typical FPMD run durations are very short (tens of ps), therefore, high temperatures were used to increase probability to observe some diffusion jumps. Due to a much longer time scale, diffusion under experimental conditions can be observed at notably lower temperatures than in our simulations. However, the qualitative model of the phenomena remains valid.

At 1200 K, the energy of helium atoms is sufficient to jump over a BO-containing triangle; thus on-site rotations of the mixed dumbbell are possible. Therefore, at high temperatures, helium can change triangles without rotation. On the other hand, helium jumps were observed between two adjacent basal planes through a tetrahedral-like configuration. As a result, mixed interstitials diffuse three-dimensionally at higher temperatures.

3.2 Interstitial helium pairs

As with many metals, helium interstitials in beryllium attract each other. FPMD calculations show two types of helium interstitial pairs: in-basal plane and out-of-basal plane (see Figure 1). The in-basal plane configuration diffuses by in-basal plane rotations and is essentially caged within a triangle. However, even at 800 K, out-of-basal plane rotations with formation of out-of-basal plane pairs are possible. In spite of the fact that the out-of-basal plane configuration has significantly higher binding energy (1.35 eV cf. 0.83 eV for in-basal plane), a reverse transformation was also observed in FPMD run at 800 K.

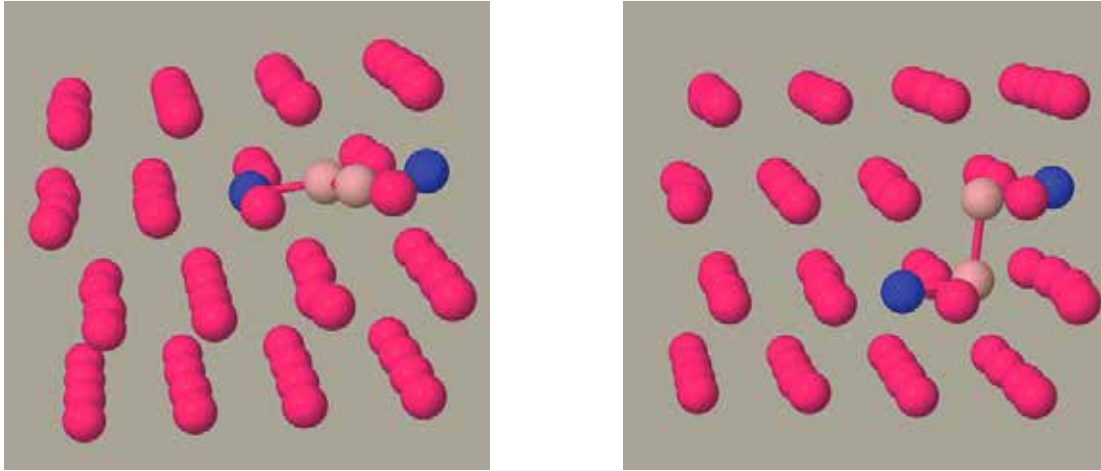


Figure 1: Pairs of interstitial helium. (a) In-basal-plane pair ($E_b=0.83$ eV), (b) out-of-basal plane pair ($E_b=1.35$ eV). Helium atoms are colored rose, while beryllium atoms constituting mixed dumbbells are colored blue.

3.3 Substitutional helium

In beryllium, as in many other metals, helium is strongly bound to vacancies. The 3 eV binding energy of helium suggests that it is almost irreversibly trapped by vacancies. However, a comparison of the energies of single interstitial helium atom and substitutional helium plus self-interstitial suggests that interstitial helium is energetically favorable and, thus, a kick-out reaction might be possible (if the activation barrier is not too high):



It should be noted that substitutional helium is immobile and requires another vacancy for diffusion (see e.g. [9]). Therefore, substitutional helium can be transported only by helium-vacancy clusters. This explains our interest in the properties of small helium-vacancy clusters, described in the next section.

3.4 Helium vacancy clusters

Previous research [1, 3] indicates that di-vacancy clusters are unstable in beryllium. DFT calculations recently predicted the same behavior for tungsten [10] and aluminum [11, 12]. In this work, we calculated the binding energies of helium atoms with di-vacancy clusters in various orientations. Helium atoms effectively stabilized di-vacancy clusters in one basal plane and in adjacent planes, but did not stabilize di-vacancy along c axes, where vacancies are separated by an additional

basal plane. The binding energy of He_1Vc_2 cluster with respect to decay into two separate vacancies and helium interstitial is about 3.0-3.7 eV depending on di-vacancy orientation. Certainly the binding energies, with respect to the decay into substitutional helium and vacancy, are significantly lower: 0.3-0.4 eV.

Two diffusion jumps of He_1Vc_2 cluster were observed in FPMD simulations at 1000 K. Diffusion of the in-basal-plane cluster appears to occur by a classical ring mechanism in the basal plane. Initial and final configurations of the jump were relaxed using static *ab initio* and the migration barrier was estimated using the drag method. The jumping atom was fixed along the direction of the jump while it was allowed to relax in two other directions. To avoid shifting of the lattice as a whole one atom, or, in some cases, two atoms far from the jumping atom, was fixed in all three directions.

The observed in-basal plane jump sequence occurs through the intermediate dissociated configuration (see Figure 2):

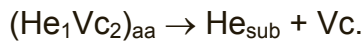


Figure 2 shows that two further in-basal plane jumps are possible. One jump (aa3) results in the dissociation of the He_1Vc_2 cluster while the other (aa2) does not require dissociation. Surprisingly, the jump without dissociation (aa2) has a higher migration barrier (1.6 eV) than those with dissociation: 0.9 eV for aa3 and 0.7 eV for aa1. The later one is the lowest energy migration path, which was observed in the ring diffusion mechanism described above.

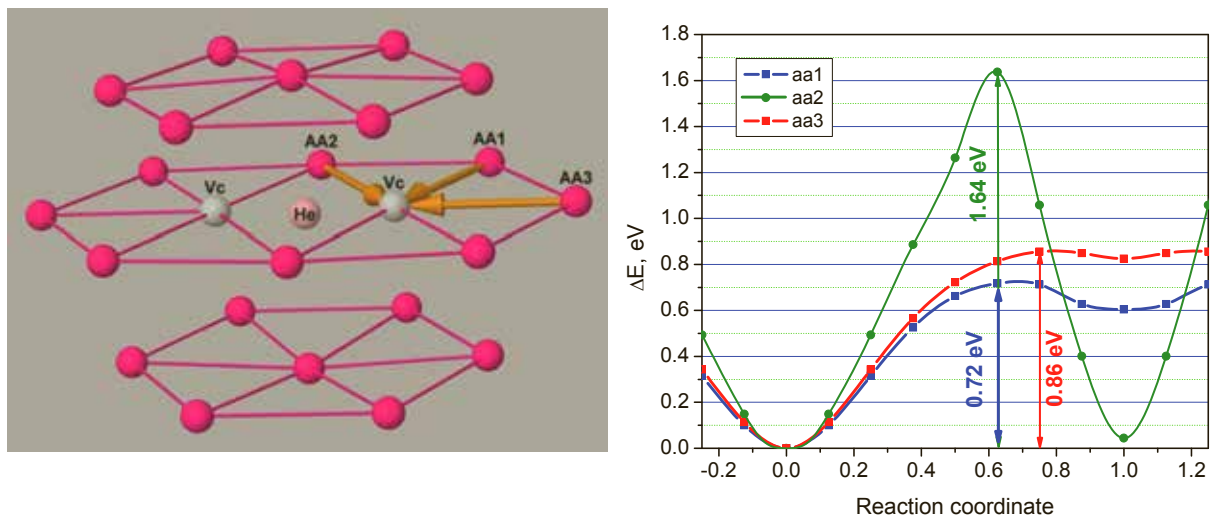


Figure 2: (a) Three possible in-basal-plane jumps of beryllium atoms (labeled as aa1, aa2 and aa3) into He_1Vc_2 complex situated in the same basal plane. In cases aa1 and aa3 dissociation of basal $(\text{He}_1\text{Vc}_2)_{\text{aa}}$ complex occurs: $(\text{He}_1\text{Vc}_2)_{\text{aa}} \rightarrow \text{He}_{\text{sub}} + \text{Vc}$. In case aa2 the $(\text{He}_1\text{Vc}_2)_{\text{aa}}$ complex changes its orientation. (b) Energy profiles corresponding to these migration pathways.

To complete the study, we calculated the diffusion barriers for three possible beryllium atom jumps from the adjacent basal plane. Two jumps occur when beryllium atoms (labeled as ac1 and ac2) jump into a vacancy (see arrows in Figure 3a). The helium atom is pushed into another vacancy, which is not the nearest neighbor of the vacancy left behind by the jumping atom. In these cases, the helium-vacancy cluster dissociates since helium cannot occupy both vacancies. In case of the third jump (ac3), the newly formed vacancy is the nearest neighbor of the helium atom. Therefore, helium takes an intermediate position between the vacancies;

however, the vacancies are now in different basal planes and helium is between these planes. The results of these calculations are presented in Figure 3b.

In the case of HeVc_2 cluster dissociation (ac1 and ac2), the migration barriers are rather high (about 1.4 and 1.2 eV, respectively). Formation energy of the non-basal cluster $(\text{He}_1\text{Vc}_2)_{\text{ac}}$ is only 0.1 eV higher than that of the basal cluster $(\text{He}_1\text{Vc}_2)_{\text{aa}}$. However, the migration barrier for the jump between these configurations is 1.4 eV.

This analysis suggests that the HeVc_2 cluster migrates preferentially in the basal plane at approximately the same rate as vacancy (0.7 eV); however, it has to overcome a double barrier (1.4 eV) to move between basal planes. On the other hand, the barrier for dissociation (ac2) is slightly lower (1.2 eV). So the HeVc_2 cluster dissociates, rather than jumps out of the basal plane.

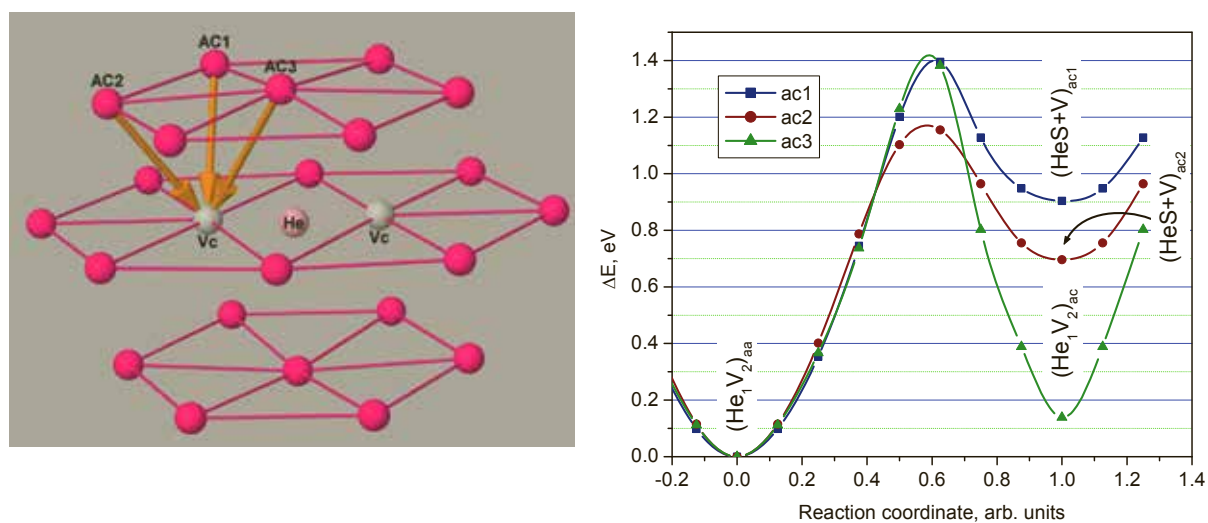


Figure 3: (a) Three possible jumps of beryllium atoms labeled as ac1, ac2, and ac3 from one basal plane into basal $(\text{He}_1\text{Vc}_2)_{\text{aa}}$ complex situated in the adjacent basal plane. In the cases ac1 and ac2, the dissociation of the $(\text{He}_1\text{Vc}_2)_{\text{aa}}$ complex occurs. In case ac3, a new $(\text{He}_1\text{Vc}_2)_{\text{ac}}$ non-basal complex forms. (b) Energy profiles corresponding to these migration pathways.

4. Conclusions

A combination of static and dynamic *ab initio* methods proved useful for the study of point defect migration pathways.

Static relaxations show that the mixed He-SIA dumbbell is the ground-state for helium at interstitial positions in beryllium. Interstitial helium is a fast diffuser: mixed dumbbells diffuse two dimensionally (within one basal plane) at low temperatures; however, they can jump between adjacent basal planes (three-dimensional diffusion) at higher temperatures. Mixed dumbbells are bound to each other in planar and non-planar configurations. These dumbbell configurations are mobile and diffuse by rotation within basal planes or by jumps between adjacent basal planes.

Substitutional helium diffuses only as a vacancy cluster. FPMD calculations showed that the He_1Vc_2 cluster migrates by a classical ring diffusion mechanism. Calculations of diffusion barriers revealed that this cluster diffuses only two dimensionally (in the basal plane) since the barrier for the jump between two adjacent basal planes is higher than the barrier for the cluster dissociation.

The anisotropy of helium diffusion for interstitial helium and helium-vacancy clusters with a preferential mobility within basal planes should have significance for further simulations of the microstructure development in neutron-irradiated beryllium.

Helium is essential for stabilization of unstable vacancy clusters. As a direct consequence, voids cannot grow in beryllium under electron irradiation, while helium bubbles can be formed under neutron irradiation due to helium produced by nuclear transmutations. Thus, it is possible to conclude that the presence of transmutation helium is necessary for the development of porous microstructure in irradiated beryllium.

Acknowledgements

We greatly appreciate the computer time granted for *ab initio* calculations in the frame of EFDA HPC-FF initiative. This work, partly supported by the European Communities under the contract of Association between EURATOM and Karlsruhe Institute of Technology, was carried out within the framework of the European Fusion Development Agreement modeling program. The views and opinions expressed herein do not necessarily reflect those of the European Commission.

References

- [1] M. Ganchenkova and V. A. Borodin, "Ab initio study of small vacancy complexes in beryllium," *Phys Rev B*, vol. 75, pp. 054108/1-5, 2007.
- [2] M. Ganchenkova, V. A. Borodin and N. R. , "Hydrogen in beryllium: Solubility, transport, and trapping," *Phys Rev B*, vol. 79, pp. 134101/1-11, 2009.
- [3] M. Ganchenkova, P. Vladimirov and V. Borodin, "Vacancies, interstitials and gas atoms in beryllium," *J Nucl Mater*, vol. 386, pp. 79-81, 2009.
- [4] A. S. Bakai, A. N. Timoshevskii, S. A. Kalkuta, P. Vladimirov and A. Moeslang, "On the influence of vacancies on the electronic properties of beryllium," *Low Temp Physics*, vol. 33, no. 10, pp. 889-891, 2007.
- [5] G. Kresse and J. Hafner, "Ab initio Molecular-Dynamics for Liquid-Metals," *Phys Rev B*, vol. 47, pp. 558-561, 1993.
- [6] J. Perdew, Y. Wang and E. Engel, "Liquid-Drop Model for Crystalline Metals - Vacancy-Formation, Cohesive, and Face-Dependent Surface Energies," *Phys Rev Lett*, vol. 66, pp. 508-511, 1991.
- [7] G. Kresse and D. Joubert, "From ultrasoft pseudopotentials to the projector augmented-wave method," *Phys Rev B*, vol. 59, p. 1758, 1999.
- [8] H. Monkhorst and J. Pack, "Special points for Brillouin-zone integrations," *Phys Rev B*, vol. 13, p. 5188, 1976.

- [9] G. Kresse, W. Bergermayer, R. Podloucky, E. Lundgren, R. Koller, M. Schmid and P. Varga, "Complex surface reconstructions solved by ab initio molecular dynamics," *Appl Phys A-Mater*, vol. 76, pp. 701-710, 2003.
- [10] A. S. Bakai, A. N. Timoshevskii and B. Z. Yanchitsky, "On chemical bonding and helium distribution in hcp beryllium," *Low Temp Phys*, vol. 37, no. 9-10, pp. 791-797, 2011.
- [11] O. S. Bakaj, A. M. Timoshevsky and B. Z. Yan-Cytsky, "On Inertness of Helium in Beryllium," *Metallofizika I Noveishie Tekhnologii*, vol. 31, no. 6, pp. 735-739, 2009.
- [12] P. Zhang, J. Zhao and B. Wen, "Retention and diffusion of H, He, O, C impurities in Be," *J Nucl Mater*, vol. 423, no. 1-3, pp. 164-169, 2012.
- [13] V. Borodin and P. Vladimirov, "Kinetic properties of small He-vacancy clusters in iron," *J Nucl Mater*, Vols. 386-388, pp. 106-108, 2009.
- [14] C. Becquart and C. Domain, "Ab initio calculations about intrinsic point defects and He in W," *Nucl Instrum Meth B*, vol. 255, pp. 23-26, 2007.
- [15] K. Carling, G. Wahnstrom, T. Mattsson, A. Mattsson, N. Sandberg and G. Grimvall, "Vacancies in metals: From first-principles calculations to experimental data," *Phys Rev Lett*, vol. 85, pp. 3862-3865, 2000.
- [16] L. Yang, X. Zu and F. Gao, "Ab initio study of formation, migration and binding properties of helium-vacancy clusters in aluminum," *Physica B*, vol. 403, pp. 2719-2724, 2008.

Appendix 1: Organisation



10th IEA International Workshop on Beryllium Technology

September 19-21, 2012

Karlsruhe Institute of Technology,
Karlsruhe, Germany

Previously, the focus of the workshop has been on beryllium technology in fusion engineering development. Since 2005, the scope is expanded to include fission applications of beryllium as well.

The objective of this workshop is to disseminate results of research and technology development in areas relevant to beryllium utilization in nuclear power systems, both fission and fusion. Papers presenting original research in these topical areas are solicited for presentation and publication.

The BeYOND-IV Workshop “Beryllium Opportunities for New Development” will be held in connection with the BeWS-10. BeYOND is working as a communication platform for researchers and industry with the aim to bring ITER to life and to prepare a “fast track” for DEMO.

INTERNATIONAL ORGANIZING COMMITTEE

<i>Anton Möslang (Chair)</i>	<i>Karlsruhe Institute of Technology, Germany</i>
<i>Christopher Dorn</i>	<i>Materion Brush Inc., Brush Beryllium & Composites, U.S.A.</i>
<i>Victor Pansyrny</i>	<i>A. A. Bochvar Institute, Russia</i>
<i>Masaru Nakamichi</i>	<i>Japan Atomic Energy Agency, Japan</i>
<i>Irina Tazhibayeva</i>	<i>Institute of Atomic Energy of National Nuclear Center, Kazakhstan</i>

PROGRAM AND LOCAL ORGANIZING COMMITTEE

<i>Pavel Vladimirov (Chair)</i>	<i>Karlsruhe Institute of Technology, Germany</i>
<i>Aniceto Goraieb</i>	<i>Karlsruhe Beryllium Handling Facility GmbH</i>
<i>Vladimir Chakin</i>	<i>Karlsruhe Institute of Technology, Germany</i>
<i>Peter Kurinskiy</i>	<i>Karlsruhe Institute of Technology, Germany</i>

Appendix 2

WORKSHOP PROGRAM

Wednesday, September 19					
		8:30	–	9:00	Registration
		9:00	–	9:15	Welcome A. Moeslang
Plenary Session					
Chair: G. Longhurst					
V. Barabash	ITER, EU	09:15	–	09:45	Materials for the ITER Blanket First Wall
M. Nakamichi	Japan	09:45	–	10:15	Beryllide R&D as Advanced Neutron Multiplier for DEMO Reactors in Japan
L. Ryczek	Materion, USA	10:15	–	10:45	Materion: Be supply status
Break (25 min)		10:45	–	11:05	
Chair: A. Möslang					
I. Kupriyanov	Russia	11:05	–	11:35	Review of beryllium activities in Russia
M. Zmitko	F4E, EU	11:35	–	12:05	Development and qualification of beryllium materials for the EU TBM
Technical Session 1: HIDOBE-01 PIE					
Chair: M. Zmitko					
L. Magielsen	NRG	12:05	–	12:35	NRG contribution to the HIDOBE01 PIE
Lunch		12:35	–	14:00	
V. Chakin	KIT	14:00	–	14:25	Current status and results of HIDOBE-01 PIE at KIT
E. Alves	ITN	14:25	–	14:50	Chemical reactivity of irradiated be pebbles under oxidizing atmosphere
A. Fedorov	NRG	14:50	–	15:15	Analysis of tritium retention in beryllium pebbles irradiated in EXOTIC, PBA and HIDOBE-01 experiments
S. van Til	NRG	15:15	–	15:40	Preliminary results from HIDOBE01 PIE on Russian pellet grades
Break (25 min)		15:40	–	16:05	
Technical Session 2: Irradiation behavior & waste management					
Chair: A. Fedorov & T. Shibayama					
T. Kulsartov	IAE NNC RK	16:05	–	16:30	Thermo-desorption study of irradiated beryllium of various grades
E. Pajuste	ICP Uni. of Latvia	16:30	–	16:55	Tritium behavior in neutron irradiated beryllium pebbles regarding their microstructure
C. Dorn	Materion	16:55	–	17:20	Investigation for lifetime expansion of Be reflector
	Bus to hotel	17:30			
IOC Meeting		19:30			Gastdozentenhaus, Karlsruhe

Thursday, September 20

Technical Session 2 (cont'd): Irradiation behavior & waste management

Chair: V. Chakin

I. Kupriyanov	Bochvar Institute	9:00	–	9:25	Experimental simulation of beryllium damage under intense transient plasma loads
A. Posevin	RIAR	9:25	–	9:50	Beryllium decontamination from radioactive impurities by hydroxide precipitation

Technical Session 3: Beryllides

Chair: E. Alves & M. Nakamichi

M. Nakamichi	JAEA	9:50	–	10:15	Development of granulation process of beryllide as advanced neutron multiplier for demo reactors in Japan
Y. Natori	Kaken Inc.	10:15	–	10:40	Synthesis of beryllides powder for advanced neutron multiplier

Break (20 min)

T. Shibayama	JAEA	11:00	–	11:25	Recent progress of irradiation effects study on Be ₁₂ Ti by plasma sintering method
P. Kurinskiy	KIT	11:25	–	12:50	Characteristics of microstructure, swelling and mechanical behavior of titanium beryllide samples after high-dose neutron irradiation at 740 and 873 K
D. Wakai (J.-H. Kim)	JAEA	12:50	–	12:15	Optimization of sintering conditions in plasma sintered beryllide
K. Munakata	Akita Uni.	12:15	–	12:40	Study on oxidation resistance of titanium beryllide fabricated by spark plasma sintering and surface analysis of the sample exposed to water vapor

Lunch

K. Wada	Akita Uni.	14:00	–	14:25	Oxidation behavior of beryllium and titanium beryllide fabricated by plasma-sintering method direct comparison of oxidation behavior by water vapor
J.-H. Kim	JAEA	14:25	–	14:50	Oxidation property of plasma sintered beryllide
J. Reimann	KIT	14:50	–	15:15	First measurements of beryllide vapor pressures

Break (15 min)

Technical Session 4: Casting, molding of Be and Be-alloys/ use of BeO in fuel technology

Chair: C. Dorn

G. Schuster	Materion	15:35	–	16:00	Investment casting of Be alloys
C. Kräher	GVT	16:00	–	16:25	Design of a molding process of beryllium and beryllides: from a suspension of metal powder and liquid paraffin to semi-finished parts
Z. Sattinova	Kazakh-British Tech. Uni.	16:25	–	16:50	Numerical research of ceramics formation process by the hot molding method
J. Malone	IBC Advanced Alloys	16:50	–	17:15	Enhancement of the Thermal Conductivity of Uranium Oxide by Fine-Grained Beryllium Oxide for Fission Applications

Bus KIT CN-hotel 17:20

Bus KIT CN- Restaurant 18:15

Bus hotel - Restaurant 18:30

Workshop Banquet 19:30 Restaurant Buschmühle

Friday, September 21

Technical Session 5 (Parallel): Safety & Technology

Chair: D. Radloff

P. Humrickhouse	INL	09:00	–	09:25	Beryllium dust explosion experiments
L. Ryzcek,	Materion	09:25	–	09:50	New Beryllium Materials
G. Schuster	Materion	09:50	–	10:15	Anodized coatings for Be and Be-Al alloys
H. Schween	HIMA	10:15	–	10:30	Management systems in safety engineering

Technical Session 5 (Parallel): Modeling of irradiation defects in hcp metals

Chair: P. Vladimirov.

S. Golubov	ORNL	09:00	–	09:25	Radiation damage in hcp materials: Exp. & Theory
V. Borodin	KIAE	09:25	–	09:50	Self-interstitial diffusion in beryllium
M. Ganchenkova	MEPhI	09:50	–	10:15	Columnar interstitial clusters in beryllium and zirconium
P. Vladimirov	KIT	10:15	–	10:30	Role of He in swelling of neutron irradiated beryllium

Break (15 min) 10:30 – 10:45

BeYOND Industrial Forum IV

A. Goraieb	KBHF	10:45	–	11:00	Welcome
S. Philipp	HIMA	11:00	–	11:20	Safety nonstop
K. Furmanns	KIT / IFL	11:20	–	11:40	Cooperation in the safety area
Signing MoU with HIMA		11:40	–	12:00	

LAB-LUNCH at KBHF 12:20 – open end

14:30 – 15:00 **Guided laboratory tours**

Round Table for discussion

Appendix 3: Participants

Name	Organization	Country
Eduardo Alves	ITN/IST	Portugal
Vladimir Barabash	ITER	France
Tobias Baur	KIT	Germany
Mümin Beyoglu	GVT	Germany
Vladimir Borodin	NRC Kurchatov Institute	Russia
Robert Buckingham	General Atomics	USA
Vladimir Chakin	KIT	Germany
Alexey Chuvilin	Ulba	Kazakhstan
Christopher Dorn	Materion Brush Inc.	U.S.A.
Anthony Dutton	IBC Advanced Alloys Corp.	Canada
Mario Epp	HIMA	Germany
Alexander Fedorov	NRG	The Netherlands
Roland Fritz	KIT	Germany
Kai Furmans	KIT	Germany
Mark Gallile	CERN	Switzerland
Cedric Garion	CERN	Switzerland
Christoph Gebert	GVT	Germany
Radmir Giniyatulin	Efremov Institute	Russia
Leonid Gitarskiy	Saulovisc	Russia
Elena Golenkova-Zakharova	IBC Advanced Alloys Corp.	France
Stas Golubov	ORNL	USA
Aniceto Goraieb	KBHF GmbH	Germany
Paul Humrickhouse	Idaho National Laboratory	USA
Michael Källberg	SCK•CEN	Belgium
Jae-Hwan Kim	Japan Atomic Energy Agency	Japan
Regina Knitter	KIT	Germany
Zoltan Köllö	KIT	Germany
Christian Kräher	GVT	Germany
Igor Kupriyanov	A.A. Bochvar Research Institute	Russia
Petr Kurinskiy	KIT	Germany
Markus Lemmens	Lemmens Medien	Germany
Glen Longhurst		USA
Peter Mählmann	TROPAG	Germany
James Malone	IBC Advanced Alloys Corp.	Canada
Kenzo MUNAKATA	Akita University	Japan
Patricia Murphy	Materion Brush Inc.	UK
Masaru Nakamichi	Japan Atomic Energy Agency	Japan
Yuri Natori	Kaken Inc,	Japan
Simon Niemes	KIT ITEP TLK	Germany
Elina Pajuste	University of Latvia	Latvia
Marie-Joëlle PORET	ACAL BFI FRANCE	FRANCE
Florian Priester	KIT	Germany
Joerg Reimann	KIT	Germany
Marco Roellig	KIT	Germany
Doris Roth	GVT	Germany
Lawrence Ryczek	Materion Brush Inc.	USA
Fabian Schneck	KIT	Germany
Wolfram Schüssler	AVEDAS	Germany
Gary Schuster	Materion Brush Inc.	USA
Heiko Schween	HIMA	Germany

Zázilia	Seibold	KIT	Germany
Victor	Sizenev	Semenovish	Russia
Keith	Smith	Materion Brush Inc.	USA
Judith	Stoll	KIT	Germany
Thomas	Stoll	KIT	Germany
Andreas	Trenkle	KIT	Germany
Pavel	Vladimirov	KIT	Germany
Michael	Voss	TROPAG	Germany
Kohei	Wada	Akita University	Japan
Daisuke	Wakai	Japan Atomic Energy Agency	Japan
Marcel	Wéber	SCK•CEN	Belgium
Kazuo	Yonehara	Japan Atomic Energy Agency	Japan
Wolfgang	Zeder	MATERION	Germany
Milan	ZMITKO	Fusion for Energy (F4E)	Spain

